Petrogenesis of a variscan migmatite complex (NW Portugal): petrography, geochemistry and fluids

Maria Areias da Silva

Programa Doutoral em Geociências
Especialização em Petrologia e Geoquímica

Departamento de Geociências, Ambiente e Ordenamento do Território

2014

Orientadora
Maria dos Anjos Ribeiro, Professora Associada, Faculdade de Ciências UP

Coorientadora
Armanda Dória, Professora Auxiliar, Faculdade de Ciências da UP

Dedicated to all the geologists whose work I relied to make this thesis. Thank you!

Author's Acknowledgements

All my teachers were very important to my training as a geologist. Since the beginning of the degree I realized that the Department of Geology at the University of Porto (now DGAOT) has a group of professionals characterized by their commitment to support the students in their learning process. I still think that I was lucky to study with this group of people. Thank you all for your support and sympathy.

During the last four years I was fortunate to work with two persons that illustrate the quality of professionals in this department: Maria dos Anjos Ribeiro and Armanda Dória. Thanks for the constructive criticism. Thank you for the encouragement, the clarity of the guidelines and relevant information. Thank you for the welcoming environment for the discussion of ideas. Thank you for being interested in the research I am conducting. Thank you for the honest, direct, and wise behaviour model.

Very special thanks to José Francisco Santos and Sara Ribeiro from University of Aveiro for the unconditional support and help in carrying out the isotopic analyses and in its interpretation.

Thanks to colleagues who oiled with their sympathy and patience my working days.

Infinite thanks to my family and friends who supported me in difficult times.

Abstract

Mindelo Migmatitic Complex (MMC) outcrops in the coastal zone north of Porto (Portugal) and consists of a set of migmatitic and granitic lithologies.

All migmatites represent the sum of a series of processes occurring in parallel, or sequentially, under the influence of various factors and generally show lithological heterogeneity. In MMC was recognized the presence of metagreywackes and calc-silicate rocks that remain as resisters, patch-metatexites, banded-metatexites, diatexites, leucogranites, two-mica granites and aplite-pegmatites.

Field relationships, accurate petrographic observations, geochemistry, Sm-Nd and Rb-Sr isotopic signature and SHRIMP zircon analyses allowed making a comprehensive characterization of various aspects of the rocks cropping out in this area and their relationship with the metasedimentary rocks in its surroundings.

The dominant process for generating the MMC migmatites was partial melting, being the Injection a minor contributor.

The data obtained by the diverse analytical methods suggest that the Schist-Greywacke Complex (SGC) metasediments cropping out in the neighbouring of MMC were the protolith that originated the migmatitic lithologies. Moreover, a co-genetic relationship between the different lithologies of MMC was inferred. The chemical and mineralogical dissimilarity between them result from their derivation from different crustal levels and different melting rates rather than of a marked difference in the protolith lithologies.

A metamorphic gradient was observed from the coastal zone to the interior showing a gradual transition from the sillimanite-K-feldspar zone to sillimanite, staurolite-, biotite- and chlorite-zone. The metamorphic sequence, the mineralogical associations and the geometric relations Si/Se suggest that the process in the origin of the metamorphic gradient has a regional character, reached moderate pressure and temperature conditions and is related with the first Variscan deformation phase. During the last Variscan deformation phase (D3) an increase in temperature and decompression occurred, conditioned by the installation of the two-mica syn-tectonic granites. A first metamorphic event (M1), attaining condition of $P > 490$ MPa and $560 < T > 600$ ºC, reflects the burial and heating. This metamorphic event was followed by decompression and temperature increase leading to andalusite and cordierite

development during a later metamorphic event (M2). The migmatization and anatexis are the result of the last metamorphic event.

The melting has occurred in several structural levels and thus at different pressure and temperature conditions, resulting in rocks with specific characteristics: i) in shallow levels (<350 MPa) migmatites are formed essentially by fluid-present partial melting followed by fluid-absent incongruent biotite melting producing peritectic cordierite, quartz, plagioclase and minor amounts of K-feldspar. The *melt* segregation led to its crystallization in dilatant sites forming massive bodies and veins of leucogranite.; ii) in slightly deeper levels the melting rate is higher, which leads to the formation of diatexites that intruded metatexites; (iii) at deeper levels higher pressure permits the occurrence of muscovite and biotite melting reactions that produced a large amount of typical two-mica granite melts. This material rises in the crust and incorporates abundant xenoliths forming a very heterogeneous granitic body.

It is suggested that multiple fluid pulses affected the MMC in subsolidus conditions: a first pulse with K-bearing fluids, a second pulse with boron-bearing fluids and a third pulse containing silica-bearing aqueous-fluids.

The K-bearing fluids affected all the MMC lithologies and caused structurally controlled sub-solidus K-metasomatism, revealed by: i) the filling of miarolitic cavities and micro-fracturing; ii) alteration processes in the metagreywacke and calc-silicate nodules; iii) replacement of plagioclase crystals in leucosomes, leucogranites and two-mica granites; iv) wide variation in the K content, especially in leucosomes and leucogranites (unrelated to the silica content), and the inverse correlation between the K and the Na_2O+CaO content in this lithologies.

The existence of leucogranites and two-mica granites showing localized replacement of biotite by tourmaline and symplectitic intergrowth of tourmaline + quartz + K-feldspar, the occurrence of tourmalinites associated with fractures and the character post-kinematic of tourmaline in the SGC metasediments, as well as the occurrence of aplite-pegmatite veins showing abundant tourmaline suggest that latte boron-rich fluids also affected the MMC and surrounding metasedimentary sequence.

The entrainment of later silicate aqueous fluids is inferred from: i) the muscovitization of tourmaline, biotite and plagioclase all over the MMC; ii) presence of quartz-veins cutting all the lithologies; iii) large quartz-crystals bands in some calc-silicate nodules that include the mineral paragenesis of the fresh rock; iv) retrograde alteration of staurolite, garnet, andalusite and biotite in the metasedimentary sequence.

The several pulses of different fluids that affected the MMC are probably related to the installation of the variscan syn and late- D3 tectonic granites since their influence is more intense in the neighbouring of the granitic bodies and the isotopic signature of the aplite-pegmatites coincide with the isotopic signatures of the Central Iberian Zone syn-tectonic granites studied by Beetsma (1995).

U-Pb SHRIMP analytical procedure was performed in zircons from a diatexite sample. Zircons show an inhered core and an overgrowth rim. The ages measured in the inhered cores are mostly Ediacaran (75%), showing a concentration peak around 590 Ma. The overgrowth rims show Variscan ages (Carboniferous) between 319 ±11 and 309 ±3 Ma and are suggested to reflect the age of the anatectic process. The Ediacaran age to the protolith and the Carboniferous ages for the anatectic process are also confirmed by Rb-Sr system results.

The Mindelo Migmatite Complex represents an example of migmatites formed in low pressure conditions and illustrates some of the reactions involving melting in high grade pelitic rocks and subsequent mineral alterations due to infiltration of late different fluids.

Key-words: LP-HT migmatites, anatexis processes, fluids, metamorphic gradient.

Resumo

O Complexo Migmatítico do Mindelo (CMM) aflora na área costeira a norte do Porto (Portugal) e é composto por um conjunto de litologias migmatíticas e graníticas.

Todos os migmatitos representam a soma de uma serie de processos que ocorrem em paralelo ou sequencialmente, sob a influência de vários factores e geralmente apresentando heterogeneidade litológica. No CMM foi reconhecida a presença de metagrauvaques e rochas calcossilicatadas que permanecem como *resisters,* metatexitos "mosqueados", metatexitos bandados, diatexitos, leucogranitos, granitos de duas micas e aplitopegmatitos.

As relações de campo, petrografia, geoquímica, assinatura isotópica de Sm-Nd e Rb-Sr e a análise de zircões pelo método de SHRIMP permitiram uma caracterização abrangente das rochas aflorantes nesta área e da sua relação com os metassedimentos do Complexo Xisto-grauváquico aflorantes na sua proximidade.

O processo dominante para a geração dos migmatitos foi a fusão parcial e anatexia, tendo o processo de injecção uma contribuição menor.

Sugere-se que os metassedimentos do Complexo Xisto-grauváquico (CXG) são o protólito que originou as litologias do MMC tendo como base as relações de campo, a similitude litológica, composição química e assinatura isotópica idênticas e idade de zircões coincidente. Foi também estabelecida uma relação cogenética entre as litologias graníticas e migmatíticas aflorantes no MMC. A heterogeneidade litológica parece ter resultado essencialmente da ocorrência de processos anatéticos em diferentes níveis estruturais e com diferentes taxas de fusão.

Foi assinalado um gradiente metamórfico desde a zona costeira para o interior (para Este) que apresenta transição gradual desde a zona da sillimanite-feldspato-potássico, silimanite, estaurolite, biotite e, finalmente, zona da clorite. A sequência metamórfica, as associações minerais e as relações geométricas sugerem que o processo que gerou as zonas metamórficas tem um caracter regional, atingindo pressões e temperaturas moderadas relacionadas com a primeira fase de deformação Varisca. Durante a terceira fase de deformação Varisca ocorre aumento de temperatura e descompressão, condicionadas pela instalação dos granitos de duas micas sin-tectónicos. O primeiro evento metamórfico terá atingido condições de P > 490 MPa e T ~580 ºC. Após este primeiro evento ocorre um segundo evento, em condições de

baixa pressão (< 350 MPa) e alta temperatura. A migmatização e anatexia seriam resultantes deste último evento metamórfico.

A fusão ocorreu em vários níveis estruturais e, por isso, sob diferentes condições de temperatura e pressão, resultando em rochas com características específicas: i) em níveis superficiais (< 350 MPa) ocorre fusão parcial em regime hidratado, originando principalmente leucossomas trondhjemíticos, seguida por fusão incongruente de biotite com produção de cordierite peritética, quartzo, plagioclase e quantidades menores de feldspato potássico - os leucogranitos e os veios de leucogranito são o resultado da migração de leucossomas trondjemiticos; ii) a níveis ligeiramente mais profundos, a taxa de fusão é superior levando à formação de diatexitos que intruem os metatexitos; iii) em níveis mais profundos ocorrem reações de fusão de moscovite e biotite que produzem grandes quantidades de fundido representativo de granito de duas micas. Este material eleva-se na crusta e incorpora abundantes xenólitos formando um corpo granítico muito heterogéneo.

Em condições subsolidus, vários tipos de fluidos afectaram as rochas do CMM: um primeiro pulso de percolação de fluidos ricos em potássio, um segundo pulso contendo fluidos ricos em boro e, por último, fluidos silicatados.

Os fluidos ricos em potássio afetam todas as litologias do Complexo Migmatítico de Mindelo provocando metassomatismo potássico estruturalmente controlado com feldspatização da plagioclase, preenchimento de cavidades miarolíticas e desenvolvimento de megacristais de feldspato em alinhamentos bem definidos. Posteriormente, fluidos ricos em boro levam à turmalinização parcial de leucogranitos, granitos de duas micas e da sequência metassedimentar, à ocorrência de turmalinitos em zonas de falha, assim como à instalação de aplitopegmatitos com turmalina que cortam todas as outras litologias. O mais recente influxo de fluidos aquosos levou à muscovitização da turmalina, biotite, plagioclase, andaluzite, cordierite e estaurolite.

Os vários pulsos de percolação de fluidos podem estar relacionados com a instalação dos granitos sin a tardi-tectónicos, uma vez que a sua influência é mais intensa junto aos corpos graníticos e a assinatura isotópica dos aplitopegmatitos coincide com a assinatura isotópica dos granitos sin-tectónicos da ZCI estudados por Beetsma (1995).

Foram realizadas análise de zircões de uma amostra de diatexito por SHRIMP e obtidas idades com base no método U-Pb. Os zircões apresentam um núcleo herdado e um bordo sobrecrescido. As idades medidas para o núcleo são principalmente Ediacáricas (75%) com um pico de concentração próximo dos 590 Ma. Os bordos

sobrecrescido apresentam idades Carboníferas (Variscas) entre os 319 ±11 e os 309 ±3 e considera-se que representam a idade do processo anatético. A idade Ediacárica para o protólito e a idade Carbonífera para o processo anatético são confirmadas pelos resultados do sistema Rb-Sr.

O Complexo Migmatítico do Mindelo representa um exemplo de migmatitos originados sob baixa pressão. Migmatitos em vários estágios de evolução afloram nesta área, o que permitiu inferir a evolução destas rochas durante o processo anatético e as alterações mineralógicas posteriores, devido à infiltração de vários tipos de fluidos.

Palavras-chave: Migmatitos BP-AT, processos anatéticos, fluidos, gradiente metamórfico.

Table of Contents

The **table of figures** is located in **Appendix F** due to take excessive volume.

Abbreviations:

CIZ – Central Iberian Zone

DBSZ – Douro Beiras Shear Zone

IM – Iberian Massif

MMC – Mindelo Migmatite Complex

SGC – Schist-Greywacke Complex

Mineral abbreviations accordingly Recommendations by the IUGS Subcommission on the Systematics of Metamorphic Rocks: Web version 01.02.07

CHAPTER I – INTRODUCTION

"I think that there is only one way to science – or to philosophy, for that matter: to meet a problem, to see its beauty and fall in love with it; to get married to it, and to live with it happily, till death do you part - unless you should meet another and even more fascinating problem, or unless, indeed, you should obtain a solution. But even if you obtain a solution, you may then discover, to your delight, the existence of a whole family of enchanting though perhaps difficult problem children for whose welfare you may work, with a purpose, to the end of your days."

Karl Popper

1.1. Objectives

In 2008 the 8th meeting of the Structural Geology Group took place. One of the field-trips, monitored by M. A. Ribeiro, was on the costal line north of Porto. Recently graduated, I was fascinated to discover "so close to home" a type of rock on which I had just heard about: "migmatites".

After examining the previous studies on the area, only general descriptions about these lithologies in papers published back in the 60s were found, as well as a didactic approach realized by Lopes (2008) and Ferreira (2011). Thus, it was concluded that this migmatitic massif and surroundings require further investigation. That was the task we intent on the realization of this PhD thesis.

As is characteristic of migmatite areas, in Mindelo Migmatite Complex (MMC) distinct lithologies crop out, both of sedimentary and magmatic origin, namely: metagreywackes, patch-metatexites, banded-metatexites, diatexites, leucogranites, two-mica granites and aplite-pegmatites (and later lamprophyres that will not be studied in this thesis).

This work seeks to answer some questions about the conditions governing the genesis of these rocks, specifically:

1 – Did partial melting produce the migmatites?

In fact there are processes other than partial melting that can produce rocks resemble migmatites, showing light-colored patches, layers and veins in a dark host, namely sub-solidus segregation and injection of vein of felsic magma into a host of another composition. To answer this question it is necessary to find evidences of partial melting. That can be provided by accurate petrographic studies since there are several microestrutural criteria that can be used to infer the former presence of melt.

2 – What is the relationship between the surrounding lower-metamorphic grade metasediments and migmatites?

In intimate relationship with the migmatites there are several granitic massifs and metasedimentary sequences. The metasedimentary sequence adjacent to the Mindelo Migmatite Complex has been associated with the Schist-Greywacke Complex (Douro-Beiras Super Group) (*e.g.* Teixeira *et al.* 1965; Pereira *et al*., 1992). More recently, it was assigned more specifically to the Beiras-Group (Oliveira *et. al.,* 1992). In an attempt to understand the relationship between migmatites and surrounding rocks the study was distributed into two distinct sectors:

- Sector 1, covers the coastal area, from Póvoa do Varzim to Leça da Palmeira, where crop out the migmatitic lithologies and the spatially associated granites.
- Sector 2, includes an area parallel to the Sector 1, from Aguçadoura to Fânzeres, where crops out the Douro-Beiras Super Group. This metasedimentary sequence will be called “Schist-Greywacke Complex (SGC)” from now on, in accordance with the classic denomination (Carrington, 1950).

3 - What is the metamorphic zoning and field gradient in the area?

The field relations, structure and metamorphic gradient of the two Sectors was studied in an attempt to understand the spatial and temporal relationship between deformation and metamorphic blastesis and pressure / temperature conditions that controlled the metamorphism and migmatization.

4 - What was the protolith of these migmatites?

The metasediments cropping out in the vicinity of migmatites may or may not be the protolith that give rise to the migmatitic lithologies. To respond to this question, field relations, geochemistry and isotopic chemistry (Rb/Sr, Sm/Nd and U/Pb) studies were conducted in an attempt to understand if the chemical and isotopic characteristics of metasediments and metatexites are coincident or whether, conversely, are distinct.

5 - Is there a relationship between the migmatites and the granitic rocks surrounding them?

The granitic massifs that outcrop within and surrounding the migmatites were considered syn-tectonic relatively to the third variscan deformation phase and assigned to two-mica granite series in several studies (e.g. Ferreira *et al*., 1987; Pereira, *et. al*.; 1992; Almeida *et al*., 2001,2014). Field work, petrographic, geochemical and isotopic studies were made trying to find if there is a cogenetic relationship between the migmatites and these granitic rocks. That is, we try to know whether the granites derive from the same type of protolith in the same anatectic process, or if the anatectic process that gave rise to the two-mica granites is different.

6 - What was the cause of the lithological diversity and heterogeneity in the MMC?

We try to understand if the lithological diversity in the MMC is related to different anatectic events or to a single anatectic process that develops at different structural levels and consequently at different pressure and temperature conditions, resulting in rocks with specific characteristics.

7 – What types of fluids were present during the anatectic process?

Petrographic examination of fluid inclusion assemblages, microthermometric measurements and Raman spectroscopy of some samples were used to provide information about the thermal and chemical evolution of the fluids present during mineral crystallization.

8 – Is it possible to date the anatexis event?

U-Pb SHRIMP zircon dating was performed in a diatexite sample. Given the constraint of time and money that limited the dating to only one sample, it was considered that the diatexites would be the most appropriate type of lithology to provide information about the age of the geological processes that gave rise to the MMC. Diatexites show relatively high quantity of zircon and underwent a rate of partial fusion more elevated than migmatites. Leucosomes show very low zircon quantity, most of them associated with restitic biotite.

A diverse methodological approach was taken in addressing these questions: field relations were used to elucidate migmatite and surroundings organization and structure; detailed petrography and mineral chemistry were used to determine which minerals co-existed at peak metamorphism; whole-rock chemistry was used to geochemically characterize the various lithologies and establish the possible relationships between them; Rb-Sr, Sm-Nd and U-Pb isotopic studies were used to constrain age and protoliths; thermobarometric calculations were used to establish a pressure temperature framework for metamorphism; and, lastly, fluid inclusion studies helped to recognize the fluid history of the area.

1.2. Migmatites and anatexis concepts

The debate about what the migmatites represent and the processes involved in its formation was directly related to the prevailing concepts about the regional high-grade metamorphism.

Hutton (1795) believed that partial melting changed the pelitic sediments and crystalline schists in gneisses. Lyell (1855) was a step forward and held that the granites are formed where the partial melting process was stronger and more complete. However, the migmatite terminology has evolved only later, when Sederholm (1907) introduced the word *anatexis*, meaning melting or re-melting rocks, to describe all cases in which the melting was not complete. Also introduced the term *migmatite* to describe the rocks with "mixture of two genetically different constituents, being an intrusive for other ...". Mehnert (1968) made intense work in migmatites from Finland

that defined as "... a rock that consists of two or more megascopic different parts, one of which is usually in the stage more or less metamorphosed and the other showing pegmatitic, aplitic, granite or generally plutonic appearance". Ashworth (1985) refined the concept of migmatite as "a metamorphic rock located in areas of medium to high grade metamorphism, that is heterogeneous on a macroscopic scale …". Sawyer, (2008) considers that "one of these migmatite parts must have been formed by partial melting of rocks and the other must be the restitic component".

Currently it is recognized that the anatectic processes, the transport of melts and the accumulation of magmas are fundamental mechanisms by which the crust differentiates and heat and mass are redistributed in orogens (Brown, 1994; Sawyer, 1996, 2001; Brown & Solar, 1998; Vanderhaeghe, 2001; Teyssier & Whitney, 2002; Olsen *et al*., 2004; Teyssier, *et al*., 2005; Brown, 2007, 2008, 2013). Exhumed orogens commonly expose migmatite cored gneiss domes that represent former partially molten crust (Whitney *et al*., 2004). Orogenic crust differentiates through partial melting, melt segregation and extraction, melt transport, and emplacement of melt as granite into upper crustal levels.

The record of transfer of melt from segregation to emplacement is commonly preserved in migmatite terrains and migmatite-cored gneiss domes as a remnant permeability network, represented by interconnected leucosomes and granite dikes and veins (Brown, 2008; Weinberg & Mark, 2008).

The studies of migmatites are of crucial importance in the understanding of the genesis of the large volume of granitic magma. The migmatites are considered to represent the paragenesis of these magmas at the time of his generation. Thus, migmatites provide a unique perspective of a fundamental process of evolution of the earth (Sawyer, 2008a).

The migmatites are some of the most complex and aesthetically interesting rocks showing a variety of textures and structures. The most impressive consist of light-colored quartz-feldspathic segregation on a darker host, with lighter segregation often presenting a diverse and spectacular appearance, sometimes meandering, other cutting, and other still discrete, or diffuse or bent.

All migmatites represent the sum of a series of processes occurring in parallel, or sequentially, under the influence of various factors and are mechanically heterogeneous. There are four basic parts of a migmatite, although not always occur in all migmatites: 1) partial melted fractions; 2) fractions where the melt was removed; 3) fractions where the melt accumulated, or injected, and 4) fractions which do not melted

at all. Each of these fractions has its own morphology (or structure), mineral paragenesis, composition and microstructure. Consequently, there is a terminology to describe and define each of them.

The terminology used to the lithological description will be that proposed by IUGS Subcommission on the Systematics of Metamorphic Rocks (Web version of 01.02.07), namely:

Metatexite is a variety of migmatite with discrete leucosomes and melanosomes, generally preserving the former structure;

Diatexite is a type of migmatite where the darker and the lighter parts form schlieren and nebulitic structures which merge into one another;

Leucosome is the lightest-colored parts of a migmatite;

Melanosome is the darkest parts of a migmatite, usually with prevailing dark minerals;

Paleosome is a part of a migmatite representing the parent rock;

Neosome is the newly formed parts of a migmatite. The neosome generally consists of leucosome and restite;

Restite is the remnant of a metamorphic rock from which a substantial amount of the more mobile components have been extracted without being replaced;

Resister is a rock offering greater resistance to granitization than another by virtue of its composition or its 'impenetrable' fabric**.**

CHAPTER II - GEOLOGICAL SETTING

"Knowledge of Nature is an account at bank, where each dividend is added to the principal and the interest is ever compounded; and hence it is that human progress, founded on natural knowledge, advances with ever increasing speed."

G.K. Gilbert

2.1. Regional geology

Geologically, the studied area lies within the Central Iberian Zone (CIZ), the innermost zone of the Iberian Massif, one of the most complete exposures of the European Variscan Belt. It is located in the westernmost part of the European Variscan Chain, and together with the Armorican Massif defines a major mega-structure, called Ibero-Armorican Arc (Dias e Ribeiro, 1995; Ribeiro *et al*., 2007).

In this chapter we will frame the study area in the context of the European and Peninsular geology, particularly regarding the Iberian Massif and the Central Iberian Zone.

2.1.1. Variscan Orogeny

The Early Devonian to Middle Carboniferous collision of Laurasia (Laurentia + Baltica) and Gondwana, between which smaller Precambrian continental blocks (Avalonia, Armorica, Iberia and Bohemia) were squeezed, resulted in the closure of three major ocean basins, (Rheic, Theic and Galicia-Massif Central) (*e.g*., Ribeiro et al., 1990, 2007; Matte, 1991, 2001; Debelmas and Mascle, 2002). The resulting Variscan or Hercynian orogenic chain extends from Iberia to east through Central Europe into Poland.

The Variscan cycle began in the Upper Proterozoic and early Paleozoic with episodes of continental rifting, followed by the occurrence of subduction and obduction of the oceanic crusts during the Silurian/lower-Devonian and, finally, acretionary process by convergence during the period of 390-300 Ma, with amalgamation of various

continental domains of peri- (or north-) Gondwanan origin, and the resorption of the intervening oceanic domains. After the collisional stage an extension in intra-continental context occurs between 380 and 280 Ma (Matte, 1991, 2001). The orogenic variscan events affected both the Cadomian basement, which was heterogeneously reworked and overprinted, and the Paleozoic cover (Ribeiro *et al*, 2007).

The Variscan chain is characterized by axial geotectonic zones, where the oldest terrains (Upper Proterozoic to Lower Paleozoic) crop out, as well as most of the variscan granitoids. On both sides these axial zones occur Devonian-Carbonic basins with low-grade metamorphism and absence of granitoids. This symmetry shows dual convergence structures and deformation migration to the outside of the chain over time (e.g. Matte, 1991; Debelmas and Mascle, 2002). In the SW Europe Variscides the main structure is dominated by the Iberian-Armorican Arc (Ribeiro, et al. 2007).

The studied area belongs to the **Iberian Massif**. This massif had a complex evolution that is reflected in the individualization of tectonostratigraphic zones based on stratigraphic, tectonic, magmatic and metamorphic criteria and on the occurrence of exotic terranes (ophiolites) and shear zones (e.g. Lotz, 1945; Julivert *et al*., 1972; Quesada, 1991, 1992; Martinez Catalan *et al*., 2014). The tectonostratigraphic division of the Iberian Massif has evolved over time depending on the available data and the elements considered. Currently essentially six major divisions are considered, including the Cantabrian Zone, the West Asturian–Leonese Zone, the Central Iberian Zone, the Ossa-Morena Zone; the South Portuguese Zone and the Galiza-Trás-os-Montes Zone (Fig. II.1).

There are two interpretations of the geodynamic evolution of the SW Europe Variscides (including Armoricam and Iberian massifs) that consider differently the role of Variscan and Cadomian tectonics cycles to produce the present geological materials and structures. For some authors the main geological events are Variscan (*e.g.* Matte, 1991, 2001; Simancas *et al*., 2001); for others the main Variscan geological events overprint relicts of a Cadomian (and pre-Cadomian?) cycle (*e.g.* Quesada, 1992; Eguíluz *et al*., 2000; Ribeiro *et al.,* 2007; Ugidos, 2010; Pereira *et al*., 2011, 2012).

Eguíluz *et al.* (2000) and Ribeiro, *et al*. (2007) considered that the accretion of Ossa Morena Zone (OMZ) and Central Iberian Zone (CIZ), the axial zones in the Iberian Massif, took place during the Cadomian orogeny. Pereira *et al*. (2011, 2012) and Solá *et al*. (2008) consider that the contact between CIZ and OMZ is not be pre-Early

Ordovician and consequently cannot be a Cadomian suture. These authors consider that the detrital zircon populations of the Beiras-Group greywackes (Ediacaran) point to the existence of three major episodes of zircon crystallization probably associated with long-lived Neoproterozoic magmatism located near or at the northern Gondwana margin at c. 850 to 545 Ma.

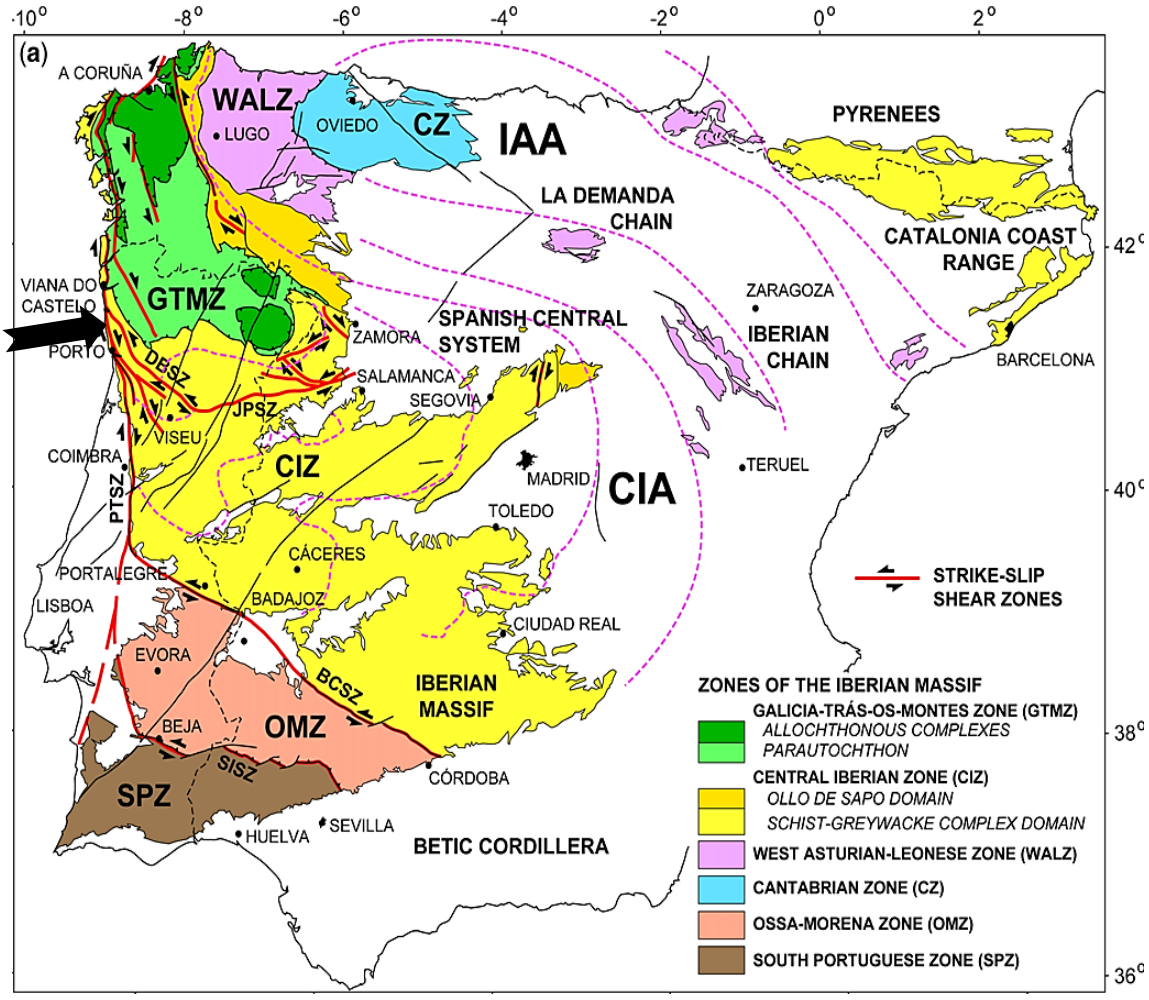

Fig.II. 1 - Outcrops of the Variscan basement in the Iberian Peninsula and subdivision of the Iberian Massif after (Martinez Catalán *et al*., 2014). Signed the location of the Mindelo Migmatite Complex (black arrow). Shear Zones: BCSZ, Badajoz-Cordoba; DBSZ,Douro-Beira; JPSZ, Juzbado-Penalva; PTSZ, Porto-Tomar; SISZ, Southern Iberian.

2.1.2. Central Iberian Zone

The lithostratigraphic sequence defined for the Central Iberian Zone (CIZ) comprises a number of units aged Neoproterozoic to Lower Devonian and Carboniferous. These units were divided in tree major domains (Fig. II.2):

- The Olho de Sapo domain is a plutono-vulcanic complex on the NE limit of CIZ characterized by the presence of Cambro-Ordovician metavolcanic and metagranitic rocks (Parga Pondal *et al*., 1964);
- The Schist-Greywacke Complex domain (Carrington da Costa, 1950) is a thick terrigenous sequence aged Neoproterozoic to Cambrian that occupies most of the CIZ and is characterized by the occurrence of a thick, monotonous succession of shales and sandstones/metagreywackes.
- Overlying this metasedimentary sequence there are several Variscan synclines/anticlines where lithologies aged from Ordovician to Devonian outcrop.

2.1.2.1. Deformation phases in Central Iberian Zone

In the Central Iberian Zone is possible to identify structures that allow distinguishing different stages of deformation, which can be integrated into two major tectonic processes: (1) extensional deformation processes coeval with sedimentation during lower Paleozoic and (2) subsequently deformation phases related to the collisional process responsible for the genesis of the Variscan Chain.

Pre-variscan deformation - Several authors recognize the existence of tectonic phases in the Neoproterozoic/Paleozoic cover, namely in Schist Greywacke Complex metasediments that although subsequent to Cadomian Orogeny, are prior to the main Variscan inversion (e. g. Sousa, 1982; Couto, 1992; Ribeiro *et al*., 1993; Ponte & Gama Pereira, 2004; Romão, 2005; Romão *et al*., 2013). The folds associated with these deformation episodes are difficult to detect, since they are obliterated by subsequent variscan deformation phases. Usually show interference structures that indicate mesoscopic folding, orientation NE-SW, with sub-vertical axial plane verging SE without associated cleavage (Ponte & Gama Pereira, 2004; Romão, *et al*., 2013).

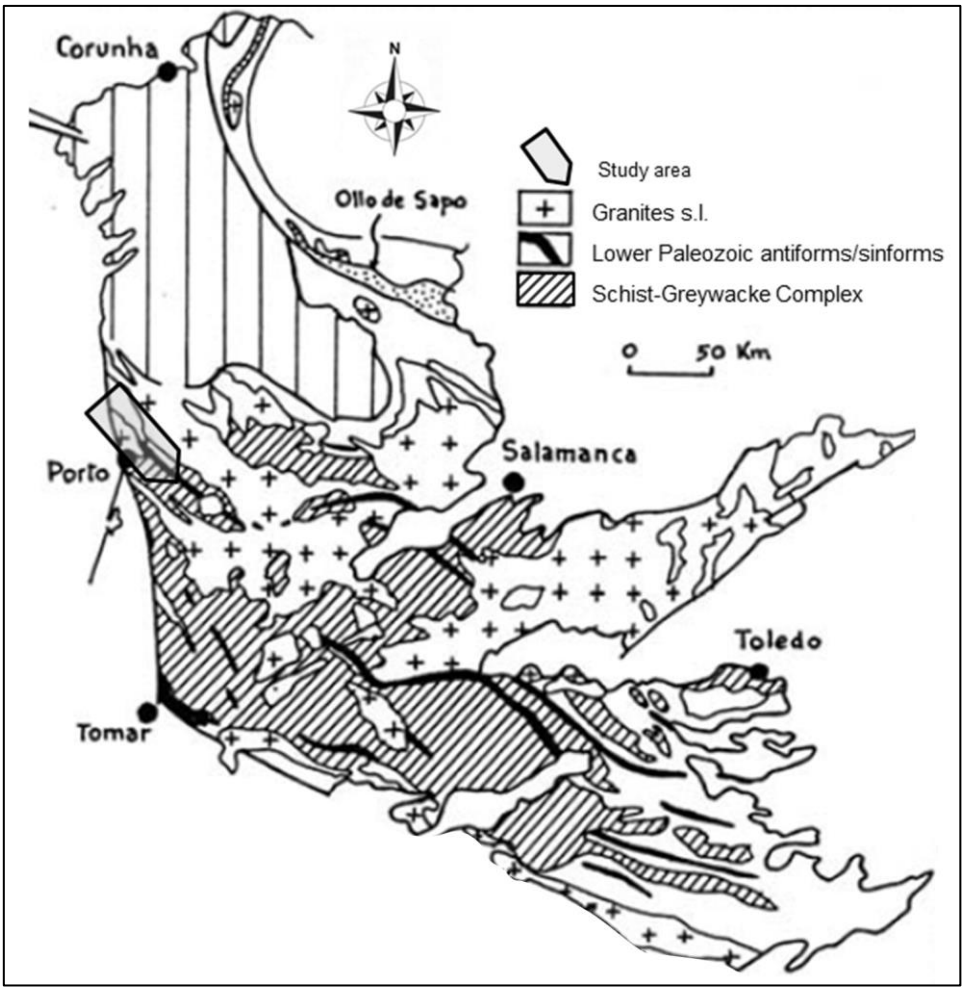

Fig.II. 2 - Major stratigraphic domains in the Central Iberian Zone with location of the study area. (After Soares de Andrade, *Lições de Geologia de Portugal*, not published)

Variscan deformation - Different authors have made the description of the structures generated by the Variscan deformation with relative consensus with regard to its geometry, but with some differences as to their chronological position, geodynamic and cinematic meaning. Generally three phases of Variscan deformation are recognized: D_1, D_2 and D_3 (e.g. Ribeiro, 1974; Noronha *et al*., 1979; Ribeiro *et al*., 1990, Dallmeyer *et al*., 1997; Romão *et al*, 2013).

Fig. II.3 represents a scheme of the main deformation events that affected the northern sector of the Iberian Massif during the Variscan cicle (Dias & Ribeiro, 1995).

1st Variscan Deformation Phase (D_1) – The main structuration of the studied region is the result of the action of the first Variscan deformation phase, D_1. This tectonic event folded all ante-Mesozoic formations of the region and is accompanied by cleavage (S_1). However, the geometry and kinematics of D_1 structures are variable and different sectors in CIZ are considered (Pereira *et al*., 1993): (1) the sector SW and S of Douro-Beiras and Juzbaldo-Penalva do Castelo Shear Zones; (2) the sector N and NE of these shear zones and the sector in the vicinity of Porto-Tomar Shear Zone.

To the sector S and SW of Douro-Beiras and Juzbaldo-Penalva do Castelo Shear Zones (the study area) the folding shows a general NW-SE (N150º to N160º) trend which is well expressed by the Armorican Quartzite Formation cartographic pattern (Couto, 1993; Ponte & Gama Pereira; 2004 Romão *et al*., 2013). The fold axes are sub-horizontal and the axial planes tend to be sub-vertical, with exception on the neighborhood of shear-zones or thrust (Ribeiro *et al*., 1990; Pereira, 1993). Regionally the S1 foliation is the most pervasive and tends to be sub-concordant with the stratification.

The genesis of granite rocks aged 379 ± 12 Ma, related to the action of depth shear zones marks the time assigned to this phase (Pereira, 1988; Pereira *et al*., 1993;). Dias *et al*. (1998) proposed the time period set between 380-360 Ma, while Noronha *et al.* (1979, 1981) considered that the migration of the tectonic front will have finished by the end of the Devonian period, i.e., about 360 Ma.

2nd Deformation Phase (D_2) – Unlike what happens with the D_1 Variscan deformation that affects in a generalized way all sectors of CIZ, the second deformation phase (D_2) was detected only in localized areas and manifests mainly through movement along the base of sub-horizontal major thrusts that laminated previous structures, especially in the N and NE sector of Douro-Beiras and Juzbaldo-Penalva do Castelo Shear Zones (Pereira *et al*., 1993). To the south sector the D_2 deformation show localized character and induced the formation of folds and shear zones with a general orientation NNW-SSE with moderate to strong inclinations to WSW and ENE vergence (Romão *et al*., 2013). Valle Aguado (2005) refers the development of localized sub-horizontal shear zones (in Porto-Viseu metamorphic belt), with development of sub-horizontal folds and foliation in metamorphic sequences of the Schist-Greywacke Complex (Beiras-Group).

These thrust movements can interact with the regional metamorphism, inducing melting of crustal materials and the consequent formation of granitic rocks (Pereira,

1988; Diez Balda, 1992; Pereira *et al*., 1993). These rocks correspond to early granodiorites, with about 320 Ma, which would have resulted from lower crust and mantle materials melting (e.g. Ribeiro M.L., 1993).

Syn-convergent distension - Subsequently to these Variscan compressive phases (D_1+D_2), a distension phase took place, leading to the Carboniferous continental sedimentation basins (e.g. Pinto de Jesus, 1986; Ferreira *et al*. 1987; Couto, 1993).

Several authors (Valle Aguado *et al.,* 1992, 2005, Diaz Balda, 1995, Martinez Catalan, 2004, 2014) consider that the extensional character of this detachment is indicated by the geometry of the metamorphic structures and the transition from initial intermediate pressure metamorphic conditions (Barrovian type) to a HT-LP regime indicating a decompressive regional metamorphic episode, coeval with the syn-convergent extensional phase. Also suggest a narrow time-span between the thermal peak and the intrusion of granitic melts (Valle Aguado, 1992; Valle Aguado *et al*., 1993). This major extensional event is attributed to a large-scale gravitational collapse of the thickened continental crust (e.g. Noronha *et al.,* 1979; Escuder Viruete *et al*., 1994; Dıéz Balda *et al.*, 1995; Ábalos *et al*., 2002).

3rd Deformation Phase (D_3) - After deposition of the Carboniferous sediments there was a new episode of deformation now in intra-continental context, that appear to have occurred at the same time as active erosion and subsidence of the Upper Carboniferous basin was taking place. The D_3 deformation event ends with the inversion of this basins (Couto, 1993; Valle Aguado *et al.* 2005; Romão *et al*., 2013).

This deformation phase generated folds with axial plans oriented N100º to N130º plunging 65º-90° to S. The D_3 event locally developed a S_3 crenulation cleavage sub-parallel to the axial plane of the folds, which in some places is the main cleavage (Couto, 1993). Ribeiro *et al*. (2008) consider that this phase generates structures parallel to the first D_1 structures that are bent or reactivated during D_3.

The early granodiorites aged 320 Ma supported all the D_3 deformation and the Westphalian B conglomerates include fragments of some of these granitoid (Ribeiro, *et. al*., 1993). The age attributed to this phase is c. 314 Ma to 308 Ma based in syn-kinematic granitoids ages (Noronha, 1979; Valle Aguado *et al*., 2005). Acciaioli *et al*., (2003) dated micas developed during this deformation phase by the Ar-Ar method.

Biotite from a sample where the last recorded metamorphic event was of an early D_3 stage yielded an age of 333.5±4.4 Ma. In contrast, measurements on muscovite that resulted from fluid ascent during the late episodes of D_3 gave a result of 312.8±3.3 Ma. Therefore, the third Variscan deformation phase must have operated during a significant period: at 335-330 Ma folding of the previous structures was taking place, whilst at *ca*. 310 Ma major late-D3 shear zones and the emplacement of granites were active (Acciaioli *et al*. 2003).

Late deformational episode - At the end of the collisional process the decrease of temperature led to the transition of ductile to brittle behavior causing the genesis of a tardi-Variscan extensive network of fractures (Parga, 1969; Arthaud & Matte,1975; Ribeiro, 1980).

A first fracturing episode (D_4 phase), led to the genesis of two conjugated fracture systems: the main sinistral NNE-SSW to ENE-WSW and a subsidiary dextral system NNW-SSE a NW-SE. The chronology of this episode is marked by the age of alkaline granites (280 ± 10 Ma), whose emplacement was controlled by these structural accidents (Ribeiro *et al*., 1980; Martins *et al*., 2001, 2009, 2011).

A second episode generated inverse fractures with N-S orientation and NNE-SSW to NE-SW (N40º) kink-bands (Ribeiro *et al*., 1990; Couto, 1993; Romão *et al*., 2013).

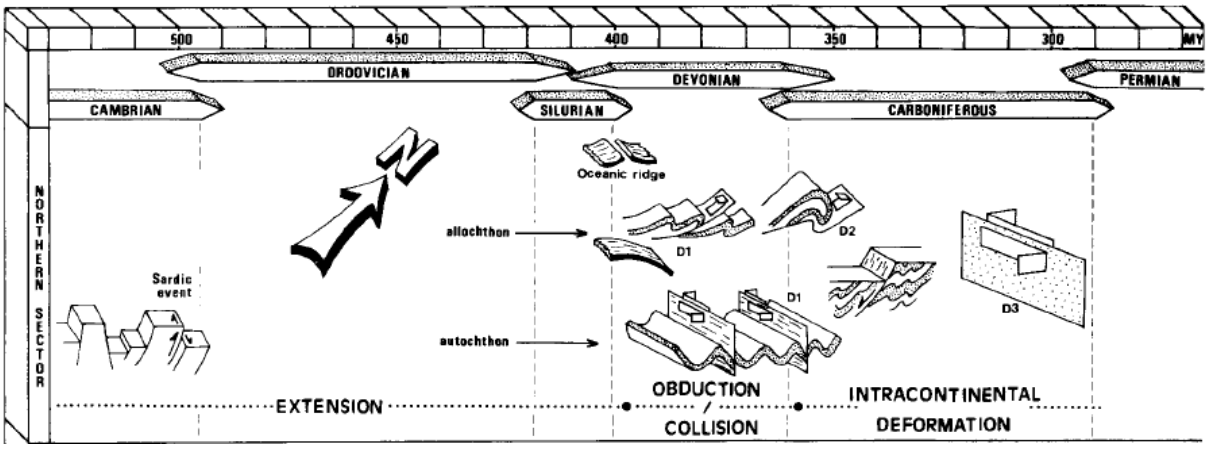

Fig.II. 3 - Time scheme of the main deformation events that affected the northern sector of the Iberian Massif during Variscan Orogeny (Dias & Ribeiro, 1995).

2.1.2.2. Metamorphism in Central Iberian Zone

It is advocated by several authors that the Variscan metamorphism is structured in metamorphic bands following a NW-SE orientation, according to the main structural directions of the Variscan Chain (Bard, 1978; Martinez & Ibarguchi, 1983; Castro *et al,* 2002). In these bands the metamorphic grade decreases within a few kilometres, perpendicular to its axis, from granulite or amphibolite to greenschist metamorphic facies. Still there are some issues about the meaning of the architecture of these metamorphic bands (Ribeiro, 1992). Bard (1978) considers that the existence of metamorphic alternating bands is associated to deep fracturing structures, while others make the metamorphic features coincide with 3rd Variscan phase antiform structures related to thermal axis, almost invariably marked by syn-tectonic plutonism (e.g. Oen, 1970; Martinez *et al*.,1988; Castro *et al.,* 2002; Valle Aguado *et al.,* 2005) (Fig. II.4).

The metamorphic evolution the early stages of deformation took place at intermediate pressure and low temperature conditions (Barrovian metamorphism) as a result of crustal thickening. Only under the basal thrust of the nappes in alochtonous terrains the high pressure conditions were recorded. The initial P and T gradients are modified during the last deformation phase and have evolved to low pressure conditions associated with thermal gradients varying from low to high temperature, the latter being spatially and temporally associated with the granite plutonism (Ribeiro M. L., 1992, Ábalos *et al*., 2002; Castro *et al.,* 2002; Arenas & Martínez Catalán, 2003, Valle Aguado, 2005, Martinez Catalán *et al.* 2014). The relationship between the low-P and high-T metamorphism and the granitoid emplacement is widely accepted considering that the advective heat has been an important mechanism on the development of thermal domes of the Iberian Massif (Martinez *et al*, 1988; Reavy, 1989; Acciaioli, 1997; Castro *et al*., 2002; Valle Aguado, 1992, 2005).

Some authors (Oen, 1970; Reavy, 1989; Acciaioli, 1997, 2005) consider that in some areas only a single low-P and high-T event is registered associated with granitic intrusions. In these areas only thermal metamorphism with a prograde zoning from the chlorite- to the biotite-, andalusite- and sillimanite-zones is registered, being the staurolite and chloritoid the result of these metamorphic event in Fe rich rocks. Acciaioli (1997), considers that the metamorphism is low-P (syn -tectonic and syn-magmatic) and nearly isobaric, although locally present peaks of syn-tectonic pressure in the early stages of D_3 deformation phase. The shear zones have favoured the channelling of fluids and the genesis and emplacement of granites, causing an addition of thermal

effects and subsequent metamorphism. In the shear zones a coeval mineral assemblages reflect P values slightly higher than the pressure of regional paragenesis. These localized metamorphic domains (>P) are coincident with areas of greater penetration of quartz-veins network, suggesting a relationship with increased fluid pressure, migration and channelling of fluids and potassium metasomatism.

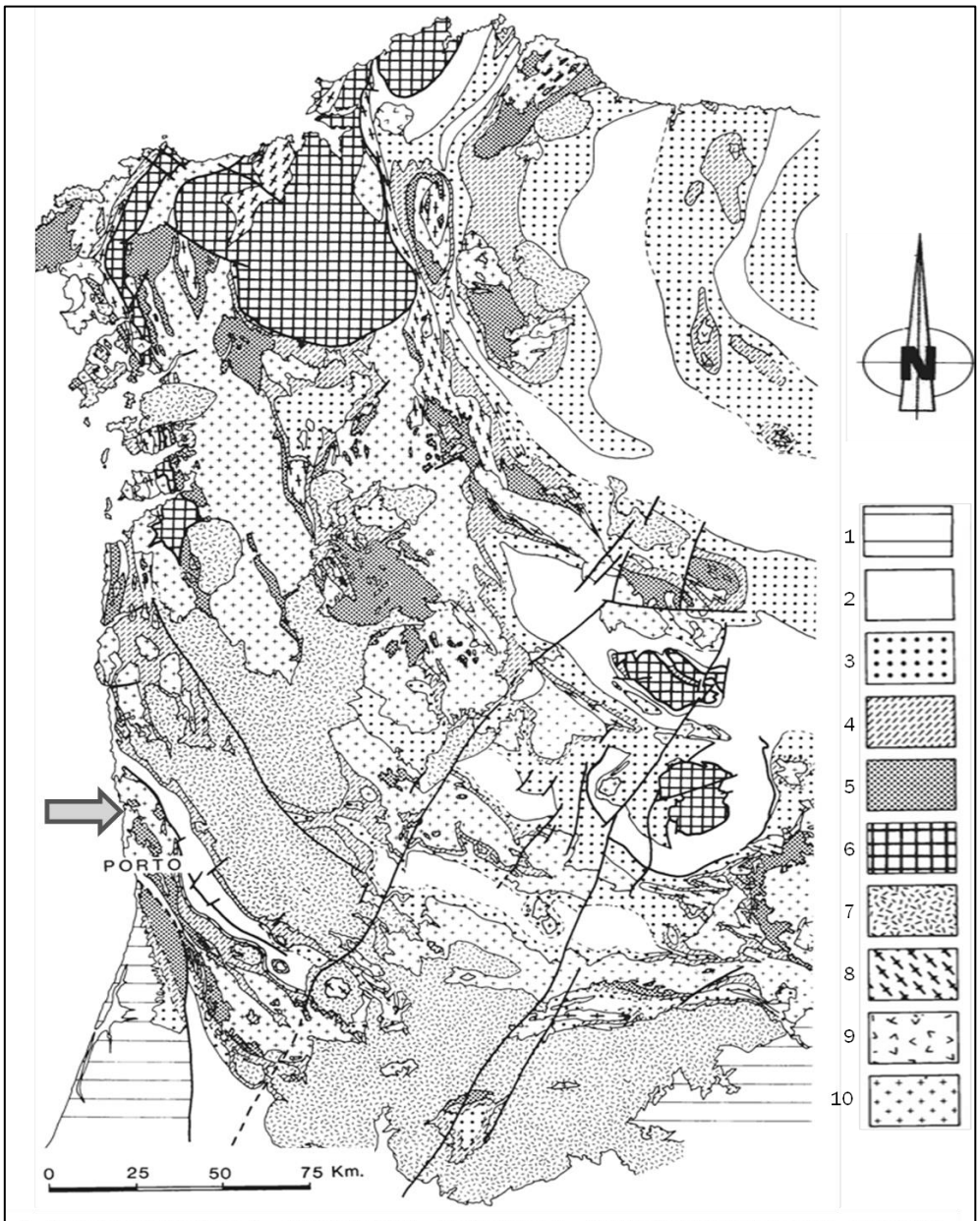

Fig.II. 4 – Distribution of metamorphic zones and variscan granitic rocks in the NW of Iberian Peninsula (after Martinez *et al*., 1988 and Castro *et al*, 2002).

2.1.2.3. Granitic rocks in Central Iberian Zone

The Central Iberian Zone is the segment of the European Variscan Chain where the granitic rocks outcrop to a greater extent and have greater typological diversity. Fig. II.5 represents the distribution of Variscan granitoids in central and northern Portugal.

The magmatic activity that prevailed during the Variscan orogenic cycle developed along different deformational stages. Thus, the magmatic rocks mainly represent orogenic granitoids, which are defined according to different age groups.

The first schemes for classification of granitic rocks were based on different criteria, namely, geochronological, structural and geochemical/petrographic, recently complemented with geochronological data.

One of the first proposals for the granitic rocks classification based on geological criteria and supported on granitoid / wall rock field relations, admitted the existence of three main groups of granites: ”oldest granites”, installed before the Variscan orogeny; the ”older granites” installed during the Variscan Orogeny e ”younger granites” installed after the Variscan Orogeny (Schermerhorn,1956).

Based on petrographic criteria, the existence of two main groups was proposed: the rare “peralkaline granites” with amphibole and/or pyroxene and the abundant “aluminous granites” only with micas (biotite/muscovite) in addition to the major minerals (Ribeiro, 1993). The late were sub-divided in two different series (Capdevila *et al*., 1973): (1) “two-mica granites” closely related to migmatites and high metamorphic grade areas and (2) “calc-alkaline granodiorites with biotite" often associated with mafic and intermediate igneous rocks.

In recent years, both structural and geochronological data, point to the definition of several intrusion times for Peninsular granitic rocks, which can be divided in three major groups: pre-orogenic granites, orogenic granites and post-orogenic granites. In the group of orogenic granites various stages of installation relatively to D_3 deformation variscan phase are distinguished (Ferreira *et al*., 1987; Pinto *et al*., 1987; Ribeiro M.L., 1993; Mateus & Noronha, 2010; Azevedo & Aguado, 2013).

Based on available data from Rb-Sr, K-Ar and U-Pb, three groups of granitic rocks can be distinguish: 1) Cambrian–Ordovician granitic rocks of 462–498 Ma (e.g. Bea *et al*., 2007; Solá, 2007; Antunes *et al*., 2009; Neiva *et al*., 2009; Rubio-Ordónez *et al*., 2012); 2) syn to late-tectonic granites aged ~336-304 Ma and 3) post-tectonic granites ~300-280 Ma (*e.g*.; Ferreira *et al.* 1987; Dias *et al*.,1998; Fernandez Suarez *et al*., 2000;

Almeida, 2001; Neiva & Gomes, 2001, Valle Aguado *et al*., 2005; Zeck *et al*., 2007; Antunes *et al*., 2008; Martins *et al*., 2009; Neiva *et al*., 2009; Solá *et al*., 2009; Carvalho *et al*. , 2010; Teixeira *et al*., 2011; Almeida *et al*., 2014). Azevedo & Valle Aguado (2013) distinguish two major cycles of magmatic activity during the Variscan Orogeny in the Portuguese sector of the Central Iberian Zone: ~ 320-310 Ma and ~ 310-290 Ma, corresponding to the installation of syn-D_3 granitoids and late-and post-D_3 granitoids, respectively.

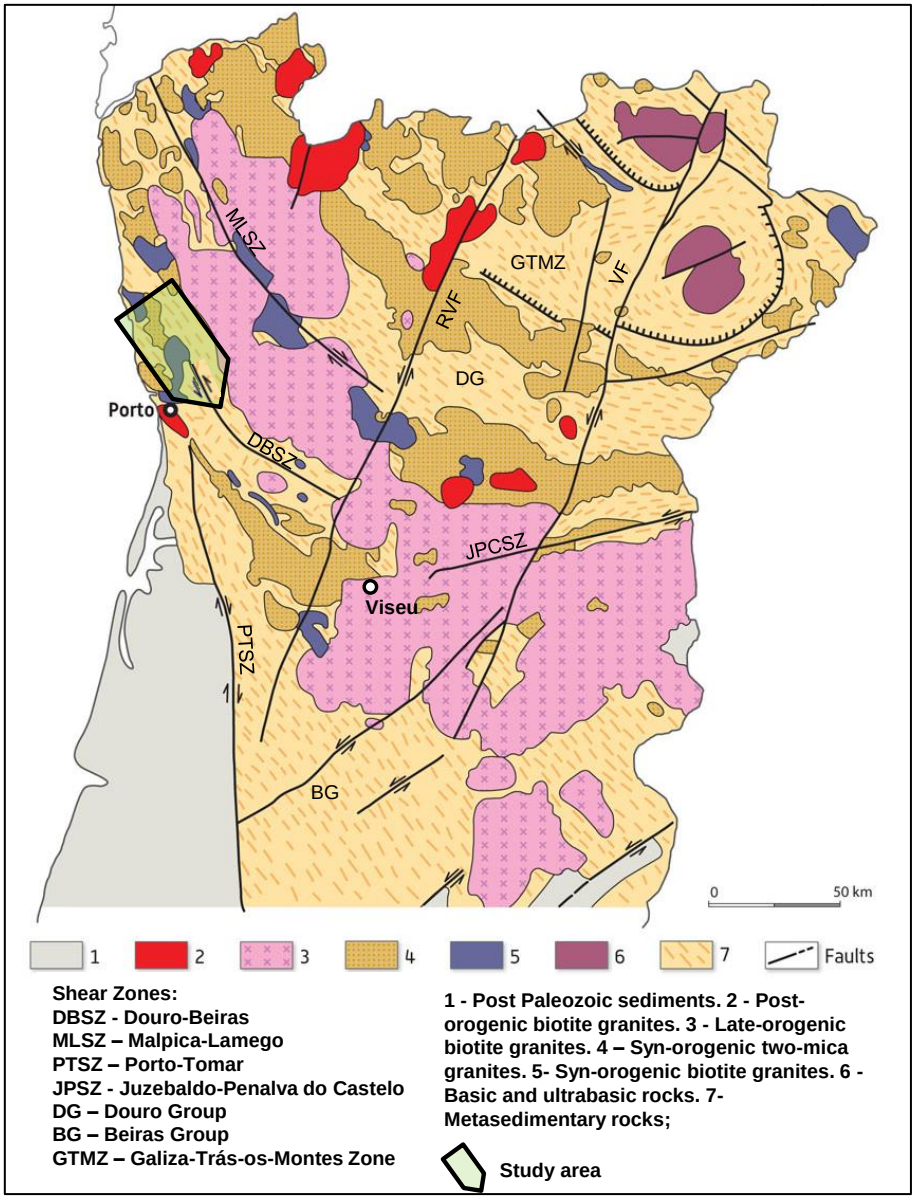

Fig.II. 5 - Distribution of variscan granitoids in central and northern Portugal with location of the study area (Modified from Ferreira *et al*., 1987).

2.2. The studied area

2.2.1. Location of the studied area and regional geology

The study area is located in the NW of Portugal and covers the metasedimentary and granitic rocks from Mindelo Migmatitic Complex (Areias *et al,* 2014) as well as the low grade to high grade metasediments dated Neoproterozoic/Cambrian that surround it. Thus, this study focused on a range of metasedimentary and granitic rocks cropping out from Póvoa do Varzim to Rates and extending south to Foz-do-Sousa (Gondomar).

The study area includes metasedimentary and granitic rocks in the vicinity of three NW-SE megastructures: (1) the Porto – Sátão antiforms/synforms; (2) the Douro-Beiras Shear Zone and (3) the Porto-Viseu Metamorphic Belt. Figure II.6 represents schematically the location of these structures and its lithological division, as well as the location of the studied area.

Porto-Sátão antiforms/synforms - In the NE sector of the study area the landscape is marked by Armorican Quartzite elevations that can be followed for several kilometers in a NW-SE direction. Among them, and from NW to SE, there are several elevations like Serra de Rates, Serra de Bougado and Serra de Santa Justa. These elevations represent Variscan antiforms (related to 1st deformational phase, D_1). In the antiforms and associated synforms marine metasediments dating from late Neoproterozoic/Cambrian to Devonian outcrop (Couto, 1993, Pinto de Jesus, 1986, Pereira *et al.*, 1992). This structure defined by Paleozoic syncline begins in Esposende (Porto), passes through Satão and ends in Salamanca (Regêncio & Portugal Ferreira,1981; Azevedo & Valle Aguado, 2013).

Douro-Beiras shear zone (DBSZ) - Adjacent to Porto-Sátão Paleozoic metassediments, to SW, there is the so-called Douro-Beiras Shear Zone extending from the vicinity of Apúlia (NW) to Viseu (SE). This structure corresponds to a sinistral shear-zone whose activity was particularly important during the entire Variscan Cycle (Dias & Ribeiro, 1991), having controlled the opening of several continental intra-mountainous sedimentary basins during the Carboniferous. These basins of NW-SE orientation are composed by conglomeratic deposits with fragments of granite,

quartzite and arkoses as well as by sandstones, shales with plant fossils and coal (Teixeira e Medeiros, 1965).

Valle Aguado *et al*. (2000) considers that the DBSZ may represent the western termination of the Juzbado–Penalva do Castelo sinistral shear system. These shear zones are an important boundary between domains with distinct structural and stratigraphic styles: from the structural point of view there is the change in vergence of major D_1 folds between northern and southern sectors and from the stratigraphic point of view these shear-zones represent a paleogeographic boundary during Schist-Greywacke Complex deposition allowing individualization between the two basins where the Douro Group and the Beiras-Group sediments were deposited (e.g. Díez Balda *et al*., 1992; Pereira *et al.,* 2007).

Porto-Viseu Metamorphic Belt - To the SW, and adjacent to the Douro-Beira Shear Zone, there is another NW-SE megastructure called Porto-Viseu Metamorphic belt (Schermerhorn, 1956; Oen, 1970; Reavy, 1989; Esteves *et al.,* 2006; Valle Aguado *et al.,* 1993, 2005; Azevedo & Valle Aguado, 2013). This metamorphic belt is composed of pelitic rocks interbedded with greywackes and relatively thin calc-silicate layers of the Schist-Greywacke Complex and constitutes a classical example of a gneiss dome showing HT-LP migmatites and anatectic granites in the core and low- to very low-grade metasediments in the limbs (Valle Aguado *et al*., 2005, Acciaioli, 1997). The core of the antiform consists of syn-tectonic two-mica granites that intruded the Schist-Greywacke Complex metasediments. The metamorphic grade of the metasediments is highest in the antiform core and decreases continuously towards the flanks. Intimately associated with the granitic rocks there are migmatitic complexes as exemplified by Mundão Anatectic Complex (Valle-Aguado *et al.*, 2010), in the Viseu region, and Mindelo Migmatitic Complex in the studied area (Areias *et al*, 2014).

Our study focuses on the metasedimentary sequence, in the NW of the Porto-Viseu Metamorphic Belt, from the lowest metamorphic grade up to the central anatectic complex. In the last published geological maps (Oliveira *et al*, 1992) these lithologies are correlated to the Schist-Greywacke Complex (Beiras-Group) whose profile-type was established by Romão (1994, 2013) in the Beiras region.

The SGC is a thick turbidity sequence that occupies the major part of Central Iberian Zone. Although the precise ages of these metasedimentary sequences are still poorly known, the maximum deposition age of the SGC has been constrained by U-Pb data of

its youngest zircon population, approximately placed at the Ediacaran-Cambrian boundary at 542 Ma (e.g., Teixeira *et al*., 2011, 2012; Pereira *et al.,* , 2012, Talavera *et al*. , 2012).

It is well exposed in Douro and Beiras regions in Portugal and in Salamanca, Extremadura, Montes de Toledo and Alcudia in Spain. Two main units have been recognized: the lower unit is of Ediacaran age and the upper unit is of Early Cambrian age. In Portugal these two units were nominated as Beiras-Group and Douro Group respectively. The existence of distinctive features between the Douro and the Beiras-Group metasedimentary sequences together with gravimetry studies led many authors to consider the existence of two independent sub-basins, whose existence was conditioned by the occurrence among them of a major crustal anisotropy associated with the Douro–Beiras and the Juzbado–Penalva do Castelo sinistral shear zones (e.g. Sousa, 1982; Silva *et al.*, 1988; Vidal *et al*., 1994; Jensen *et al*., 2007; Valladares et al., 2000; Ugidos *et al*. 2003; Rodriguez Alonso *et al*., 2004; Talavera *et al*., 2012; Villaseca *et al*., 2014). Provenance from continental deposits derived from the interior orogens in North Gondwana is proposed for Neoproterozoic sediments, whereas for the Lower Cambrian sediments a source derived from an older crust beneath those continental deposits is pointed (Valladares *et al.,* 2000; Villaseca, 2014).

The SGC presents very low to low-grade metamorphism in extensive regions and regional metamorphic zoning shows a symmetric pattern parallel to the syntectonic peraluminous granite plutons. The metamorphic field gradient is marked by condensed isograds parallel to the granites, varying in a short extension from chlorite-zone to biotite-andalusite or sillimanite-zone (Valle Aguado, 1993, 2005; Acciaioli, 1997; Ribeiro,. *et al*. 2008).

2.3. Previous studies

Previous studies conducted in MMC are scarce. Most of them were written in the sixties, for the preparation of Póvoa de Varzim and Porto geological maps.

Torre de Assunção, in 1962, published a paper where characterizes the rocks in the vicinity of Porto. In that paper he describes the “migmatitic coastal region" that considers occurring in places like Lavadores, Foz do Douro, Lavra, Angeiras and Vila Chã. In this paper there are also petrographic descriptions of the granitic intrusions of the region and of the calc-silicate rocks that outcrop within the migmatites.

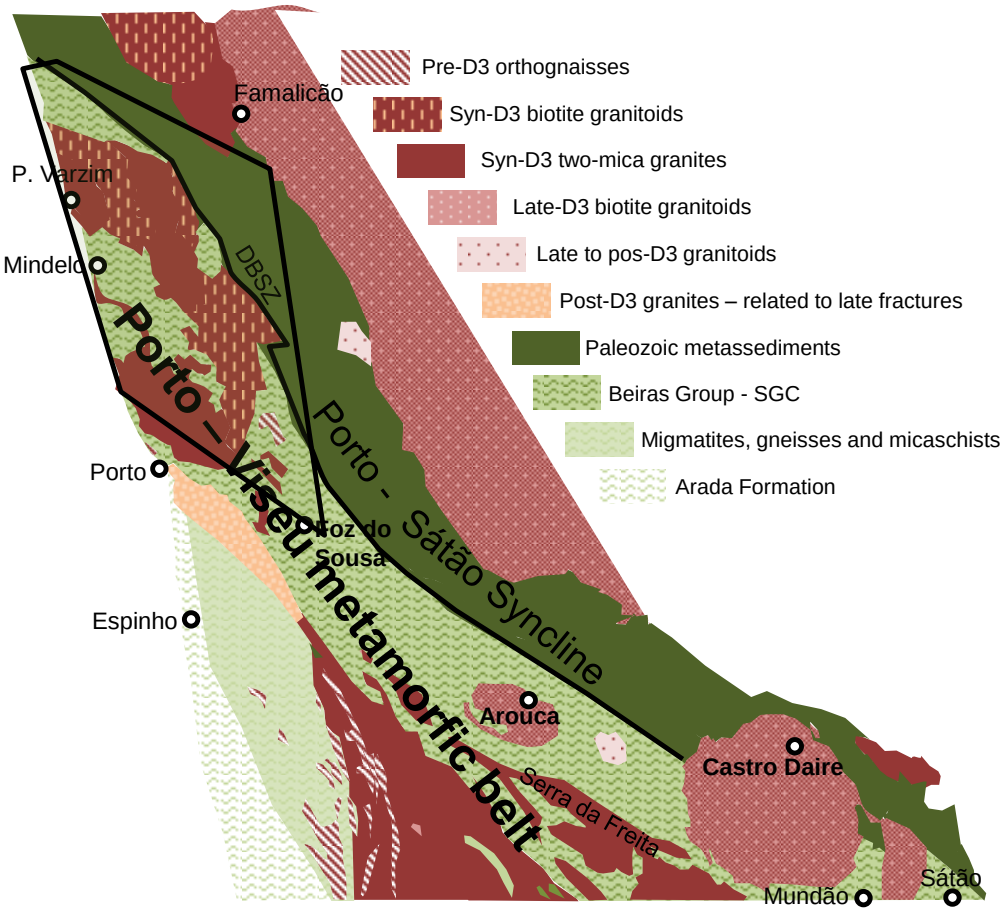

Fig.II. 6 - Simplified geological map of the study area with the major megastructures and location of the studied area (based on Ferreira *et al*., 1987 and Oliveira & Pereira, 1992).

Teixeira *et al.* (1965) in the 1: 50 000 scale Póvoa de Varzim geological map, refers a migmatitic band on the coastal zone, north of Porto, which classify as "Schist-granite-migmatitic Complex". It is mentioned the gneissic character of the formations and the occurrence of dark nodules within the migmatite, as well as granites, pegmatites and basic veins (lamprophyres).

Latter, Teixeira (1970), describes the “migmatitic-gneissic” formations north of Porto, occurring between Póvoa de Varzim and Angeiras. It considers that the Foz-do-Douro and Lavadores units are an extension, to the south, of these gneisses. Also refers that Porto Granite intruded these gneissic units and considered that this granite is pre-Silurian.

In 2001 and 2014, U-Pb geochronological studies in the Porto granite, conducted in two populations of zircon and monazite, interpreted the age 318 ± 2 Ma as the most

likely age of granite installation, being in accordance with the age constrained by the tectonic frame (Almeida, 2001, 2014; Martins *et al*. 2001).

More recently a master's thesis (Lopes, 2008b) and a PhD thesis (Ferreira, 2011) added lithological and structural field data and some petrological data in Angeiras and Vila do Conde, respectively. These works emphasized the interest of the area for teaching and divulgation of the local and regional geology. The didactic interest of this area is relevant for the diversity, complexity and beauty of geological structures as well as the prodigious exposition present in the beaches outcrops. Remember that in these beaches it is possible to show different granite rocks, metamorphic rocks, migmatitic rocks and various types of veins (pegmatitic, basic, etc.).

In the last years, during the preceding work of this thesis, several publications have emerged that focus on aspects of the petrography, geochemistry and isotopic chemistry of the area, particularly with regard to calc-silicate resisters (Ribeiro M.A. *et al*., 2011, Areias *et* al., 2012a,b,c), migmatite rocks and associated granites (Areias *et* al., 2012d; 2013a,b; 2014a,b) and pegmatitic veins (Areias *et al*. 2013c).

CHAPTER III – LITHOLOGICAL DESCRIPTION AND FIELD RELATIONS

Why may we not add Geology to the list of poetical sciences? Why shall not that science, which is the second science in eras and magnitudes, and the first, in affording scope for the imagination, be brought into favor with the Muses and afford themes for the Poet?

E. Hitchcock

3.1 - Introduction

In this chapter it will be made a description of the field relations and characteristics of the different studied lithologies. The lithological description will be divided into two distinct sectors:

Sector 1 – Between Póvoa do Varzim and Leça da Palmeira, comprising the Mindelo Migmatitic Complex and spatially associated granitic rocks;

Sector 2 - Between Laundos and Gondomar, comprising the Schist-Greywacke Complex metasediments located to SW of Beiras-Douro Shear Zone.

The location of sampling was dependent and conditioned by the existence of outcrops showing fresh or relatively fresh rocks. Since the region under study is densely populated and intensively used for agricultural and industrial production the number of outcrops in good condition is scarce. Thus, the resulting sampling distribution is quite irregular as there are several locations that do not meet the conditions for achieving a good geochemical study.

During the field work 161 mesoscopic samples of all recognized units and rock types were collected for use in the different methodologies addressed by this dissertation.

In the appendix A the coordinates of the points mentioned in the figures captions are listed (e.g. P. 450). These coordinates are the location where the photos were taken.

3.2. Sector 1 - Póvoa de Varzim ↔ Leça da Palmeira

In the coastal zone between Póvoa do Varzim and Leça da Palmeira the Mindelo Migmatite Complex (MMC) outcrops. The MMC is composed of several distinct lithologies. Like in other metatexite complexes also in MMC the most preponderant feature is the intricate way in which the lithologies relate to each other and the heterogeneous morphologies. Accordingly to field relations and petrographic observations the MMC lithologies were divided in seven different types: 1) patch-metatexites; 2) banded-metatexites; 3) metagreywacke resisters; 4) diatexites; 5) leucogranites; 6) two-mica granites and 7) aplite-pegmatites.

Fieldwork extended up from north to south along the coast. Migmatites were observed from Aguçadoura to Leça da Palmeira, but also inland, where was possible collect some fresh samples of migmatites and of two-mica granite. Towards E the occurrence of migmatites extends from the coastline to Modivas. The number of samples collected in the interior is small relative to the number of samples collected in the coastal zone. This is mainly due to the limited number of outcrops in this heavily populated area.

Figures III.1 and III.2 represent geological sketches of the Mindelo Migmatite Complex, and Migmatite Zone, respectively. The location and type of sampling is marked with a colour code. These geological sketches are based on the geological map scaling 1:200 000 with modifications based on field observations. Patch-metatexites, banded-metatexites and diatexites, with some greywackes, are prevalent in the central part of the MMC, called in this thesis “Migmatitic Zone” (MZ). This zone extends from north to south along about 6 km from Vila Chã to Angeiras. Out of MZ leucogranites crop out especially to the north and to the south of the migmatitic zone and two-mica granites predominate in an extensive area that surrounds both migmatites and leucogranites.

The entire Sector shows heterogeneity of lithologies and intricate relationship between them. In the Migmatitic Zone there are several dykes and small intrusive two-mica granite bodies, leucogranites and aplite-pegmatites. Moreover, within the two-mica granites there are abundant masses of metatexites and diatexites mostly incorporated by the two-mica granites as xenoliths of variable dimension. As an example of this heterogeneity, Figure III.3 shows an outcrop in Vila Chã where in the space of 100 x 50m metatexites, diatexites, aplite-pegmatites and leucogranite veins crop out. Figure III.4 presents an outcrop in Vila do Conde where within two-mica granite, leucogranites, diatexites and metagreywacke bodies are shown.

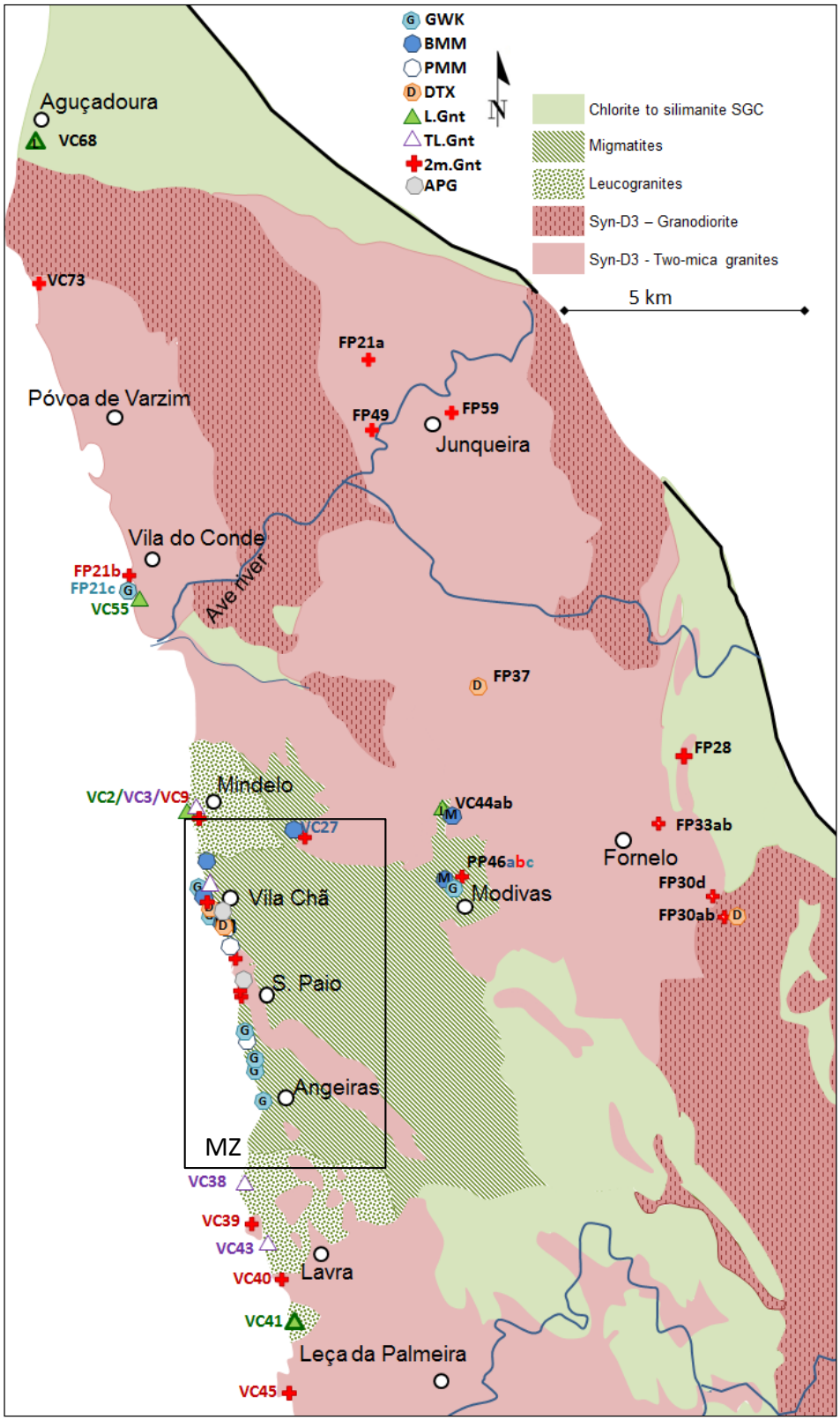

Fig. III. 1 – Geological sketch of Sector 1 based on field observations and geological map. Also signalled the location and lithological type of sampling. The migmatite zone (MZ) is marked by the black rectangle and is more detailed showed in the Fig. III.2. Legend key: GWK – metagreywackes; BMM – banded-migmatites; PMM – patch migmatites; DTX – diatexites; L.Gnt – leucogranites; TL.Gnt – tourmaline-bearing leucogranites; 2m.Gnt – two-mica granites ; APG – aplite-pegmatites; SGC – Schist-Greywacke Complex.

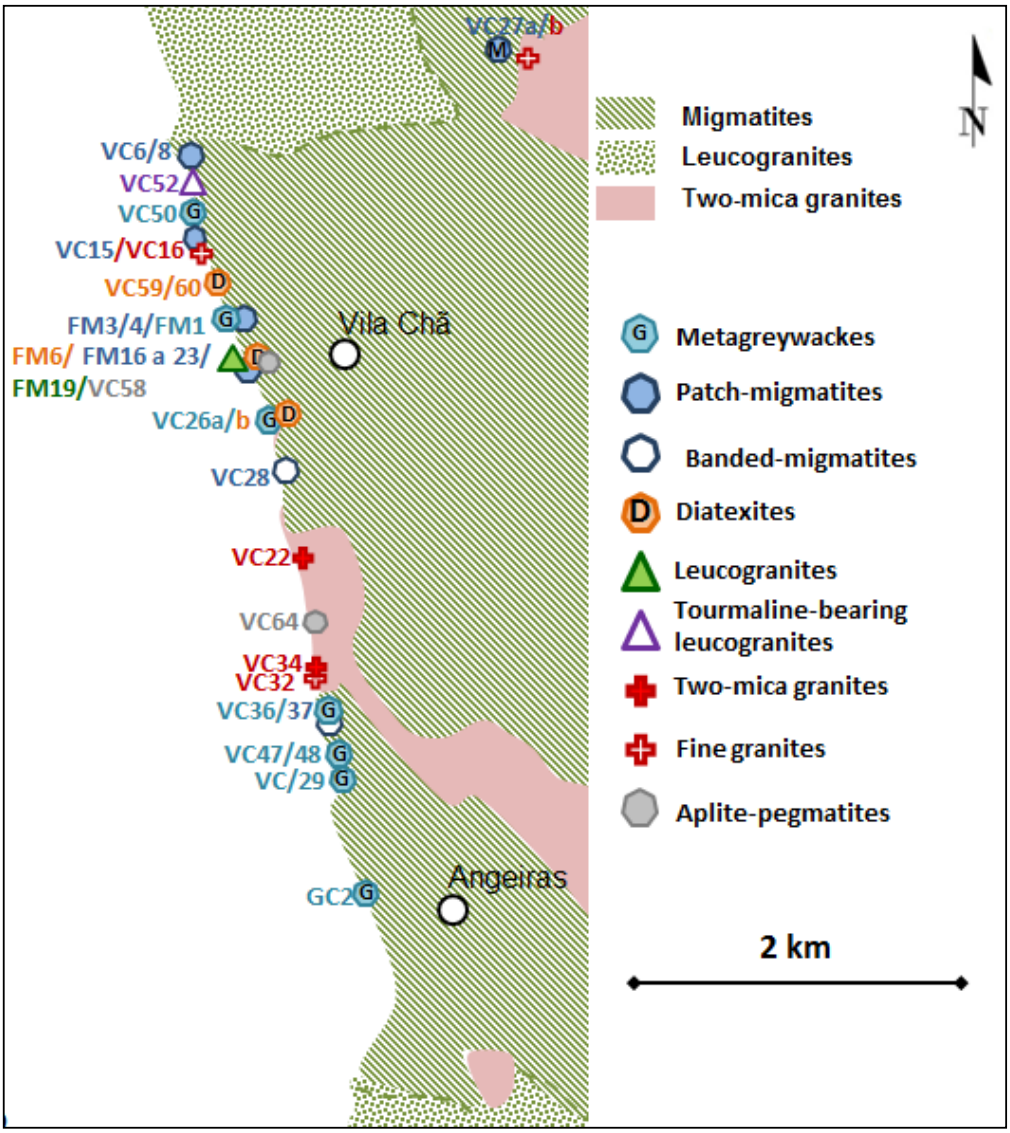

Fig. III. 2 – Detail of Fig.III.1 showing the geological sketch of Mindelo Migmatite Complex – Migmatite Zone. Also signalled the sampling location and lithological type.

3.2.1. Metatexitic rocks

In the Metatexite Zone (MZ) the dominant lithology showing varied morphology and structure are the banded-metatexites. Banded-metatexites crop out over a wide area in Metatexite-zone forming a splendid mosaic of roughly dark and light layers and beautiful folds. Most of them consist of discrete discontinuous centimetric-thick layers of medium grained quartz- and plagioclase-rich light leucosomes alternating with millimetric to centimetric thick dark melanosomes (Figs.III.5 and III.6).

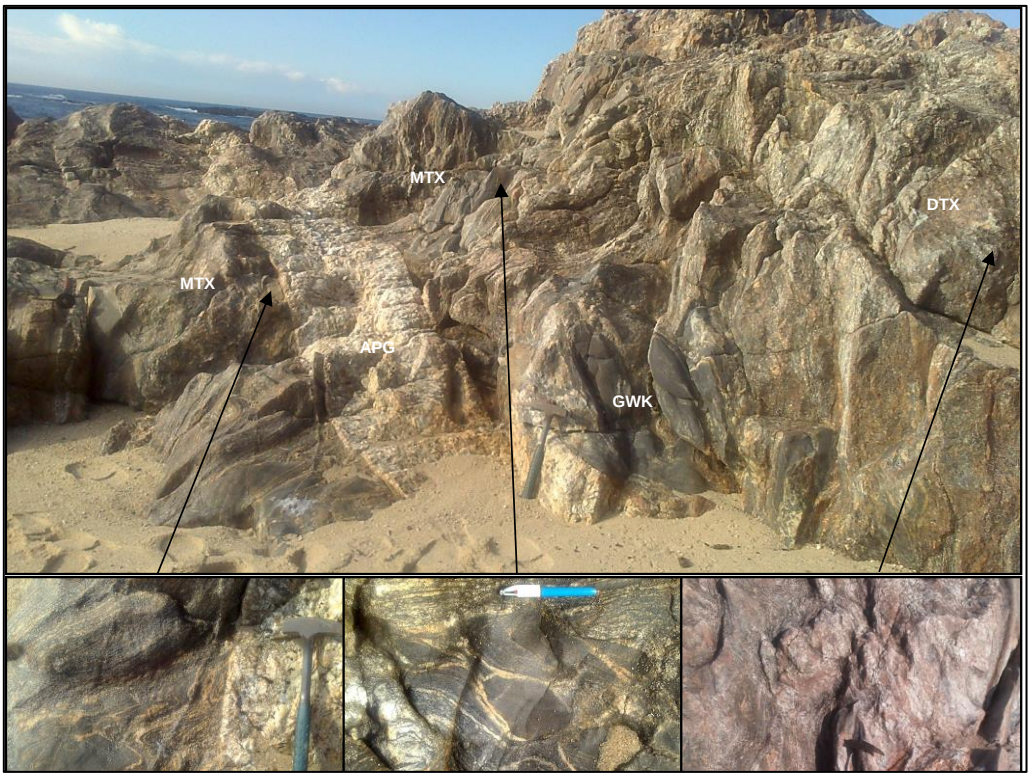

Fig. III. 3 - Field photograph showing lithological heterogeneity in an outcrop were metatexite predominates. MTX – metatexite; GWK – metagreywacke; APG – aplite-pegmatite (P. 462-Vila Chã).

Fig. III. 4 – Field photograph showing lithological heterogeneity in an outcrop where two-mica granite predominates. DTX – diatexite; GWK – metagreywacke; L.Gnt – leucogranite; 2m.Gnt – Two-mica granite (P. 577-Vila do Conde).

Leucosomes are coarse grained, white colored and can be classified using a two-fold division based on relationships with surrounding banded-metatexites – they are either concordant or discordant to local foliation. Concordant leucosomes are in petrographic continuity with discordant leucosomes (with similar microstructure, mineralogy and mode) (Fig. III.6) and they filling dilatant sites.

Metatexites in the vicinity of the leucogranites (see Fig. III.1) show darker colour and high melanosome/leucosome ratio consistent with residual composition, substantial leucosome extraction and passive enrichment in residual minerals after the removal of melt (Figs. III.5A and III.28A).

Banded-metatexites are intensely folded (Figs. III.5A and III.6D). The structural aspects related to the deformation will be described further in the final of the chapter.

Patch migmatites are rare and occur always associated with thick layers of metagreywacke resisters that inhibit more widespread partial melting in these rocks. They are dominated by paleosome and are characterized by the occurrence of small scattered patches of leucosome resulting from discrete partial melting (Fig. III.7). There are two types of patch leucosomes: type I is composed essentially of quartz, sillimanite and cordierite (Fig. III.7A) and type II is composed essentially of large crystals of quartz and plagioclase (Fig. III.7B). The last type of leucosome incorporates the first type of leucosome and minerals from melanosome. Dark *selvedges* border both type of patch leucosomes, generally being inferred to be the result of local (*in situ*) segregation of melt (e.g. Sawyer, 2008).

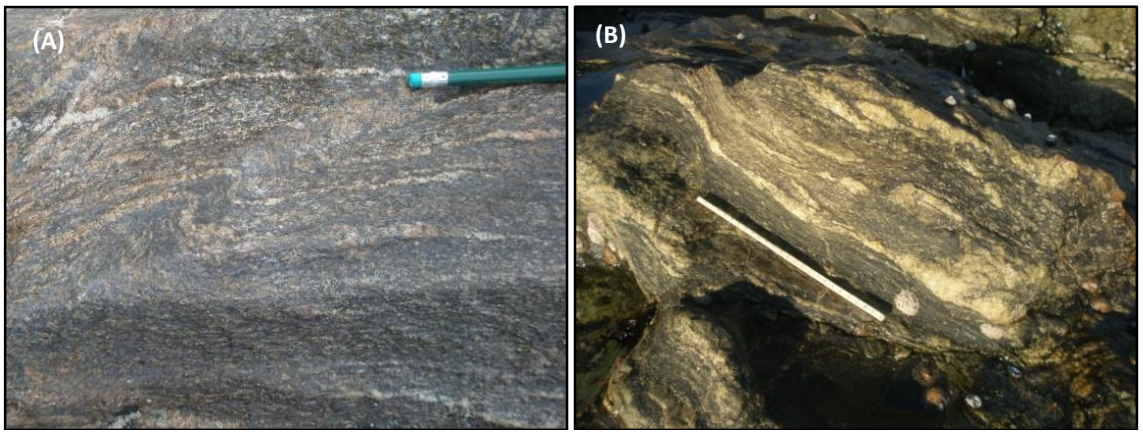

Fig. III. 5 – Field photographs showing aspects of banded-metatexites. A) Banded-metatexite showing textural features consistent with residual composition after the removal of melt (P.492); B) Banded-metatexite showing roughly layers of leucosome (P.587).

Fig. III. 6 – Field photographs showing aspects of banded-migmatites. A and B) Banded-metatexite and transverse leucogranite dike exhibiting petrographic continuity (with similar microstructure, mineralogy and mode) with concordant leucosome (P.707 and 587 respectively); C) Banded-metatexite showing segregation of leucosome and accumulation in dilatant site. The leucosome is coming from various parts of the metatexite that connected in the accumulation site (P.462); D) Folded banded-metatexite (P. 686).

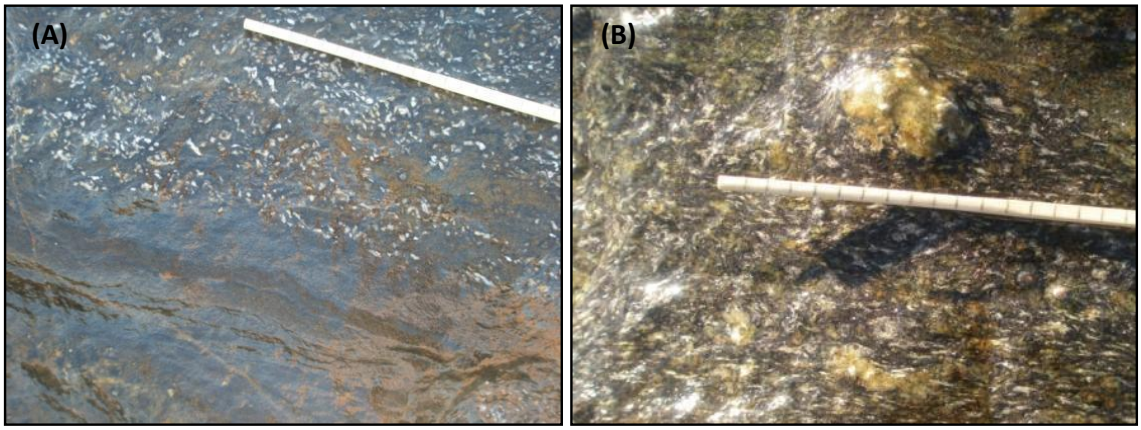

Fig. III. 7 – Field photographs of patch-metatexites. A) Layer of patch-metatexite parallel to a layer of metagreywacke resister (P.681); B) Patch-metatexite showing quartz feldspathic leucosome (Type II). Within the leucosome there are fragments of the type I leucosome and melanosome. Note the dark *selvedge* around the leucosome patchs. (P.615).

3.2.2. Metagreywackes and calc-silicate rocks

Within the metatexites there are dark metagreywacke layers and nodules. These rocks crop out as tabular layers varying thicknesses from centimetric to metric, alternating with pelite metatexites (with metapelite high proportion) (Figs. III.8 to III.12). Most of them have lenticular geometry. This geometry is usual in migmatitic areas where "tick layers of metagreywacke appear to detach from the metatexite and progressively transformed from tabular to round to lenticular shapes as they are incorporated into the migmatite" (Sawyer, 2008). These lenticular bodies are generally called schollen.

Within most of the metagreywacke layers and lenticular bodies there are calc-silicate nodules that stand out from the metagreywacke by its darker color. From now on these rocks will be called calc-silicate nodules (CSN). These bodies show sub-cylindrical or ovoid shape, and can be in vertical position, oblique or horizontal position within the metagreywacke layers (Figs. III.9 and III.10). The diameter varies from a few centimeters to about 50 cm at most. The length reaches about 1.5 m. It is important to note that the nodular calc-silicates are completely surrounded by the metagreywackes. This is, the calc-silicate rocks are totally inserted in the metagreywackes and do not occur as independent layers. However, there are some metagreywacke bodies without any calc-silicate nodule. Thus, the calc-silicate nodules seem to be an inherent feature of the metagreywackes, which show preferred concentration of calc-silicate minerals in specific sites.

Most of the calc-silicate nodules show two distinct concentric zones: a core zone (CZ) containing clinopyroxene and an outer zone (OZ) with amphibole. The relative thickness of these zones is highly variable. There are calc-silicate nodules where the core zone prevails and the outer zone is relatively thin, and others, were the outer zone is dominant or even exclusive.

Around some of the metagreywackes there are signs of partial melting (migmatized metagreywackes) revealed by the formation of layered concentric leucosomes. The leucosomes occur as concentric thin layers contouring the more calcic nodular portions of the metagreywackes and pass gradually to more pelitic and less calcic, banded-metatexites (Fig. III. 11).

Some of the metagreywacke and calc-silicate bodies show evidence of being affected by later fluids. The fluid entered the rock after the metamorphic peak that established the dominant mineralogy of these rocks (visible in unaffected rocks). These rocks show the following aspects (Fig. III.12): 1) retrograde calcite development in the most

Ca rich core-zone; 2) lighter color bands between the calc-silicate and the metagreywacke related to preferred cloritization of biotite; 3) silica infiltration bands composed of large quartz crystals that include the calc-silicate assemblage.

Fig. III. 8 - Field photographs of metagreywackes and calc-silicate nodules. A) Metagreywacke lenticular bodies showing calc-silicate nodules within (P.462). B) Lenticular metagreywacke resister body and calc-silicate nodule showing core-zone (CZ) and outer-zone (OZ). (P.462). Abbreviations: CSN – Calc-silicate nodule; GWR – Metagreywacke resister; BMM – Pelitic metatexite.

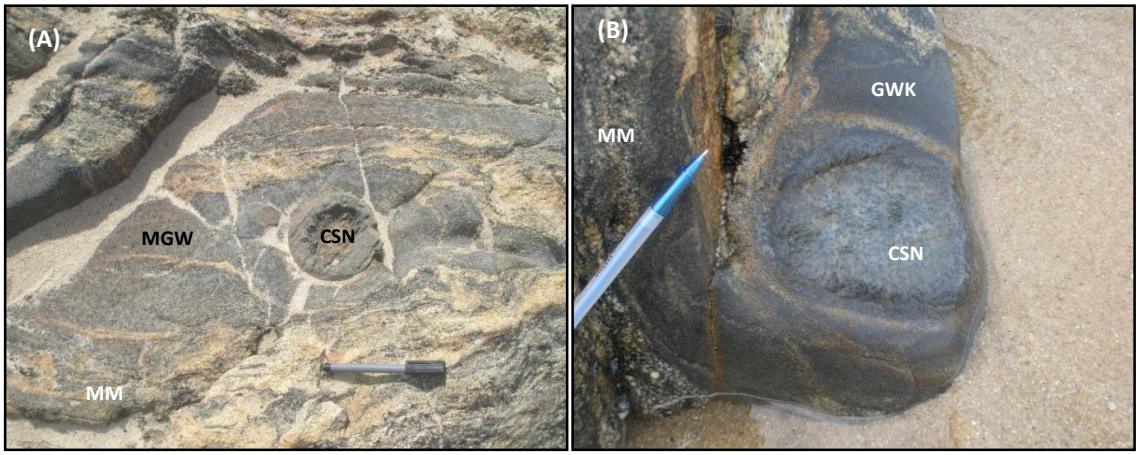

Fig. III. 9 - Field photographs showing aspects of metagreywackes and calc-silicate nodules. A) Vertical cylindrical calc-silicate nodule within tabular metagreywacke layer; B); Calc-silicate nodule containing relatively high proportion of diopside zone (core zone) and a tiny rim of outer zone (Horizontal plan). Abbreviations: CSN – Calc-silicate nodule; GWK – Metagreywacke; MM – Pelitic metatexite.

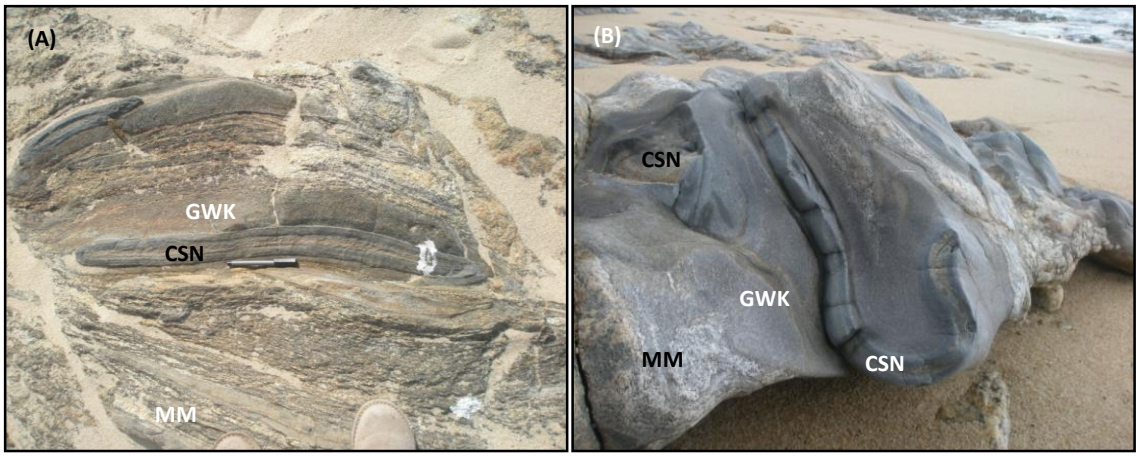

Fig. III. 10 – Field photographs showing aspects of calc-silicates: A) Ellipsoidal calc-silicate nodule and metagreywacke parallel to migmatitic foliation (P. 702); B) Calc-silicate cylindered nodule within rounded metagreywacke schollen (P. 463); A – horizontal plan; B – vertical plan). Abbreviations: CSN – Calc-silicate nodule; GWK – Metagreywacke; MM metatexite.

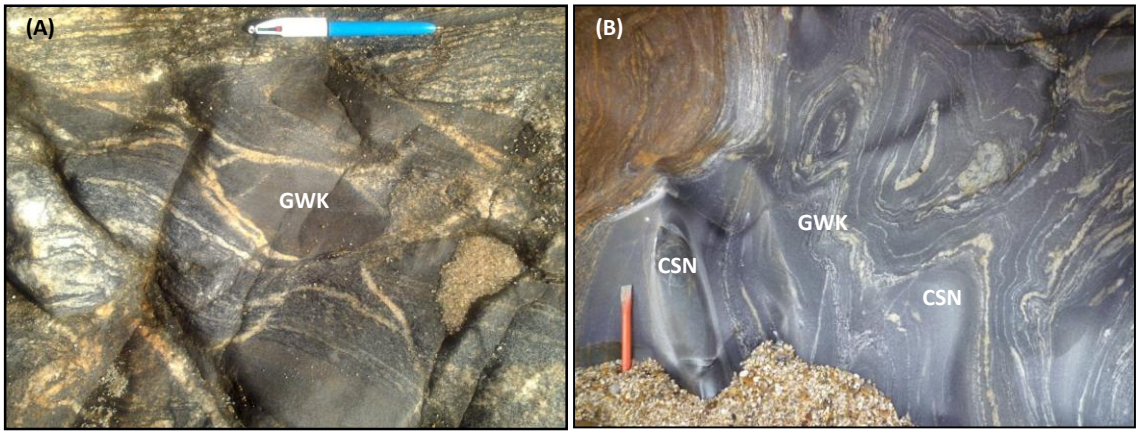

Fig. III. 11 – Field photographs of migmatized metagreywackes showing concentric accumulation of leucosome.. (A= P. 538 and B = P.462). Abbreviations: CSN – Calc-silicate nodule; GWK – Metagreywacke.

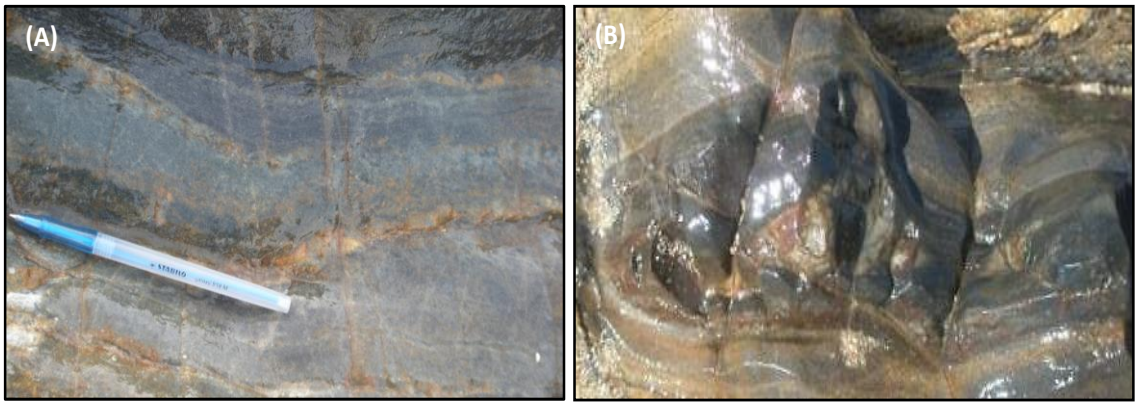

Fig. III. 12 – A) Calc-silicate resisters showing lighter bands resulting from infiltration of silica-rich fluids (P. 616); B) Calc-silicate nodule showing clearer core related with late alteration and subsequent secondary calcite development (P. 580).

3.2.3. Granitic Rocks

Within and surrounding the metatexite zone several distinctive granitic rocks crop out. These different granitic rocks show complex relationship with the metatexites and different mesoscopic aspect. Diatexites crop out as mesocratic massive bodies or dykes, showing granitic appearance and containing abundant schlieren and some schollen within. Leucogranites crop out as white granitic bodies showing rare residual dark schlieren. Two-mica granites occur mostly in massive bodies around the migmatitic zone but also cutting the migmatites. It exhibits uniform mineral distribution, typical of granite, although showing rare schlieren.

Diatexites (DTX) crop out within the metatexite zone both as bodies of few tens of square meters and as metric thick dykes (Figs. III.13 and III.14). In both cases the contact between diatexites and metatexites is sharp. The melt-depleted remains of pelitic layers (biotite schlieren) stand out as dark alignment within the rock. The schlieren gives to the rock a mesocratic appearance although with nuances derived of the variability in the intensity of schlieren that, although generally abundant, are more intense in some areas of the diatexite bodies. The matrix is composed mostly of dispersed medium-grained crystals of quartz, feldspars and rare biotite. However, most of the biotite occurs in the schlieren as well as sillimanite, cordierite and rare garnet. Large crystals of muscovite occur in some of the diatexites, principally in those showing signs of being affected by structurally controlled fluids and show coarse grained quartz and muscovite (Fig. III.14).

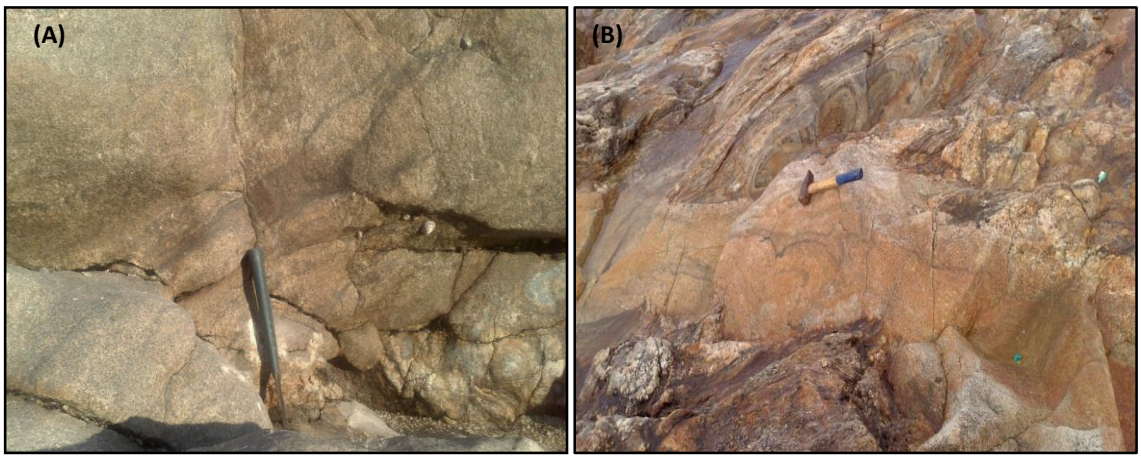

Fig. III. 13 - Field photographs showing several aspects of diatexites. A) Diatexite showing dark schlieren (P. 462). B) Diatexite dyke cutting the metatexite rocks (P. 705).

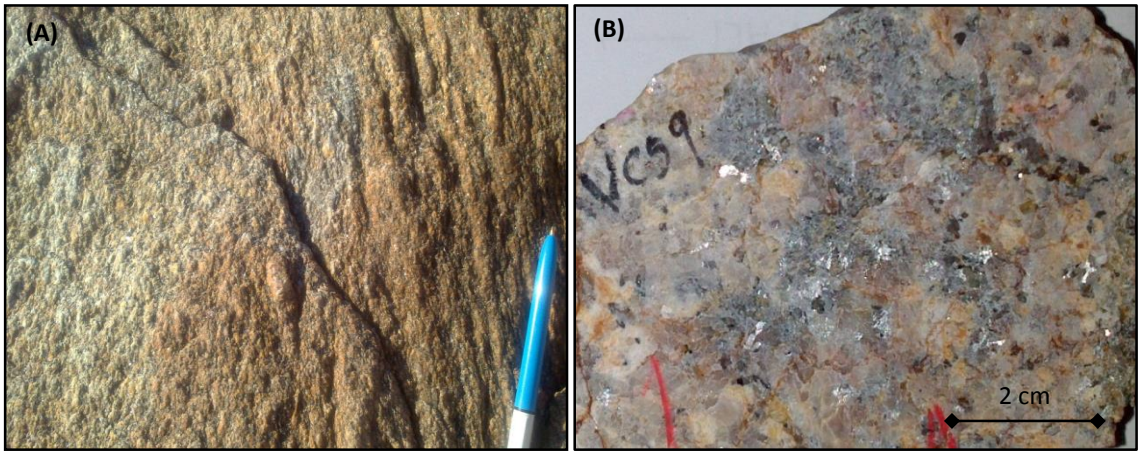

Fig. III. 14 - A) Diatexite showing intense dark schlieren; B) Photograph of a diatexite hand sample showing large white-mica crystals and coarse-grained quartz.

The leucogranites (L.Gnt) outcrop immediately north and south of the Migmatite Zone where they occur as bodies with several tens of square meters but also occur as veins that cut the migmatites and even the metasedimentary sequence in the vicinity of the migmatite complex (Fig. III.1). The most relevant feature of the leucogranites is the light colour and scarcity of biotite or other dark minerals. The grain size varies from medium-grained to coarse-grained. (Figs. III.15 and III.16).

Leucogranites are composed mostly of quartz and feldspars, and some biotite associated with sillimanite and rare garnet clustered in aligned dark spots. These dark agglomerates seem to result from the dissolution of aligned pelitic restitic xenoliths (Figs. III.15A and III.15B). Pelitic and metagreywacke xenoliths are abundant (Fig.III.16). Unlike diatexites and *in situ* leucosomes, cordierite is absent in the leucogranites.

Few K-feldspar megacrystals occur in the leucogranites matrix. K-feldspar also develops in miarolitic cavities, indicating the existence of later K-bearing fluids that filled the open spaces in the leucogranite (Fig. III.16A).

Locally the biotite clusters disappear and they are replaced by tourmaline clusters with the same texture as the biotite clusters. These tourmaline-bearing leucogranites (TL.Gnt) occur as metric thick tabular bodies both within the metatexites and within the leucogranites (Fig. III.17). It is possible to find unaffected portions of leucogranite within the tourmaline-bearing leucogranites (Fig.III.17B). This suggests that the tourmaline-bearing parts of the leucogranites result from structurally controlled flow of fluids that cause the tourmalinization of biotite.

The transition between leucogranites and metatexites is gradual. There is a progressive increase in the amount of schlieren in the transition from the leucogranites to metatexites. Also the network of veins of leucogranite is more intense within the metatexites near the bodies of leucogranite.

Fig. III. 15 - Field photographs of leucogranite. A) General aspect of leucogranite showing a light matrix with dark aligned biotite spots (P. 482). B) Aligned Schlieren of residual material inside leucogranite (P.485).

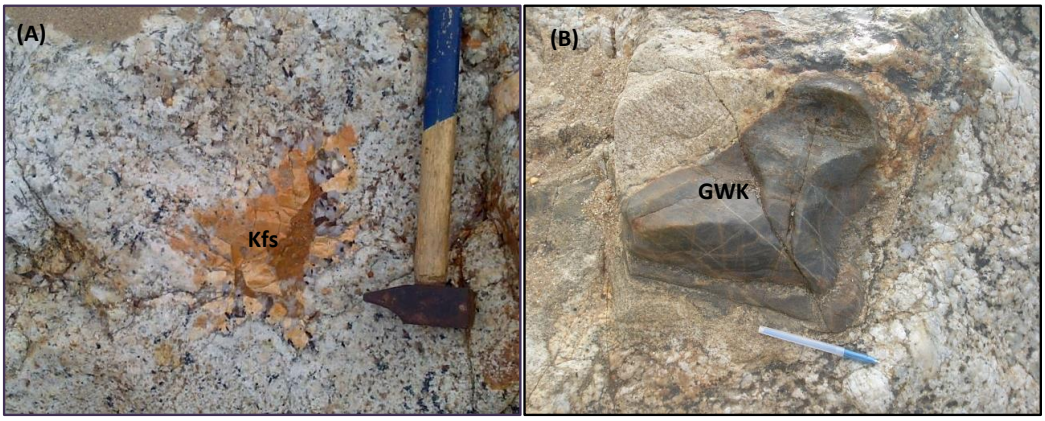

Fig. III. 16 - A) Leucogranite showing development of K-feldspar (Kfs) in miarolitic cavity (P.709). B) Metagreywacke (GWK) xenolith inside leucogranite (P.437).

Fig. III. 17 – Field photographs of tourmaline-bearing leucogranite. A) Leucogranite showing dark spots of tourmaline (P.709); Tourmaline-bearing leucogranite dyke containing a small portion of biotite bearing leucogranite (P. 487).

Two-mica granites crop-out north, south and east of leucogranites and migmatites and also as small bodies (hundred square meters) within migmatites (see Fig.III.1). Generally show medium-grain size, locally containing few K-feldspar megacrystals. Biotite is mostly dispersed in the quartz-feldspathic matrix but also forming dark schlieren, although more rarely than in diatexites (Fig. III.18).

There are several granitic dikes and veins, generally fine-grained, which cut the migmatites. In the low grade metasedimentary sequence (SGC) surrounding the metatexite zone, porphyritic two-mica granites occur.

The two-mica granite bodies include abundant fragments (xenoliths) of metagreywacke resisters as well as metatexites (Figs.III.19A and III.19B). These xenoliths generally show preferred orientation parallel to the schlieren.

Locally, feldspar megacrystals developed in well-defined structural alignments, showing preferred orientation striking N120º to N130º (Figs. III.19C and D).

Fig. III. 18 – Field photographs of two-mica granites. A) Medium grained two-mica granite with scarce K-feldspar megacrystals (P.606); B) Two-mica granite with aligned schlieren (P. 575).

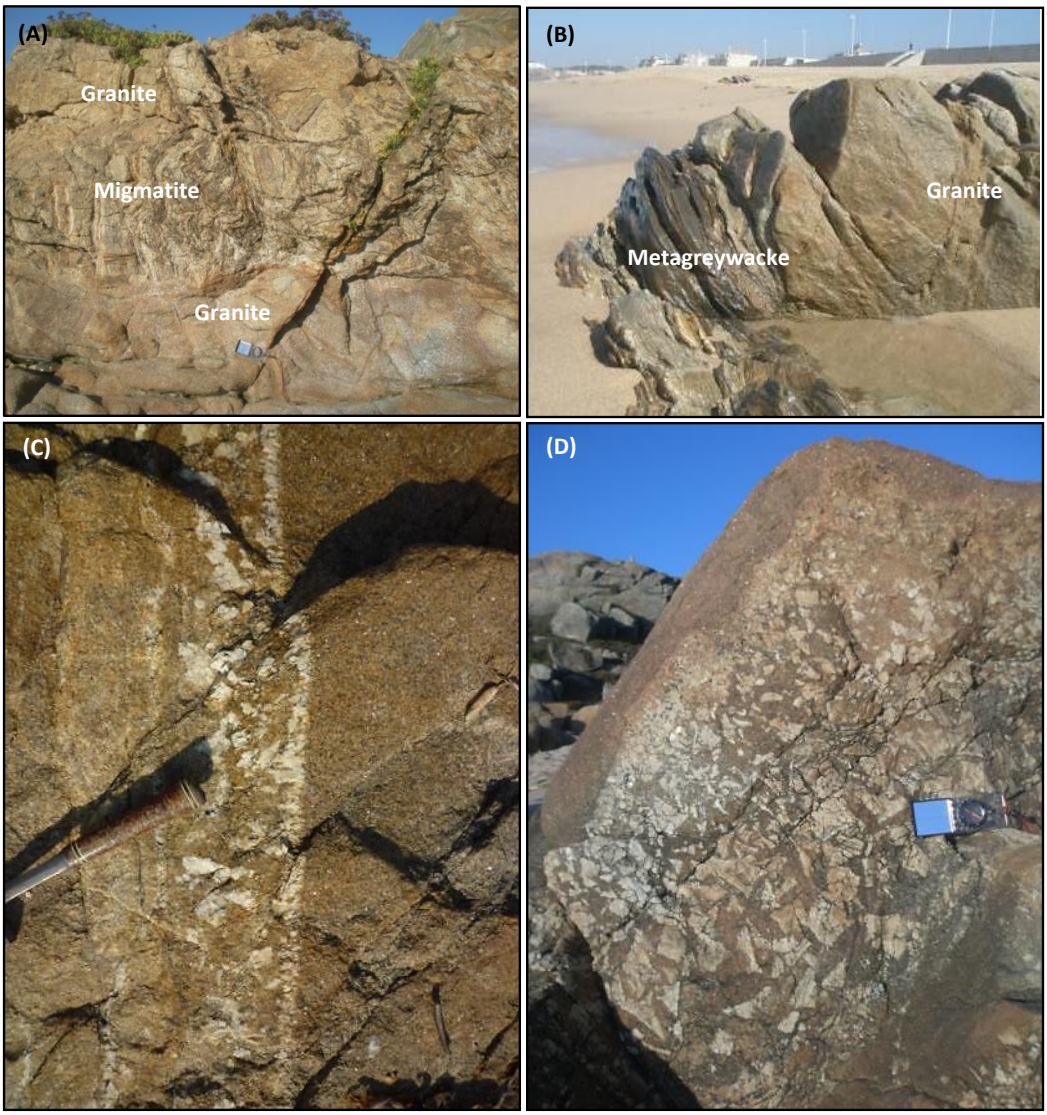

Fig. III. 19 – Field photographs of two-mica granites. A) Migmatite xenolith within two-mica granite (P583); B) metagreywacke xenolith within two-mica granite (P. 580); C and D) Strips of K-feldspar megacrystals developing in the granitic matrix in well-defined corridors striking N130º, 70º SW (P.608 and 587).

3.2.4. Aplite-pegmatites

Cutting all lithologies mentioned above there are several aplite-pegmatite veins showing centimetric to metric thickness and length > 10 m meters. These veins are characterized by its internal structure with compositional bands, generally showing (Fig. III.20):

- In the centre there is an aplitic band with quartz + plagioclase + tourmaline + garnet;
- Occurring symmetrically on one side and the other of the aplitic band, there is an intermediate band containing K-feldspar and plagioclase large grains;
- In the contact with the host rock there are quartz and plagioclase intergrowths showing comb-structure.

The thickness of each compositional band is variable, specially the intermediate band that could have few centimetres to more than a meter. In the last case the biggest modal percentage is clearly of K-feldspar that could form huge accumulations more than 1.5 m tick (Fig. III.20C). There is also repetition of the banding, i. e., some aplite-pegmatites show intermediate- and aplite-bands alternating several times.

In the granite zone, there are aplite-pegmatites that develop over the K-feldspar megacrystal alignments. In these type of aplite-pegmatites there is an inner part constituted by K-feldspar centimetric crystals inserted in the granitic matrix and bordered symmetrically by the aplite-pegmatite showing the typical zonation (Fig. III.21). Thus, the aplite pegmatite develops accordingly to the direction of the K-feldspar alignments and, eventually, from the alignment itself. This suggests that the K-feldspar alignments and the aplite-pegmatite emplacement could be related to the same event.

Locally, e specially associated with the leucogranites and with the aplite-pegmatites there are masses of muscovite agglomerates that give to the rocks a satin appearance. When associated with the pegmatites the development of muscovite occurs preferentially in the contacts with the wall-rock, although veins constituted exclusively by muscovite and minor quartz could also occur (Fig. III.21B).

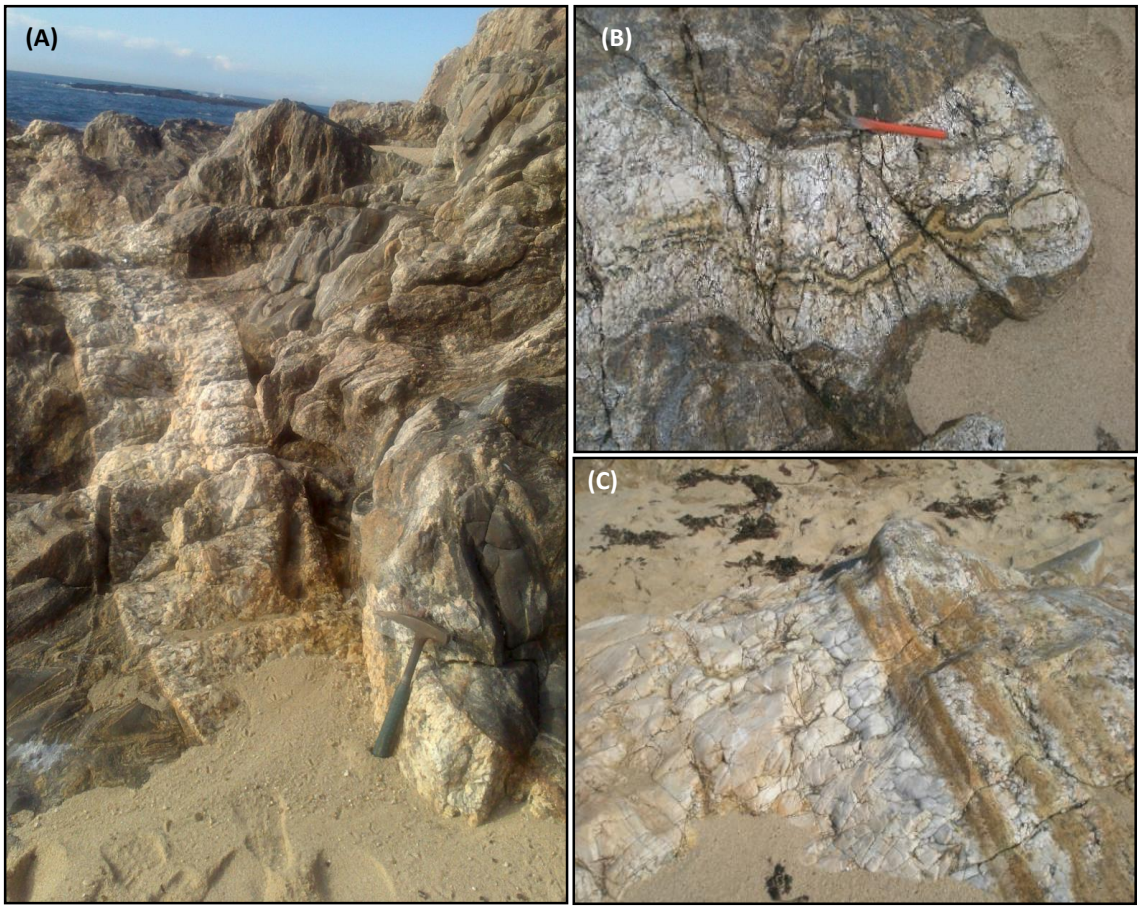

Fig. III. 20 – Field photographs showing aspects of aplite-pegmatite veins. A) Aplite-pegmatite cutting the migmatites; B, Aplite pegmatite showing zoning structure (P. 463); C) Huge K-feldspar development in the intermediate zone of aplite-pegmatite (P. 440).

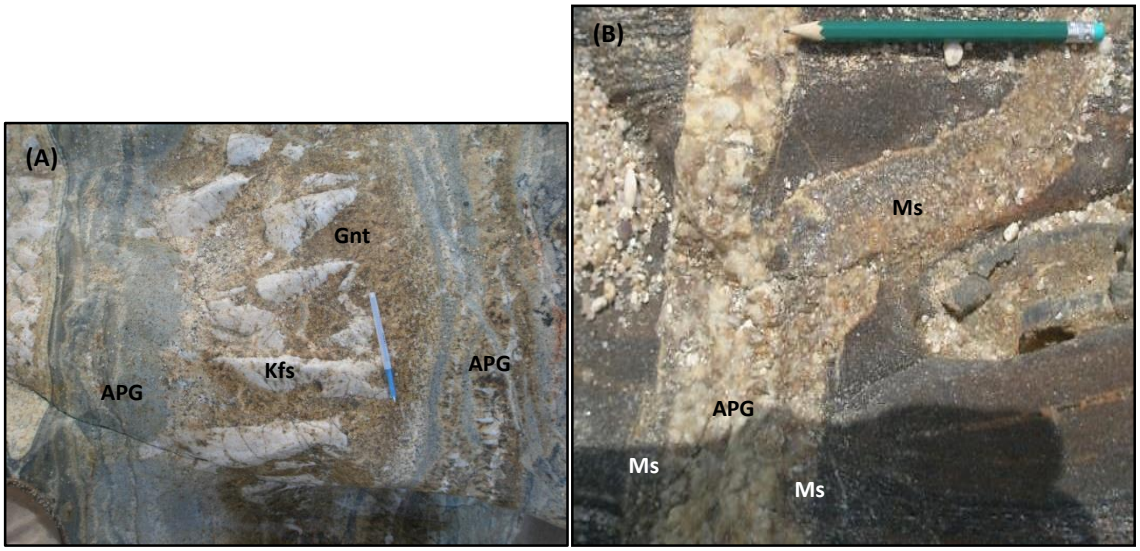

Fig. III. 21 - A) K-feldspar megacrystals (Kfs) alignments within granite (Gnt), symmetrically bordered by aplite-pegmatite (APG) (P. 792) ; B) Pegmatite vein bordered in both sides by muscovitic agglomerates in the contact with the wall-rock (P. 499). From a certain point the muscovitic masses derive from the pegmatite vein and form an independent "vein".

3.2.5. Structure

All over the MMC several deformation structures are observed. These various structures are the result of the action of various stages of deformation and/or anatexis concomitant with deformation.

3.2.5.1. Stratification

The best way to get information about the stratification would be to measure the contacts between the metagreywackes and the pelitic metatexites. However, the metagreywacke lenticular bodies show all possible orientations between NE-SW to NS (parallel to migmatite foliation). Also, in the vertical plan, the orientation of the lenticular bodies of metagreywacke shows pronounced heterogeneity (Fig. III.22). This is the result of the metagreywacke layers disruption coeval with melting under dynamical conditions, forming lenticular bodies dispersed in the migmatite matrix, that usually are called schollen or rafts (Sawyer, 2008a and b).

However, it was possible measure the stratification in some rare metagreywacke thicker layers (>50 cm), without evidence of disruption and in patch-migmatite layers preserved within metagreywackes (Fig. III.23).The metagreywacke layers show a planar surface striking N020º to N050º. The patch-migmatites show the same NE-SW preferential orientation, varying from N025º to N050º.

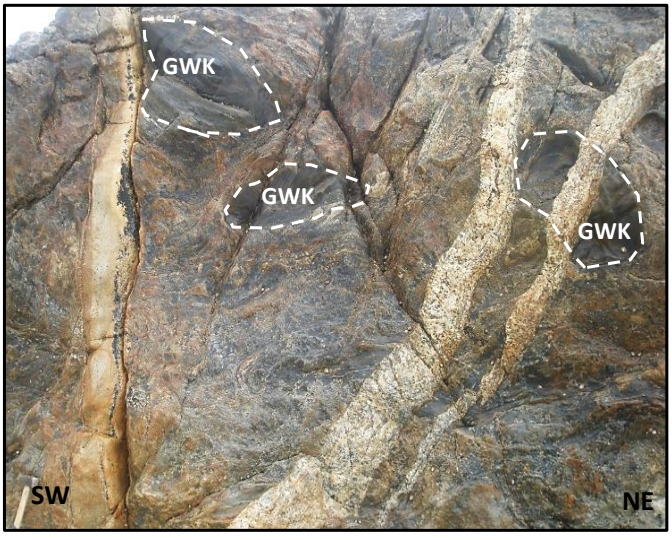

Fig. III. 22 –Metagreywacke showing random orientation within heterogeneous metatexite. Three aplite/pegmatite veins cut the earlier structure (Vertical plan).

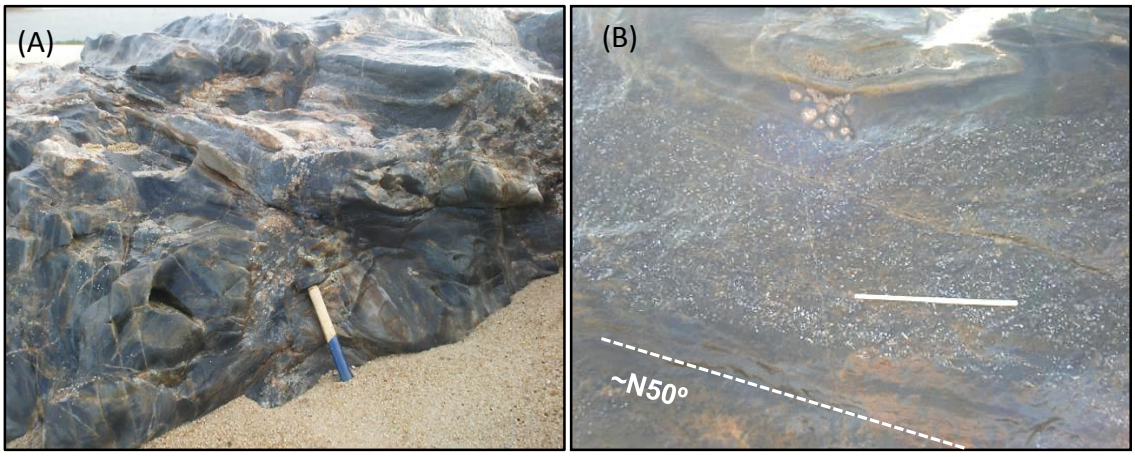

Fig. III. 23 – Field photographs showing S0 planar structures. A) Thick metagreywacke layer striking approximately N30º. B) Patch-migmatite layer striking N50º (horizontal plan view). (Horizontal plan).

3.2.5.2. Foliation

In MMC/MZ the most penetrative planar structure is the migmatite foliation (S_n). This foliation is well marked in the metatexite zone and is defined by the preferred orientation of melanosome minerals (biotite and sillimanite) and by the gneissic layering formed by leucosome and melanosome (Fig. III.24).

The good definition of the migmatitic foliation allowed the measurement of data in order to be used in a stereographic projection (Fig. III.25). The stereographic projection revealed the occurrence of three concentration peaks:

- The main concentration peak strikes from N160º to N000º dipping 70º to 90º to E. This migmatitic foliation shows the typical alternating banding with millimeter to centimeters thick leucosomes.
- The other concentration peak strikes from N025º to N045º dipping 60º SE to 90º.
- To the south of S. Paio (Fig.III.1) there is a gradual transition to a sub-horizontal foliation. This foliation strikes from ~NS to NE-SW, dipping from 50º to 10º E. The sub-horizontal foliation is predominant between the S. Paio granitic massif and the granitic massifs that outcrop in Leça da Palmeira (see Fig. III.1).

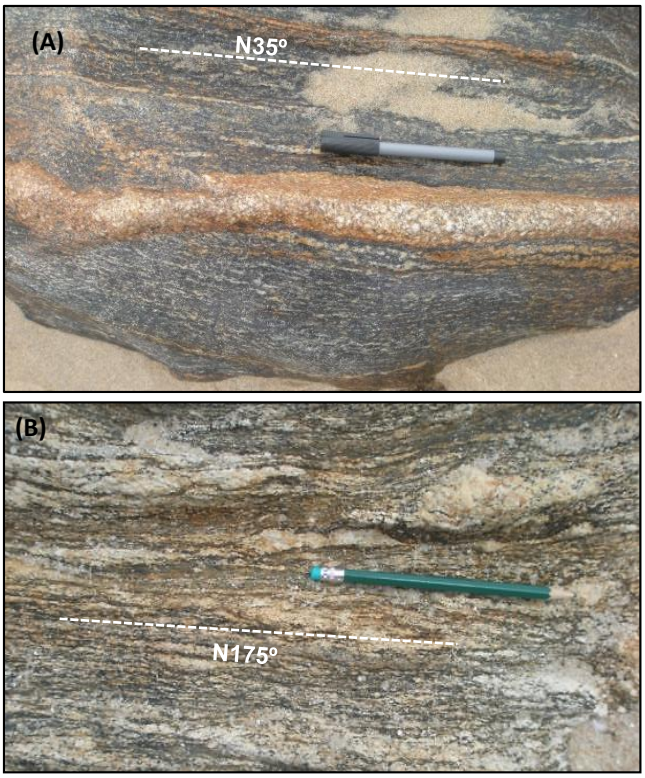

Fig. III. 24 – Field photographs showing migmatitic foliation (S_n). A) Foliation striking N035º in P. 494 and B) Foliation Striking N175º in P. 497. Both attitudes are widespread in metatexite zone, although NS predominates. (horizontal plan).

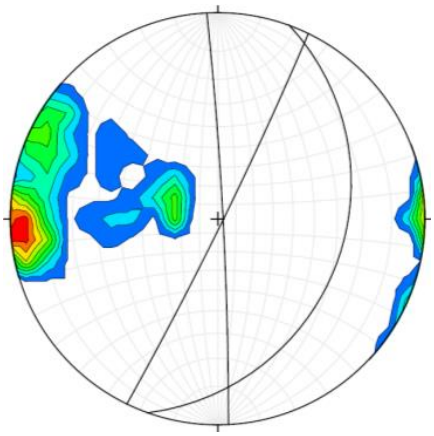

Fig. III. 25 - Density diagram of S_n planes in MMC/MZ. There are two concentration peaks around N177º and N026º dipping 85º to NE. To the south of the S. Paio Granite the dip is progressively more sub-horizontal, with average dipping 27º to E.

The migmatitic foliation is folded by a late deformation phase. Thus, after the action of D_n, a later D_{n+1} phase affected the migmatitic foliation, but was not enough intense to transpose S_n and form a new foliation. There are several features related to this later deformation phase, that suggest a simply shear character, namely:

- Folds related to this deformation phase show strong asymmetry (Fig. III. 26)
- In the most intensely deformed layers the metagreywacke schollen have rounded morphology and the calc-silicate nodules within show curved shape or asymmetric mantled shape (Fig. III.27);
- There are boudinated leucosomes along S_n foliation (Fig. III.28A and B);
- Some metagreywacke schollen parallel to S_n show shortening and amalgamation (Fig. III.28C).

The D_{n+1} asymmetric folds bend the melanosome and leucosome homogeneously, suggesting that when folding occurred the banding was almost completely formed and was affected as a whole. Also the boudinage in leucosomes and the amalgamation of schollen suggests that the anatexis predates the latter deformation phase.

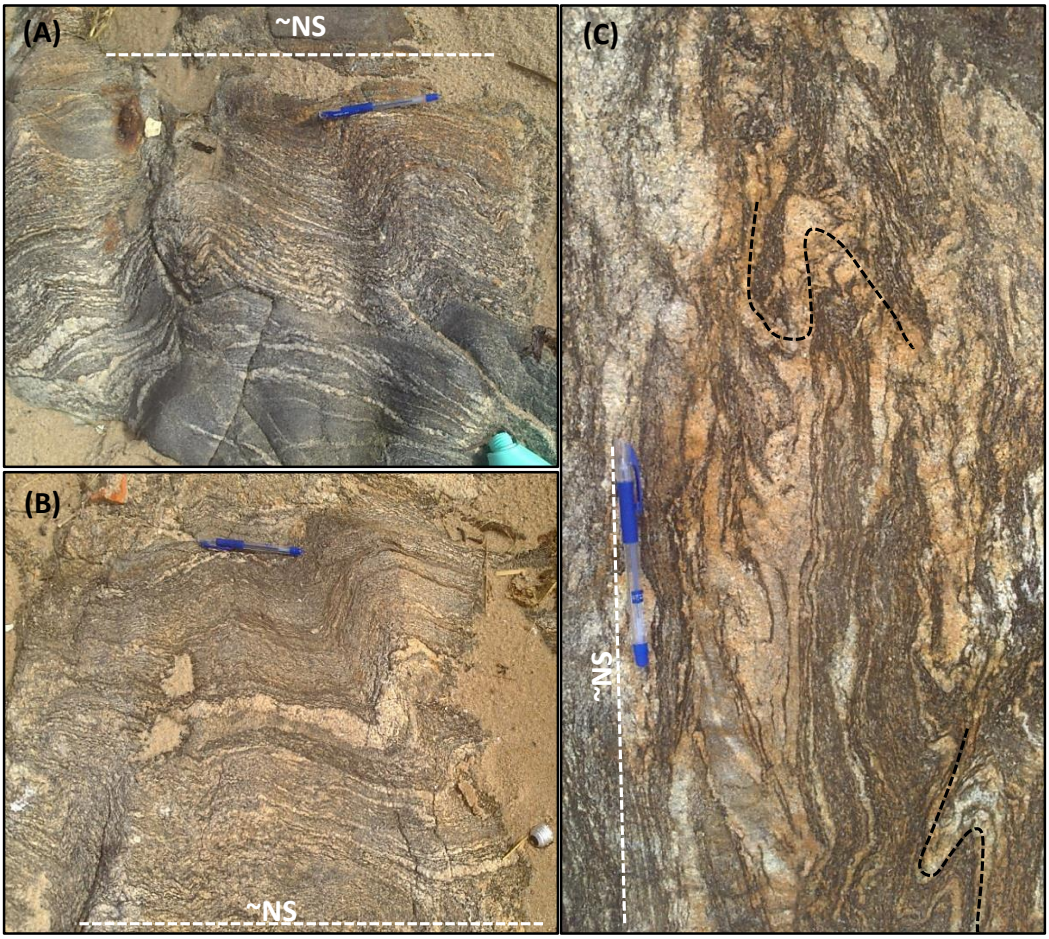

Fig. III. 26 – A and B) Field photographs showing asymmetric folding affecting the S_n (~NS) migmatitic foliation. The leucosomes thickness is homogeneous in the hinges and limbs of the folds (P. 711). C) Fold Interference patterns resulting from action of D_{n+1} in previous S_n folds. (P.710; horizontal plan).

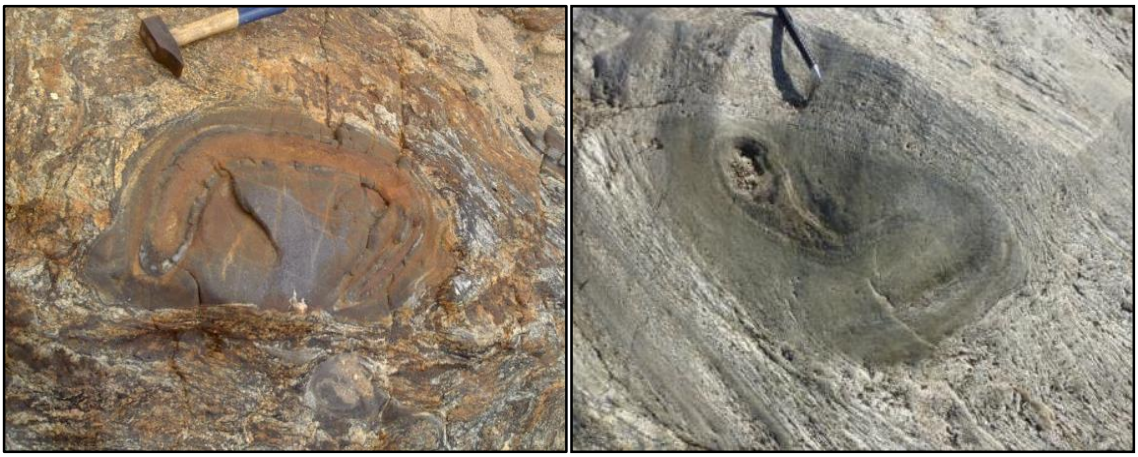

Fig. III. 27 – Field photographs showing rounded metagreywacke schollen containing folded calc-silicate nodules. A) P. 701 and B) P.439.

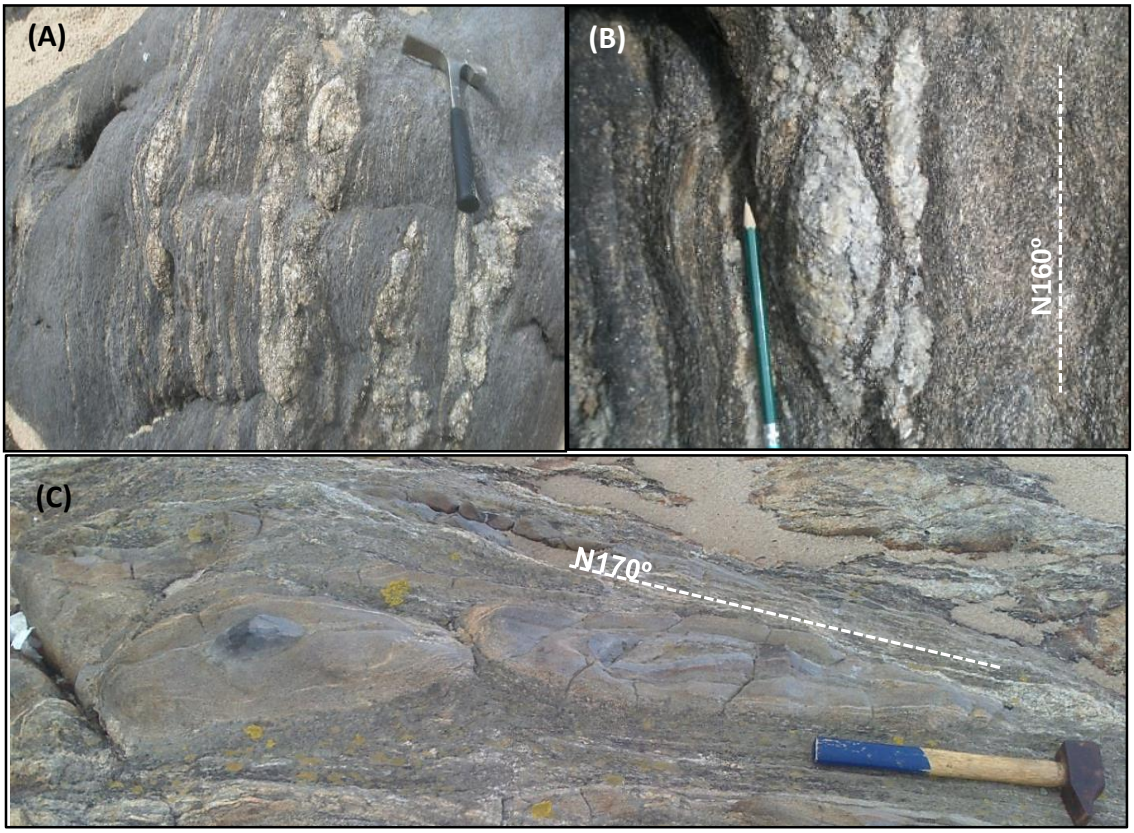

Fig. III. 28 - A and B) Boudinated leucosomes in residual melanosomes (P. 507 and 504); C) metagreywacke schollen showing shortening and amalgamation (P.710).

As referred before, the granitic rocks of MMC are anisotropic, with evidence of a foliation resulting from a magmatic flow, which is locally overlapped by a later foliation in ductile-brittle regime.

The anisotropy associated with magmatic flow is more or less penetrative, being marked by the orientation of K-feldspar megacrystals, pelitic xenoliths and dark schlieren that generally show preferred orientation striking NW-SE (Fig. III.29). However, in the granitic dykes, the orientation of the schlieren is parallel to the dyke's walls (Fig. III.13B).

In general, all the granitic rocks show signs of minor solid state deformation. However is notorious the existence of corridors of intense deformation, as is the case of Leça da Palmeira two-mica granite (sample VC45, see Fig.III.1) and Fornelo two-mica granites (samples FM30 and FM33, see Fig. III.1). In these areas, the foliation that developed in ductile-brittle regime caused the development of CS-like shear structures with orientation ~N120º (Fig. III 30A).

Aplite-pegmatite veins have sharp contacts with the migmatites and two-mica granites showing predominant striking N110º to N140º with peak concentration around N120º, 80º NE (Fig. III.30). Although the aplite-pegmatites show straight and sharp contacts with the wall rocks, internally they show evidences of a deformational regime during its emplacement. Folded layers (Fig. III.31) and deformed plagioclases are a common feature in these rocks (see chapter IV).

The described structural characteristics suggest that MMC structures are the result of two deformation phases, the first corresponding to the regional D_1 and the second correspond to the regional D_3. The migmatization is coeval with the last D_1 stages and continue during D_3 non-coaxial phase. The granite emplacement occurred under deformational regime related to the last regional D_3 deformation phase.

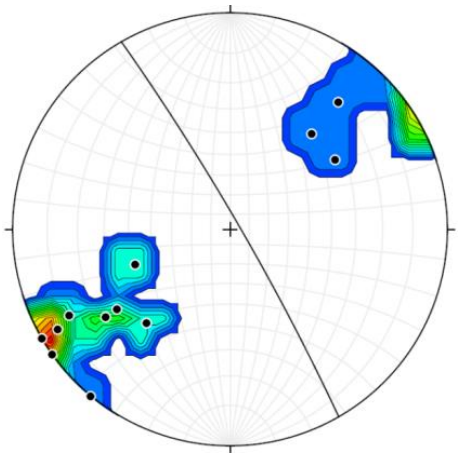

Fig. III. 29 - Density diagram of schlieren and xenoliths in two-mica granites showing concentration peak striking N150º, and variable dip.

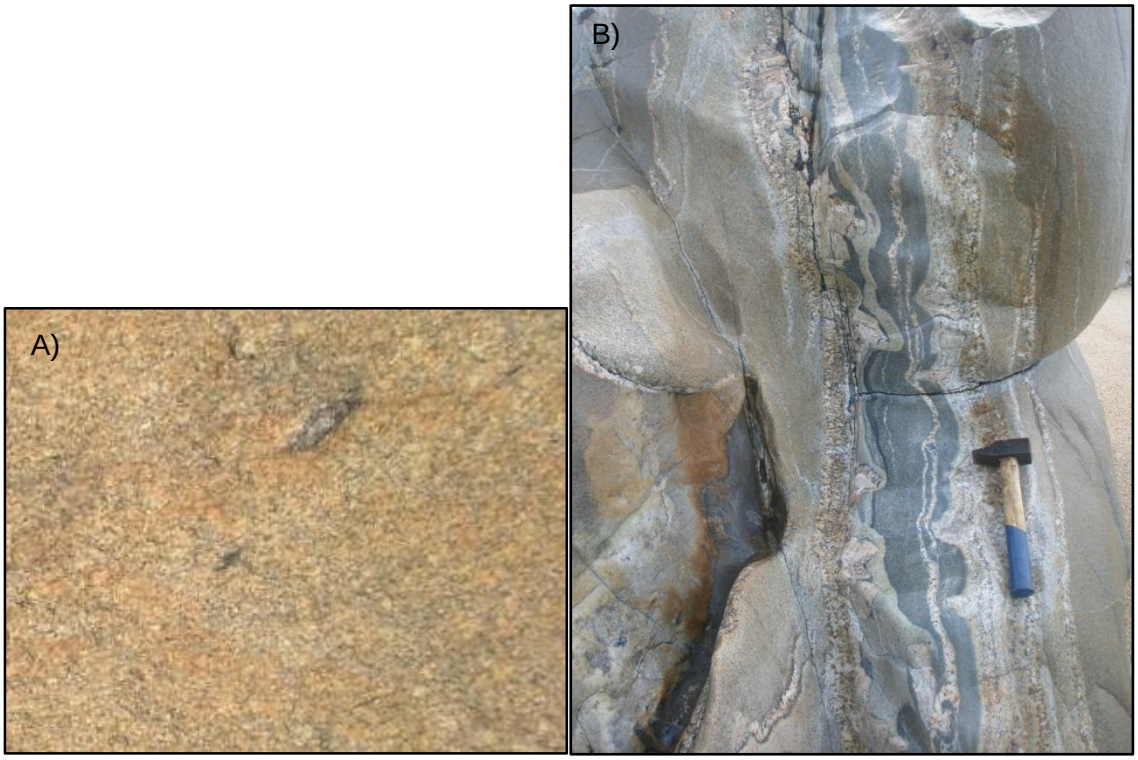

Fig. III. 30 – A) Granite showing ductile-brittle deformation.B) Internal structure in of an aplite-pegmatite vein.

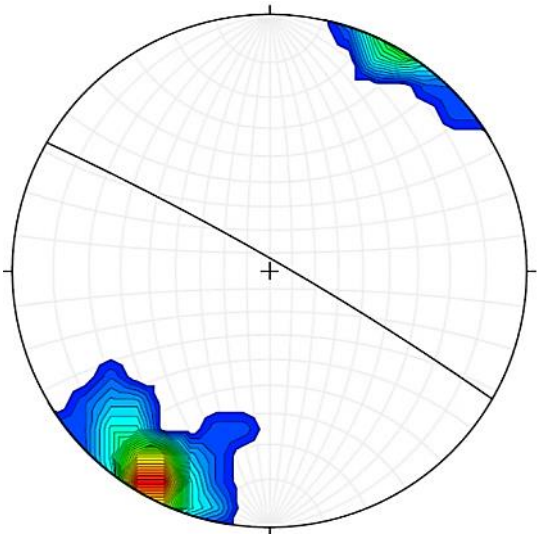

Fig. III. 31 - Density diagram of aplite-pegmatite veins in MMC, showing peak concentration N120º, 85º NE.

3.3. Sector 2 - Aguçadoura ↔ Fânzeres

Sector 2 is located to the SW of Douro-Beiras Shear Zone in the NE flank of Porto-Viseu metamorphic Belt. Localities like Laundos, Aguçadoura, Alvarelhos, and Fânzeres are situated in this Sector (Fig. III.32).

The field work to the N of Alvarelhos was hampered by the intense human activity and subsequent lack of outcrops as well as the state of alteration of the few existing outcrops. In the Fânzeres zone the access to fresh rocks was easier. 25 samples representative of the lithologies and metamorphic grade were collected.

Sector 2 covers metasediments of "Schist-Greywacke Complex – Beiras-Group" (Pereira *et al*. 1992) and consists of thick sequences of alternating shales and metagreywackes, occasionally interspersed with quartzites and metaconglomerates.

These metasediments contact with several granitic massifs that embody the core of the Porto-Viseu antiform like Stº André granite, Ermesinde granite, Barcelinhos granite, Póvoa granite, Porto granite, Fânzeres, Gondomar, and Pedregal granites (this terminology reflects the one used in the last published geological map; Pereira et al., 1992). There are several granite porphyries, especially situated in Alvarelhos, intrusive in the metasediments. To the W the metasedimentary sequence passes gradually to the MMC migmatites.

In this sector, gradations from weakly metamorphosed to strongly metamorphosed rocks can be seen. From the west towards the east the metamorphic grade varies in few kilometres (max 10 Km) from sillimanite-zone and staurolite/sillimanite-zone (adjacent to granites) passing to staurolite/almandine zone, to biotite-zone and finally to chlorite-zone. The description of lithologies will be taken from west to east highlighting the metamorphic grade of the different units.

From the Mindelo Migmatite Complex towards east, the outcrops are rare and intensely altered. However, it is possible to observe a gradual transition from migmatites to sillimanite-zone metasediments as it moves toward east. The transition zone is very heterogeneous showing zones where sporadic granites cut the metatexites passing gradually to zones where granites prevail although containing great amount of metatexitic xenoliths. Gradually, the metatexites disappear and sub-vertical layers of sillimanite-schists, metagreywackes and metaconglomerates occur (Fig. III.33). In Fânzeres the sillimanite occurs only in metasediments adjacent to the granitic intrusions.

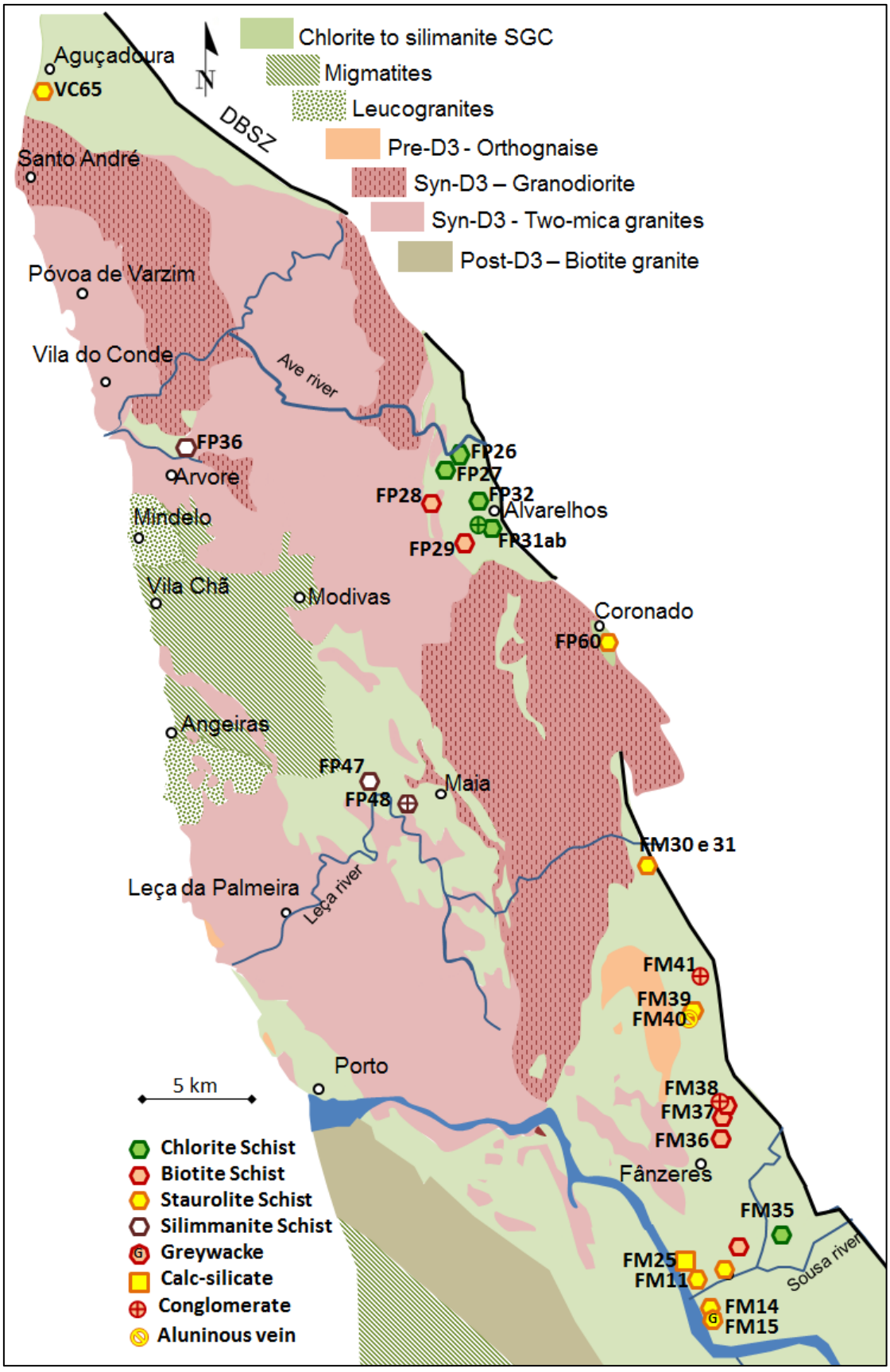

Fig. III. 32 – Geological sketch showing Sector 2 with representation of the sampling location and lithological type.

Fig. III. 33 – Metaconglomerate and sillimanite-schist near Maia (P. 704).

To the E, the sillimanitic rocks disappear (except near granites) and staurolite-bearing rocks crop out in a NNE-SSE range, between Aguçadoura and Fânzeres (Fig. III.32).

Staurolite-zone rocks unit is composed of mica-schists, metagreywacke and rare intercalations of calc-silicate rocks associated with the metagreywackes. Mica-schists are dominant and the metagreywacke/calc-silicate layers show centimetric thickness (Fig. III.34).

Mica-schists show granolepidoblastic texture and demarcation in quartz-feldspathic and micaceous domains with variable thickness. Staurolite porphyroblasts are abundant and can reach 5 cm in length along the longest axis. Staurolite porphyroblasts show an internal foliation. In most of them this internal foliation is oblique and truncated by the external foliation (S_n) that generally is anastomosed around staurolite porphyroblasts (Figs. III.35A, 35B and 35D). There are also lenticular quartz that resulted from metamorphic segregations that show the same relation with the main foliation as the staurolite porphyroblasts. Garnet porphyroblasts are less abundant than staurolite and some of them occur included in the larger staurolite crystals (Fig. III.35D).

There are folded quartzite layers showing axial plan parallel to S_n. These folds are symmetric and tight or isoclinal (Fig. III.36A). A later D_{n+1} deformation phase crenulated the S_n foliation and folded the quartz veins parallel to S_n. Both the crenulation and the folds are asymmetric (Figs. III.35B and 35C). The crenulation is not penetrative and

shows variable intensity. The staurolite-schists from Fânzeres show less intense and less penetrative crenulation than the staurolite-schists from Aguçadoura.

Locally, in the contact with the Paleozoic metasediments and associated with fault zones, there are dark layers of tourmalinites, mostly showing replacement of micas by tourmaline.

Locally, and restricted to bands of about 2 to 3m, large sillimanite/kyanite “veins” were developed, where the replacement of staurolite and the great size of the aluminosilicates are notoriuos (Fig. III. 36B).

From west towards east the dimension of staurolite porphyroblasts decreases till they disappear. The staurolite-schists are replaced by schists with biotite porphyroblasts in the biotite-zone (Fig. III.37). The dominant lithologies of this metamotphic zone are biotite-schists showing granolepidoblastic texture interbedded with metric metaconglomerates, whose size of clasts decreases towards the top (Fig. III.37B). These lithologies are composed of biotite, quartz, plagioclase and rare garnet. The structures are the same as the structures present in the staurolite-zone.

In the region of Alvarelhos – Fornelo several dykes of porphyritic granite intruded these metasediments leading to the development of tiny andalusite crystals in a small area around the intrusion.

Towards east the dimension of the biotite porphyroblasts decreases and the biotite-schist show a gradual transition to chlorite-schists, so to the chlorite-zone.

In the chlorite-zone the grey phyllites are the dominant lithology and they show a laminated texture with variable thickness from centimetric to metric (with a higher proportion of metapelites) (Fig. III. 38).

The lithologies mentioned above are interspersed by metaconglomerate layers with variable thickness (from 1 to 10 m). The metaconglomerates are composed of very coarse-grained quartz elongated grains, usually with dimensions between 1 and 3 cm in the greatest axis. The quartz grains are surrounded by white-mica films (Fig. III.39).

In Alvarelhos, in the top of the unit, close to the Carboniferous contact, a level of satin dark phyllites with kaolinite was found (Fig. III.38C). Couto (1993) refers the occurrence of the same type of lithology in the top of Montalto unit (SW of the Valongo anticline).

3.3.1. Structure

The geometry of the planar structures is similar in all metamorphic zones, since in all of them the overlap of three main ductile phases is evident.

The bedding is oriented N160º to N170º plunging to NE with high inclination. The main foliation (S_n) observed in the field is defined by the phyllosilicates and opaque minerals and varies from N160º to 200º. This cleavage is crenulated by a later deformation phase, which is also represented by asymmetric folded quartz veinlets parallel to S_n.

In the microstructural level it is possible to detect, in all metamorphic zones a previous foliation (S_{n-1}) which is preserved in quartzose bands and in the most protected regions adjacent to porphyroblasts, as well as inside the staurolite porphyroblasts.

The first phase generated a pervasive cleavage (S_n) which is dominant in this Sector. A later deformation (D_{n+1}) phase folded and reoriented and / or reactivated the earlier S_n foliation, which is revealed by the ubiquitous presence of asymmetric crenulation cleavage and mesoscopic folds.

Stereographic measurements of the principal foliation indicate two concentration peaks from N177º/87º E to N010º/62º E and N152º/82º E. The NW-SE (~N152º) peak occurs in metasediments that show intense crenulation and other features suggesting reorientation by the latter deformation phase (Fig. III.40).

Fig. III. 34 - Field photographs showing staurolite schist and metagreywacke layer (S0=N010º; 68º N).

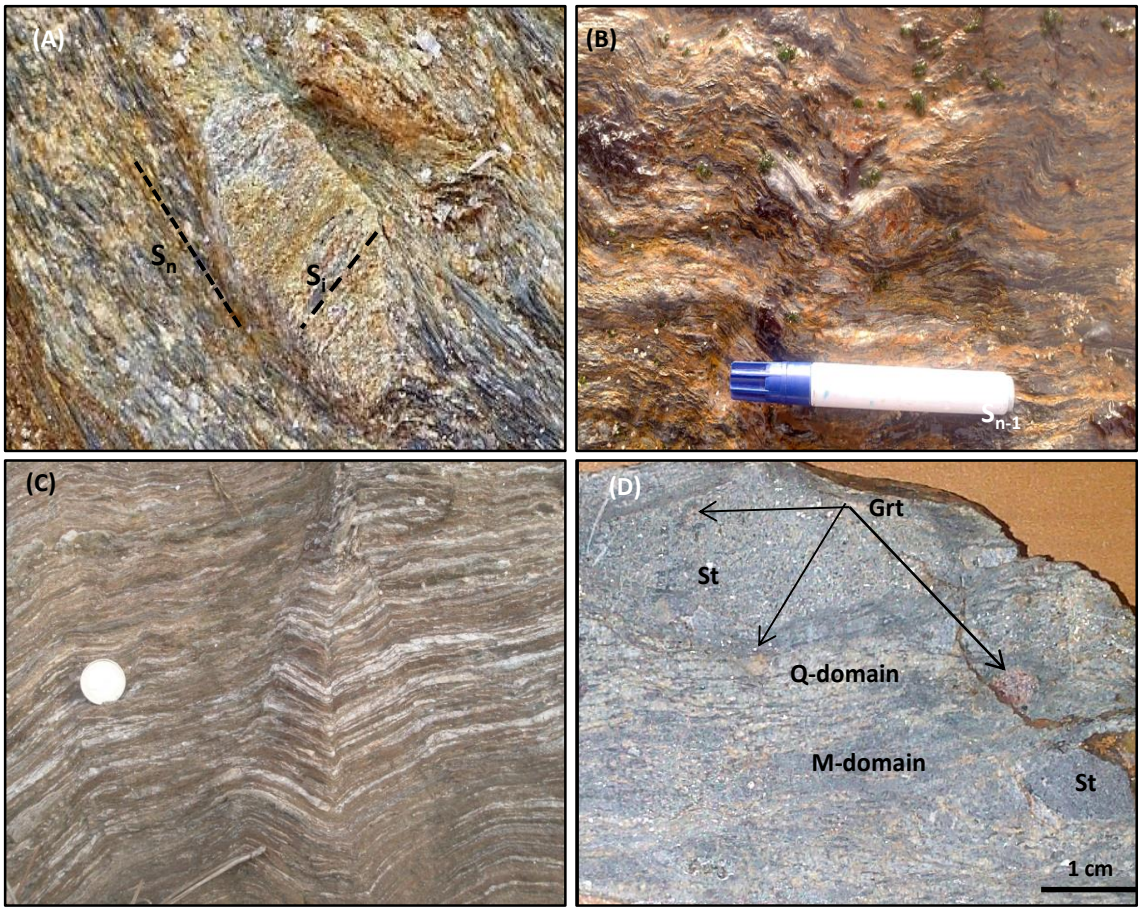

Fig. III. 35 – A) Staurolite-schists showing staurolites with major axis parallel to S_n. Staurolite porphyroblasts show internal foliation (Si) oblique and truncated by S_n (P. 454; vertical plane); B) Staurolite-schist from Aguçadoura showing crenulation cleavage affecting S_n (P.791; horizontal plane); C) Metamorphic segregation banding composed by quartzose and micaceous domains parallel to S_n foliation. The S_n foliation is crenulated by a later deformation phase (Vertical plan; P. 456); D) Staurolite-schist hand-specimen showing the micaceous and quartz-feldspathic domains, the staurolite porphyroblasts (St) and garnet (Grt) porphyroblasts dispersed in the matrix and also inserted in the staurolite.

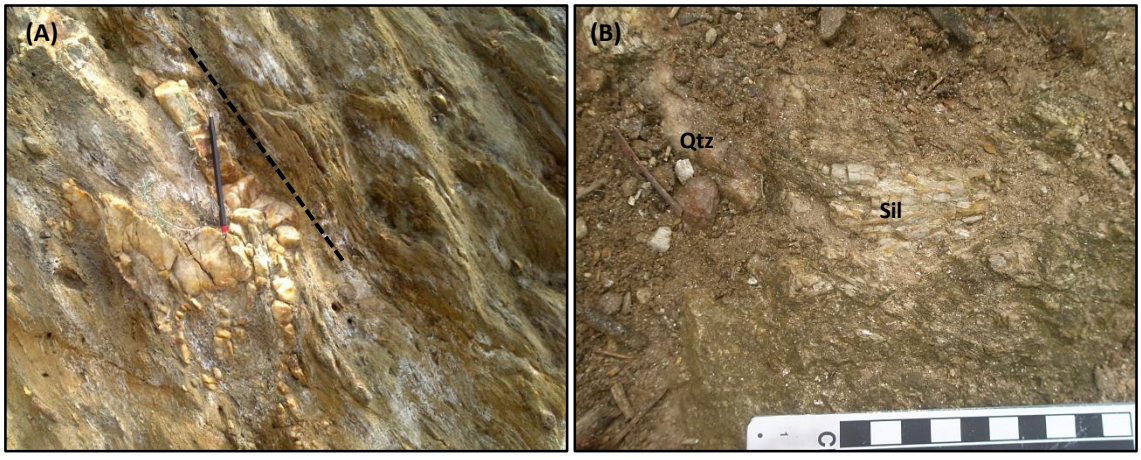

Fig. III. 36 – A) Folded quartzite showing axial plan parallel to S_n. B) Aluminosilicate “vein” in the staurolite-zone (P. 779).

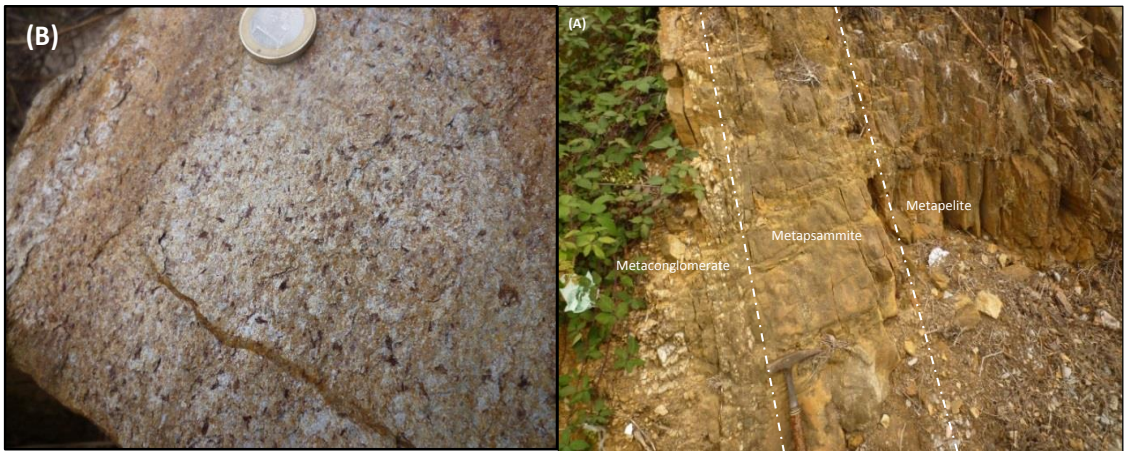

Fig. III. 37 – Field photographs showing aspects of biotite-zone. A) Biotite-schist showing biotite porphyroblasts (P.460); B) Normal sequence from metaconglomerate to metapelite.

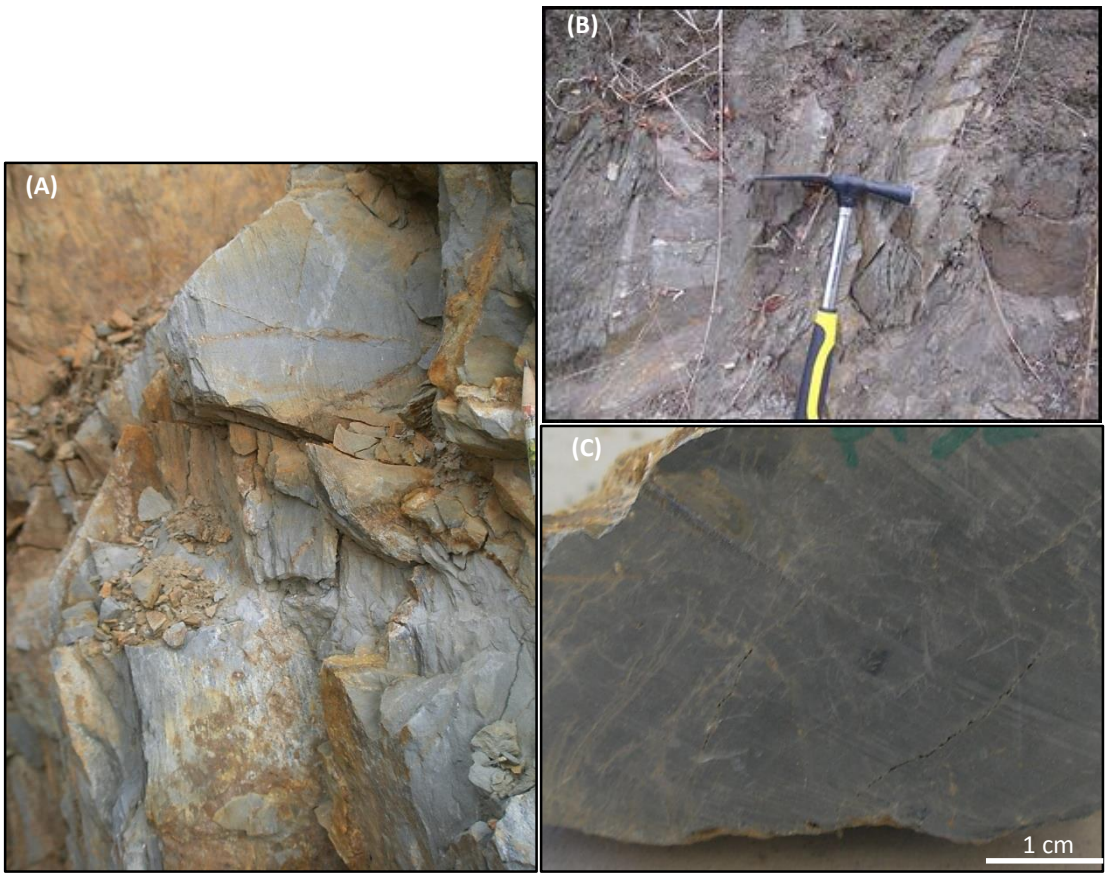

Fig. III. 38 – Field photographs showing aspects of chlorite-schists. A) Chlorite-schist showing crenulation (vertical plane; P.554). S_n= N5; 60 E; crenulation: N120º, 90º; B) Chlorite-schist alternating with metasiltite (P. 632; S_n = N155º, 80º NE e S0 = N169º, subvert.); C) Hand specimen of the satin dark phyllites level cropping out in the top of the chlorite-schists unit

Fig. III. 39 - A) Metaconglomerates from Gondomar (P. 784) showing elongated quartz clasts and mica around the clasts; B) Metaconglomerate hand specimen from Alvarelhos (P. 648)

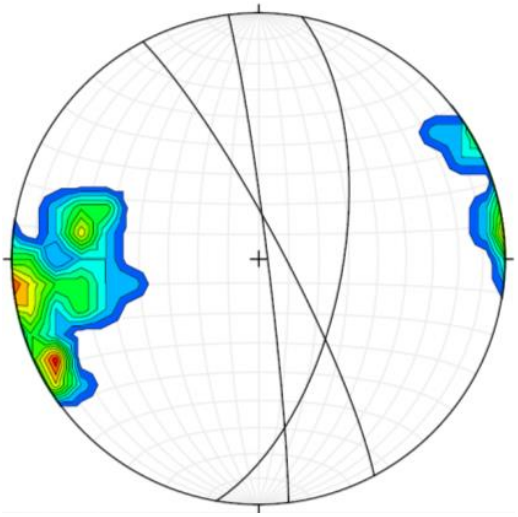

Fig. III. 40 - Density diagram to S_n poles in Sector 2. There are two concentration peaks. One varied from N177º/87º E to N010º/62ºE and the other is ~N152º/82º E. The NW-SE (~N152º) peak occurs in metasediments that show intense crenulation and other features suggesting reorientation by the latter deformation phase.

3.4. Synthesis

The field observation and sampling were done in an area of about 300 km^2. In this area metasediments and granitic rocks crop out. From west to east the metamorphic grade decreases rapidly from sillimanite-K-feldspar-zone, to sillimanite-zone, staurolite-zone biotite-zone and chlorite-zone. These observations are in agreement with previous studies in the Porto-Viseu Metamorphic Belt that refer a metamorphic field gradient

marked by condensed isograds parallel to the granites, varying in a short extension from chlorite-zone to sillimanite-zone (*e.g*. Schermerhorn, 1956; Oen, 1970; Reavy, 1989; Couto, 1993; Acciaioli, 1997; Valle Aguado *et al.,* 1993, 2005; Esteves *et al.,* 2006; Ribeiro, M.A*. et al*. 2008; Azevedo & Valle Aguado, 2013).

In Sector 1 there is great heterogeneity of lithologies and intricate relationship between them, which is a typical characteristic of the migmatitic zones (*e.g*. Brown, 2008; Sawyer, 2008). Granitic anatectic rocks predominate in this Sector, although in the coastal zone it is possible to observe extensive range of migmatites and minor granitic masses (metatexite zone – MZ). There are also metagreywackes and calc-silicate lithologies that remain as resisters within the more pelitic metatexites.

In the MZ patch-metatexites, banded-metatexites, diatexites, leucogranites and two-mica granites crop out (Fig. III.1).

The contacts between the granitic rocks and the metatexites are distinct: the passage from metatexites to leucogranites is gradual, while the contacts with diatexites and two-mica granites are abrupt. The latter contains huge fragments of metatexites and calc-silicate rocks within.

The metatexite zone shows interconnected leucosomes and granite dikes and veins that cut the metatexites. The younger veins, cutting all the referred lithologies are aplite-pegmatitic.

The lithostratigraphic sequence cropping out in the Sector 2, which consists of alternating shales and metagreywackes, is similar to the metasedimentary lithologies cropping out in Mindelo Migmatite Complex. However, the metagreywacke layers proportion and thickness seem to be higher in the last, while the quartzites and metaconglomerates are absent. The pelitic lithologies mark the gradational metamorphic grade from west to east with development of sillimanite immediately after the Migmatitic Zone and also in contact with the granitic bodies, followed by staurolite development in pelitic and psammitic lithologies. To the east the biotite and chlorite porphyroblasts are the markers of the metamorphic grade.

The principal foliation and fold axial plans in the Sector 1 and Sector 2 show predominant striking to NNE-SSW (varying from N170º to N025º). The folds related with this phase are isoclinal and tight.

These planar structures were affected by a latter deformation phase that crenulated the foliation in the more pelitic lithologies and folded the more competent layers. The folds

and other structural aspects related to these last phase (boudinage and amalgamation of schollen) are asymmetric and indicate non-coaxial strain for these last phase.

The migmatitic banding and mineral alignments that mark the foliation in the Sector 1 are parallel to the SGC main foliation present in Sector 2. Accumulation of leucosome occurs in the hinges of D_n folds and other dilatant sites, while the later asymmetric folds show uniform distribution of leucosome. This suggests that migmatization started in the end of the principal deformation phase (D_n) and continued during the last deformation phase (D_{n+1}).

The orientation of structures in the MMC (Sector 1) and in the SGC (Sector 2) seems to be related to the first Variscan ductile phase (D_1) later reoriented, reactivated and crenulated by the last deformation phase (D_3) that is simultaneous of the thermal peak and decreasing pressure conditions (Ribeiro M.A *et al*., 2008). In some segments the reorientation of structures is complete. The two-mica granites emplacement is syn-tectonic with D_3 since the orientation of magmatic foliations is the same as the main orientation of the Paleozoic structures. The dispersion of orientation in the structures of Sector 1 and Sector 2 could be related to the ante-Variscan deformation episode that folded the ante-Paleozoic metasediments (Couto, 1992; Ribeiro *et al*., 1993; Ponte & Gama Pereira, 2004; Romão, 2005; Romão *et al*., 2013).

CHAPTER IV – PETROGRAPHIC DESCRIPTION

"Every now and then one paints a picture that seems to have opened a door and serves as a stepping stone to other things."
Pablo Picasso

"A picture can tell a thousand words, but a few words can change its story."
Sebastyne Young

4.1. Sector 1 – Mindelo Migmatite Complex

4.1.1. Petrography of metatexites

Banded-metatexites predominates in the Metatexite Zone but locally patch-metatexites also crop out. Patch-metatexites are characterized by the predominance of melanosome over leucosome. Leucosomes consist of small scattered patches less than 10 mm, dispersed in the melanosome and generally surrounded by dark selvedgs (Fg.III.7). Banded-metatexites are characterized by the occurrence of aligned bands of melanosome intercalated with bands of leucosome of variable thickness and proportion (Fig.III.6).

Patch-metatexites melanosomes show granolepidoblastic texture with anastomosed foliation marked by aligned biotite and sillimanite. The foliation drapes around biotite + sillimanite aggregates that look like pseudomorphs after staurolite, although staurolite was never observed in this rocks (Fig. IV.1.1A).

In the banded-metatexites the melanosome minerals are aligned, forming continuous bands separated from each other by leucosomes, developing a gneissic foliation (Fig. IV.1.1B). The gneissic foliation is disturbed in folded metatexites (Fig. IV.1.1C).

Melanosomes are composed of biotite + sillimanite + garnet + quartz + plagioclase + cordierite ± secondary muscovite. Zircon, monazite, apatite, rutile and ilmenite are widespread accessory minerals.

Biotite arises either in elongated crystals oriented parallel to the bands or in smaller grains with random orientation (Fig. IV.1.2). Biotite crystals show xenomorphic textures and symplectitic intergrowths related with corrosion and melt forming reactions (Figs IV.1.2C and D).

Sillimanite can be fibrolitic, pseudomorphing biotite, or prismatic when associated with quartz (Fig. IV.1.3). It is mostly concentrated in melanosomes although also occurs as alternating strips, aligning parallel to the melanosome bands, within leucosomes. There are textural aspects that suggest replacement of sillimanite by cordierite (Fig. IV.1.3D).

Garnet is rare, xenomorphic and shows replacement coronas with cordierite + sillimanite + quartz (Fig. IV.1.4).

Most of the cordierite is located in the frontier between melanosome and leucosome, although also occurs within melanosomes. It is generally xenomorphic or pseudomorphic after biotite and is associated with biotite and quartz (Fig. IV.1.5). Quartz and plagioclase grains occurring in the melanosomes are xenomorphic and smaller than the ones occurring in the leucosomes.

Muscovite is essentially secondary, replacing biotite or plagioclase (Fig.IV.1.6).

Leucosomes from patch-metatexites show two distinct types: Type I leucosomes are composed of sillimanite + cordierite + quartz + plagioclase (Fig. IV.1.7). Type II leucosomes are composed of large crystals (magmatic) of quartz + plagioclase ± K-feldspar and contain fragments of Type I leucosome. K-feldspar is rare and always associated with plagioclase or in fine films around biotite crystals.

Leucosomes from banded-metatexites show large anhedral to subhedral crystals of quartz + plagioclase ± K feldspar. These large crystals include small grains of anhedral or rounded quartz, plagioclase, biotite and accessory minerals. Fragments of melanosome are entrained in the leucosome (Figs. IV.1.8 and IV.1.9).

Both patch-metatexites and banded-metatexites show several textures typical of partial melting (e. g. Sawyer, 2008a; Holness, 2008), either in leucosomes or in melanosomes, namely:

- Presence of peritectic cordierite (Fig. IV.1.5);
- Magmatic microstructures in leucosome crystals (Figs. IV.1.8, IV.1.9 and IV.1.12);
- Plagioclase, quartz and cuspate K-feldspar grain (Fig. IV.1.8);

- Magmatic rims on subsolidus cores of grains (*e.g.* magmatic rims of plagioclase$_2$ and K-feldspar enclosing anhedral remnant plagioclase$_1$ (Fig. IV.1.9);
- Quartz or K-feldspar films surrounding biotite grains (Fig. IV.1.10);
- Melt pools enclosing euhedral crystals which grew directly from the liquid (Fig. IV.1.11A).

K-feldspar is rare in metatexites (in some of them only it was detected by backscattered images, Fig. V.24). It is possible to find metatexites without any K-feldspar side by side with K-feldspar bearing metatexites less than 3 m away from each other. When it is present, K-feldspar includes all the other minerals in the assemblage, shows anhedral morphology and occurs both as product of biotite melting reaction (Fig. IV.1.10) and replacing plagioclase (Fig.IV.1.12). Textural evidence of plagioclase replacement by K-feldspar are widespread (Fig. IV.1.12), namely K-feldspar in cores of plagioclase crystal, plagioclase "inclusions" in K-feldspar which are in parallel continuity with plagioclase outside the K-feldspar and ghost myrmekites, i.e. myrmekites included in K-feldspar crystals (Collins, 2013).

It is noteworthy that the calc-silicate nodules adjacent to metatexites without K-feldspar show no replacement textures or mineralogy; however, those inserted in K-feldspar-bearing migmatites show local retrograde replacement (Sub-chapter III. 1.3.2.2.).

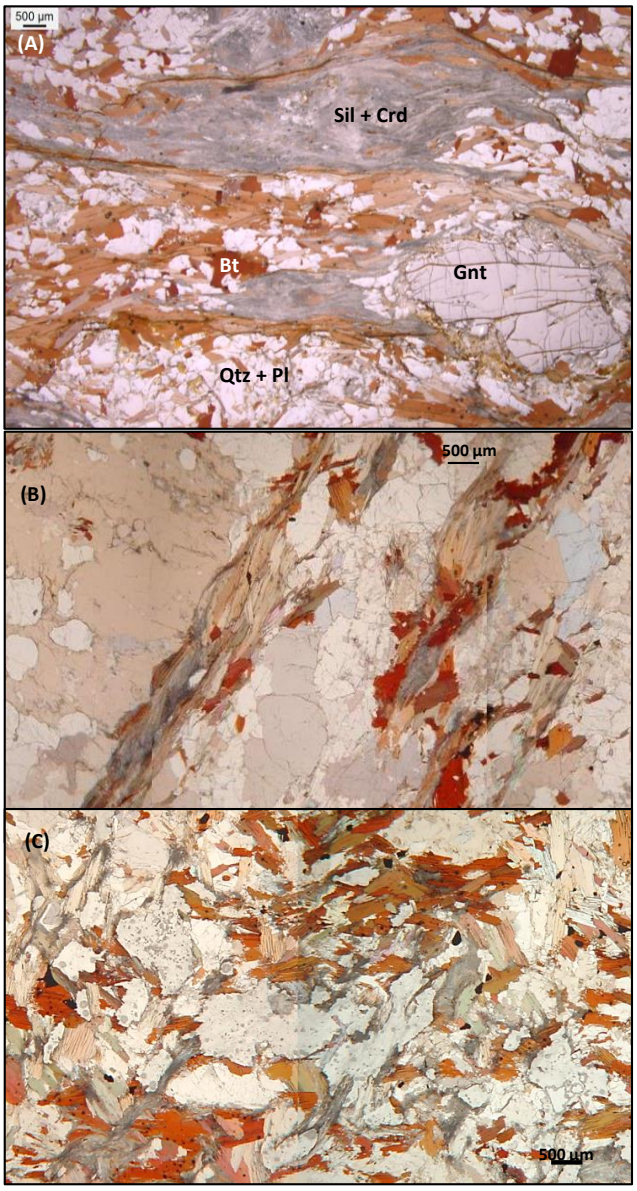

Fig. IV.1. 1– Photomicrographs of metatexites: A) Patch-metatexite B) Banded-metatexite showing migmatitic foliation marked by aligned alternating bands of melanosome and leucosome; C) Banded-metatexite showing folded foliation.

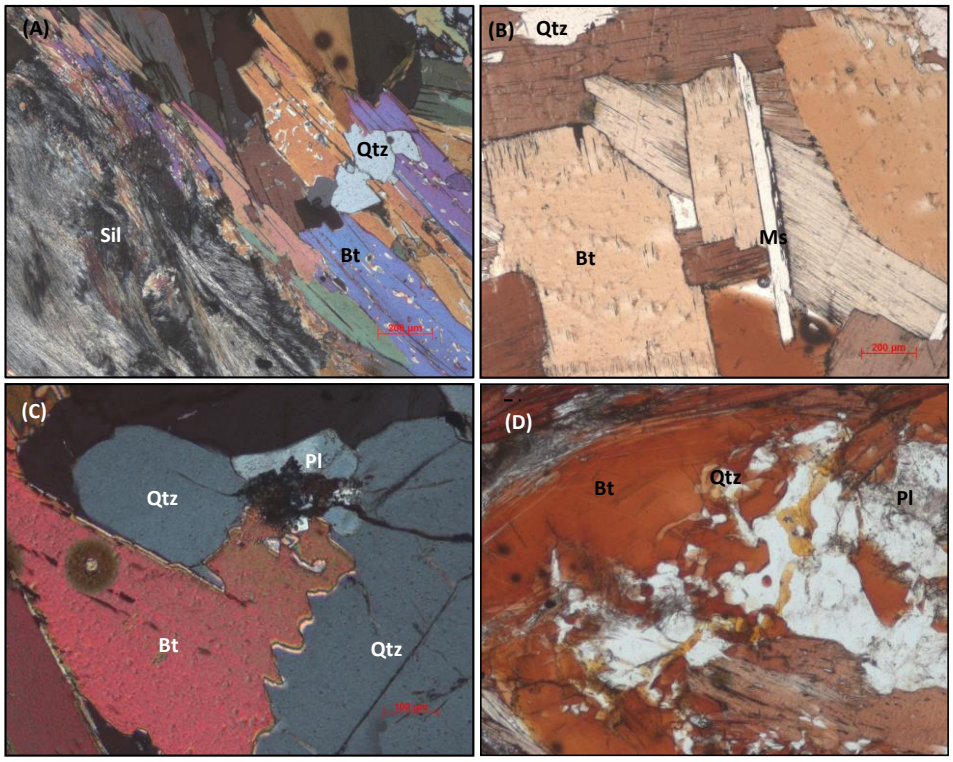

Fig. IV.1. 2– Photomicrographs showing some aspects of melanosomes. A) Melanosome showing aligned biotite and sillimanite (CPL); B) Melanosome band showing random biotite aggregates (PPL); C) Irregular border of biotite due to corrosion in contact with quartz (CPL); D) Biotite symplectitic with quartz adjacent to plagioclase (PPL).

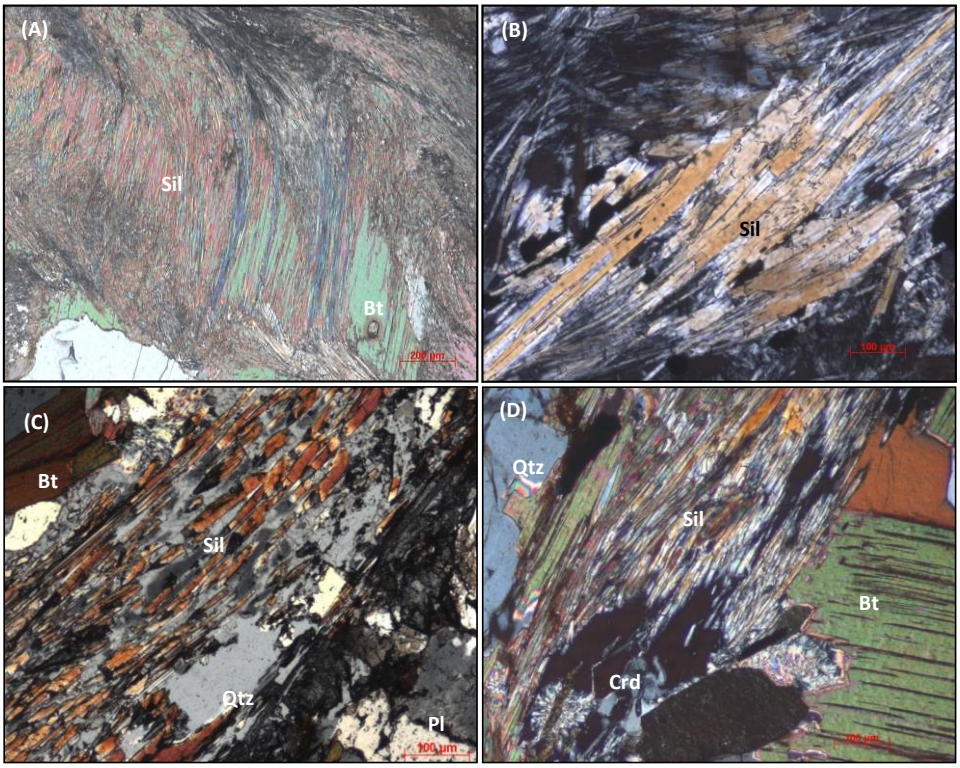

Fig. IV.1. 3 – Photomicrographs showing aspects of sillimanite. A) Fibrolitic sillimanite replacing biotite in the melanosome (PPL); B) Prismatic sillimanite in the melanosome (CPL); C) Sillimanite inserted in large quartz crystal in the leucosome (CPL). D) Cordierite replacing sillimanite in the melanosome (CPL).

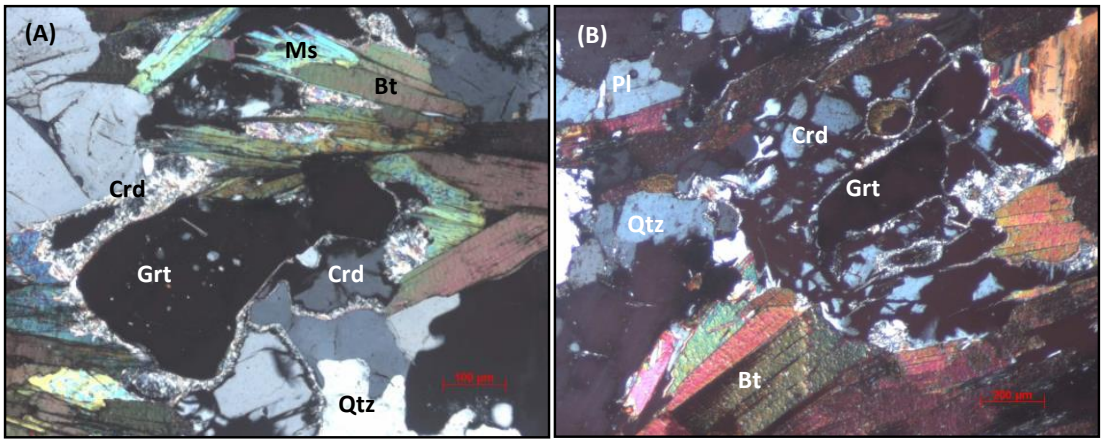

Fig. IV.1. 4 - Photomicrographs showing aspects of garnet. A) Garnet with small quartz inclusions and a tiny cordierite corona (CPL); B) Residual garnet crystal surrounded by cordierite and quartz (CPL).

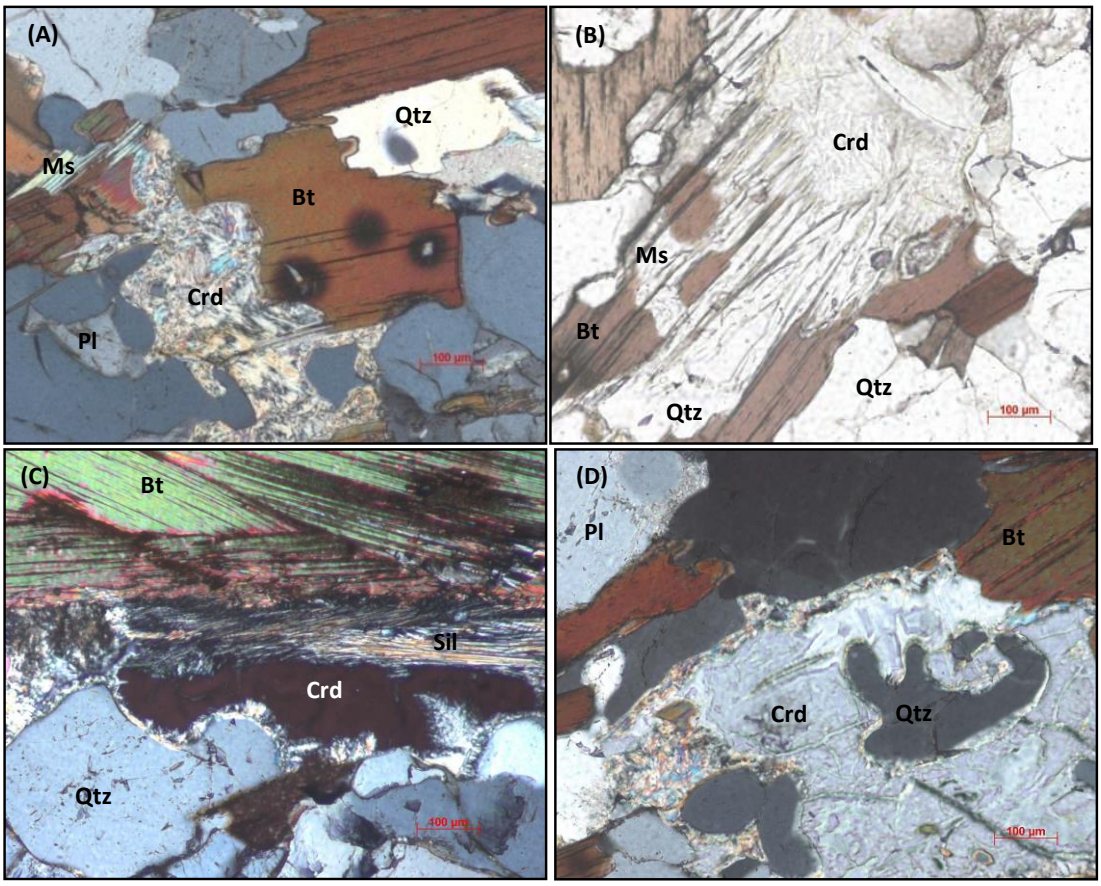

Fig. IV.1. 5 – Photomicrographs showing aspects of cordierite. A) Cordierite after biotite inserted in the leucosome (CPL). B) Cordierite and muscovite after biotite in melanosome (PPL); C) Cordierite between melanosome layer and leucosome (CPL); D) Cordierite replacing biotite and quartz and containing xenomorphic quartz inclusions (CPL).

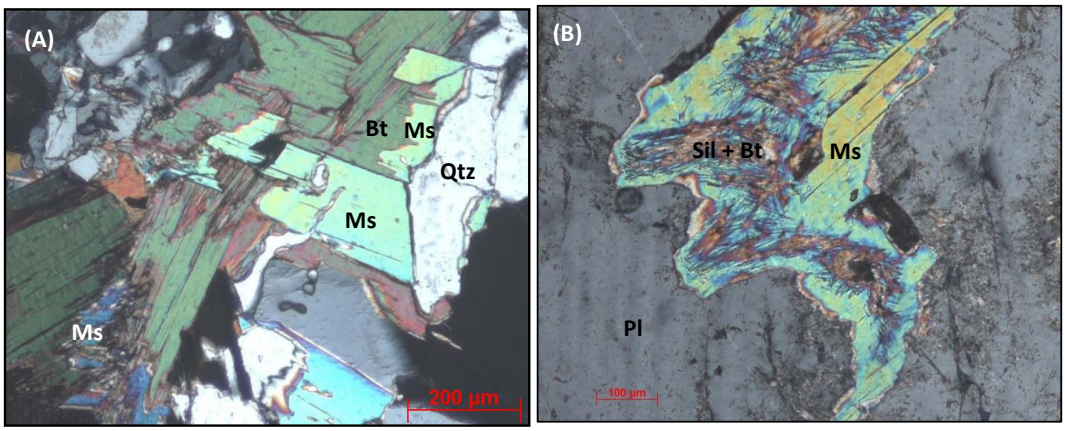

Fig. IV.1. 6 - Photomicrographs showing some aspects of biotite partial replacement by muscovite: A) in the melanosome (CPL) and B) in the leucosome (CPL).

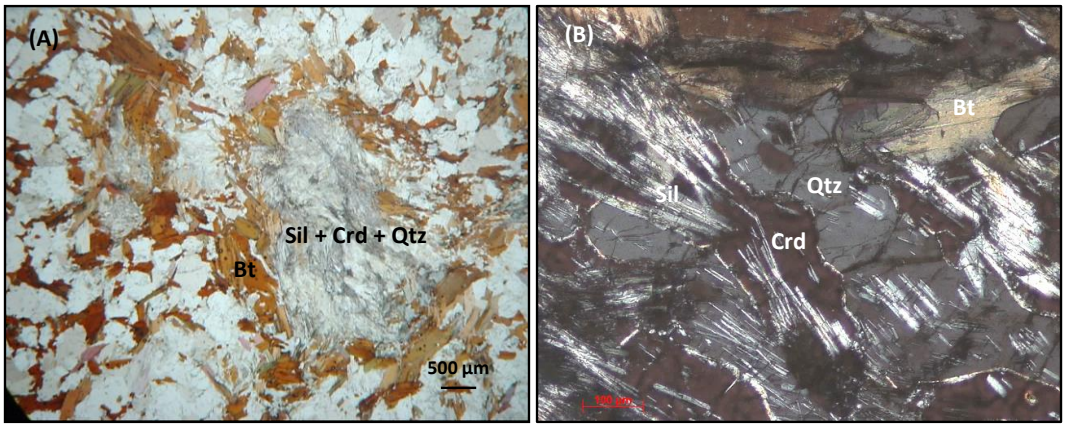

Fig. IV.1. 7 - Photomicrograph showing textural aspects of patch-metatexites: A) leucosome composed of sillimanite + cordierite + quartz surrounded by biotite selvedge (PPL); B) Detail of previous image.

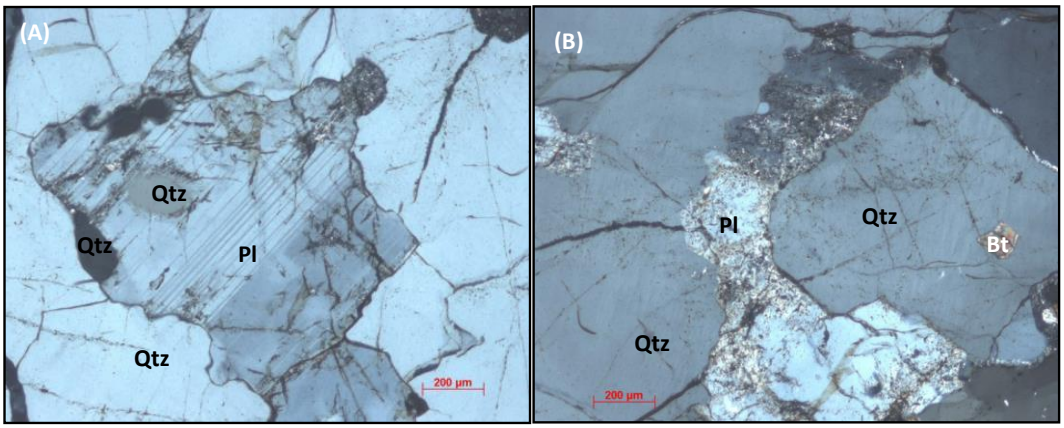

Fig. IV.1. 8 – Photomicrographs showing aspects of banded-metatexites leucosomes. A) Xenomorphic plagioclase inserted in large quartz crystal and containing quartz round inclusions (CPL); B) Cuspate plagioclase between quartz crystals(CPL).

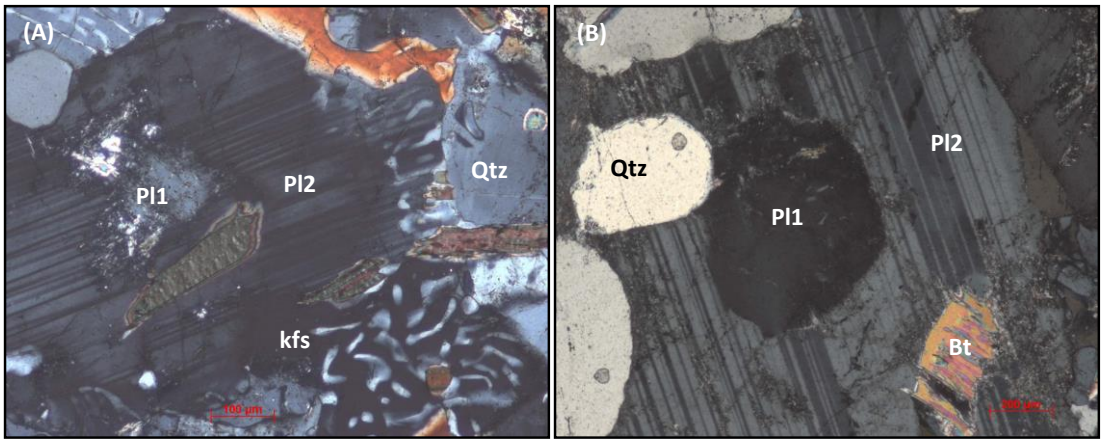

Fig. IV.1. 9 - Photomicrographs showing aspects indicative of melting reactions: A) Residual biotite and plagioclase (Pl_1) inside neo-formed plagioclase (Pl_2) and vermicular intergrowths of quartz and feldspar nucleated on plagioclase; B) plagioclase (Pl_1), quartz and biotite relicts inserted in neo-formed plagioclase larger crystal (Pl_2); (Photos in CPL).

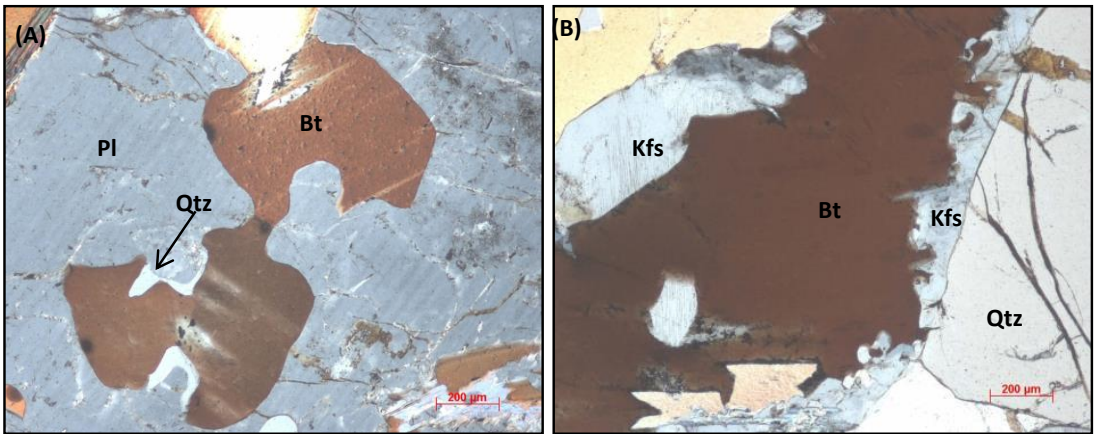

Fig. IV.1. 10- Photomicrographs showing aspects indicative of melting reactions: A) Xenomorphic biotite incorporated in large plagioclase crystal. Biotite shows a fine quartz film in the contact with plagioclase; B) Xenomorphic biotite with a K-feldspar fine film in contact with quartz; (Photos in CPL).

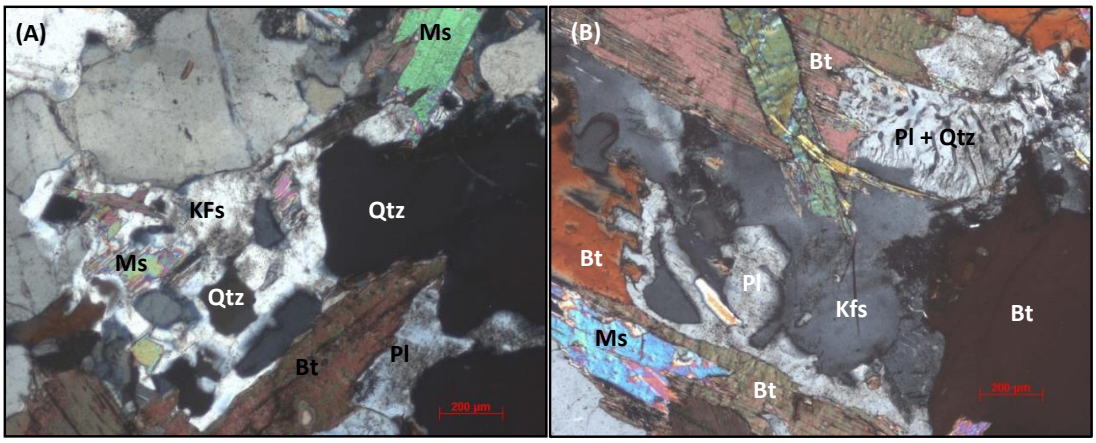

Fig. IV.1. 11 - Photomicrographs showing textural aspects indicative of melting reactions. A) Melt pool defined by feldspar enclosing subhedral quartz crystals; B) Plagioclase + K-feldspar + biotite complex intergrowths and myrmekites replacing biotite; (Photos in CPL).

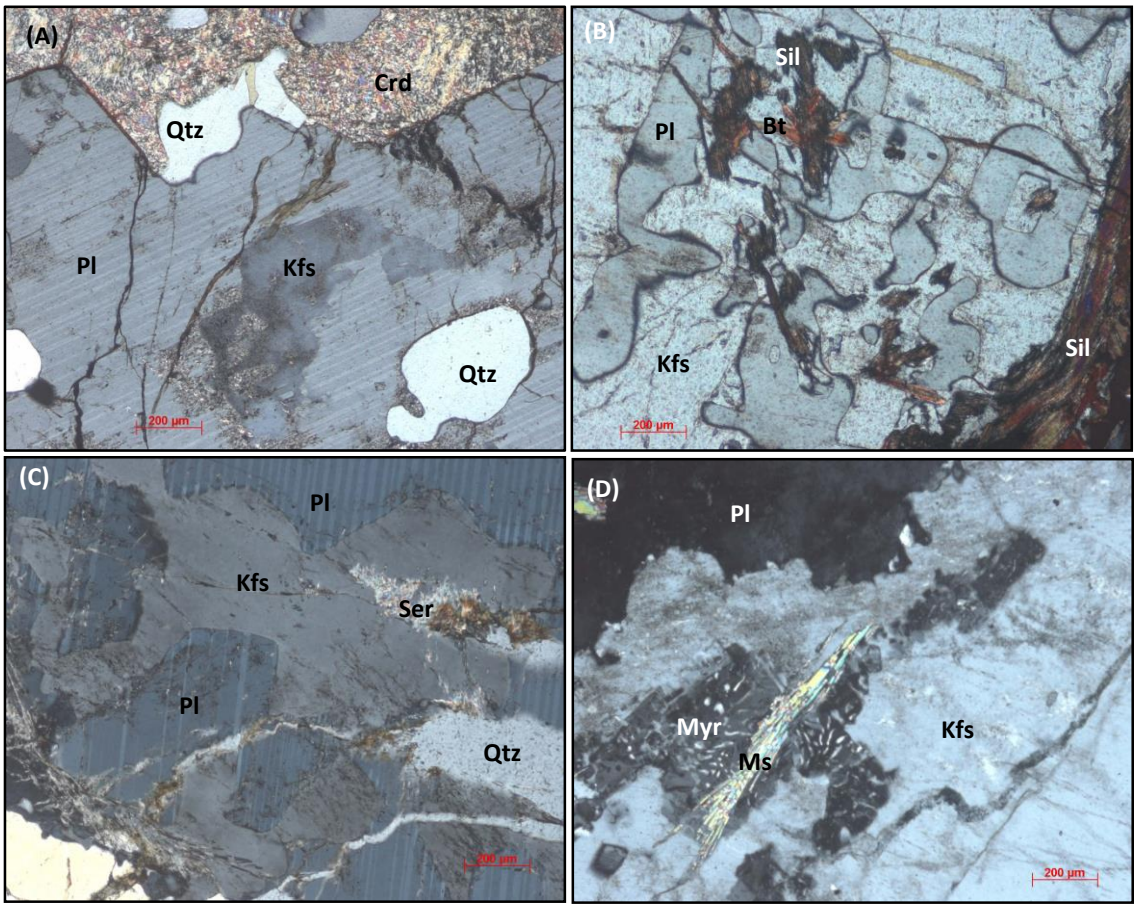

Fig. IV.1. 12 - Photomicrographs showing textural evidence of plagioclase replacement by K-feldspar. A) Incipient development of K-feldspar in the core of plagioclase; B) Plagioclase "inclusions" in K-feldspar which are in optical continuity; C) Plagioclase inclusion in K-feldspar which are in optical continuity with plagioclase outside the K-feldspar. D) Ghost myrmekite associated with muscovite within K-feldspar; (Photos in CPL).

4.1.2. Petrography of metagreywackes and calc-silicate nodules

As referred in the sub-chapter 3.2.2., dispersed in the Metatexite Zone there are dark metagreywacke layers containing calc-silicate nodules that remain as resisters within the pelitic-metatexites.

M**etagreywackes** show granoblastic texture with discrete and aligned biotite dispersed in a quartz-feldspathic matrix (Fig. IV.1.13). The mineral association is biotite + oligoclase + quartz + ilmenite ± almandine.

Where biotite is abundant the microstructure is dominated by biotite. Owing to the dominance of the mica {001} planes, some of the quartz and plagioclase grains tend to be elongate parallel to the foliation marked by the mica grains (Fig. IV.1.14A). In the samples where the quartz-feldspathic matrix prevails over the biotite, the texture is

more granoblastic, with polygonal aggregates, although most of the boundaries between quartz and oligoclase crystals are curved (Fig. IV.1.14B). Some of the plagioclase crystals show small rounded quartz inclusions (Fig. IV.1.14C). Garnet is rare and xenomorphic, randomly dispersed in the matrix (Fig. IV.1.14D).The polygonal aggregates and the accentuated curved boundaries between quartz and plagioclase is indicative of the high temperature underwent by these rocks.

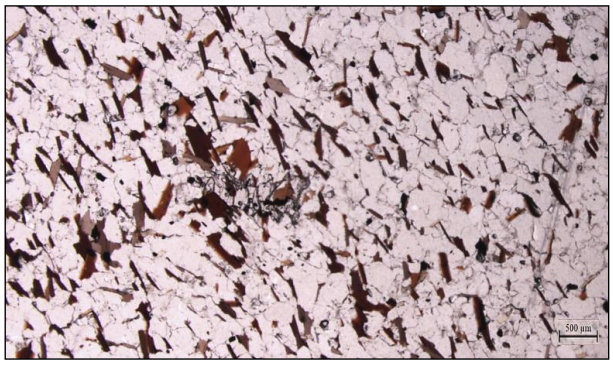

Fig. IV.1. 13 – A) Photomicrograph showing general aspects of the metagreywacke resisters (PPL).

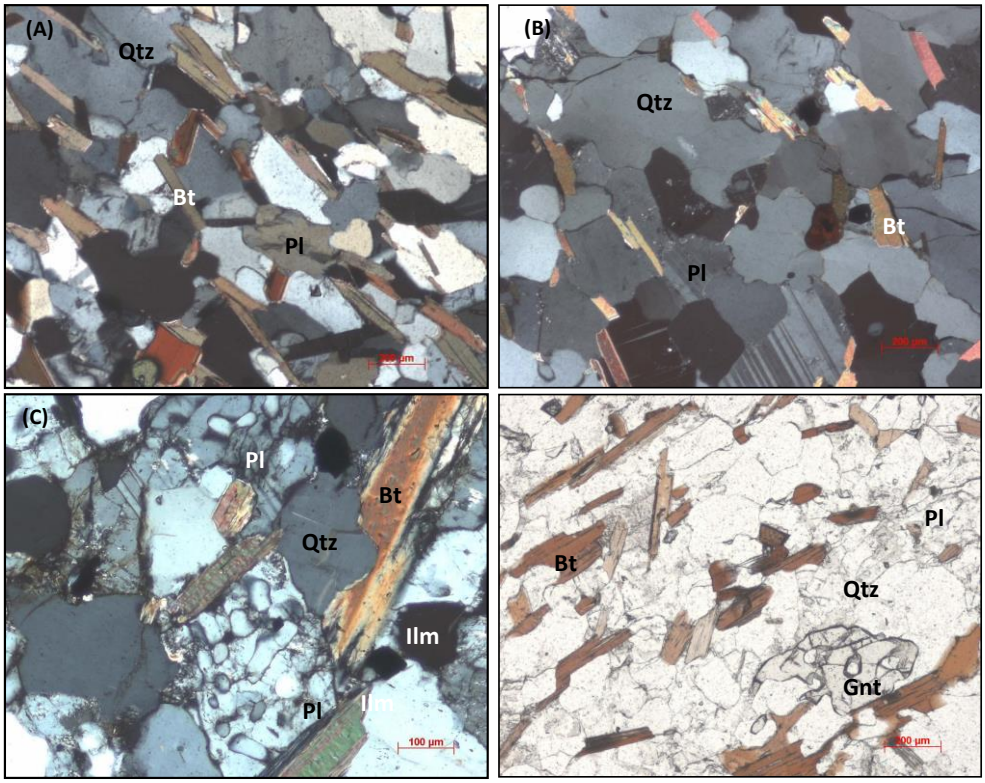

Fig. IV.1. 14 - Photomicrographs showing textural aspects of metagreywackes: A) Aligned biotite within the quartz-feldspathic matrix (CPL); B) Aggregate of quartz, plagioclase and biotite. (CPL). C) Plagioclase showing inclusions of rounded quartz; D) Xenomorphic garnet crystal within the quartz-feldspathic matrix (PPL).

C**alc-silicate nodules** show fine-grained granoblastic texture. Poikiloblasts of pyroxene, garnet and amphibole develop in a matrix consisting of plagioclase and quartz. Titanite, zircon, apatite, allanite and sulphides occur as accessory minerals (Fig. IV.1.15).

The calc-silicate nodules present two zones (eventually three zones) with the same texture but different mineralogy: a core-zone with diopside + grossular + plagioclase + quartz + sphene + allanite + sulfides and an outer-zone showing the same paragenesis except for the absence of diopside and instead, occurrence of hornblende. Some of the calc-silicate nodules show biotite in the most external part of the outer-zone, instead of hornblende (Figs. IV.1.15 to IV.1.19).

In the interface between the core-zone and the outer-zone diopside and hornblende develop in association, generally parallel to the direction of zoning (Fig. IV.1.17). However there is no evidence of retrograde replacement of diopside by hornblende. There are no replacement coronas and no replacement of diopside in the cleavages or fractures. Diopside never occurs in the outer-zone and hornblende is absent in the core-zone. Thus, this mineralogical boundary is the result of a side-by-side growth and not the result of later replacement. A similar relationship occurs between amphibole and biotite in the external part of the outer-zone, were occurs instead of amphibole.

Diopside porphyroblasts show poikilitic texture with rounded quartz and plagioclase inclusions, smaller than the same minerals crystals of the surrounding matrix (Fig. IV.1.16A). Locally it occurs in polygonal clusters with triple junctions (Fig. IV.1.16B). There are diopside, garnet and plagioclase associations that resemble a relationship host/inclusion. However, this type of association is the result of interpenetrative contacts between the crystals, since it can be observed minerals that look like both host and inclusion, i.e., the cutting angle of the irregular crystals and the perspective in two-dimensions produced what can be called "false inclusions". The only true inclusions in these minerals are quartz and plagioclase rounded crystals.

Amphibole, like diopside, is poikilitic and develops in the interstitial space between the quartz-feldspathic matrix (in association with garnet, titanite, plagioclase and allanite) (Fig. IV.1.17 and IV.1.18A).

Biotite occurs in the border of the calc-silicate nodules outer-zone, adjacent to the contact with the surrounding metagreywackes. It shows a poikiloblastic texture, mimetizing the skeletal texture of hornblende (Fig. IV.1.18B). The morphology of this biotite is quite different from that which occurs in the metagreywackes. Here is skeletal,

filling spaces between the quartz and the plagioclase of the matrix whereas in metagreywackes is always idiomorphic (compare Fig. IV.1.14 with Fig. IV.1.18B).

Garnet is poikilitic or even skeletal with inclusions of quartz and plagioclase and shows an interstitial relationship with the quartz-feldspathic matrix (Fig. IV.1.18A).

Plagioclase shows two distinct textures: (i) idiomorphic, fine-grained, forming polygonal aggregates (Fig. IV.1.19A) and (ii) slightly coarser grained, poikilitic, with lobate boundaries (Fig. IV.1.19B).

Quartz is abundant, although with variation in the modal proportion. It shows medium to fine-grain, lobate boundaries and polygonal clusters characteristic of static recrystallization (Fig. IV.1.19). Quartz inclusions in clinopyroxene, amphibole, garnet and plagioclase are rounded or irregular.

Sphene is abundant and distributed in the matrix both in the core- and in the outer-zone (Fig. IV.1.19B).

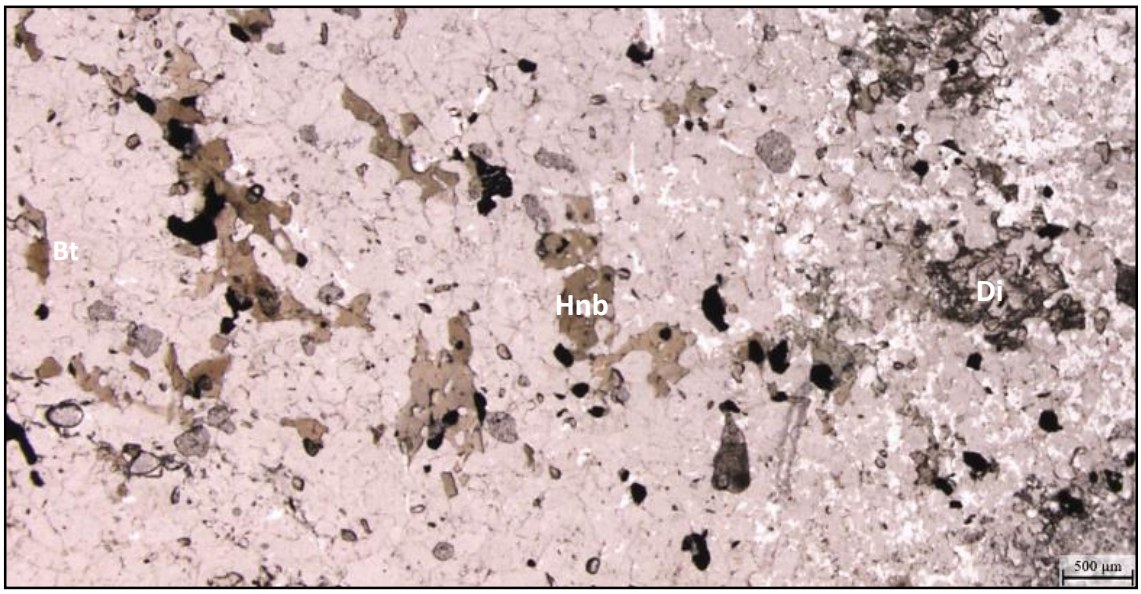

Fig. IV.1. 15 - Photomicrographs on the magnifying glass of calc-silicate nodule showing core-zone with diopside (right) and outer-zone with hornblende (left) (PPL).

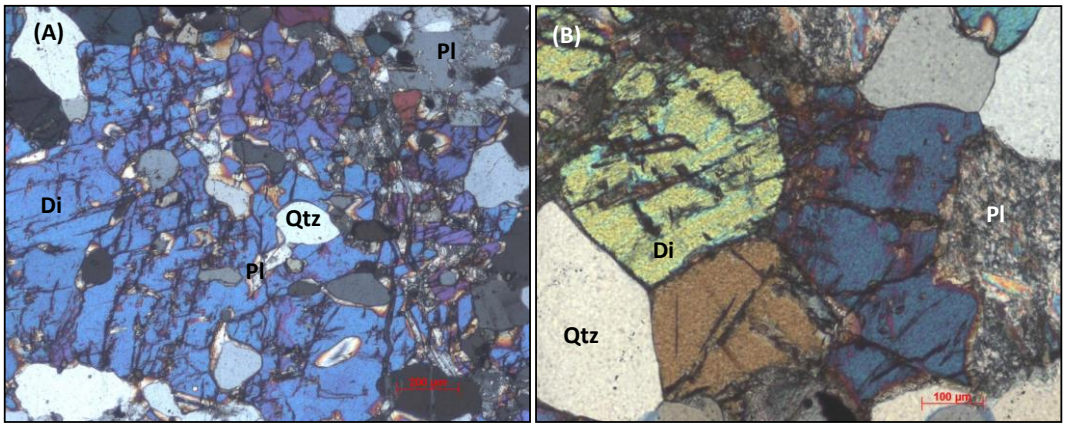

Fig. IV.1. 16 – Photomicrographs of calc-silicate nodules core-zone. A) Diopside showing poikiloblastic texture with quartz and plagioclase rounded to sub-rounded inclusions (CPL); B) Polygonal aggregate of diopside (CPL).

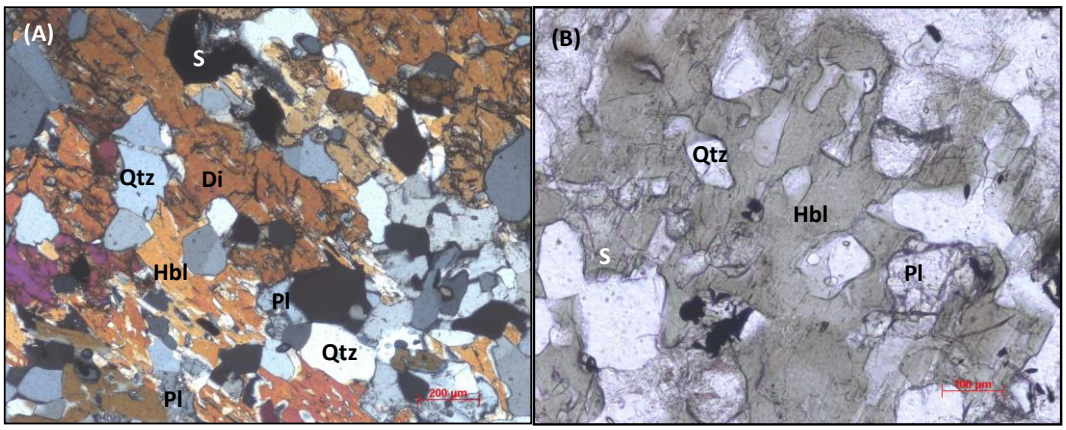

Fig. IV.1. 17 - A) Contact between diopside and hornblende in the boundary between core- and outer-zones (CPL). B) Hornblende crystal with plagioclase and quartz inclusions (PPL).

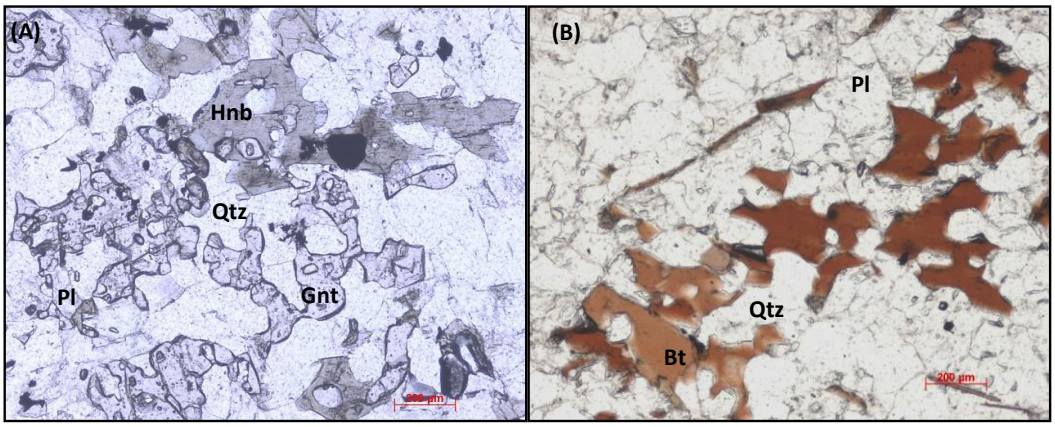

Fig. IV.1. 18 – Photomicrographs of calc-silicate nodules outer-zone: A) Skeletal hornblende and garnet crystals within the quartz-feldspathic matrix (PPL); B) Skeletal biotite in the border of the outer-zone (PPL).

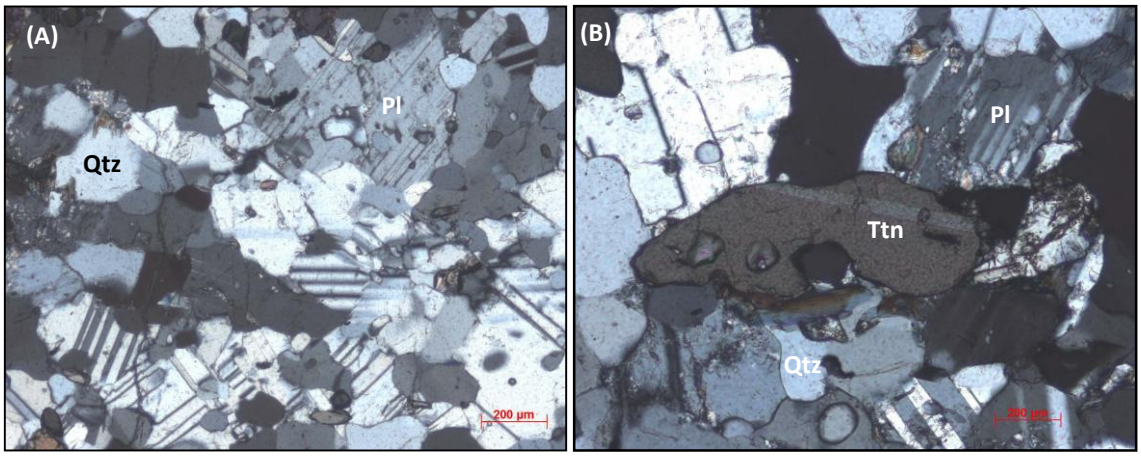

Fig. IV.1. 19 – Photomicrographs of calc-silicate nodules showing aspects of the quartz-feldspathic matrix. A) polygonal aggregate of idiomorphic plagioclase and quartz (CPL); B) Large titanite crystal within the quartz-feldspathic matrix (CPL).

4.1.2.1. Retrograde processes

Locally the metagreywacke and calc-silicate resisters show mineralogy and texture related to retrograde processes. Two types of alteration occur: in Type I the silica content is apparently unchanged and in Type II the silica content is considerably increased.

Type I retrograde process occur in calc-silicate and metagreywacke resisters situated in the vicinity of K-feldspar bearing metatexites. In these rocks plagioclase is replaced by epidote and clinozoisite in the core-zone and by sericite in the outer-zone (Figs.IV.1.20A, B and E).Diopside is replaced by actinolite (Fig.IV.1.20C) and some of the hornblende is replaced by chlorite (Fig. IV.1.20D). There are also fractures filled with epidote minerals (Fig. IV.1.20F). The metagreywackes surrounding these calc-silicate nodules do not show accentuated replacement textures. It is important to note that nodules almost completely altered, such as those described herein, and nodules without significant retrograde paragenesis, can be found at a distance of 3 meters from each other. Moreover, the altered nodules are located within K-feldspar bearing metatexites, while those with no significant changes are located within migmatites without K-feldspar in its mineral composition.

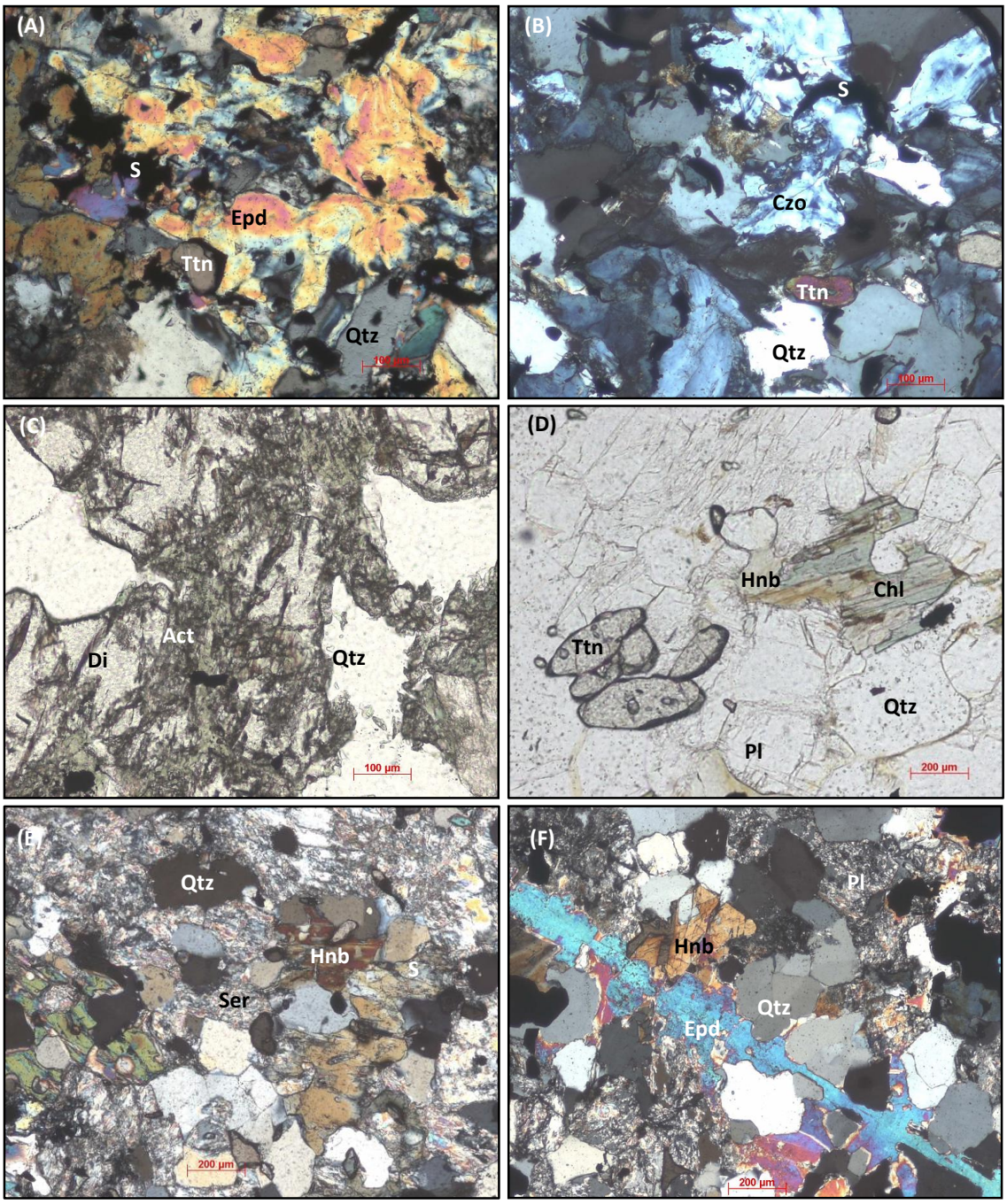

Fig. IV.1. 20 - Photomicrographs of calc-silicate nodules showing aspects of Type I retrograde alteration. A and B) Epidote minerals replacing anorthite in the core-zone (CPL); C) Actinolite replacing diopside (PPL); D) Chlorite replacing hornblende (PPL); E) Sericite replacing plagioclase in the outer-zone (CPL). E) Fracture filled with epidote (CPL).

Type II retrograde process occurs in calc-silicate and metagreywacke resisters that show sharp quartz-bands where large quartz crystals develop that include the calc-silicate paragenesis (Figs.IV.1.21, 1.22A). In the more calcic core-zone, besides quartz there are also retrograde large calcite crystals that enclose the other minerals (Fig.

IV.1.22B). The calc-silicate minerals included in the calcite and quartz bands show retrograde features. Plagioclase is almost totally replaced by clinozoisite and sericite in the core-zone and by muscovite in the outer-zone (Fig.IV.1.22). Prehnite and chlorite replace garnet and actinolite replaces diopside (Fig. IV.1.22).The metagreywackes also show quartz-rich bands, where chlorite after biotite and sericite after plagioclase occur. The alteration bands in the metagreywackes are specially situated in the frontier between the calc-silicate nodules and the metagreywackes. It is possible to see, in the same thin section, bands of completely retrograde paragenesis and bands where the biotite and the plagioclase have no alteration features (Fig.IV.1.23).

Both types of retrograde processes are local: there are samples that do not show any type of alteration, most of them show only slightly signs of retrograde alteration, and locally there is intense retrograde paragenesis. This suggests that the retrograde process is specially related to fluid infiltration and not with retrograde regional metamorphism.

Fig. IV.1. 21 - Panoramic of the sample showing Type II retrograde alteration. CZ – Core-zone; OZ – outer-zone; GWK – metagreywacke; A – crosscutting bands almost totally composed of large quartz crystals; B – large calcite crystals enclosing all the core-zone paragenesis; C – contact between quartz band and metagreywacke showing retrograde alteration of biotite and plagioclase; D – metagreywacke without retrograde alteration.

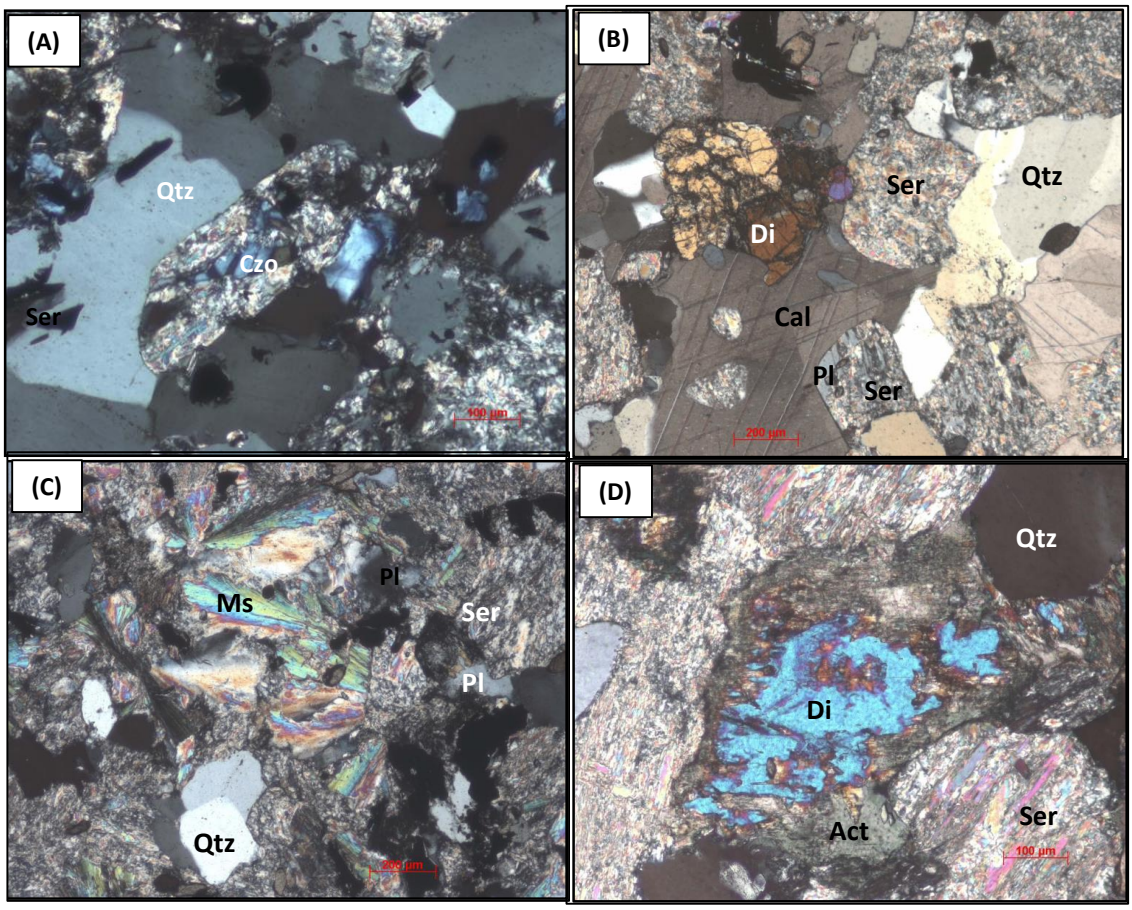

Fig. IV.1. 22 - Photomicrographs of calc-silicate nodules showing Type II retrograde alteration. A) Clinozoisite and sericite replacing plagioclase within the quartz-band; (CPL); B) Calcite crystals including diopside and sericite after plagioclase (CPL); C) Muscovite and sericite after plagioclase in the outer-zone (CPL); D) Diopside relict after actinolite replacement and surrounded by sericite after plagioclase (CPL).

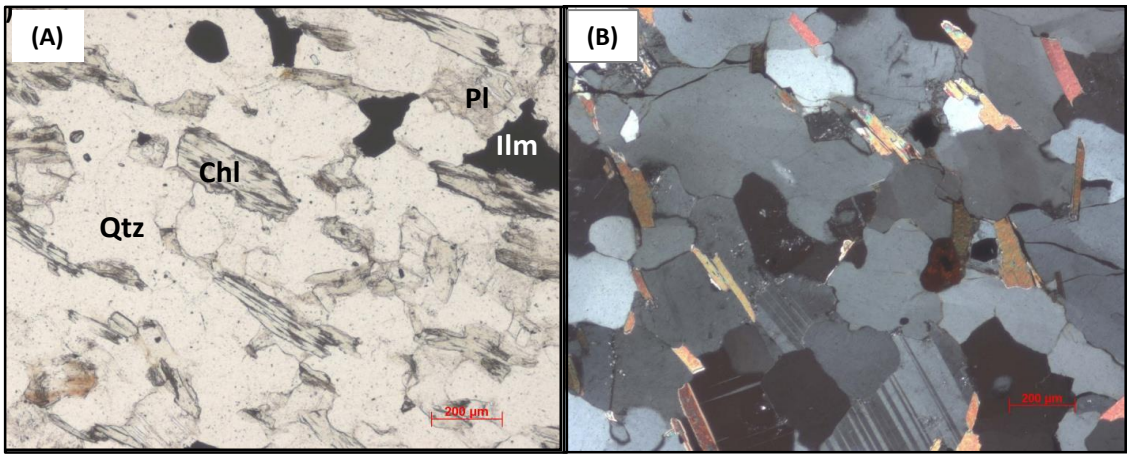

Fig. IV.1. 23 - A) Chlorite after biotite adjacent to a quartz-band in the frontier between the metagreywacke and the calc-silicate nodule (PPL); B), Biotite and plagioclase, in the same sample, without any alteration (CPL).

4.1.2.2. Migmatized metagreywackes

Some metagreywackes show evidence of having undergone partial-melting while most of them remain as resisters within the pelitic-metatexites. The migmatized metagreywackes are generally located in the outermost part of the metagreywacke resisters or between the metagreywacke schollen. It was possible to observe a gradual transition from the resister-zone to the migmatized-zone within a single thin section (Figs. IV.1.24 and 1.25). The metamorphic texture prior to fusion is preserved in the resister-zone showing fine grained granoblastic texture (Fig. IV.1.25A). A progressive increase in the grain-size occurs towards the migmatite zone, being the biotite, quartz and plagioclase crystals progressively larger. Adjacent to the migmatized zone there are biotite agglomerates associated with fibrolitic sillimanite that do not occur in the resister metagreywacke (Fig.IV.1.25B). The leucosome is composed of plagioclase and quartz large crystals that enclose smaller crystals of all the mineral assemblage present in the metagreywacke. There are cuspate grains in the leucosome and residual plagioclase within larger neo-formed plagioclase (Fig. IV.1.25D and 1.25E). Garnet shows a corona of peritectic cordierite (Fig. IV.1.25F).

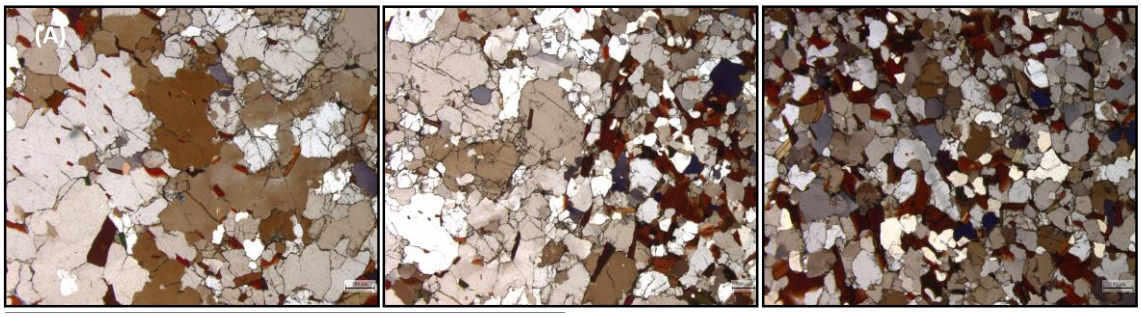

Fig. IV.1. 24 – Microphotographs showing passage from metagreywacke resister-zone (right) to the migmatized-zone (left) in the migmatized metagreywacke sample.

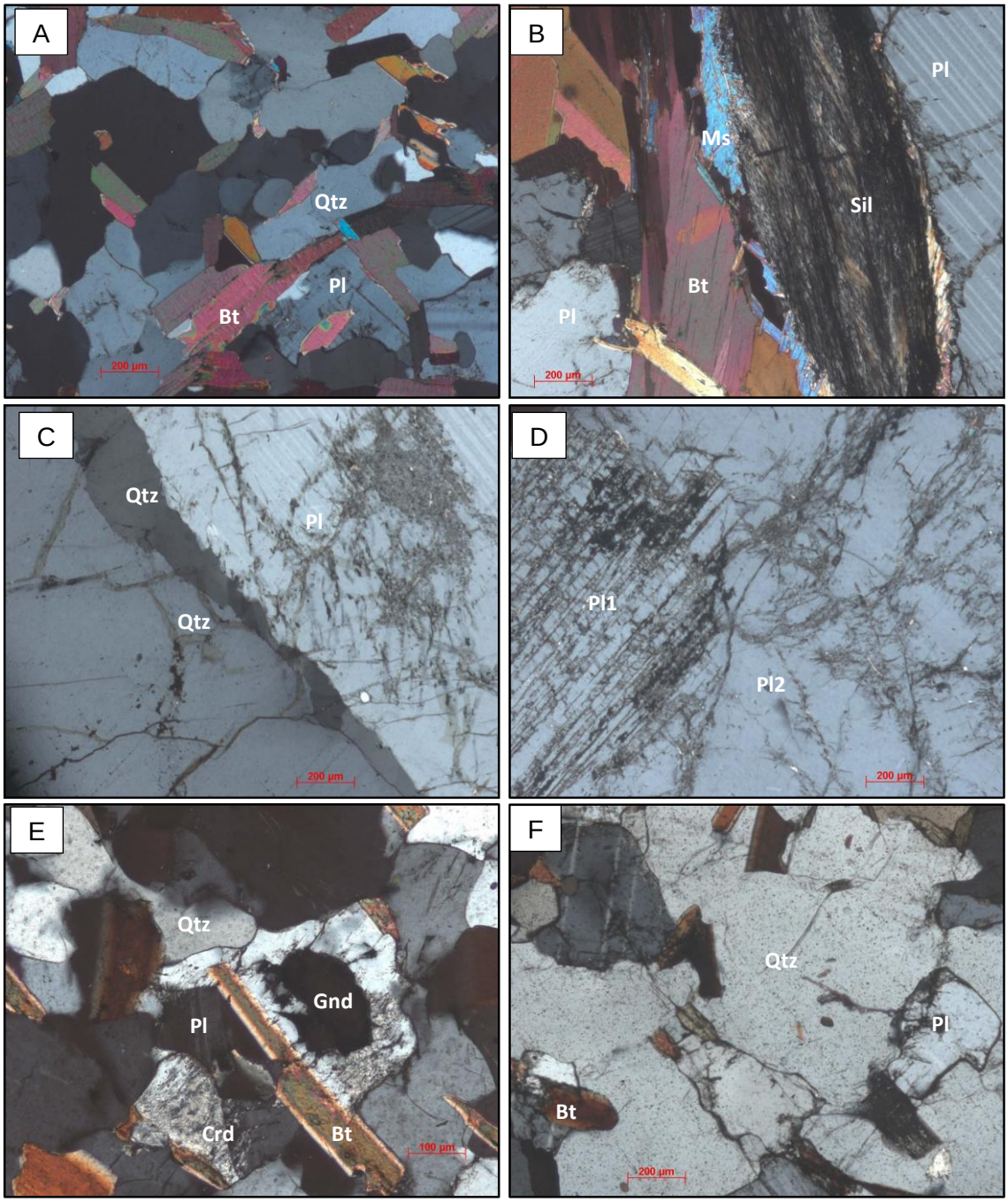

Fig. IV.1. 25 – Photomicrographs showing aspects of migmatized metagreywackes: A) Metagreywacke resister zone; B) Selvedge adjacent to the leucosome; C) Cuspate crystal of quartz between large quartz and plagioclase crystals; D) Plagioclase surrounded by neo-formed plagioclase; E) Garnet replaced by cordierite; F) Large quartz crystal containing plagioclase and biotite inclusions.

4.1.3. Petrography of diatexites

Diatexites show an equigranular matrix consisting of medium to coarse grained quartz + plagioclase + K-feldspar + biotite. Dispersed in the matrix there are abundant surmicaceous restitic enclaves (schlieren). The schlieren are composed of aligned biotite + sillimanite + cordierite ± garnet. The modal proportion of accessory minerals such as monazite, zircon and apatite is relatively high generally associated to the schlieren minerals.

Biotite occurs in aligned bands defining a foliation (Fig. IV.1.26A), or distributed in the matrix in aggregates (Fig. IV.1.26B). The biotite dispersed in the matrix show corroded borders in contact with quartz and plagioclase (Figs. IV.1.27A and B) .

Garnet is rare and restricted to the schlieren (Fig. IV.1.27C).

Fibrolitic sillimanite occurs within the schlieren, associated with biotite and skirting the matrix grains (Fig. IV.1.27D).

Cordierite is abundant. Occurs in the schlieren and also distributed in the matrix. There are tiny rounded cordierite crystals surrounded by later cordierite. The inherited crystal could be a metamorphic corroded cordierite crystal where peritectic subhedral cordierite nucleated (Fig. IV.1.28). There are several cordierite crystals inside large crystals of K-feldspar and quartz (IV.1.29A).

Plagioclase occurs as large anhedral to subhedral crystals (Pl2), most of them containing subhedral inherited plagioclase (Pl1) (Fig. IV.1.29B).

K-feldspar occurs as large subhedral crystals generally containing inclusions of all the residual or peritectic minerals, namely cordierite, plagioclase, apatite and quartz (Figs. IV.1.29A and 1.29D). There are K-feldspar inclusions that show a previous complex texture, namely corroded crystal of inherited plagioclase surrounded by newly formed plagioclase and both surrounded by K-feldspar or biotite euhedral crystals inside anhedral plagioclase that is inside K-.feldspar large crystals (Fig. IV.1.29D). These feldspar crystals will be formed after the migmatisation process incorporating inclusions with typical textures of partial melting.

Like metatexites also diatexites show myrmekite intergrowths, in most of the cases associated with micas or sillimanite suggesting a relationship between the biotite melting reactions and the occurrence of myrmekite. There are myrmekites protruding into K-feldspar crystals but most of them occur as inclusions both in K-feldspar and in quartz large crystals (“ghost myrmekite”) (Fig. IV.1.29). This suggests that myrmekites

developed in a previous process (biotite melting) and were enclosed by the later larger crystals of K-feldspar and quartz. (Fig. IV.1.30).

Flame perthites in K-feldspar, slightly deformed plagioclase and quartz crystals showing undulose extinction are evidence of fragile-ductile deformation processes affecting these rocks.

Locally the diatexites show corridors where the grain size is larger, the modal proportion of quartz increased, the biotite is intensely replaced by muscovite and there are several aggregates of radiating muscovite. This suggests that later fluids affected this rocks (Fig. V. 1.31).

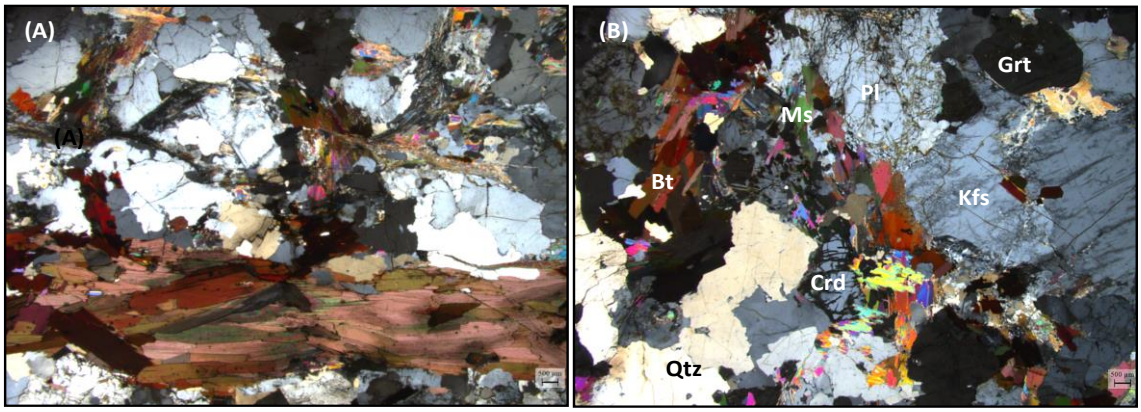

Fig. IV.1. 26 – Microphotographs showing textural aspects of diatexites

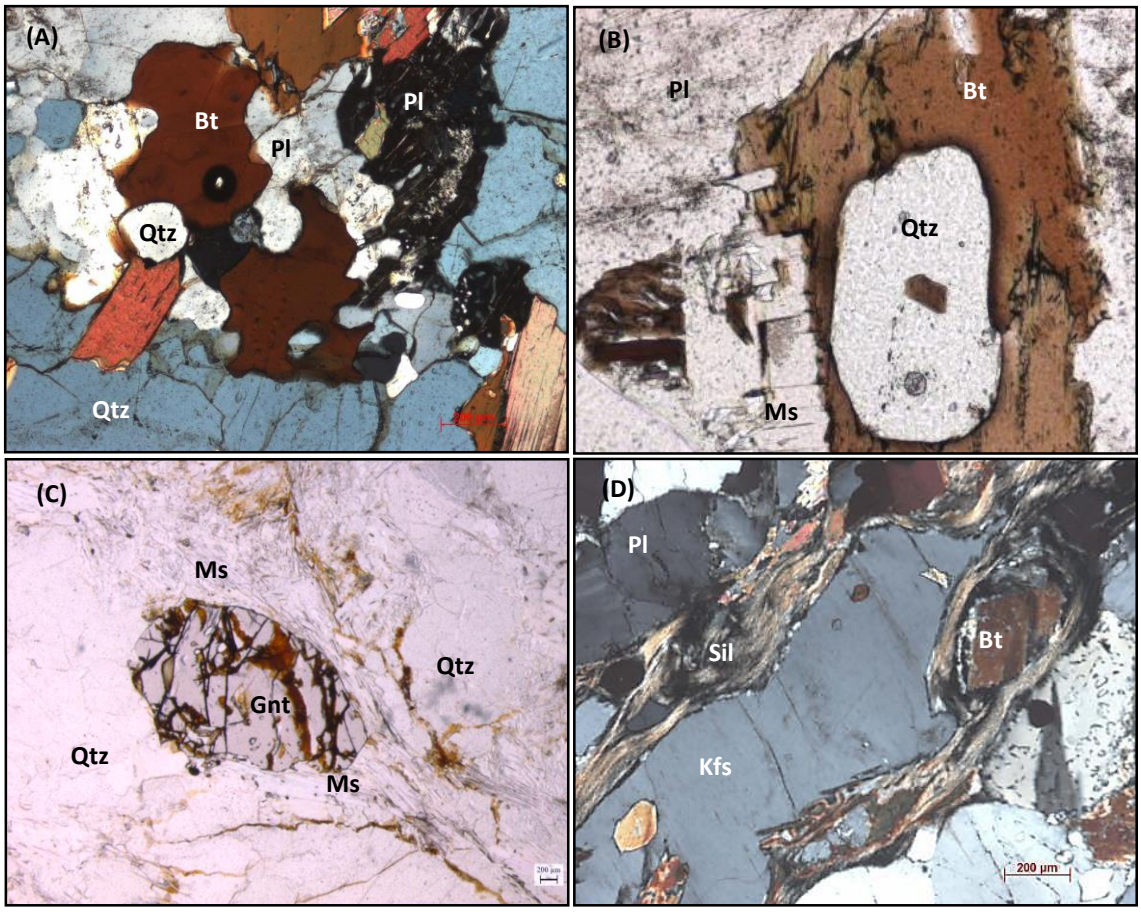

Fig. IV.1. 27 – Photomicrographs showing textural aspects of diatexites. A and B) Corroded biotite in contact with plagioclase and quartz; C) Restitic garnet surrounded by folia of muscovite (PPL); D) Fibrolitic sillimanite next to a coarse K-feldspar crystal. The K-feldspar has a morphology adapted to the space between the sillimanite schlieren (CPL).

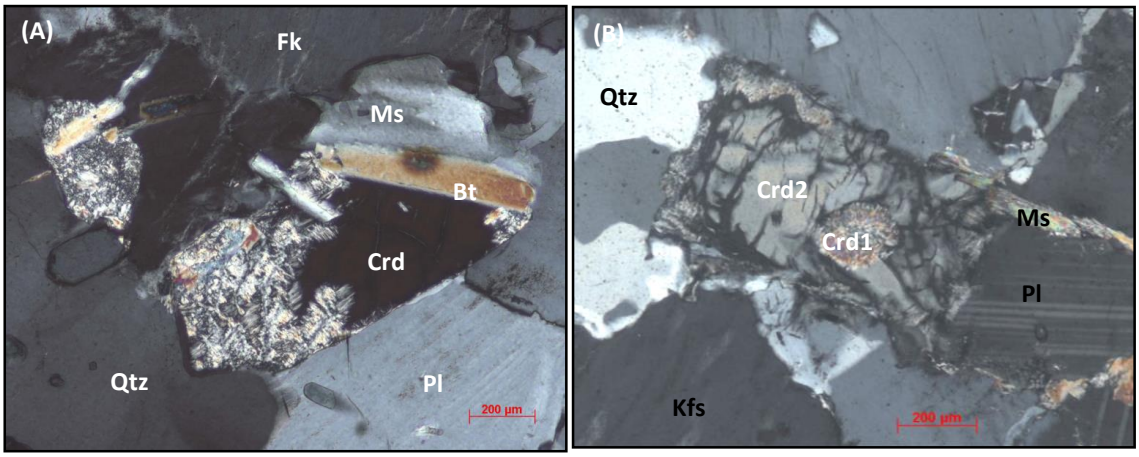

Fig. IV.1. 28 – Photomicrographs showing textural aspects of cordierite in diatexites: A) Cordierite associated with biotite and muscovite; B) Rounded and pinitized cordierite inside subhedral cordierite (CPL).

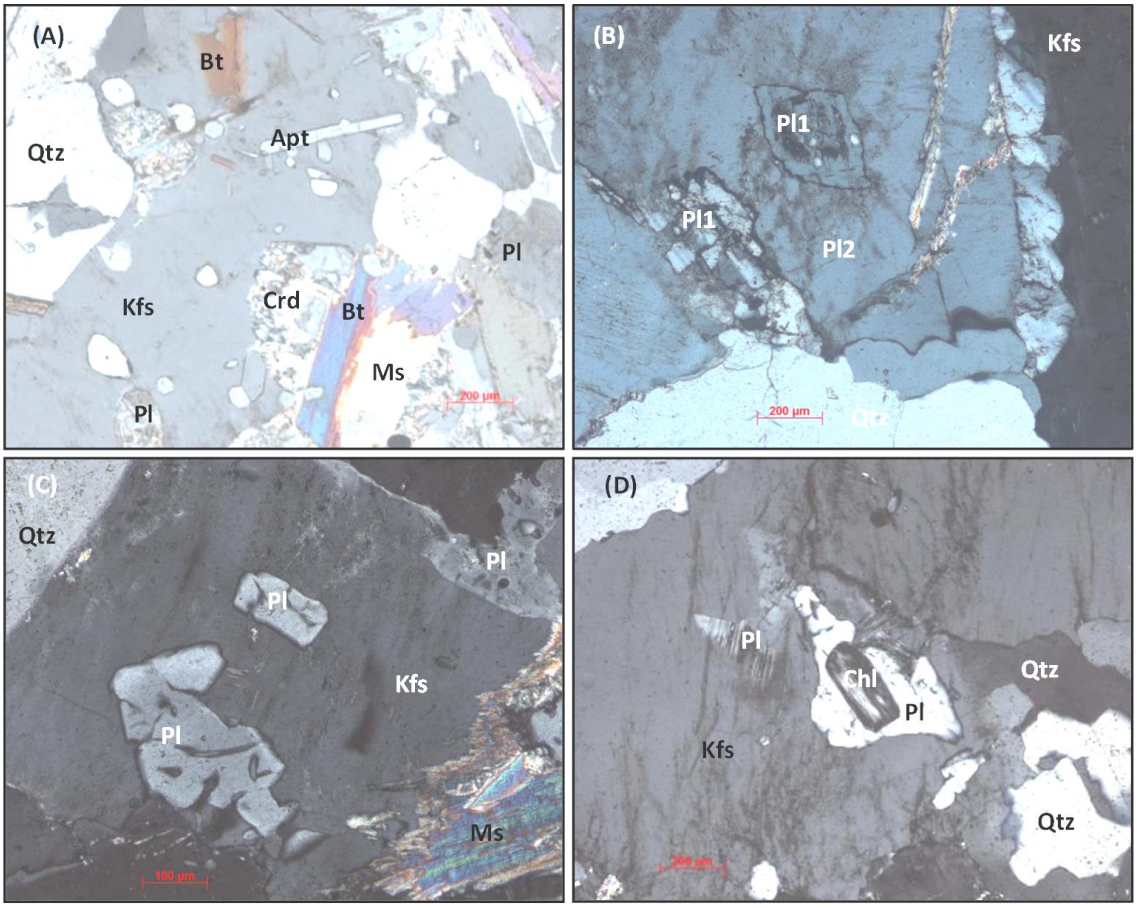

Fig. IV.1. 29 - Photomicrographs showing some textural aspects of diatexites. A) Large K-feldspar crystal containing apatite, cordierite, biotite, quartz and plagioclase inclusions; B) Zoned subhedral inhered plagioclase (Pl1) e inside magmatic large plagioclase crystal (Pl2); C) Plagioclase inclusions in K-feldspar showing vermicular quartz and irregular form. D) Chlorite after biotite inclusion in plagioclase that is inside a K-feldspar crystal.

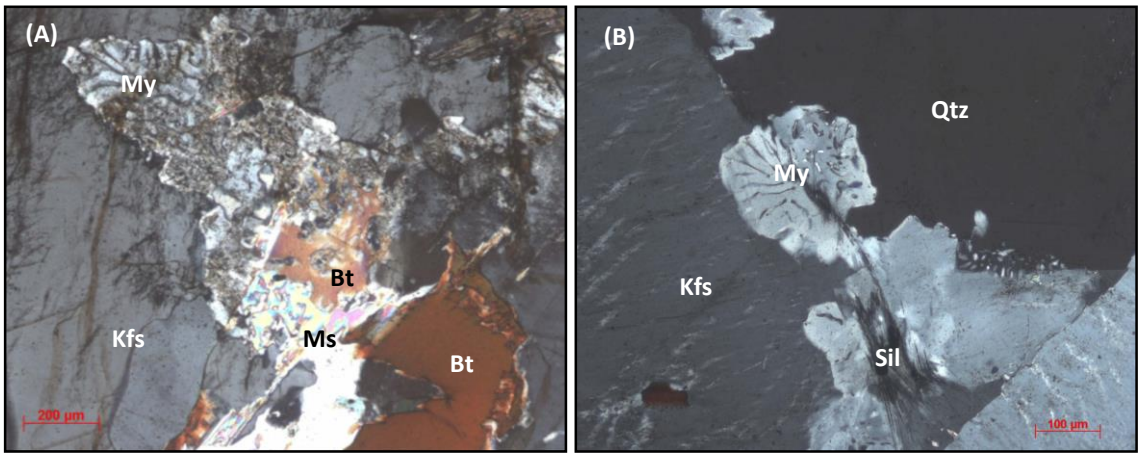

Fig. IV.1. 30 - A) Myrmekite projecting into K-feldspar associated with biotite. B) Myrmekite projecting into K-feldspar and quartz crystals associated with sillimanite. K-feldspar shows flame perthites.

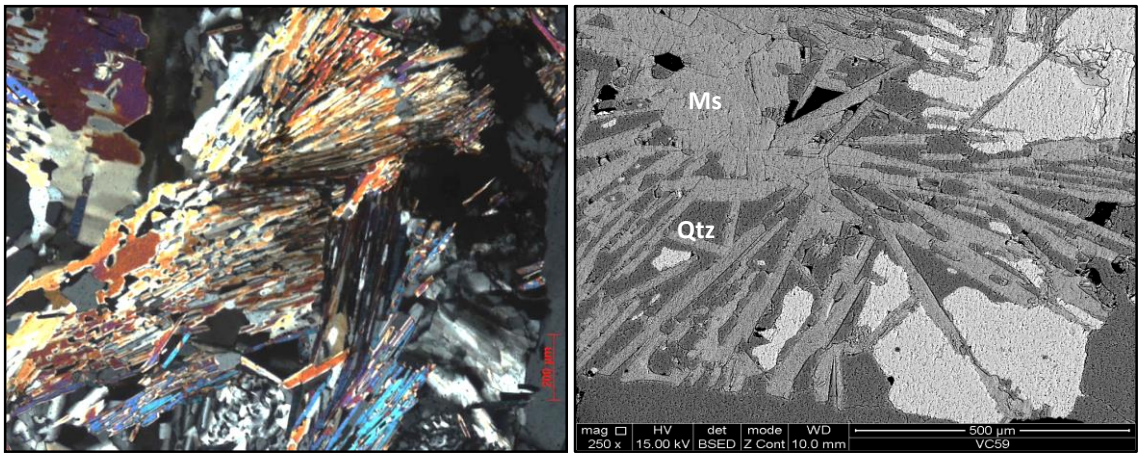

Fig. IV.1. 31 – Secondary muscovite in diatexites.

4.1.4. Petrography of leucogranites

Leucogranites show magmatic equigranular texture, although locally rare K-feldspar megacrystals occur (Fig. IV.1.32A). The mineral association is quartz + plagioclase + biotite + muscovite ± K-feldspar ± garnet ± chlorite (sec.). There are rare zircon and monazite tiny crystals dispersed in the matrix. Biotite is not abundant and generally is aggregated in clusters (Fig. IV.1.32B). Sillimanite is rare, fibrolitic and always associated with biotite (Fig. IV.1.32C). Garnet is very rare, showing corroded texture and residual aspect (Fig. IV.1.32D)

Several partial melting microstructures denounce the anatectic origin of this rock, namely (Fig. IV.1.33): i) anhedral residual biotite that locally shows evidence of partial melting reactions; ii) residual plagioclase inside larger grains of neoformed plagioclase; iii) cuspate grains of plagioclase and quartz; iv) plagioclase including rounded quartz crystals.

Like leucosomes, there are leucogranites with abundant K-feldspar and leucogranites with rare K-feldspar. In general, all the leucosome and leucogranite samples with K-feldspar show textural evidence of plagioclase replacement by K-feldspar namely K-feldspar in cores of some plagioclase crystals, occurrence of plagioclase inclusions in K-feldspar which are in parallel optical continuity and K-feldspar development in miarolitic cavities. Ghost myrmekites are also present inside k-feldspar crystals (Fig.IV.1.34).

The tourmaline-bearing leucogranites show tourmaline dispersed in the matrix (Fig. IV.1.35). Biotite is absent or very rare. Tourmaline occurs as pseudomorphs after biotite, showing pleochroic halos and quartz inclusions and/or occurs in symplectitic intergrowths with quartz in contact with K-feldspar, indicating reaction with the k-feldspar (Fig. IV. 1.35C and 1.35D).

Both leucogranite types show intense later muscovitization of biotite, tourmaline and K-feldspar and chloritization of biotite. There are also large muscovite random agglomerates that give to the rock a satin appearance and seem to result from later alteration processes (Fig. IV.1.36).

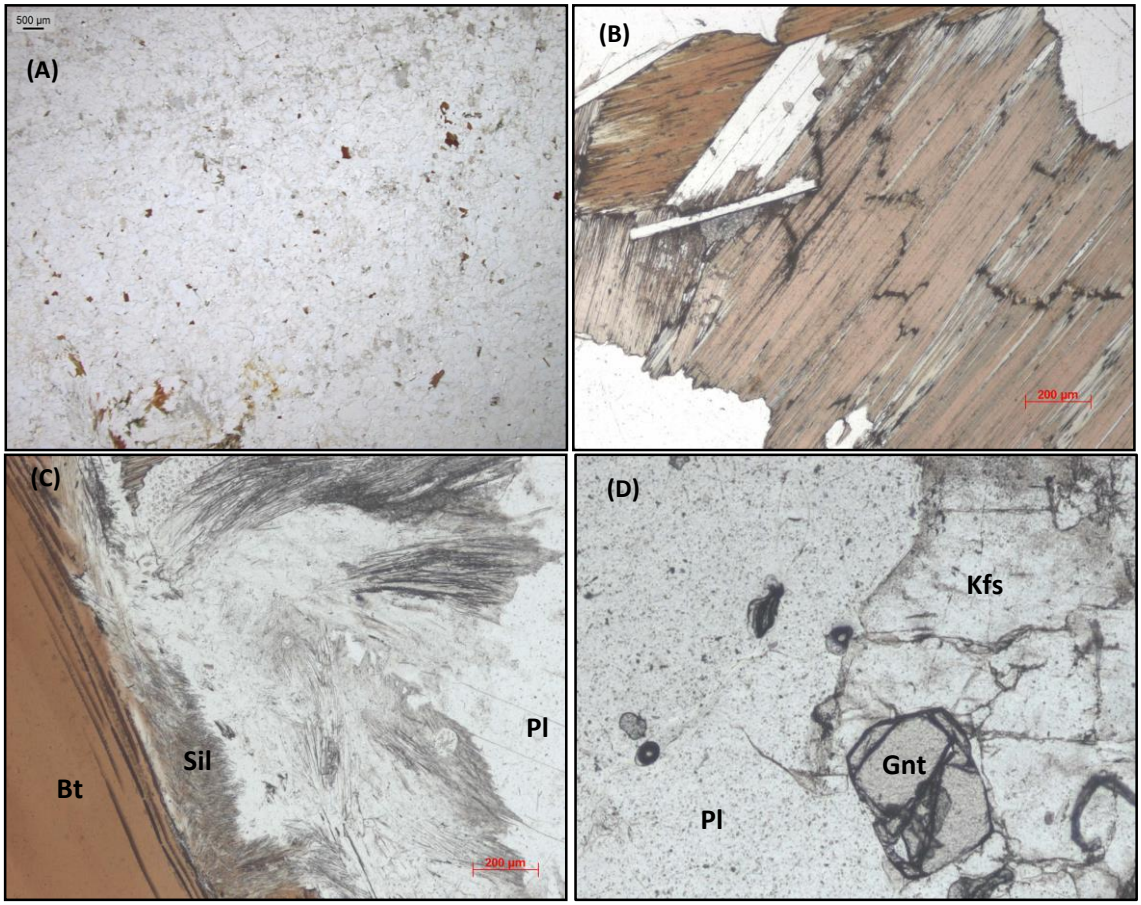

Fig. IV.1. 32 - Photomicrographs showing textural aspects of leucogranite. A) General aspect of leucogranites; B) Biotite cluster (PPL); C) Sillimanite adjacent to biotite (PPL); C) Residual garnet (PPL).

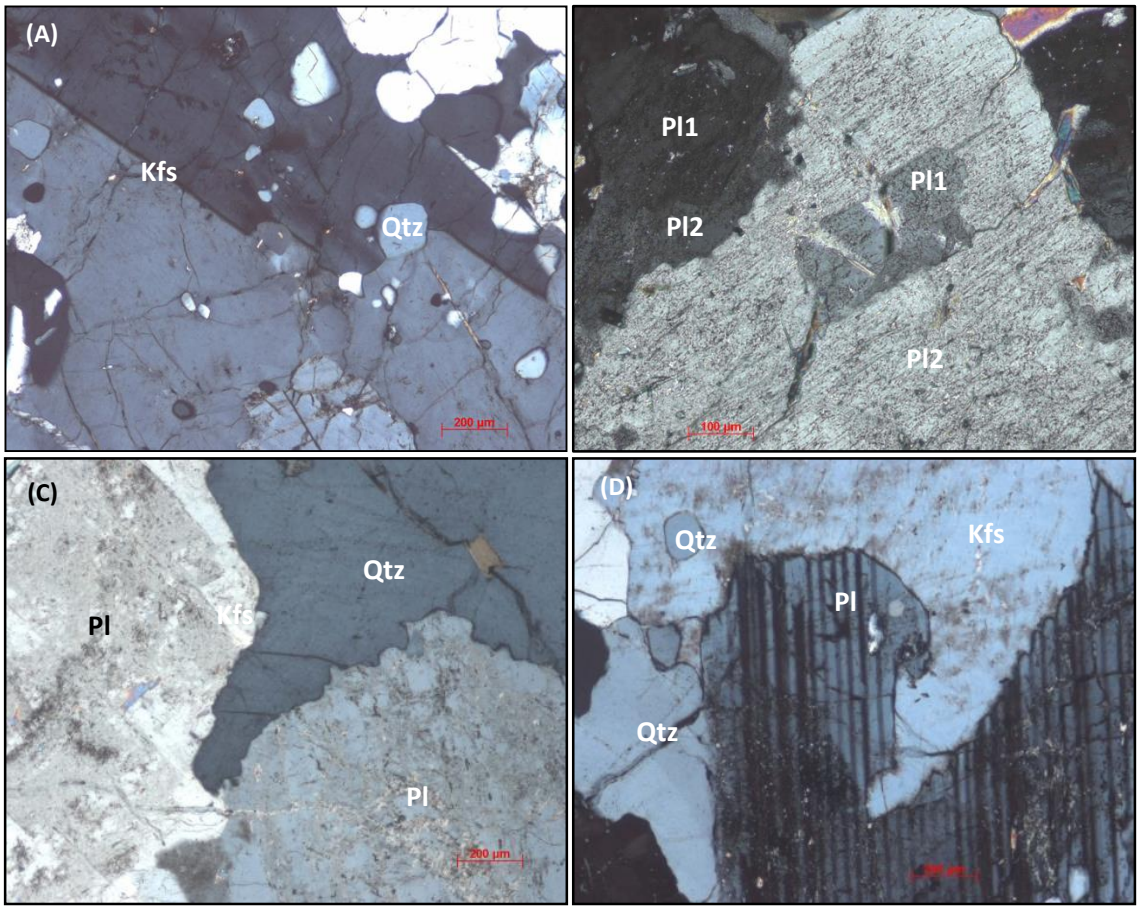

Fig. IV.1. 33 - Photomicrographs showing textural aspects of leucogranites. A) K-feldspar megacrystal showing plagioclase and quartz inclusions and Carlsbad twining; B) Residual plagioclase crystals (Pl1) and neo-formed plagioclase overgrowth (Pl2). C) Cuspate quartz and K-feldspar crystals; D) Highly irregular contact between plagioclase and K-feldspar; (Photos in CPL).

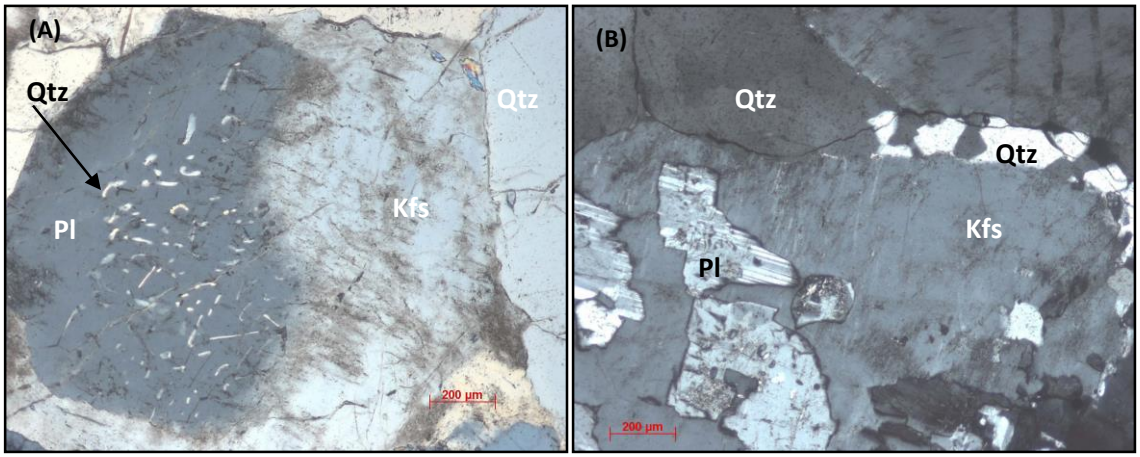

Fig. IV.1. 34 - Photomicrographs showing textural aspects of leucogranites. A) Anhedral plagioclase crystal partially replaced by K-feldspar. Vermicular quartz within plagioclase. B) K-feldspar replacing plagioclase. Plagioclase fragments included in the K-feldspar show the same optical orientation, indicating that it is a single plagioclase crystal. Highly cuspate quartz crystal showing subgrains formation restricted to the area between two feldspar grains. (Photos in CPL)

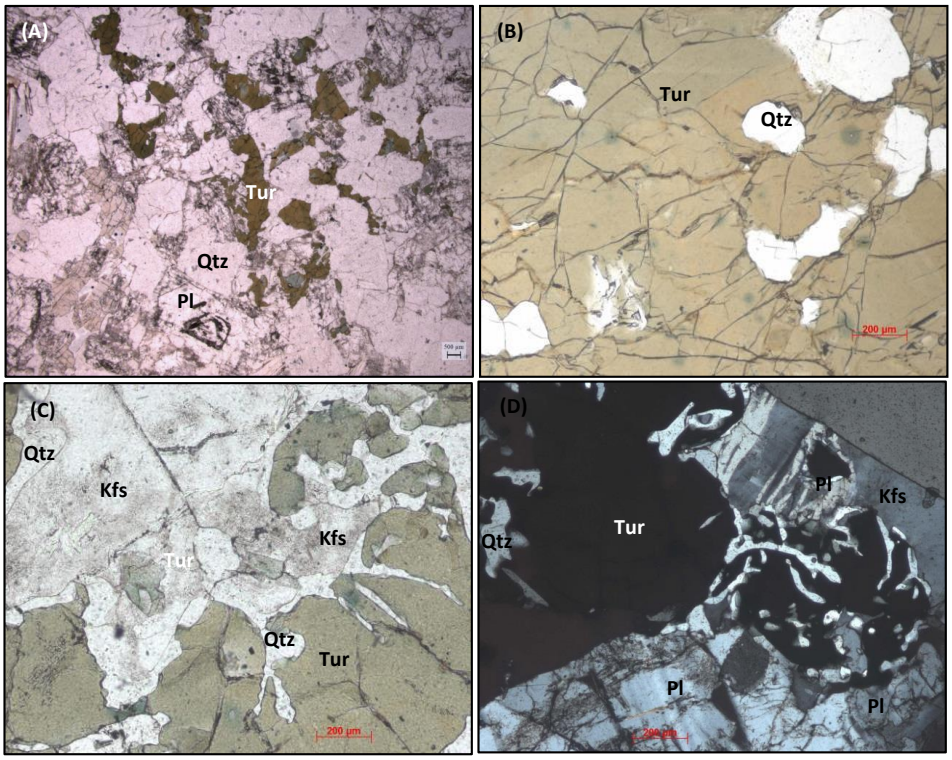

Fig. IV.1. 35 - Photomicrographs showing textural aspects of tourmaline-bearing leucogranites. A) General aspect. Tourmaline is dispersed in the plagioclase/quartz matrix (PPL); B) Large tourmaline crystal with quartz inclusions and pleochroic halos (PPL); C and D) Tourmaline showing intergrowth with vermicular quartz in the contact with feldspar (PPL and CPL).

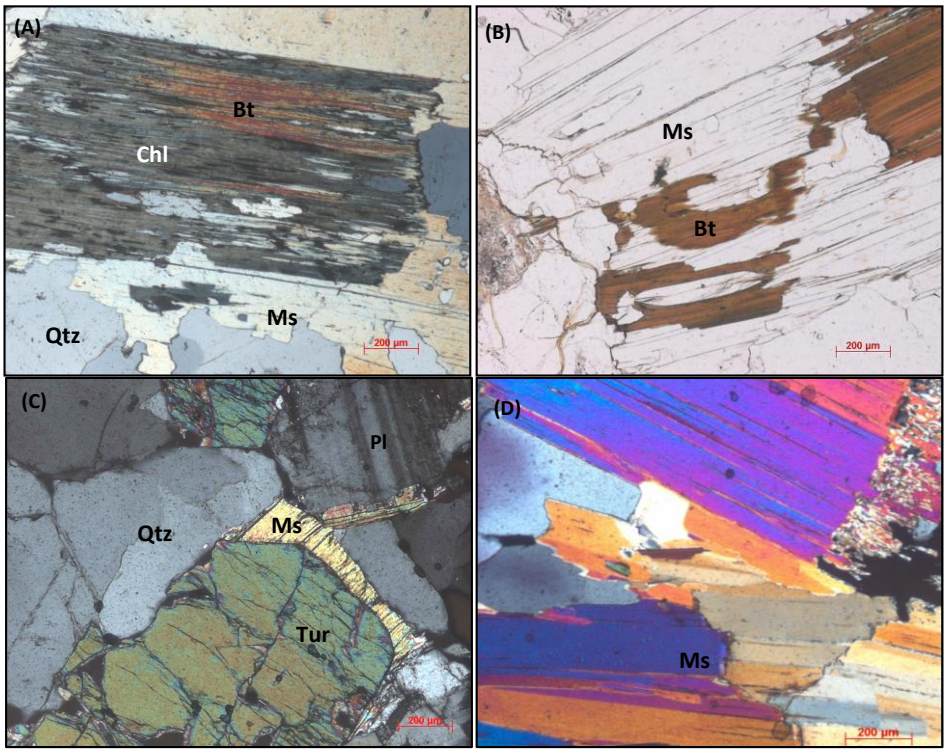

Fig. IV.1. 36 – Replacement aspects in leucogranites; A) Chlorite replacing biotite; B) Muscovite replacing biotite; C) Secondary muscovite replacing tourmaline; D) Agglomerate of secondary muscovite.

4.1.5. Petrography of two-mica granites

Two-mica granites show equigranular and phaneritic texture and are composed of quartz + plagioclase + K-feldspar + biotite + apatite + muscovite + zircon + monazite ± andalusite ± tourmaline (Fig. IV.1.37). Locally there is development of K-feldspar megacrystals (2 to 10 cm).

Rare aligned schlieren containing biotite + sillimanite ± garnet occur. Biotite in the schlieren is corroded (Fig. IV. 1.37B). Sillimanite and garnet are rare and restricted to the aligned schlieren (Fig.IV.1.37C).

Apatite is abundant and associated with biotite (Fig. IV.1.37C). Tourmaline occurs locally as pseudomorph after biotite (Fig. IV.1.37E). Most of muscovite is secondary, showing opaque minerals concentration in the cleavages (IV.1.37F).

Plagioclase occurs as medium grained euhedral crystals or showing corroded borders when associated with K-feldspar.

K-feldspar occurs as large euhedral crystals that include biotite, sillimanite quartz and plagioclase fine grained and rounded crystals and also as cuspate grains between quartz and plagioclase (Fig. IV.1.38A and 1.38B).

Myrmekite are abundant, generally associated with corroded biotite (Fig. IV. 1.37B)

Like the other rocks in MMC, two-mica granites also show textural evidence of plagioclase replacement by K-feldspar, namely plagioclase corroded crystals surrounded by K-feldspar (Fig. IV.1.38C to 1.38F). Plagioclase quartz round inclusions passed continuously to the K-feldspar crystal (Fig. IV.1.38F and E).

The corridors of K-feldspar megacrystals (Fig. III. 19) have mineral composition similar to the two-mica granites but showing larger K-feldspar crystals (5 to 10 cm), abundant and euhedral muscovite and tourmaline and more intense deformational textures (Fig. IV.1.39). K-feldspar megacrystals replace plagioclase (Fig. IV. 1.39A), filled plagioclase fractures (Fig. IV. 1.39B) and contain inclusion of quartz and plagioclase (Fig. IV.1.39C). There are deformed K-feldspar, plagioclase and muscovite crystals (Fig. IV.1.39C and 39E).

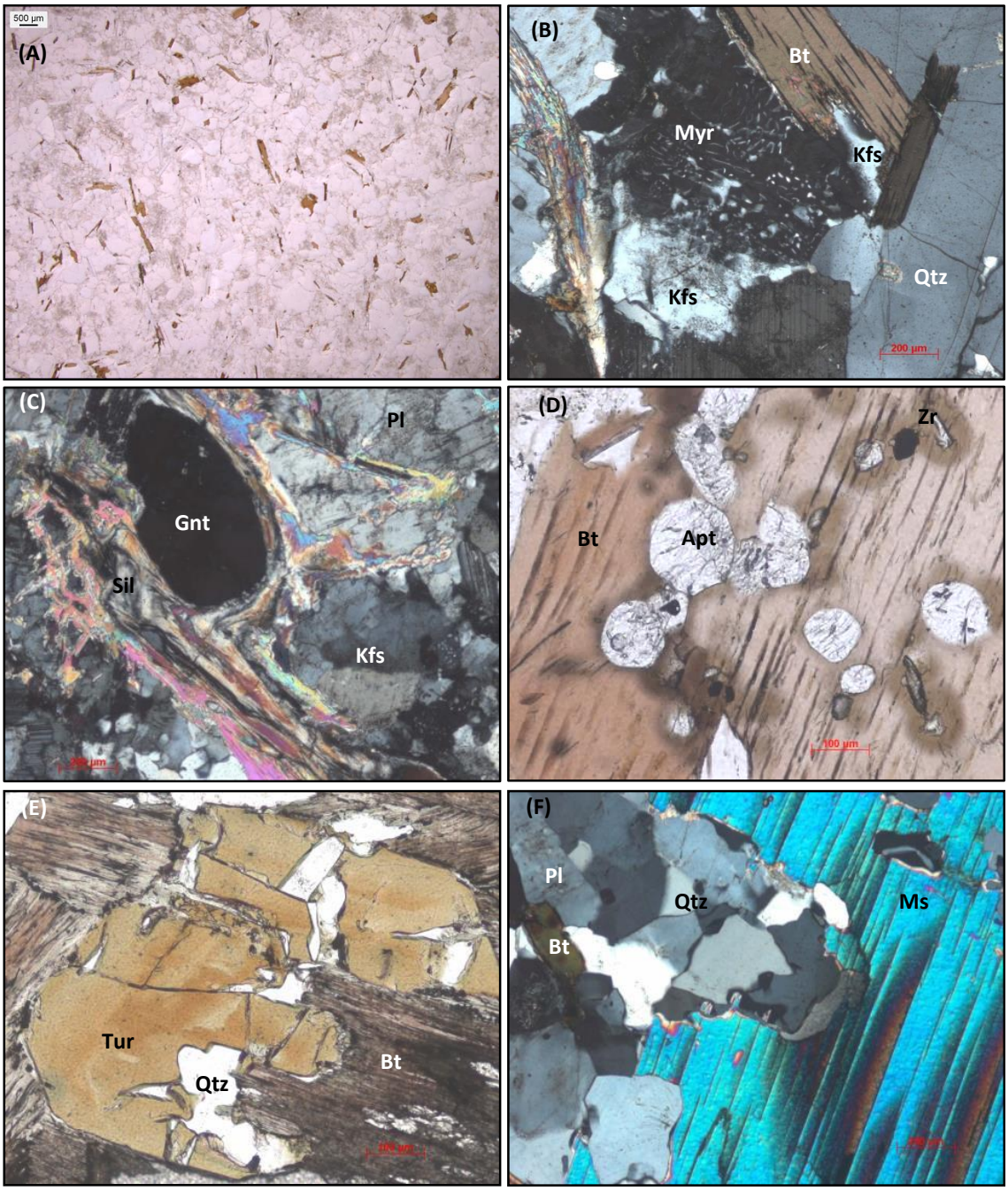

Fig. IV.1. 37 - Microphotographs showing textural aspects of two-mica granites. A) General aspect (PPL). B) Corroded biotite producing K-feldspar in contact with myrmekite (CPL); C) Garnet and sillimanite folia in the schlieren (CPL); D) Biotite containing apatite and zircon inclusions (CPL); E) Tourmaline associated with quartz and biotite (PPL); F) Muscovite showing concentration of opaque minerals in the cleavages (CPL).

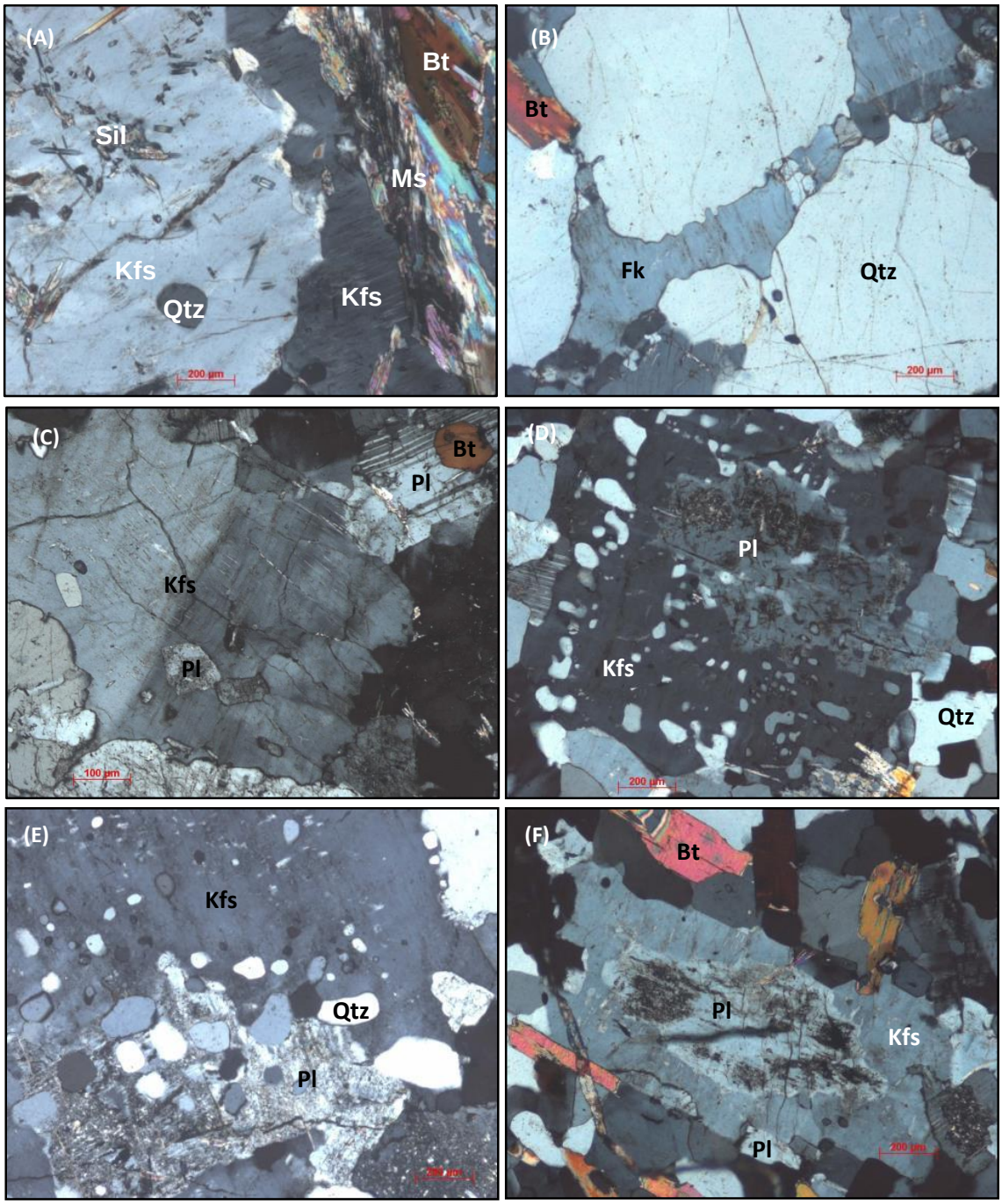

Fig. IV.1. 38 - Microphotographs showing textural aspects of two-mica granites. A) K-feldspar anhedral large crystal containing sillimanite and quartz inclusions. Cuspate K-feldspar between K-feldspar and micas; B) Cuspate K-feldspar between two quartz crystals; C) K-feldspar containing plagioclase rounded inclusions and irregular borders. Plagioclase containing biotite inclusion showing rounded corners. D) Anhedral plagioclase crystal surrounded by K-feldspar. The K-feldspar shows quartz vermicules or quartz blebs inclusions in the border; E) K-feldspar replacing plagioclase. The quartz inclusions in plagioclase remain as inclusions in K-feldspar although showing smaller size. F) K-feldspar pseudomorphic after partially replaced plagioclase. Plagioclase is intensely corroded in the center and fragments of the same plagioclase crystal border the pseudomorph. (All photos in CPL).

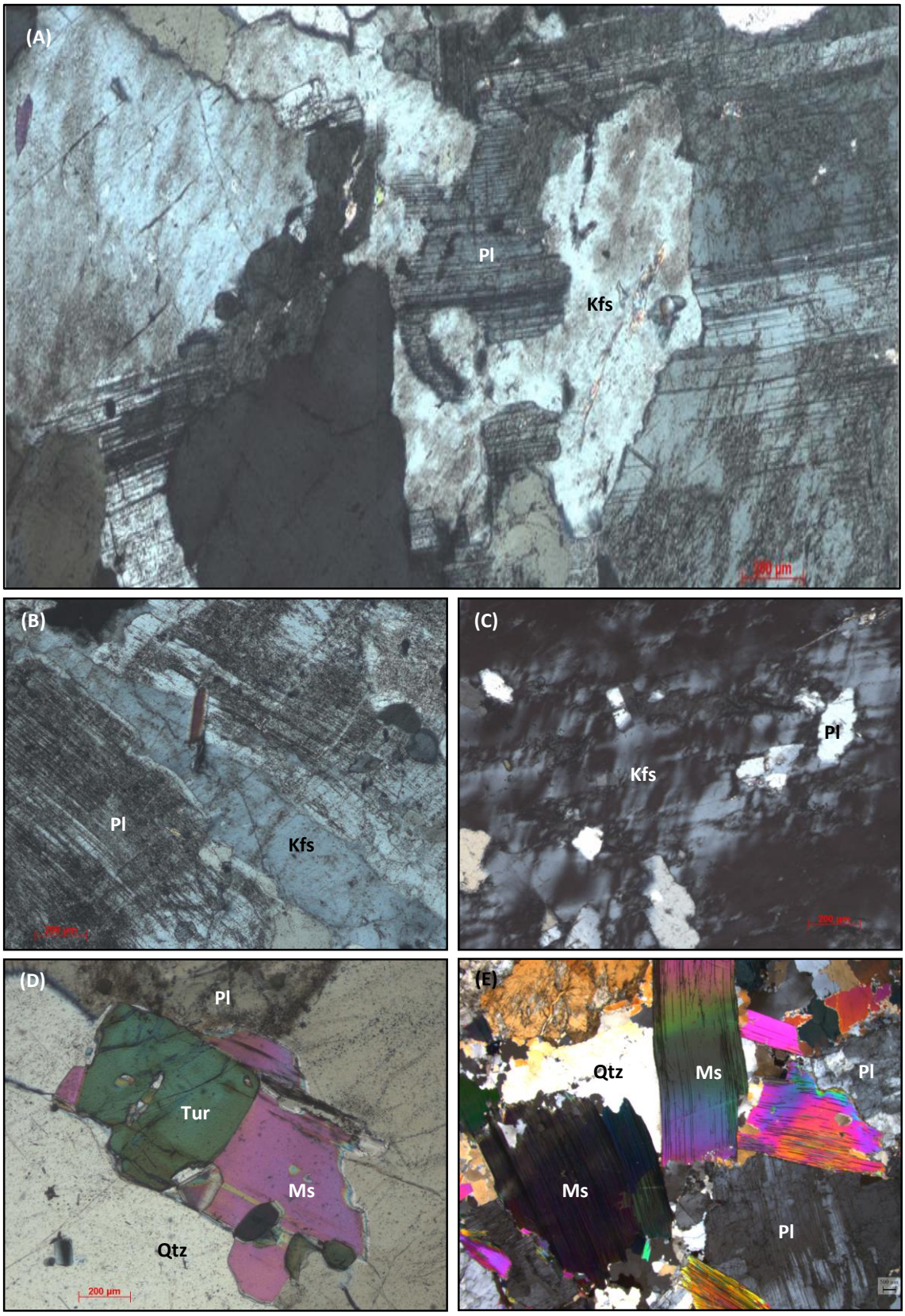

Fig. IV.1. 39 - Microphotographs showing textural aspects of K-feldspar corridors within two-mica granites. A) K-feldspar replacing plagioclase; B) Cuspate K-feldspar filling plagioclase fracture; C) Deformed K-feldspar large crystal containing zoned plagioclase inclusions; D) Tourmaline replaced by muscovite; E) Deformed muscovite dispersed in the matrix.

4.1.6. Petrography of aplite-pegmatite veins

Aplite-pegmatite veins cut all the previous lithologies forming sharp contacts with metatexites, diatexites and two-mica granites. Most of the aplite-pegmatite veins show three distinct zones comprising:

- Aplitic central zone composed of quartz + albite and aligned trails of tourmaline and garnet. The quartz/plagioclase grain size is coarser beyond the tourmaline trails, towards the contact with the wall rock. Very rare anhedral biotite occurs. There is no muscovite in the internal zone (Fig.IV.1.40).
- Intermediate coarser-grained zone showing perthitic feldspar, albite, quartz, muscovite and tourmaline. The feldspar, quartz and plagioclase crystals seem to be distributed in the fine-grained aplitic matrix, since they are surrounded by fine grained minerals identical to the aplite zone and contain several mineral inclusions from the aplite. The borders of the large minerals include the aplite minerals that delimited them (Figs.IV.1.40 and 1.41).
- Quartz-albite fringe adjacent to host rock showing parallel elongated albite/quartz intergrowths. The albite contains abundant submicroscopic apatite inclusions (Figs. IV.1.41).

There are fine-grained muscovite, quartz and tourmaline agglomerates that appear to be pseudomorphs after K-feldspar megacrystals Plagioclase is partially replaced by muscovite as well as the rare biotite (Fig. IV.1.42).

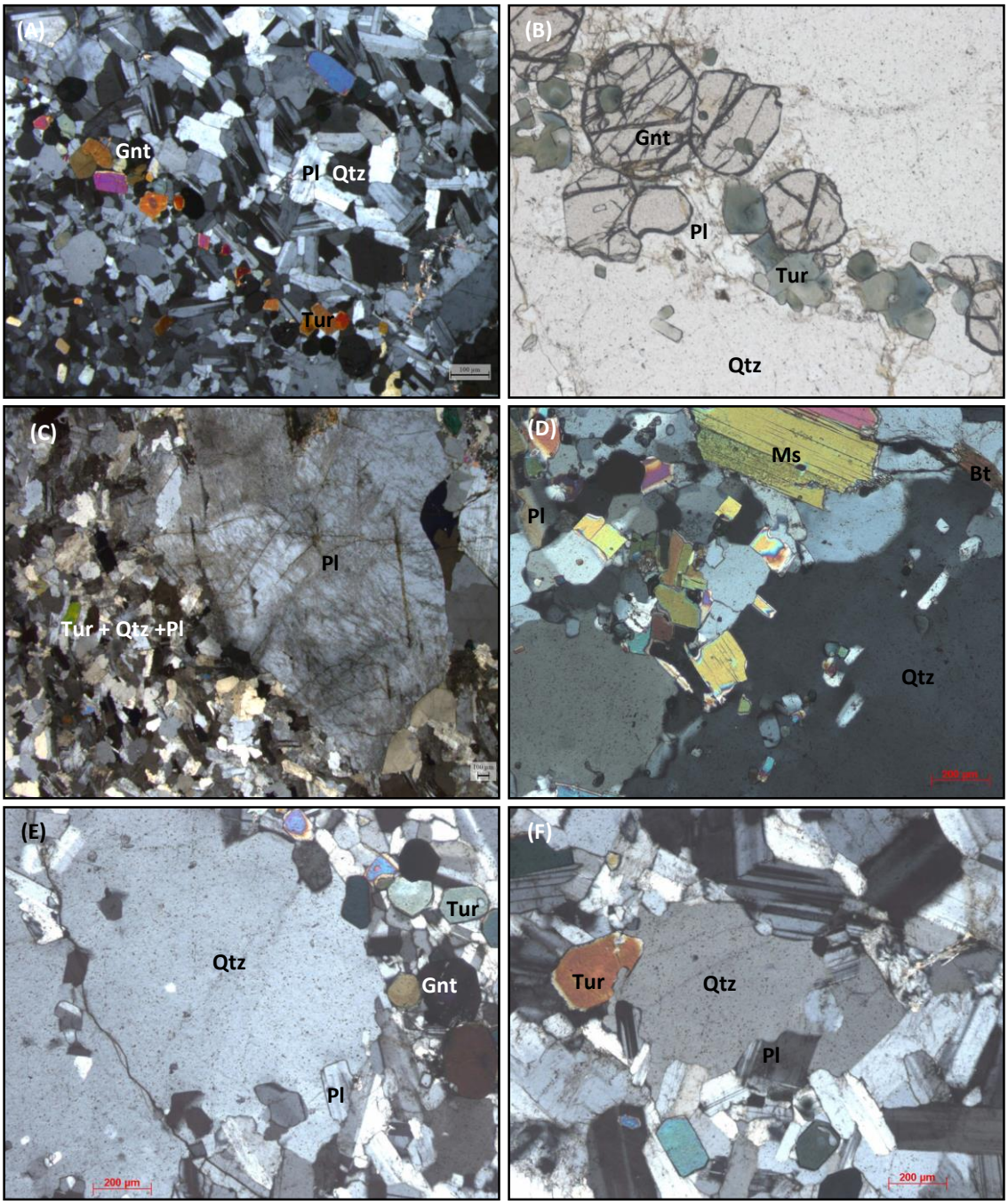

Fig. IV.1. 40 – Photomicrographs showing textural aspects of aplite-pegmatite veins. A) Aplitic internal zone showing fine grained quartz/plagioclase matrix and an aligned band with fine-grained tourmaline and garnet. There is an increase in grain size beyond the tourmaline band, towards the intermediate zone (CPL); B) Detail of the previous picture showing the tourmaline/garnet band (PPL); C, D, E and F) beginning of the intermediate coarse grained zone, showing large plagioclase and quartz crystals in contact with aplite. The borders of large crystals have inclusions of the aplitic matrix (CPL).

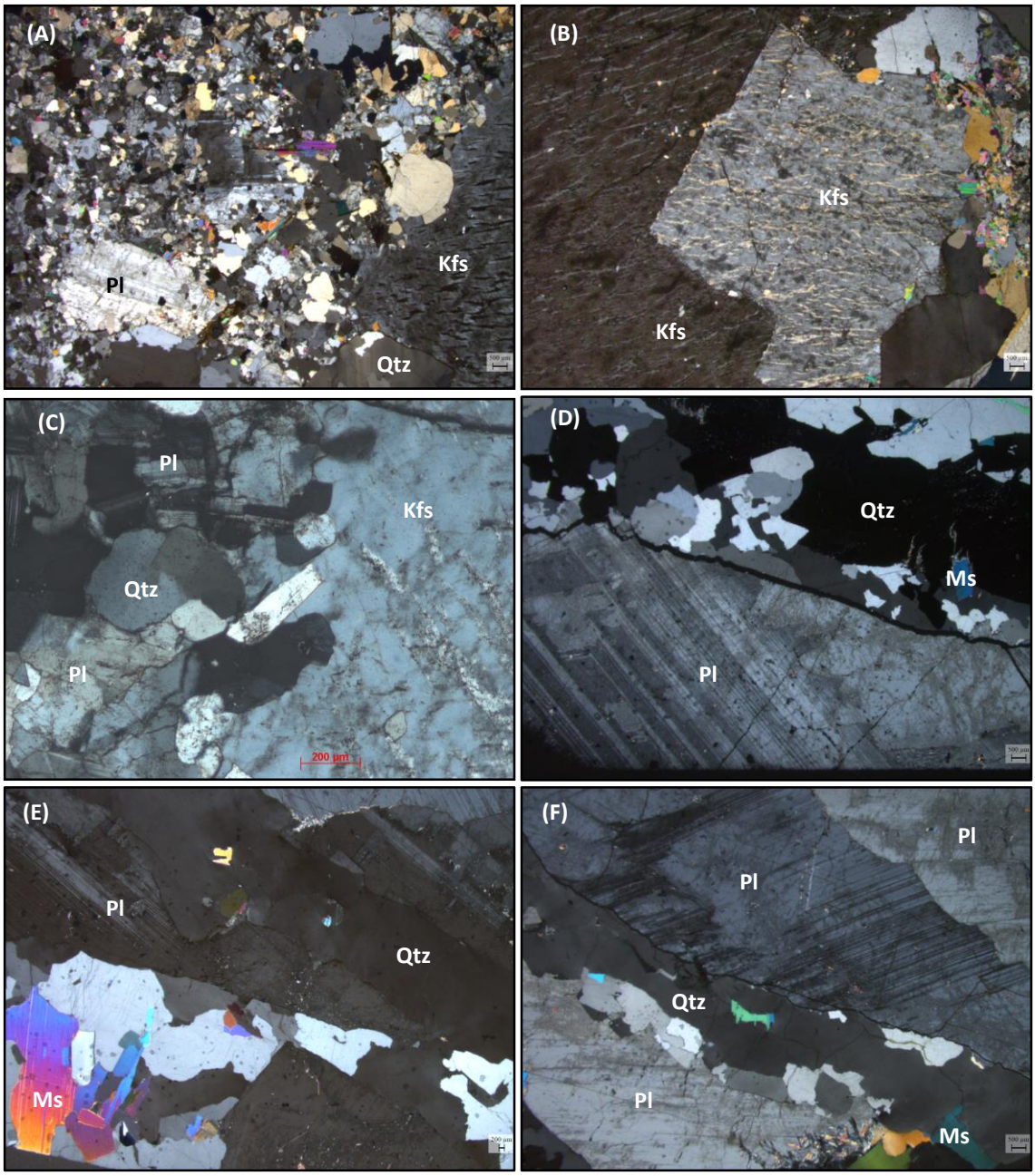

Fig. IV.1. 41 - Photomicrographs showing textural aspects of aplite-pegmatite veins: A, B and C) Intermediate zone showing perthitic K-feldspar crystals; D, E and F) Comb structure zone showing parallel elongated plagioclase and quartz intergrowth. (All photos in CPL).

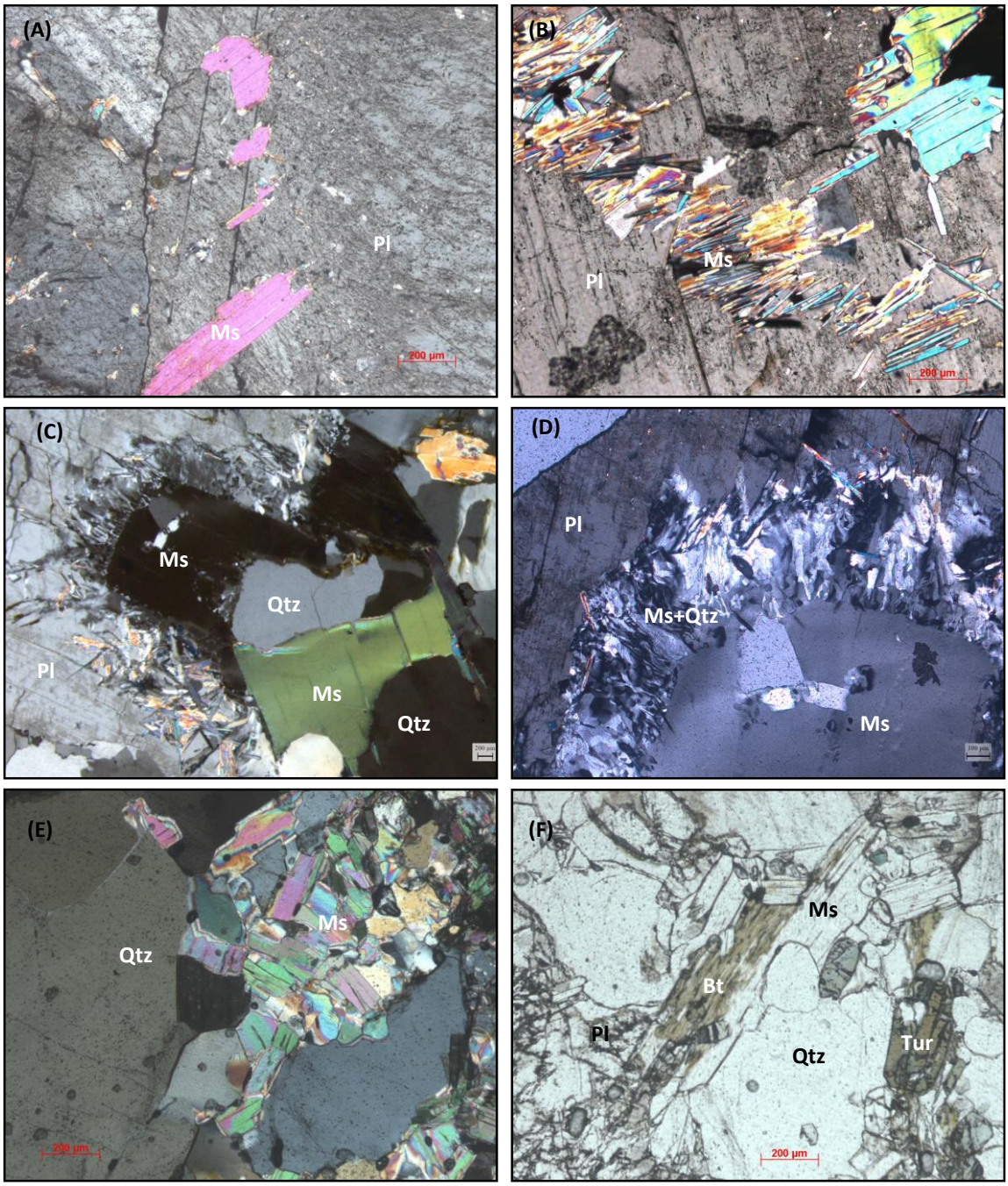

Fig. IV.1. 42 – A, B, C and D) Muscovite replacing plagioclase (CPL); E) muscovite agglomerates in the Intermediate zone; F) Rare biotite in the intermediate zone (PPL).

4.1.7. Synthesis and discussion

The textural and compositional evidence suggest that the dominant process for generating the MMC migmatites was partial melting. Injection is not a major contributor since there are no traceable field relations between the leucosomes in the analyzed outcrops and the granitic intrusions (except for leucogranites). In addition, the diverse compositions exhibited by the leucosomes over short distances argue against a common intrusive source, as well as the diversity of granitic rocks associated with the metatexites

Textural evidence of partial melting processes are widespread both in metatexites and in granitic rocks. Moreover, the abundance of peritectic cordierite and relicts of sillimanite + biotite in leucosomes support an anatectic origin through an incongruent melting reaction involving biotite and sillimanite as the reactants and cordierite plus K-feldspar as incongruent products. The following reaction in the KFMASH system is consistent with the observed textures and seems to be one of the melt-producing reactions of these migmatites:

$$Bt + Qtz + Sil = Crd + Kfs + L$$

The lithological heterogeneity present in MMC is common in migmatitic/anatectic terrains and must result from differentiation in the partial melting rates. The more calcic metagreywackes did not melted at all, the patch-metatexites show a low rate volume of melt, represented by the patchy leucosomes, the banded-metatexites show a similar proportion of leucosome and melanosome, the diatexites show larger volume of leucosome relatively to restitic phases and two-mica granites contain only few remaining restitic phases.

The structural level where the partial melting started could also be different since diatexites and two-mica granites show intrusive contacts with the metatexites and contain metatexitic xenolith, indicating a generation at greatest depth. Leucogranites, however, have a different relationship with metatexites, showing gradual transition. The modal proportion of feldspars and quartz is relatively high and the biotite is scarce. Apparently the leucogranites cropping out at the north and south of the Metatexite Zone are the result of massive segregation of leucosomes that dragged a few pieces of restitic phases. The proportion of these restitic phases is higher in the areas adjacent to the metatexites and progressively lower away from the Metatexite Zone.

The leucosomes are coarser-grained than the surrounding host-rock and show igneous fabrics. The average grain-size of the plagioclase and quartz in leucosomes is ~10 times larger than that of the corresponding host-rocks. In general, the plagioclase and quartz leucosome crystals have restitic plagioclase, biotite, cordierite inclusions. This fact can be explained by the continued growth of plagioclase and quartz in a melt with high amount of solid phases that are incorporated as inclusions in the larger crystals, as is expected in rocks showing limited rate of partial melting.

The presence of abundant peritectic cordierite in melanosomes and in restitic schlieren in diatexites indicates low-pressure anatectic conditions. The absence of peritectic garnet (the rare garnet crystals show residual character) and the absence of orthopyroxene, indicate temperatures below 810º considering the system NCKFMASHTO (Brown, 2013, White, 2008). The thermobarometric conditions prevailing in MMC condition will be discussed in the chapter VII.

Two-mica granites and diatexites show approximately equal modal proportion of K-feldspar and plagioclase. Metatexites and leucogranites show great heterogeneity in the K-feldspar modal proportion. In fact, there are metatexites and leucogranites where K-feldspar was not detected while others show high modal proportion. Within two-mica granites there are well defined corridors where the K-feldspar crystals reach 10 cm and evidence of plagioclase replacement by K-feldspar are observable in all the MMC lithologies. Moreover, calc-silicate rocks adjacent to K-feldspar bearing metatexites show marked alteration textures and mineralogy. Thus, it seems that sub-solidus K-metasomatism has influenced the composition and contributed to the heterogeneities of the MMC lithologies. Evidence that the K-metasomatism occurs at temperatures below the solidus exists in places where K-feldspar projects into microfractures in plagioclase and where broken plagioclase crystals are surrounded by the K-feldspar so that plagioclase islands are created in parallel optic continuity with the adjacent, unbroken plagioclase crystal, as well as the filling of miarolitic cavities by K-feldspar. Several studies described K-feldspar megacrysts as having been formed by K-metasomatism, especially in deformation zones and associated with a specific type of myrmekite (e.g. Pitcher & Berger, 1972; Barton & Sidle, 1994; Collins 1997). Recent studies show that mineral-water interface reactions could occur that cause minerals to develop porosity so that fluids can flow through a granitic rock and produce large scale replacements (Putnis & Putnis 2007; Putnis, 2009; Putnis & John 2010; Putnis & Austrheim 2010; Putnis & Ruiz-Agudo 2013). These authors considered that K-

metasomatism could produce more albitic plagioclase, quartz and K-feldspar accordingly to the following reactions:

$CaAl_2Si_2O_8/NaAlSi_3O_8 + K^{+1} \rightarrow KAlSi_3O_8 + NaAlSi_3O_8/\ CaAl2Si_2O_8 + SiO_2 + Ca^{+2} + Al^{+3}$

$CaAl_2Si_2O_8 + 4SiO_2 + 2K^{+1} \rightarrow 2KAlSi_3O_8 + Ca^{+2}$

$NaAlSi_3O_8 + K^{+1} \rightarrow KAlSi_3O_8 + Na^{+1}$.

Tourmaline was not detected in metatexites, diatexites and most of the leucogranites. However, tourmaline-bearing leucogranites and two-mica granites containing rare tourmaline locally occur. Tourmaline in two-mica granites is rare and is associated with biotite. Tourmaline in leucogranites is, in general, the only ferromagnesian mineral present since biotite is absent or very rare. Tourmaline is subhedral to anhedral, contains pleochroic halos and also occurs in symplectitic intergrowths in contact with K-feldspar.

Granitic melts are likely to be undersaturated in tourmaline from the start of their crystallization, and their initial boron contents will be limited by the abundance of tourmaline in their source rocks. Most leucogranitic magmas will initially crystallize biotite, cordierite or garnet, but not tourmaline (Deer *et al*., 1997). In the pneumatolytic phase tourmalinization can occur by introducing boron-rich fluids. Generally, biotite is the first mineral to be replaced and subsequently K-feldspar (Deer *et al*. 1992). The leucogranites with tourmaline spots could be the result of complex metasomatic process involving migrating boron-rich fluids which cause the breakdown of biotite and locally reacted with feldspar to give tourmaline plus quartz (symplectitic intergrowth).

Late magmatic fluids enriched in B are probably responsible not only for accessory tourmaline in MMC, but also for the occurrence of late tourmaline in metapelites and tourmalinites associated with quartz veins in the surrounding metasedimentary sequence (sub-chapter 4.2 and 4.3.).

Tourmaline shows later replacement by muscovite, biotite is replaced by muscovite and chlorite + rutile, cordierite is pinitized and plagioclase and K-feldspar are replaced by sericite and muscovite. There are calc-silicate nodules and metagreywackes that show intense later silicification and quartz veins cut all the MMC lithologies. Locally, the diatexites and leucogranites show coarse grain size, abundant muscovitization of feldspars and occurrence of radiating muscovite aggregates. This indicates that later aqueous silica-rich fluids also have played a role in the MMC.

4. 2. Sector 2 - Aguçadoura ↔ Fânzeres

Sector 2 is located to SW of Douro-Beiras Shear Zone and comprises the NE flank of Porto-Viseu antiform (to NE from the antiform core granitic intrusions) and covers lithologies related to the "Schist-Greywacke Complex – Beiras-Group". The petrological description will be made accordingly to the metamorphic zones, from chlorite-zone to sillimanite -zone.

4.2.1. Chlorite-zone

In the chlorite-zone the chlorite-schists and the metaconglomerates were studied.

Chlorite-schists are fine-grained and show alternating micaceous-rich and quartz-feldspathic–rich bands parallel to the principal continuous cleavage defined by chlorite and white-micas (Sn). The textural aspect of the cleavage indicates a sedimentary origin since there are bands with different size and irregular borders. There are also parallel quartz veinlets (Fig. IV.2.1).

The mica-rich bands are composed of white micas, chlorite and abundant opaque minerals that define a slaty cleavage. The quartz-feldspathic bands are composed mainly of quartz, minor plagioclase and dispersed white-mica flakes (Fig. IV.2.2).

The continuous Sn cleavage is locally crenulated. A Dn+1 deformation phase crenulated Sn and formed a discrete cleavage and microlithons (Fig.IV.2.3). The quartz veinlets are folded showing fold attenuation coincident with the concentration of micas along the crenulation cleavage (Fig. IV.2.3).

Metaconglomerates are composed of large quartz grains and fine-grained quartz agglomerates surrounded by phyllosilicates. Phyllosilicate aggregates contour the quartz and are composed of white-mica and chlorite associated with opaque minerals and late tourmaline. These agglomerates contour the quartz grains and form a marked cleavage that is parallel to the quartz grains elongation. This Sn cleavage is locally crenulated. Mica alignments circumvents the larger quartz crystals, indicating that the morphology of quartz clasts prevail over cleavage. The larger quartz grains show ondulose extinction, subgrains formation and bulging. The fine-quartz agglomerates are composed of quartz, rare plagioclase and dispersed white-mica flakes parallel to the Sn. The quartz grains show ondulose extinction and are elongated parallel to the main cleavage (Sn) (Fig. IV.2.4).

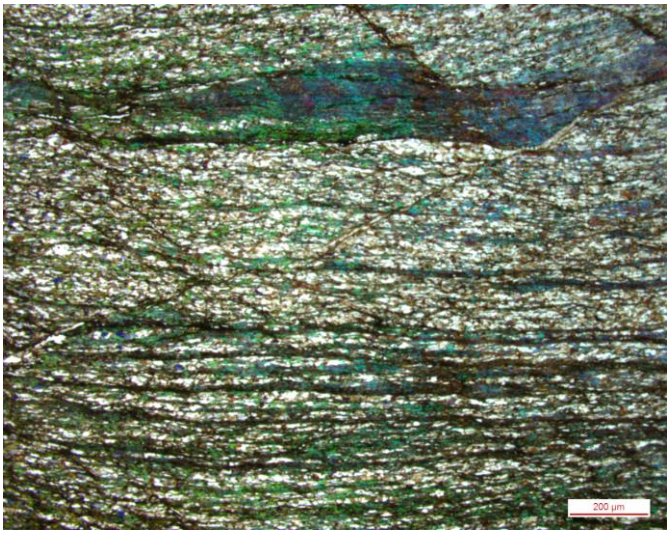

Fig. IV.2. 1 – Photograph showing general aspect of chlorite-schists.

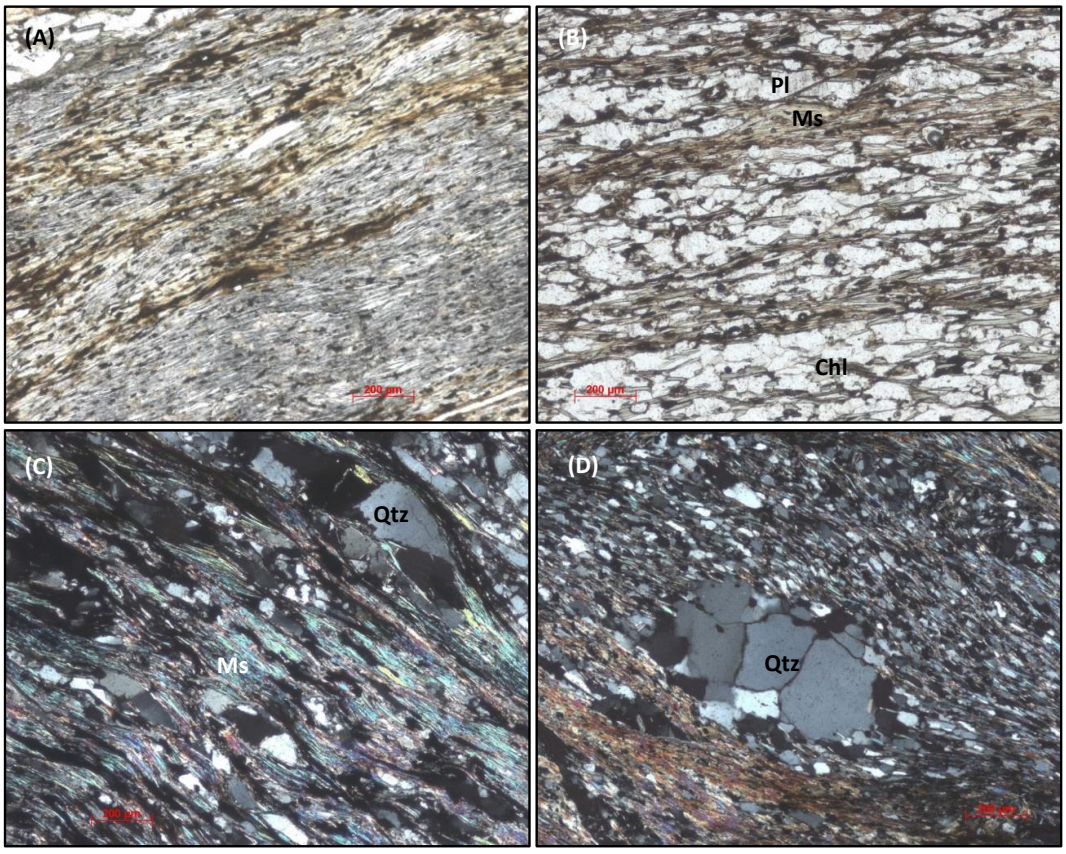

Fig. IV.2. 2 - Photomicrographs showing textural aspects of chlorite-schists. A) Micaceous band composed of white-micas/chlorite/opaque minerals forming alignments that define a continuous slaty cleavage; B) Quartz domain showing fine-grained quartz and plagioclase and minor chlorite and white-mica alignments. C) Cleavage anastomosing around quartz crystals elongated parallel to Sn cleavage. D) Sample cut perpendicularly to the bedding showing lenticular coarser-grained quartz agglomerate.

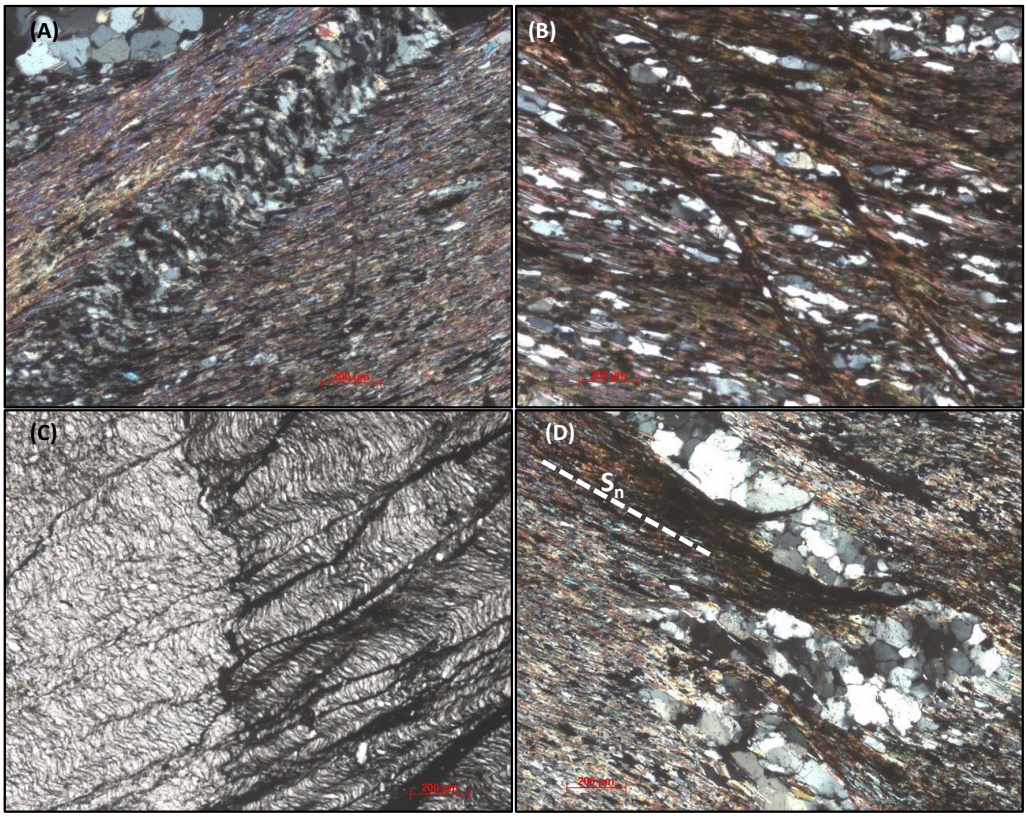

Fig. IV.2. 3 – Photomicrographs of chlorite-schists showing discrete crenulation cleavage and folded quartz veinlet showing fold attenuation coincident with the concentration of micas along the crenulation cleavage.

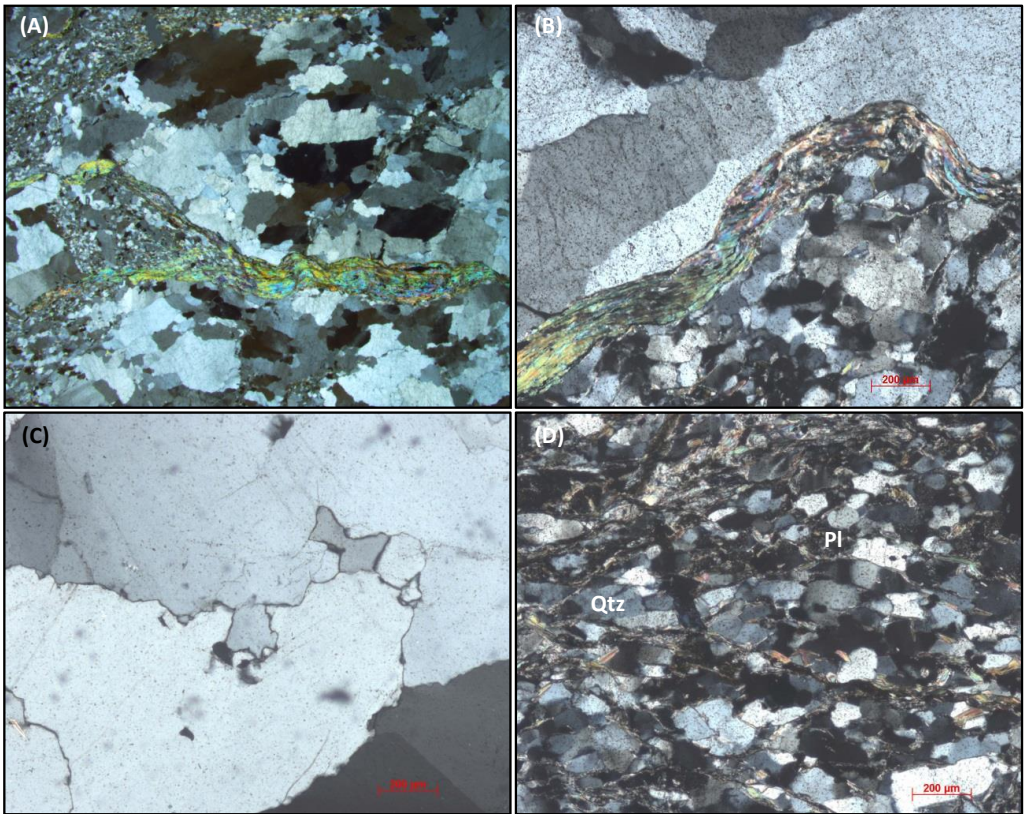

Fig. IV.2. 4 – Photomicrographs showing textural aspects of metaconglomerates layers in the chlorite-zone.

4.2.2. Biotite-zone

In biotite-zone the biotite-schists, metaconglomerates and metagreywackes were studied.

Biotite-schists show coarser grain-size than chlorite-schists, granolepidoblastic texture and are composed of biotite + muscovite + quartz + plagioclase ± chlorite ± garnet. There are zircon, monazite, apatite, ilmenite, rutile and tourmaline as accessory minerals.

In the transition from chlorite- to biotite-zone the cleavage is defined by muscovite, opaque minerals and elongated quartz and plagioclase. The biotite porphyroblasts resulted from the replacement of chlorite and are dispersed as “starks” in the matrix (Fig. IV.2.5A).To the upper limit of the biotite-zone, the biotite porphyroblasts replace mimetically the aligned muscovite and define the foliation (Sn) (Figs. IV.2.5B to 5F). In this part of the biotite-zone rare garnet porphyroblasts develops (Fig.IV.2.5B) and the delimitation in quartz-domains and micaceous-domains is more evident. Quartz shows elongation parallel to the foliation in the micaceous bands and more isotropic morphology in the quartzose domains.

Biotite-schists adjacent to the porphyritic granites develop late andalusite (outcropping in Alvarelhos; Fig. IV.2.5C).

The crenulation affecting Sn cleavage is widespread, folding the micaceous domains and also the quartzose domains (Fig. IV.2.5D and 5E).

There are retrograde replacement of biotite by chlorite, muscovite and sericite, and dispersed late tourmaline.

Metaconglomerates in the biotite-zone are similar to the metaconglomerates in the chlorite-zone, showing large quartz clasts, fine grained quartz and plagioclase aggregates, both surrounded by aligned mica. However, in these rocks, biotite grains develop in the micaceous bands replacing white-micas, especially in the vicinity of the quartz large crystals. The biggest quartz clasts are, in this zone, transformed into smaller grained polygonal aggregates with triple junctions due to thermal effects (Fig. IV.2.5F).

Metagreywackes in the biotite-zone are composed of quartz, plagioclase and biotite. Ilmenite, zircon, apatite and tourmaline occur as accessory minerals. Micas are aligned and define a foliation. The texture is typical of aggregates dominated by crystal faces (Vernon, 2004). Biotite occurs in numerous small aligned mica flakes. The

quartz/quartz interfaces meet mica {001} quartz interfaces at approximately 90◦ or are joined to the edges of the mica flakes.

The quartz/quarts and quartz/plagioclase contacts are curved but intense dynamic or static recrystallization features are absent (no undulose extinction, no bulging, no subgrains) (Fig. IV.2.6).

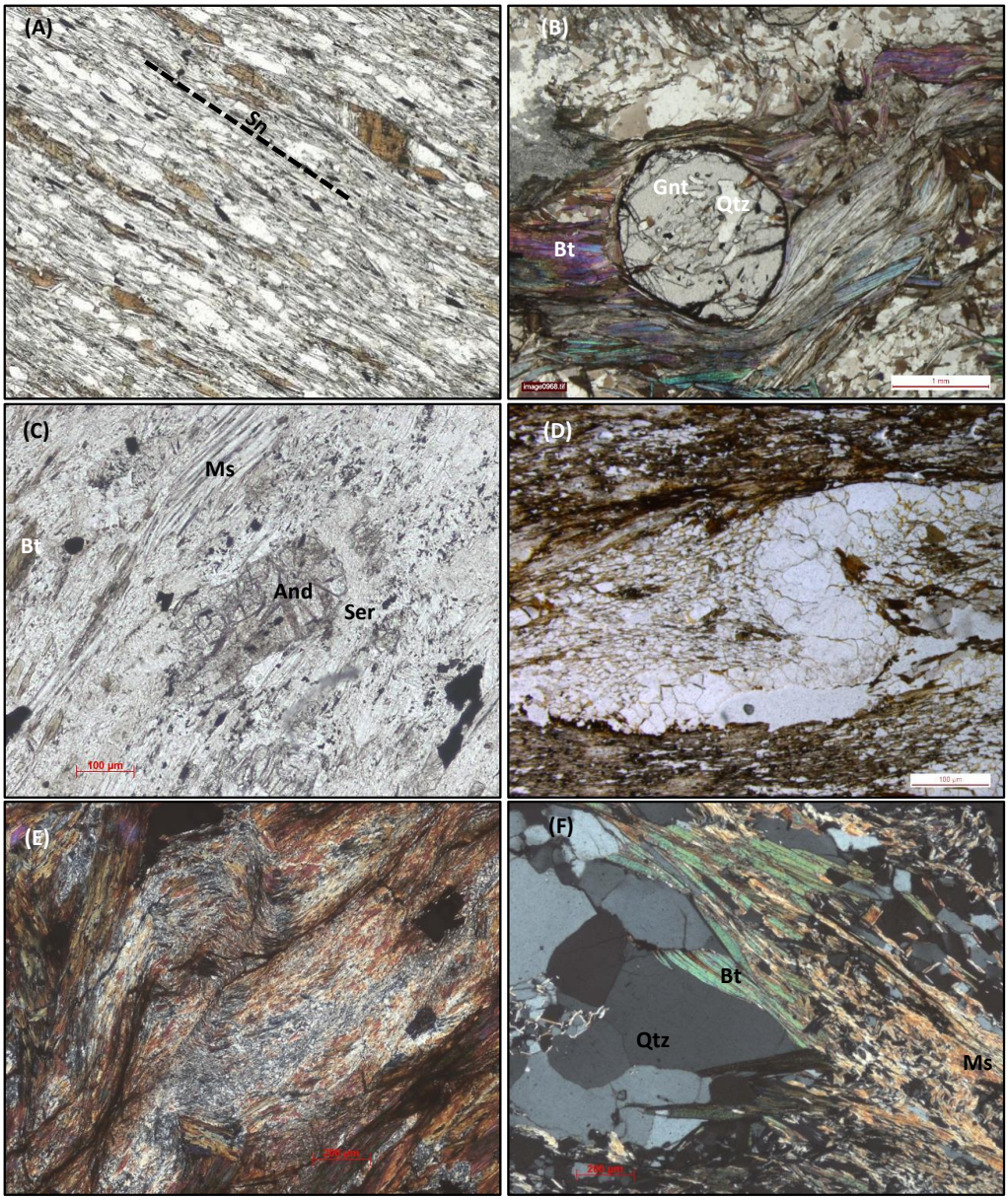

Fig. IV.2. 5 - Photomicrographs showing textural aspects of biotite-schists. A) Biotite-schist from the base of biotite-zone showing granolepidoblastic texture with biotite porphyroblasts; B) Garnet within the micaceous domains in the top of biotite-zone; C) Biotite-schist located in the vicinity of a porphyritic granite showing andalusite and retrograde muscovite and sericite. D and E) Folded quartz veinlet and crenulation cleavage affecting Sn; F) Metaconglomerate showing biotite and polygonal quartz.

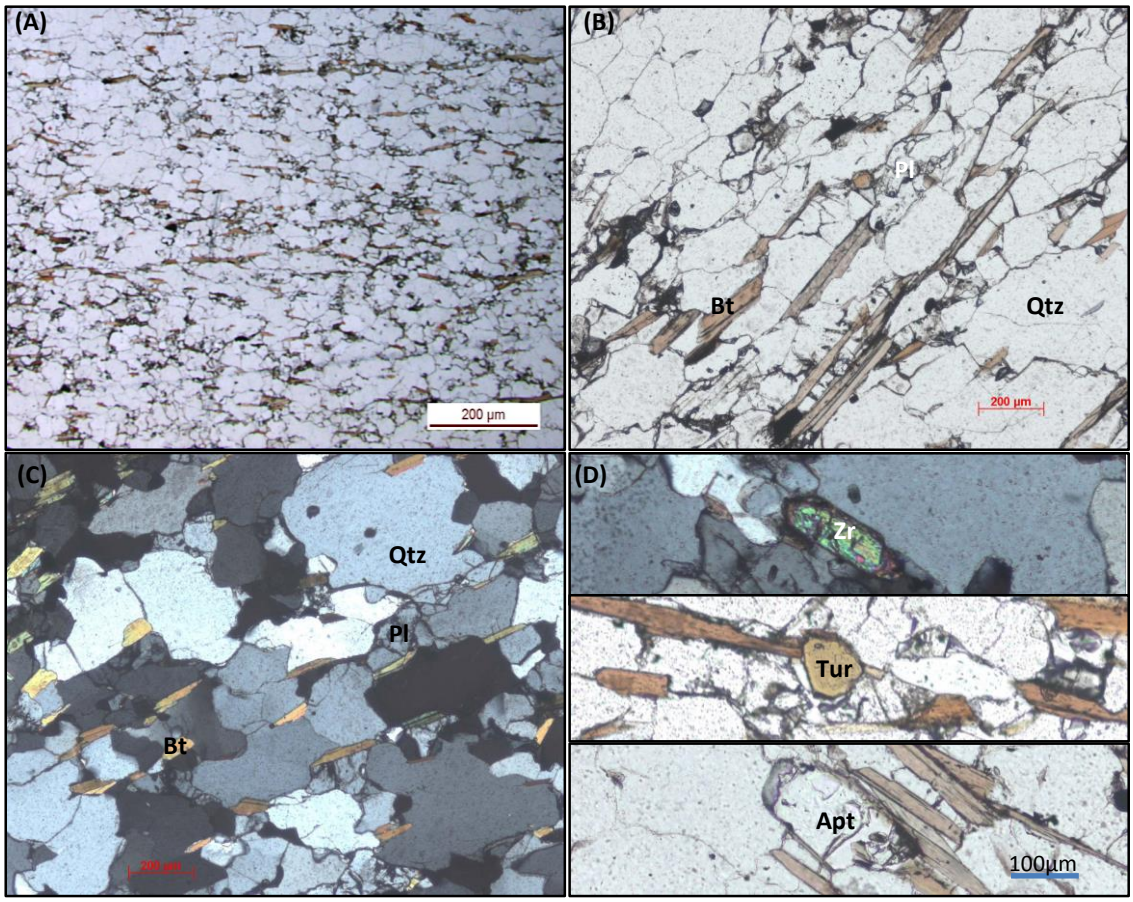

Fig. IV.2. 6 - Photomicrographs showing textural aspects of metagreywackes in biotite-zone. A) Magnifying glass photo showing aligned biotite flakes (PPL). B) Detail of the previous photo PPL); C) Photomicrograph showing curved contacts between quartz/quarts and quartz/plagioclase but not dynamic recrystallization features (no ondulose extinction, no bulging, no subgrains (CPL); D) Zircon, tourmaline and apatite dispersed in the quartz-feldspathic matrix (CPL and PPL).

4.2.3. Staurolite-zone

In the staurolite-zone staurolite-schists and calc-silicate rocks were analyzed.

The staurolite-schists are characterized by the mineral assemblage quartz + plagioclase + biotite + almandine + staurolite + andalusite + cordierite + ilmenite + iron oxides + tourmaline + apatite + zircon.

The texture is granolepidoblastic showing major quartz-feldspathic domains alternating with micaceous domains showing bands of aligned biotite agglomerates (Fig. IV.2.7). Staurolite, almandine, andalusite and cordierite blasts are dispersed in the matrix, both in the micaceous bands and in the quartz-feldspathic domains, although prevailing in micaceous bands (Fig. IV.2.7). The relative proportion of micaceous and quartz-

feldspathic domains is wide-ranging, occurring zones where the micaceous domains prevail and zones where the quartz-feldspathic domains prevail.

The quartz-feldspathic domains show polygonal or elongated fine-grained quartz and plagioclase and aligned but dispersed biotite. The modal amount of plagioclase is variable, occurring bands where the quartz predominates (approximately 90%) and areas where the plagioclase reaches about 40%.

The micaceous domains show agglomerates of aligned biotite, ilmenite, tourmaline and a lower modal percentage of quartz and plagioclase.

Three planar anisotropies are patent in these rocks: i) the main foliation, Sn, defined mainly by biotite (and muscovite + chlorite pseudomorphs after biotite), quartz and opaque minerals (ilmenite) elongated in the same direction; ii) a previous cleavage (Sn-1) is preserved in quartz-feldspathic domains *(microlitons)* and also as folded inclusion trails inside staurolite porphyroblasts (Figs. IV.2.8 and IV.2.16); and iii) a crenulation cleavage, that locally bends the main foliation (Sn) (Fig. IV.2.9).

Biotite occurs as fine-grained aligned crystals dispersed in the quartz-feldspathic domains and as aligned agglomerates parallel to Sn in the micaceous domains. Biotite in micaceous domains shows two different textures: i) elongated crystals aligned parallel to Sn and ii) as transverse “stacks” similar to those in biotite-zone (Fig.IV.2.10). These different types of biotite could result from two processes:

- Biotite that developed in dynamic conditions (aligned) and late biotite growing in static conditions (stacks);
- Biotite that replaces muscovite (aligned) and biotite that replaces chlorite stacks.

This last hypothesis is suggested by the similar morphology and by the late alteration processes that show muscovitization of the aligned biotite and chloritization of the transverse biotite (Fig. IV.2.23).

Garnet is rare (less than two crystals in most of the thin-sections), shows idiomorphic to sub-idiomorphic morphology and occurs both in the quartz-feldspathic domains and in the micaceous domains. When located in the quartz-feldspathic domains is poikilitic, almost skeletal, containing rounded quartz inclusions slightly smaller than the quartz in the matrix (Fig. IV.2.11B). In the micaceous domains, garnet is less poikilitic, containing few quartz inclusions with heterogeneous size. The Sn foliation is wrapped around the garnet porphyroblast and the inclusions trails are oblique to Sn (Fig. IV.2.11A). Garnet

also occurs as inclusion inside the largest staurolite porphyroblasts. Most of the porphyroblast are totally or partially replaced showing prograde substitution by biotite/staurolite/plagioclase pseudomorphs after garnet (Fig. IV.2.11C and D). In samples showing late retrograde alteration with muscovitization and cloritization of biotite, garnet is replaced by chlorite (Fig. IV.2.23).

Staurolite occurs in micaceous domains and in the quartz-feldspathic domains. When exclusively in quartz-feldspathic domains, shows poikiloblastic to skeletal texture with random quartz inclusions. When exclusively in micaceous domains, only contains tiny graphite inclusions. However, most of the staurolites show a complex inclusion pattern that records a long history of mineral growth. The following aspects can be highlighted:

1 - Staurolite porphyroblasts are contoured by the Sn foliation (Figs. IV.2.12 and IV.2.17);

2 – Some staurolite porphyroblasts preserve evidence of bedding and Sn-1. That is revealed by:

- The smallest staurolite porphyroblasts show apparently heterogeneous quartz inclusions trails (Si), oblique to each other and truncated by Sn (Fig. IV.12A). The heterogeneity of the Si pattern suggests that the staurolite porphyroblasts grew over a folded Sn-1 cleavage;
- Bedding and Sn-1 are preserved in the largest staurolite porphyroblasts. These have overgrown the compositional layering or bedding preserving the alternating quartz-rich and quartz-poor bedding planes parallel to Sn-1 foliation. The quartz rich layers remain as quartz-rich bands within the staurolite porphyroblasts and the micaceous-rich layers are replaced by staurolite, leaving graphite tiny inclusions that remain aligned parallel to the bedding layers marking a Sn-1 foliation (Fig. IV.2.13).
- The internal foliation (Si) is curved at the edges of some staurolite porphyroblast showing inclusions trails that are continuous to Sn-1 cleavage preserved in the low strain sites adjacent to staurolite (Fig. IV.2.14). The sense of curvature of the foliation at one end of the porphyroblast is opposite to that at the other end (‘millipede structure’) (Figs.IV.2.15);
- There are microlithons impressed in the staurolite porphyroblasts by inclusions trails. These are defined by relics of quartz-rich *versus* quartz-poor layers (Q and M-domains). The quartz-rich “microlithons” are defined by quartz and ilmenite

inclusions and the quartz-poor micaceous domains are defined only by ilmenite and graphite inclusions (Fig. IV.2.16).

3 – The borders of the biggest staurolite porphyroblasts show trails of elongated and aligned ilmenite inclusions parallel to Sn. This results of the continuous porphyroblast growth after the Sn main foliation having drape around the staurolite crystal (Bell & Johnson, 1989a, Figs. IV.2.17 and 2.18).

4 – Some samples show staurolite fine-grained crystals dispersed in the matrix that show static growth, no foliation deflection and no inclusions (Fig.IV.2.19).

5 – Adjacent to most staurolite porphyroblasts there are pressure-shadows, where quartz has recrystallized occupying dilatant sites adjacent to the porphyroblast. The position of the pressure-shadow, extending parallel to the Sn foliation, indicates the formation of the pressure shadow during Dn deformation phase.

6 – The crenulation cleavage (Dn+1) is not recorded in Si staurolite inclusion trails.

7 – Andalusite replaces staurolite and late retrograde processes provoke replacement of staurolite by muscovite and biotite agglomerates or by sericite in the borders and in fractures (Fig. IV.2.23).

The staurolite porphyroblasts can be inferred to have grown during the Dn deformation phase that folded and transposed an earlier Sn-1 cleavage. Some of them, however, continue to grow after the last stages of progressive development of Sn, which is revealed by the replacement of the phyllosilicates that define the Sn foliation wrapped around the staurolite porphyroblasts.

Andalusite porphyroblasts occur both dispersed in the micaceous domains and in association with staurolite. All the porphyroblasts overgrow the Sn foliation showing Si parallel to Se, which is revealed by straight inclusion trails of elongated ilmenite and biotite (Si) in continuity to the matrix Sn foliation (Fig. IV.2.21). There are andalusite porphyroblasts overgrowing the crenulation cleavage and showing mimetic development over the crenulation (Fig. IV.2.21D). There are evidences of staurolite replacement by andalusite + biotite revealed by staurolite relics inside andalusite porphyroblasts (Fig. IV.2.20). This indicates that andalusite grew after the development of the Sn foliation and that the earlier staurolite porphyroblasts were replaced by andalusite.

Tourmaline occurs as dispersed crystals in the staurolite-schists and overlaps Sn foliation without deflection in the surrounding matrix (Fig. IV.2.22A). In the tourmalinites

associated to fault-zones all the phyllosilicates were replaced by tourmaline that mimetized the previous foliation (Fig. IV.2.22B). This suggests the entrainment of later boron-rich fluids in the metasedimentary sequence.

Retrograde processes affect the staurolite-schists, what is revealed by the substitution of staurolite by sericite, muscovite and biotite, the replacement of garnet by chlorite, replacement of biotite by chlorite and muscovite and replacement of andalusite by sericite (Fig. IV.2.23).

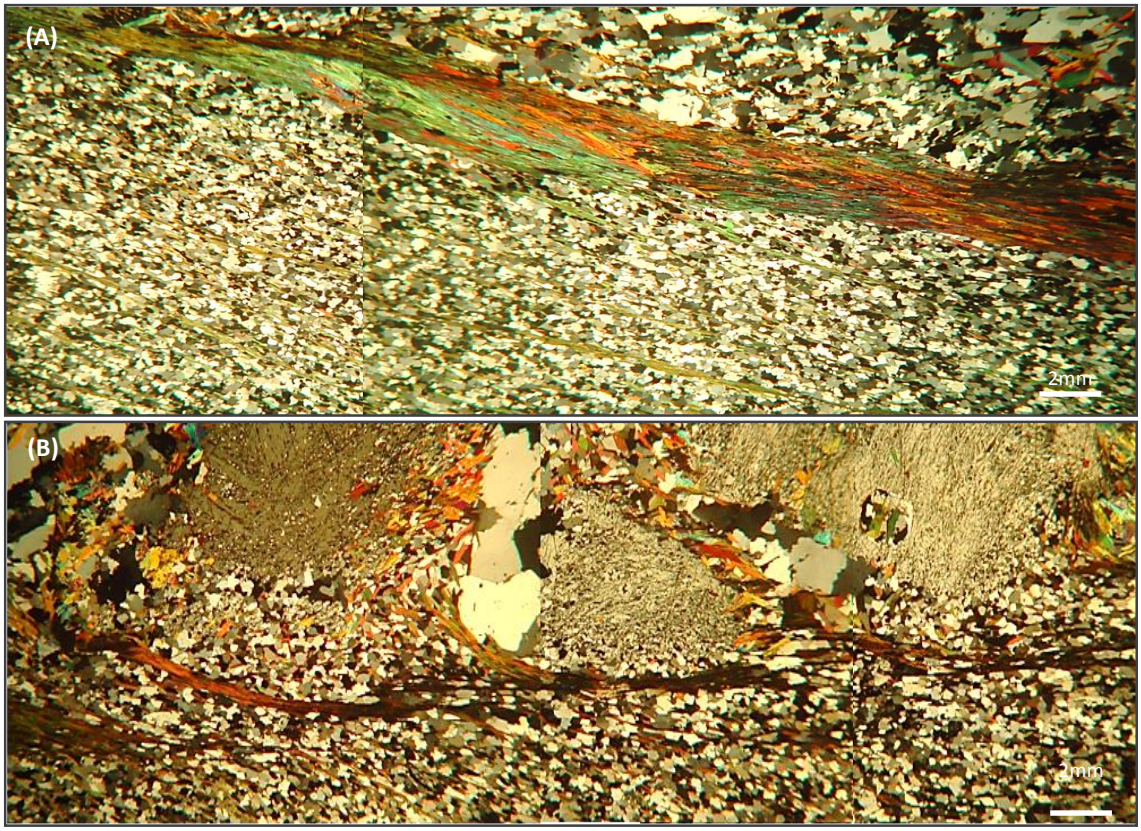

Fig. IV.2. 7 – A) Photomicrographs of staurolite-schists showing quartz-feldspathic domains and micaceous domains. Quartz-feldspathic domains contain fine-grained quartz and plagioclase crystals and rare aligned biotite. Micaceous domains contain biotite aligned agglomerates (CPL). B) Photomicrographs showing three staurolite poikiloblasts. Included in staurolite there are a pseudomorph after garnet (CPL).

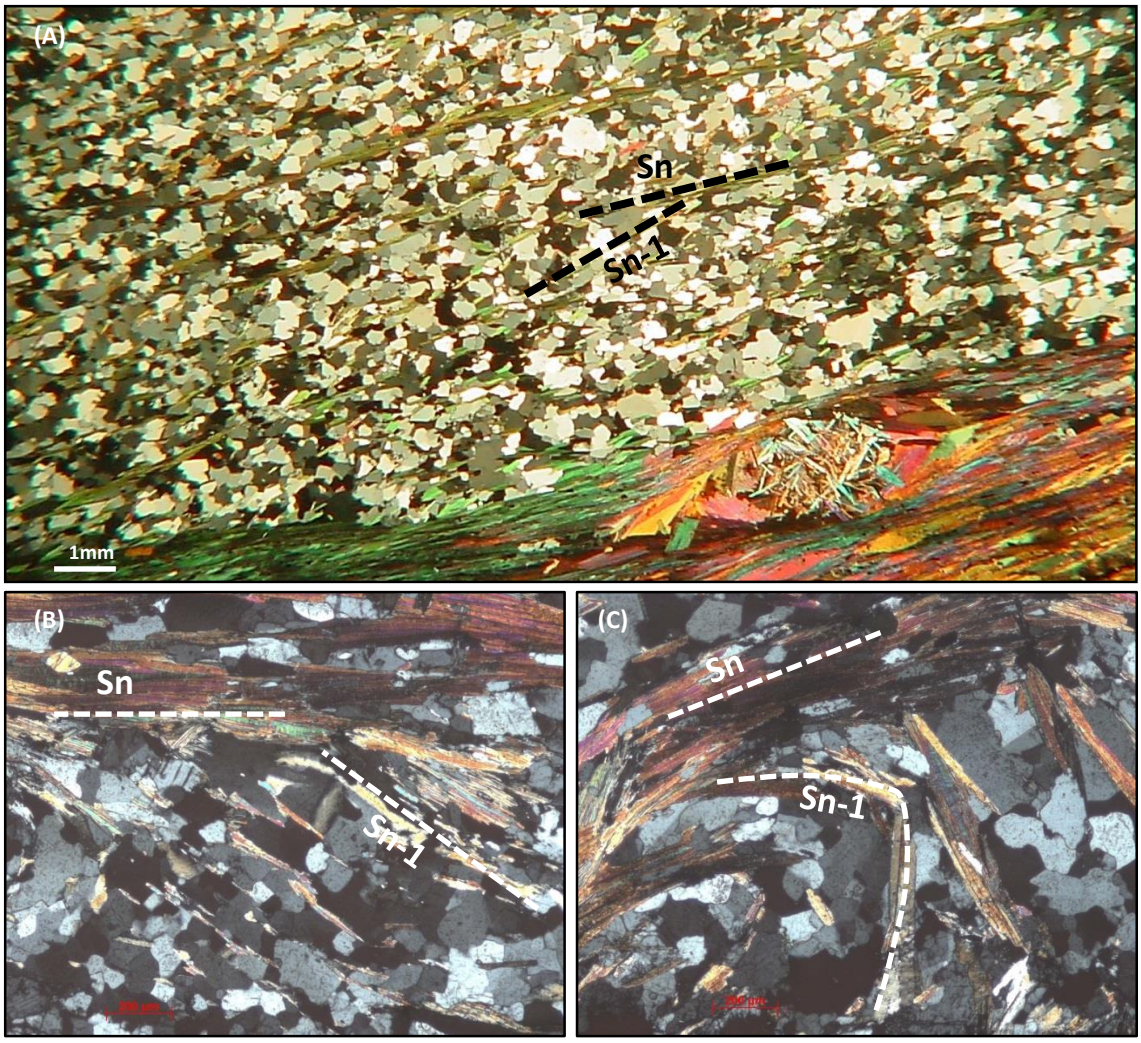

Fig. IV.2. 8 – Photomicrographs showing textural aspects of staurolite-schists. A) Panoramic photo showing micaceous domain and quartz-feldspathic domain. In the quartz-feldspathic domain can be distinguished the Sn foliation parallel to the micaceous domain and an oblique Sn-1 cleavage; B and C) Sn-1 cleavage truncated by Sn; (All photos in CPL).

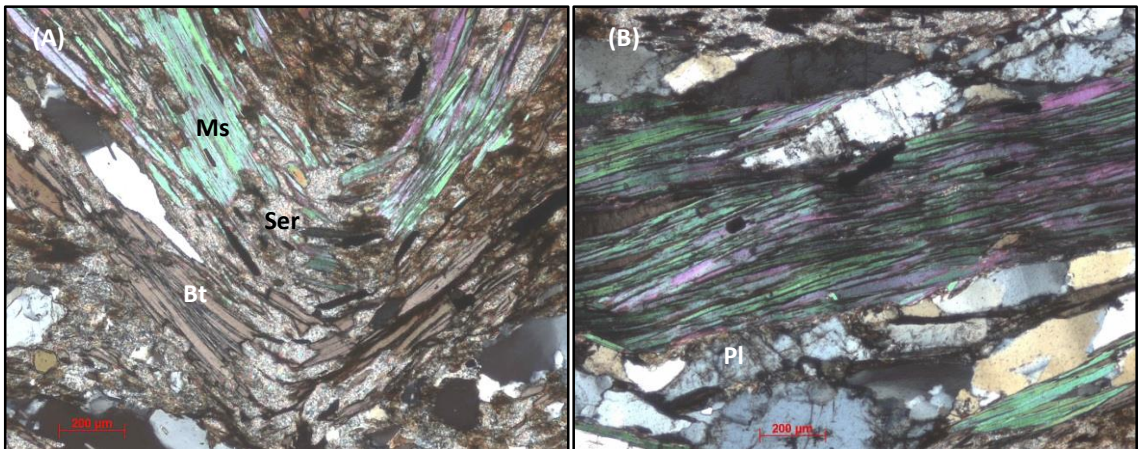

Fig. IV.2. 9 - Photomicrographs showing folding affecting the Sn cleavage (All photos in CPL).

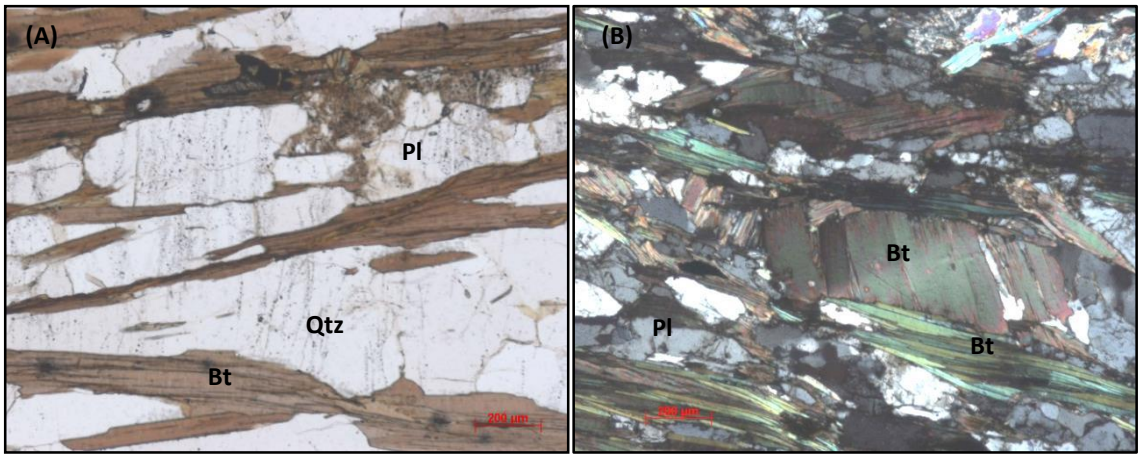

Fig. IV.2. 10 – Photomicrograph showing textural aspects of biotite in staurolite-schists. A) Biotite in quartz-feldspathic domains; B) Biotite in micaceous domains showing two different textures: fine elongated flakes marking Sn foliation and biotite as “stacks”.

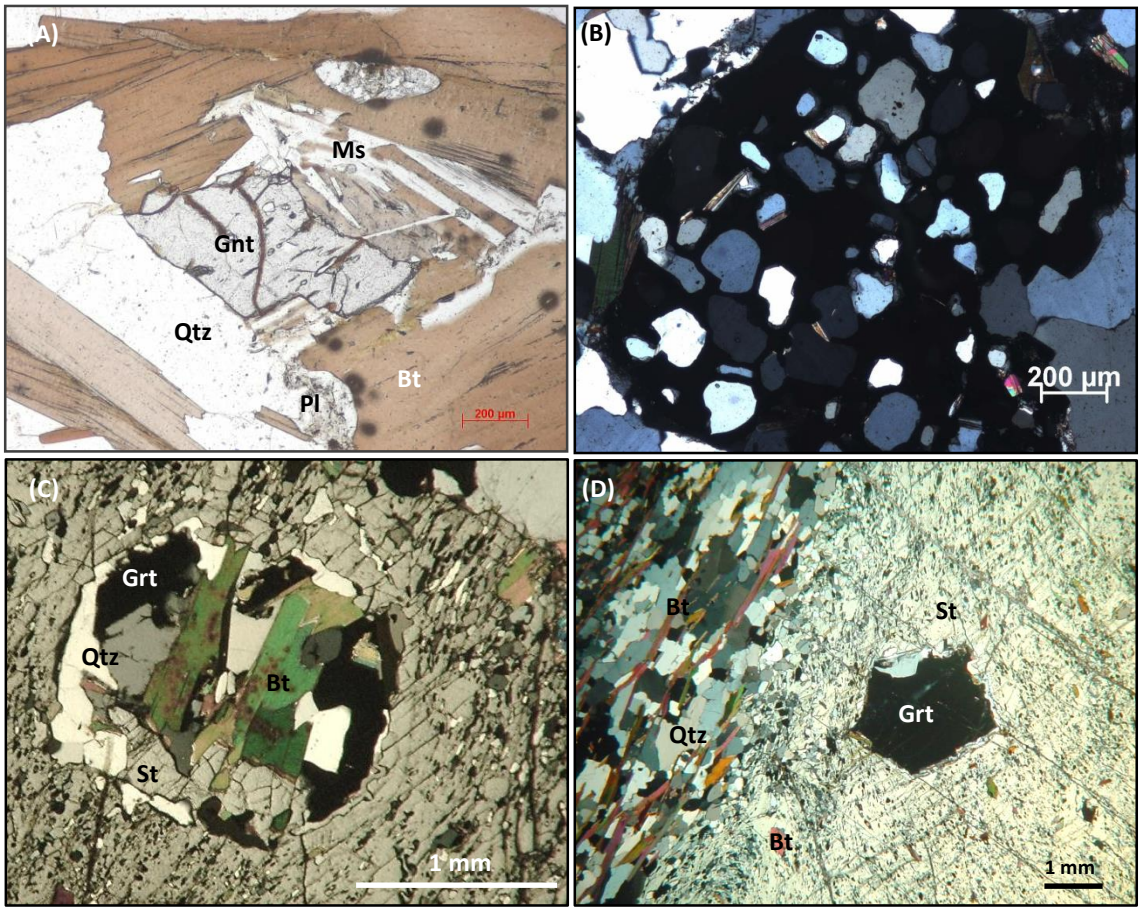

Fig. IV.2. 11 - Photomicrograph showing textural aspects of garnet in staurolite-schists. A) Garnet in micaceous domain (PPL); B) Poikilitic garnet in quartz-feldspathic domain. (CPL); C and D) Garnet inside staurolite (CPL).

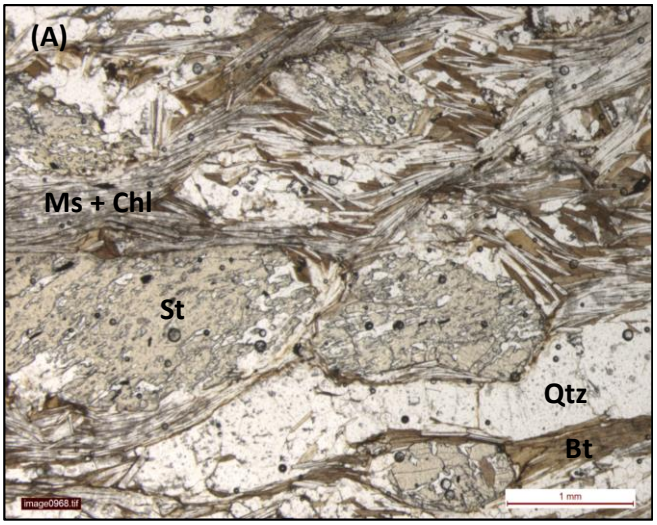

Fig. IV.2. 12 – Photomicrograph showing textural aspects of staurolite in staurolite-schists. Conspicuous staurolite porphyroblasts showing abundant quartz inclusions defining an heterogeneous internal pattern (Si), discordant to the Sn foliation, which is strongly flattened around staurolite. Note the heterogeneity of the Si pattern.

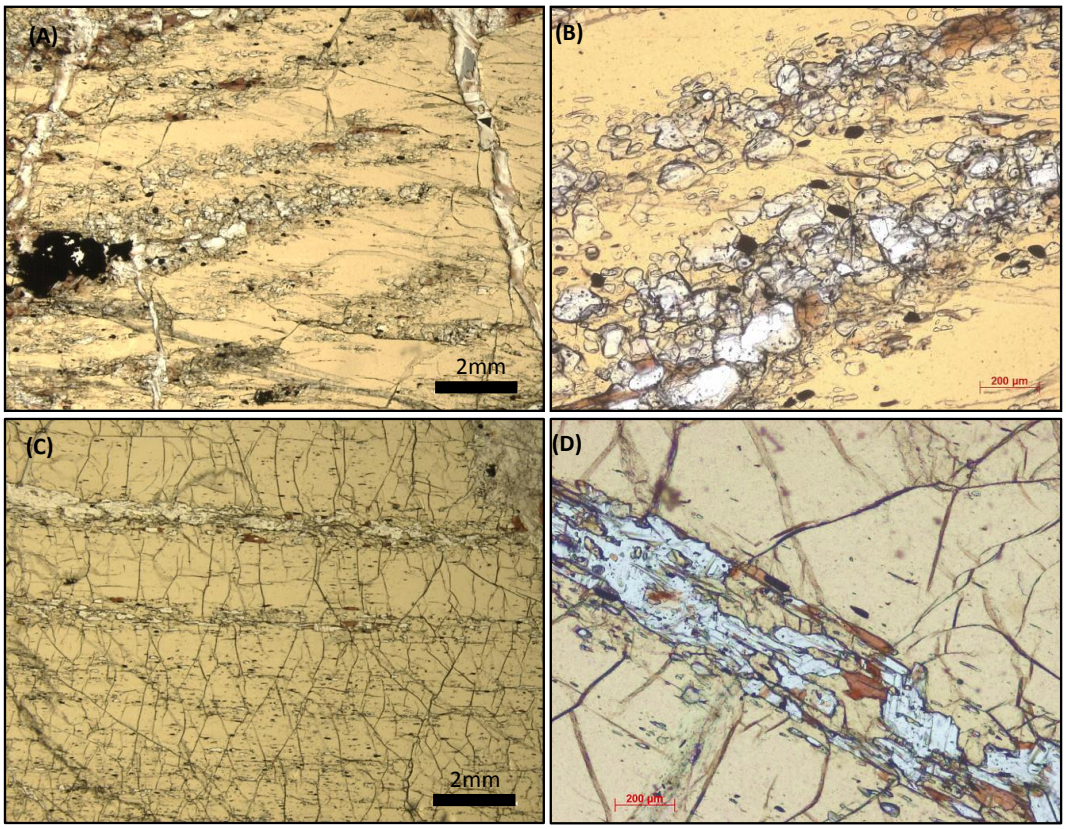

Fig. IV.2. 13 - Photomicrographs showing staurolite porphyroblasts fossilising the bedding and Sn-1 parallel to the bedding. The micaceous bands were replaced by staurolite leaving aligned graphite as inclusions and the quartz-rich bands are revealed by the quartz aligned inclusions trails. These inclusions trails are not parallel to the exterior foliation.

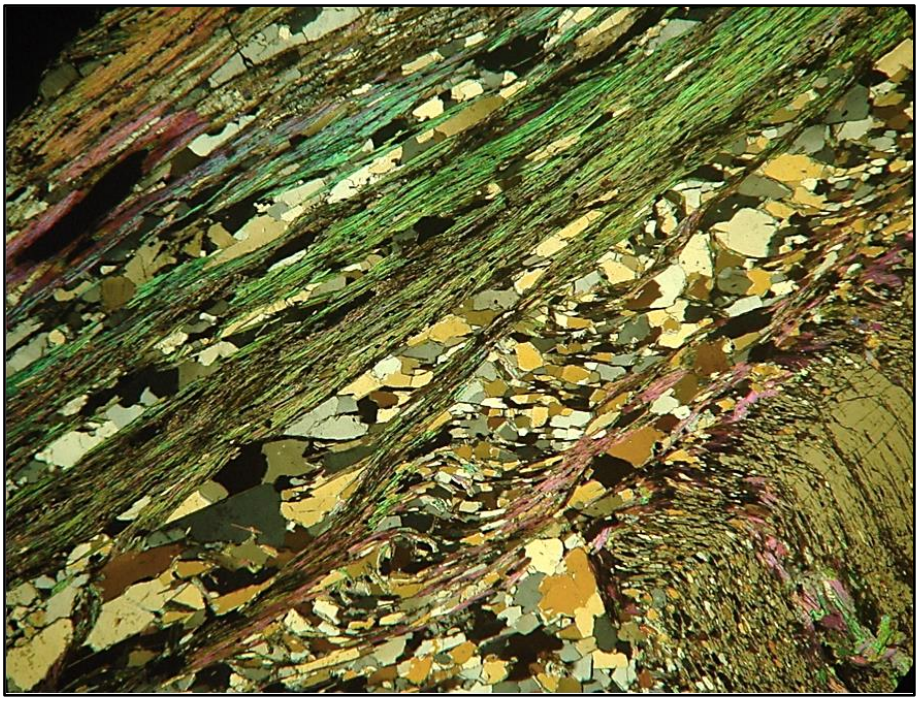

Fig. IV.2. 14 – Photomicrographs showing textural aspects of staurolite-schists. Sn cleavage defined by biotite and secondary muscovite. Quartz fine-grained crystals are elongated parallel to Sn. The low-strain site adjacent to staurolite porphyroblast reveals residual crenulation microfolds (Sn-1) that have been obliterated in the unprotected areas of the matrix. The staurolite poikiloblast quartz inclusions trails are continuous to Sn-1 crenulation cleavage. The curvature of Si at the edges of the staurolite porphyroblast indicates that the crenulations began to form as the porphyroblast completed its growth.

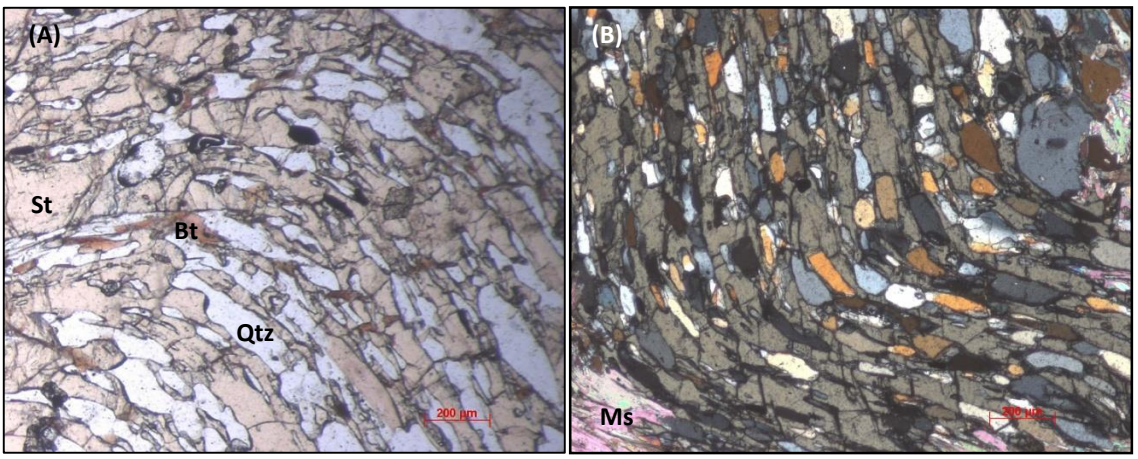

Fig. IV.2. 15 - Folded quartz trails in the border of the staurolite porphyroblasts, top and bottom, respectively. The sense of curvature of the foliation at one end of the porphyroblast is opposite to that at the other end (‘millipede structure’).

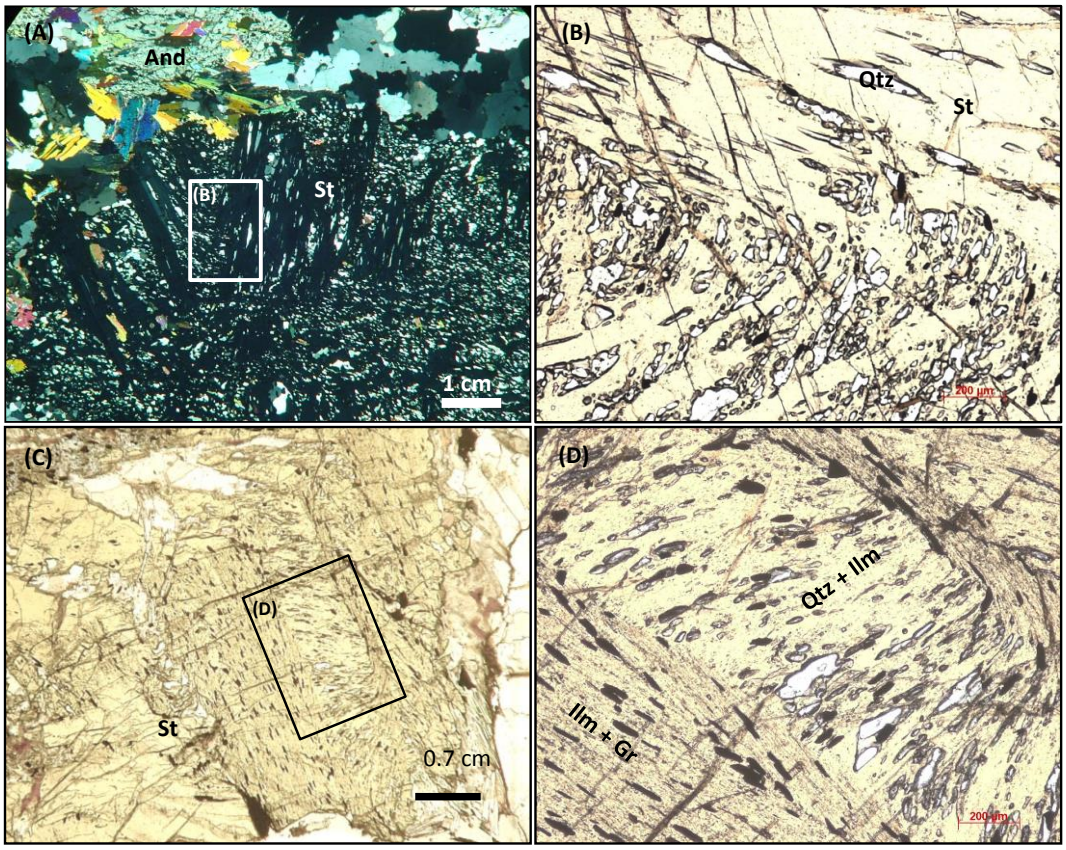

Fig. IV.2. 16 - Photomicrographs showing textural aspects of staurolite-schists. A) Staurolite showing fossilized "microlithons" defined by folded trails of quartz truncated by oblique elongated inclusions (Si); B) detail of previous figure; C) Staurolite showing fossilized "microlithons" impressed by quartz and ilmenite inclusions inside staurolite porphyroblast. D) Detail of previous picture showing relics of quartz-rich (Q-domains) versus quartz-poor layers (M-domains). The quartz-rich "microlithons" are defined by quartz and ilmenite inclusions which preserve the previous foliation and the micaceous domains are defined only by ilmenite and graphite (Gr) inclusions.

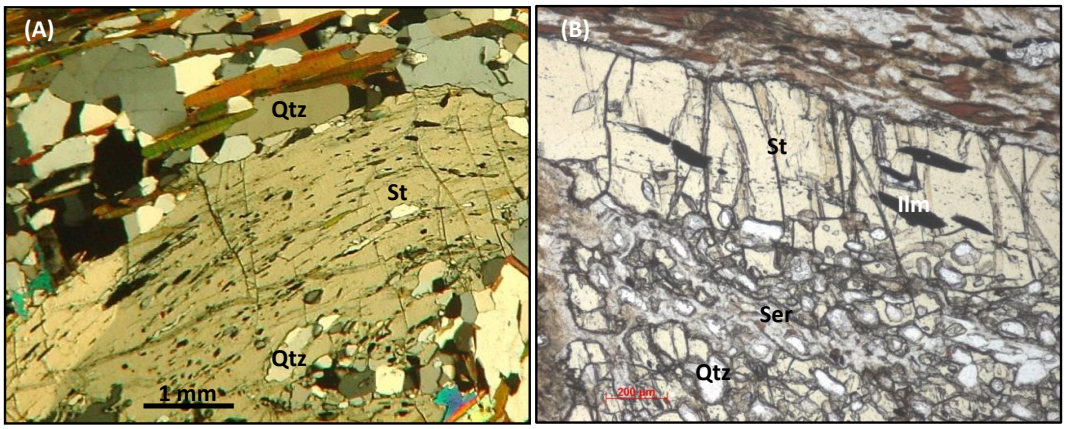

Fig. IV.2. 17 – Photomicrographs showing textural aspects of staurolite in staurolite-schists. A) Border of staurolite showing aligned ilmenite and graphite inclusions trails parallel to Sn external foliation. Note that inclusions trails record the deformation caused by the deflection of Sn around the porphyroblasts. B) Staurolite edge showing ilmenite and graphite inclusions trails parallel to external Sn foliation.

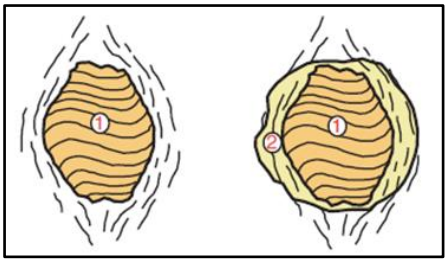

Fig. IV.2. 18 - Sketches showing progressive growth stages of an hypothetical porphyroblast during progressive, foliation-forming deformation of the matrix, according to the model of Bell & Johnson (1989).

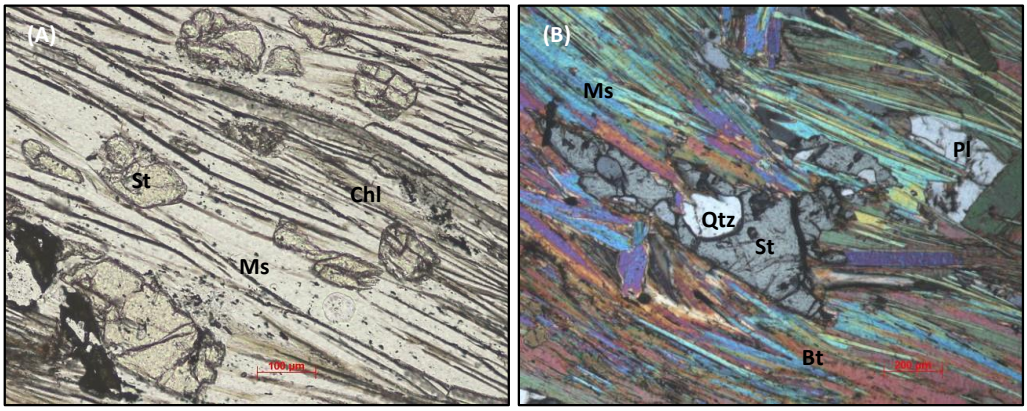

Fig. IV.2. 19 – Photomicrographs showing staurolite porphyroblasts overlapping on Sn foliation without deflection in the surrounding matrix suggesting they grew under static conditions.

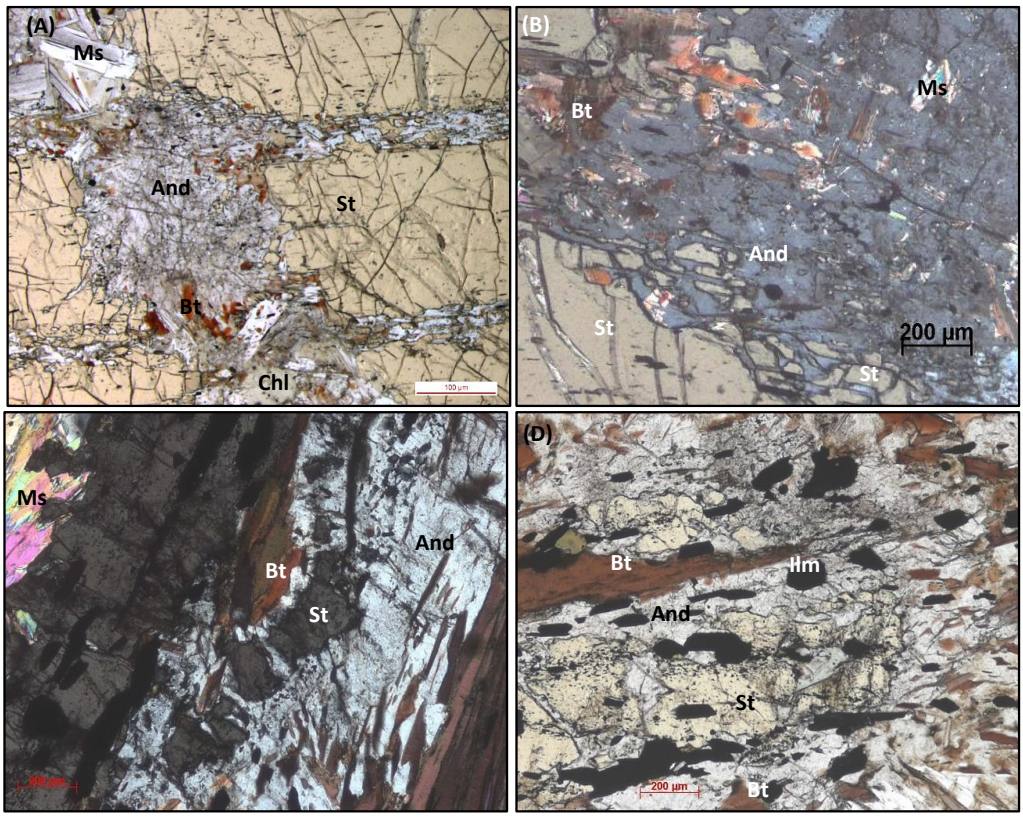

Fig. IV.2. 20 – Photomicrographs showing staurolite replacement by andalusite and biotite

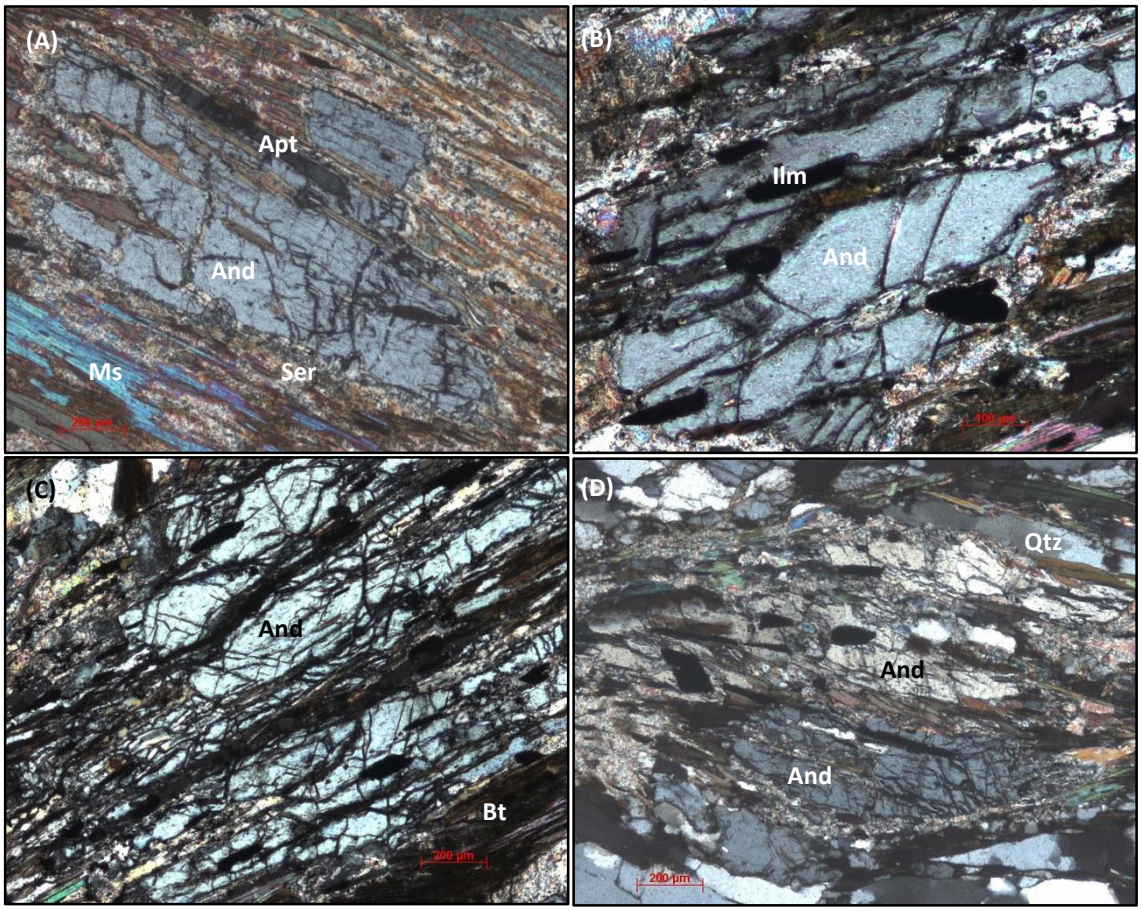

Fig. IV.2. 21 – Photomicrographs showing andalusite porphyroblasts in staurolite schists. A,B andC) The Sn foliation is not deflected by andalusite and Si is parallel to Se. D) The andalusite porphyroblasts show slightly flexure mimetic of previous structures (Sn folded by Dn+1).

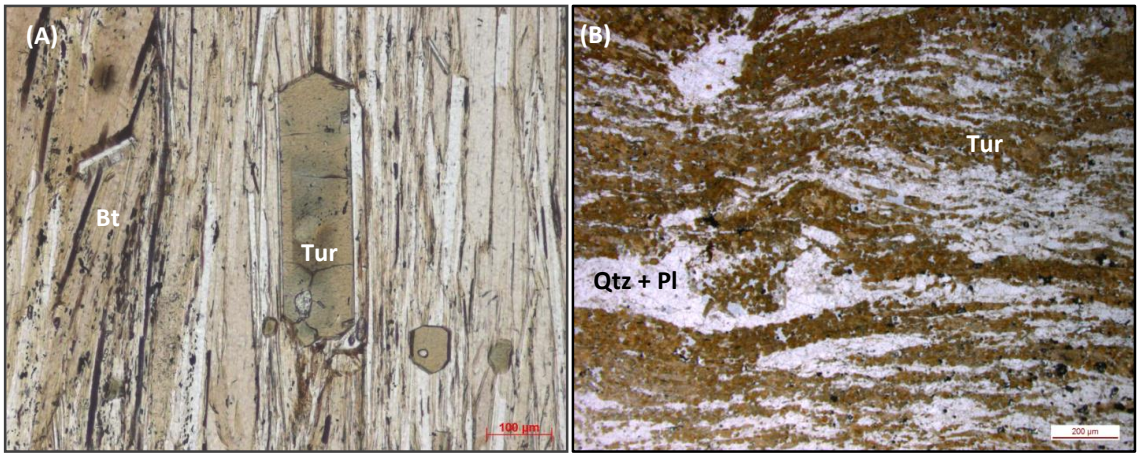

Fig. IV.2. 22 – Photomicrographs showing tourmaline textural aspects in staurolite schists. A) Tourmaline overlapping Sn foliation without deflection of the surrounding matrix; B) Tourmalinite associated to a fault in staurolite-zone. All the phyllosilicates were replaced by tourmaline that mimetized the previous foliation.

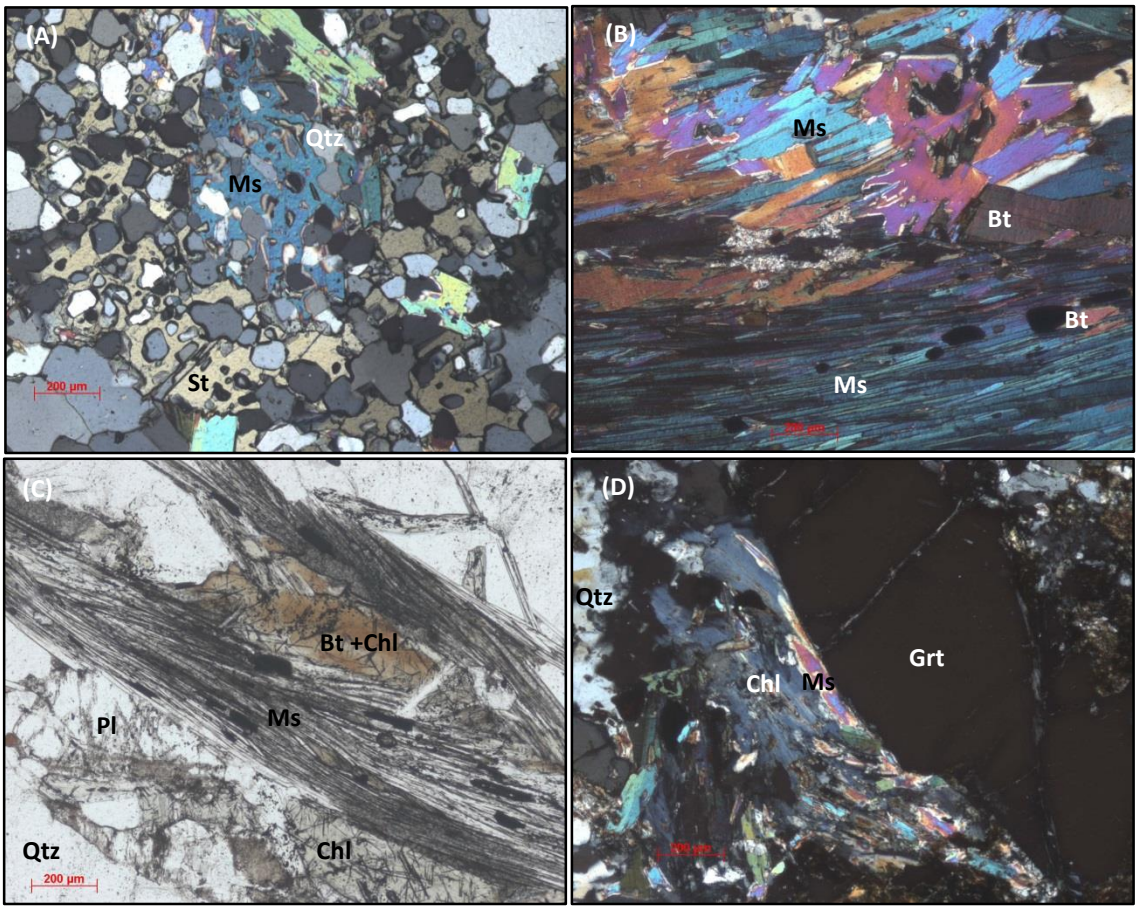

Fig. IV.2. 23 - Photomicrographs showing alteration aspects in staurolite-schists. A) Muscovite partially replacing staurolite in quartz-feldspathic domain. Muscovite shows the same poikilitic texture as the staurolite. B) Random flakes of muscovite replacing staurolite (top) and aligned muscovite replacing biotite and mimetizing biotite alignment; C) Chlorite replacing transverse biotite and muscovite replacing aligned biotite. D) Chlorite + muscovite+ quartz replacing garnet.

4.2.3.1 - Calc-silicate rocks

The calc-silicate rocks in the staurolite-zone show the mineral assemblage: amphibole (hornblende) + quartz + plagioclase (anorthite) + garnet + titanite + ilmenite + pyrrhotite ± epidote (sec) ± chlorite (sec) ± smectite (sec).

The matrix is quartz-feldspathic showing polygonal quartz and minor amount of anorthite. Titanite is dispersed in the matrix. Hornblende occurs as aligned crystals most of them pseudomorphs after actinolite. Garnet is poikilitic, containing quartz inclusions with heterogeneous size and distribution. Late alteration processes show replacement of anorthite by epidote and replacement of hornblende by chlorite and smectite (Fig. IV.2.24).

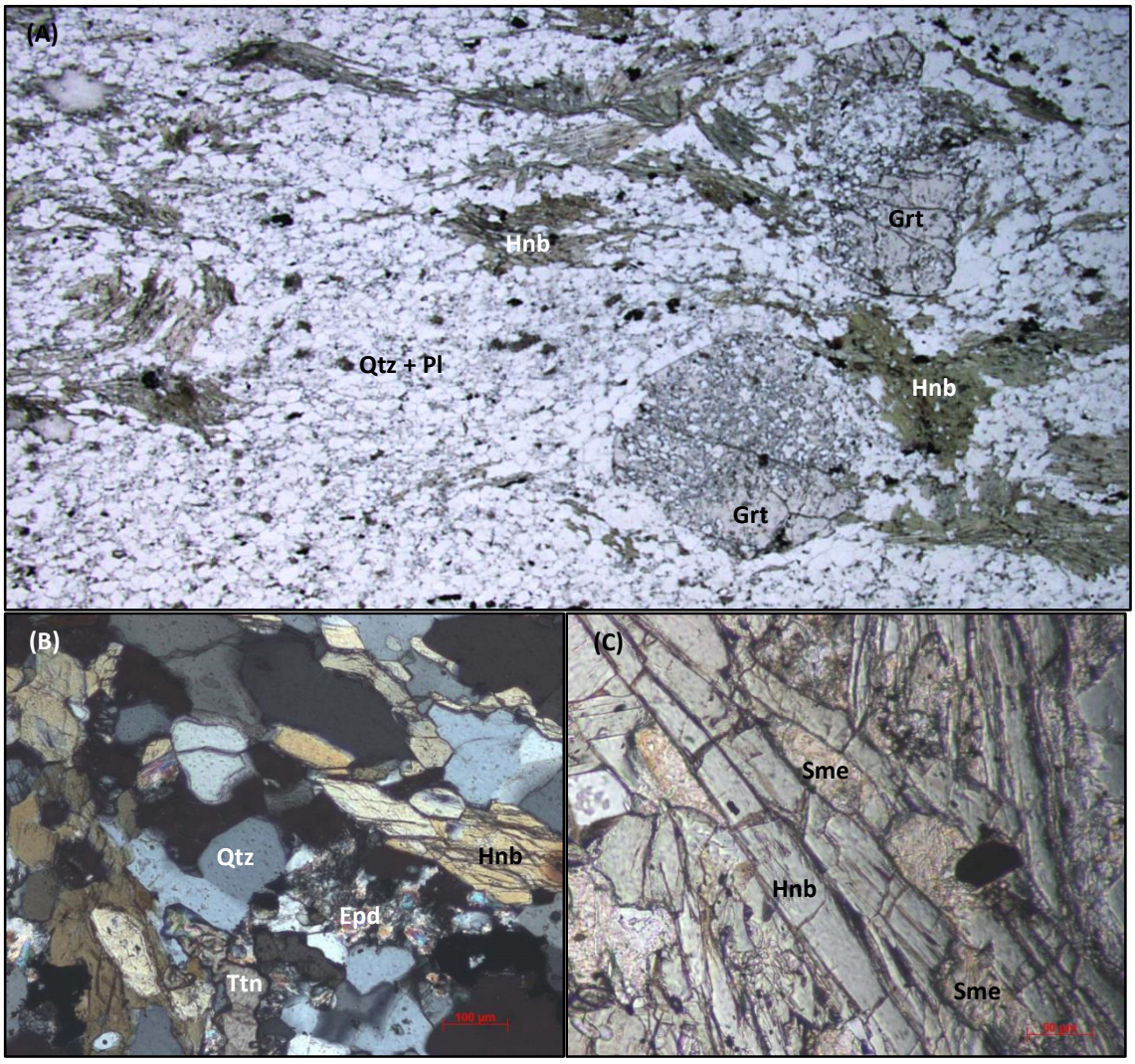

Fig. IV.2. 24 - Photomicrograph showing textural aspects of calc-silicate rocks in the staurolite-zone. A) General aspect of the sample (PPL). B) Amphibole and titanite associated with epidote and quartz (CPL); C) Smectite after hornblende (PPL).

4.2.3.2. "Aluminosilicate veins"

The aluminosilicate veins occurring in the staurolite-zone are composed of muscovite + sillimanite + andalusite + kyanite ± quartz (Fig. IV.2.25). Muscovite is abundant and occurs in radiating aggregates or as large flakes. Large prismatic sillimanite crystals occur associated with muscovite. Fibrolitic sillimanite is also abundant. Kyanite and andalusite occur in idiomorphic crystals dispersed in the rock. Staurolite is rare, shows aluminosilicate vermicular inclusions and is replaced by andalusite, which suggests a later emplacement of the aluminosilicate veins.

The idiomorphic texture and the linear contacts between the aluminosilicate crystals and the absence of reactional textures suggest textural equilibrium between the aluminosilicate minerals.

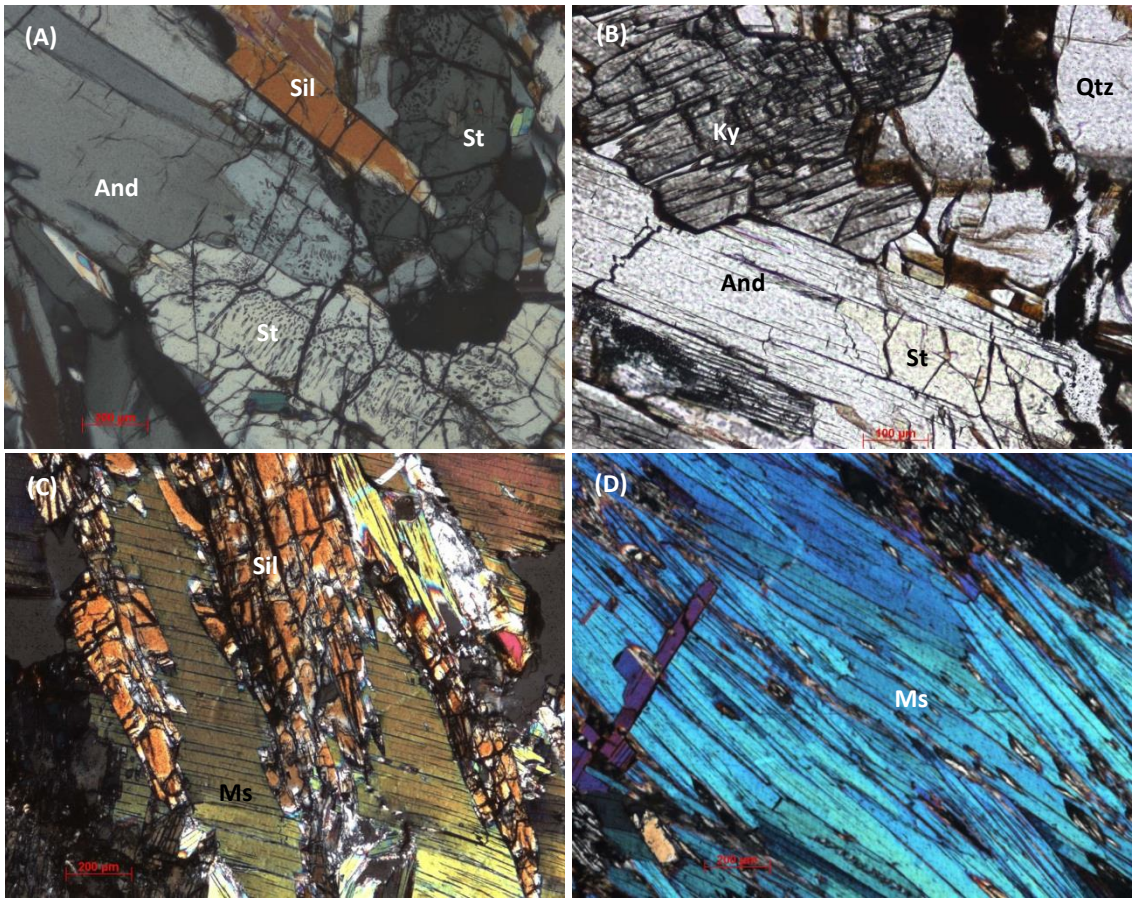

Fig. IV.2. 25 – Photomicrographs showing aspects of aluminosilicate "veins": A) Staurolite partially replaced by andalusite and containing aluminosilicate vermicular inclusions. B) Staurolite replaced by andalusite associated with quartz and kyanite; C) Sillimanite and muscovite intergrowths; D) Muscovite agglomerate.

4.2.4. Sillimanite-zone

Sillimanite-zone is restricted to areas adjacent to the MMC or in contact with the granitic massifs in Fânzeres.

In the metaconglomerates (Figs. IV.2.26A and B), micas skirting the quartz grains are replaced by clusters of sillimanite. The mineral assemblage is: quartz + biotite + sillimanite (and retrograde muscovite + chlorite).

In schists the sillimanite replaces biotite, which defines the Sn foliation (Figs. IV.2.26C and D). The mineral assemblage is: quartz + plagioclase + biotite + sillimanite ± muscovite. There are some aspects that suggest incipient partial melting, namely plagioclase overgrowth and cuspade quartz crystals. It is important to highlight the absence of staurolite, andalusite or cordierite in these samples.

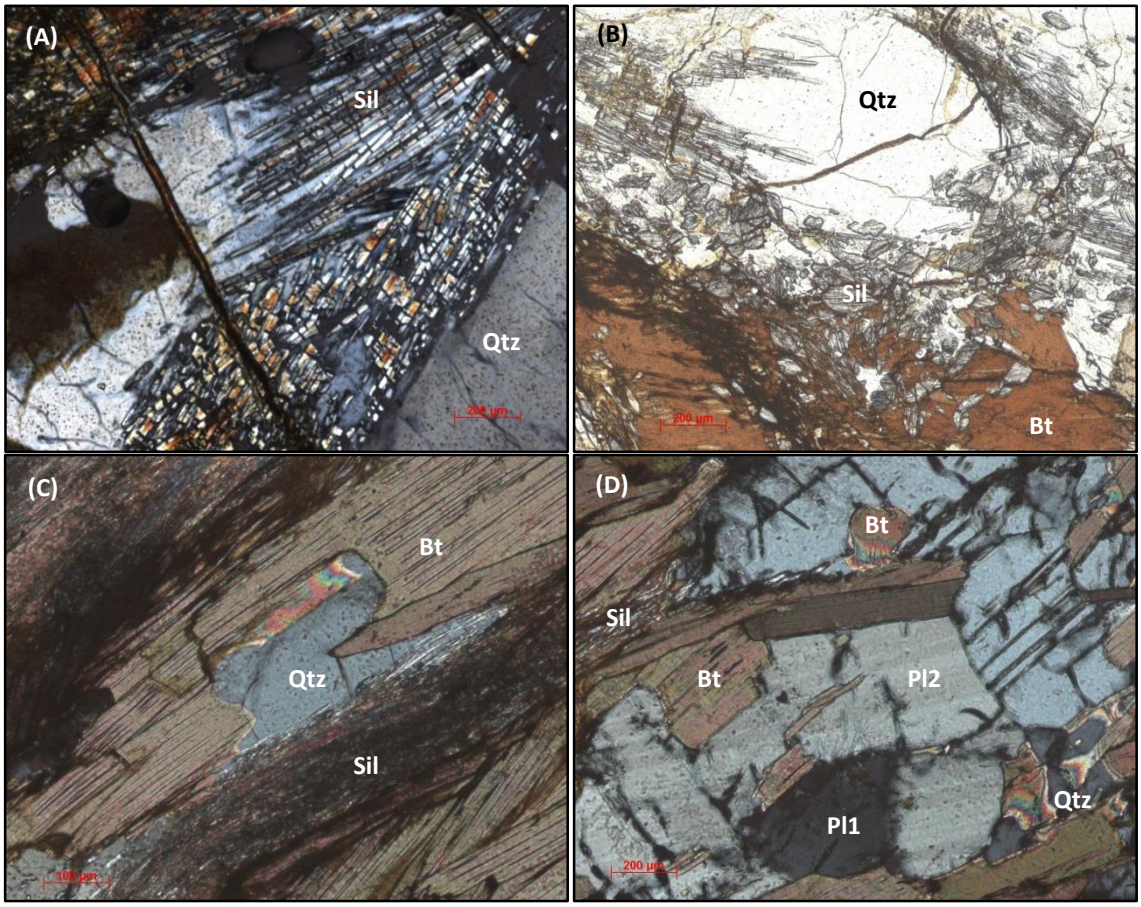

Fig. IV.2. 26 – Photomicrographs showing textural aspects of sillimanite-zone rocks. A and B) Metaconglomerate showing replacement of biotite by prismatic sillimanite; C and D) Sillimanite-schists showing fibrolitic sillimanite replacing biotite and evidence of initial partial melting as cuspate quartz and plagioclase overgrowth.

4.2.5. Metamorphic conditions in Sector 2

In this sub-chapter we will discuss the mineral assemblages and their relationship with the possible metamorphic condition found in Sector 2, from chlorite-zone to sillimanite-zone.

It is known that mineral assemblages and compositions of minerals are controlled either by the bulk composition of the rock or/and by metamorphic factors, notably the pressure and temperature conditions (Turner, 1948). The bulk rock composition is fundamental to understand the sequence of assemblages displayed by the analyzed rocks.

The system K_2O-FeO-MgO-Al_2O_3-SiO_2-H_2O (KFMASH) is useful and appropriate to the study the metamorphic conditions of pelitic rocks containing Fe and Mg bearing minerals (Bucher & Grapes, 2011).

Figure IV.2.27 represents the bulk rock composition of biotite- and staurolite-schists in the AFM diagram as well as the composition of the aluminosilicate-vein present in the staurolite-zone. The pelites bulk composition is characterized by “A” parameter values between 0.40 and 0.53 and XFe between 0.43 and 0.48. Moderate to low values of Mn, generally < 0.04 and low CaO content. This values are considered typical of pelites although they show slightly low Al and high Mg content. The bulk composition of these rocks determines its behavior during metamorphism.

As was observed in the petrographic studies, the mineral zone sequence of index minerals in Sector 2 is: Chl → Bt →Grt → St →Sil. Chloritoid, kyanite or pyrophilite were not detected during the petrographic observations. Figure IV.2.28 represents a sequence of assemblages displayed as an arrangement of schematic AFM diagrams in the KFMASH system (AFM-diagrams) in a Barrovian metamorphism context (after Bucher & Grapes, 2011) where the bulk-rock composition of the studied pelitic rocks is marked (red diamond). The analysis of AFM diagrams sequence allows to understand the particular paragenesis found, form Chlorite- to migmatite-zone, namely the appearance of garnet before staurolite since, generally, in higher Al rocks staurolite predates garnet (Spear, 1995; Bucher & Grapes, 2011) and the absence or rarity of chloritoid and aluminosilicates in the staurolite-zone (common in higher Al rocks). The staurolite first appearance occurs at ~560 ºC to the bulk composition of this pelitic rocks (Fig. IV.2.28h).

Figure IV.2.29 shows the distribution of mineral assemblages for typical pelitic bulk-rock composition showing relatively low Al and moderate Fe contents (Bucher & Grapes, 2011). In all fields muscovites, quartz and H_2O are present in addition to the indicated minerals (the curve 1 represents the breakdown of muscovite to K-feldspar). It is notably that this type of rock will not develop sillimanite along a Barrovian type geotherm and that it will not contain kyanite at any P and T conditions. Chloritoid occurs only at pressures higher than 500 MPa. This can explain why the staurolite-schists do not contain aluminosilicates in equilibrium with staurolite and why chloritoid was not detected in the biotite-zone samples. The coexistence of aluminosilicate with staurolite is only possible in rocks that contain higher Al content. Considering the first occurrence of staurolite at 560 ºC, the peak pressure conditions attained by these rocks was at least 490 MPa (Fig. IV.2.29 – red shaded area).

As referred, the staurolite-schists are interbedded with calc-silicate rocks. This rocks show the mineral paragenesis amphibole + quartz + garnet + anorthite + titanite. Diopside is absent. Considering X_{CO2} normal values to calc-silicate rocks, and the system SiO_2-MgO-CaO-H_2O-CO_2 (Spear, 1995), the diopside starts to develop between 550 and 600 ºC. Thus, using this data, it is possible to constraineven more the metamorphic conditions during this metamorphic event to temperatures between 560 and 600 ºC (Fig. IV.2.29 – red shaded area).

The development of andalusite at staurolite expenses and showing a blastesis/deformation relationship indicative a post-kinematic character, suggests that a decompression process occurred after the attainment of the first metamorphic event conditions (M1). Sillimanitic rocks near the granitic intrusions could be the result of increasing temperature and decompression (Bucher & Grapes, 2011). The PT conditions of this metamorphic event were delimited in the pseudosection diagram in the field of andalusite (orange shaded area; Fig. IV.2.29) and indicated P < 380 MPa and T > 530 ºC.

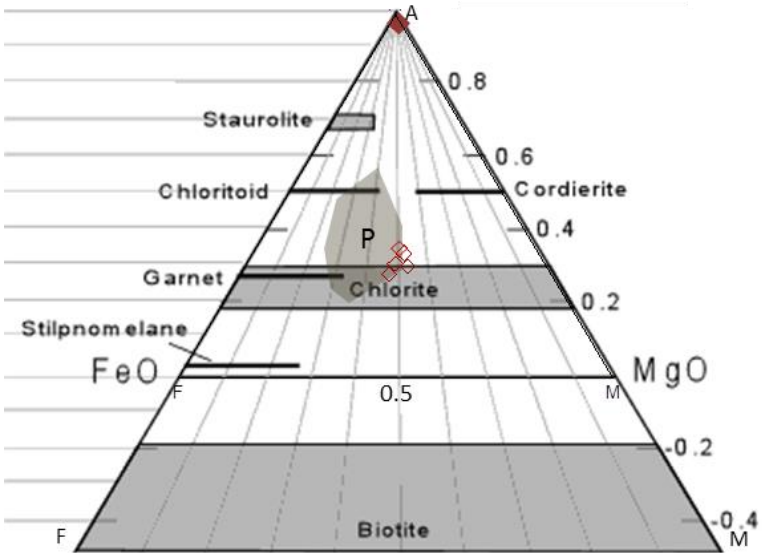

Fig. IV.2. 27 - AFM diagram. Compositions for typical pelitic composition is represented by "P" (Bucher & Grapes, 2011). Staurolite schist composition show XFe between 0.4 and 0.6 and "A" parameter between 0.3 and 0.4. The composition of aluminosilicate vein shows A= 0.98 (red filled diamond).

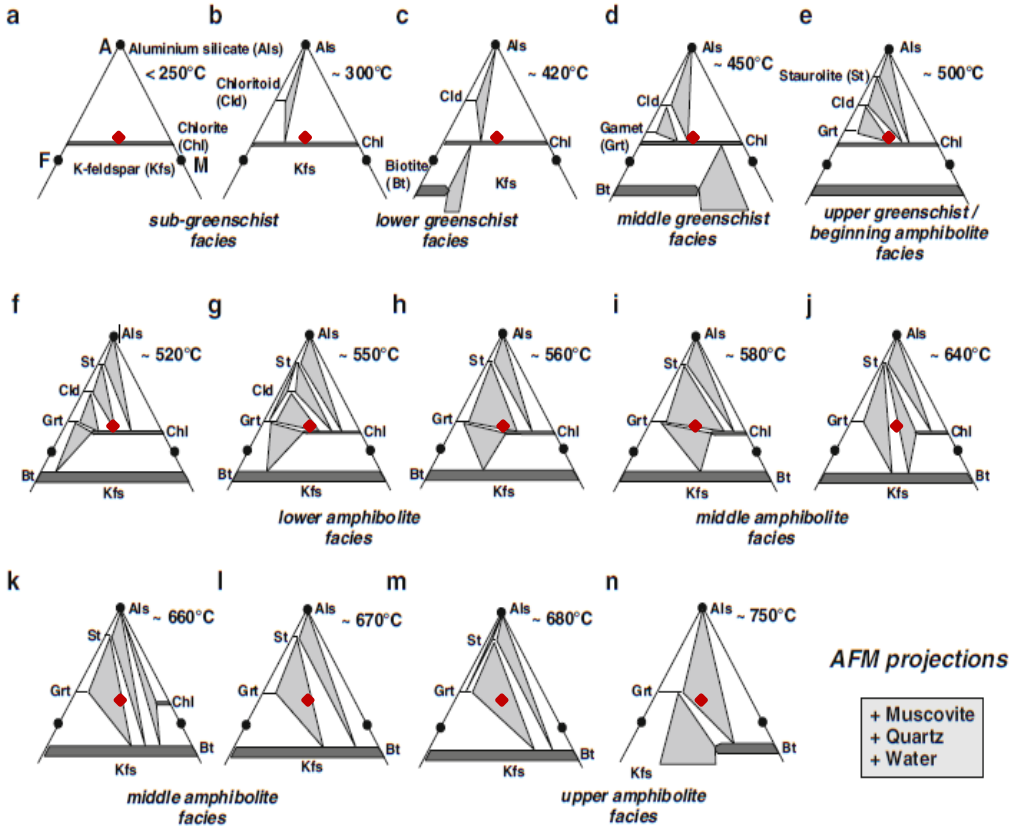

Fig. IV.2. 28 - Arrangement of assemblages displayed as a sequence of schematic AFM diagrams in the KFMASH system (AFM-diagrams) along Barrovian type geotherm (after Bucher & Grapes, 2011). The bulk rock composition of sector 2 pelitic rocks is indicated by the red diamond.

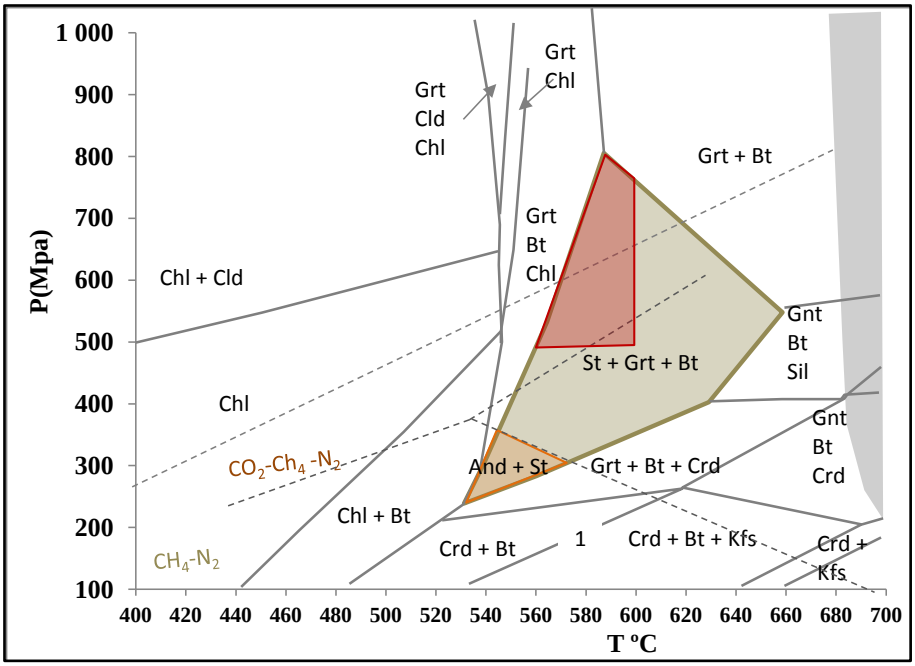

Fig. IV.2. 29 - Stable assemblages in metapelitic rocks that originally contained Chl–Ms–Qtz (model system KFMASH). Note that this type of rock will not develop sillimanite in a Barrovian type geotherm and does not contain Ky at any P and T. The fields that contain Kfs do not carry Ms (high T low P). The central amphibolite facies assemblage is Grt–Bt–St (shaded in green). Delimited the stability field of the staurolite-schists paragenesis at a first metamorphic event (M1) and during a second metamorphic event were andalusite replaces and coexists with staurolite.

4.2.6. Synthesis and discussion

In sector 2, the chlorite, biotite, staurolite and sillimanite metamorphic zones already identified by other authors for the Porto-Viseu Metamorphic Belt (e.g. Accioaioli, 1997; Valle Aguado *et al.,* 1993, Ribeiro *et al*., 2008, 2014) were recognized. It was also observed the spatially delimited occurrences of "veins" showing the anomalous mineral association muscovite/quartz/ aluminosilicates as well as small contact aureoles around porphyritic granites in the biotite-zone were reported.

Three distinct deformation phases were observed: i) the oldest (Dn-1) is defined by residual foliation (Sn-1) which is only found in quartzose domains and in the staurolite and garnet inclusions trails. It is parallel to S0 and probably of diagenetic character; ii) A second phase (Dn) causes a penetrative foliation (Sn) which is characterized by phyllosilicates and ilmenite alignment and inclusions trails in the border of the staurolites; iii) The last deformation phase (Dn+1) redirected, transposed and / or crenulated the previous foliations.

It is considered that Dn-1 is likely to have diagenetic character or correspond to an earlier not penetrative deformation phase. Sn corresponds to the first Variscan deformation phase (D1) and Dn+1 to the third deformation phase (D3) (considering D2 the deformation phase correlated with the allochthonous thrusts).

The blastesis period probably was contemporaneous of the end of crustal thickening caused by the thrusting of the allochthonous units. Andalusite blastesis is late-D3 deformation phase which suggests decompression and increased temperature during this last phase.

The metamorphic sequence, the mineralogical associations and the geometric relations Si / Se suggest that the process that originated the metamorphic zones has a regional character, reached moderate pressure and temperature conditions and is related to D1 deformation phase. During D3 an increase in temperature and decompression process occurred, conditioned by the granitization and installation of the two-mica syn-tectonic granites.

A first metamorphic event (M1), attaining condition of $P > 490$ Pa and $560 < T > 600$ ºC, reflects thinckening and heating. These conditions were followed by decompression and temperature increase leading to andalusite and cordierite development during a later metamorphic event (M2). The sillimanite-zone and migmatization are the result of the last metamorphic event.

Figure IV.2.30 represents the blastese/deformation relation as deducted by the petrographic studies.

Aluminosilicate-bearing quartz veins are observed in metamorphic rocks of several orogens, including the Alps, the Himalayas and the North-American Cordillera (Sauniac & Touret, 1983; Kerrick, 1990; Cavosie *et al.,* 2002; Putlitz et al., 2002) as well in contact aureoles (e.g. Cesare, 1994). Also in the Serra da Freita region, to the south of the studies area, Acciaiolli (1997) found the same mineral association. The processes of Al transfer and the source of the fluids that originate these lithologies are not completely understood. For example, some studies infer transport of Al by regional fluid flow, associating Al mobility with large channelized fluid fluxes (Ague, 2003; Bucholz & Ague, 2005) or typical regional fluxes arising from the devolatilization of metasediments (Acciaioli, 1997; Beitter *et al.,* 2008). Other studies provide evidence that the Al needed to form aluminosilicate veins can be derived locally from adjacent wallrocks by diffusion through a pore fluid phase (Widmer & Thompson, 2001). They generally are considered to record near peak, high-temperature conditions (Cavosie *et al.,* 2002; Putlitz *et al*., 2002).

The contact between the aluminosilicate vein and the host-rock is sharp. However, the staurolite-schist adjacent to the aluminosilicate vein shows a zone of about 20 cm where sillimanite, andalusite and kyanite develop, although showing low modal proportion, that decreases gradually from the contact with the vein. This suggests that the K-Si-Al were transported regionally by fluids from out of the local rock system, what is also corroborated by the relatively large size of the “vein” (> 2 m) and the abundant presence of secondary muscovite plates and quartz.

The circulation of B- K- Al- Si-rich later fluids (syn- to post-D3) is also suggested by the abundance of late tourmaline, by the muscovitization of staurolite, biotite, andalusite, cordierite and plagioclase and by the chloritization of biotite and garnet, as well as by the abundance of quartz veins and tourmalinites associated with fault-zones. These late alteration processes are more evident in the regions proximal to the granitic intrusions. This could indicate a relation between the crystallization of the granites and the circulation of later fluids.

Fig. IV.2. 30 - Blastesis/deformation connections based on the mineral assemblages present in the diverse metamorphic zones and their relationship with the foliations.

CHAPTER V - MINERAL CHEMISTRY

To trace the series of these revolutions, to explain their causes, and thus to connect together all the indications of change that are found in the mineral kingdom, is the proper object of a Theory of the Earth.

John Playfair (*The Huttonian Theory of the Earth*; 1802)

5.1. Introduction

In order to characterize the different mineralogical phases, present in the studied rocks, polished thin sections were analysed by microprobe/WDS and by SEM/EDS. Metagreywackes, calc-silicate rocks, metapelites and granitic rocks minerals were analysed and the results are reported in Appendix B. The sampling is distributed as follows:

- Eight calc-silicate nodules and metagreywacke samples, one of which occurs in the Staurolite-zone.
- One biotite-schist and two staurolite-schist samples from sector 2 (Fânzeres and Aguçadoura);
- Six patch-metatexite and banded-metatexite samples;
- Four diatexite samples;
- Two tourmaline-bearing leucogranite samples;
- Three two-mica granite samples;
- Two aplite-pegmatite samples.

WDS analyses were performed using the JEOL model JXA-850 electronic microprobe at the Laboratório Nacional de Energia e Geologia em S. Mamede de Infesta, Porto and at the Laboratório de Microssonda Electrónica of Faculdade de Ciências da Universidade de Lisboa, using a JEOL JXA-8200 electronic microprobe. The quantitative analyses were collected using an accelerating potential of 15 kV and a beam current of 20 nA. The counting time for each element was 20s except for Rb, Cs and Sr which was 60s and beam diameter of 1 mM was used for most tests except for

the micas where the beam was defocus up to 8 µm to prevent migration of the lighter elements such as the case of fluorine mica.

SEM/EDS analyses were performed using a High resolution (Schottky) Environmental Scanning Electron Microscope with X-Ray Microanalysis and Electron Backscattered Diffraction analysis: Quanta 400 FEG ESEM / EDAX Genesis X4M, at CEMUP – Centro de Materiais da Universidade do Porto. Samples were coated with a C thin film, by vapor deposition, using the JEOL-JEE 4X Vacuum Evaporator equipment.

The structural formulas of the different minerals were calculated as follows:

Pyroxene - based on 6 oxygen atoms and the formula $M_2M_1T_2O_6$;

Amphibole - based on 23 oxygen and the formula $A_{0-1}B_2C_5T_8O_{22}$ $(OH,F)_2$;

Garnet - based on 24 oxygen atoms and the formula $A_3O_2T_3O_{12}$;

Epidote – based on 12,5 oxygen atoms and the formula $X_2Y_3Z_3(O,OH,F)_{13}$;

Feldspars - based on 8 oxygen atoms and the formula (Ca, Na, K) Al (Al, Si) Si_2O_8;

Biotite and muscovite - based on 24 oxygen atoms and the formula $X_2Y_{4-6}Z_8O_{20}$ $(OH,F)_4$;

Staurolite – based on 23 Oxygen atoms and the formula $(Fe,Mg,Zn,Li)_2Al_9Si_4O_{22}(OH)_2$;

Tourmaline – based on 31 (O,OH,F) and the formula $XT_3Z_6B_3Si_6(O,OH)_{30}(OH,F)$.

5.2. Pyroxene

Pyroxene occurs exclusively in the core-zone of the calc-silicate nodules. In migmatites, in granitic rocks or in metagreywacke resisters, pyroxenes were not detected.

In the Morimoto *et al*., (1988) diagram the pyroxenes from all fresh samples classify as diopside although in more altered samples (VC28) the composition is Fe richer (hedembergite). There are minor amounts of Mn (< 0.58 p.f.u.) and Na (< 0.024 p.f.u.) (Figs. V.1 and V.2).

Analytical traverses did not exhibit systematic compositional zoning, although could occur heterogeneous patchy zoning within the grains, showing slight variations in Fe/Mg and Mn content (Figs. V.1 to V.3). These variations are mostly related with the

substitution of Mg by Fe, the same process that occurs in the more altered samples and probably resulted from incipient alteration processes.

Minerals of intermediate composition between diopside and hedembergite occur in calcium rich metasediments which undertake regional metamorphism forming by the reaction (Deer, 1992):

$$\text{Hornblende} + \text{Calcite} + \text{Quartz} \leftrightarrow \text{Diopside} + \text{anorthite} + 3CO_2 + H_2O.$$

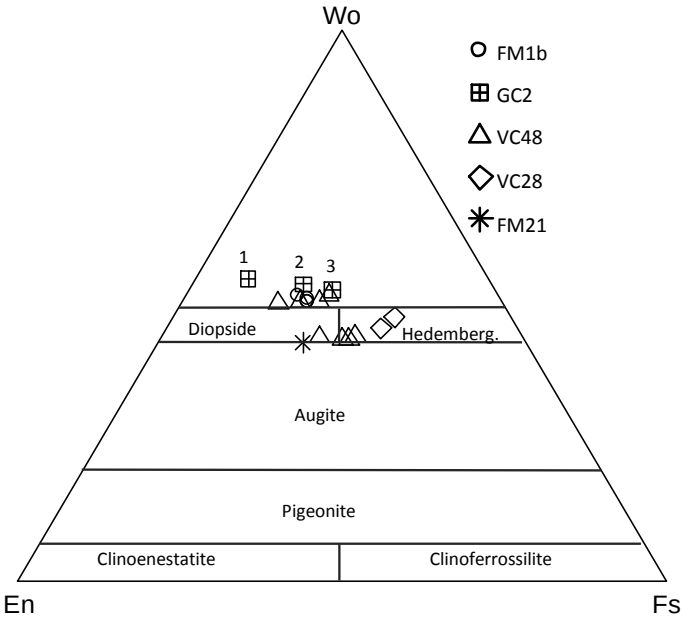

Fig. V. 1 - Classification diagram for pyroxenes (Morimoto, *et al*, 1988). Clinopyroxene from calc-silicate nodules is diopside with variable content in #Mg. The more hedembergite composition belongs to a sample showing intense Type II alteration. The numbers refers to different points within a single diopside crystal (see Fig. V.3).

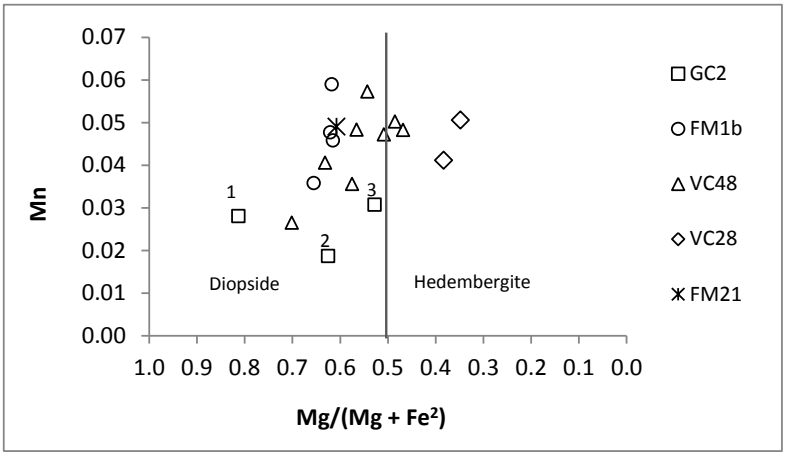

Fig. V. 2 - #Mg *versus* Mn compositional variation in pyroxenes from the calc-silicate nodules.

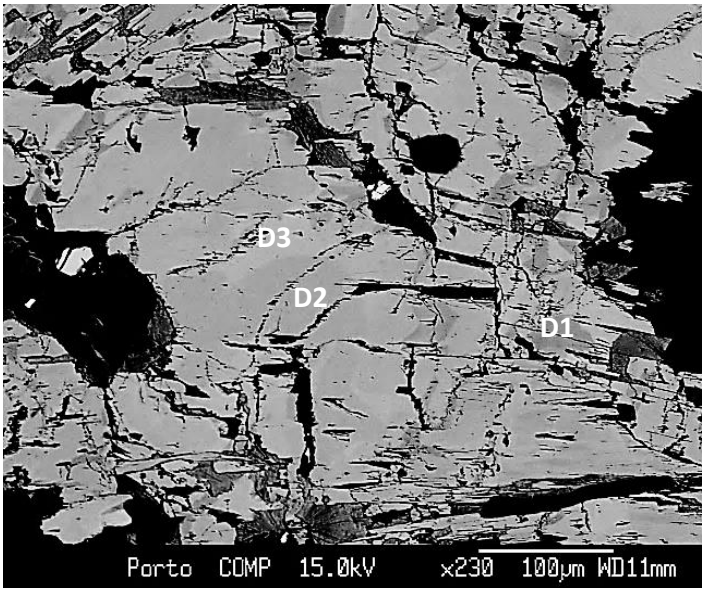

Fig. V. 3 – Backscattered image of diopside. It is possible observe a patchy zoning, showing slight variations in Mg and Fe content within the grains.

5.3. Amphibole

Amphibole occurs in the outer-zone of the calc-silicate nodules and in the rims that mantle diopside in altered samples. The amphibole in calc-silicate rock from lower metamorphic grade (Staurolite-zone) was also analysed.

All the amphiboles show Ca > 1,5 and (Na+K) < 0.5, belonging to the calcic-amphibole category. On the Mg/(Mg+Fe) *versus* Si (p.f.u) diagram for calcic amphiboles with low Na+K content (Leake *et al*, 1977), the analysed amphiboles from calc-silicate nodules are classified as magnesiohornblendes (Fig. V.4 and V.5A).

Amphibole from lower-grade (Staurolite-zone) calc-silicate rocks is also magnesiohornblende, although containing slightly less Si and Mg (p.f.u.) and higher Al^t than the hornblende from MMC calc-silicate nodules (Fig. V.4 and V.5B).

The amphibole that replaces diopside is actinolite in calc-silicate nodules with Type I alteration (GC2) and ferro-actinolite in calc-silicate nodules showing Type II alteration (VC28) (see sub-chapter III.1.3.2.2).

The Na + K average is low (< 0,1), Ti average is ~0,051 to Mg-hornblende and ~0,033 to actinolite.

Hornblende crystals do not show compositional zoning in unaltered samples. In more altered samples hornblende shows a tiny border of more actinolitic composition.

The composition of calcic amphiboles in metamorphic rocks is sensitive to pressure and temperatures but also to bulk rock composition and oxygen fugacity. Generally in low metamorphic grade the composition is actinolitic. With increasing of metamorphic grade the amphibole becomes hornblende and in high grade is tchermakitic or pargasitic (Deer *et al*., 1997).

The transition from greenschist to amphibolite facies can be represented by the reaction which was referred to occurring experimentally at about 550 °C (2 kbar) (Deer *et al*., 1992, 1997):

Albite + chlorite + epidote + actinolite ↔ hornblende + plagioclase

Chlorite + epidote + quartz ↔ hornblende + anorthite

Tremolite + chlorite + epidote + quartz ↔ hornblende + H_2O

Typical hornblendes of regional metamorphic rocks are stable within the range 550º to 900 ºC. In water-rich environment hornblendic amphiboles could be stable in high P-T conditions (Jan & Howie, 1981). Actinolite is characteristic of rocks that formed at temperatures below 550 ºC, at low pressure or as products of retrograde metamorphism (Dear, *et al.* 1997).

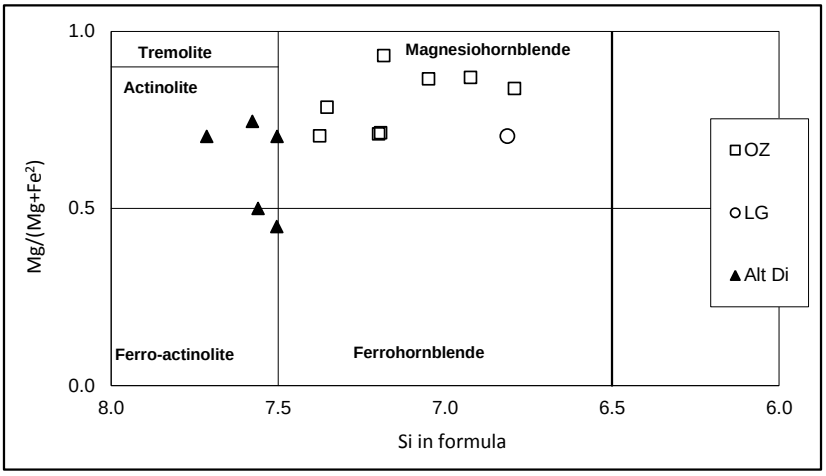

Fig. V.4 – Diagram #Mg *versus* Si for amphiboles classification after Leake *et al.* (1997). Calc-silicate nodules amphiboles (OZ) and amphiboles from staurolite-zone (LG) classify as magnesiohornblende. Amphiboles occurring as alteration coronas in diopside crystals (Alt.Di) classify as actinolites.

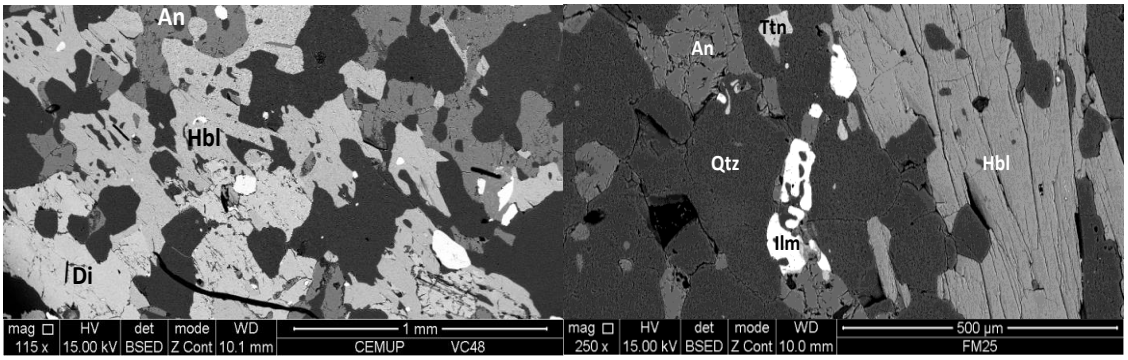

Fig. V. 5 – Backscatter images of hornblende: A) Hornblende and diopside in the contact between core-zone and outer-zone; B) Staurolite-zone calc-silicate sample (FM25) showing hornblende, quartz, anorthite, titanite and ilmenite.

5.4. Epidote

The epidote minerals in the analysed samples are solid solution between epidote and clinozoisite and, based on textural criteria, are interpreted as secondary. This hypothesis is confirmed by the low pistacite component[1] (Pst < 11,4%) (Fig. V.6). Epidote occurs uniformly distributed in the matrix, generally replacing anorthite (saussurization), and filling fractures in the nodules that underwent Type I retrograde alteration (Fig. V.7). Saussurization retrograde process is frequent in the studied rocks were clinozoisite replaces anorthite through the reaction (Deer et al., 1992).

$$4\text{Anorthite} + H_2O \leftrightarrow 2\text{Clinozoisite} + 2\text{Quartz} + Al_2O_3$$

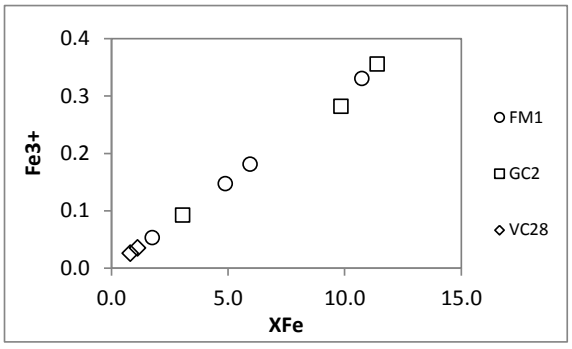

Fig. V. 6 – Pistacite component versus Fe^{3+} for calc-silicate rocks epidote group minerals.

[1] $[Fe^{3+}/(Fe^{3+}+Al^{VI})]$

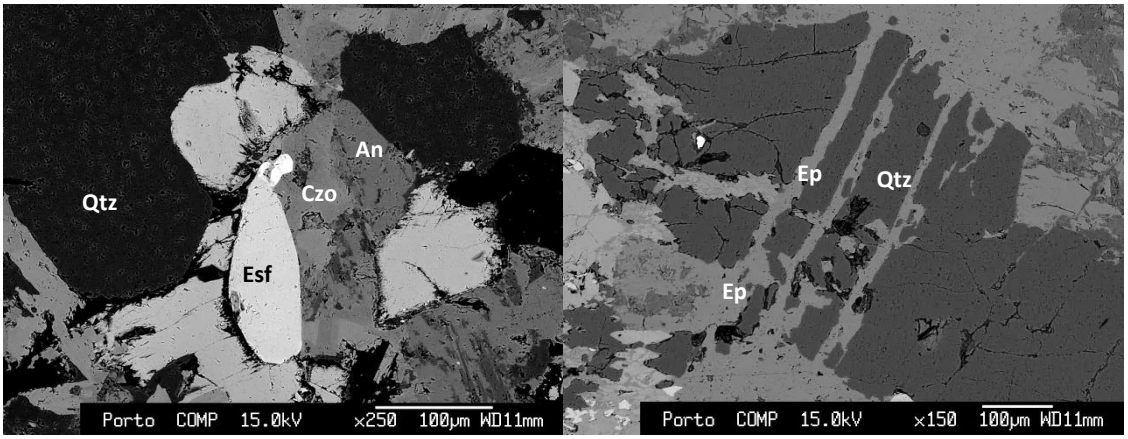

Fig. V. 7 – Backscatter images from calc-silicate nodules. A) Epidote minerals replacing anorthite; B) Epidote filling fractures.

5.5. Garnet

Garnet group minerals occur in calc-silicate nodules, metagreywackes, migmatites and leucogranites. Mineral analyses were performed in all the garnet bearing lithological types.

5.5.1. Garnet from metagreywackes and calc-silicate rocks

Garnet crystals were analysed from calc-silicate nodules with and without retrograde replacements, Staurolite-zone calc-silicate rocks and metagreywackes. The following can be highlight:

- Garnet from the calc-silicate nodules shows chemical composition variation from the core to the outer-zone. At the core-zone grossular and andradite components are higher (88 < #Grs > 90; 2 < #And < 7). Towards the outer-zone the Ca component decreases (28 < #Grs < 23) and Fe, Mg and Mn components increase (#Alm = 50; #Py = 10; #Sp = 14) (Fig. V.8A).
- In the core-zone was found rare garnet enclosed in diopside whose composition shows less Ca and more Fe and Mn than the matrix garnet (Fig. V.8A).
- The garnet composition from the Staurolite-zone calc-silicate sample is similar to the garnet composition of calc-silicate nodules outer-zone (Fig. V.8).
- Metagreywacke garnet is almandine with moderate Mn and Mg component (51%<#Alm<65%; 21<#Sp<28; #Py~13) (Fig. V.8 and V.12).

- Only the samples that show clear retrograde alteration processes contain zoned garnets, showing a profile where Ca component decreases and Fe + Mn components increase towards the crystal edge (Fig. V.9 and V.11B).
- In samples showing Type II retrograde alteration grossular is replaced by retrograde prehnite (Fig. V.11A). According to Deer *et al*. (1992) the stability field of prehnite is established by the reaction:

  5 prehnite = 2 grossular + 2 zoisite + 3 quartz + $4H_2O$ (at 400 ºC ; 2-4 Kbar when $P_{H2O} = P_{total)}$

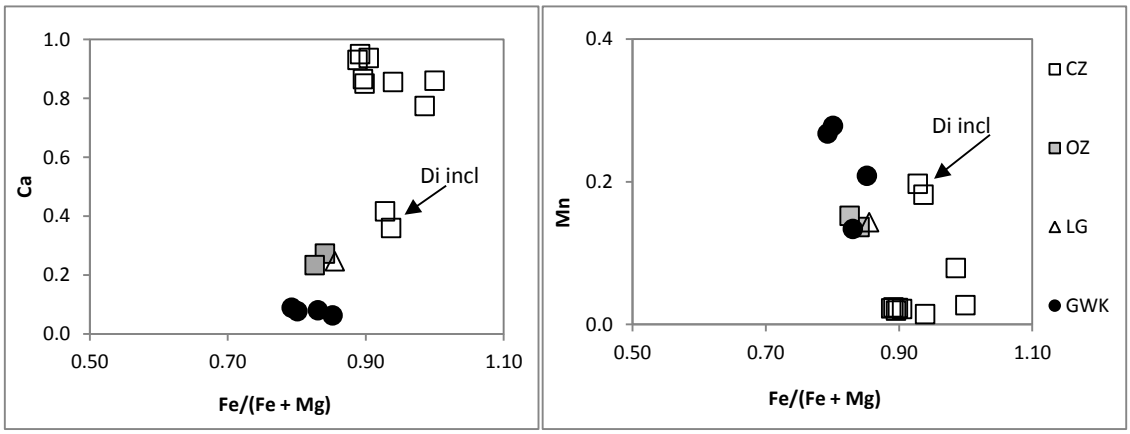

Fig. V. 8 - Fe/(Fe+Mg) *versus* grossular and spessartine components (p.f.u.) for garnets from calc-silicate nodules, metagreywackes and low-grade calc-silicate rock. (Legend key: CZ – calc-silicate nodule core-zone; OZ – calc-silicate nodule outer-zone; GWK – metagreywacke resister; LG– staurolite-zone calc-silicate rock).

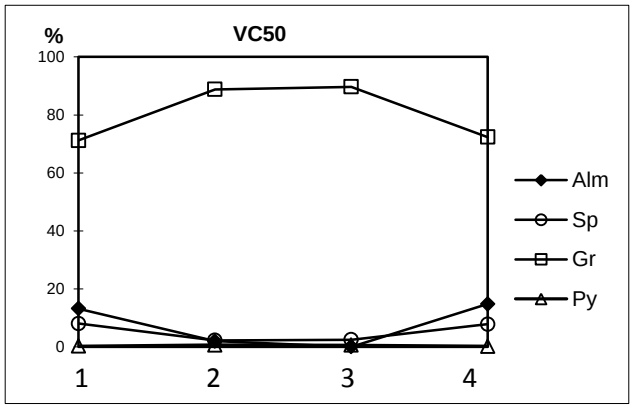

Fig. V. 9 - Compositional profiles for a garnet crystal from sample VC50. Profile showed in Fig. V.11. Legend Key: Alm – almandine; Sp – spessartine; Gr – grossular; Py – pyrope.

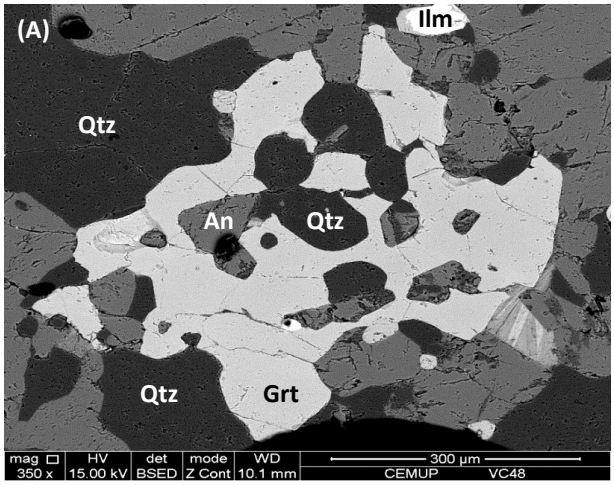

Fig. V. 10 – Backscatter images from calc-silicate samples. Grossular in the core-zone showing skeletal texture.

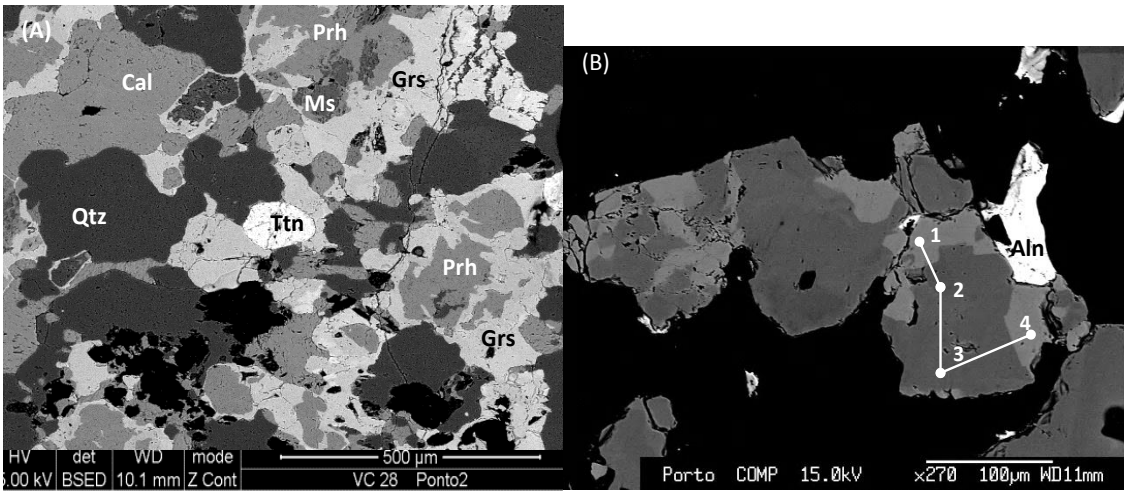

Fig. V. 11 - Backscatter images from calc-silicate nodules showing retrograde processes. A) Prehnite replacing grossular in Type II retrograde alteration. B) Zoned garnet with location of analysed pointes (Fig.V.9).

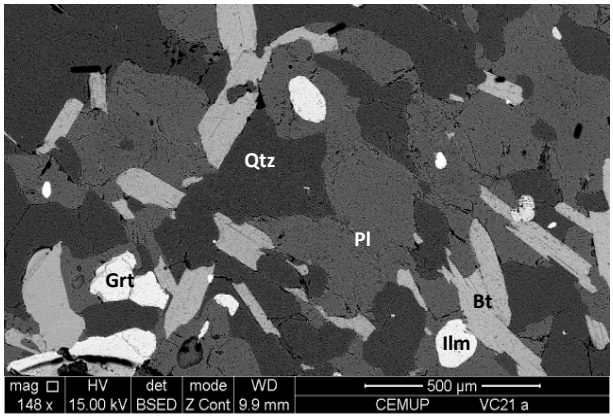

Fig. V. 12 – Backscattered image of metagreywacke sample showing garnet + andesine (Pl) + biotite + quartz.

5.5.2. Garnet from metapelites and granitic rocks

Garnets occurring in staurolite-schists from Fânzeres and staurolite-schists from Aguçadoura were analysed. In MMC rocks, were analysed garnets from patch- and banded-metatexites, the residual garnets from diatexites and leucogranites, as well as the garnets from aplite-pegmatites. Summarizing their main characteristics the following can be highlighted:

- Garnet from staurolite-schists is almandine (~77%) with ~13% pyrope, ~7% grossular and ~4% spessartine. The garnet from the Fânzeres sample shows a composition slightly different from the Aguçadoura sample. The last one shows more intense retrograde alteration and the garnet is Mn richer and Fe poorer (Fig. V.13). Analytical traverses did not exhibit systematic compositional zoning in the Fânzeres staurolite-schist garnet but the compositional profile in garnet from Aguçadoura shows a border slightly enriched in Fe and Mg and depleted in Ca and Mn (Fig. V.14).
- Garnet from patch-metatexites is sub-euhedral, shows a cordierite plus biotite substitution corona and is associated with sillimanite, biotite, plagioclase and quartz in the melanosomes. Almandine component varies between 70 and 73%, pyrope ~16%, grossular ~3% and spessartine ~8%. The compositional profile does not show any variation from the core to the border of the crystal (Fig. 15A).
- Garnet from banded-metatexites shows composition similar to the patch-metatexite garnet although showing slightly more Mn and less Mg (Fig. V.13).
- Garnet from diatexite is rare, corroded and surrounded by fibrolite and biotite. Almandine component varies between 67 and 77%, pyrope component varies between 8 and 12%, grossular component is ~2% and spessartine component is ~10%. The garnet compositional profile shows a border depleted in Mg and Fe and enriched in Mn (Figs. V.15B).
- Garnet from leucogranites shows texture and composition similar to the garnet from metatexites and diatexites. Almandine component is ~75%, pyrope 6 to 12%, grossular ~1% and spessartine ~13%. Like in garnets from diatexites, the compositional profile also shows a border depleted in Mg and Fe and enriched in Mn (Fig. 16A).
- Garnet from aplite-pegmatite is euhedral and associated with tourmaline, albite and quartz. Is an almandine–spessartine garnet (58-62 % almandine; 37-39% spessartine) with very low Mg and Ca (< 2%). The F component is about 6%. A

compositional profile shows only a small decrease in Fe and increase in Mn content towards the garnet rim (Figs. V.13, V.16 and V.17B).

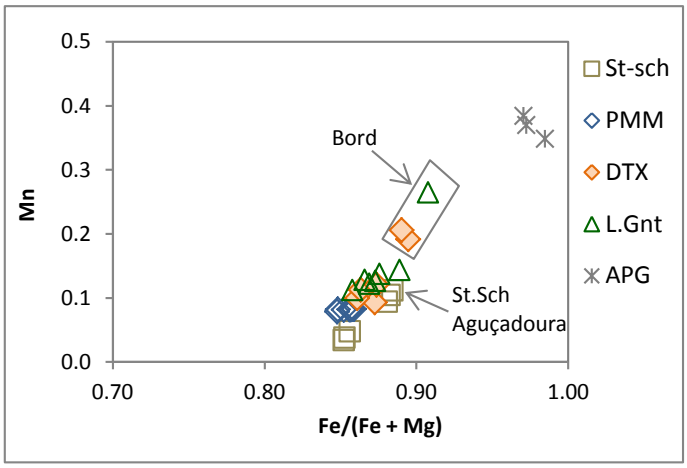

Fig. V. 13 - Fe/(Fe+Mg) *vs* Mn composition for garnets in Sector 1 and Sector 2. Legend key: St-sch – staurolite-schists; PMM – patch-metatexites; DTX – diatexites; L.Gnt – leucogranites; APG – aplite-pegmatites.

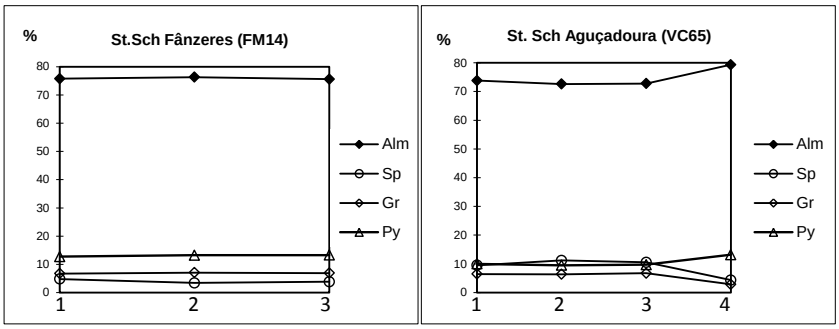

Fig. V. 14 - Compositional profile for staurolite-schist garnet from Fânzeres (sample FM14) and from Aguçadoura (sample VC65).The composition is similar although the garnet from Aguçadoura shows a border slightly enriched in Fe and Mg and depleted in Ca and Mn.

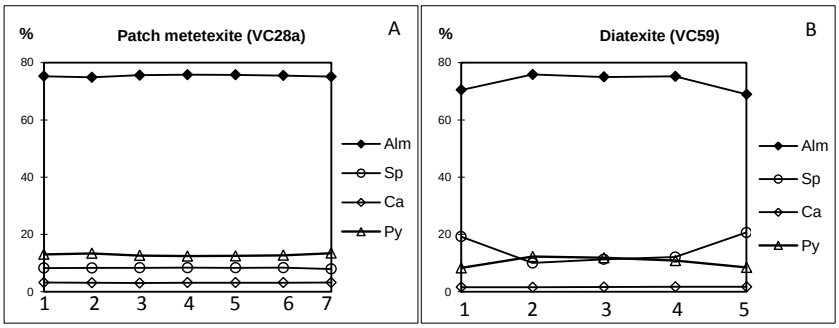

Fig. V. 15 – Compositional profile for patch-metatexite and diatexite samples garnet. The garnet from diatexite does not show compositional variation. The garnet from diatexite is depleted in Mg and Fe and enriched in Mn in the borders.

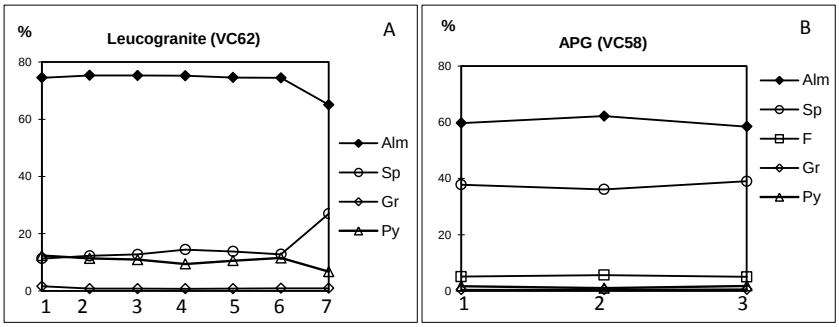

Fig. V. 16 - Compositional profile for leucogranite (sample VC62) and aplite-pegmatite (sample VC58) garnets. The garnet from leucogranite is depleted in Mg and Fe and enricher in Mn in the border. Garnet from aplite-pegmatite is almandine/spessartine with high F component. In the core is slightly richer in Fe and poorer in Mn.

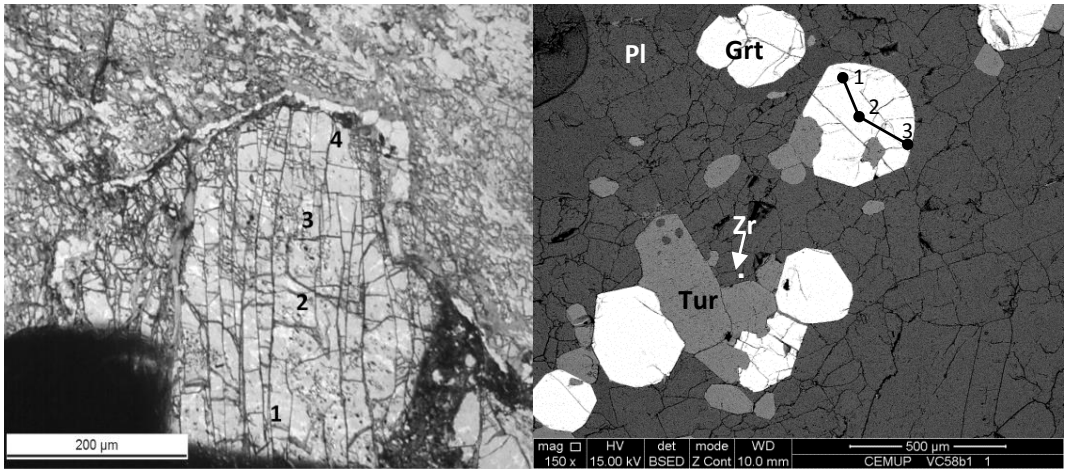

Fig. V. 17 - A) Garnet inside a large crystal of staurolite in staurolite-schist from Aguçadoura. Points localization of the profile in Fig. V.14B; B) Garnet from aplite-pegmatite with the points location of the profile in Figure V.16B .

5.5.3. Synthesis

The garnet present in the calc-silicate nodules belongs to the ugrandite series while the garnet present in metagreywackes, migmatites and granitic rocks belongs to the pyralspite series.

In the calc-silicate nodules the garnet Ca content decreases and Fe, Mg and Mn content increases from the core-zone to the outer-zone. The garnet from lower-metamorphic grade (Staurolite-zone) shows a composition similar to that of the outer-zone of the calc-silicate nodules from MMC. The bulk-rock composition of the nodules varies from the core-zone to the outer-zone, containing higher Ca and Mn in the core-zone and lower Mg in outer-zone (Fig. VI.18). Thus, it is likely that the variation in

garnet Ca and Mg content from core- to outer-zone is related to the variation in the bulk-rock content. The variation in Mn content is not correlated with the bulk-rock content. However, as the core-zone contains diopside high modal proportion, that is absent in the outer-zone, and diopside concenters more Mn than amphibole, is possible that the Mn has been allocated preferably in the diopside structure in the core-zone and in the garnet structure in the outer-zone. In the samples showing later alteration the Fe and Mn contents increase to the border of the garnet crystal.

In metapelitic rocks, the garnets from Staurolite-zone and patch-metatexites show similar composition. However the Mn content in Aguçadoura and in the Metatexite Zone is slightly higher. The whole-rock composition of MMC lithologies and Aguçadoura schists also revealed an increase in the Mn content relatively to the whole-rock composition of staurolite-schists from Fânzeres. Thus, the difference in Mn could reflect the host rock composition.

It is notorious the similarity in composition and texture between the garnets from metatexites and from granitic rocks. This suggests that garnets from diatexites and leucogranites are residual, as is also suggested by their scarcity and corroded texture.

The garnets from staurolite-schists and patch-metatexites do not show any zonation. However the garnets from granitic rocks and from the more altered staurolite-schist sample (VC65) show a tiny border with a composition slightly different from the core. The garnet from granitic rocks shows increase in Mn and decrease in Fe content in the border. This probably is related with an exchange ion processes between the melt and the residual garnet, as is suggested by the abrupt differences between the core and the border. The border of the garnet from the Aguçadoura schist shows slightly higher Fe and less Mn and Ca. The zonation may be related with retrograde processes since this sample is intensely affected by later fluids.

5.6. Feldspars

5.6.1. Feldspars from metagreywackes and calc-silicate rocks

Plagioclase and K-feldspar analyses were performed on calc-silicate nodules core-zone and outer-zone and in metagreywackes. Summarizing their main characteristics the following can be highlighted (Figs. V.18 to V.21):

- Calc-silicate nodules core-zone plagioclase is anorthite.

- Plagioclase from calc-silicate nodules outer-zone is slightly less calcic than plagioclase from core-zone. Classifies between anorthite and bytonite.
- The Staurolite-zone calc-silicate sample contains anorthite.
- In the sample showing Type I retrograde alteration a single K-feldspar crystal was detected in the outer-zone. Its composition is relatively rick in K and Ba and poor in Ca and Na. This suggests that K-rich fluids affected these rocks as well as the adjacent migmatites (Fig. V.18 and V.23B).
- Plagioclase from metagreywacke is oligoclase to andesine.
- Analyses were performed in the sample of metagreywacke that underwent partial migmatization, both in the zone without signs of partial melting and in the migmatized-zone. The composition of the plagioclase is the same in the fine-grained plagioclase crystals from metagreywacke resister part and in the large grained plagioclase from migmatized-zone. Compositional profiles show no variation from cores to borders (even in crystals that show textural dissimilarities; Figs. V.20 and V.21). A tiny border of more albitic composition surrounds some of the larger grains in the migmatized-zone.

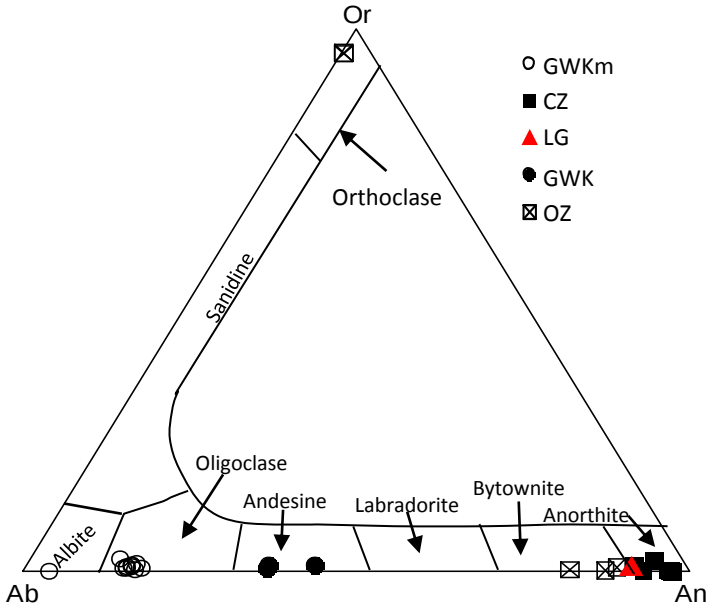

Fig. V. 18 - Feldspar classification diagram (Deer *et al*., 1992) for calc-silicate nodules, metagreywackes and staurolite zone calc-silicate rocks. Legend key: GWK.m – Migmatized metagreywacke; CZ – calc-silicate nodules core-zone; ; LG – low-grade calc-silicate rocks; GWK – metagreywacke resister; OZ – calc-silicate nodules outer-zone.

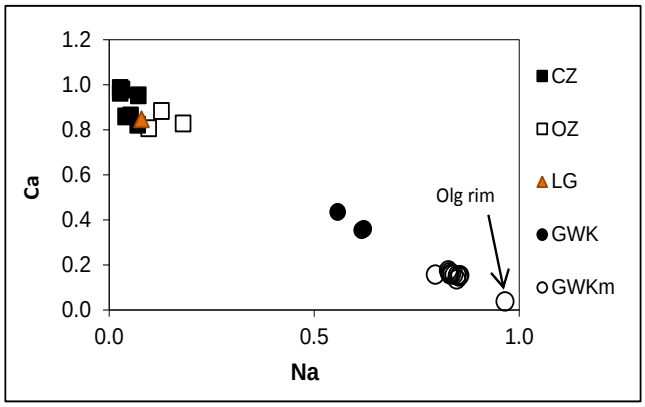

Fig. V. 19 – Ca *vs*. Na (p.f.u.) of plagioclases from calc-silicate nodules core-zone and outer-zone, metagreywackes and lower-grade calc-silicate rock. Legend key: CZ – calc-silicate nodules core-zone; OZ – calc-silicate nodules outer-zone; LG – low-grade calc-silicate rock; GWK – metagreywacke resisters; GWK.m – metagreywacke showing evidences of partial melting.

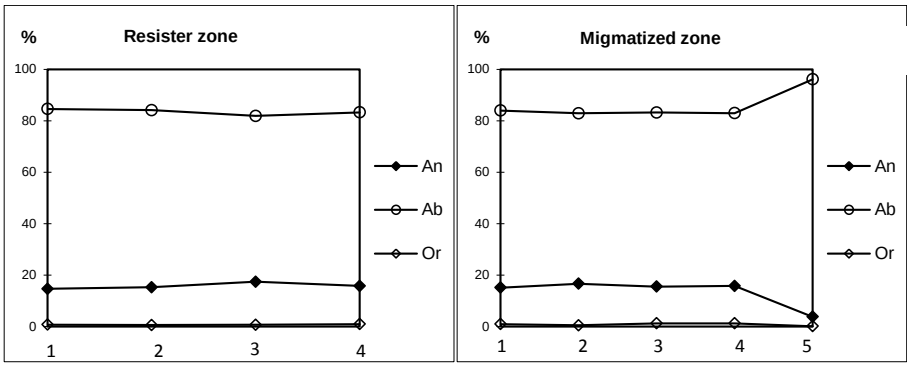

Fig. V. 20 – Compositional profile of the plagioclase from (A) metagreywacke resister zone and (B) migmatized zone in sample FP21c. The composition is similar in both zones and throughout the plagioclase crystals. Only a tiny border in plagioclase larger crystal from migmatized zone shows more albitic composition.

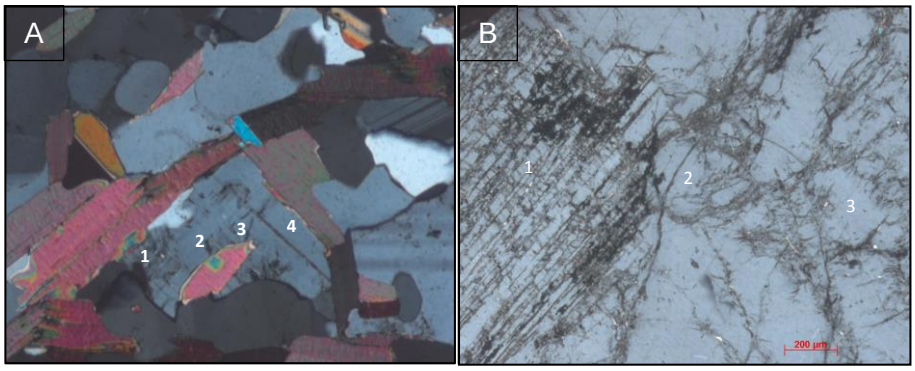

Fig. V. 21 – Photomicrographs of metagreywacke partially migmatized: A) Plagioclase from metagreywacke sample showing signs of partial melting (FP21c). A) Zone with only minor signs of partial melting were plagioclase is fine grained and B) zone showing intense partial melting were plagioclase is coarse-grained and shows a residual core surrounded by magmatic plagioclase. Location of the analysed points in Fig. V.20 (point 4 is outside of the picture).

5.6.2. Feldspars from metapelites

Plagioclase and K-feldspar analyses were performed on biotite-schists, staurolite-schists, patch-metatexites and banded-metatexites. Summarizing their main characteristics the following can be highlighted (Figs. V.22 and V.23):

- Plagioclase from biotite-schists classifies as albite (An_3);
- Plagioclase from staurolite-schists also classifies as albite, although showing a more calcic composition ($An_{7\ to\ 8}$);
- Plagioclase from metatexites is oligoclase ($An_{17\ to\ 26}$), both in melanosome and in leucosome.
- Some oligoclase crystals from leucosome show a very thin albite border, especially in the contact with K-feldspar or associated with fractures.
- K-feldspar in the leucosomes is orthoclase (#Or = 82 to 86). In some metatexites K-feldspar is only detectable in backscattered images were occur as incipient tiny crystals inside plagioclase (Fig. V.24A).
- Plagioclase from myrmekites in metatexites is more albitic (An_{12}) than the plagioclase in melanosomes and leucosomes (Fig. 24B).

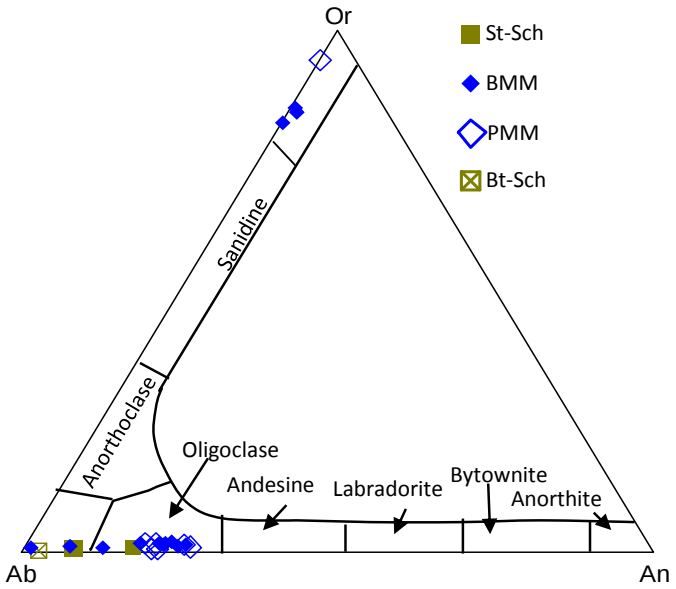

Fig. V. 22 - Feldspar classification diagram (Deer *et al*., 1992) for metapelites and metatexites. Legend key: St.Sch – staurolite–schists; BMM – banded-metatexites; PMM – patch-metatexites; Bt-Sch – biotite-schists.

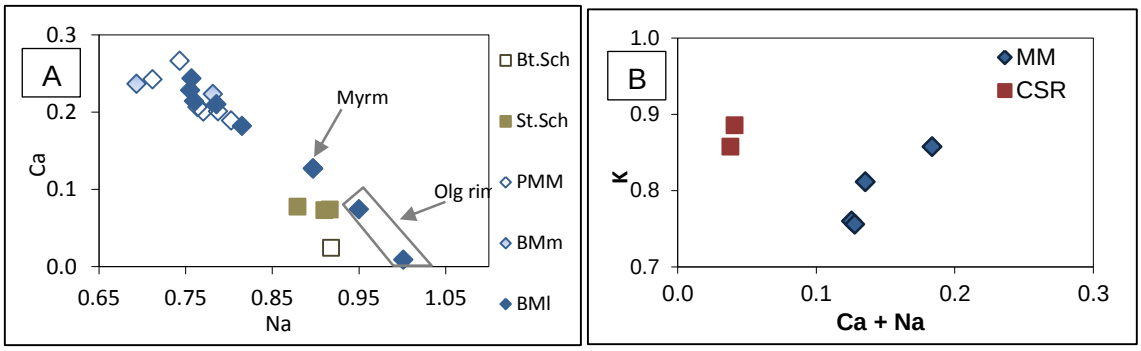

Fig. V. 23 – A) Ca *vs*. Na (p.f.u) diagram for plagioclase from metapelites and metatexites. B) K *vs* Na+Ca (p.f.u) for K-feldspar from metatexites and calc-silicate rock. Legend key: Bt.Sch – biotite-schists; St.Sch – staurolite-schists; PMM – patch-metatexites; BMm – banded-metatexites melanosome; BMl – Banded-metatexites leucosome; Olg rim – Oligoclase albitic rim); CSR – calc-silicate rocks; MM - metatexites.

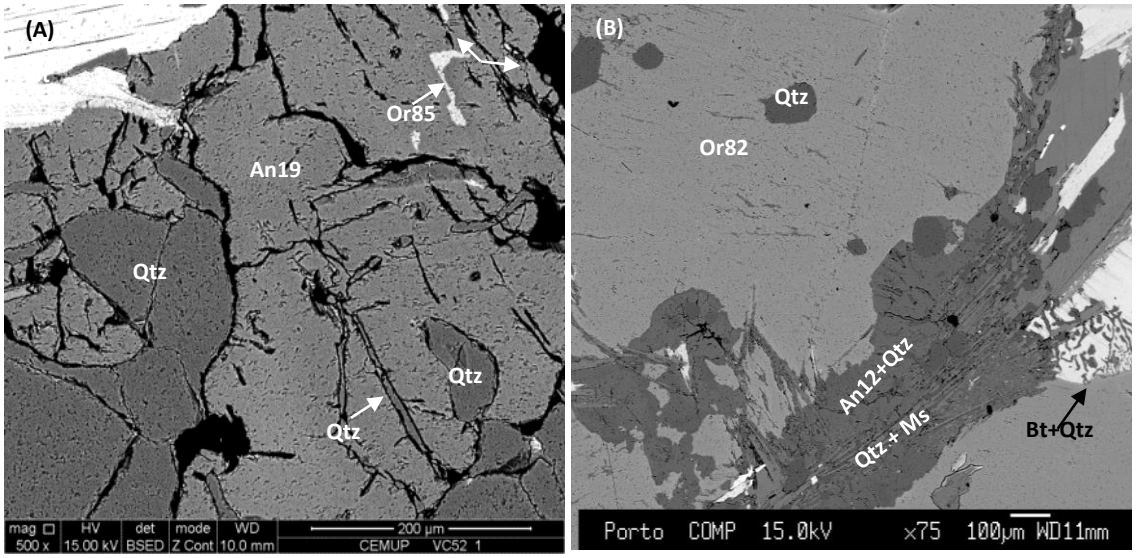

Fig. V. 24 – Backscattered image from: (A) patch-metatexite plagioclase with vermicular quartz inclusions. Note the incipient grow of orthoclase within plagioclase, only detected in the backscattered image. (B) Albite tiny rim and vermicular quartz in the plagioclase border that contacts whit the orthoclase.

5.6.3. Feldspars from granitic rocks

Analyses were performed in plagioclases from diatexites, leucogranites, two-mica granites and aplite-pegmatites. The aplite-pegmatites analyses were taken from aplite inner zone, intermediate zone and comb-structure border.

Summarizing their main characteristics the following can be highlighted (Fig. V.25 and V.26):

- Plagioclase from diatexite matrix is oligoclase (An_{17-21}). Albite (An_{6-2}) occurs as tiny rims in oligoclase or associated with fractures within oligoclase (Figs. V.26 and V.27). Besides the albitic rim, oligoclase does not show any zoning.
- Leucogranites contain both oligoclase crystals and albite crystals (An_{14-7}) (Figs. V.25 and V.26). The Ca content of this oligoclases is lower than the Ca content of oligoclase from diatexites. Some larger plagioclase crystals show normal compositional zoning, passing from An_{16} to An_6 towards the border of the crystal (Fig.V.30). Albite crystals do not show compositional zoning. There is also an albitic rim in some oligoclase crystals.
- Two-mica granites contain both oligoclase crystals and albite crystals (An_{22-2}) (Figs. V.25 and V.26). There is also an albitic rim in some oligoclase crystals. Some crystals show heterogeneous zoning (Figs.V.30).
- The perthites composition is albitic (An_7) (Fig.V.35).
- Plagioclase from aplite-pegmatite, both in aplite-zone, in intermediate zone, in comb-structure zone and in perthites is albite (An_{1-5}).

- Diatexites K-feldspars show two slightly distinct compositions: crystals showing #Or ranging from 77 to 81 and higher Ca, Na and Ba content and crystals showing #Or ranging from 87 to 91 and lower Ca, Na and Ba content (Figs. V.25, V.31 and V.33).
- Leucogranites K- feldspar is orthoclase with #Or ranging from 88 to 95 and low Ca, Na and Ba content. The modal proportion of K-feldspar crystals in leucogranites varies from high to moderate to absent and the majority of crystals clearly replace plagioclase.
- Two-mica granite K-feldspar is orthoclase with #Or ranging from 87 to 97. The Na and Ca contents are relatively low but Ba is higher than in leucogranites.
- K-feldspar from aplitopegmatite is orthoclase showing #Or ranging from 91 to 93 (Fig. V.25 and V.31).
- Crystals showing heterogeneous zoning occur in all the lithologies. There are also crystals without any zoning (Fig. V.32 to V.35).
- All the lithologies show incipient development of K-feldspar within plagioclase crystals (Figs. V.33 to V.35), showing high K content.

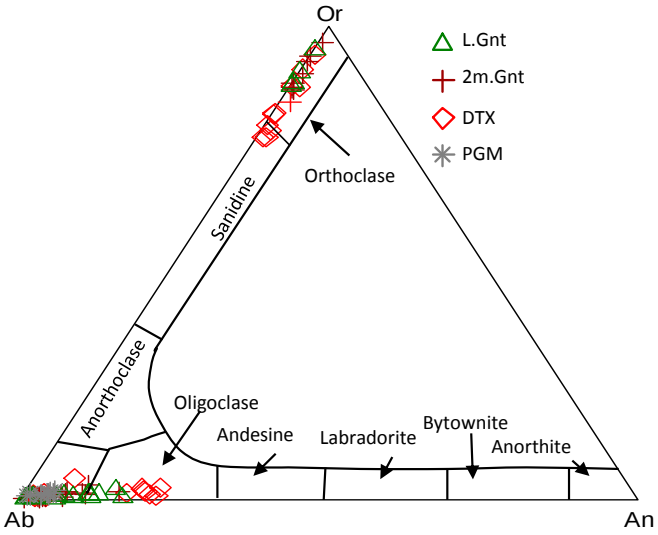

Fig. V. 25 - Feldspar classification diagram (Deer *et al.*, 1992) for granitic rocks. Legend key: L.Gnt – leucogranites; 2m.Gnt – two-mica granites; DTX- diatexites; PGM – aplite-pegmatites.

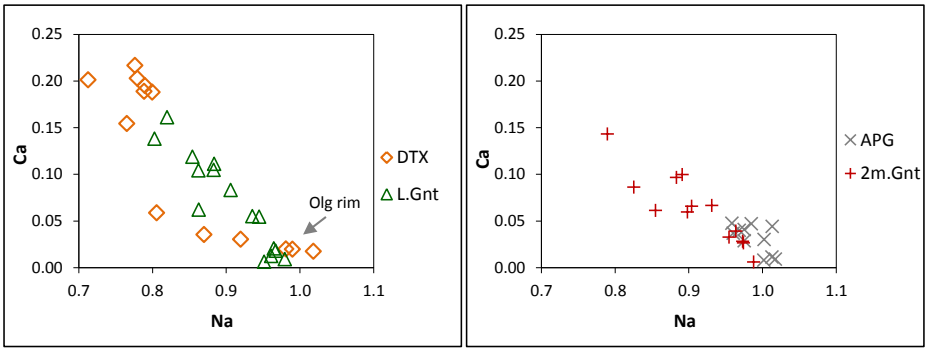

Fig. V. 26 - Ca *vs*. Na (p.f.u.) diagram for granite rocks plagioclase. Legend key: DTX- diatexites; L.Gnt – leucogranites; 2m-Gnt – two-mica granites; APG – aplite-pegmatites; Olg rim – oligoclase rim).

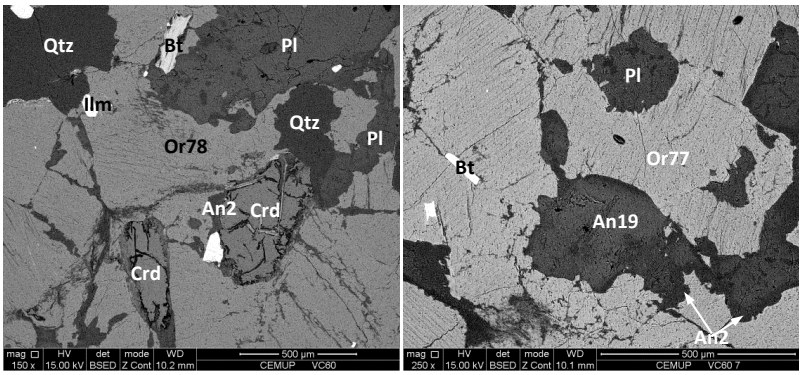

Fig. V. 27 – A) Backscattered image from diatexite sample showing oligoclase with an albite rim in the contact with K-feldspar. B) Major feldspar crystal associated whit oligoclase. Oligoclase shows an albitic rim.

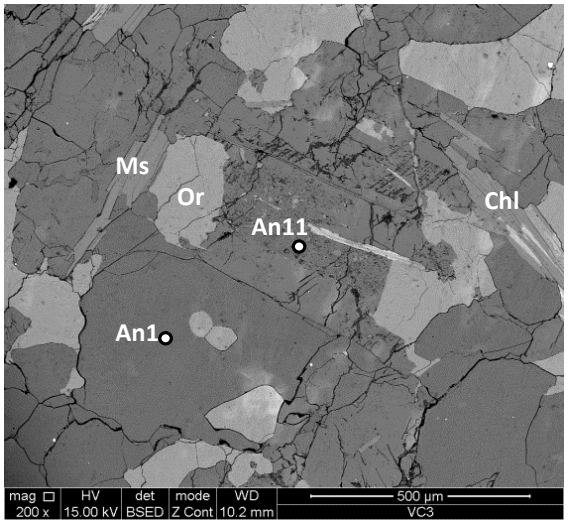

Fig. V. 28 – Backscattered image of leucogranite plagioclase showing an oligoclase core and albite crystals. K-feldspar replaced plagioclase.

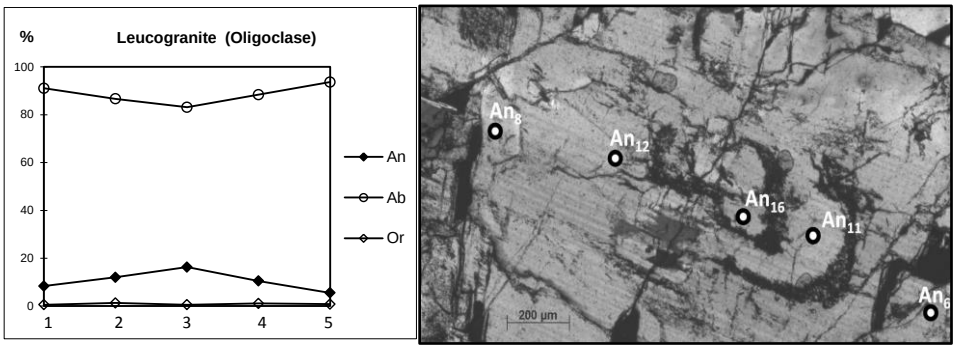

Fig. V. 29 – Profiling points in zoned plagioclase from leucogranites.

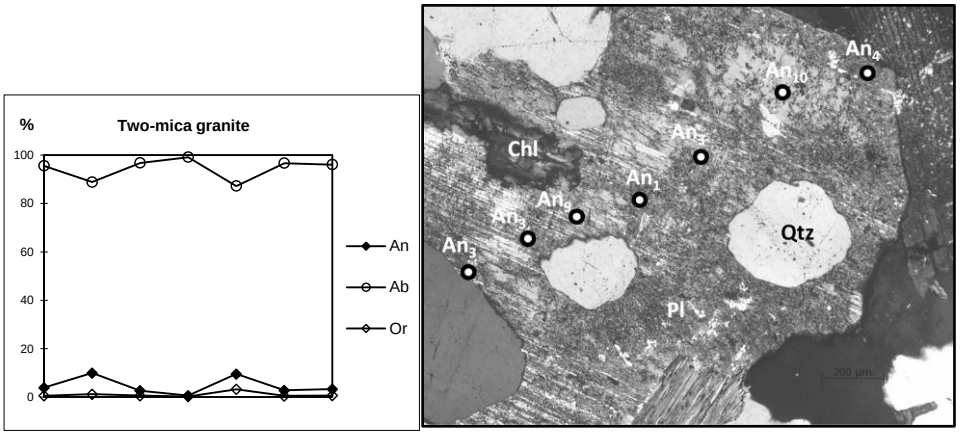

Fig. V. 30 – Profiling points from a two-mica granite plagioclase crystal showing heterogeneous patchy zoning.

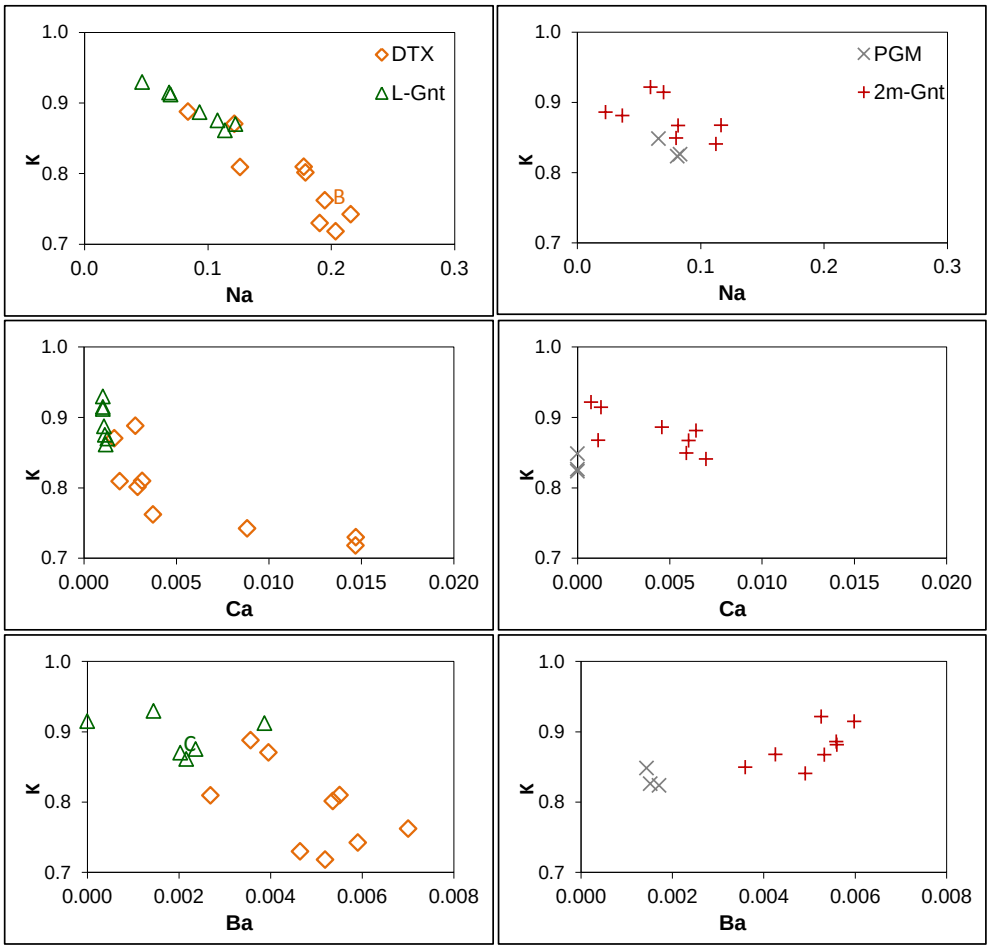

Fig. V. 31 – K vs Na, K Vs Ca and K vs Ba (p.f.u.) diagrams for K-feldspar from MMC granitic rocks. Legend key: DTX-diatexites; L.Gnt – leucocratic granites; 2m-Gnt – two-mica granites; PGM – aplite-pegmatites.

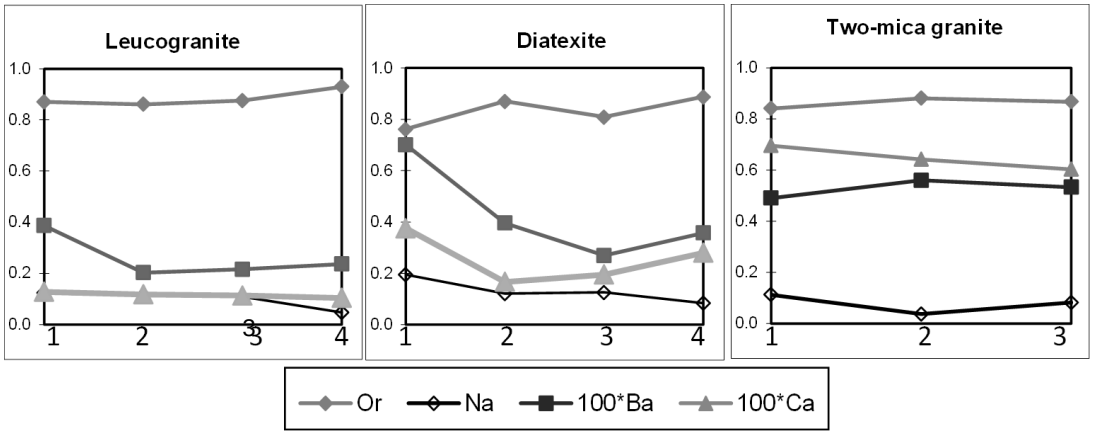

Fig. V. 32 –Variation in K, Na and Ba (p.f.u.) in K-feldspars from leucogranite, diatexite and two-mica granite.

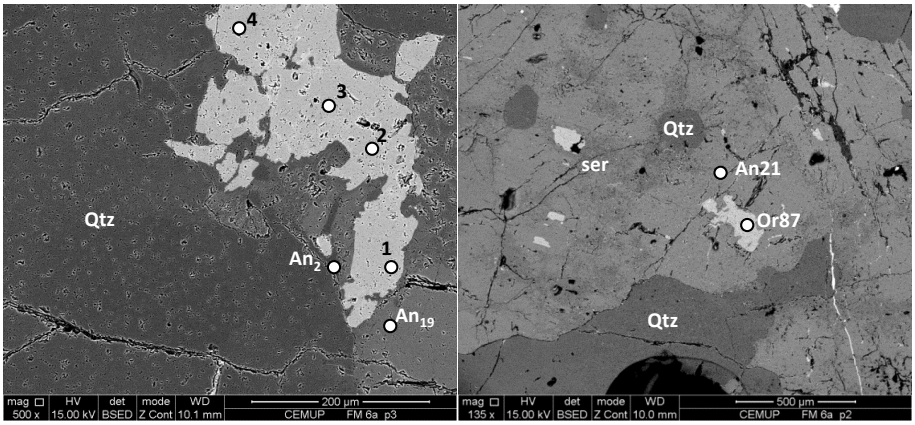

Fig. V. 33– Backscattered image showing diatexite orthoclase large crystal and profile points of Figure V.32; B) Incipient development of orthoclase within oligoclase.

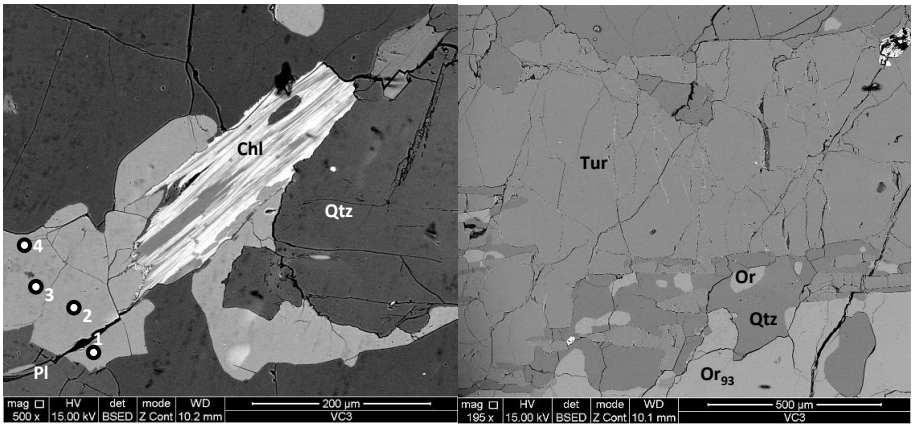

Fig. V. 34 – Leucogranite backscattered image showing: A) Orthoclase and profile points of Figure V.32. B) Orthoclase associated to tourmaline and quartz.

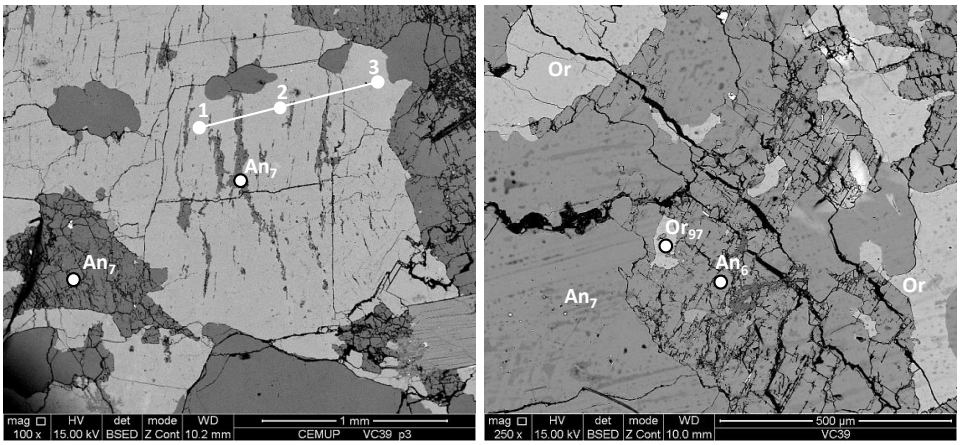

Fig. V. 35 – A) Backscattered images of two-mica granite showing: A) perthitic feldspar showing plagioclase and quartz inclusions and profile points of Figure V.3; B) Incipient orthoclase occurrence within plagioclase large crystal.

5.6.4. Summary

The characteristics of the analysed feldspars permit to highlight some aspects:

Albite from biotite-schist and staurolite-schists is characteristic of low to medium-metamorphic grade rocks.

The plagioclase composition from calc-silicate nodules and metagreywackes mainly reflects the change in whole-rock chemical composition.

In metatexites and diatexites, textural evidences of restitic oligoclase surrounded by magmatic plagioclase are common. It is noted that the composition of the restitic plagioclase and the surrounding magmatic plagioclase is similar, generally in the oligoclase field, without any zoning. Moreover, in samples showing partial migmatization, although the texture and size of plagioclase are very different in partially melted areas and in areas of the sample without signs of partial melting, the composition of plagioclase is identical. Thus, in these rocks there are no appreciable difference in plagioclase composition between the leucosomes and the host rock, a common observation in migmatites (Johannes, 1988; Ashworth, 1979, 1985). Ashworth suggested that subsequent to crystallization the leucosome plagioclase re–equilibrated with the surrounding metamorphic rock producing a homogeneous plagioclase composition in the migmatites.

Plagioclases from diatexites show the same composition and texture as the plagioclases from metatexites, including the albitic rim. This suggest, as expected, that diatexites result from the same process as metatexites but showing higher partial melting rate.

Oligoclase from leucogranites and two-mica granites is Ca poorer than in diatexites and coexists with albite crystals in the matrix (that are absent in migmatites). Whole-rock Ca content is also variable, being the diatexites richer than leucogranites and two-mica granites. However, the Ca content of pelitic metatexites is also low and the plagioclase shows the same Ca richer composition as in diatexites. Thus, this suggests that plagioclases from leucogranites and two-mica granites are more fractionated than the source-rock plagioclases. In rocks formed by partial melting the phase relations dictate that plagioclase compositions should be more sodic in the anatectic melts than in the protoliths (Ashworth, 1979). Moreover, the existence of separate crystals of K-feldspar and albite is synonymous of subsolvus granites, that is, granites that

crystalized at low-temperature (Philpootts, 1989). Thus, it is possible that leucogranites and two-mica granites crystalized at lower temperatures than metatexites.

When occurs, the plagioclase zoning is not homogeneous: some crystals show a gradual transition from core to border and others show patchy zoning. The more albitic crystals do not show any zoning. In magmatic systems, plagioclase is, most communally, zoned (except if the crystals are isolated from the melt). The progressive normal zoning can result from temperature decrease during crystallization of the magma that originated these granitic rocks. Unzoned plagioclase may occur but is not common in magmatic rocks (*e.g*. Hibbard, 1995; Vernon, 2004). Thus, the patchy zoning and the absence of zoning in the oligoclase crystals is probably related with the inhered character of these plagioclase crystals in rocks where the rate of partial melting is low. In these conditions, necessarily the space to grow is limited giving rise to crystals that do not grow evenly and grow constrained by the limited space available. The albitic rims in metatexites and diatexites and the unzoned albite crystals in leucogranites and two-mica granites could be related with later fractionation phases that are relegated to intergranular positions and rims-growth on larger plagioclase crystals (Hibbard, 1995).

K-feldspar is absent in most of the metatexites and leucosomes, rare in some and abundant in others. The same occurs in leucogranites. In diatexites and two-mica granites the modal proportion of K-feldspar is higher and the distribution is homogeneous. There are many K-feldspar crystals that replace plagioclase, both at incipient scale or at large scale. The incipient crystals within plagioclase show higher K content, are anhedral and do not follow the cleavages of the host crystal, being considered as resulting from nucleation (replacement) and not saturation (exsolution) (Vogel, 1970; Deer *et al.*, 1992). The larger ortoclase crystals show heterogeneous zoning in all the lithological types. The myrmekite plagioclase is more albitic than the plagioclase from the migmatites matrix. This also suggests that some of the K-feldspar (especially in metatexites and leucogranites) is the result of K metasomatic processes that replaces plagioclase (e.g. Putnis *et al*. 2007), in agreement to the petrographic and field observations.

5.7. Biotite

Biotites were analysed on metagreywackes, calc-silicate nodules, biotite-schists, staurolite-schists, metatexites, diatexites, leucogranites and two-mica granites.

5.7.1. Biotites from metagreywackes and calc-silicate nodules

Analyses were taken from calc-silicate nodule border, metagreywacke resisters and migmatized metagreywackes.

Besides the texture and morphology (Fig. V.36), also the biotites composition from metagreywackes and calc-silicate nodules is different. According to Foster (1960) nomenclature (Fig. V.37), biotites from metagreywackes classify as Mg-biotites and biotites from calc-silicate classify as eastonites, showing higher Mg content (Fig. V.38). The Ti, Mn and K content is similar in the two types of rocks. Biotites from calc-silicate nodules show Al^{iv} and F contents slightly higher than the F and Al^{iv} contents of biotites from metagreywackes (Fig. V.38). On the FeO - MgO - Al_2O_3 diagram (Gokhale, 1968) all biotites plot on the metamorphic biotites field (Fig. V.39).

Migmatized greywacke sample is composed of two zones: a zone that shows evidences of partial melting and other zone that remains as resister, without any signs of partial melting. Biotites from the two zones were analysed.

The biotites from migmatized metagreywacke show slightly lower Mg content than the biotites from metagreywacke resister, overlapping the composition of pelitic-metatexites biotites (Fig. V.38). Within the migmatized metagreywacke the biotites show similar composition in the part of the rock that remains as resister and in the migmatized zone. Only Mn and F show slight variation that is not related with the position of biotite in metagreywacke resister zone or in migmatized zone. This suggests complete re-equilibrium of the biotites during migmatization processes.

5.7.2. Biotites from metapelites and metatexites

Analyses were taken from biotite-schists and staurolite-schists from SGC (Sector 1) and from patch- and banded-metatexites from MMC (Sector 2). Biotite is the only ferromagnesian mineral phase occurring in metapelites and metatexites.

According to Foster nomenclature (1960) biotite-schists contain Fe-biotite, staurolite-schists and metatexites contain Mg-biotite (Fig. V.40).

Low-grade biotites (from Biotite-zone) show a composition richer in Fe and poorer in F, K, Na and Mn than the biotites from the other lithologies. #Fe in biotites from staurolite-schists and metatexites is similar. However the Ti, Mn, F and K content of biotites from metatexites is higher than of biotites from staurolite-schists, with exception of biotites resulting from staurolite alteration were the F content is higher (Fig. V.41).

The leucosome biotites have slightly higher #Fe and Ti content than the biotites from melanosome (Fig. V.41). These biotites are generally inside plagioclase or quartz major leucosome crystals. Figure V.42 display backscattered images showing textural aspects of biotites from patch-metatexites, banded-metatexites and leucosomes. All the analysed biotites from metapelite rocks plot on metamorphic field in the FeO - MgO - Al_2O_3 and MgO-TiO_2-(FeO+MnO) (Gokhale, 1968) diagrams (Fig. 43).

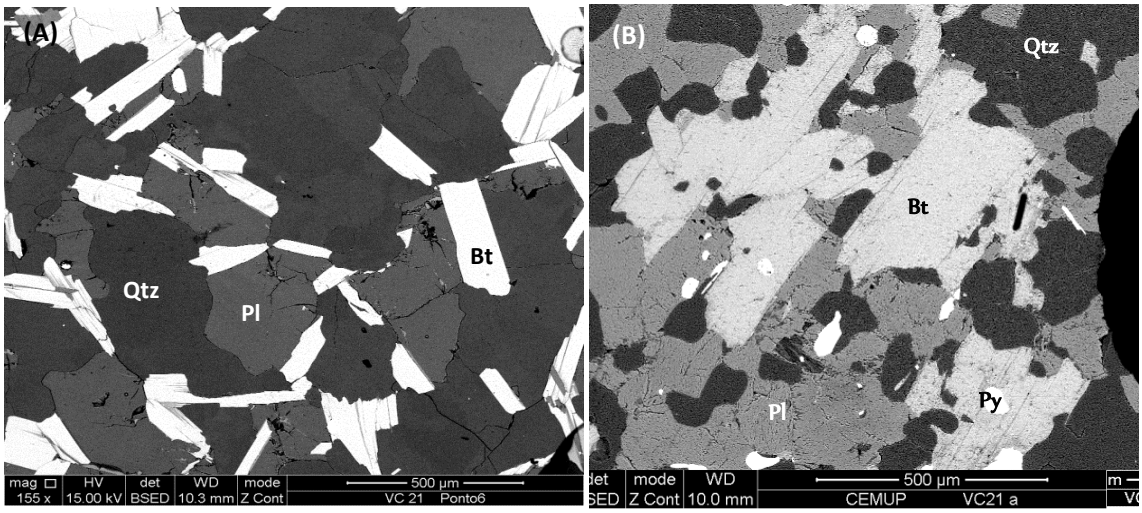

Fig. V. 36 – Backscattered image from: A) Metagreywacke; B) Calc-silicate nodules outer-zone. Note the distinct morphology and relation with other minerals.

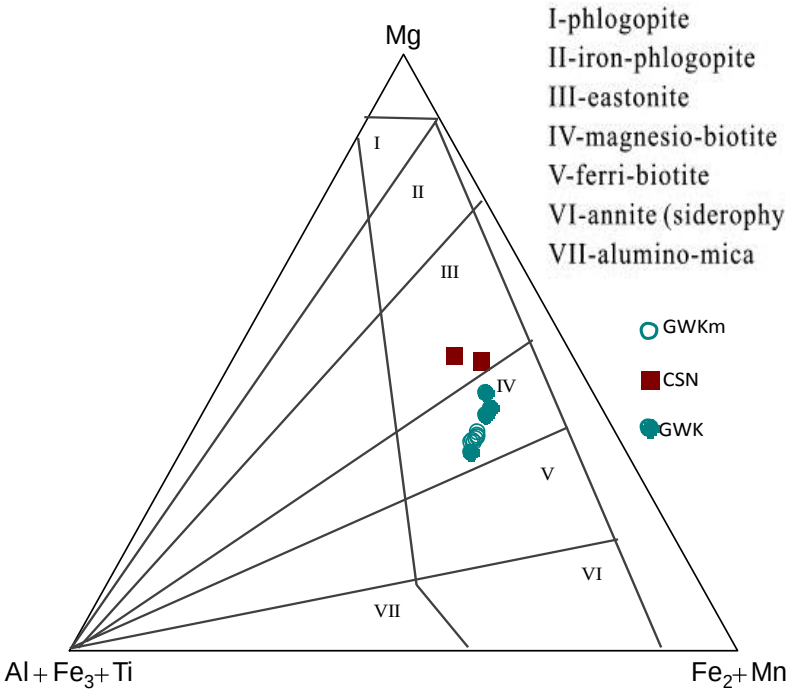

Fig. V. 37 – Foster (1960) classification diagram. Greywacke micas classify as magnesio-biotite and calc-silicate micas classify as eastonites.. (Key: GWK.m – greywacke metatexite; CSN – calc-silicate nodule; GWK – metagreywacke resister).

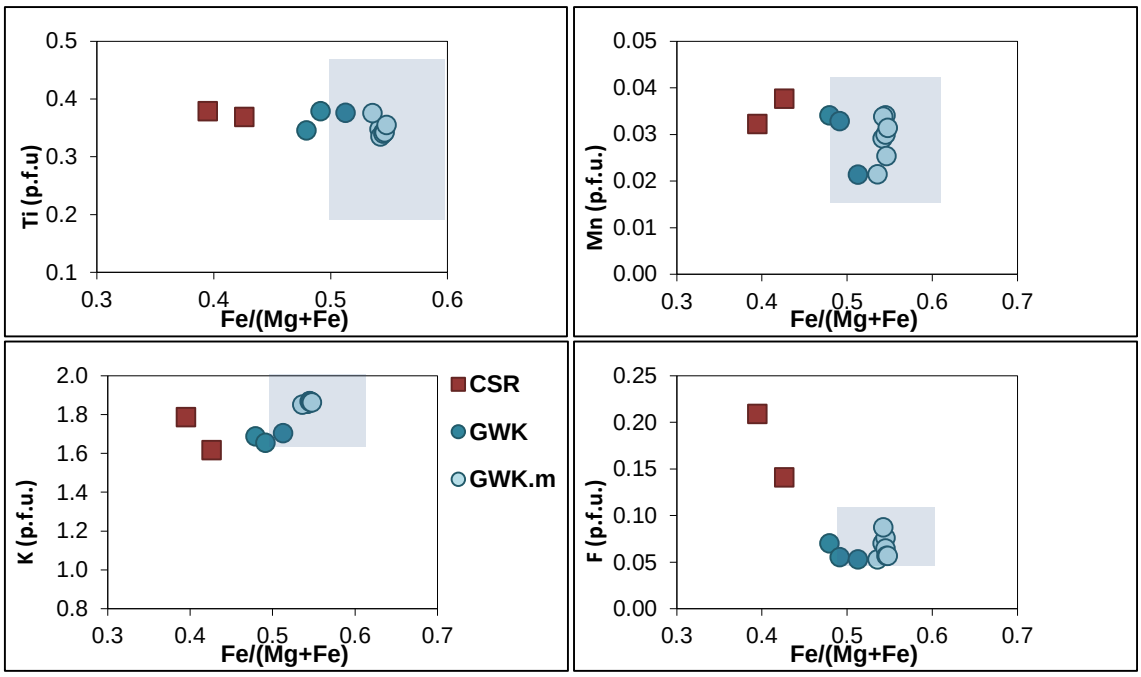

Fig. V. 38 - Ti versus #Fe compositional variation diagrams for metagreywacke and calc-silicate biotites. The calc-silicate biotites have more Mg than biotites from metagreywackes. The shaded space represents the composition of metatexite biotites for comparison. Key: CSN – calc-silicate nodule; GWK – metagreywacke resister; GWK.m – migmatized greywacke.

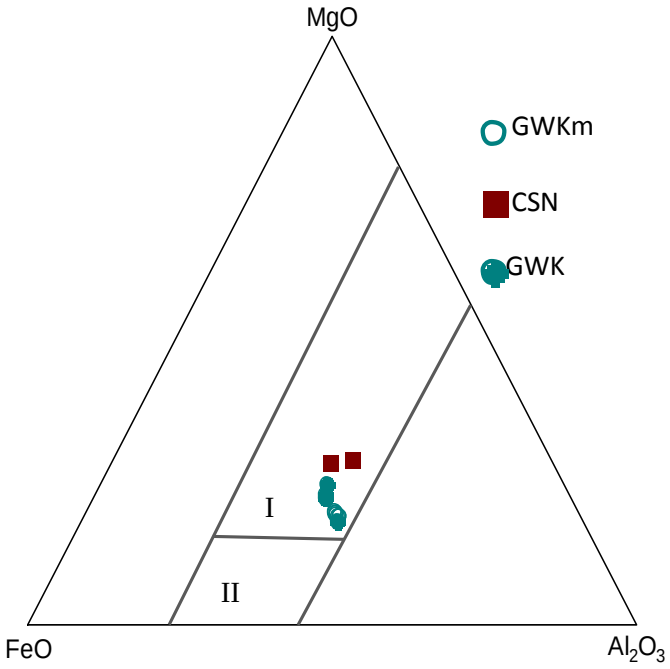

Fig. V. 39 – Greywacke biotite compositions on the FeO - MgO - Al_2O_3 diagram. Fields from Gokhale (1968): I - metamorphic rocks biotite, II - igneous rocks biotite. Metagreywacke and calc-silicate biotites plot on metamorphic field. Key: GWK.m – migmatized metagreywackes; CSN - calc-silicate nodule; GWK – metagreywacke resister.

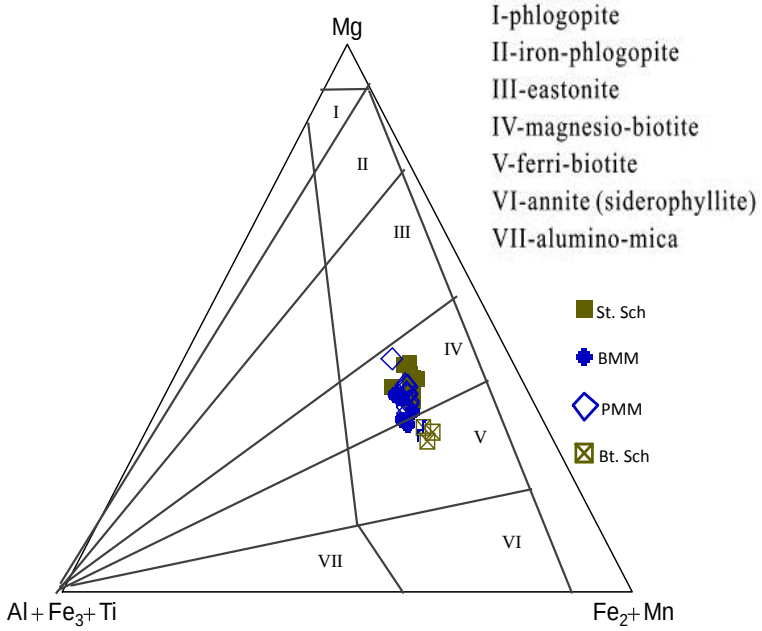

Fig. V. 40 - Foster (1960) classification diagram. Metapelite and metatexite tri-octahedral micas are essentially magnesio-biotite. Key: St.Sch – staurolite-schists; BMM – banded-metatexites; PMM - patch-metatexite; Bt.Sch – biotite-schists.

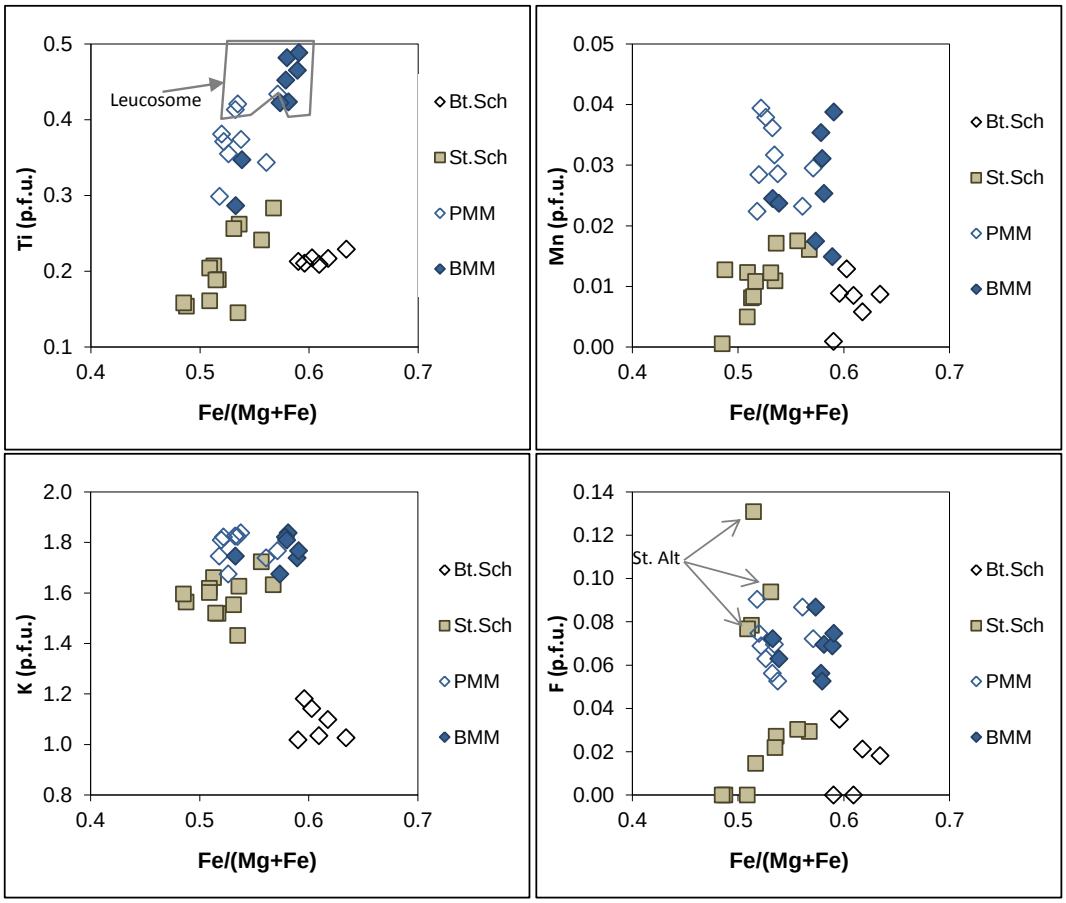

Fig. V. 41 - Compositional variation diagrams for metapelite and metatexite biotites. Legend key: Bt.Sch – biotite-schists; St.Sch – staurolite-schists; PMM - patch- metatexites; BMM – banded-metatexites.

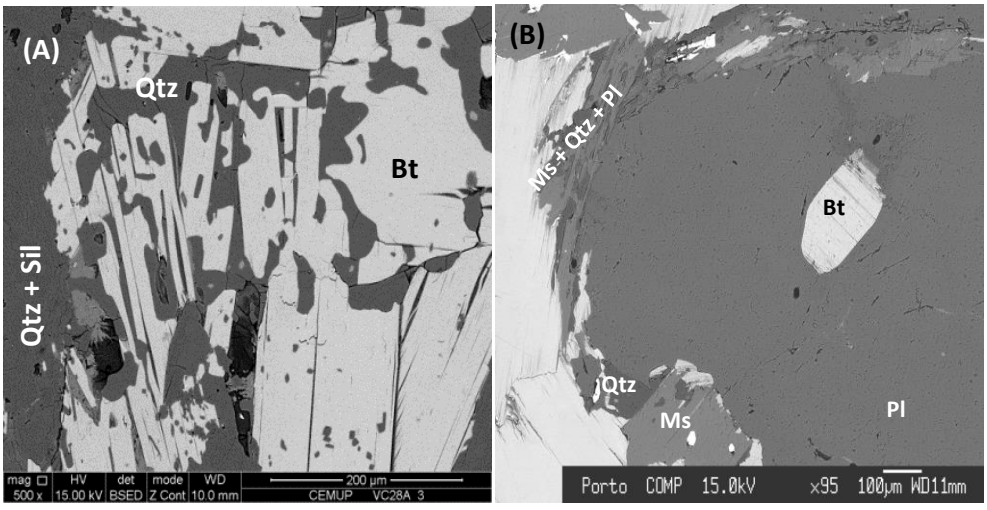

Fig. V. 42 – Backscattered images showing: A) Melanosome biotite in patch-metatexite showing quartz + sillimanite intergrowths; B) Leucosome biotite included in a plagioclase large crystal.

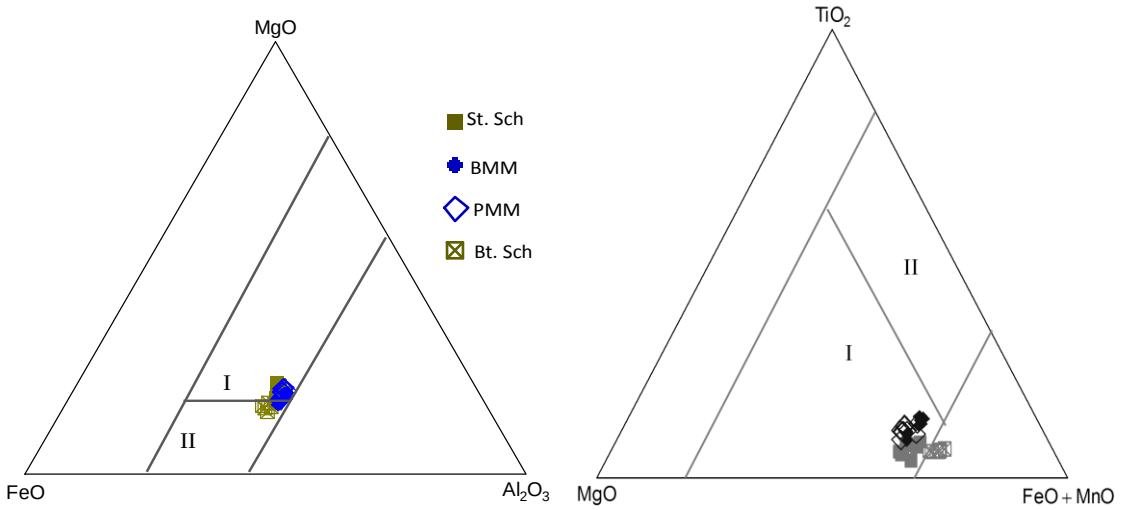

Fig. V. 43 – A) Metapelite and metatexites biotite plots on (FeO - MgO - $Al_2O_{3)}$ and (MgO – TiO2 – FeO+MnO) diagrams from Gokhale (1968): I - metamorphic rocks biotite, II - igneous rocks biotite. All the analysed biotites from metapelites and metatexites plot on the metamorphic field, inclusive the biotites found in leucosomes. Legend Key: St.Sch – staurolite-schists; BMM – banded-metatexites; PMM - patch-metatexite; Bt.Sch – biotite-schist.

5.7.3. Biotites from granitic rocks

Biotites from diatexites, tourmaline-bearing leucogranites and two-mica granites were analysed. The rare biotites occurring in leucogranites matrix show intense chloritization and thus were not considered in this study. Biotite is the only ferromagnesian mineral phase occurring in the MMC granitic rocks.

According to the Foster (1960) nomenclature (Fig. V.44), the Gokhale (1968) classification (Fig. V.45) and the Ti, Mn, K, Na, Al^{iv} and #Fe contents (Fig. V.46) the following can be highlighted:

- Biotites from diatexites classify as Mg-biotites and plot as metamorphic type biotites. The Ti content varies from 0.23 to 0.33 (p.f.u.), slightly lower than metatexites. Mn, K and Al^{iv} contents are similar to the metatexites biotites.
- The rare biotite from tourmaline-bearing leucogranites classifies as Fe-biotites and plot as igneous type biotites. Ti content is variable but similar to the other lithologies. Mn content is clearly higher and Na and Mg content is lower in these biotites. Biotite adjacent to tourmaline shows a distinct composition with lower Ti and F content and higher Fe and Mn content (classifying in the transition to syderophilite).
- Two-mica granites show two distinct types of biotite that classifies as Mg-biotites and as Fe-biotites and plot as metamorphic and as igneous type biotites,

respectively. The Fe-biotites have lower K and higher F contents than the Mg-biotites.

The chemical composition of biotite is an important indicator of the granitic rocks types in which they occur. Its composition is classically used to estimate the conditions of crystallization of the parental magma such as chemical composition, oxygen and halogen fugacities (e.g. Speer, 1984; Nachit *et al*, 1985, Abbel-rahmam, 1994). The Al_t *vs.* Mg diagram after Nachit *et al*. (1985) and the FeO – Mg - Al_2O_3 diagram after Abell-Rahmam (1994) distinguish biotites from potassic-aluminum series to alkaline series. All the biotites from MMC granitic rocks plot in the field of alumino-potassic series in the Nachit *et al*. (1985) diagram, more specifically in the field of the rocks where biotite coexists with cordierite (Fig. V.47). However, cordierite is absent in the two-mica granites and in leucogranites. On the Abell-Rahmam (1994) diagram all the biotites from granitic rocks plot on the field of "peraluminous series including S type granites" (Fig.V.48A).

Compositional profiles of biotites from diatexites and two-mica granites show slightly zoning from core to border. However, the zoning is not homogeneous since a single element could be depleted in the border of some biotites and enriched in the border of others (Fig. V.49).

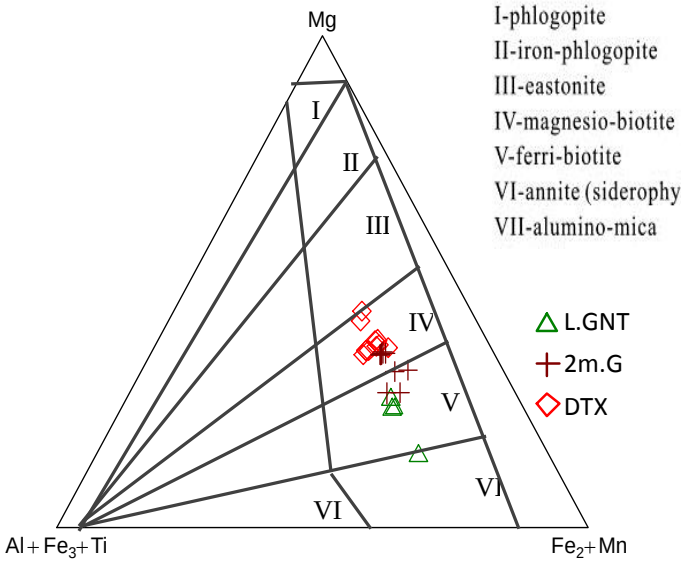

Fig. V. 44 - Mica classification diagram of Foster (1960). Diatexite biotites classify as Mg-biotites, two-mica granite (GNT) biotites classify as both Mg and Fe-Biotites and leucogranite biotites plot as Fe-biotites. Legend key: L.Gnt – leucogranites; 2m.Gnt – two-mica granites; DTX – diatexites.

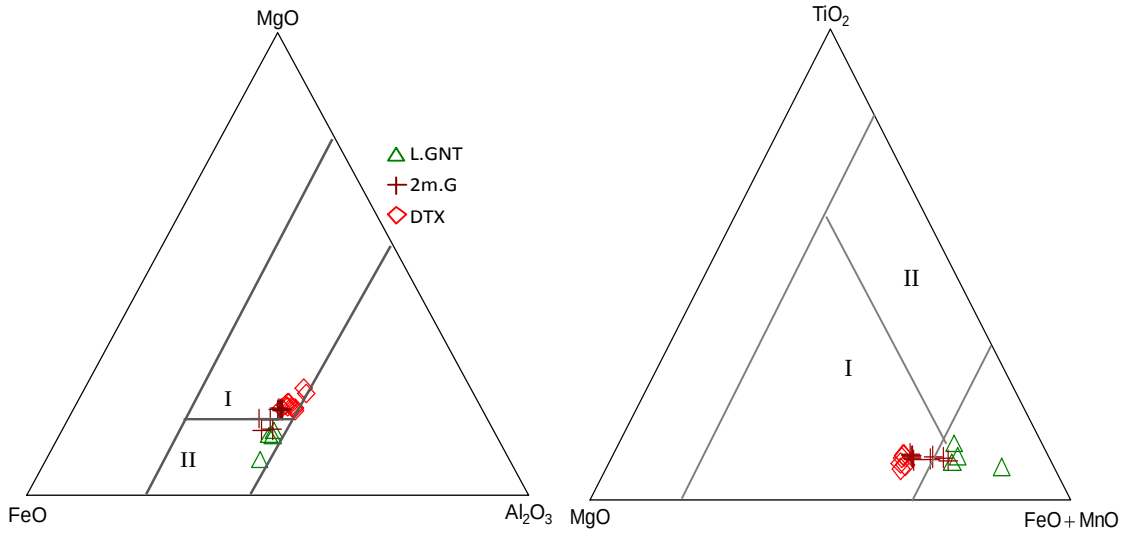

Fig. V. 45 - Granitic rocks biotites composition plotted on the FeO - MgO - Al_2O_3 and MgO-TiO_2-FeO+MnO diagrams. Fields from Gokhale (1968): I - metamorphic rocks biotites, II - igneous rocks biotites. Key: L.Gnt – leucogranites; 2m.Gnt – two-mica granites; DTX – diatexites.

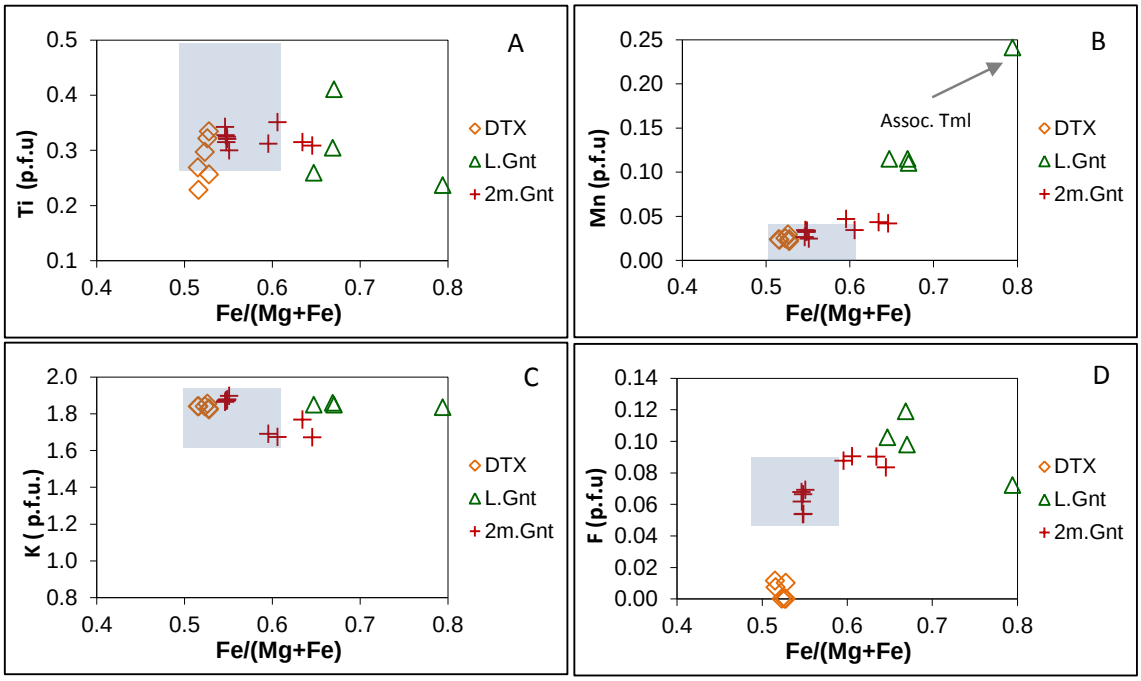

Fig. V. 46 - MMC granitic rocks representation in the #Fe versus Ti, Mn, K and Na diagrams. The shaded space represents the composition of biotites from metatexites. Legend key: L.Gnt – leucogranites; 2m.Gnt – two-mica granites; DTX – diatexites.

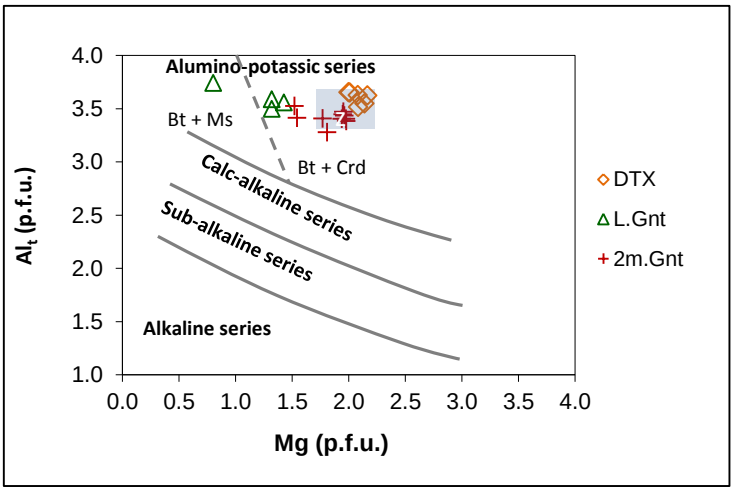

Fig. V. 47 – MMC granitic rocks representation in the Al_t *vs*. Mg diagram of Nachit *et al*. (1985). Abbreviations: Bt + Ms – Alumino-potassic series where biotite coexists with muscovite; Bt + Crd – Alumino-potassic series where biotite coexists with cordierite.

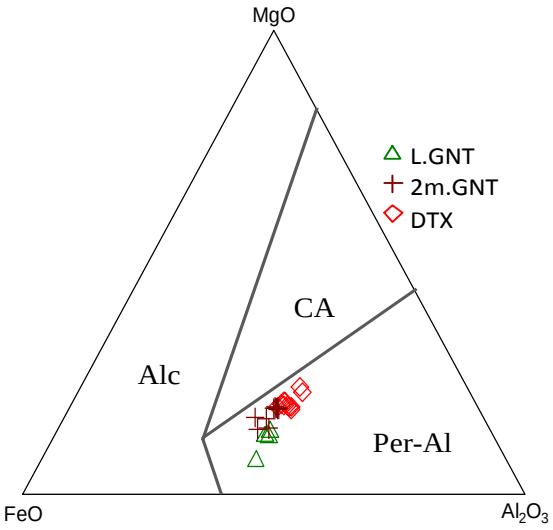

Fig. V. 48– MMC granitic rocks representation in the FeO-MgO-Al2O3 diagram. Fields from Abell-Rahmam (1994): Alc – Anorogenic alkaline series biotites; CA - Calc-alcaline series biotites; Per-Al - Peraluminous series biotites). Legend key: L.Gnt – leucogranites; 2m.Gnt – two-mica granites; DTX – diatexites.

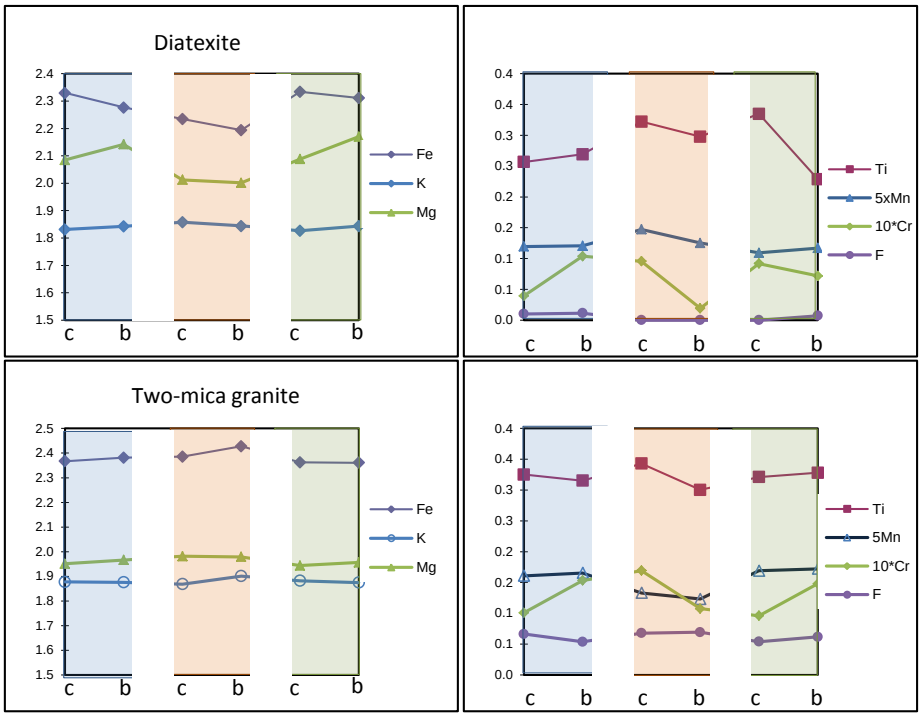

Fig. V. 49 - Profile diagrams for three biotites from diatexites and three biotites from two-mica granites (each colour shading represents a different biotite crystal). The variation is not homogeneous since there are biotites where an element is enriched in the border of some biotites and depleted in the border of others. Obs: b = border; c = core.

5.7.4. Summary

The composition of biotites depends on a number of interdependent variables, namely P, T, fO_2, fH_2O, and element activities. According to the data presented above we can highlight the following:

The biotites from metamorphic rocks plot in the metamorphic biotite field and seem to reflect mostly the partition of elements with coexistence ferromagnesian minerals. For example, in calc-silicate rocks, as M^4 sites in amphibole take Fe in preference to Mg, the distribution of iron is shifted somewhat in favour of that mineral, being the biotite more riche in Mg (Gorbatschev, 1970). This could explain the Mg-rich biotite from calc-silicates relative to metagreywackes, although the whole-rock #Mg in calc-silicate rock is slightly lower than in metagreywackes.

The biotite from staurolite-schists is Mg richer than biotite from biotite-schists. This can be related with the increase in metamorphic grade (Feet, *et al*., 2003 and references therein) and can be explained by the partition of elements in staurolite-schists, since

staurolite carries iron in 4-coordination, which is a type of lattice site not easily occupied by Mg in silicates, so the distribution of Mg is anticipated to be strongly in favour of biotite (Gorbatschev, 1970, Guidoti, 1984).

From staurolite-zone biotites to migmatite biotites the Ti content increases substantially, what could be related with the metamorphic grade increase (Guidotti, 1984; Henry & Guidotti., 2002; Feet *et al*., 2003).

Mn, K and F contents also increase in the MMC biotites relatively to the staurolite-zone biotites. This is consistent with the hypothesis that oxidized F- and K-bearing fluids entrained the MMC lithologies (Gunow *et al*., 2008; Bath *et al*., 2013), as is suggested by field and petrographic observations.

Biotites inserted as inclusions in the leucosome crystals have slightly higher Mg content than the biotites from melanosomes. This could indicate that this biotites where included in the minerals from leucosomes before the development of cordierite, that provoke a repartition of Mg between this two minerals in the melanosomes.

The biotites from migmatitic-greywacke do not show substantial differences between the migmatized-zone and the unmigmatized-zone, indicating a rebalancing of the composition of biotite that affects both sides of the rock.

The biotites from diatexites retain their metamorphic character and show a composition similar to the metatexites biotites (except in the F content that is higher in the migmatites biotites), being mainly of restitic origin. This suggests that diatexites result of anatexis of the same metapelites that originated the metatexites and show moderate degree of partial melting and melt production, being the magmatic texture mostly impressed by the recrystallization of plagioclase, quartz and K-feldspar large crystals.

The biotites from tourmaline-bearing leucogranite plot as igneous biotites in the diagram of Gokhale (1968), due to its relatively low Mg content. However, the field and petrographic observations indicate that these biotites have a restitic character and were affected by latter fluids. This is also suggested by its high F contents, especially in the biotite associated with tourmaline.

The biotite from two-mica granites presents igneous and metamorphic character, indicating that some biotite could be restitic and other could be newly-formed of magmatic origin. The petrographic observations also suggest this double origin since there are anhedral and euhedral biotite crystals in the two-mica granites matrix. This

would be expected in a rock resulting from anatexis of metamorphic rocks but showing a higher rate of partial melting than the diatexites.

Although not all the MMC granitic rocks show cordierite, its biotites plot in the field of alumino-potassic series containing biotite and cordierite due to their relatively high Mg content. This is also in agreement with the origin mostly restitic for this biotites since they show a composition similar to the composition of the biotites from metatexites.

5.8. White-mica

White micas were analysed from metapelites, metatexites and granitic rocks.

White-micas from low-grade metapelites (Chlorite- and Biotite-zone) are aligned along the main foliation. The higher grade metasediments white-micas (Staurolite and Migmatite-zones) essentially resulted from staurolite, biotite, plagioclase and K-feldspar alteration processes.

According to the white-micas classification of Deer *et al.* (1962, 1992), white-micas from all the studied lithotypes are muscovites where the X position is essentially occupied by K and the Y position by Al (Fig. V.50).

Regarding paragonite and celadonite components the studied muscovites show the following characteristics (Fig. V.51):

- Muscovite from chlorite-schists shows a ratio celadonite/paragonite of about 1;
- Paragonite component is prevalent on biotite from staurolite-schists;
- Celadonitic component is prevalent in biotites from metatexite; the muscovites that result from feldspars alteration show low paragonitic component;
- Muscovite from granitic rocks shows predominance of celadonitic component;
- Paragonitic component prevails in the Micas from aplite-pegmatites.

The distinction between primary and secondary origin is the major question concerning the occurrence of muscovite in igneous rocks. The primary status of muscovite in many two-mica granites is questionable. The larger interstitial muscovite crystals in granites could have formed in equilibrium with magma, or have formed in the solid state at any P-T condition below the stability curve of muscovite (Feet *et al.,* 2003). Muscovite can crystallize from granitic magma at pressures above 3.5 kbar, but at lower pressures muscovite can only form in the solid state (Deer *et al.,* 1992).

It was considered that magmatic muscovites are richer in Ti, Al and Na and poorer in Mg and Si (Deer *et. al.,* 1997). As referred, in staurolite-schists, metagreywackes and metatexites all the muscovites are secondary. In these rocks, the muscovites that clearly substitute biotite show relative high Ti and Na content. It is the case of the muscovites in metatexites (Fig. V.53A) and in diatexites (Fig. V.53B). The content in Ti and Na is related with the replaced mineral, since the muscovites replacing feldspar show minimal Ti and Na content and muscovites replacing biotite show the higher Ti content. Muscovites after staurolite show moderate Ti content and high Na content (Fig. V.53A and 54). Muscovites from calc-silicates, that replace plagioclase, also show low Ti and Na content.

Muscovites from diatexites are all anhedral and clearly result of replacement of biotite or feldspars, or occur as radial aggregates in diatexite veins (Fig. V.55 and V.57B). The Ti content is highly variable and like in metatexites is related with the replaced mineral. The hydrothermal radiating aggregates show the lower Ti content (Fig. 54B).

Two-mica granites and leucogranites show both, muscovites that replace biotite or feldspars and large plates of euhedral muscovite dispersed in the matrix (Fig. V.57A). The euhedral muscovites do not occur in all the samples since these muscovites only occur in samples that show other signs of hydrothermal alteration, like chloritization of biotite and sericitization of plagioclase. Spatially are related with zones where the granitic rocks show fracturing and are slightly deformed. The Ti and Na composition is similar to the diatexite and metatexite muscovites (Fig. 53). The core and border of two subhedral muscovites from two-mica granites were analysed. The border is slightly depleted in Ti and $Mg+Fe_t$ and enriched in Na.

Since the composition of muscovites depend of the replaced mineral the use of Miller *et al.,* (1981) and Monier *et al*. (1984) diagrams is inconclusive, since the muscovites that replace biotite or staurolite plot in the field of primary origin. The muscovites clearly replacing feldspars plot in the fields of secondary/hydrothermal muscovites but muscovites replacing biotite have Ti content similar to the primary muscovites (Fig. 54).

To conclude about the existence of primary muscovite in two-mica granites and leucogranites it will be necessary more accurate studies, although a secondary origin seem to be more probable regarding the texture of the muscovites, the coexistence of other hydrothermal replacements and the inexistence of euhedral muscovites in some of the two-mica granites samples.

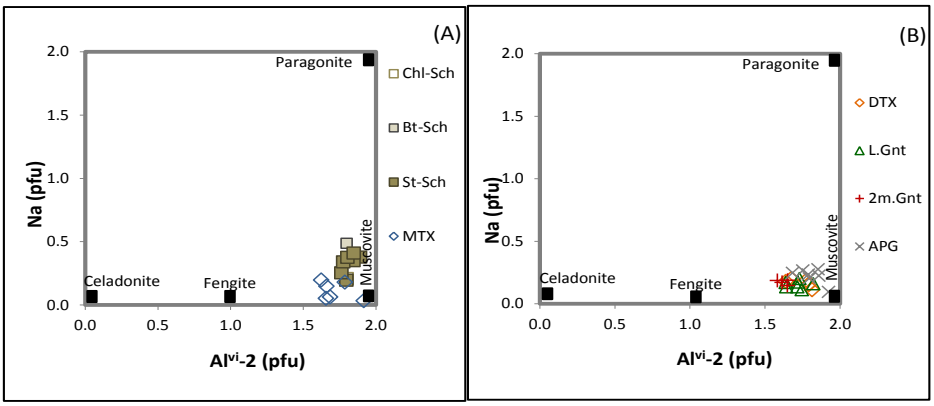

Fig. V. 50 – Representation of the white micas in the Na *vs.* Al^{VI}-2 classification diagram (after Deer et al., 1962,). (A) metapelites and (B) granite rocks. Legend Key: Chl-Sch – chlorite-schists; Bt.Sch – biotite-schists; St.Sch – staurolite-schists; MTX - metatexites; CSN – calc-silicate nodules; DTX – diatexites; L.Gnt – leucogranites; 2m-Gnt – two-mica granites; APG – aplite-pegmatites.

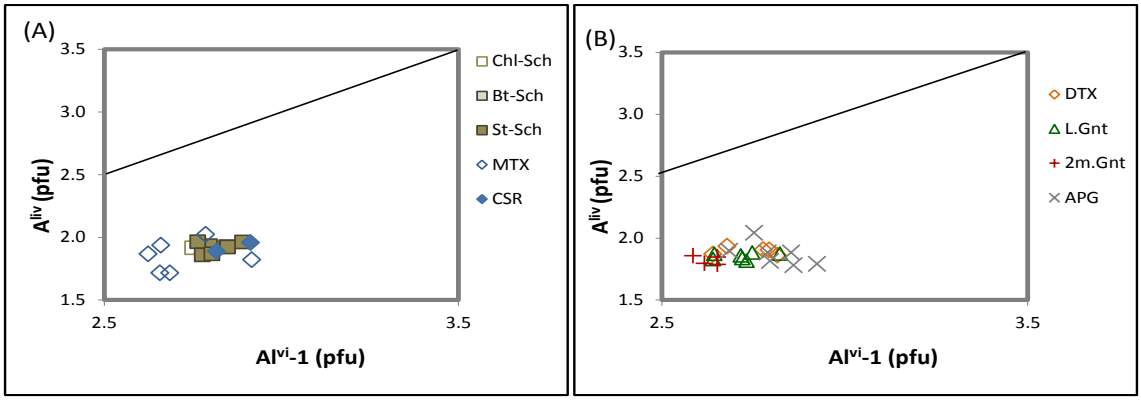

Fig. V. 51 – Al^{IV} versus Al^{VI} – 1 diagram showing trend-line that represents the phengite substitution. All the analysed muscovites have $Al^{VI}/(Al^{VI}-1) < 1$ and do not follow the phengite substitution trend. Legend Key: Chl-Sch – chlorite schists; Bt.Sch – biotite-schists; St.Sch – staurolite-schists; MTX - metatexites; CSN – calc-silicate nodules; DTX – diatexites; L.Gnt – leucogranites; 2m-Gnt – two-mica granites; APG – aplite-pegmatites.

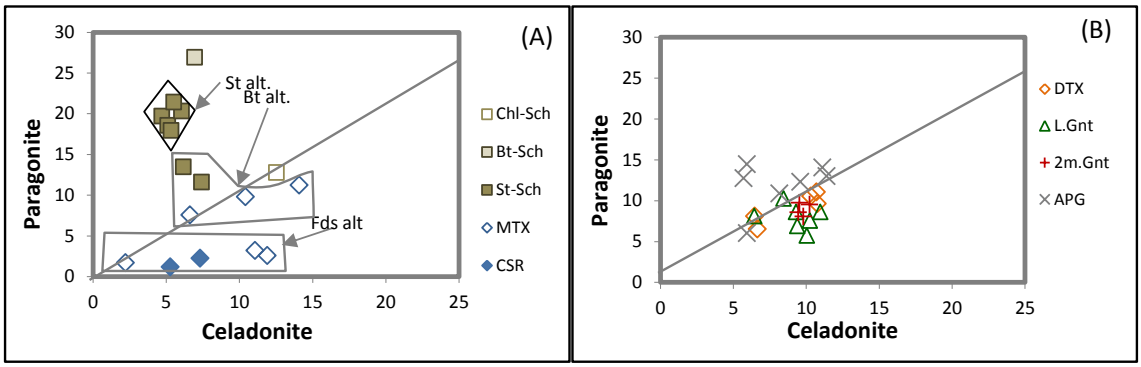

Fig. V. 52 – Celadonite versus paragonite component diagram for (A) metapelites and (B) granite rock white-micas. Legend Key: Chl-Sch – chlorite-schists; Bt.Sch – biotite-schists; St.Sch – staurolite-schists; MTX - metatexites; CSN – calc-silicate nodules; DTX – diatexites; L.Gnt – leucogranites; 2m-Gnt – two-mica granites; APG – aplite-pegmatites.

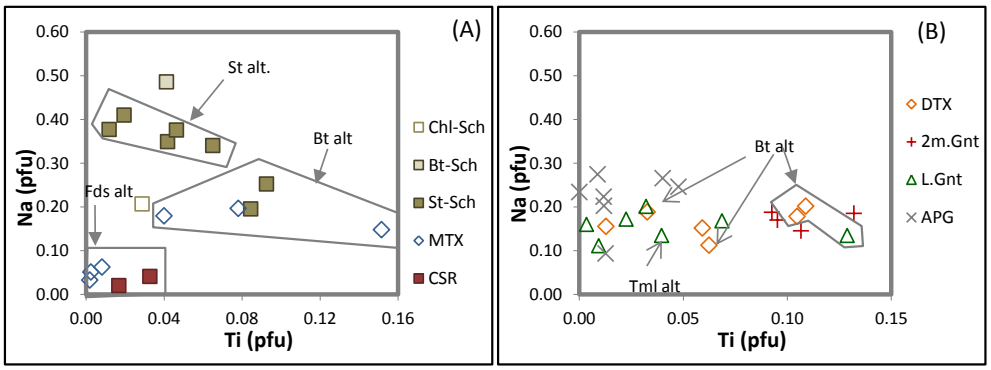

Fig. V. 53 – (A) Ti versus Na diagram for metapelite and metatexite muscovites; (B) Ti *versus* Na diagram for granitic rocks muscovites. Legend Key: Chl-Sch – chlorite-schists; Bt.Sch – biotite-schists; St.Sch – staurolite-schists; MTX - metatexites; CSR – calc-silicate nodules; DTX – Diatexites; L.Gnt – leucogranites; 2m-Gnt – two-mica granites; APG – aplite-pegmatites.

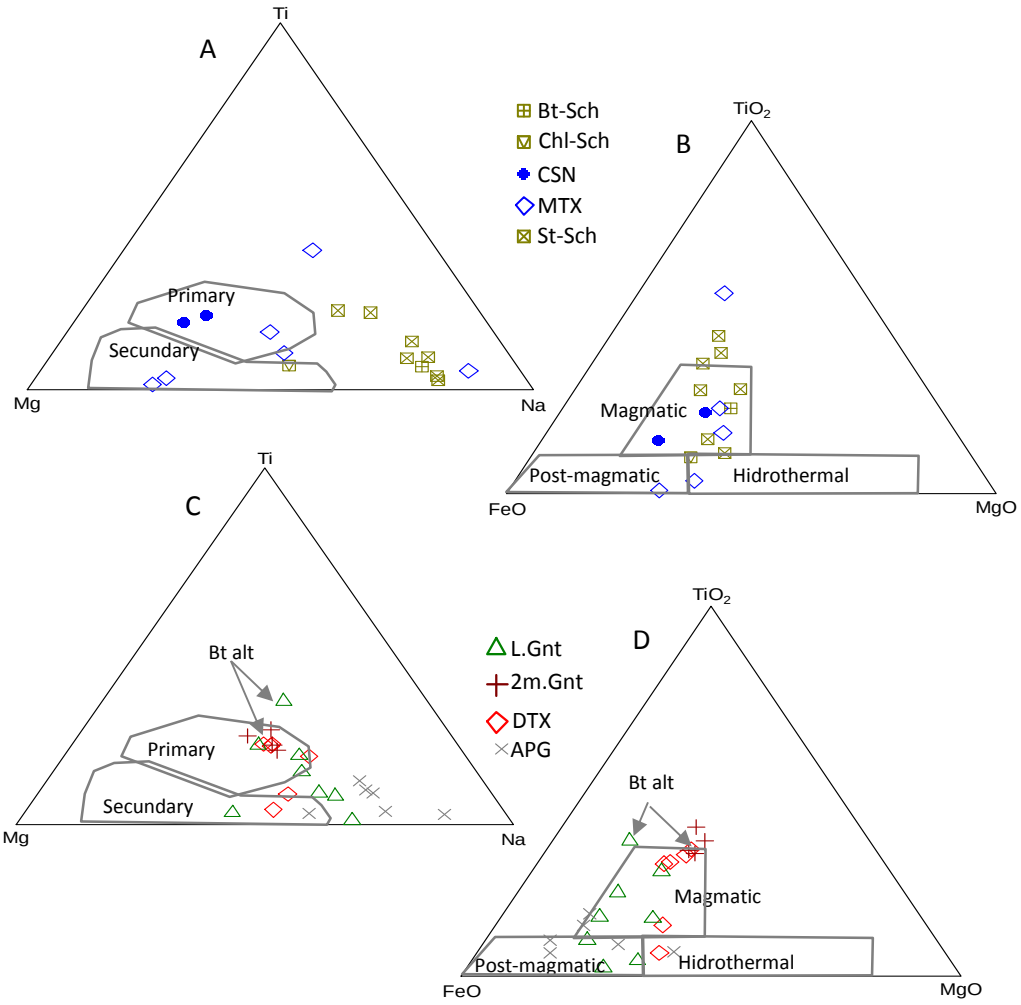

Fig. V. 54 - Projection of muscovites in Miller *et al*. (1981) diagram (A and C) and Monier *et al.* (1984) diagram (B and D) for discrimination of primary and secondary muscovites. Key: Bt.Sch – biotite-schists; Chl-Sch – Chlorite-schists; CSN – calc-silicate nodules; MTX –metatexites; St.Sch – staurolite-schists; L.Gnt – leucogranites; 2m-Gnt – two-mica granites; DTX – Diatexites; APG – aplite-pegmatites

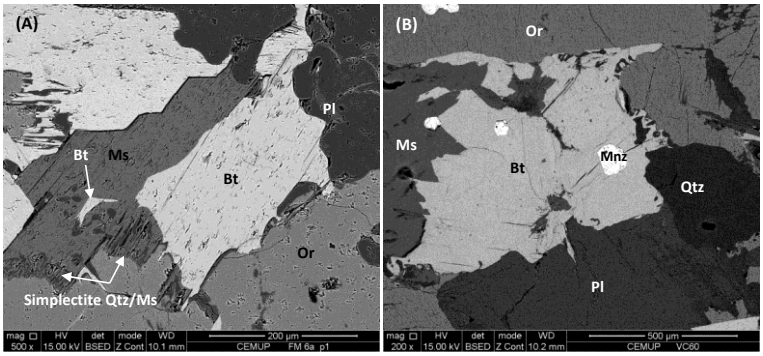

Fig. V. 55 – Backscatter Electron Images from diatexite of (A) primary biotite with crystal faces replaced by muscovite and showing symplectitic border and (B) reequilibrated xenomorphic biotite replaced by muscovite and showing symplectitic border.

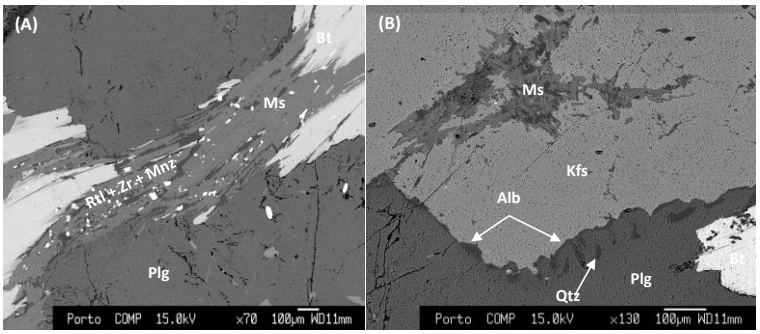

Fig. V. 56 – Bachscattered images of metatexites showing muscovite replacing biotite and replacing K-feldspar.

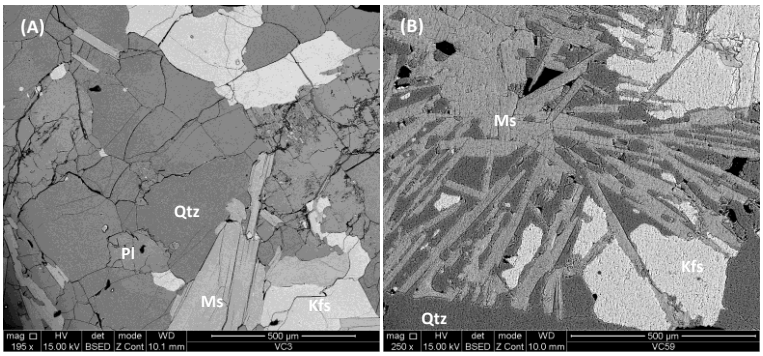

Fig. V. 57 – Backscattered images showing A) euhedral to subhedral muscovite in leucogranite; B) Radial aggregate of muscovite associated with quartz in diatexite.

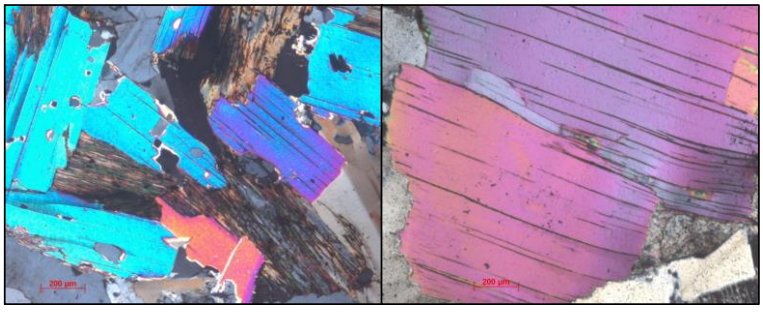

Fig. V. 58 – Euhedral muscovite in two-mica granites associated with chlorite after biotite.

5.9. Staurolite

Staurolites are characterized by an internal zone containing great amount of quartz inclusions and an external rim showing mostly ilmenite inclusions. Most if the staurolites show hydrothermal alterations zones with development of secondary micas. Were made profiles across the staurolite crystal, from the core to the edges (Figs.V.59 and V.60) and also in staurolite pseudomorph after garnet and staurolite surrounding garnet (Fig.V.61). The following can be pointed out:

- The composition of staurolite has little variation from sample to sample. In general classify as Fe-staurolites (0.77< #Fe < 0.80 p.f.u.) showing low Zn, Mn and Cr content (< 0.037, < 0.034 and < 0.019 p.f.u. respectively). The Fe content is inversely correlated with Si+Al (r^2 = 0.7). The H_2O content varies between 1.86 and 3.19 w%;
- There are no systematic differences across the vertical or horizontal profiles;
- There are no systematic variation between the quartz inclusion zone, the opaque mineral inclusion zone and the free inclusion zone;
- The only systematic chemical variation is observed in the staurolite adjacent to the alteration zone (point 9, 15 and 16; Fig. V.59). These points show a sharp drop in the Fe, Mn and Zn contents and an increase in the Al+Si content;
- The staurolite pseudomorph after garnet has more Fe and less Si+Al than the staurolite surrounding garnet (Fig. V.61).

The slight, non-systematic chemical variations observed across the staurolite crystals suggests that the compositional dissimilarities are more probably related to the staurolite structure and hydrothermal alteration processes than to metamorphic processes.

Sector-zoning in staurolite related to the development of distinctly different compositions accordingly to the crystallographic distinct faces of a growing staurolite crystal is well known (e.g. Hollister, 1970).

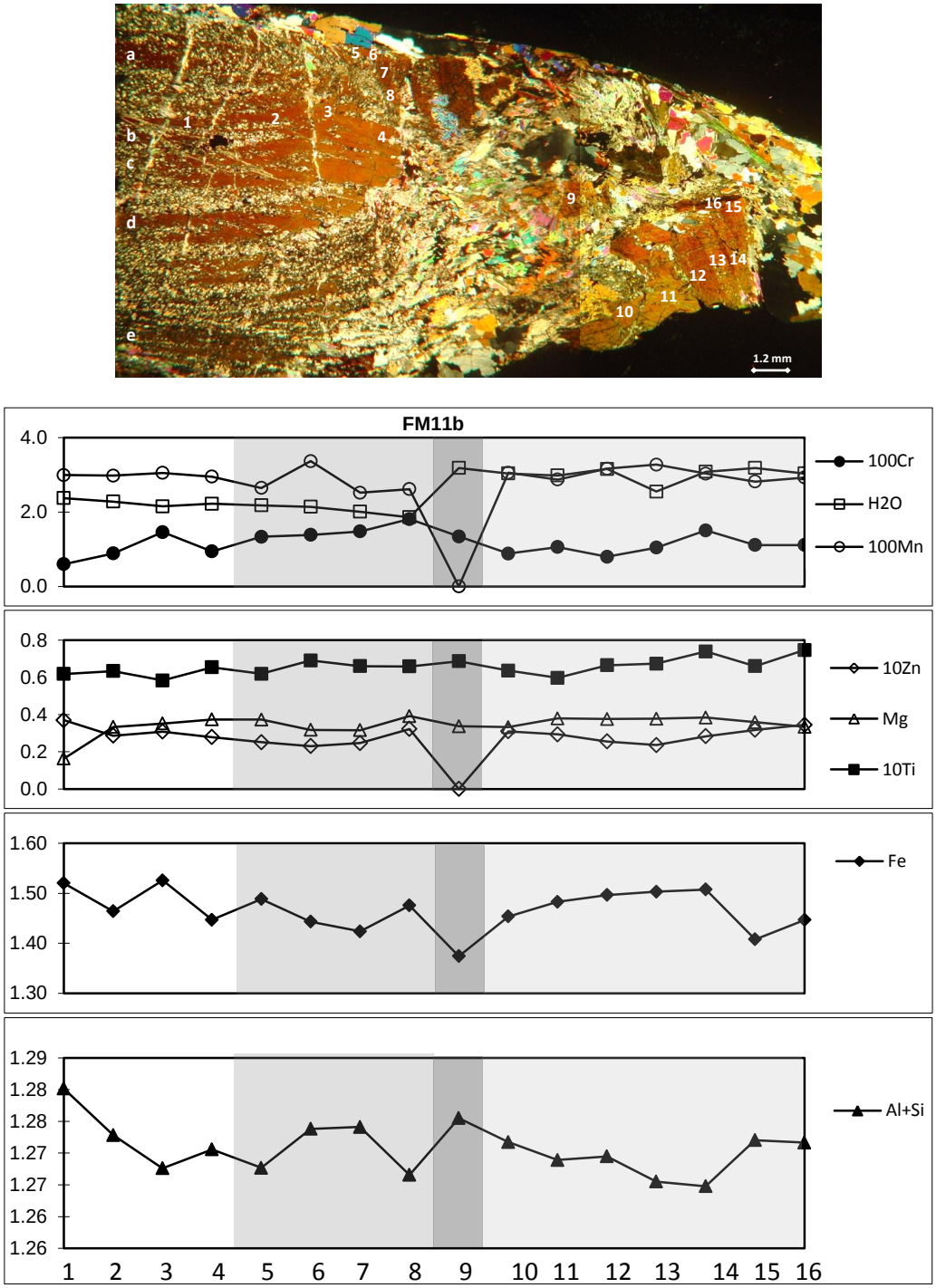

Fig. V. 59 - Staurolite profile in core-zone (1-4), upper edge (5-8), alteration zone (9) and border (10-16) for several elements. From inner zone to the upper edge there are no significant differences; From the inner part towards the alteration zone and the border the water content increases and the Cr content decreases. On the alteration zone there are a sudden decrease in Zn, Mn and Fe. Ti shows a flat profile.

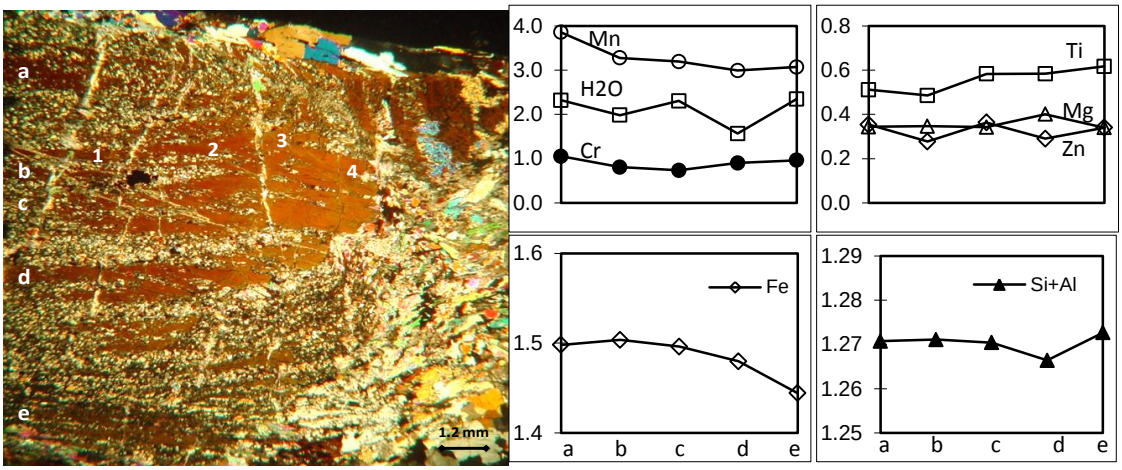

Fig. V. 60 – Vertical central profile (a to e).

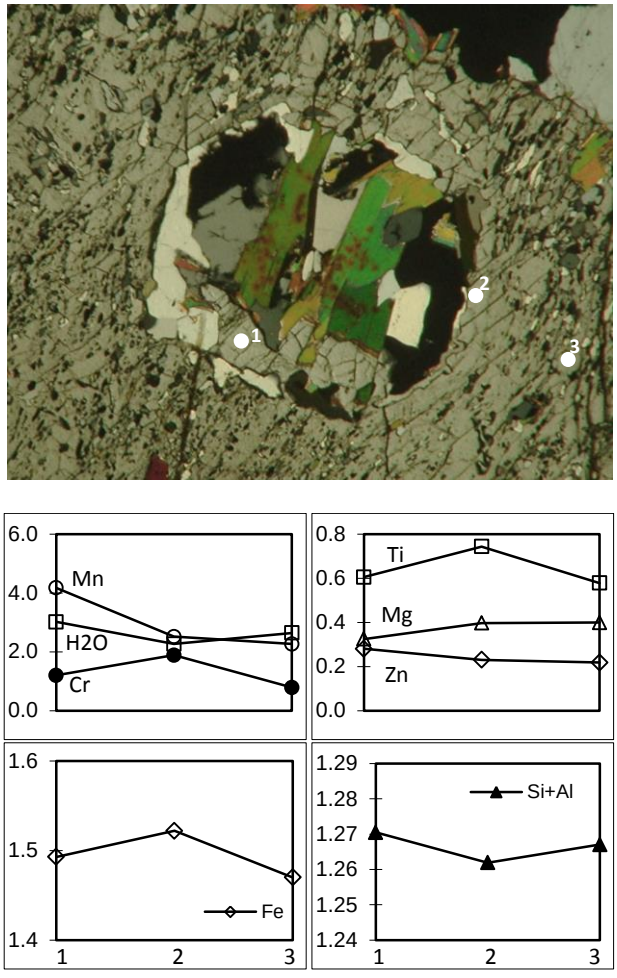

Fig. V. 61 – Staurolite replacing garnet (1-2) and surrounding garnet (3; with opaque and quartz inclusions). The staurolite replacing garnet has more Fe and less Si+Al than the staurolite surrounding garnet.

5.10. Tourmaline

Analyses were performed on tourmalines from leucogranites and from aplite-pegmatites.

The analyzed tourmalines chemical composition corresponds to schorl. In all the samples the Z-site is fully occupied by Al and the X-site is predominantly occupied by Na (Fig. V.63).

Tourmaline from aplite-pegmatites shows 0.15 < #Mg < 0.50, sodium ranging from 0.55 to 0.72 (p.f.u.) and very low Ca content ranging from 0.023 to 0.05 p.f.u.. Some tourmalines show a tiny border with slightly differences in the Fe, Ti, Mn and Mg contents (Figs. V.65A and V.66A).

Tourmaline from leucogranites shows 0.30 < #Mg < 0.42, sodium ranging from 0,56 to 0,74 p.f.u. and low Ca content (< 0,01 p.f.u.). Titanium contents are low (0.025 to 0.089 p.f.u.). Compositional profiles show a border enriched in Mg and Ti and depleted in Mn, although with some heterogeneous variation. The Ti content in this crystal is especially low (~0.25 p.f.u.), except in one of the borders where there is a abrupt increase to values equivalent of the other crystals (~0.8 p.f.u.) (Figs. V.65B and V.66B).

On Henry & Guiddoti (1985) diagrams (Fig.V.64) all the tourmalines plot on the Li-poor granite and associated pegmatites field.

Fe-Mg tourmaline is a common accessory mineral in evolved granites, associated hydrothermal products and pegmatites and is widespread in the European Hercynian Belt leucogranites (Pivec *et al*. 1998), including in Portuguese granites and pegmatites (Neiva, 1974; Neiva *et al*., 2007).

Neiva *et al.,* (2007) found systematic differences in composition and zoning in tourmalines from magmatic and hydrothermal origin. These authors consider that “magmatic tourmaline is either unzoned or shows an increase in Fe/(Fe+Mg) and a decrease in Mg from core to rim, while hydrothermal tourmaline is either oscillatory zoned or shows an increase in Al and a decrease in Fe and Mg from core to rim; hydrothermal tourmaline shows lower content in Fe/(Fe+Mg) than magmatic tourmaline”.

The tourmaline from leucogranite show lower Fe content (#Fe ~0.63) than the aplite-pegmatites tourmalines (#Fe ~0.77). Also the zoning is heterogeneous. This suggests

that the tourmaline from leucogranites is of hydrothermal origin, what is in agreement with the petrographic observations. Aplite-pegmatites tourmalines are enriched in Mn. The same enrichment in Mn is found in the aplite-pegmatites garnets, what indicates that these minerals reflect the Mn-rich composition of the host rock.

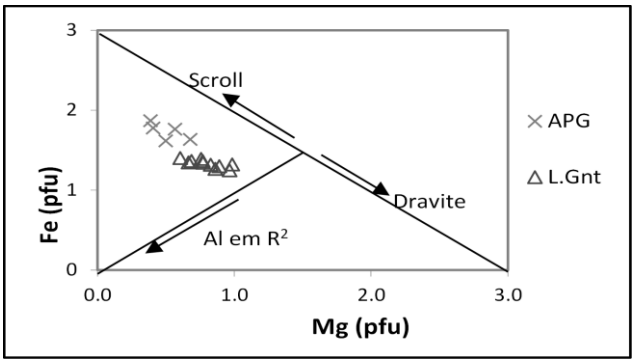

Fig. V. 62 – Classification diagram for staurolites with fields defined by London and Manning (1995). All the tourmalines plot on the scroll field. Key: APG – aplite-pegmatite; L.Gnt – leucogranite.

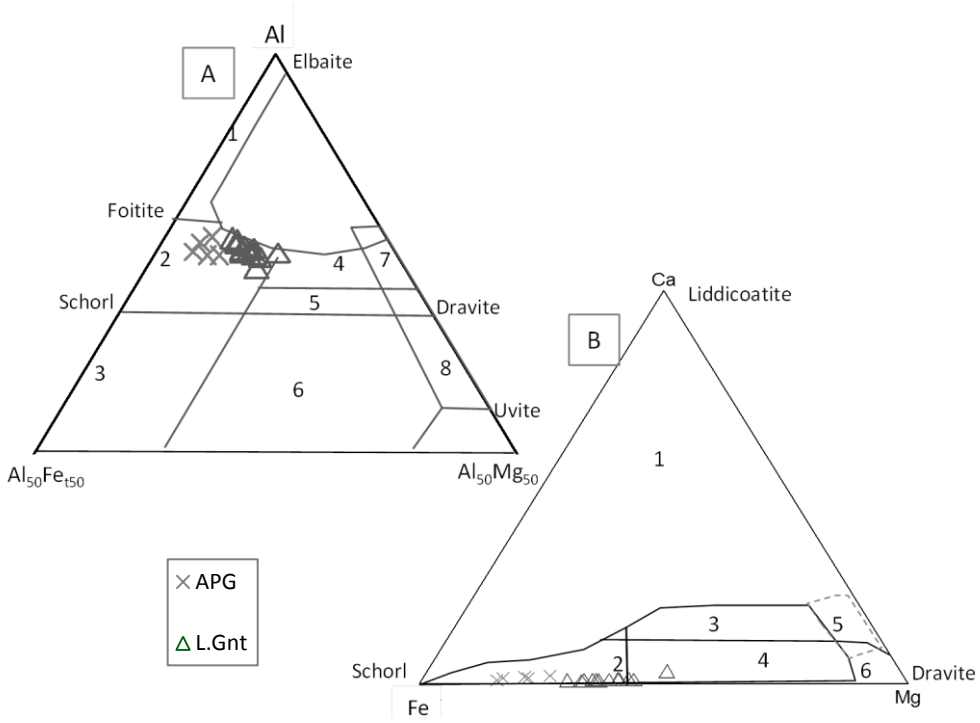

Fig. V. 63 – **A)** Ca- Fe_t -Mg and diagram of Henry & Guidotti, (1985) (molecular proportions) for tourmaline from leucocratic granite (L.Gnt) and aplitopegmatite (APG). The fields represent: I - Li-rich granite pegmatites and aplites; **2 - Li-poor granites and pegmatites**; 3 - Ca-rich metapelites and metagreywackes; 4 - Ca-poor metapelites or metapsammites rocks and quartz-tourmaline rocks; (5) Metacarbonates; 6 -Meta-ultramafic rocks; **B)** Fet – Al – Mg diagram The fields represent: 1 - Li-rich granite pegmatites and aplites; **2 – Li-poor granites and pegmatites**; 3 - hydrothermal altered granites 4 / 5- Metapelites /psammites; 6 - Fe3*-rich quartz-tourmaline rocks 7 - Low-Ca meta-ultramafic rocks 8 - Metacarbonates and meta-pyroxenites Legend key: APG – aplite-pegmatite; L.Gnt – leucogranite.

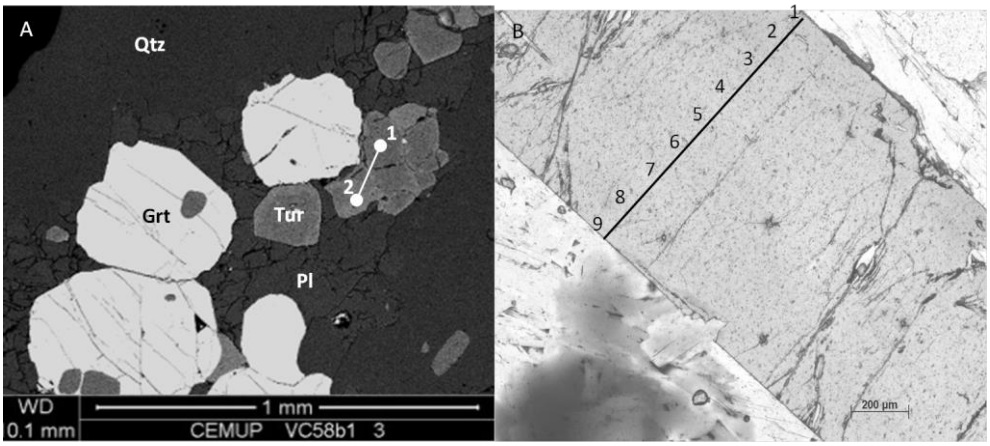

Fig. V. 64 – A) Backscattered image of tourmaline in aplite-pegmatite (A) and leucogranite (B) showing location of analyses referred in Fig. 66.

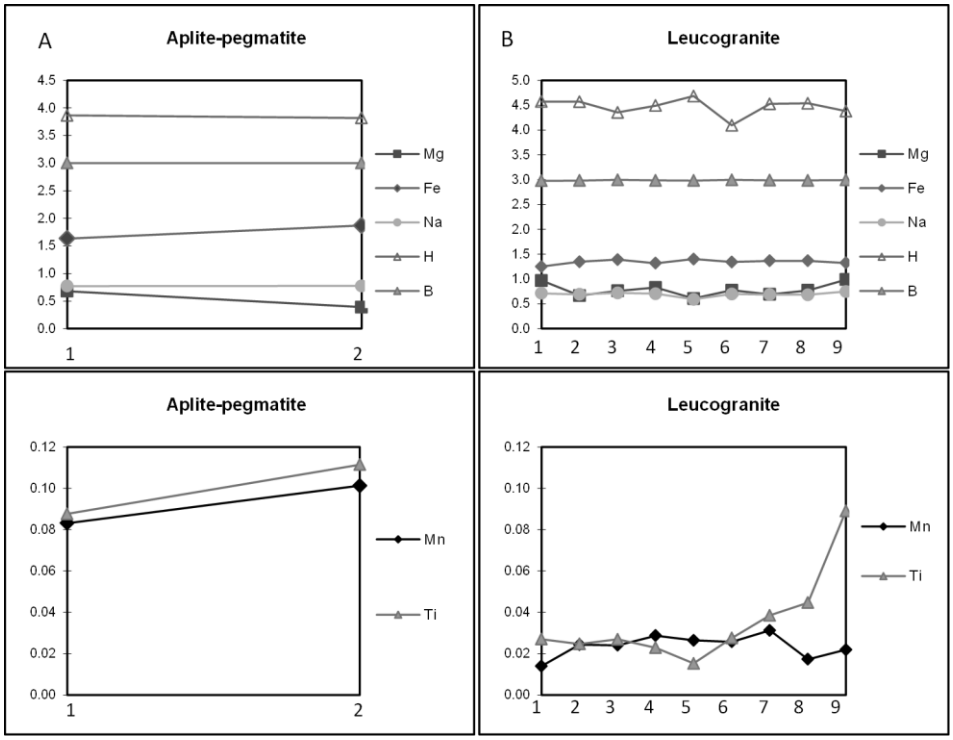

Fig. V. 65 – Profile of analysed points in tourmaline from leucogranite and tourmaline from aplite-pegmatite. The location of analysed points is in Fig. V.66.

CHAPTER VI – GEOCHEMISTRY

"**I consider nature a vast chemical laboratory in which all kinds of composition and decompositions are formed."**

Antoine Lavoisier

6.1. Introduction

Whole-rock major and trace-element analyses were carried out using ICP and ICP-MS (inductive coupled plasma / mass spectrometry) procedures at "Activation Laboratories" (Ancaster, Ontario). Fused samples are diluted and analysed by Perkin Elmer Sciex ELAN 6000, 6100 or 9000 ICP/MS. Three blanks and five controls (three before sample group and two after) are analysed per group of samples. Duplicates are fused and analysed every 15 samples. Instrument is recalibrated every 40 samples. Precision and accuracy for concentrations ≥100× the minimum detection limit (MDL) was generally better than ±5 percent relative, and in many cases such as for major elements was better than ±1 percent relative. For concentrations approximately 10× the MDL, precision and accuracy were about ±10–20 percent relative depending on the method used. The Cu, Pb, Zn, Ni, Ag, As and Sb values provided by Fusion ICP/MS, are semi-quantitative and are provided for general information, thus were not used in this work.

The samples selected for the chemical analyses were chosen on the basis of a previous petrographic study and covering all lithologies of the study area, distributed as follow:

Sector 1 – In this Sector samples were analysed from metagreywacke resisters and calc-silicate nodules, metatexites, leucosomes and granitic rocks including three metagreywacke samples, four calc-silicate samples, twelve metatexite samples (two patch-metatexite and ten banded-metatexite samples), two leucosome samples, five diatexite samples, seven leucogranite samples (four leucogranite samples and three tourmaline-bearing leucogranite samples), fourteen two-mica granites s.l. samples

including medium to coarse-grained granites (nine samples), fine-grained granites (two samples) and porphyritic granites (three samples from Ferreira, 2011).

Sector 2 – In this Sector samples were analysed from Schist-Greywacke Complex including one quartzite (or metasiltstone) sample, one pelite sample from biotite-zone, one calc-silicate sample, two psammite and four pelite samples from staurolite-zone. Three of the staurolite-schists samples are from Fânzeres and one is from Aguçadoura (Fig. III.32).

The results of chemical analyses are presented in Appendix C.

6.2. Geochemistry of metasedimentary rocks

6.2.1. Major elements

The lithological diversity of metasedimentary rocks under study, although matched by different metamorphic evolution, is the major cause of the differences in lithogeochemistry composition.

Various classification schemes for clastic sediments based on whole-rock chemical data have been established (e.g. Pettijohn *et al*. 1972; Herron, 1988). Figures VI.1 and VI.2 represent the Herron (1988) classification diagram and ACF diagram (Eskola, 1915; with fields of Barton *et al*, 1991 and Winter, 2001) applied to MMC and SGC samples that were used to give an idea of the lithogeochemical types present in Mindelo Migmatite Complex (MMC) and Schist-Greywacke Complex (SGC) metasediments. Herron (1988) diagram distinguishes between lithologies according to whole-rock major elements chemistry based on SiO_2/Al_2O_3 *vs.* Fe_2O_3/K_2O ratios and their proportion reflects the sedimentary evolution. With an increasing SiO_2/Al_2O_3 ratio the grain size also increases, as do the grade of recycling and the maturity of the sediment. The Fe_2O_3/K_2O ratio is used as an indicator of mineralogical stability and distinguishes lithic fragments from feldspar. Eskola diagram with fields defined by Barton *et al.*, (1991) and Winter (2001) takes into account the Ca, Na, Mn, and Mg besides Al, K and Fe giving a broader classification.

These diagrams are used to emphasize the lithological diversity of MMC, SGC and PLZ, in spite of their application to low-grade metasedimentary contexts. Although in many post-depositional and metamorphic processes the element mobility does not

appear to be an important factor in determining the lithogeochemical composition (McLennan *et al.,* 1991; Rollinson, 1993), in high grade metamorphic conditions some chemical mobility may occur during the metamorphic processes (Barbey & Cuney, 1982).

All the lithologies in the MMC are relatively rich in Ca (average of 11wt.% of CaO in calc-silicate nodules, 2 wt.% in metagreywackes and 2,5 to 0,4 wt.% in metatexites). MMC metasedimentary lithologies can be divided in:

- Metagreywackes show low variation in major elements composition. CaO content between 2 and 3 wt.%, SiO_2 average content ~74 wt.%, Al_2O_3 average content 14,8 wt.%, Fe_2O_3 content ~4,7 wt.%, K_2O average content 1,5 wt.% and Na_2O average content ~ 2,6 wt.%.
- Calc-silicate nodules plot in Fe-shale (Fig. VI.1) and marls field (Fig. VI.2). Calc-silicate classification in the Herron diagram is conditioned by their very low K and Na content and high Ca content (content average of 0,76 wt.%, 0,51 wt.% and 11 %wt.%, respectively). SiO_2 content is lower than the metagreywackes SiO_2 content (57 and 67 wt.%). Calc-silicates showing Type II alteration plot in the sandstone field due to its higher silica content.
- Metatexites plot between shale and greywacke fields (Fig. VI.1) and in the pelite field (Fig. VI.2). They show SiO_2 between 57 and 72 wt.%, Al_2O_3 between 13,5 and 21,0 wt.%, Fe_2O_{3t} between 3,9 and 8,8 wt.%, Na_2O between 1,0 and 3,4 wt.% and K_2O between 2,1 and 6,1.

SGC samples are composed of:

- Biotite-schists and staurolite-schists show similar composition and occupy the shale (Fig. VI.1) or pelite (Fig. VI.2) fields. SiO_2 content varies between 56 and 64 wt.%, Al_2O_3 content between 17 and 24 wt.%, Fe_2O_{3t} average content ~7 wt.%, K_2O average content ~4 wt.%. Na_2O content is variable in staurolite-schists (0,5 to 2 wt.%). This variability is reflected in mineralogy of the units, since there are layers showing higher plagioclase modal proportion and layers were quartz is dominant, as referred in Chapter III.
- Staurolite-bearing metapsammites (staurolite-schist showing low-mica content) are staurolite-schists samples collected in the thicker quartz-feldspathic domains as referred in the chapter III. The SiO_2 content is ~84 wt.%, Al_2O_3 content ~6 wt.%, Fe_2O_{3t} ~3 wt.% and, Na2O ~ 1 wt.% K_2O ~1 wt.% in average.

- Metasiltstones and quartzites from biotite-zone show low K_2O content and high SiO_2 (~90 wt.%) what projects this sample in the Fe-sandstone field in Herron (1988) diagram, although the Fe content is similar to the other lithologies.
- Calc-silicate rocks from staurolite-zone plot in the transition marl/ greywackes in ACF diagram and in Fe-Sandstone field in Herron diagram. The composition is similar to the calc-silicate nodules from MMC but showing slightly higher silica and lower Fe_2O_{3t} and CaO contents.

The geochemical classification is broadly coincident with the petrographical observations.

Leake (1964) proposed a diagram to distinguish volcanogenic metasedimentary sequences based on the Niggli parameters (si *versus* (al + fm) – (c + alk)) for pelitic rocks (Fig. VI.2). None of the studied samples plot in the field of volcanogenic rocks in the diagram. The same samples plot out of the mafic rocks field defined by Winter (2001) in the ACF diagram (Fig. VI.3).

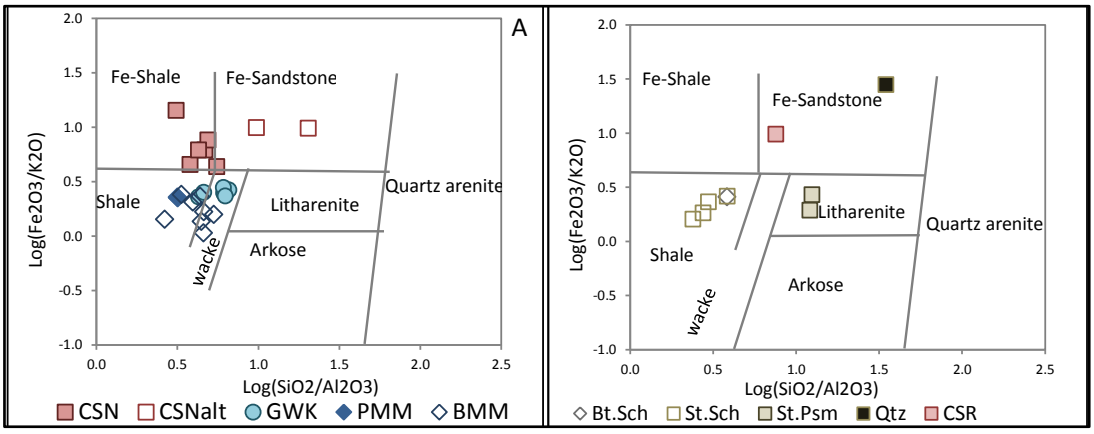

Fig.VI. 1 – Whole-rock analyses from (A) Mindelo Migmatite Complex and (B) Schist-Greywacke Complex projected in Herron (1988) diagram. Legend key: CSN – calc-silicate nodule; CSNalt – Calc-silicate nodules showing type II retrograde alteration; GWK – metagreywackes; PMM – patch-metatexites; BMM – Banded-metatexites; Bt.Sch – biotite-schists; St. Sch – staurolite-schists; St.Psm – staurolite psammites; Qtz – quartzites; CSR – calc-silicate rock.

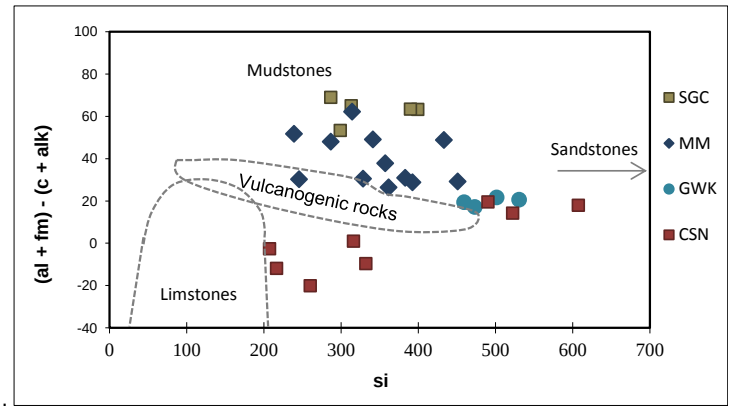

Fig. VI. 2- Diagram based on Niggli parameters si *versus* (al + fm) – (c + alk) with delimitation fields by Leake's (1964) for Schist-Greywacke Complex pelitic rocks (SGC) and Mindelo migmatite Complex metatexites (MM), metagreywackes (GWK) and calc-silicate nodules (CSN).

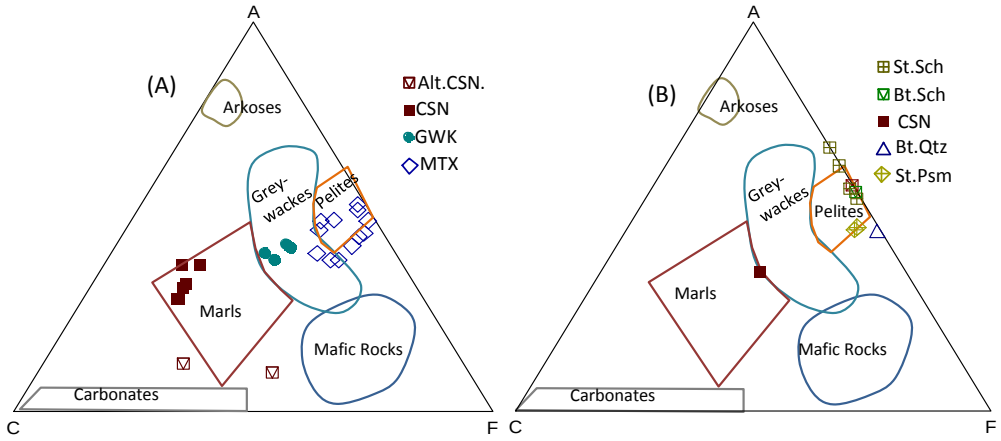

Fig.VI. 3 – Whole-rock analyses from (A) Mindelo Migmatite Complex, (B) Schist-Greywacke Complex projected in ACF diagram (Eskola, 1915) with fields of Barton *et al*., (1991) and Winter (2001). Legend Key: CSN – Calc-silicate nodules showing type II retrograde alteration; CSN – calc-silicate nodule; GWK – metagreywackes; PMM – patch-metatexites; BMM – Banded-metatexites; Bt.Sch – biotite-schists; St. Sch – staurolite-schists; St.Psm – staurolite-psammites; Qtz – quartzites; a = $[Al_2O_3 + Fe_2O_3] - [Na_2O + K_2O]$; c = $[CaO] - 3.33[P_2O_5]$; f = [FeO + MgO + MnO] in molar proportions.

6.2.2. Multielement diagrams

Trace elements are useful tracers of the petrogenetic processes and of their geotectonic context, namely the alkali elements (K, Rb, Cs), the alkaline-earth elements (Sr, Ba) the rare-earth elements (REE), the high field strength elements (HFSE) (Ti, Nb, Ta, Hf, Zr), and Th and U.

The analysis of the trace elements content in metasedimentary rocks using multi-elemental diagrams normalized to a standardized average is one of the ways to the

interpretation of its distribution and fractionation during the petrogenetic processes. The Neoproterozoic Iberian Average Shale - NIBAS (Ugidos *et al*., 2010) is one of these standardized averages. Further examples of the widely standardized averages for multi-elemental normalization of metasedimentary rocks are NASC (North American Shale Composite) (Gromet et al., 1984), PAAS (Post-Archaen Australian Shale) (Taylor & McLennan, 1985) and the UCC (Upper Continental Crust) (Taylor & McLennan, 1985).

The elements were selected in the following sequence: 1) elements associated with feldspars and micas and related to crustal sources like Ca, Mn, Sr, Na, Ba, Rb, K, U; 2) elements associated with heavy minerals, with lower mobility in the sedimentary/metamorphic processes like Th, Zr, Y, Ti and Al; 3) elements associated with basic sources and dark micas and quite immobile like Fe, Mg and V; and 4) elements associated with metasomatic processes or volatile phases like Nb and Ta.

The normalization to NIBAS (Ugidos *et al.,* 2010) was made by sector and by lithology. Below, the most important aspects of these multi-elemental diagrams are highlighted (Figs. VI.4 and VI.5):

Sector 1 (MMC):

- Calc-silicate nodules show positive anomaly in Ca, Mn and Sr related with the high Ca content and negative anomaly in alkalis and associated elements as well as in ferromagnesian elements. The samples relative to calc-silicate rocks showing Type I and Type II retrograde alteration (GC2, FM21a, VC50 and FM16a) are richer in K, Rb and Ba than the samples without any signs of alteration. The Type II retrograde alteration provokes also a relative depletion in Ca, Mn and ferromagnesian elements (and increase in silica as referred before);
- Metagreywacke from MMC show Ca, Mn and Sr positive anomaly. All the other elements show slight depletion relative to NIBAS. The composition is quite homogeneous although the samples that show signs of partial melting (FP21c and FP46c) contain slightly more Ba, Rb, K and P than the metagreywacke resisters.
- Metatexites are enriched in Ca, Mn, Sr and Ti relative to NIBAS, although in variable proportions and always less than metagreywackes. The variability in Ca is related to the distance from metagreywackes, being the Ca richer adjacent to metagreywackes. The migmatized metagreywackes composition is in general intermediate between metagreywacke resister and pelite metatexites compositions

showing a gradual transition between the metagreywackes layers and the adjacent pelitic metatexites.

- Patch-migmatites (VC28 and VC37c) show a composition similar to the NIBAS and to the banded-metatexites although the sample VC37 shows an excess of Ca and Sr.

Sector 2 (SGC):

- In SGC the pelitic lithologies show variation in LILE, especially in Ca, Mn and Na content. The staurolite-schist from Aguçadoura (VC65) is the richest in Na, Ca and Sr. The HSFE composition is similar to NIBAS, although showing Ti enrichment. The staurolite-psammites are depleted in all the elements relative to NIBAS except Ca, Zr and Ti. The quartzite from biotite-zone is depleted in most elements except SiO_2.

The average compositions of MMC metatexites and SGC pelites normalized to NIBAS were plotted in a multielement diagram for comparison (Fig. VI.6). The average composition of metatexites is quite similar to pelites from SGC. Only the Ca, Sr and Mn content is slightly higher in metatexites. However, if compared to staurolite-schist from Aguçadoura (VC65) the chemical composition is almost coincident. The SGC average composition is quite similar to NIBAS although the Ti content is slightly higher and Nb and Ta slightly lower.

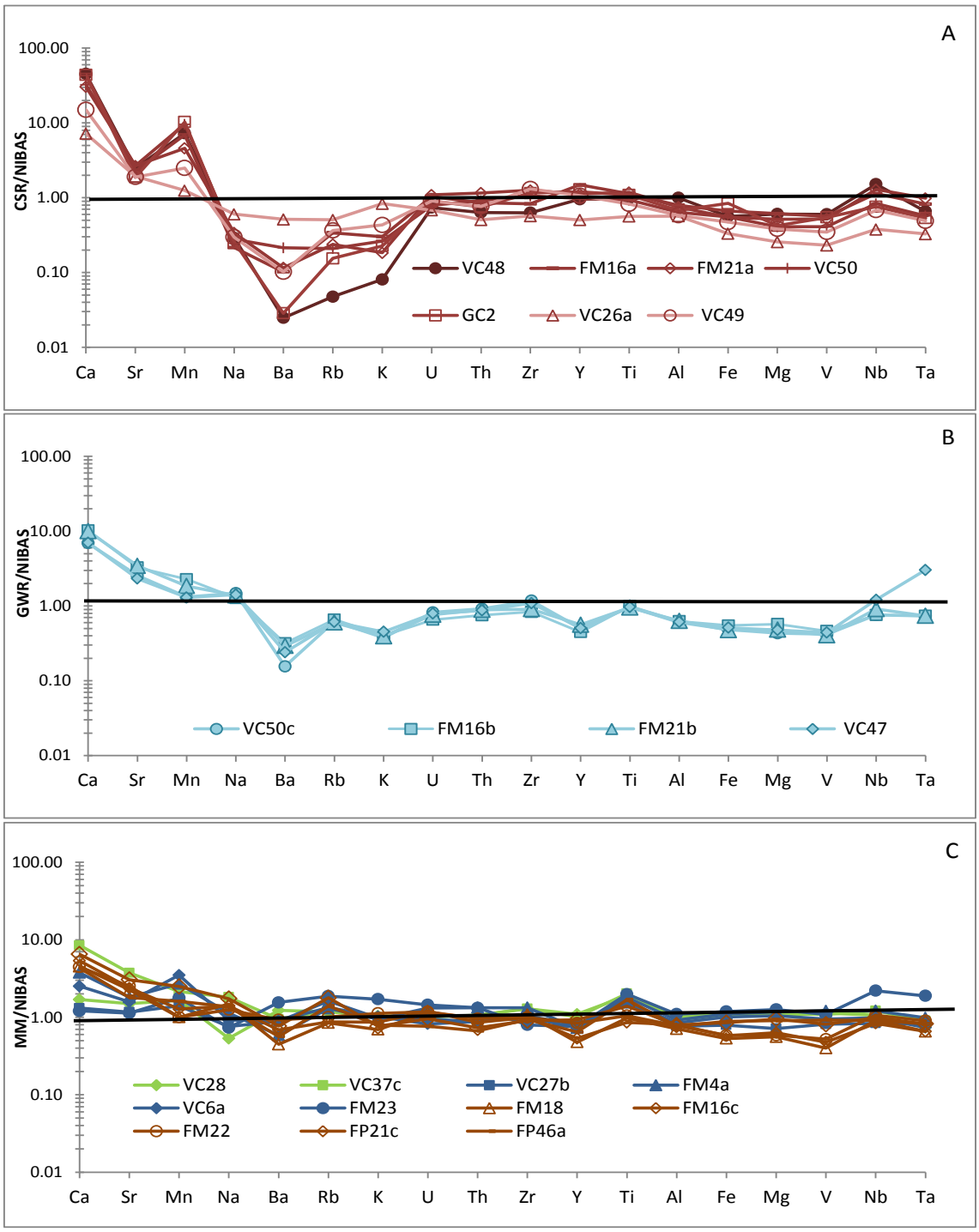

Fig. VI. 4 – Multielement diagram for MMC lithologies normalized to NIBAS. A) Calc-silicate nodules including sample without signs of alteration (VC48 and FM21a), samples showing type I alteration (FM16a, Vc50 and GC2) and samples showing type II alteration (VC26a and VC49); B) Metagreywackes; C) Metatexites including patch-metatexites (VC28 and VC37c), pelitic banded-metatexites (VC6a, FM23, VC27b and FM4a) and migmatized metagreywackes (FM22, FP21c; FP46a, FM16c).

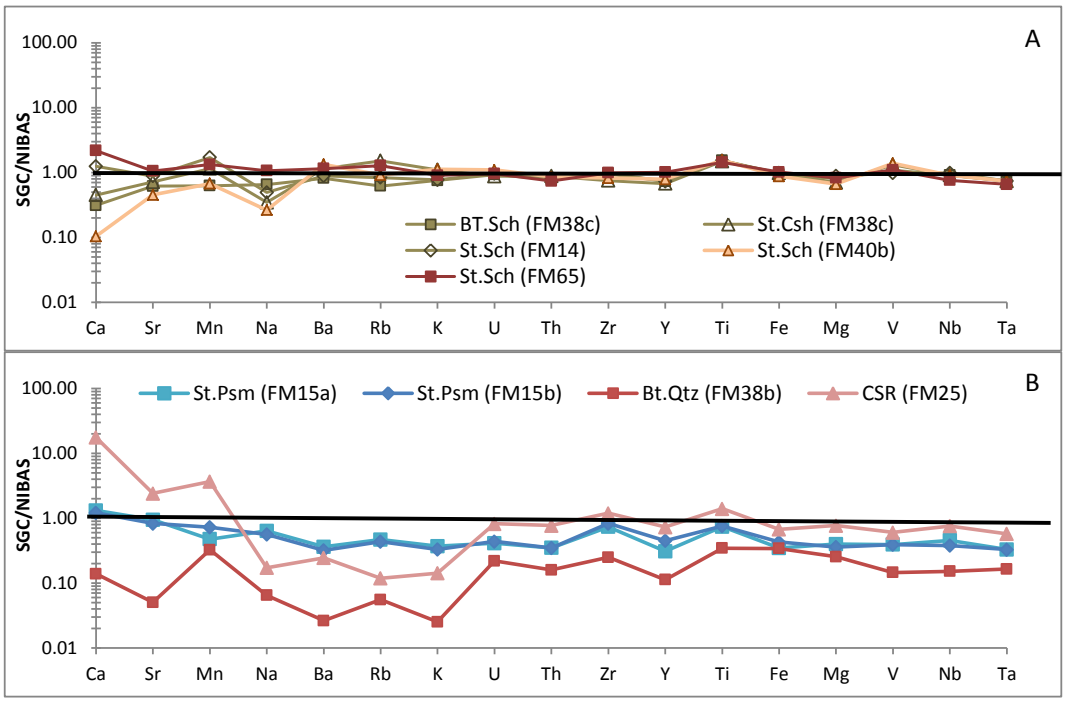

Fig. VI. 5 – Multielement diagram for SGC lithologies normalized to NIBAS: A) Pelitic lithologies from biotite-schist to staurolite-schists. B) Staurolite-psammites, quartzite from biotite-zone and calc-silicate rock from staurolite-zone. Legend Key: St.Psm –staurolite-psammite from staurolite-zone; Bt.Qtz – quartzite from biotite-zone; Bt.Sch – biotite-schist; St.Sch – staurolite-schist.; CSR – calc-silicate rock.

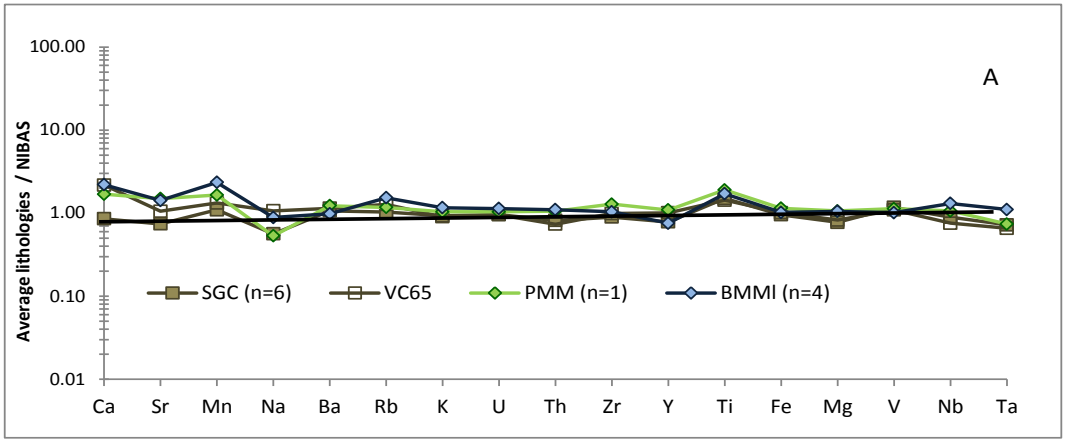

Fig. VI. 6 – A) Projection of pelitic banded-metatexites, pelitic patch-metatexites and SGC pelitic samples average compositions. Legend key: VC65 – staurolite-schist from Aguçadoura; SGC – Schist-Greywacke Complex average composition of samples from Fânzeres and Aguçadoura; PMM –pelitic patch migmatite sample; BMM – average composition of pelitic metatexites;

6.2.3. Rare Earth Elements

The rare earth elements (REE) are regarded as amongst the least soluble trace elements and are relatively immobile during low-grade metamorphism, weathering and hydrothermal alteration. They present a very low concentration in hydrothermal and meteoric solutions, therefore the REE in sediments are chiefly transported as particulate matter and reflect the composition of their source (Taylor & McLennan, 1985). However, in high metamorphic grade or when the water/rock ratio is very high the REE are not totally immobile and caution must be taken in interpreting the REE patterns. In clastic sediments the single most important factor contributing to the REE contents is its provenance, thus, nevertheless the necessary caution, REE patterns can faithfully represent the original composition of the parent rock (Rollinson, 1993).

Figures VI.7 and VI.8 represent the REE profiles normalized to chondrite, (Boynton, 1984) for MMC metagreywackes, calc-silicate nodules, metatexites and Schist-Greywacke Complex samples.

All samples reveal a REE profile with negative Eu anomaly and light rare-earth elements enrichment in respect to heavy rare-earth elements, the ratio La_N/Yb_N is positive, with higher fractionation of light than heavy REE as is typical of terrigenous rocks (Condie, 1993). The massive incorporation of vulcanoclastic detritus in these lithologies is discarded by the REE profiles (besides major elements, Fig.VI.3) since sediments near active volcanic arcs often show flatter REE patterns, less well-developed Eu anomalies and lower REE abundances (Plank and Langmuir, 1998).

The main characteristics of the REE patterns can be summarized as follow:

Sector 1 (MMC):

- Metagreywackes show homogeneous profiles, both in light REE and in heavy REE. They have the lowest REE total content ($\sum REE_n$ ~ 323 ppm in average). The HREE profile is flattened relatively to the LREE profile.
- Calc-silicate nodules show higher REE content than metagreywackes although with parallel profiles ($\sum REE_n$ ~ 550 ppm in average). The samples showing Type II retrograde alteration (VC26 and VC49) show depletion in REE although the REE profile is parallel to the other calc-silicate samples.
- Metatexites show relatively high REE content similar to NIBAS. However, is notorious the higher REE content in pelitic metatexites than in migmatized

greywackes, although showing continuous variation ($\sum REE_n$ ~558 ppm and ~446 ppm in average, respectively). LREE profiles are similar to each other and parallel to NIBAS. HREE profile is slightly more fractionated in migmatized greywackes than in pelitic metatexites. Patch-metatexites have REE pattern similar to the banded-metatexites pattern.

Sector 2 (SGC):

- In the SGC the pelitic lithologies have a REE profile similar to NIBAS and almost coincident with each other showing $\sum REE_n$ ~ 510 ppm in average.
- The staurolite-psammites (FM15a and FM15b) shows lower REE content ($\sum REE_n$ ~ 235 ppm in average) and greater HREE flattening.
- The quartzite from biotite-zone (FM38c) has the lowest REE content although showing a REE pattern sub-parallel to the other lithologies.
- Calc-silicate rock from staurolite-zone shows a REE profile similar to the REE profile of the MMC calc-silicate nodules although with slightly less total REE content and lower Eu negative anomaly (Fig.VI.7A).

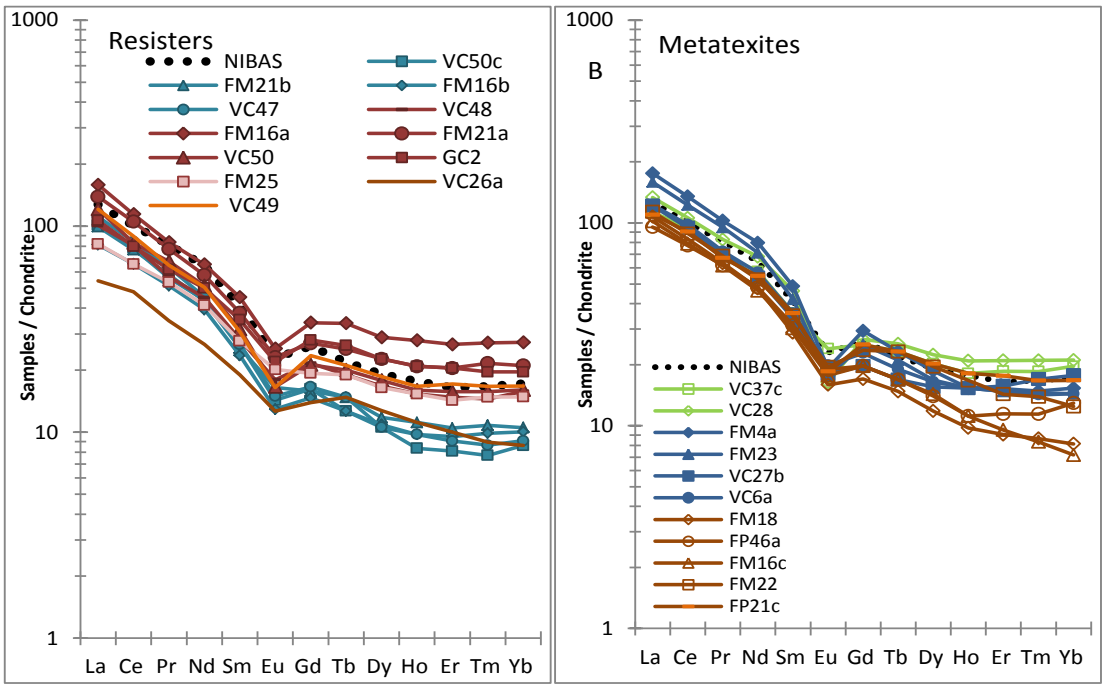

Fig. VI. 7 - Chondrite-normalized (Boynton, 1984) REE profiles for calc-silicate and metagreywacke resisters. A) Samples VC49 and VC26a correspond to calc-silicate rocks showing type II retrograde alteration. Sample FM25 corresponds to calc-silicate rock from staurolite-zone; B) Chondrite-normalized (Boyron, 1984) REE profiles for patch-metatexites (green), pelite banded-migmatites (blue) and migmatized greywackes (brown). The NIBAS REE profile is also plotted.

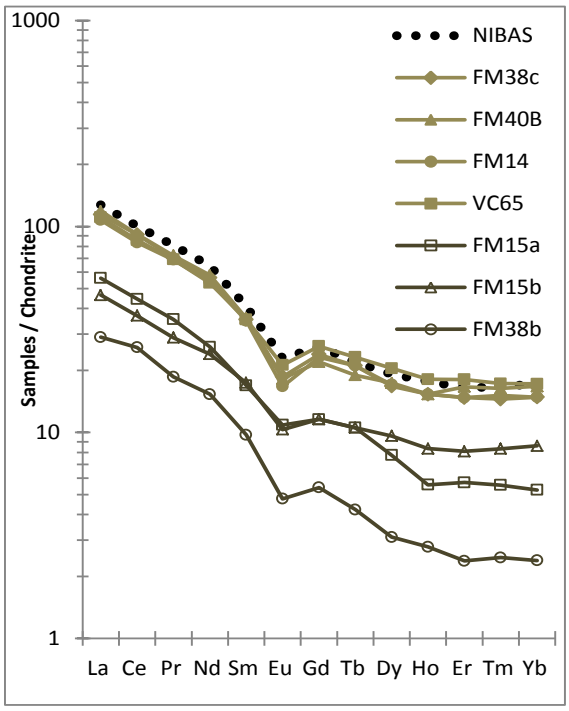

Fig. VI. 8 - Chondrite-normalized (Boynton, 1984) REE profiles for SGC lithologies. The pelitic lithologies show a REE profile similar to NIBAS. The staurolite-psammites (FM15a and FM15b) shows lower REE content and the greater flattening of HREE. The quartzite from biotite-zone (FM38c) has the lowest REE content although showing a profile sub-parallel to the other lithologies.

The presence of quartz has a dilution effect on REE concentrations and the heavy minerals as zircon, monazite and allanite have a significant but erratic effect on the REE pattern of an individual sample (Rollinson, 1993). To understand the influences of this minerals in the REE content the samples were projected in binary diagrams ∑REE *versus* Zr, Th, Al_2O_3 and Y and these elements *versus* the ferromagnesian elements (Figs. VI.9 and VI.10). The following can be highlighted:

- In SGC and MMC pelitic lithologies the REE content is correlated with Th, Y and Al_2O_3 content. Zr seems not to be so determinant in the total REE content.
- Ferromagnesian elements correlate with Th especially in the more pelitic samples (the less ferromagnesian samples from migmatized metagreywackes show similar Th content). Considering that Th is associated with monazite, this suggests that monazite is linked to biotite in pelitic lithologies and dispersed in the matrix in more greywacke lithologies.

- Al_2O_3 correlates with ferromagnesian elements in metatexites but not in the SGC pelite lithologies, where most likely the Al_2O_3 is associated with staurolite besides biotite.
- Metagreywacke and calc-silicate nodules show ∑REE positive correlation with Y (r^2=0.80), There is no correlation with Zr or Th. The linear positive correlation coefficients between ∑REE and Y, suggests that Y-bearing heavy minerals were important in hosting the REE in the metagreywackes and calc-silicate nodules. Since Y is strongly partitioned into garnet the REE content is probably associated with this mineral in these lithologies. In fact, calc-silicate nodules show higher garnet content and its REE content is also higher than the metagreywackes REE content.
- The presence of quartz in quartzite lithologies and in calc-silicate nodules showing Type II alteration processes have an effect similar which is revealed by REE profiles parallel to the pelitic samples but showing lower REE content.

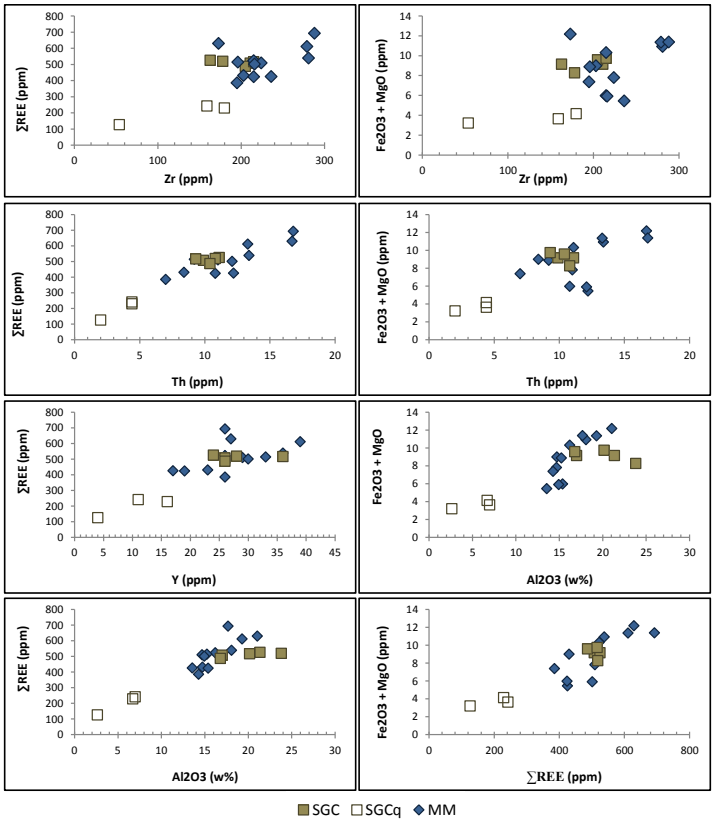

Fig. VI. 9 – Diagrams relating ∑REE with Zr, Th and Y and the relationship of these elements with the ferromagnesian elements for Metatexites and SGC lithologies. Legend Key: SGC – Schist-Greywacke Complex pelitic samples; SGCq – SGC psammitic and quartzite samples; MM – metatexites from MMC.

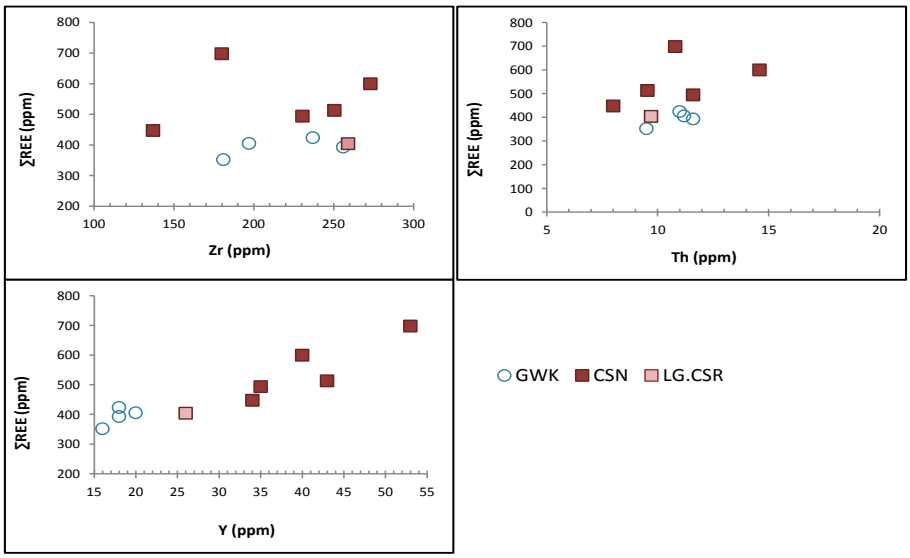

Fig. VI. 10 - Diagrams relating ∑REE with Zr, Th and Y for metagreywackes and calc-silicate rocks. Legend key: GWK – metagreywackes, CSN – calc-silicate nodules; LG-CSN calc-silicate rock from staurolite-zone. The ∑REE is mostly related to Y content.

6.2.4. Core and outer-zone of calc-silicate nodules

As referred before the calc-silicate nodules show two distinct zones and are always inserted in metagreywacke layers. In order to evaluate the compositional variation within the zoned calc-silicate nodules, core-zone, outer-zone and surrounding metagreywackes were separately analyzed in two nodules (VC50 and GC2, both with 10 cm length) (Fig. VI.11).

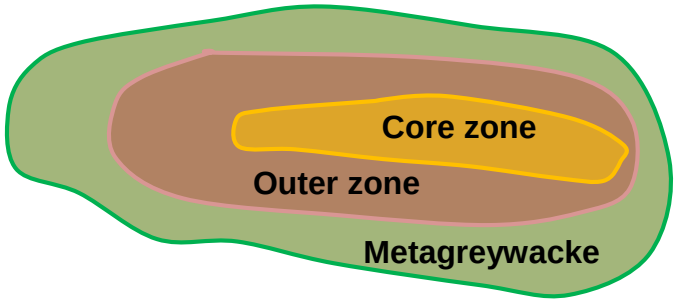

Fig. VI. 11 – Calc-silicate nodule schematic representation showing core-zone, outer-zone and surrounding metagreywacke.

Enrichment/depletion diagrams are a convenient way to show the relative enrichment and depletion in trace or major elements (Rollinson, 1883). Figure VI.12 represents enrichment/depletion diagrams that compare the relative concentrations of the nodules core-zone and outer-zone and the relative concentration of nodules outer-zone and surrounding metagreywacke. In these set of diagrams it is possible define the elements that are specially concentrated in each of the analyzed zones. The following can be highlighted:

- The core-zone is the most enriched in Ca, Mn, Fe, Y and REE (especially La).
- The elements Mg, P, Sr, Co, Ti, Al, Sc, Nb are specially concentrated in the outer-zone (intermediate between calc-silicate nodules and metagreywackes) relatively both to core-zone and to metagreywacke.
- The metagreywackes are the most enriched in Na, Ba, Rb and Sr.

Figure VI.13A shows the REE profile (normalized to chondrite, Boynton, 1984) for core-zone and outer-zone of the same nodules. It is evident the highest REE content in the core-zone. Figure VI.13B represents ACF diagram (Eskola, 1915) with delimited fields for diverse metasomatic composition types (after Barton *et. al*., 1991 and Winter, 2011). None of the samples plots in the skarn field or other metasomatic composition.

Zoned calc-silicate nodules associated with high grade metamorphic rocks, in amphibolite/granulite facies conditions and normally associated with pelitic and semi-pelitic migmatite rocks are well reported (e.g. Buick *et al*., 1993, Morand, 1994; Owen, 1994; Hudson & Kearns, 2000; Morel, 1961).

In high metamorphic grade, most of the nodules show an inner-zone with higher temperature assemblage (with clinopyroxene as index mineral) and an outer-zone with lower temperature assemblage (with amphibole or biotite as index minerals). Obviously the metamorphic conditions are the same all over the nodule. The zonation is in general explained by metasomatic diffusion (Buick *et al*., 1998; Owen *et al*., 1994) or as a result of metamorphism affecting compositionally zoned cemented psammites (Hudson & Kearns, 2000; Morel, 1961).

It is unlikely that the zoning was formed only by syn-metamorphic boundary diffusion metasomatism since (Fonteilles, 1978; Coelho, 1993):

- The chemical gradient between core-zone and the metagreywacke is not enough to promote the exchanges. For example, SiO_2 content is comparable between the core-zone of calc-silicates and the metagreywackes (71 to 73 wt.%

in GC2 and 64 to 75 wt.% in VC50) and Al_2O_3 content is similar (~12 wt.%). Only Ca and Mn are higher in core-zone (12 to 2 wt.% and 0.6 to 0.06 respectively).

- The outer-zone composition is not quantitatively intermediate between the two supposed reactants rocks. Several elements (including some considered immobile like Al, Sc and Ti) are concentrated in the outer-zone that is in-between the core-zone and the metagreywackes. If the concentration in these elements is lower in both the zones that surround the outer-zone, it is unlikely that they could result of diffusion processes between them.

Moreover, the zoning formation exclusively by infiltration fluids is also inconsistent, considering that (Fonteilles, 1978; Korzinsky, 1979; Barton, 1991; Coelho, 1993):

- The concentric morphology of the zoning. Generally the infiltration metasomatism depends on external fluids structurally controlled and shows linear shape;
- Absence of monomineralic zones common in infiltration metasomatic fronts;
- Absence of water induced textures or paragenesis in the zoned calc-silicate nodules without any signs of retrograde alteration (e.g. no replacement textures, no wollastonite);
- Absence of precipitated minerals in veins or other kind of open spaces.

In ACF diagram with fields represented compositions for metasomatic types (after Barton *et al.* 1991) none of the samples plot in the metasomatic fields (Fig. VI.13B).

These factors allied to the variability in composition from nodule to nodule and variability on CZ/OZ thickness ratio can only be explained by pre-metamorphic constraints. However, in the calc-silicate nodules affected by Type I and Type II retrograde processes the higher concentration of K, Ba and Rb is evident in altered rocks (0.48 to 0,95 wt.% for K, 45 to 75 ppm for Ba and 18 to 30 ppm to Rb).

The characteristics of the calc-silicate nodules from MMC suggested that the gradual mineral differentiation from core- to outer-zone (Fig. VI.12) could have resulted from variation of the original mineralogy of the nodules and cementation processes and did not resulte from metasomatic processes. The same origin is proposed by Hudson and Kearns (2000) and Morel (1961) for other high metamorphic grade zoned calc-silicate nodules. The cementation process probably starts with Ca-Mn richer calcite and progressively changes to Mg-P-richer calcite. These leads to centrifugal decrease in

Ca and Mn and increase in Mg and P content towards the border of the nodule. These centrifugal changes reflect the dynamics of nodular growth (Gluyas, 1984). The gradual change in composition of the cement leads, in higher metamorphic grade, to the development of different mineralogy, adequate to the composition, between the core and outer-zone, namely the occurrence of diopside in the core-zone and hornblende in the outer-zone**.** After that some of the zoned nodules were affected by external K-rick or/and silica-rich fluids.

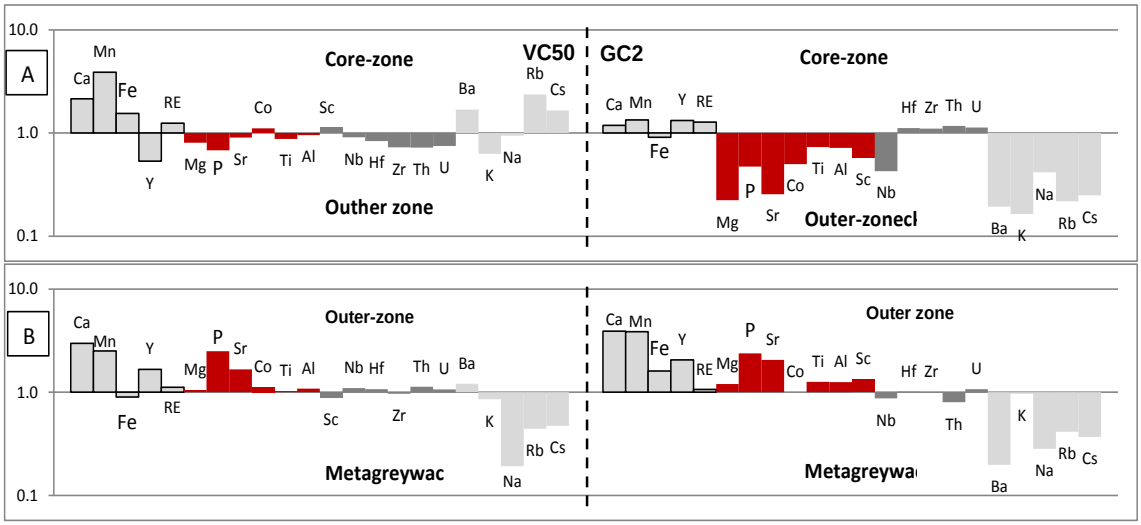

Fig. VI. 12 - Enrichment/depletion diagrams that compare the element concentrations of the nodules core-zone relative to the outer-zone (A) and the relative concentration of nodules outer-zone relative to the surrounding metagreywacke (B) of the same nodule (VC50 and GC2). The elements Mg, P, Sr, Co, Ti, Al, Sc are specially concentrated in outer-zone (intermediate zone) relatively both to the core-zone and to the metagreywackes.

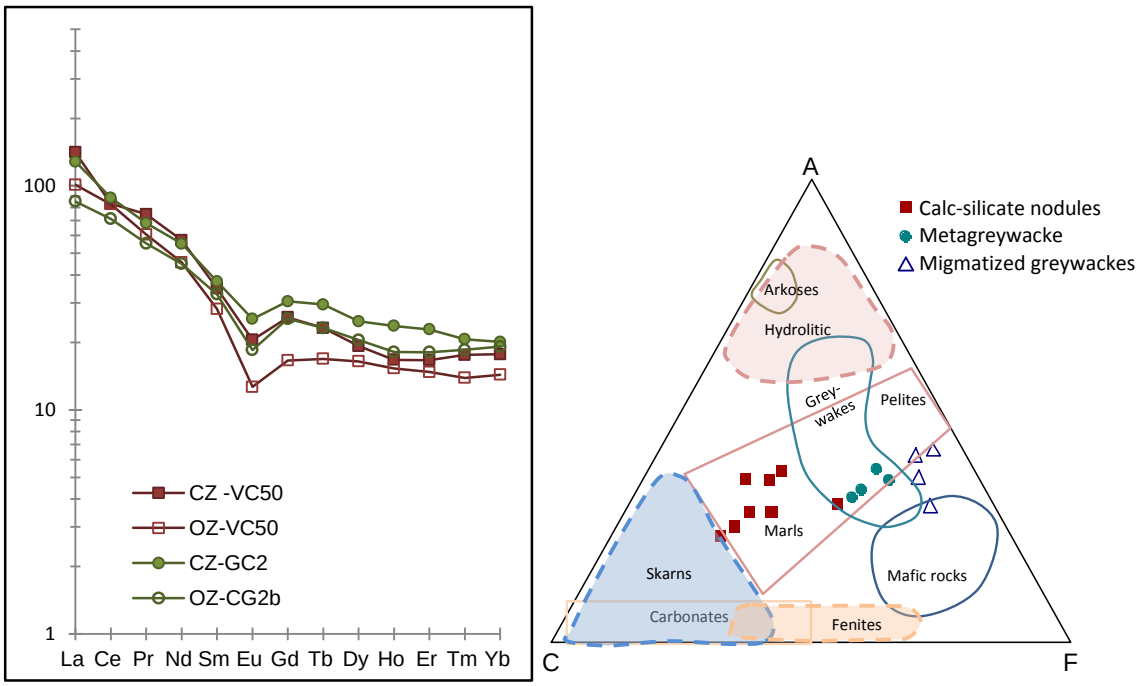

Fig. VI. 13 – A) Comparison between the REE profiles of calc-silicate core-zone (CZ) and outer-zone (OZ) of two nodules (VC50 and CG2). B) ACF diagram (Eskola, 1915). General bulk compositions of unaltered arkoses, pelites, metagreywackes, marls, carbonates and basic rocks are represented by shaded fields; compositions for metasomatic types are represented by outlined dotted lines (after Barton *et .al*., 1991 and Winter, 2011).

6.2.5. Summary

The lithogeochemical study of the lithostratigraphic units in Sector 1 and 2 allowed the following observations and conclusions:

Samples of sector 1 (MMC) consist of migmatized pelites and metagreywackes (metatexites) as well as Ca-rich metagreywackes and calc-silicate nodules which have resisted to migmatization (resisters). All lithologies show crustal signature and compared to NIBAS have similar composition although showing Ca, Sr, Mn, Rb and Ti slightly higher content and Ta and Nb lower content.

Samples of sector 2 (SGC) are composed of metapelites, quartzites and metapsammites as well as scarce calc-silicate rocks. The metapelitic rocks show composition similar to pelitic metatexites of sector 1 (MMC), especially those collected in Aguçadoura, either in major- as in trace elements. The calc-silicate rocks from sector 2 show similar composition to the calc-silicate rocks from MMC.

The REE profiles of all the lithologies are typical of metasedimentary rocks. The REE content is similar in metapelites from sector 1 and sector 2. In sector 1 and 2 the REE content is directly correlated with heavy accessory mineral content (particularly those which concentrate Th) and to ferromagnesian elements. This means that these minerals are associated with biotite, the more frequent ferromagnesian mineral present (garnet is rare). In metagreywacke rocks the REE are particularly associated with garnet (Y content).

The calc-silicate nodules zonation could fundamentally have resulted from variation on the original mineralogy of the nodules, generated by diagenetic/cementation processes that leads to centrifugal decrease in Ca and Mn and increase in Mg and P content toward the border of the nodule. These compositional differences conditioned distinct metamorphic paragenesis, which are not related to different PT conditions.

6.3. Geochemistry of granitic rocks

6.3.1. Introduction

Granitic rocks are granular rocks consisting of quartz, plagioclase and K-feldspar with variations in the ferromagnesian minerals content. This type of paragenesis can be originated in a number of different processes including partial melting of various crustal components, evolution of mantle melts or a mixture of crustal and mantle sources (Frost *et al*., 2001). Its origin, source, evolutionary processes, emplacement at different structural levels and in different tectonic environments promote great diversity within the granitic rocks. This variety of sources led to a corresponding variety of classification schemes, which include the presumed origin of the granitoid, mineralogy, geochemistry and tectonic environment.

The sampling includes leucosomes (LCS), diatexites (DTX) leucogranites (L.Gnt), tourmaline-bearing leucogranites (TL.Gnt) and two-mica granites s. l. including medium-grained granites (2m.Gnt), fine-grained granites (F.Gnt) and porphyritic granites (P.Gnt). Leucosomes were collected in *in situ* banded-metatexites (VC8) and in veins cutting the metatexites (FM19). Leucogranites were collected from leucogranite masses (VC2, VC3 – Vila Chã and VC43 - Lavra) and from leucogranite-veins outcropping in the metatexite zone (VC52 - Vila Chã) and in the surrounding metasedimentary sequence (VC44b - Malta, VC55 – Vila do Conde and VC68 - Aguçadoura). Two-mica granites were collected in Lavra (VC39), Leça (VC45), S. Paio (VC22 and VC34); Vila do Conde (FP21a and FP21b), Junqueira (VC49 and VC50) and Fornelo (FP30a); fine-grained granites dikes from Vila Chã (VC16 and VC32) and porphyritic granites dikes from Fornelo (after Ferreira, 2011). Aplite-pegmatite veins were collected in S. Paio (VC64) and in Vila Chã (VC58). The designation two-mica granites *s.l*. is used when the two-mica granites, the fine-grained granites and the porphyritic granites are considered together.

6.3.2. Chemical-mineralogical characteristics

The most traditional petrographic classification of granitoids is based on the modal abundance of quartz, plagioclase and alkali feldspar (Streckeisen, 1974). However, in this work we chose to consider the normative classification and chemistry of granitic

rocks due to the coarse grain size of the rocks and the presence of solid solutions that limit the modal analysis. The following classification diagrams were used:

Diagram Q'-ANOR of Streckeisen and Le Maitre (1979) (Fig. VI.14) using the normative compositions (Barth mesonorme, 1958). The Q-ANOR diagram was derived empirically by Streckeisen and Le Maitre (1979) as a CIPW normative equivalent to the IUGS classification of Streckeisen (1974) matching to the upper triangle of QAPF diagram. It employs the parameters Q=100*(Qtz/(Qtz+Ab+Or+An)) and ANOR= (100*An/(An+Or)).

Diatexites plot mostly as syenogranites or in the frontier between syenogranites and monzogranites and show high Q'. One of the samples (FP46) plot out of diagram field due to its high silica content (74,02 wt%) and low Ab+An+Or proportion.

Leucosomes and leucogranites plot in the field of alkali feldspar granites, although one sample of leucogranite and one sample of tourmaline-bearing leucogranite plot in syenogranites and monzogranite field, due to their low K content. Like in diatexites, one sample from Malta (FP44b) shows higher proportion of silica relatively to An+Ab+Or and plot out of the diagram.

Two-mica granites, including fine-grained granites and porphyritic granites, and aplite-pegmatites plot in the field of alkali feldspar granites.

Diagram SiO_2 *versus* K_2O from Le Maitre *et al*. (1989) (Fig. VI.15). The projection of MMC granitic rocks show that leucogranites plot in the fields of low, medium, higher and very high K content, what is a reflex of their great K content variation (from 1,44 to 7,37 wt%). Leucosomes show also very high K content (~6,6 wt%). The other MMC granitic rocks plot in the field of high K content showing lower dispersion. Aplite-pegmatites show medium K_2O content. The silica content variation is low and there are no correlation between the K_2O content variation and the SiO_2 variation.

The B-A diagram as proposed by Debon & Le Fort (1983) with classification fields for various types of peraluminous rocks designed by Villaseca *et al*. (1998) (Fig. VI.16). The B = Fe + Mg + Ti parameter reflects the content of mafic minerals and the A = Al – (K + Na + 2Ca) parameter reflects the amount of aluminum incorporated into feldspars (calculations are based on millications).

All the granitic rocks from MMC plot in the peraluminous domain. Leucosomes, leucogranites, two-mica granites *s. l.* and aplite-pegmatites plot in the felsic peraluminous field (with exception of one sample of leucosome that show more ferromagnesian elements content). Diatexites show higher ferromagnesian elements content and plot in the highly to moderately peraluminous fields.

Diagram of Debon & Le Fort (1988) (Fig.VI.17). These diagrams are considered effective in distinguishing evolutionary trends, as well as in the establishment of types of magmatic associations and in defining different subtypes. The aluminous associations and evolutionary trends are divided in: (1) mesocratic and sodium-potassium association following a silica-potassic evolutionary trend; (2) leucocratic association following a silica-sodic evolutionary trend and (3) meso to leucocratic and potassic association following a silica evolutionary trend.

All lithologies plot in the leucocratic to sub-leucocratic associations (only one sample of diatexite plot in mesocratic field) and the potassic association is dominant. Leucogranites show variation in K and Na that causes the dispersion between potassic, sodic-potassic and sodic associations. Aplite-pegmatites plot in the field of leucocratic/ sodic associations. The MMC granitic rocks do not follow any well-defined evolutionary trend both regarding the individual lithologies or considering the lithologies as a whole, since the distribution of samples is scattered and some overlaps each other.

Frost *et al.* (2001) classification scheme that is composed of three indexes (Fig. VI.18):

Fe-number - Fe-number is calculated as weight proportion of FeOt/(FeOt+MgO). Fe number determine whether the rocks are mainly magnesium or ferroan and provide information about the history of differentiation of the granitic magma. The iron enrichment is used to distinguish between granitoids from different tectonic environments. Frost *et al.* 2001 proposed the terms “ferroan” for rocks where the Fe is more abundant than Mg and “magnesian” for rocks were the Mg is more abundant than Fe. Mg is considered more abundant than Fe if the ratio FeO/(FeO+MgO) < 0,5.

MMC granitic rocks plot as magnesian granitoids, except the aplite-pegmatites and one sample of leucogranite that plot as ferroan granitoids. Diatexites and leucosomes are the most magnesian rock types. One sample of porphyritic granite is highly magnesian.

MALI (modified alkali-lime index) is expressed by the composition and abundance of feldspar or other minerals containing K and Na relatively to the silica content. Many magmatic igneous suites show similar trends in $Na_2O + K_2O - CaO$ *versus* SiO_2 diagrams that can be divided in Calcic, calc-alkalic, alkali-calcic and alkali fields (Frost *et al.* 2001).

MMC granitic rocks show some dispersion in the MALI and do not follow any particular trend. Diatexites and leucogranites show high MALI dispersion and plot in calcic, calc-alkalic and alkali-calcic field. The former due to their CaO variable content (0,61 to 1,12) and the lasts due to their high K_2O and Na_2O variation. Two-mica granites *s.l.* and leucosomes plot as alkali-calcic. Aplite-pegmatites plot as calc-alkalic and alkali-calcic due to their low K content (~2.96 in average). Thus, in the MMC, the variations are principally related with Na_2O and K_2O content since there are not accentuated variations in the CaO content (only diatexites show slightly higher CaO content).

Aluminium Saturation Index (ASI): A=NK vs. ASI diagram, where A/NK stands for molecular $Al_2O_3/(Na_2O + K_2O)$ and ASI for molecular $Al_2O_3/(Na_2O + K_2O + CaO - 1{,}67*P_2O_5)$. In fact, it is the A/CNK parameter of Shand (1943), corrected for the Ca content in apatite. ASI makes the chemical discriminant between peraluminous granitoids (ASI > 1) and metaluminous granitoids (ASI < 1).

All the granitic rocks in MMC are peraluminous showing ASI > 1.17. Diatexites follow a trend distinct from the trend of leucogranites and two-mica granites due to its higher Ca content.The peraluminous granitoids have more Al that can be accommodated in feldspars and must have another aluminous phase present (Frost *et al.,* 2001). In the case of diatexites, the phase is mostly biotite and cordierite and in the case of two-mica granites is biotite and rare andalusite. Given the terminology used by Bea *et al.* (1987), specifically for the Variscan Massif granitoids with SiO_2 content > 62%, it appears that all the granitic rocks from MMC belong to strongly aluminous series (A / (CNK) > 1.15).

In summary, the MMC granitic rocks are magnesian, peraluminous and range from calc-alkalic to alkali-calcic in the Frost classification.

Rb-Ba-Sr diagram proposed by Bouseily & El Sokkary (1975) (Fig. VI.19). The relationship between Rb - Ba - Sr in granitoids has been used to define paths of differentiation in granitic series, as well as to distinguish between granite formed exclusively by magma from those formed by metasomatism or in intimate association with the host rocks (anomalous granites).

Metatexites, diatexites, leucosomes and leucogranites plot on the anomalous granites field that is considered represent granitoids formed by metasomatism or in intimate association with the host rocks (anatexites). Tourmaline-bearing leucogranites show higher Rb and Sr content relatively to the tourmaline-absent leucogranites and plot in the field of differentiated granites. Two-mica granites (including fine-granites and granitic porphyry) plot on the normal granites field showing variable differentiation. The porphyritic granites show slightly higher differentiation than the other two-mica granite types. On the contrary, fine-grained granites show lower differentiation. The aplite-pegmatites show pronounced differentiation, plotting in the extension of the field of highly differentiated granites.

Diagram Na-K-Ca of Raju & Rao (1972) (Fig. VI.20): This ternary diagram demarks the field of granitic rocks originated by magmatic processes from granitic rocks originated by metamorphic/metasomatic processes. In general, the granite rocks from MMC plot close to the magmatic origin granites but in the metamorphic/metasomatic fields (except three diatexite samples due to its higher Ca content). The authors considered that the granitic samples that plot outside the magmatic field and the samples with considerably higher K content could most probably indicate K-metasomatism.

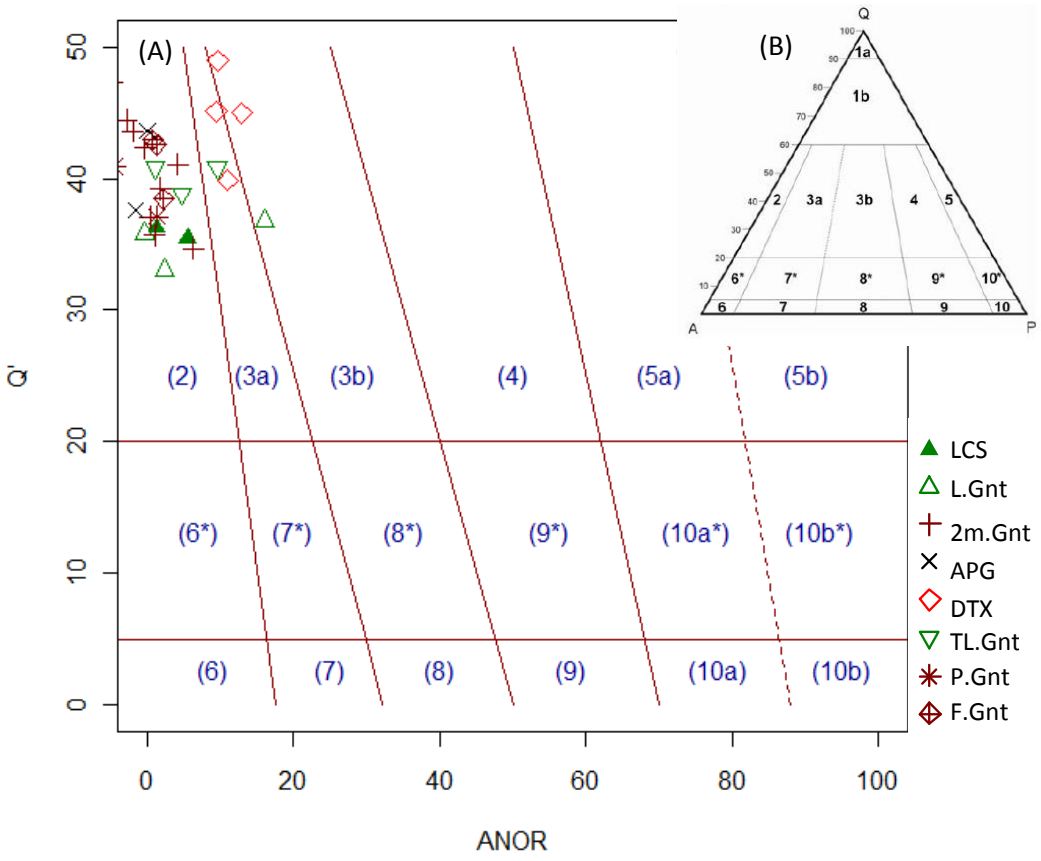

Fig. VI. 14 – Classification of MMC granitic rocks using the normative compositions in the diagram Q'-ANOR of Streckeisen and Le Maitre (1979). B) Modal classification of oversaturated plutonic rocks corresponding to the upper triangle of QAPF Streickeisen (1974). The numbers in both diagrams match to the same classification. Fields: (2) – Alkali feldspar granites; (3a) – Syenogranites; (3b) – Monzogranites. Legend key: LCS – leucosomes; L.Gnt – leucogranites; 2m.Gnt – two-mica granites; APG – aplite-pegmatites; DTX – diatexites; TL.Gnt – tourmaline-bearing leucogranites; P.Gnt – porphyritic granites; F.Gnt – fine-grained granites.

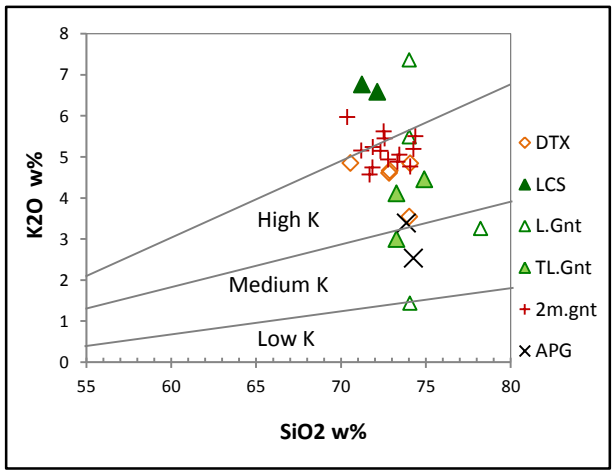

Fig. VI. 15 – Projection of MMC granitic rocks on the K_2O *versus* SiO_2 diagram of Le Maitre *et al*. (1989). Legend key: DTX – diatexites; ; LCS – leucosomes; L.Gnt – leucogranites; TL.Gnt – tourmaline-bearing leucogranites; 2m.Gnt – two-mica granites s.l. ; APG – aplite-pegmatites.

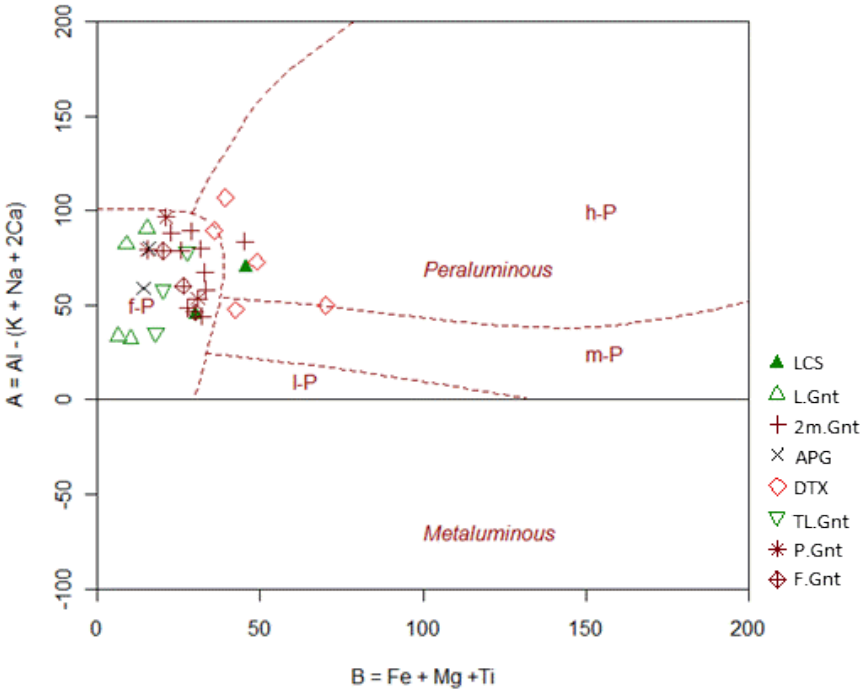

Fig. VI. 16– B-A diagram as proposed by Debon & Le Fort (1983) modified after Villaseca *et al.* (1998) with fields for various peraluminous rock types. The calculations are based on millications. Abbreviations: l-P = Low peraluminous; m-P – moderate peraluminous; h-P – high peraluminous and f-P felsic peraluminous. Legend key: LCS – leucosomes; L.Gnt – leucogranites; 2m.Gnt – two-mica granites; APG – aplite-pegmatites; DTX – diatexites; TL.Gnt – tourmaline-bearing leucogranites; P.Gnt – porphyritic granites; F.Gnt – fine-grained granites.

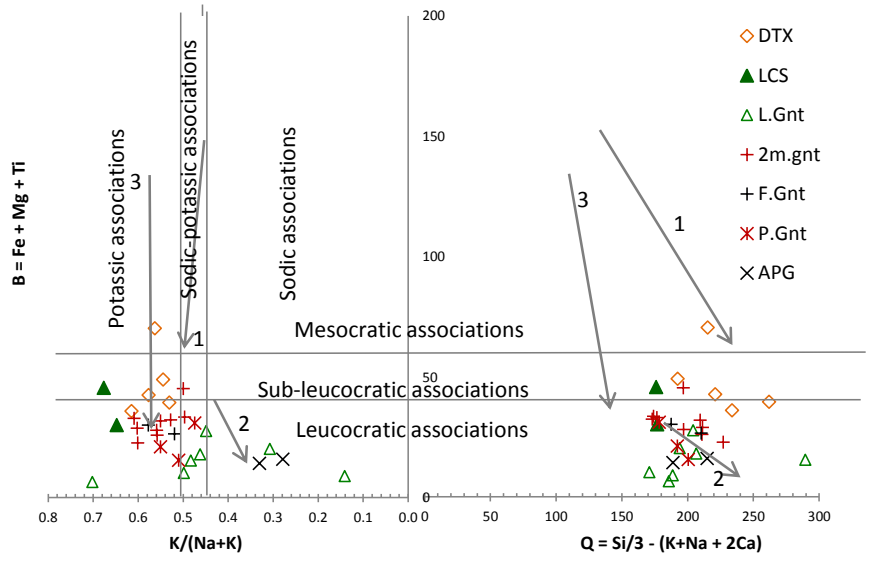

Fig. VI. 17 – Projection of MMC granitic rocks in the Debon & Le Fort (1988) diagram distinguishing evolutionary trends and magmatic associations. 1 - Mesocratic and sodium-potassium association with silico-potassic evolutionary trend, 2 - Leucocratic and sodium association, with silico-sodic evolutionary trend; 3 - meso to leucocratic and potassic association with silica evolutionary trend. Legend key: DTX – diatexites; LCS – leucosomes; L.Gnt – leucogranites; 2m.Gnt – two-mica granites; F.Gnt – fine-grained granites; P.Gnt – porphyritic granites; APG – aplite-pegmatites.

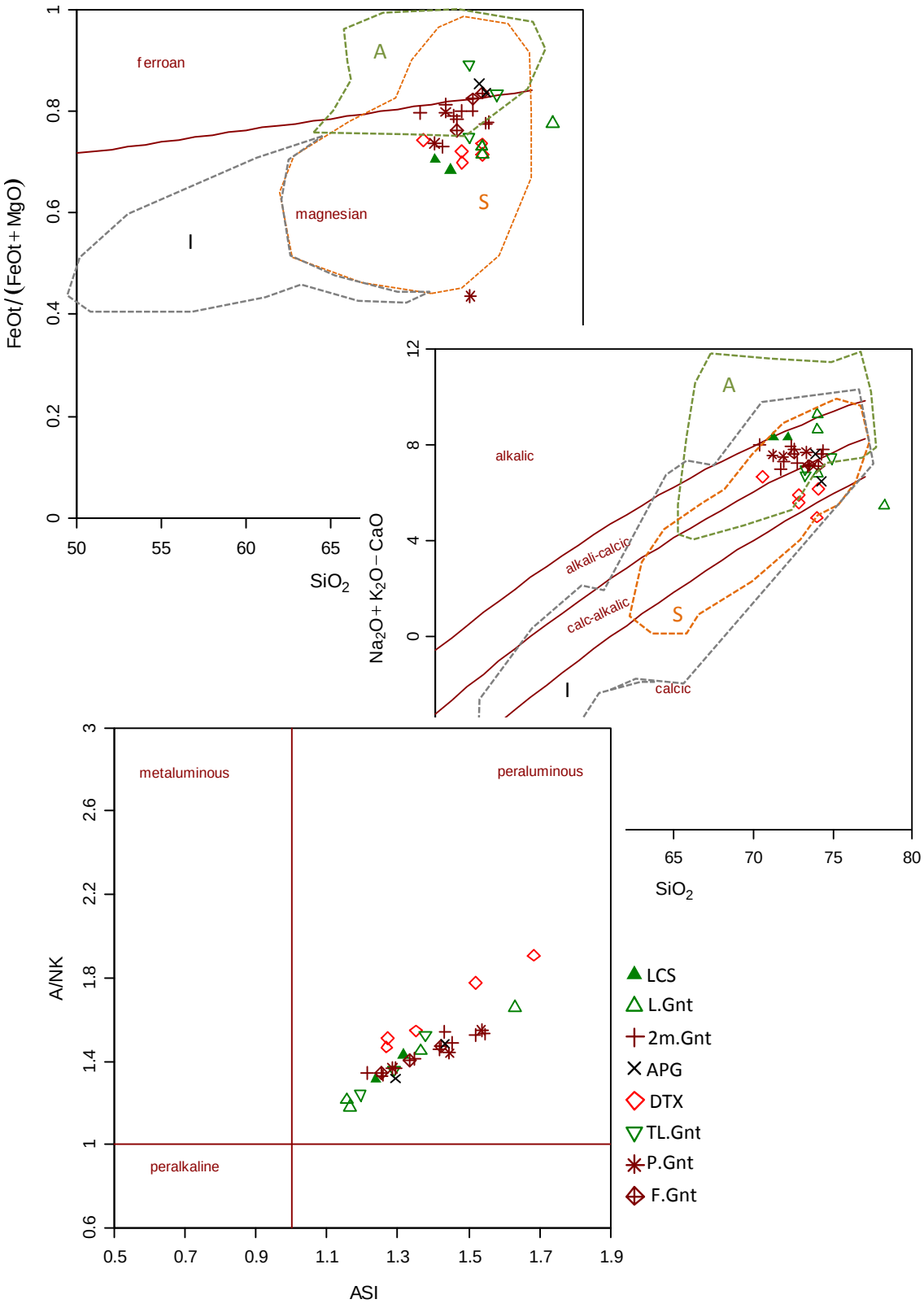

Fig. VI. 18 – Frost *et al*. (2001) classification scheme for MMC granitic rocks. Legend key: LCS – leucosomes; L.Gnt – leucogranites; 2m.Gnt – two-mica granites; APG – aplite-pegmatites; DTX – diatexites; TL.Gnt – tourmaline-bearing leucogranites; P.Gnt – porphyritic granites; F.Gnt – fine-grained granites.

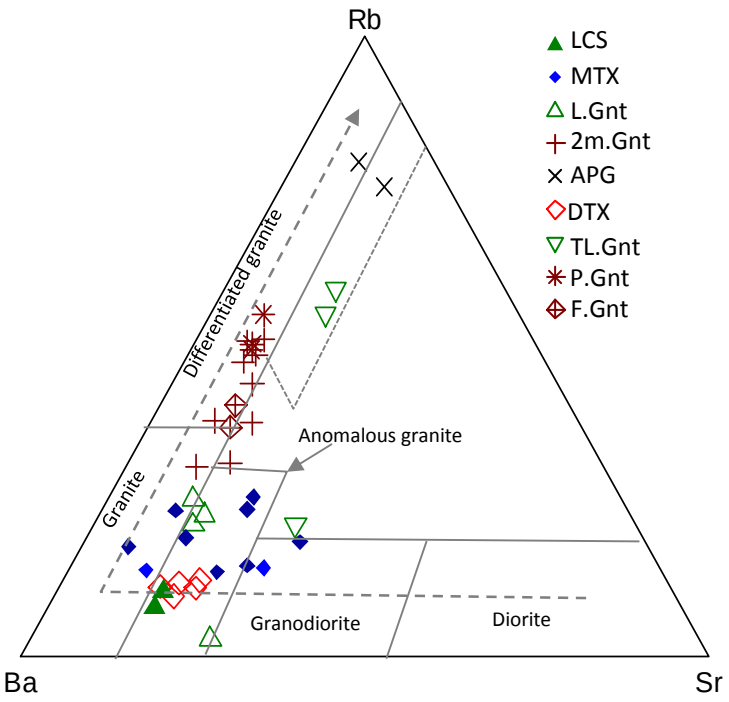

Fig. VI. 19 - Rb - Ba - Sr diagram of El Bouseily & El Sokkary (1975) for MMC granitic rocks and metatexites. Legend key: LCS – Leucosome; MTX – Metatexite; L.Gnt – leucogranite; 2m.Gnt – two-mica granites; APG – aplite-pegmatites; DTX – diatexites; TL.Gnt – tourmaline-bearing leucogranites; P.Gnt – porphyritic granites; F.Gnt – fine-grained granites.

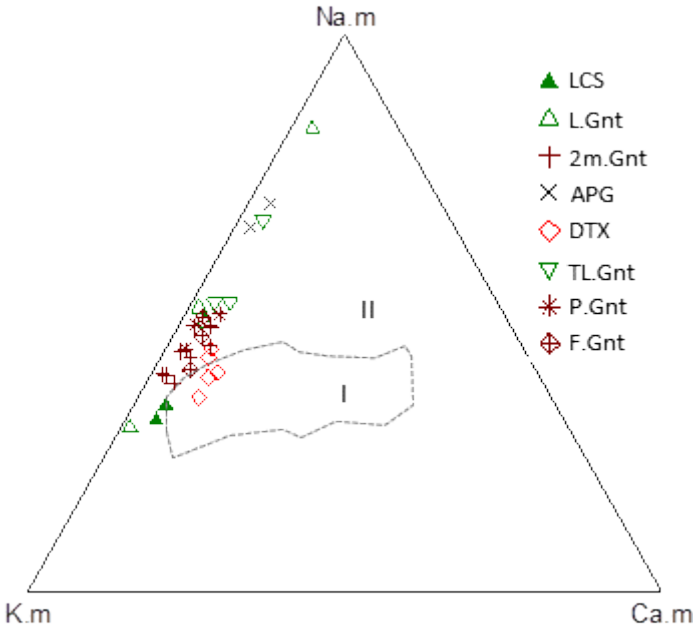

Fig. VI. 20 -Diagram Na-K-Ca (in milications) of Raju & Rao (1972). Fields: I - magmatic granitic rocks; II – replacement granites rocks. Legend key: LCS – Leucosomes; L.Gnt – leucogranites; 2m.Gnt – two-mica granites; APG – aplite-pegmatites; DTX – diatexites; TL.Gnt – tourmaline-bearing leucogranites; P.Gnt – porphyritic granites; F.Gnt – fine – grained granites.

6.3.3. Tectonic discrimination

Several authors (ex. Batchelor & Bowden, 1985; Foster *et al.* 2001, Pearce *et al*.; 1984) consider that magmas produced in different tectonic environments can be distinguished based on their chemical composition. The exclusive use of chemical diagrams to distinguish the geodynamic context of granite emplacement, without any other independent data, must always be done with care, since it can lead to wrong conclusions. In fact, competing factors, independent of the tectonic environment, could determine the composition of granitic rocks. In particular the anatectic granites composition is mostly a function of the protolith rock composition and of the melt crystallization history, being the tectonic environment secondary (Rollinson, 1993; Foster *et. al*, 2001).

Batchelor & Bowden (1985) propose a tectonic environment discrimination considering the parameters R1 and R2 based on major elements (Fig. VI.21) which distinguishes between granites from mantle fractionates, pre-orogenic granites, post-collisional uplift granites; late-orogenic granites, anorogenic granites, syn-collisional granites and post-orogenic granites.

Pearce *et al*. (1984) suggest a set of diagrams using HFSE such as Ta, Zr, Y and Nb that are the most stable under various conditions and hydrothermal metamorphism (Fig. VI.22). For granitic rocks these authors proposed distinguish four kinds of tectonic environment: ORG - granites of oceanic rift, fore-arc and back-arc; VAG - oceanic volcanic arc and active margins granites; WPG - intra-plate granites in attenuated crust and island arcs; COLG - collisional granites, syn-tectonic, associated with continent-continent collision and continent-arc.

In both diagrams two-mica granites *s. l.* plot in the field of syn-collisional granites. Diatexites and leucosomes plot in the field of post-orogenic granites in the Bachelor and Bowden (1985) diagram and mostly in the field of Oceanic Volcanic Arc granites and Active Margins in the Pearce *et al.* (1984) diagrams. Leucogranites plot between the syn-collisional and active margins fields.

In the Whalen *et al*. (1987) 1000Ga/Al vs. Zr or Zr+Nb+Ce+Y discriminant diagrams (Fig. VI.23) the MMC granitic rocks plot in the field of S or I-type granites and fall outside the A-type compositional field. Two-mica granites, aplite-pegmatites and one sample of tourmaline-bearing leucogranites plot in the field of fractionated felsic granites. Diatexites plot in the frontier between fractionated and unfractionated granites and leucosomes and leucogranites clearly in the unfractionated granites field.

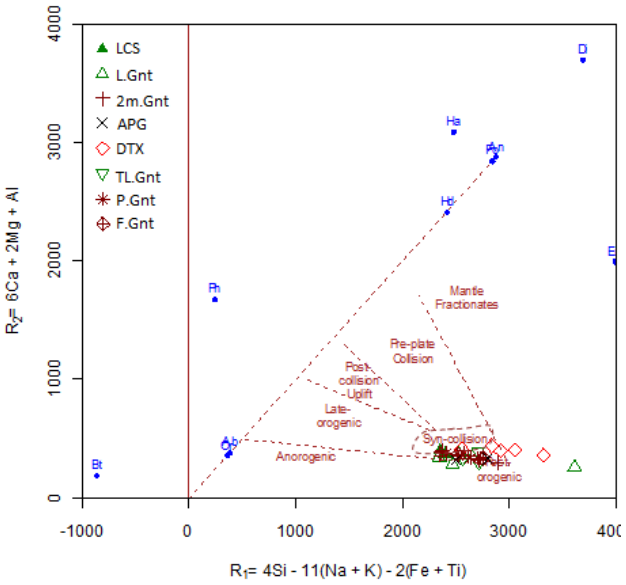

Fig. VI. 21 – Projection of MMC granitic rocks in the Batchelor and Bowden (1985) discrimination diagram, which distinguishes between granites from fractional mantle, pre-orogenic granites, post-collisional uplift granites, late-orogenic granites, anorogenic granites, syn-colisional granites and post-orogenic granites. Legend key: LCS – Leucosomes; L.Gnt – leucogranites; 2m.Gnt – two-mica granites; APG – aplite-pegmatites; DTX – diatexites; TL.Gnt – tourmaline-bearing leucogranites; P.Gnt – porphyritic granites; F.Gnt – fine-grained granites.

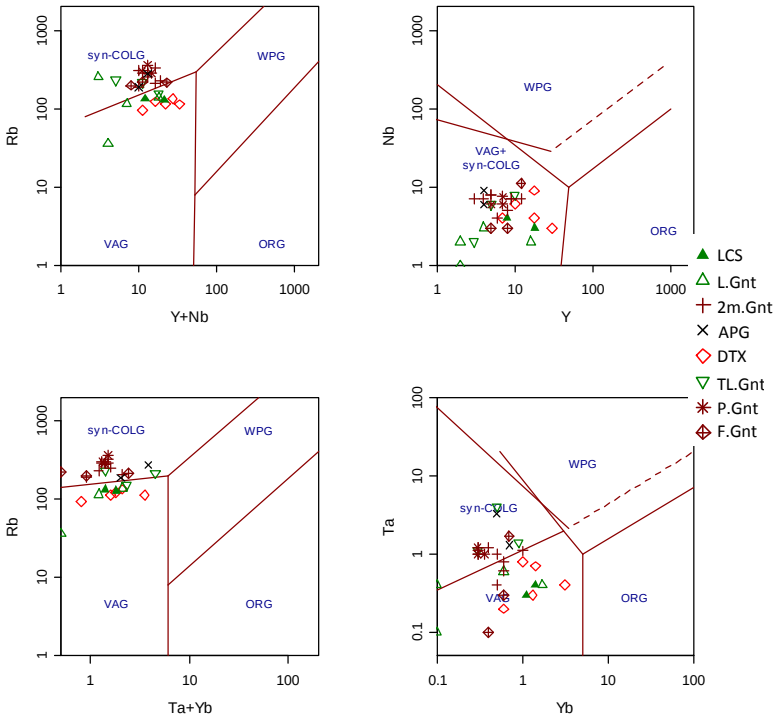

Fig. VI. 22 – Projection of MMC granitic rocks in a suite of four diagrams for discrimination of geotectonic environment of granitoid rocks proposed by Pearce *et al.* (1984). Abbreviation: ORG - Ocean Ridge Granites; VAG - Volcanic Arc Granites; WPG - Within Plate Granites; syn-COLG – syn-Collisional Granites. Most of the two-mica granites and the aplite-pegmatites plot on the syn-collisional granites field and most of the diatexite, leucosome and leucogranite plot on volcanic arc granites field. Legend as in Fig. VI.21.

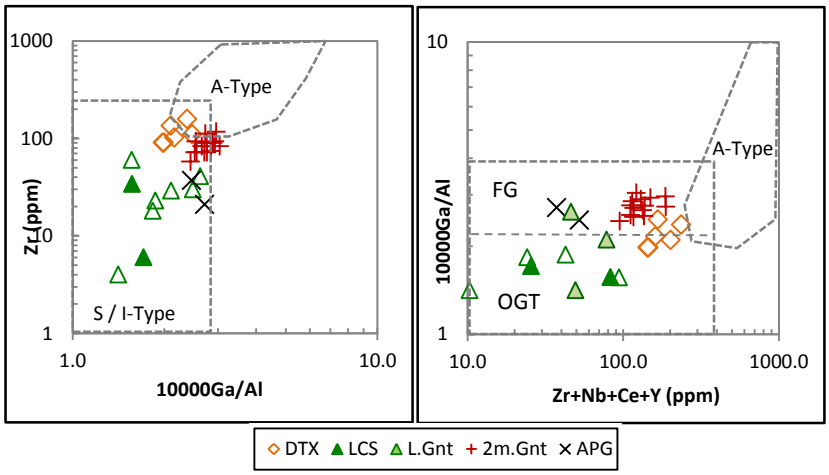

Fig. VI. 23 - 10000Ga/Al vs. Zr and Zr+Nb+Ce+Y vs 10000 Ga/Al discrimination diagram (Whalen et al., 1987). Abbreviations: OGT (unfractionated M-, I- and S-type granites) and FG (fractionated felsic granites). Legend key: DTX – diatexites; LCS – Leucosomes; L.Gnt – leucogranites; 2m.Gnt – two-mica granites; APG – aplite-pegmatites.

6.3.4. Variation Diagrams

Harker variation diagrams are used to understand the processes occurring during the evolution of magmas. The correlation patterns between selected elements provide an indication in this regard since they are generally related to mixtures of magmas, addition or subtraction of solid phases by contamination or fractional / partial melt crystallization. Fractional crystallization is considered responsible for most of the correlations between major elements in Harker diagrams. In the case of partial melting the correlation patterns are controlled by the geochemistry of the solid phases that are being added to the melt. In the case of fractional crystallization with assimilation, the patterns of correlation show variability which is related to the inclusion of country rock in the magma during fractionation (Rollinson, 1993).

Figures VI.24 and VI.25 show the projection of major and selected trace elements *versus* SiO_2 for MMC granitic rocks. All the granitic rocks from MMC show relatively high SiO_2 content (two-mica granites ~72,6 wt.%, leucogranites ~74,0 wt.% and diatexites ~72,9 wt.% in average). Two-mica granites and diatexites K_2O content is 5,2 and 4,5 in average. In leucogranites the K_2O content is highly variable ranging from 1,4 to 7,4 wt.%. The ferromagnesian elements content is low in two-mica granites and leucogranites (1,38 and 0,78 in average, respectively). Diatexites show the higher FeO + MgO content (2,78 wt.% in average), CaO (0,9 wt.% in average), Ba, Sr, Y, Zr and La contents. Leucogranites show the lowest ferromagnesian, HSFE and TiO_2 contents, high variation in K_2O content and high Na_2O and Ba contents. Two-mica granites s.l.

show the highest P_2O_5 (0,39 in average) and Rb contents (specially the granitic porphyry). However there are no systematic variations relative to SiO_2 from two-mica granites to fine granites to porphyritic granites.

Considering the lithologies independently or considering the granitic rocks as a whole there are no evident correlations between major or trace elements and the silica content. Only a slight inverse correlation between SiO_2 and Al_2O_3 is observed. This suggests that the classic model of fractional crystallization is not the principal process influencing the lithological diversity in the MMC granitic rocks.

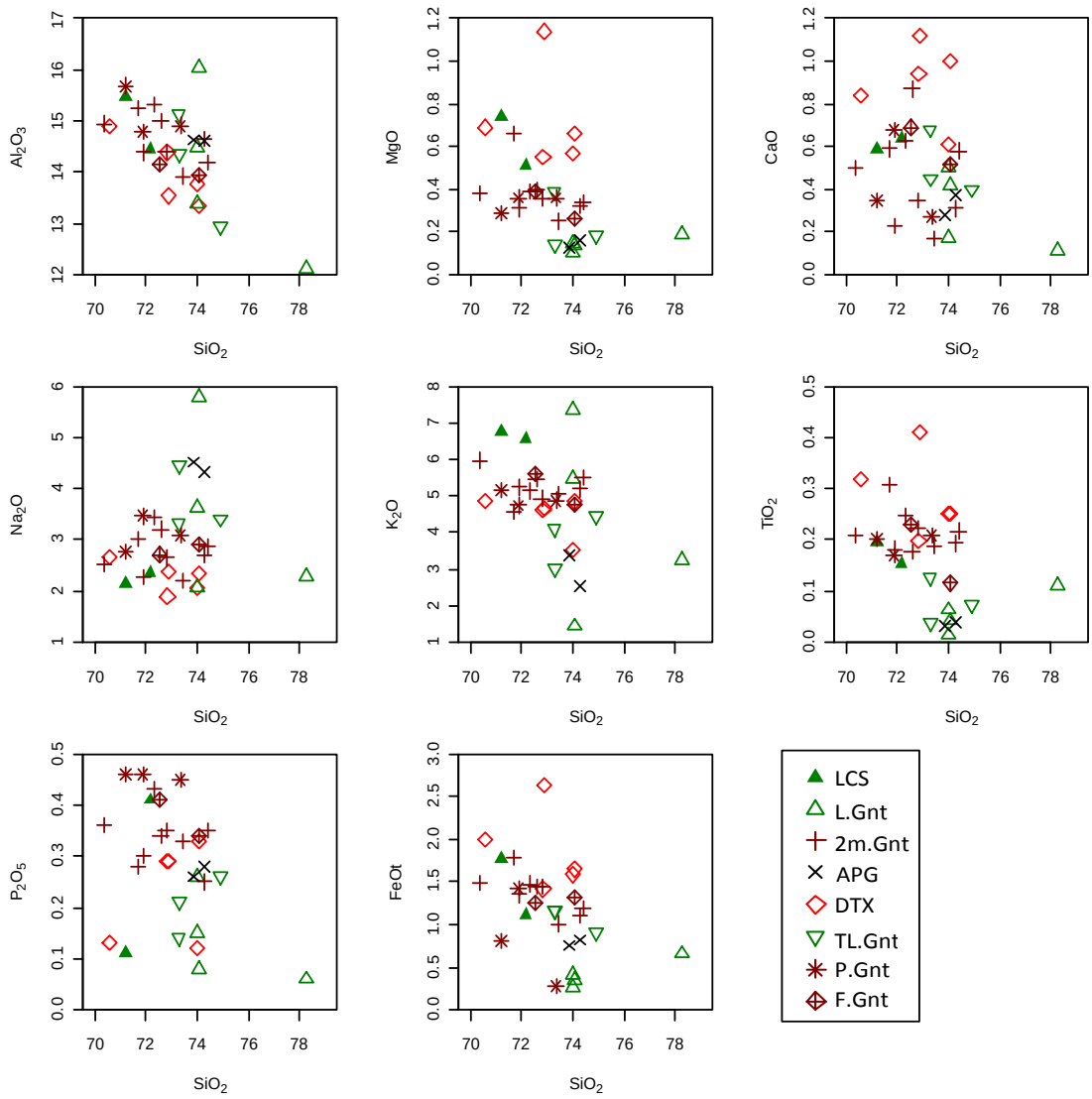

Fig. VI. 24 – Harker diagrams for MMC granitic rocks projecting major elements *versus* silica content. Legend key: LCS – Leucosomes; L.Gnt – leucogranites; 2m.Gnt – two-mica granites; APG – aplite-pegmatites; DTX – diatexites; TL.Gnt – tourmaline-bearing leucogranites; P.Gnt – porphyritic granites; F.Gnt – fine granites.

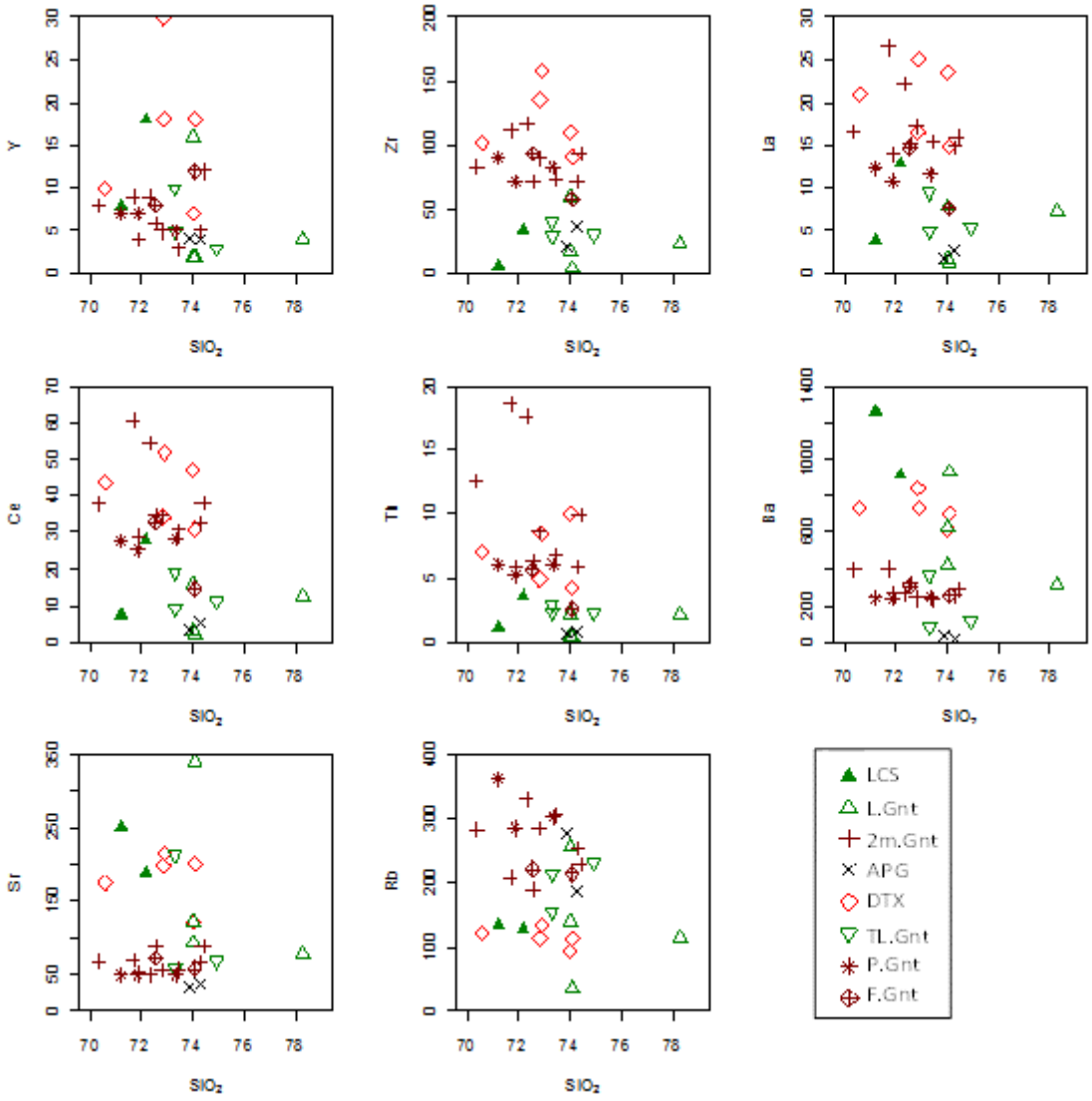

Fig. VI. 25 – Harker diagrams for MMC granitic rocks projecting selected trace elements *versus* silica content. Legend key: LCS – Leucosomes; L.Gnt – leucogranites; 2m.Gnt – two-mica granites; APG – aplite-pegmatites; DTX – diatexites; TL.Gnt – tourmaline-bearing leucogranites; P.Gnt – porphyritic granites; F.Gnt – fine granites.

Figures VI.26 and VI.27 show the patterns defined by major and selected trace elements *versus* the content in mafic components (Fe_2O_3t + MgO) for the MMC granitic rocks. A notable feature is the positive correlation between TiO_2, CaO and HSFE content and the content in mafic minerals (in this case biotite since it is the only mineral that contains Fe_2O_3 and MgO in these rocks).

In contrast, the elements compatible in reactant phases during the melting processes (Rb, Ba and Sr) show a higher range of variation with no clear correlation with mafic components. These elements are concentrated in minerals that are key reagents in the

melting reactions that produce granites, e.g., biotite, quartz, plagioclase and garnet (Sawyer, 2008).

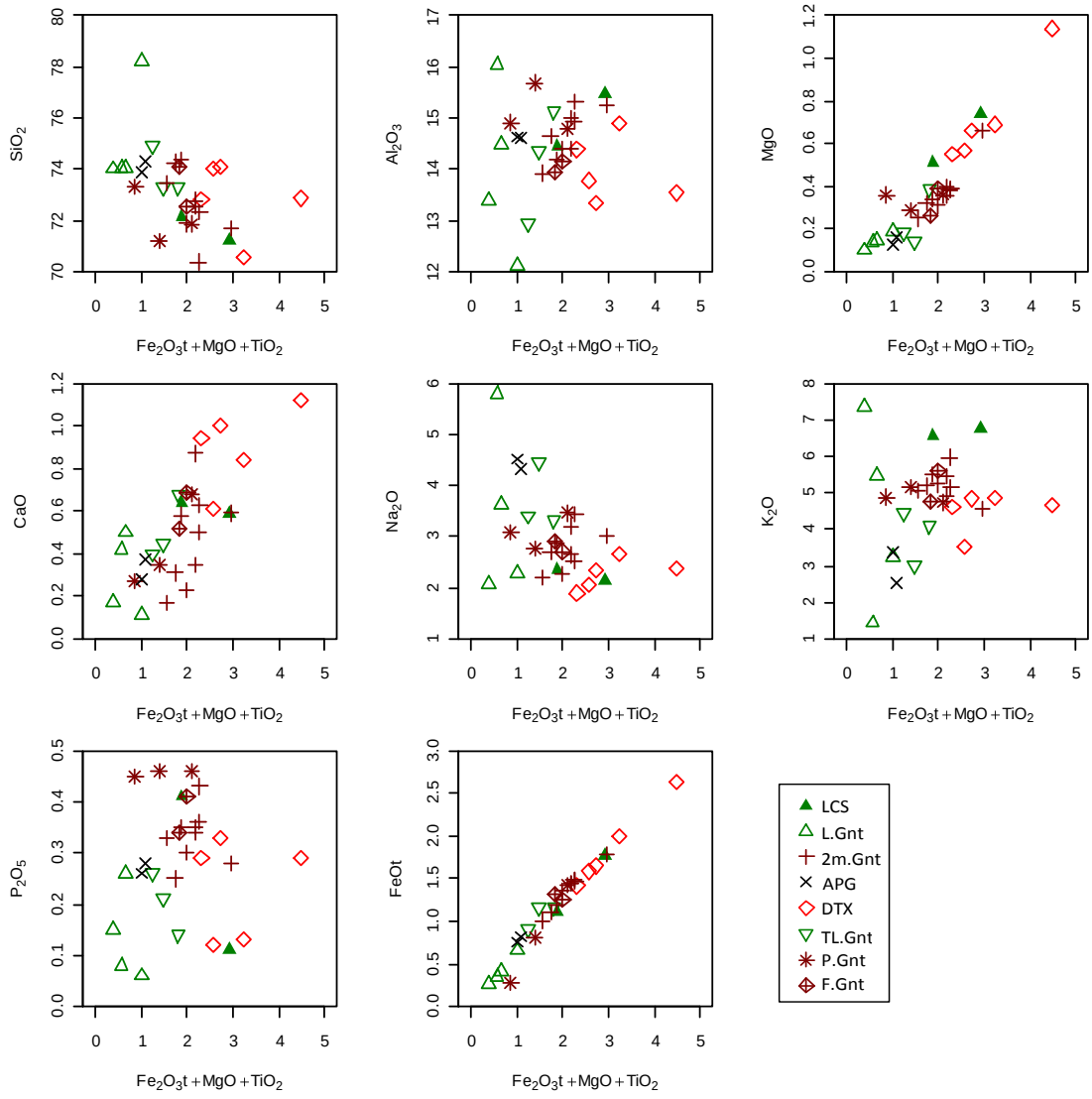

Fig. VI. 26 - Projection of major elements contents *versus* mafic components to the MMC granitic rocks. Legend key: LCS – Leucosomes; L.Gnt – leucogranites; 2m.Gnt – two-mica granites; APG – aplite-pegmatites; DTX – diatexites; TL.Gnt – tourmaline-bearing leucogranites; P.Gnt – porphyritic granites; F.Gnt – fine granites.

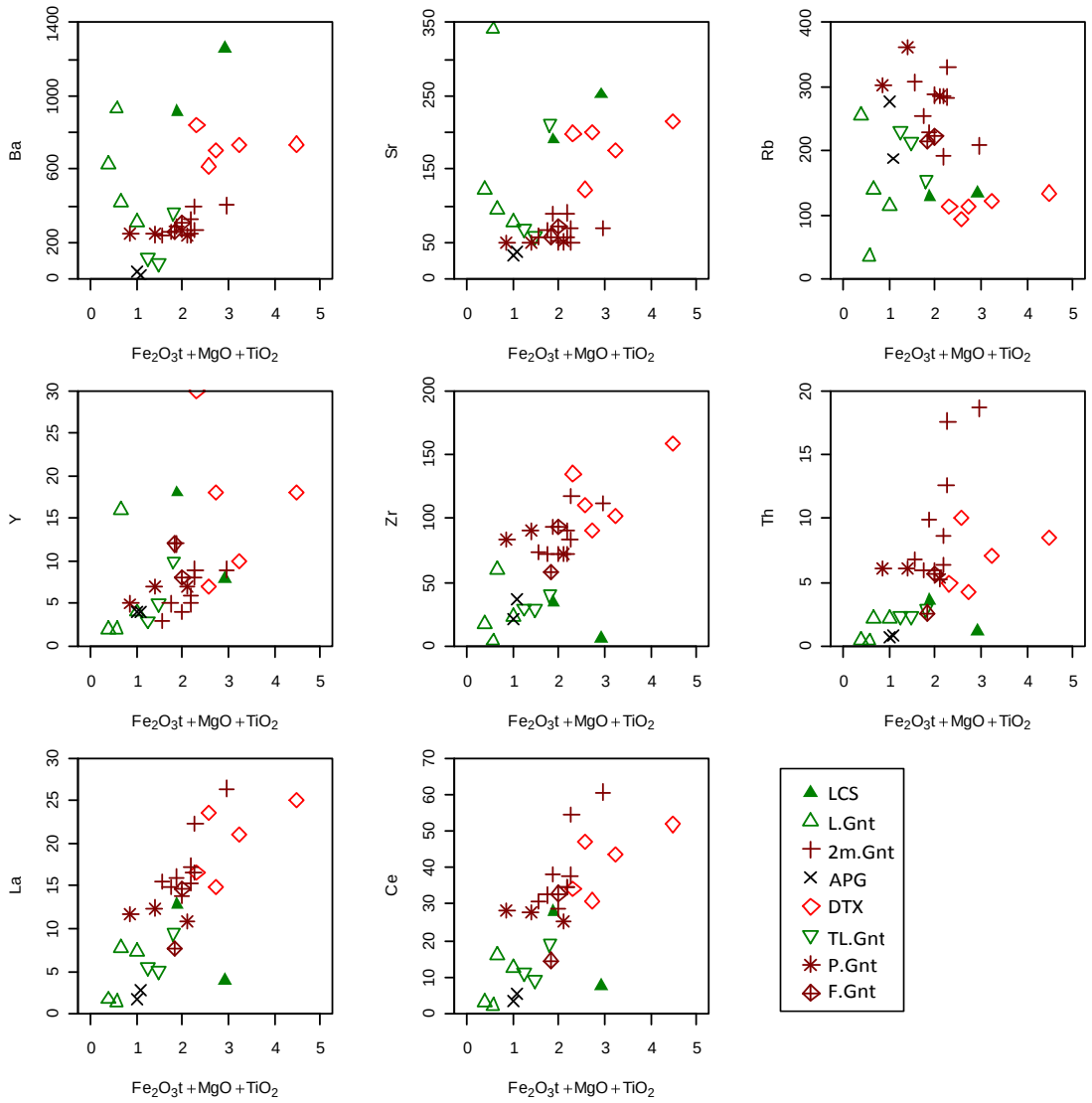

Fig. VI. 27 - Projection of selected trace elements contents *versus* mafic components to the MMC granitic rocks. Legend key: LCS – Leucosomes; L.Gnt – leucogranites; 2m.Gnt – two-mica granites; APG – aplite-pegmatites; DTX – diatexites; TL.Gnt – tourmaline-bearing leucogranites; P.Gnt – porphyritic granites; F.Gnt – fine granites.

6.3.4.1. Large Ion Lithophile Elements variation diagrams

Close geochemical association of potassium and rubidium has led to the extensive use of K/Rb ratio in petrogenetic analysis of igneous systems as a potential indicator of petrogenetic evolution, in particular to the separation between primary and secondary trends (Shaw, 1968). Being larger in size, rubidium accumulates in residual melts more rapidly than does potassium. Hence, with progressive differentiation the K/Rb ratio of rocks should decrease with increasing acidity. Therefore K/Rb ratios can indicate the extent and direction of differentiation in a suite of igneous rocks (Tombale *et al.,* 1984).

Shaw (1968) compiled K and Rb data for a variety of igneous rock types and defined several igneous fractionation trends on the Rb vs K diagram. It was established a main trend that characterize K and Rb concentrations in rocks ranging from granite to continental basalts. The "main trend" lies near a K/Rb ratio of 230 and shows an increase in Rb and K with magmatic differentiation. A second trend which diverges to higher K/Rb ratios at very low K concentrations is defined by ocean tholeiite basalts. The third trend is the pegmatitic-hydrothermal trend showing extreme Rb concentration relative to nearly constant (or even decreasing) K resulting in a trend parallel to the Rb axis.

Figure VI.28A and B represents the K *vs.* Rb diagram and K/Rb *vs.* K_2O for MMC granitic rocks compared with Show's Main Trend. MMC granitic rocks display high K and Rb contents showing K/Rb ratio between 105 in aplite-pegmatites to 422 in leucosomes (in average).

Diatexites, leucosomes and tourmaline-absent leucogranites show high K/Rb ratio and plot above Shaw's "main trend" related to their lower Rb content. *In situ* leucosomes show the highest K content to moderate Rb content. This confirms the low differentiated character of these lithologies. Two-mica granites, aplite-pegmatites and tourmaline-bearing leucogranites plot below the Shaw's "main trend", showing a moderate to highly differentiated character. Aplite-pegmatites show the lower K/Rb values as is typical of highly differentiated rocks. The aplite-pegmatite samples do not plot in continuity with any of the other granitic rocks.

Also is notorious that the MMC granitic rocks do not follow the normal differentiation trends since diatexites and two-mica granites show a trend parallel to the Rb axis and leucogranites show highly dispersion in K content that is not related with the Rb content nor with the hydrothermal increasing of Rb. Thus, it seems that the differentiation trend of two-mica granites is related to hydrothermal processes. The variation in leucogranites shows a hydrothermal component (increase in Rb in tourmaline-bearing leucogranites) but also another influence that cannot be associated with magmatic neither with hydrothermal differentiation. This suggests the influence of later metasomatic processes.

As mentioned before, the K_2O content variation in MMC granitic rocks is not related to silica content. In SiO_2 versus K_2O diagram (Fig. VI.28C) two-mica granites and diatexites show a trend almost parallel to the silica axis with little variation of K_2O

content. In contrast, leucogranites have an opposite behavior, showing strong potassium enrichment relatively to SiO_2 variation (following a vertical trend in the diagram). The K_2O content in leucogranites is correlated with CaO+ Na_2O content (r^2 = 0,9, except sample FP44b that show low Na_2O relatively to SiO_2 content). This demonstrate extremely high gains of K at the expense of Na and Ca, suggesting the occurrence of a feldspatization process that is not accompanied by increasing acidity, probably post-magmatic, associated with K-metasomatism/potassic alteration (Pirajno, 1992). These data are in agreement with petrographic observations since there are several indications of plagioclase replacement by K-feldspar.

The initial concentration of Rb, Sr and Ba in granitic rocks is controlled by processes of fractional crystallization and is dependent on their relative partition coefficients. It is expected that concentration of Sr and Ba decrease and Rb increase in residual fluids with increasing crystallization. This translates to a relative increase in Rb upwards in the granite series with a reciprocal decrease in Ba and Sr, being the deviation to the expected trends as being a function of geochemical modification due to alteration. Bivariate trace element plots of Rb vs. Sr or Rb vs. Ba tend to be the most sensitive to crystal fractionation as shown by numerous authors; for example Hunter (1973), Kleeman & Twist (1989).

Figures VI.28E and VI.28F represents the Rb vs. Sr and Sr vs CaO diagrams for MMC granitic rocks. In general the lithologies showing higher Sr content have lower Rb content. However the behavior is different of each lithology. Two-mica granites show low Sr and high Rb content, low Sr variation and a slight correlation between Sr and Rb. (r^2=0,57). Diatexites, leucosomes and leucogranites show low Rb content and high variation in Sr content, without evident correlation between Rb and Sr variations. Aplite-pegmatites show the lowest Sr content. The usual relation between Sr and CaO content only is evident in diatexites (r^2=0,96).

Ba *vs.* Rb/Sr diagram (Fig. VI.28H) shows marked individualization between the different lithologies. Diatexites, leucosomes and leucogranites show low Rb/Sr content and high Ba content and slightly correlation between Sr and Rb (r^2=0.5). Two-mica granites show variation in Rb/Sr content (due to Rb variations) and low variation in Ba content. Aplite-pegmatites show lower Ba content and do not follow the same pattern as any of the other lithologies.

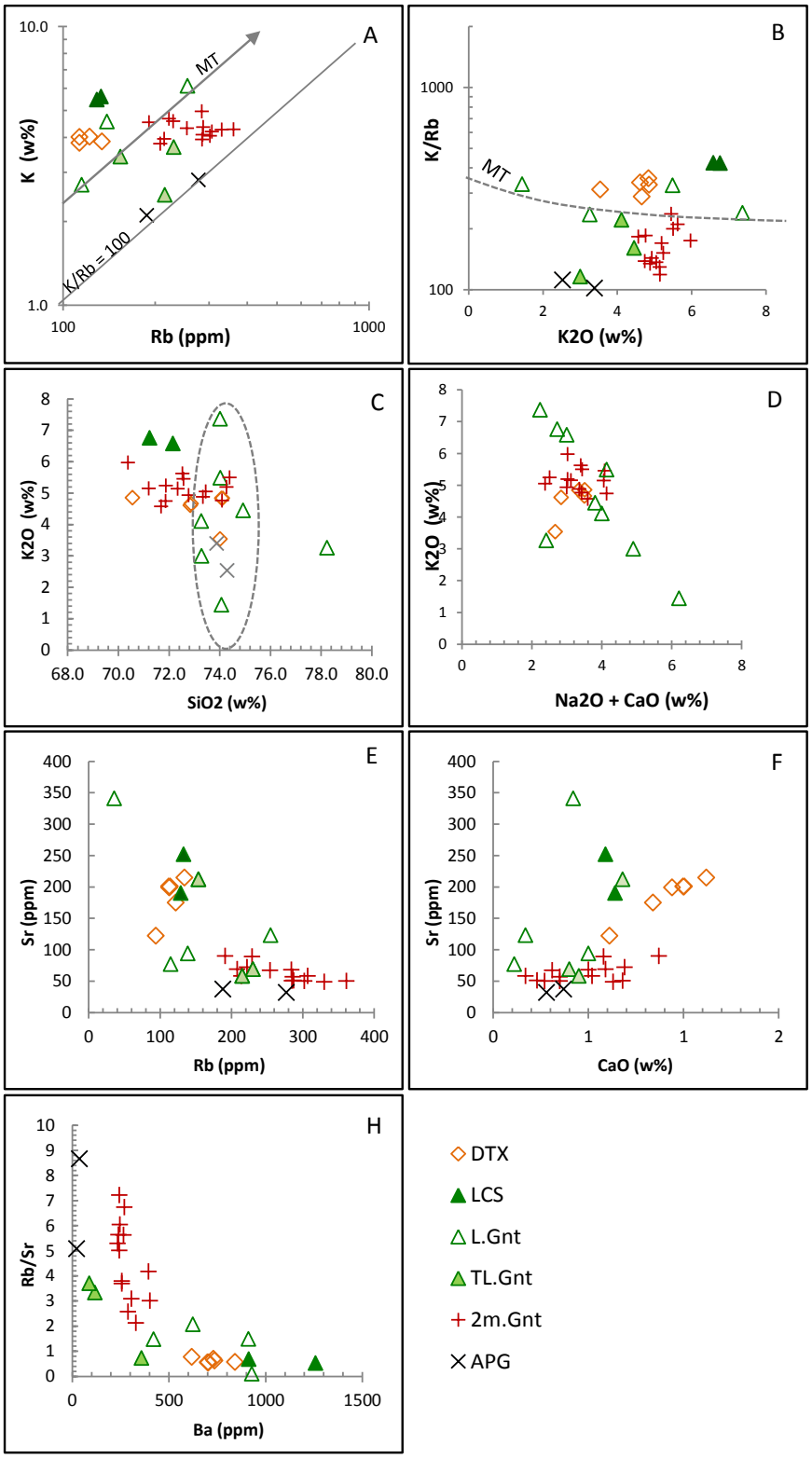

Fig. VI. 28 – Projection of MMC granitic rocks in the: A) Rb *vs.* K (wt.%) diagram compared with Shaw's main trend (MT). B) K_2O (wt.%) versus K/Rb diagram for MMC granitic rock compared with Shaw's main trend. C) SiO_2 vs. K_2O diagram; D) K2O vs. Cao+Na2O diagram; E) Rb vs. Sr diagram; F) Sr vs. CaO diagram; H) Rb/Sr vs. Ba diagram. Legend key: DTX – diatexites; LCS – leucosomes; L.Gnt – leucogranites; TL.Gnt – tourmaline-bearing leucogranites; 2m.Gnt – two-mica granites; APG – aplite-pegmatites.

6.3.4.2. HSFE variation diagrams

The recognition that REE, Y, Th and U-rich accessories minerals may play an important role in controlling the geochemistry of crustal melts is well stablished (e.g. Watson, 1988; Watt et al., 1996; Bea, 1996; Sawyer, 2008). Crustal rocks always contain REE, Y, Th, U-rich accessory minerals which usually account for an elevated fraction of REE, Y, Th and U contents in bulk rock (*e.g*. Gromet & Silver, 1983; Sawka, 1988) and may therefore disturb or even completely mask the effects produced by major minerals during melting and crystallization (Miller & Mittlefehdlt, 1982; Yurimoto *et al.,* 1990, Bea & Montero, 1999). The geochemistry of HSFE reflects the behaviour of accessories and some key major minerals such as garnet, feldspars and amphibole, and may therefore give valuable information about the conditions of partial melting, melt segregation and crystallization of granite magmas in different crustal regimes (Bea, 1996).

Figure VI.29A, 29B and 29C represents the TiO_2 *vs* Zr, TiO_2 *vs*. Mg and La + Ce *vs* Zr diagrams for MMC granitic rocks. Diatexites show the highest HSFE and MgO content, two-mica granites show moderate content and leucogranites show the lowest HSFE content. Leucosomes, although showing low Zr and La+Ce contents have moderate MgO and TiO_2 contents. TiO_2 correlates with the MgO and Zr content and Zr content with the La + Ce content.

Figure VI.29D represents the U *vs.* Th diagram to the MMC granitic rocks. Comparing with average standard granite (Condie, 1993) the Th/U ratio is lower for all the lithologies. Diatexites show Th/U values slightly lower but closer to metatexites (Th/U = 2,12) and follow the same trend (except one sample), showing Th content ~8,9 ppm in average and U content 4,3 ppm in average. Leucogranites and leucosomes show low Th/U values (1.3 and 0,7 respectively) and have low Th and U contents. Two-mica granites s.l. show variability in the Th/U ratio ranging from 2,8 to 0,55 which is exceptionally low compared to the Th/U ratios of average granite (3,5 to 4, Roger & Adams, 1978) and do not follow the Th/U trends. They show high U content (7,2 ppm in average) much higher than the average granite of 4 ppm (Roger e Adams, 1978). The Th content (10 ppm in average) is low relatively to the average granite of 18 ppm. Fine granites and porphyritic granites show the lowest Th content and the lowest ferromagnesian elements content. Aplite-pegmatites show very low Th content that plot them beyond the scope of the diagram, although the U content is similar to two-mica granites. It seems that the diatexites Th and U contents is inherited from the

metatexites with some depletion in both. However, the other MMC granitic rocks apparently were produced by a process that excludes the accessory minerals containing Th, in special the leucogranites and leucosomes.

The higher U content in two-mica granites *s.l.* could be related to the presence of magmatic xenotime since xenotime unlike monazite exhibits a substantial preference of U over Th (e.g., Forster 1998). The same author (Foster, 1999) find that magmatic Uraninite is widespread as an accessory mineral in peraluminous variscan granites and is the dominant contributor to the bulk-rock U content, showing only insignificant portions of the thorium concentrations which are predominantly controlled by monazite-group minerals.

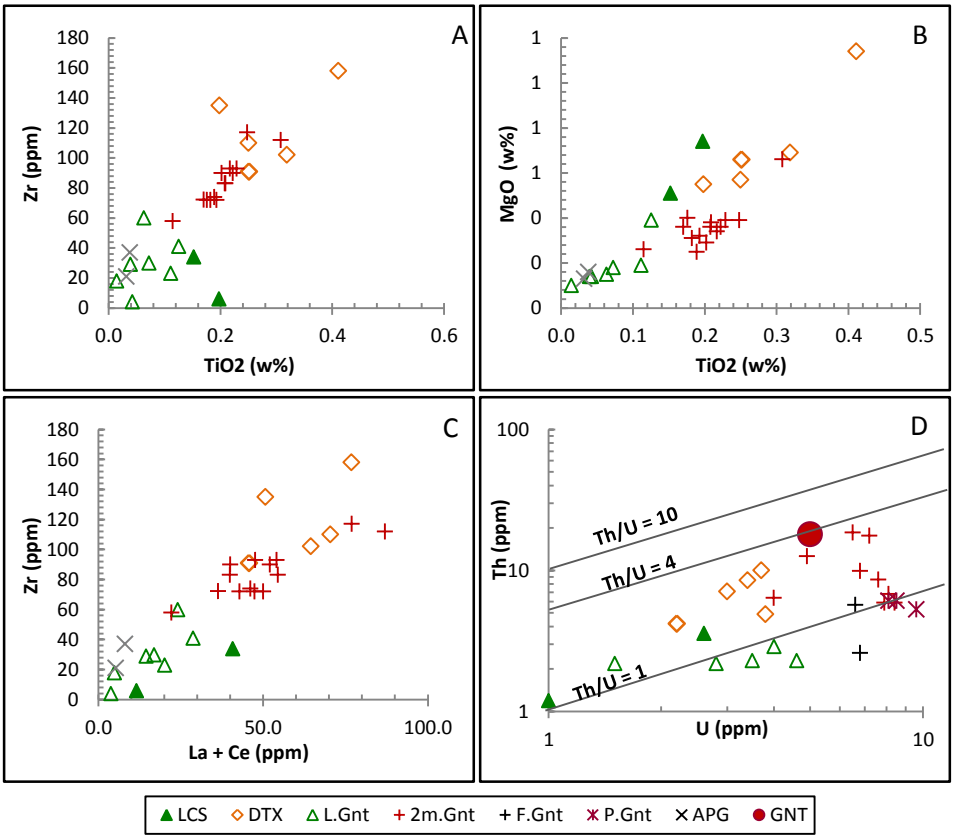

Fig. VI. 29 - Variation diagrams TiO_2 vs Zr, TiO_2 vs MgO, La+Ce vs Zr and Th *vs.* U for MMC granitic rocks. Legend key: LCS – leucosomes; DTX – diatexites; L.Gnt – leucogranites; 2m.Gnt – two-mica granites; F.Gnt – fine-grained granites; P.Gnt – porphyritic granites; APG – aplite-pegmatites; GNT – average standard granite (Condie, 1993).

6.3.5. Multielement diagrams

Figure VI.30 represent multielement diagrams for MMC granitic rocks normalized to the average of medium-grained sin-F_3 two-mica granites from NW of Portugal (Pereira *et al*., 1992; n=14 for two-mica and n=54 for trace elements). The multielement patterns show the high dissimilarity between the distinct MMC granitic lithologies compositions, in special in what concerns minor and trace elements. The following can be highlighted:

- Diatexites are enriched in ferromagnesian elements, Ca, Sr, Ba Zr and Ti and depleted in Mn, P, Na, K, Rb, U, Ta and Nb relatively to the normalization standard.
- Leucosomes show multielement pattern similar to diatexites but exhibiting anomalous low Zr content, less ferromagnesian elements and higher K content.
- Leucogranites show higher compositional variation, low ferromagnesian and HSF elements content, high Ba and Sr. Tourmaline-bearing leucogranites stand out from tourmaline absent leucogranites by their lower Ba and Sr content and higher Ta and Rb content.
- Two-mica granites, fine-grained granites and porphyritic granites show low compositional variation and a pattern more approximate to the normalization standard. However it is notorious the lower Ca, Mn, Na, Rb, U, Zr, Y, Ta and Nb content that distinguishes the MMC two-mica granites *s.l.* from the normalization standard medium-grained two-mica granites analysed by Pereira et al., 1992. Fine-grained granites show slight variations in the Ta and Nb contents and porphyritic granites show lower Fe, Ca and Mn contents.
- Aplite-pegmatites are poorer in Ca, Sr, K, Rb, Ba, ferromagnesian and HSF elements and richer in Mn, Na, Ta and Nb content relatively to both other MMC granitic rocks and to the normalization standard.

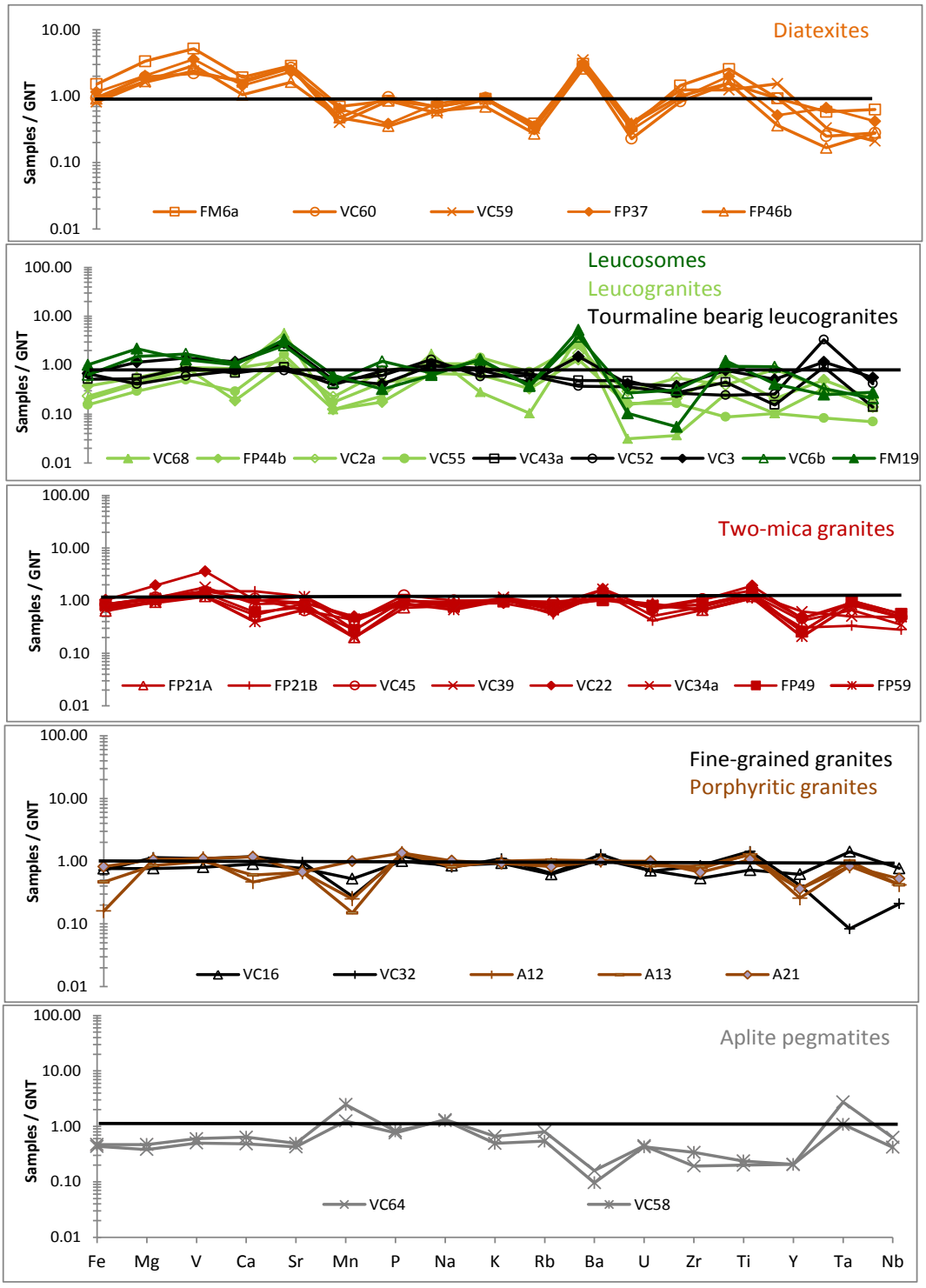

Fig. VI. 30 – A) Diatexites from Vila Chã (FM6, VC59 and VC60), Malta (VC46b) and Fornelo (VC37); leucosome *in situ* (VC8) and leucosome vein (FM19) from Metatexite Zone. B) Leucogranites from Mindelo (VC2), Malta (FP44b), Vila do Conde (VC55) and Aguçadoura (VC68) and tourmaline-bearing leucogranites from Mindelo (VC3), Vila Chã (VC52) and Lavra (VC43a). C) Two-mica granites from Lavra (VC39), Leça (VC45), S. Paio (VC22 and VC34); Vila do Conde (FP21a and FP21b), Junqueira (VC49 and VC50) and Fornelo (FP30a). D) Fine-grained granite dikes from Vila Chã (VC16 and VC32) and porphyritic granites dikes from Fornelo, and D) Aplite-pegmatite from S. Paio (VC64) and Vila Chã (VC58).

6.3.5.1. Rare earth elements

Rare Earth Elements pattern diagrams normalized to Chondrite (Boynton, 1984) for MMC granitic rocks are shown in Figures VI.31, VI.32, VI.33 and VI.34. The observations of REE patterns allows highlight the following:

- Diatexites REE pattern is characterized by moderate total REE content, absence of Eu anomaly and variable HREE fractionation.
- Leucosomes REE pattern is characterized by low total REE content, positive Eu anomaly and variable HREE fractionation. Leucosome *in situ* (VC8) show higher REE content and smaller Eu anomaly than leucosome vein (FM19).
- Leucogranites REE pattern is characterized by low REE total content, positive Eu anomaly and variable HREE fractionation. The leucogranites (both with and without tourmaline) situated in the zone immediately adjacent to the Metatexite Zone (Mindelo and Lavra) show higher REE total content and lower Eu positive anomaly than the leucogranites dispersed in dikes that intrude the metasedimentary sequence (samples VC55 and VC68).
- Two-mica granites REE pattern is characterized by moderate REE content, accentuated negative Eu anomaly and marked REE fractionation.
- Fine granites show a REE pattern similar to two-mica granites but with higher variation in REE content and HREE fractionation.
- Porphyritic granites show a REE pattern very similar to two-mica granites.
- Aplite-pegmatite REE pattern is characterized by low total REE content, negative Eu anomaly and low HREE fractionation.

Many investigators have shown that a large part of the total budget of some trace elements, including REE, Y, Th, U, Hf and Zr is located in accessory minerals and are conditioned by the distribution coefficient of these elements between the anatectic melt and the residuum (e.g. Bea 1996; Watt *et al*., 1996; Bea & Monteiro, 1999). Diagrams with the ∑REE, LREE and HREE content versus Zr, Th, Y, and P_2O_5 (Figs. VI.35, VI.36 and VI.37) show that these processes of distribution are clearly observed in MMC granitic rocks:

In diatexites the ∑REE show a positive correlation with Zr (r^2=0.95). Leucogranites show ∑REE correlation with Zr, Th and Y (r^2=0.5, 0.76 and 0.86 respectively). In two-mica granites the ∑REE correlation is especially related to Zr and Th content (r^2= 0,76 and 0.86 respectively) (Fig. VI.35).

As expected, Th content correlates with Nd content and with ∑LREE suggesting that monazite strongly influences LREE concentrations in the MMC granites. However, in two-mica granites there are an enrichment in Th that do not follow the monazite Th/Nb ratio (0.26) suggesting other mineral apart monazite could influence the Th content in these rocks (Fig. VI.36A). The Y content correlates with Ho and near the chondrite Y/Ho ratio of 27.5 suggesting a relation between the Y-bearing minerals, namely garnet and xenotime and the ∑HREE.

The Eu anomaly is related to the leading role of accessory minerals with respect to plagioclase. The lower the Th and Zr content smaller is the negative Eu anomaly in diatexites and two-mica granites. The leucogranites and leucosomes, with positive Eu anomaly, show the minor amount of these elements. The Na_2O/CaO ratio is inversely correlated with Eu positive anomaly (Fig. VI. 37).

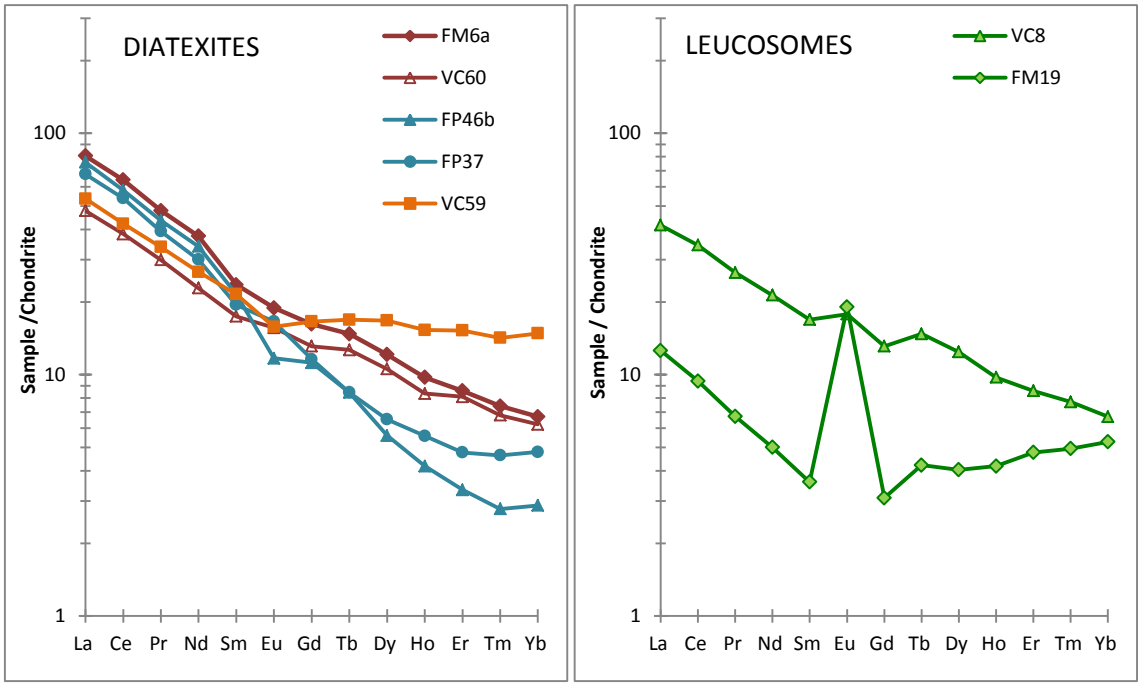

Fig. VI. 31 – Rare Earth Elements pattern diagrams normalized to Chondrite (Boynton, 1984). A) Diatexites from Vila Chã (FM6, VC59 and VC60), Malta (VC46b) and Fornelo (VC37) and B) Leucosome *in situ* (VC8) and leucosome vein in Metatexite zone (FM19).

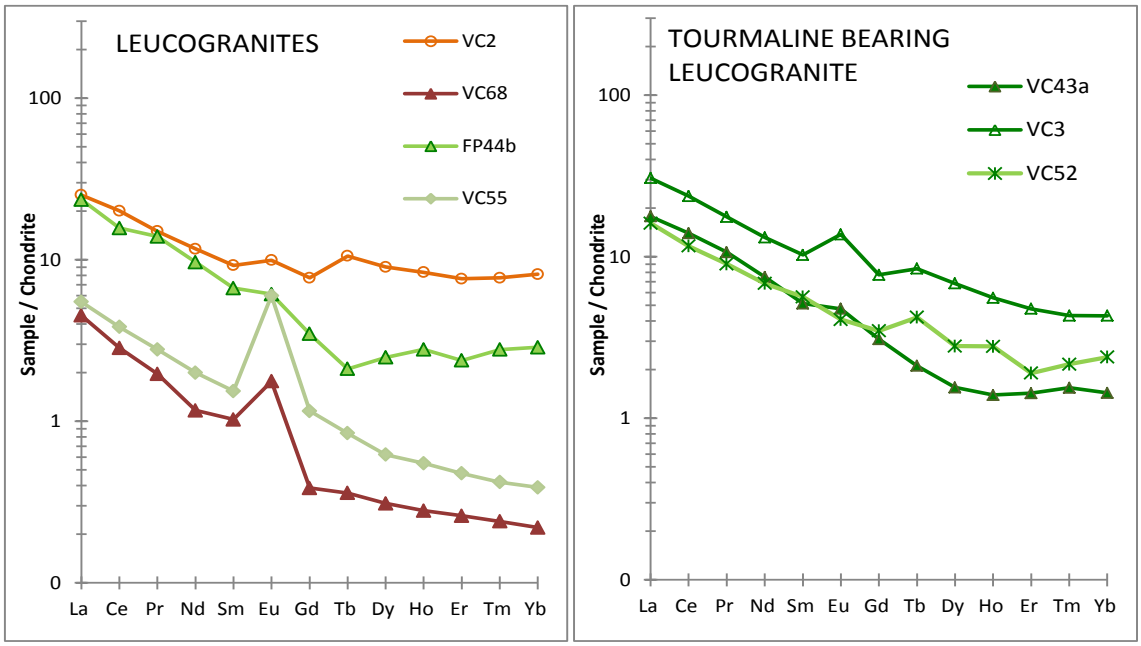

Fig. VI. 32 - Rare Earth Elements pattern diagrams normalized to Chondrite (Boynton, 1984) to A) Leucogranites from Mindelo (VC2), Malta (FP44b), Vila do Conde (VC55) and Aguçadoura (VC68); B) tourmaline-bearing leucogranites from Mindelo (VC3), Vila Chã (VC52) and Lavra (VC43a).

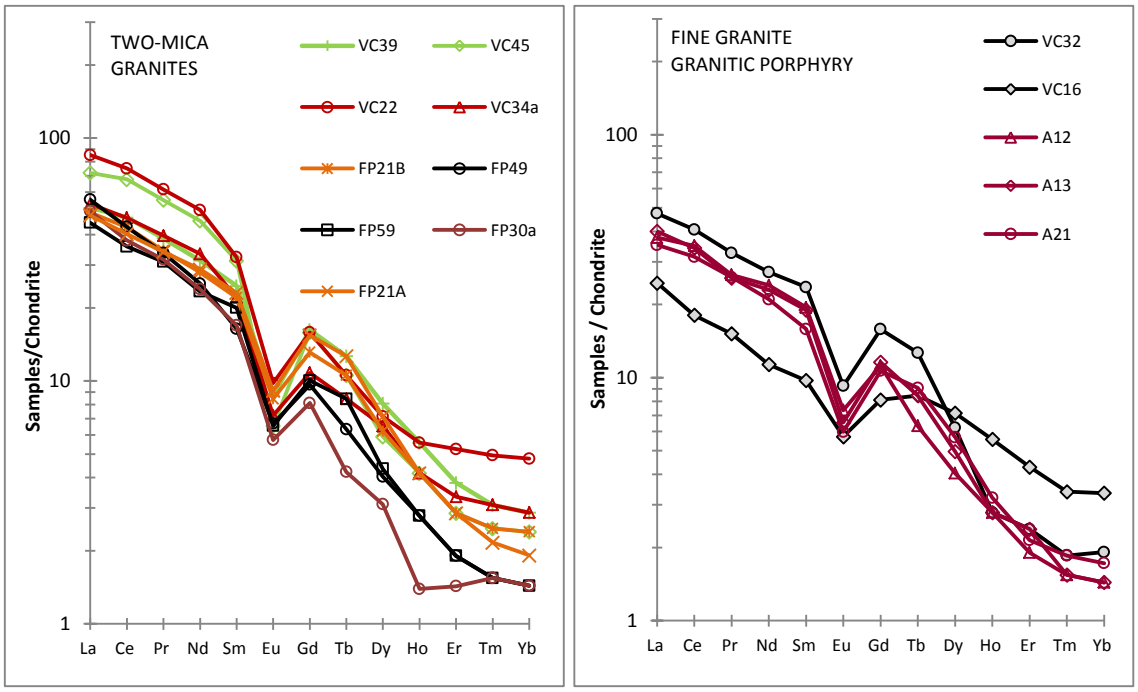

Fig. VI. 33 - Rare Earth Elements pattern diagrams normalized to Chondrite (Boynton, 1984) to: A) Two-mica granites from Lavra (VC39), Leça (VC45), S. Paio (VC22 and VC34); Vila do Conde (FP21a and FP21b), Junqueira (VC49 and VC50) and Fornelo (FP30a). B) Fine granites from Vila Chã (VC16 and VC32) and porphyritic granites from Fornelo (porphyritic granites data from Ferreira, 2011).

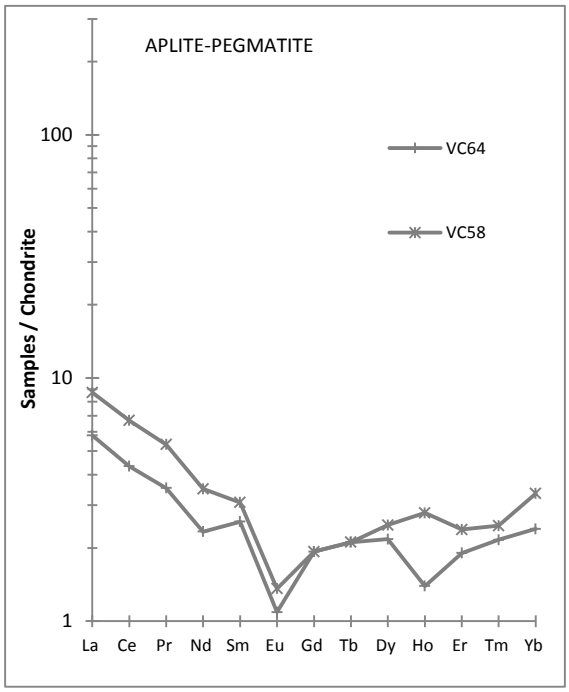

Fig. VI. 34 - Rare Earth Elements pattern diagrams normalized to Chondrite (Boynton, 1984) to aplite-pegmatite from S. Paio (VC64) and Vila Chã (VC58).

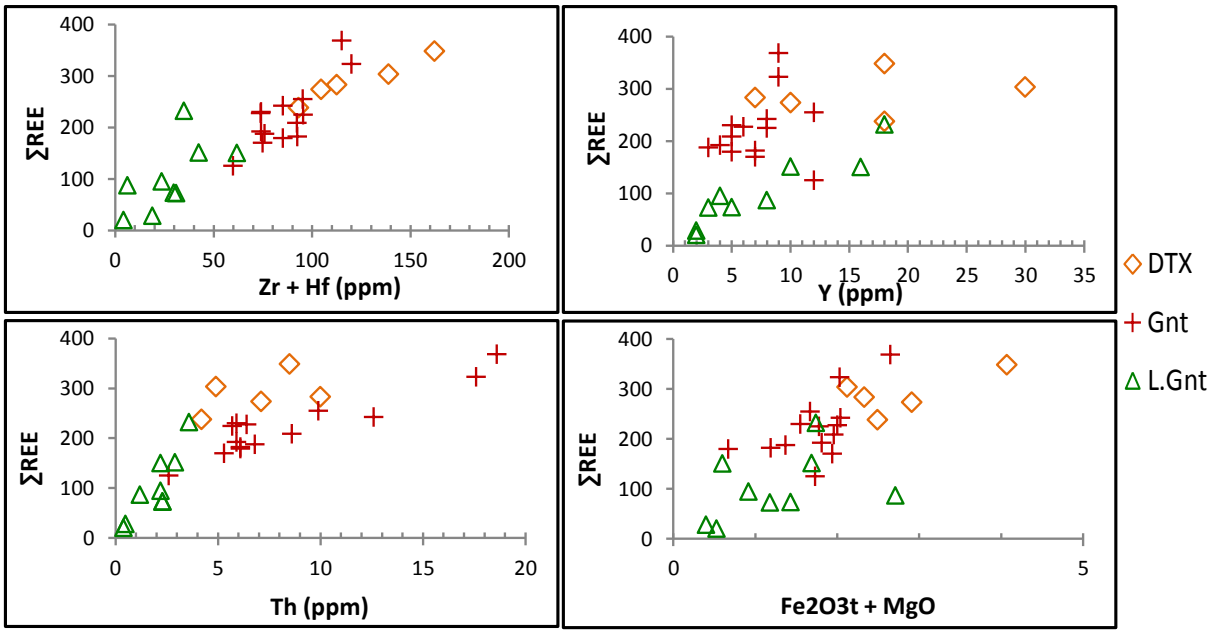

Fig. VI. 35 – Binary diagrams showing the relation between total REE content and elements associated with acessorry minerals (Zr, Hf, Th and Y) in granitic rocks from MMC. Legend key: DTX – diatexites; L.Gnt – leucosomes, leucogranites and tourmaline-bearing leucogranites; Gnt – two-mica granites s.l..

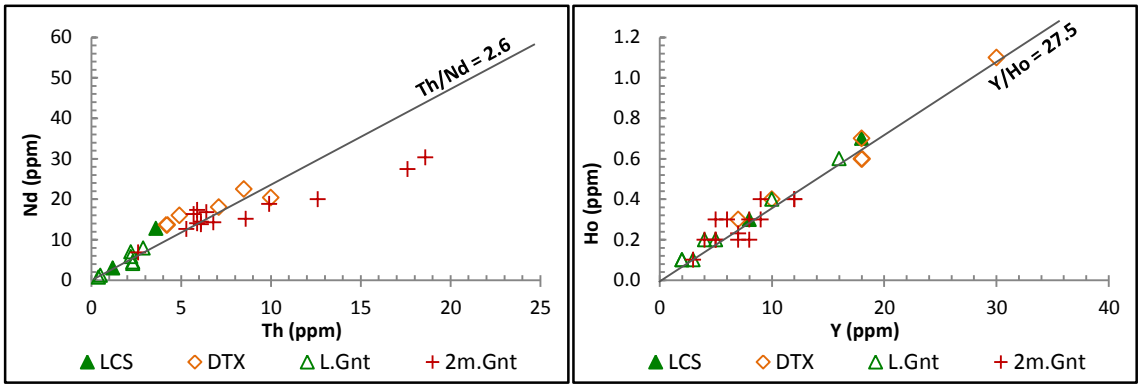

Fig. VI. 36 – Projection of MMC granitic rocks in Nd vs.Th and Ho vs. Y diagrams showing the relation between the LREE and Th content and HREE and Y content, respectively. Legend key: LCS – leucosomes; DTX – diatexites; L.Gnt – leucogranites; 2m.Gnt – two-mica granites.

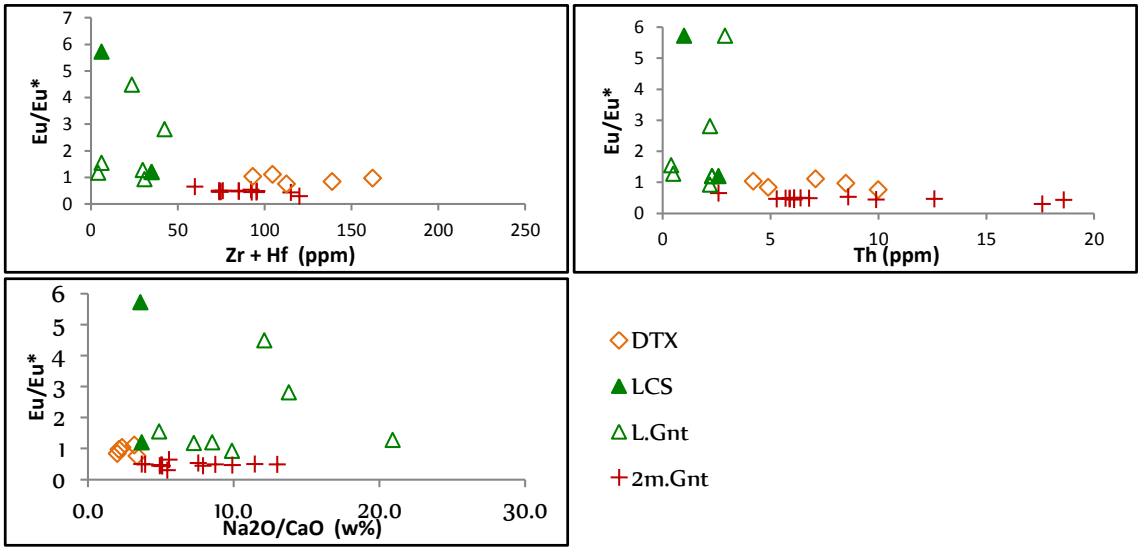

Fig. VI. 37 - Binary diagrams showing the relation between Eu anomaly and the content in elements associated with accessory minerals (Zr, Hf, Th) and plagioclase fractionation (relation between Na_2O/CaO) in MMC granitic rocks. Legend key: DTX – diatexites; L.Gnt – leucosomes, leucogranites and tourmaline-bearing leucogranites; Gnt – two-mica granites s.l..

6.3.6. Comparison with other granitoids

6.3.6.1. Comparison with S- and I-type granites

The concept of I- and S-type granites was introduced in 1974 by Chappell & White to account for the observation that the granites in the Lachlan Fold Belt have properties that generally fall into two distinct groups. This has been interpreted to result from derivation by partial melting of two different kinds of source rocks, namely sedimentary for S-type granites and older igneous rocks for I-Type granites (Chappel & White,

2001). Like S-type granites, the MMC granitic rocks are highly peraluminous, showing normative corundum between 2,0 and 6,0 and high silica content. The Harker variation diagrams show overlap and irregular distribution as is expected in S-Type granites.

Figure VI.38A represents the projection of MMC granitic rocks in K_2O vs Na_2O diagram showing the fields corresponding to granites occurring in other regions of the globe, namely S and I-type granites from Australian Lachlan Fold Belt (Chappel & White 1974), leucogranites from European Variscan (Stussi, 1989) and Himalayas belt (Vidal *et al*., 1982). MMC granitic rock plot in the S-type granite field showing high K_2O and Na_2O content and its composition is close to Himalayan leucogranites as referred before by Vidal *et al*. (1982) for the two-mica Hercynian granites. The leucogranites variation in K_2O and Na_2O content is notorious and make them plot in- and-out of the S-Type granites field, suggesting later processes (Fig. VI.38). Chappell and White (2001) consider that Ca is a much better discriminant between S- and Y-Type granites. Figure VI.38B represent the diagram CaO vs Fe_2O_3t for the MMC granitic rocks with delimitation of I and S type granites. All the MMC granitic rocks plot in the S-type granites.

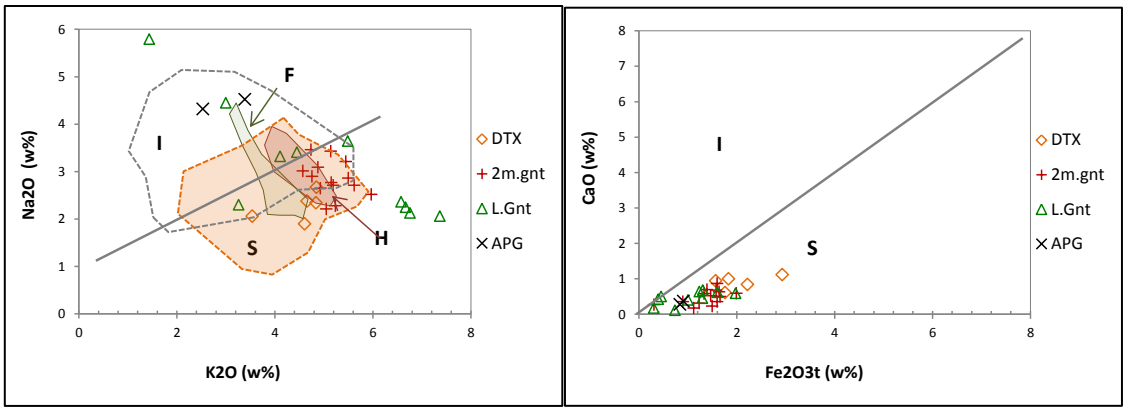

Fig. VI. 38 – Projection of MMC granitic rocks in K_2O vs Na_2O and in CaO Vs. Fe_2O_3t diagrams. Also represented the fields corresponding to S and I-type granites from Lachlan Fold Belt (Chappell and White 2001) and leucogranites from European Variscan and Himalayas belts. Abbreviations: S – S-type granites; I – I-type granites; H – Himalayan leucogranites (Vidal et al, 1982);F - French massif alumino-potassic granites (Stussi, 1989).

6.3.6.2. – Comparison with CIZ granites of N Portugal

In agreement with petrographic and structural interpretation made by several investigators, the granitoids of NW of Portugal can be divided into the following types: ante-Hercynian gneiss and / or early Hercynian generally called early granitoids; two-mica Hercynian granites (mesocrustal genesis) and biotite granites with calcic plagioclase considered Hercynian to late-Hercynian (deep crustal genesis) (Pereira *et al*., 1992 and references therein). The different types of granitic rocks show some differences from the chemical point of view that allow to characterize and evaluate the genetic processes that governed its emplacement and crystallization (Pereira *et al.* 1992).

In terms of major elements these three different granitoids overlap each other, although in general silica is higher in the early gneisses (~ 72% wt.) decreasing slightly in the two-mica granites but remaining above 70 wt.% in biotitic granitoids (~69 wt%). The Na_2O and K_2O show variability although early gneisses show a highly potassic character (~ 5.6 wt.% in average). CaO, MgO TiO_2 and P_2O_5 show generic enrichments in biotitic granitoids.

In order to overcome the difficulty in individualize the types of granitic rocks Pereira *et al*., (1992) propose the use of trace elements that consider a good way to delimit areas pertaining to the different granitic types. In the ternary diagrams Sr – Zr – 30Y and in the binary diagrams TiO_2 *versus* Y two-mica granites show random distribution related to the response of different melting intensity in sedimentary rocks of initial varied composition (Ugidos & Bea, 1976), and the biotite granites evidence trends of magmatic differentiation. The early granites tend to plot separated from the two-mica and biotite granitoids.

Figure VI.39 represent the projection of MMC granitic rocks in the diagrams Zr-Sr-30Y and TiO_2 *vs.* Y with delimitation fields for two-mica granites, biotite granites and early granites defined by Pereira *et al*. (1992). Most of the samples from MMC granitic rocks plot out of any specified fields. Although nearer to two-mica granites than to biotite granites, the lower Zr and Y content distinguish geochemically the MMC lithologies from the other granitoids.

Figure VI. 40 represents the multielement diagram for MMC two-mica granites normalized to medium grained two-mica granites form NW of Portugal (Pereira *et al*., 1992). As seen in the sub-chapter 6.3.5. all the MMC granitic rocks show depletion in Mn, Rb, U, Y, Nd and Ta and enrichment in Ba and V relatively to the two-mica

granites analysed by Pereira et al. (1992). It is interesting the notorious lower Fe, Mn, Na, Rb, U, Zr, Y, Nd and Ta and enrichment in Ba Ti and V contents in MMC two-mica granites that separate them from the medium-grained two-mica granites studied by Pereira *et al*. (1992) in the NW of Portugal. Relatively to the early gneissic granites the multielement pattern is also different although with coincidence in K and Ba enrichment and Na, Rb, Zr and U depletion.

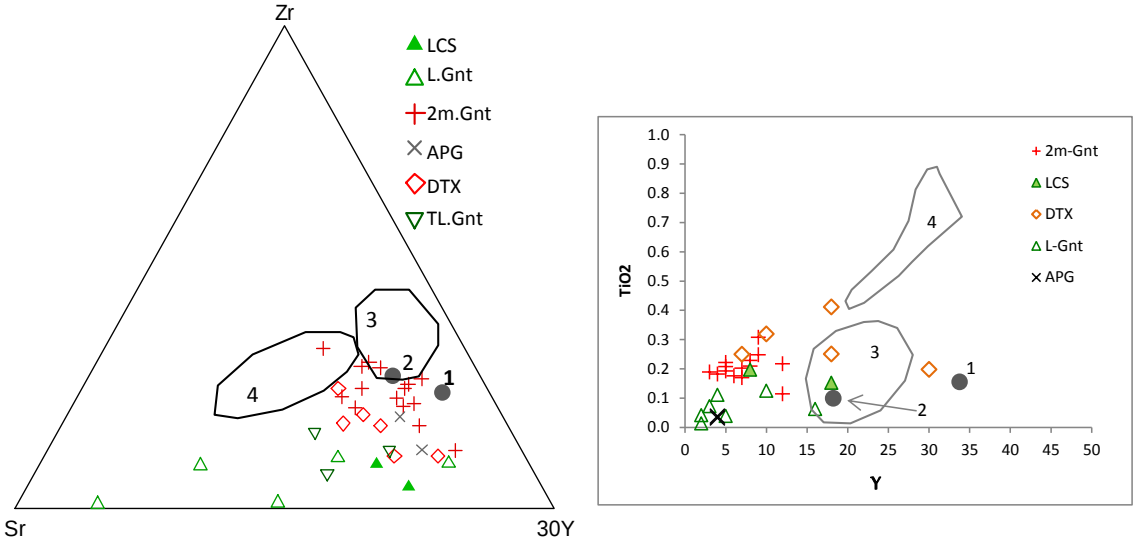

Fig. VI. 39 - Zr-Sr-10Y and Y *vs.* TiO_2 diagram with delimitation of the NW Portugal two-mica granite, orthogneiss and granodiorites fields according to Pereira *et al*., 1992. The majority of samples plot out of any specified fields. Legend: 1 – Orthogneiss (pre-orogenic); 2 – Gneissic granite (ante-D3); 3 – Two-mica granite; 4 – Granodiorites s.l.. Legend key: LCS – leucosomes; L.Gnt – leucogranites and tourmaline-bearing leucogranites, 2m.Gnt – two-mica granites. APG – aplite-pegmatites; DTX – diatexites; TL.Gnt – Tourmaline-bearing leucogranites.

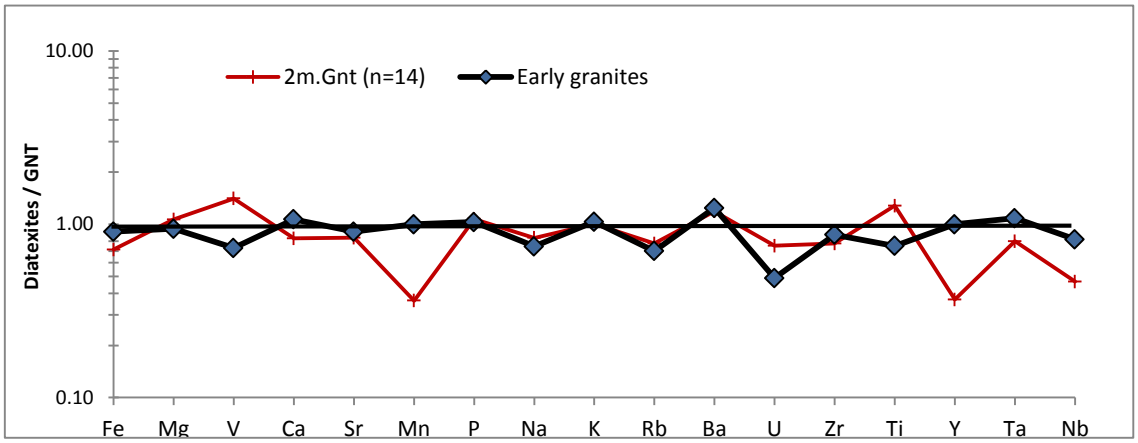

Fig. VI. 40 – Multivariate diagram for MMC average two-mica granites and early granites normalized to medium grained two-mica granites from Pereira *et al.* (1992).

6.3.7. Summary

The different granitic rocks types were classified as diatexites, leucosomes, leucogranites, tourmaline-bearing leucogranites, medium to coarse grained two-mica granites, fine-grained two-mica granites and porphyritic granites, accordingly to their field relations and petrographical textures and mineralogy.

The most significant characteristic shared by all of these granitic rocks is their S- type affinity (highly peraluminous, high SiO_2, K_2O and low CaO and Na_2O contents), and the lower MnO, U, Y, Ta, Nb contents and higher Mg, V, Sr and Ba contents relatively to the two-mica granites from CIZ in NW of Portugal. However, the MMC granitic lithologies show different mineralogy and chemical composition:

- Diatexites are classified generally as syenogranites showing magnesian and calcic to alkali-calcic character (accordingly to the Frost (2001) classification). They are enriched in Ca, HSFE, Ba and Sr relatively to the other MMC lithologies. The REE profile is characterized by high REE total content and absence of Eu anomaly. The only differentiation processes observed are related with the ferromagnesian content that influences the HSFE content;
- Leucosomes *in situ* and leucosome-veins in the Metatexite Zone are classified as alkali feldspar granites showing magnesian and alkalic-calcic character. They are characterized by high K, Sr and Ba content. The ferromagnesian content is close to the diatexites but the Zr content is lower. REE pattern is characterized by low REE content and positive Eu anomaly. The leucosome *in situ* shows higher HSFE content and lower Eu positive anomaly than the leucosome-veins;
- Leucogranites are classified as alkali feldspar granites and syenogranites, showing magnesian and alkali-calcic to calc-alkali character (Frost, 2001). They are characterized by high variation in K content that is not correlated with silica content but is inversely correlated with CaO+ Na_2O content and by their low ferromagnesian and HSFE content. REE pattern is similar to leucosomes, showing Eu positive anomaly and low REE total content. Tourmaline-bearing leucogranites although showing similar HSFE and REE patterns, stand out from of tourmaline-absence leucogranites by their lower Ba and Sr and higher Ta and Rb content;
- Two-mica granites are classified as alkali feldspar granites showing magnesian and alkali-calcic character. They are characterized by higher P, Rb and U content relatively to the other MMC granitic lithologies showing a composition in general

intermediate between the diatexites and leucogranites. REE profile is characterized by moderate REE content, Eu negative anomaly and high HREE fractionation. The fine-grained granites show a composition similar to two-mica granites but low differentiation character and variable HREE fractionation due to their Y content. Porphyritic granites show composition similar to two-mica granites although with slightly more differentiated character and lower ferromagnesian elements and Th content.

- Aplite-pegmatites show a quite different composition, poor in ferromagnesian elements and richer in volatile elements and Mn. The REE pattern shows low REE content, Eu negative anomaly and low REE fractionation.

Like other S-type granites, the MMC granitic rocks do not show clear correlation between silica content and major or minor elements, indicating that the magmatic differentiation by fractional crystallization is not an important process of differentiation in these rocks. The only observed correlations are between ferromagnesian elements and HSFE, indicating that the entrainment of mafic components and accessory minerals in the melt is the most important process of differentiation in the MMC granitic rocks. The mafic components and HSFE content individualize diatexites and leucosomes (higher content) from two-mica granites (moderate content) from leucogranites (low content).

Also the LILE discrimination diagrams are liable to individualize the different MMC granitic rocks. Diatexites, leucosomes and leucogranites are characterized by the high Ba and Sr content, close to metatexites composition, revealing their low differentiated character. Two-mica granites show higher Rb content revealing a more differentiated character. However, the evident deviation of the trends, accepted as significant of increasing crystallization processes, suggests the occurrence of latter processes that altered the MMC granitic rocks. Hydrothermal processes seem to have affected two-mica granites as revealed by the K/Rb ratios. The differentiation in leucogranites seems to be more related with K-metasomatism as suggest the petrographic observations, the random distribution of K, the correlation between K and $CaO+Na_2O$, the lack of relation between K and Rb and the strong potassium enrichment relatively to silica variation, that accompanies these styles of alteration (Pirajno, 1992)

The major elements composition of MMC granitic rocks is similar to the major elements composition of two-mica granitic series of the Variscan Belt and to the Himalayan leucogranites. Concerning the composition of two-mica granites series of NW of Portugal the MMC two-mica granites show also similar major elements composition

although the minor and trace elements composition reflect some particularities, namely in what concerns the depletion in Fe, Mn, Na, Rb, U, Zr, Y, Nd and Ta and enrichment in Ba, Ti and V contents.

6.4. Chemical relations between SGC metasediments, metatexites and granitic rocks

6.4.1. Variation diagrams

The understanding of the sequence and processes of migmatite formation benefits from using the whole-rock chemical composition. This type of analysis, used for classification of rocks and interpretation of the petrogenetic context, in the case of migmatites and related anatectic granites can still have an important role in understanding the processes occurring during its formation, definition of the protolith composition and the various parts of neossome (Sawyer, 2008).

Most geological processes produce sets of rocks defining patterns or trends in the variation diagrams, because the processes advance in some lithologies more strongly than on others. To interpret these trend patterns is essential to obtain relations between the composition of the starting material and the composition of the final products to understand the changes that occur during the processes in the mineral paragenesis and modal proportions. The bivariate diagrams using an element that characterizes the residue *versus* an element representing the anatectic melt can provide information about the migmatization processes (Sawyer, 2008).

Figure VI.41 represents SiO_2 *vs.* Fe_2O_3 + MgO, SiO_2 *vs.* Na_2O + CaO, K_2O *vs.* CaO + Na_2O and Fe_2O + MgO *vs.* K_2O bivariate diagram used to interpretation of general sets and trends of granitic rocks and metatexites from MMC. One sample from SGC in staurolite-zone from Aguçadoura (the sample with composition most approximate to patch migmatites) was considered to represents the protolith (P) and *in situ* leucosomes were considered to represent the initial anatectic melt. Also the composition of experimental anatectic melts of pelitic protolith was plotted for comparison (Sawyer, 2008).

SiO_2 *versus* Fe_2O_3 + MgO diagram (Fig. VI.41A) shows that two metatexite samples (FM23 and FM4) and the patch-migmatites represent residual metatexites showing

higher concentration in ferromagnesian minerals and lower SiO_2 content than the protolith. The other banded-metatexite samples show depletion in ferromagnesian minerals and increase in silica content. These results are compatible with petrographic observations since the residual samples show high concentration in biotite, sillimanite and cordierite and darker colour than the other banded-metatexites. Metatexites follow the trend for anatectic melt + residuum that goes from protolith to granitic rocks which suggests a continuous relation between metatexites and the granitic rocks in MMC. The greywacke and calc-silicate resisters have compositions that fall outside the protolith field and do not follow the same trend as metatexites. Diatexites and two-mica granites are concentrated around the leucosomes and thus are considered typical anatectic melts (Sawyer, 2008). Comparing to experimental anatectic melts the MMC granitic rocks are less SiO_2 rich and show slightly higher ferromagnesian content.

SiO_2 *versus* Na_2O + CaO diagram (Fig. VI.41B) shows that within metatexites there is no coherent correlation between the silica content and the alkalis content. Within granitic rocks also there is no correlation between silica and alkalis content but there is a tendency of leucogranites to concentrate melt-produced plagioclase or quartz (especially those cropping-out in distal sites) relative to other lithologies.

K_2O *versus* CaO + Na_2O and K_2O *versus* Fe_2O_3 + MgO diagram (Fig. VI.41C) show enrichment in residual plagioclase in metatexites. All the granitic rocks plot in the field of melts contaminated with residuum, except one sample of leucogranite that show K enrichment relatively to leucosomes. The K_2O content in leucogranites is variable although with tendency to correlate with CaO + Na_2O content. In the samples containing < 4 wt% of K_2O (blue line in the diagram) K-feldspar is absent or is very rare. That includes metatexites, diatexites and leucogranites.

In summary the metatexites show both a residual character (PMM, FM23 and FM4 samples) with enrichment in biotite, cordierite and rarely garnet (only in the rare Ca-rich pelitic layers – sample VC32c) or enrichment in plagioclase and quartz relative to protolith. The former reflect melt segregation and the latter melt accumulation. The zone of melt segregation is mostly detected in Vila Chã, near the Mindelo leucogranites. The diatexites and two-mica granites show a composition similar to anatectic melts since they do not differ greatly from leucosomes, although with tendency to slightly accumulate melt produced plagioclase. The leucogranites show higher scattering with tendency to accumulate melt produced plagioclase and quartz. None of the diagrams follow the trend of fractioned melts.

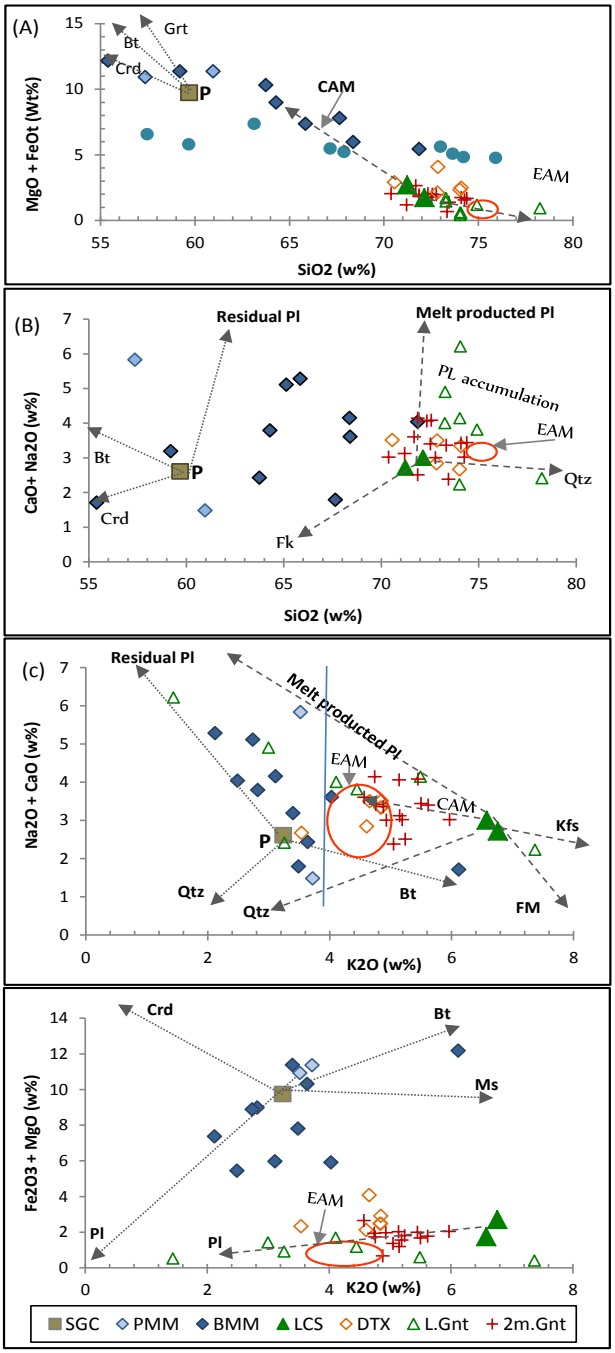

Fig. VI. 41 – Diagrams plotting compatible *vs.* incompatible element. A SGC sample was considered to represent the protolith (P) and *in situ* leucosomes were considered to represent the initial anatectic melt. Abbreviations: FM - trend of fractional melts; CAM – trend of melts contaminated with residuum; EAM – field of experimental anatectic. Legend Key: SGC – sample from Schist-Greywacke Complex; PMM – patch-metatexites; BMM – banded-metatexites; DTX – diatexites; LCS – leucosomes; L.Gnt – leucogranites; 2m.Gnt – two-mica granites.

6.4.2. Multielement diagrams

Figure VI.42 represents a multielement diagram where the average composition of the MMC rocks was normalized to the staurolite-schist from Aguçadoura. It is clear the similarity in the composition between the SGC sample and the pelite metatexites average composition. However there are a slight enrichment in Mg, Mn, Th, Nb and Ta content and depletion in Na, V and Y content in metatexites.

The granitic rocks show in general lower Mn, Ta, Nb, ferromagnesian and HSF elements than the protolith and the metatexites. The diatexites, leucosomes and leucogranites show similar content in Ba, Sr and Rb to the metatexites, although diatexites show higher Ca and Sr content. Two-mica granites *s.l.* show the lower Ca and Sr content and K, Rb, Na, U, Nb and Ta enrichment relatively to the other lithologies (except tourmaline-bearing leucogranites and aplite-pegmatites).

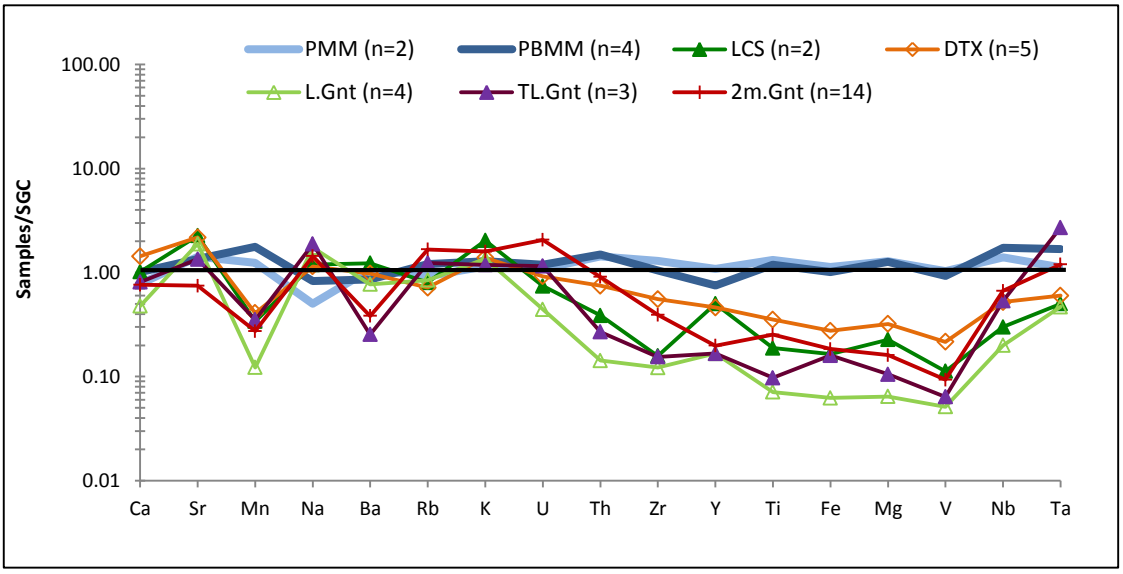

Fig. VI. 42 – Multielement diagram with values moralized to staurolite-schist sample for average composition of MMC Rocks. Legend Key: PMM – patch-metatexites average; BMM – banded-metatexites average; DTX – diatexites average; LCS – leucosomes average; L.Gnt – leucogranites average; TL.Gnt – tourmaline-bearing leucogranites average; 2m.Gnt – Two-mica granites *s. l.* average.

6.4.3. Rare Earth Elements

Figure VI.43 represents the REE patters for each lithological type average, where is well reflected the specificity of the REE patterns of diatexites, leucogranites and two-mica granites *s.l.*.

The REE content of granitic rocks is lower than that of metatexites. Diatexites, leucosomes and leucogranites show REE fractionation similar to metatexites but very distinct Eu anomaly. Two-mica granites *s.l.,* show Eu negative anomaly but larger HREE fractionation.

Figure VI.44A represents binary diagram related ferromagnesian content with total REE content. As referred before the REE total content of all the MMC lithologies are related with the mafic components (biotite). Two-mica granites also show this positive correlation but it is notorious the abrupt enrichment in Th that does not follow the trend of other lithologies. These observations are better reflected in the Sc vs. Th/Sc diagram (Fig. VI.44B) where is notorious the abrupt enrichment in Th relatively to Sc. However the LREE content of two-mica granites and diatexites is similar. In migmatites the LREE fractionation is directly correlated to Th content (r^2=0.6) and HREE content is inversely correlated with the Y content (r^2=0.7). However, in two-mica granites no correlation is observed. This suggests that Th in two-mica granites is not exclusively associated with monazite. This could be related to the fact that monazite and zircon commonly have different average grain size, and probably monazite was preferentially dissolved in two-mica granites since the differential flux of trace elements into the melt during dissolution of accessory phases is a function of dissolution rate and surface area, which are correlated to grain size and the degree of under-saturation of the melt with respect to the element(s) concerned (Watson, 1996). Magmatic xenotime is a possible Th containing mineral as well as U in the two-mica granitic rocks.

The distribution of yttrium, rare-earth elements (REEs), zirconium, and hafnium may be used to verify whether Y, REEs, Zr, and Hf in rocks or minerals have been deposited from pure silicate melts or modified by aqueous fluids (Bau, 1996). Unlike other magmatic rocks, highly evolved magmas are rich in components such as H_2O, Li, B, F, P, and/or Cl and often show non-chondritic Y/Ho and Zr/Hf ratios and reveals that non-CHARAC (CHARAC: charge-and-radius-controlled) trace-element behaviour prevails in highly evolved magmatic systems. Fluid metasomatism (specialy F–rich fluids) has been proposed to account for nonchondritic Zr/Hf values in granitic rocks

(Bau, 1996; Veksler *et al*., 2005), but other authors maintain that this ratio can be explained by crystal fractionation (Pan, 1997).

Figure VI.44D represents the Y/Ho vs. Zr/Hf diagram for MMC rocks and SGC pelitic samples. The most marked feature observed in the diagram is the overlap between SGC samples, metatexites and granitic rocks from MMC and the proximity to CHARAC values, if compared to fractionated/evolved granites (e.g. Eibenstock granite pluton, Calamity Peak pluton, Pleasant Ridge Granite).

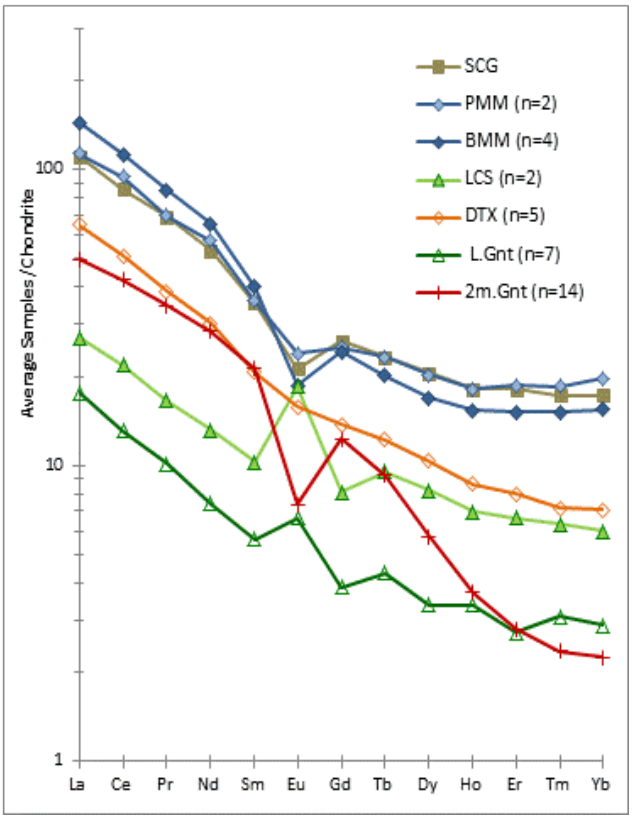

Fig. VI. 43 - Rare Earth Elements pattern diagrams normalized to Chondrite (Boynton, 1984) to Schist-Greywacke Complex and MMC rocks averages. Legend Key: SGC – Schist-Greywacke Complex from Aguçadoura; PMM – patch-metatexites average; BMM – banded-metatexites average; DTX – diatexites average; LCS – leucosomes average; L.Gnt – leucogranites average; TL.Gnt – tourmaline-bearing leucogranites average; 2m.Gnt – Two-mica granites *s. l.* average.

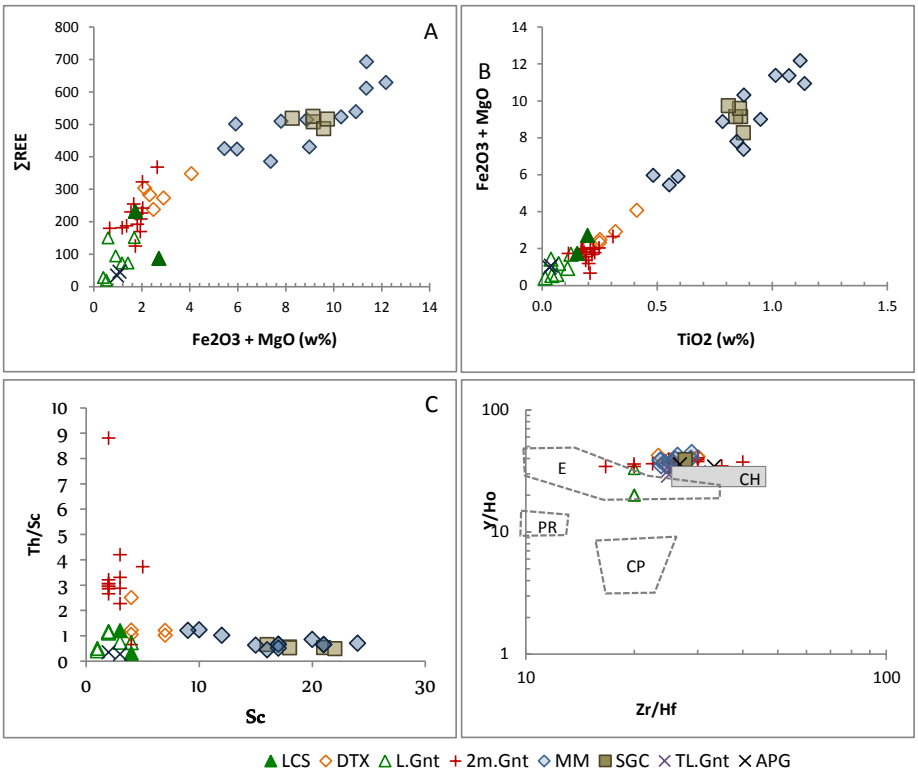

Fig. VI. 44 – Variation diagrams for MMC granitic rocks, relating A and B) ferromagnesian elements to REE and TiO_2. C) Th/Sc and Sc; D) Y/Ho vs. Zr/Hf; Abbreviations: E - Eibenstock granite pluton; CP - Calamity Peak pluton; PR - Pleasant Ridge Granite. Legend; Key: LCS – leucosomes;. DTX – diatexites; SGC –Schist-Greywacke Complex pelitic samples; L.Gnt – leucogranites; 2m.Gnt – Two-mica granites; MM – metatexites.

6.5. Geochemical characteristics and anatectic processes

One of the most distinctive aspects of the MMC granitic rocks is their lithological, mineralogical and textural variation, the lack of evidence of magmatic differentiation by fractional crystallization, the low ferromagnesian, Ta-Nb and HSF elements content and the positive correlation between mafic components and HSFE and REE.

Melting experiments performed by Garcia-Arias *et al*. (2012) have shown that two protoliths of virtually the same major and trace-element composition yield melts showing different trace-element composition at the same P-T-%H_2O conditions. The reason resides in the different solubility of accessory phases. In felsic rocks, the main trace elements are hosted in accessory phases rather than in major phases (Watson et al., 1989; Wolf & London, 1994; Bea, 1996, 1999). Rb, Sr and Ba, other trace elements

of petrogenetic interest, are incorporated by major phases (Harris and Inger, 1992; Bea, 1996). It was verified that the mineral phases release their trace-element content proportionally to their melting ratio. Other experimental studies show that melts formed by partial melting of crustal material at T: 800°C have relatively low FeO and MgO contents (Johannes & Holtz, 1996). Most crustal melts generated at these "low" temperature conditions (%H_2O and P have much less influence), have a leucogranitic composition, except for those melts carrying residuum minerals. Experimental peraluminous melts generated at higher temperatures (T=850-950°C), have higher FeO, MgO and CaO contents reaching monzogranite/granodiorite composition, although controlled by the chemistry of the protolith (Johannes & Holtz, 1996).

Considering that MMC granitic rocks are the result of melt segregation from a pelite protolith, lower ferromagnesian and HSFE contents relatively to both metatexites and two-mica granites from NW of Portugal should be expected and could be explained by the retention of biotite, zircon, monazite and other accessory minerals in the residual phases. The other anatectic two-mica granites from NW of Portugal probably underwent much higher melt-rate and consequent incorporation of ferromagnesian and heavy minerals than the granitic rocks from MMC.

The Mn and Y lower content of all the MMC granitic rocks (exception for aplite-pegmatites) could be related with the same process since Mn and Y are widely distributed as accessory elements in garnet and this mineral is mostly associated with the melanosomes, being rare in the granitic rocks.

Ta and Nb low content are influenced by two factors – in diatexites, leucosomes and tourmaline-absent leucogranites is exclusively related with the ferromagnesian elements content what suggests the retention of these elements in rutile associated with biotite and to the residual phase - the same processes that influenced the other HSFE content. However, tourmaline-bearing leucogranites, although showing major and HSF elements contents similar to the tourmaline-absent leucogranites show an increase in Nb and Ta content and a low Nb/Ta ratio (2.5 in average). The high Ta content of tourmaline-bearing leucogranites and aplite-pegmatites correlates positively with Rb. This suggest that an addition of internally derived fluids played a key role in the variation of the Nb/Ta ratio since generally granitic rocks show a positive correlation between Ta and Rb, Li and F that are strongly enriched in the evolved rocks (Dostal & Chatterjee, 2000). Two-mica granites from MMC show low Ta and Nb content relatively to the two-mica granites from NW of Portugal due to the anatectic process and retention in residua. The higher content relatively to the other MMC granitic rocks

is due to hydrothermal differentiation and higher melt ratio, *i.e.* both processes could have actuated in these last rocks.

The high V, Ti and Ba content in all the MMC granitic rocks probably relates with characteristics of the protolith since SGC metasediments and the metatexites also show enrichment in these elements.

These observations reinforces the hypothesis that the MMC granitic rocks resulted from anatectic processes with variable melt-rate but still in intimate association with the metasedimentary protolith. Thus, the chemical and mineralogical dissimilarity between the MMC granitic rocks could result from their derivation from different crustal levels, different fusion rates and/or different melt segregation process rather than from a marked difference in the source lithologies involved.

The relationship between MMC granitic rocks, metatexites and SGC is suggested by several geochemical characteristics, namely:

- The SGC samples and metatexites similar composition;
- The Ba – Rb - Sr overlap between SGC samples and metatexites, diatexites, leucosomes and leucogranites (Sr is slightly lower in SGC pelitic samples due to its low Ca content). Two-mica granites and tourmaline-bearing leucogranites show higher Rb content and lower Ba content.
- The SGC samples Y/Ho and Zr/Hf composition overlaps the MMC lithologies composition.
- The continuous differentiation between MMC granitic rocks, metatexites and SGC samples in what concerns HSFE.
- All the differences between SGC samples/metatexites could be explained by the anatectic processes and/or fluids entrainment that are corroborated by the field relations and petrological observations.

It is likely that a first fluid-present melting pulse took place in MMC and produced most of the leucogranites and leucogranite-veins. This hypothesis is corroborated by the following observations:

- The leucogranite chemical composition, namely the high HSFE depletion relatively to metatexites and the distinct REE patterns can be produced by removal of leucosome before complete equilibration due to the inhibited dissolution of accessory phases (Watt *et al*., 1996) and are expected in leucosomes formed

during the early stages of segregation and extraction (Brown, 2013). Evidence for channelized flow and deformation-enhanced melt segregation on an outcrop scale is present all over the MMC, where melt migration occurs over several distances.

- Leucogranites (and *in situ* leucosomes) show high variability in the K_2O content and consequent heterogeneity in K-feldspar abundance. The K content is inversely correlated with Na_2O+CaO content is reflected in the replacement of plagioclase by K-feldspar in these lithologies. The SGC metasediments and consequently most of the migmatites are poor in potassium and phosphorous. So, the few K-bearing metatexites cannot be identical in composition to the primary rock; an addition of potassium must have taken place. This indicates that locally, in structurally controlled zones, occurred K-diffusion that metasomatized some leucogranites and metatexites. Thus, the initial melt composition was essentially trondhjemite and became granitic by large-scale K-diffusion. Several authors postulate that K-poor leucosomes formed preferentially by H_2O fluxed melting of mainly plagioclase and quartz (*e.g.* Patiño Douce and Harris, 1998. Conrad *et al*. 1988; Garcìa-Casco *et al*. 2001, Jung, 2005; Zeng *et al*., 2005b).
- Fluid-present melting, which mainly consumes plagioclase and minor amounts of mica, will produce strong Sr enrichment and marked Rb and Ba depletion (Harris and Inger, 1992). MMC leucogranites are characterized by low Rb/Sr values, much lower than the two-mica granite values (average Rb/Sr = 1.07 and 4.44 respectively) and higher Ba/Sr values (average Ba/Sr = 0.38 to leucogranites and 0.22 to two-mica granites).
- The positive Eu anomaly observed in most leucosomes and leucogranites also argues in favour of prevailing fluid-present melting, inasmuch as fluid-absent melting is known to have negative Eu anomalies (Harris and Inger, 1992).
- It was proposed (Brown, 2013; Milord *et al*., 2001) that mica-bearing leucosomes without incorporation of peritectic minerals in mica-bearing hosts are more likely to be the product of fluid-present melting whereas leucosomes that carry nominally anhydrous (peritectic) minerals, such as cordierite, garnet or pyroxene, are more likely to be a product of fluid-absent hydrate-breakdown melting. In fact, as previously referred, the leucosomes and leucogranites are cordierite free (unlike diatexites).
- Fluid-absent melting experiments in low-pressure conditions indicated that the production of pronounced amounts of melt at low-P and beyond 800º ºC requires the presence of a fluid phase during partial melting (Spicer, 2011).

So, it is suggested that leucogranites result from fluid-present melting in the first stages of migmatization, involving essentially quartz and plagioclase through the reaction:

$$Qtz + Pl + H_2O = Melt \quad (1)$$

The melt produced was rapidly segregated and crystalized in dilatant sites north and south of the metatexite zone and in veins across the metasedimentary sequence and the metatexite zone.

The fluid source for this first melt could result from the aqueous fluid already in the pores, leads to water saturated melting, at least initially or to water-added melting due to infiltration of H_2O (as an aqueous fluid) into hot rocks (Sawyer, 2010). Oxygen isotopes studies show that the source for infiltrating fluids could be basically metamorphic water (δ18O unchanged) (Scaillet *et al.,* 1996; Sawyer, 2010) or basically seawater (δ18O reduced) (Wickham & Taylor, 1987; Holloway *et al.,* 2008).

The availability of water for melting reactions decreases since water is rapidly dissolved into the melt (Sawyer, 2008). Thus, and in agreement with the observed textures, the migmatization continues by fluid-absent biotite breakdown reactions (Brown, 2008; White, 2008):

$$Bt + Pl_1 + Sil + Qtz = Crd + Pl_2 (\pm Kfs) + Melt \quad (2)$$

$$Bt + Sil + Qtz = Crd + Kfs + Melt \quad (3)$$

These reactions take place in relatively shallow crustal levels. The peritectic cordierite and the absence of peritectic garnet or ortopyroxene (either in metapelites or in metagreywackes) indicate that melt occurred at $P < 4$ Kbar and $T < 760$ ºC (assuming that chemical equilibrium is attained; White, 2008).

The diatexites show mineralogical and chemical composition coherent with *in situ* partial melting containing all the same mineral phases as the banded-metatexites but the leucosome/melanosome ratio is much higher with consequent relatively low ferromagnesian elements and HSFE content. They show the sequential evolution from low melt-fraction metatexites to high melt-fraction diatexites. The absence of resisters within diatexites and its higher Ca content (higher than metatexites) is an outcome of calc-silicate metagreywackes incorporation in their composition, which gives them a calc-alkaline character. This suggests that the melting temperature and consequently the melting rate were probably higher for diatexites than metatexites. The abrupt contacts between diatexites and metatexites suggest that the diatexites intruded metatexites and have been formed at deeper levels. However the P-T conditions and

melting reactions of diatexites and migmatites formation were not much different since the mineralogy is identical.

In MMC several factors must be taken into account with regard to the relationship between two-mica granites and migmatites:

- Two-mica granites have a truly intrusive character: there are numerous sills, dikes and other bodies of two-mica granites which cut the migmatite rocks and incorporate migmatite xenoliths;
- The mineralogical and chemical composition of two-mica granites is different from that of migmatites and leucogranites. The former have andalusite which is absent in migmatites and have more K-feldspar and apatite. Cordierite is present in migmatites but not in two-mica granites. This is reflected in the chemical composition since two-mica granites show a different REE, higher K and P content and Rb/Sr ratio. This could indicate a different protolith or a different anatectic process.
- The content in rubidium, which is quite independent of that of potassium, is similar to the hydrothermal pegmatitic trend of Shaw (1968) and may be an indication of the part played by a fluid phase during the late history of the granite.

It is known that at low *P* (below ≈ 3.5 Kbar) only biotite breakdown melting reactions occur, as muscovite is typically consumed in subsolidus conditions (Holland & Powell, 2002; White, 2008; Spicer, 2011). However, at deeper levels (about 5 kbar) muscovite persists at higher temperature and both muscovite and biotite melting reactions occur with rising temperature. So, the anatectic processes at deeper levels could result of the muscovite breakdown reactions at moderate P (White, 2008):

Ms + Pl + Qtz = Als + Kfs + Melt (3.5 < P < 6 Kbar; T < 800 ºC) (4)

This reaction generates large amounts of melt showing the typical mineralogical and chemical composition of MMC two-mica granites. This is confirmed by the enrichment in Rb and depletion in Sr and Ba relatively to the metasedimentary protolith, characteristic of melts generated by incongruent melting of muscovite under fluid-absent conditions (Harris & Inger, 1992).

The textures and geochemistry of the MMC rocks suggests that multiple fluid pulses affected the MMC in subsolidus conditions: a first pulse with K-bearing fluids, a second pulse with boron-bearing fluids and a third pulse containing silica-bearing aqueous-fluids.

The K-bearing fluids aforementioned affected all the MMC lithologies and caused structurally controlled sub-solidus K-metasomatism. This is suggested by:

- Presence of K-feldspar in some metatexites and spatially associated calc-silicate rocks and absence in adjacent metatexites. The same occurs in some leucogranites that show much higher K-feldspar modal content and abrupt enrichment in K content.
- The textures observed in these metatexites and leucogranites. In fact, all the leucosomes and leucogranite samples containing K-feldspar show textural evidence of plagioclase replacement by K-feldspar, namely K-feldspar in cores of plagioclase crystals, occurrence of plagioclase inclusions in K-feldspar which are in parallel optical continuity with plagioclase outside of the K-feldspar and K-feldspar development in miarolitic cavities, etc. (Chapter III).
- The two-mica granites wall rocks (SGC metasediments) are poorer in potassium (~3,3 wt.%) and usually their only potassium-rich mineral is biotite. Therefore, the huge amounts of potassium-rich granite (~ 5,2 wt.%) cannot result exclusively from segregations *in situ.* Like leucosomes and leucogranites, some two-mica granites and diatexites also show replacement of plagioclase by K-feldspar. There are two types of k-feldspar crystals: one type is magmatic (euhedral to subhedral) and the other is anhedral always replacing plagioclase. Besides, Na_2O+CaO and K_2O content are uncorrelated. This is due to the different anatectic processes that originate these last lithologies: they incorporate all the components resulting from anatectic reactions plus restites, while leucogranites resulted from melt segregations. Also the diatexite and two-mica granite resulted from higher melting rate and formed in deeper levels. So it is likely that two-mica granites and diatexites include both K-feldspar resulting from micas breakdown and also later K-feldspar resulting from K diffusion.

The occurrence of leucogranites and two-mica granites showing localized replacement of biotite by tourmaline, late tourmaline in the metasediments and the occurrence of aplite-pegmatite veins with abundant tourmaline suggest that latte boron-rich fluids also affected the MMC and surrounding metasedimentary sequence. These fluids are

unrelated to those with K since there are tourmaline-bearing lithologies without K-feldspar. The rocks affected by these fluids show abrupt enrichment in Ta, Nb and Rb and depletion in Ba relatively to the unaffected adjacent rocks.

The entrainment of later silicate aqueous fluids is inferred from: i) the muscovitization of tourmaline, biotite and plagioclase all over the MMC; ii) presence of quartz-veins cutting all the lithologies; iii) large quartz-crystals bands in some calc-silicate rocks that include all the minerals of the rock; iv) retrograde alteration of staurolite, andalusite and biotite in the metasedimentary sequence.

CHAPTER VII – FLUID INCLUSION

Geology is the study of pressure and time. That's all it takes really, pressure and time.

Red (Morgan Freeman) in movie *The Shawshank Redemption*.

``. . . and I argue that there is no necessary connection between the size of an object and the value of a fact, and that, though the objects I have described are minute, the conclusions to be derived from the facts are great."

H.C. Sorby (1858)

7.1. Introduction

Already in the XVIII century the presence of fluid inclusions in minerals was observed and used by Neptunists in support their theory. Later (in the mid-1800s) Henry Clifton Sorby microscopic studies revealed the presence of small fluid-filled cavities in minerals that were considered relics of the fluid phase which intervened in the genetic process of the host mineral and became trapped in a given moment in its history.

Technological advancements (heating-freezing stages) promote accurate studies that revealed the importance of the fluid inclusion studies as a method which, in conjunction with others, allows a better understanding of the geologic history and the evolution of a given lithotype.

During the last two decades, petrologists have directed increasing attention to the role of fluids in metamorphic and migmatitic terranes (e.g. Touret, 1977, 1981, 1985, 1986, 2001; Lamb *et al.,* 1987; Newton, 1992; Giorgetti *et al*., 1996; Guedes, 2001, Byn Fu *et al*., 2001; Guedes *et al*., 2002; Cesare *et al*., 2007; Kerkhof *et al*, 2014).

Fluids are especially important in high-grade metamorphic environments because it can lower a rock's melting point (Arzi, 1978; Ashworth, 1979). Moreover, the fluid amount and composition will control the temperature of initial melting, the amount of melt produced and the temperature of melt crystallization. In addition, the study of fluid inclusions may give an indication as to whether fluid-absent or fluid-present conditions dominated during partial melting. Indeed, it is important to determine whether anatexis occurs by dehydration melting, in which fluids are released by the breakdown of

hydrous minerals such as muscovite, biotite and hornblende (vapour-absent melting), or whether a free fluid, migrating in the middle and lower crust, played an active role during metamorphism (vapour-present melting) (Touret, 1981, 1985; Lamb & Valley, 1987; Newton, 1992).

Of additional interest are the trapping conditions of any later fluids that infiltrated the area after peak metamorphism. Such secondary fluid inclusion data may help to delineate the path followed during decompression and cooling.

As the fluid inclusions are the only direct fluid samples from which the host crystal grew, their study is conditioned on five fundamental assumptions (Roedder & Bodnar, 1997):

- The trapped fluid is representative of an homogeneous solution;
- The inclusion behaves as a closed system and, once trapped, the fluid cannot be modified;
- The volume of the cavity around the fluid inclusion neither increases nor decreases after imprisonment;
- The relation between the geological event and the trapping is identified;
- The pressure effects are negligible or known.

Methods of investigation

In any fluid inclusion study three successive steps are required: observation, measurement and interpretation. These steps should be carefully evaluated and planned (Touret, 2001).

There are several methods to study fluid inclusions. The present work was based on petrographic observations, microthermometry and Raman microspectroscopy.

A fluid inclusion petrographic study, requiring any other instrument than a conventional petrographic microscope, is the first and an essential step to stablish the temporal relationship between the different fluids, the fill degree of inclusions and evaluate whether the inclusions are suitable for fluid inclusions studies (Kerkhof, 2001, 2014).

Next to petrographic examinations, microthermometry is the most important analytical technique for characterizing fluid inclusions. It involves measuring, under the microscope, the temperatures at which phase-transitions are observed to occur in fluid inclusions.

The microthermometric measurements are performed in the range of -180 to +20 ºC (cryometry) and +20 to +600 ºC (thermometry). Among the temperatures that can be recorded, two are particularly important: the melting temperature (Tm - solid to liquid) and the homogenization temperature (Th - liquid to vapor or vice-versa). The homogenization temperatures allow, with the help of PVT diagrams, determine the density of the fluid trapped and the melting temperatures allow the determinations of fluids composition. For example, the extent to which the melting point of ice is depressed provides an indication of the bulk salinity of the inclusions.

A homogeneous fluid of a specified composition has a certain density for a given temperature and pressure. If the fluid is trapped in a closed cavity, its volume and mass will always remain constant, as the density, thus maintain its original value. If the fluid remains homogeneous, any further developments after its entrapment will happen at constant density. Thus it is possible trace a line in the PT diagram that represents an isochore, i.e. a line of equal density for each PT pair conditions.

Thus, microthermometry is a method to obtain melting and homogenization temperature data from which it is possible to calculate the salt composition or the density of the trapped fluids. The delimitation of variation of PT real trapping conditions can be obtained by the method of intersection of isochores (inclusions considered synchronous) or by intersection with geothermometers and/or geobarometers based in the mineral paragenesis.

In the analysis of fluid inclusions, Raman microspectroscopy is mostly used for identification of gases and solids in the inclusions but it is also a quick method of host mineral identification. In addition to the qualitative identification of different gas species Raman spectroscopy can also be used to calculate the composition of some the gases. Of all the components of fluid inclusions only a limited number of species can be quantitatively analysed by Raman microspectroscopy, in particular polyatomic gas phases, and some polynuclear phases in solution (Burke, 2001).

Genetic classification of fluid inclusions

Genetically, the fluid inclusions can be classified as:

- Primary: those which constitute a fluid present at the time of the mineral crystallization**.** Fluid inclusions of primary origin will occur as a single inclusion (or isolated group) in an otherwise inclusion free crystal;
- Secondary: those whose entrapment is evidenced by, for example, a period of fracturing or recrystallization; generally occur along a healed fracture or in trails

along planes that cross cut several crystals (transgranular trails), or are parallel to the mineral cleavages;

- Pseudo-secondary: those that have appearance of secondary but a meaning similar to the primary inclusions because they represent filling of fractures that occurred during the growth of the mineral. It occurs in alignments that are confined to the limits of the crystal (intergranular trails).

Diagnostic criteria for classifying genetically the fluid inclusions as primary or secondary have been proposed by Roedder (1979). When these terms are applied to massive rocks may be misleading as primarily grown minerals that are not generally preserved. In this case the terms “early” versus ”late” are more suitable for characterizing the trapping chronology. For that reason, in massive rocks, fluid inclusions can be mainly subdivided in, (i) isolated, (ii) clustered, and (iii) in trails essentially healing microcracks (Kerkhof, 2001).

7.2. Sampling and methodology

Three samples (FM19, VC51, and FP21) were selected in order to carry out the fluid inclusion studies. Sample FM19 is an *in source* leucosome that crops out in Vila Chã, at the coordinates point 462. Sample VC52 is a tourmaline-bearing leucogranite cropping out in Vila Chã, at the coordinates point 503. Sample FP21 is a two-mica granite from Vila do Conde cropping out at the coordinates point 575 (see Appendix A for coordinates points).

The fluid inclusion studies were performed in quartz. Fluid inclusion petrography, microthermometric and Raman microspectroscopy analyses were performed at the laboratories of Centro de Geologia da Universidade do Porto (CGUP), in doubly-polished wafers of about 150 µm thick. Microthermometric characterization of the fluids was performed using a calibrated Chaixmeca heating-freezing stage (Poty *et al*., 1976) for cryometric analyses, and a calibrated Linkam THMSG 600 heating-freezing stage (Shepherd *et al*., 1986) for the thermometric studies. Calibration was conducted using pure CO_2 inclusions in quartz from Calanda, Switzerland and synthetic H_2O fluid inclusions standards at T≤0ºC with melting-point standards at T>25ºC. The accuracy was ±0.1 °C during cryometric measurements and ±1 °C during heating. The degree of filling (volume of liquid phase/total volume – Flw) was estimated optically at room temperature by using volumetric charts proposed by Roedder (1984) and Shepherd *et al.* (1985). Molar fractions of CO_2, CH_4 and N_2 were determined by Raman

microspectroscopy analyses in selected individual inclusions using a Labram Dilor-Jobin Yvon Spectrometer attached to an Olympus microscope. The excitation source was a He–Ne laser with 632.8 nm wavelength operated at 20 mW. The quantification of the different species in the inclusions was obtained using a computer program developed at CGUP that follows routine procedures described by Prieto *et al*. (2012). Aqueous fluid salinity (expressed as equivalent wt% of NaCl) was calculated using the temperature of last ice melting and the equation of Bodnar (1993). Bulk composition of both types of fluids was calculated using the computer program package FLUIDS-1 (Bakker, 2003). Isochores for the non-aqueous fluids were calculated using Bakker (2003) software and the state equations of Flowers (1979). The isochores for the H_2O-NaCl inclusions were calculated from the equation of state of Knight & Bodnar (1989).

7.3. Microthermometric and Raman data

Based on its morphology, number of phases (at room temperature) and phase behaviour on cooling, four major types of fluids have been recognized in the studied samples: (i) N_2-CO_2-CH_4; ii) N_2-CH_4; iii) CO_2-N_2, and iv) aqueous fluids (H_2O-NaCl). Microthermometric and Raman microspectroscopy data are reported in Appendix D.

7.3.1. Leucosome - FM19

Sample FM19 is an in source leucosome, *i.e.,* the product of anatectic melt that has migrated away from the place where it formed but still within the confines of the source layer (Fig. III.6C). It is essentially composed of coarse-grained quartz + plagioclase + K-feldspar and contains dispersed fragments of restitic biotite + sillimanite (Fig. VII.1). K-feldspar is abundant (~38% in modal composition) and englobe all the other minerals as inclusions. The later alteration processes were limited to biotite muscovitization. The solid state deformation was not very intense although some quartz crystals evidence slightly ondulose extinction and K-feldspar crystals show incipient flame-perthites. The studied quartz shows subhedral to anhedral coarse-grains (1 to 4 mm). Its morphology and texture point to a magmatic origin. However, taking in account the lithology, some of this coarse quartz grains may have grown from fine-grained crystals nucleated in the metamorphism process. This is also suggested by the numerous round quartz inclusions in leucosome plagioclase and K-feldspar crystals.

Fig. VII. 1 –Thick double-polished section of sample FM19

At room-temperature this sample is essentially characterized by the presence of monophasic and two-phase liquid+vapour (L+V) aqueous fluid inclusions trapped in quartz (Fig. VII.2 to VII.4)

Monophasic inclusions were observed in intragranular trails (Simmons & Richter, 1976; Kranz, 1983), which never cross-cut quartz grain boundaries, and occasionally isolated. They are mainly polygonal to ellipsoidal in shape; ranging in size from 2 to 17 µm (av. 13.1 µm). Even though the inclusions look like monophasic, a presence of a thin film of liquid (not visible under the microscope) cannot be excluded.

The two-phase aqueous inclusions occur in clusters associated with the monophasic inclusions and in alignments that cut the previous intragranular trails.

Monophasic inclusions

The monophasic inclusions show two sub-types (Fig. VII.10 and VII.15):

- Mixed N_2 - CO_2 - CH_4- inclusions. N_2 is the dominant specie in the volatile phase ranging from 55.6 to 72.3 mole%, CO_2 content ranges from 15.1 to 29.1 mole% and CH_4 from 12.6 mole % to 16.5 mole %. In some inclusions it can be observed separation of N_2 gas and liquid in the presence of solid CO_2 when cooled to T< -150ºC The partial-homogenization temperatures ($Th_{partial}$) occur majority in the vapor phase but some inclusions homogenize in the liquid phase ranging from -132.9 to -132.4 and -135.8 to -133.2 °C, respectively. The final melting temperatures (T_m) range from -78.6 to -64.9 ºC.
- N_2-CH_4 inclusions showing $Th_{partial}$ in the range of -134.4 to -131.6 °C, all in the vapor phase. N_2 is also the dominant specie in the volatile phase ranging from 68.8 to 88.8 mole%.

Aqueous two-phase inclusions

The aqueous two-phase (H_2O-NaCl) inclusions in sample FM19 occur (Figs. VII.11 and VII.17):

- Dispersed in clusters and associated with the monophasic inclusions. The inclusions size varies between 5 and 12 µm and show a degree of filling varying from 0.70 to 0.95. Ice melting temperatures (Tm_{ice}) lie between -5.5 and -3.4 ºC corresponding to salinities of 5.6 to 8.6 eq. wt.% NaCl (average of 7.8 eq. wt.% NaCl). In this type of fluid inclusions the total homogenization (Th_{total}) occurs always in the liquid phase between 144 and 257 ºC (average of 204ºC).
- In intragranular trails showing regular shapes. The inclusions range in size from 5.4 and 27 µm (av. 11 µm) and show a degree of filling from 0.90 to 0.95. Ice melting temperatures lie between -2.2 and -1.8 ºC which corresponds to salinities of 3.1 to 3.7 eq. wt.% NaCl (average of 3.5 eq. wt. % NaCl). Total homogenization (to liquid) occurred between 164 and 208 ºC (average of 186ºC).
- In trails that cut the previous intragranular planes. These inclusions display irregular shapes, a degree of filling (Flw) varying from 0.70 to 0.95. Tm_{ice} lie between -0.7 and -0.4 ºC which corresponds to salinities of 1.2 to 0.7 eq. wt.% NaCl (average of 0.9 eq. wt.% NaCl). Temperatures of total homogenization (into liquid) range from 161 and 312 ºC (average of 245ºC). It was not possible confirm if the last type of inclusions cross-cut grain boundaries. However, its later origin relatively to the monophasic and two-phase inclusions clustered in intragranular trails is evident**.**

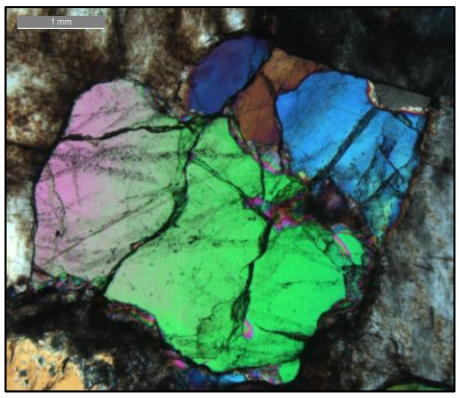

Fig. VII. 2 – Photomicrograph of the quartz from leucosome (FM19) showing fluid inclusions intragranular trails

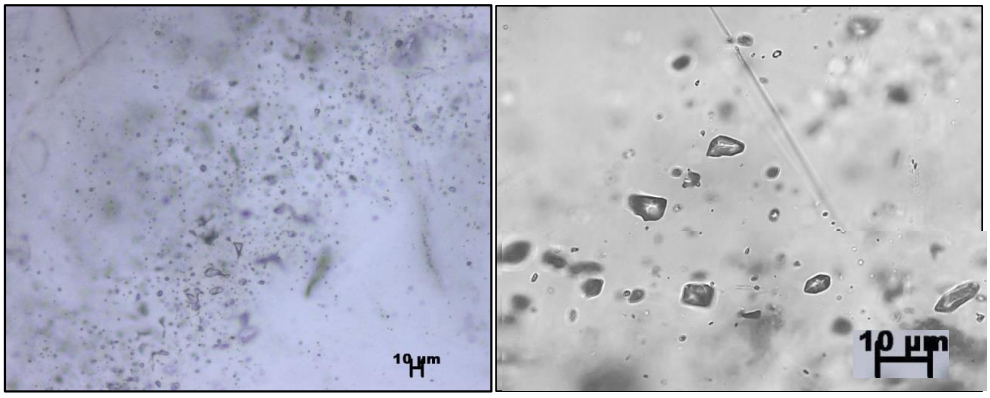

Fig. VII. 3 – Photomicrograph of the pseudo-secondary clusters of monophasic and two-phase inclusions in quartz from leucosome.

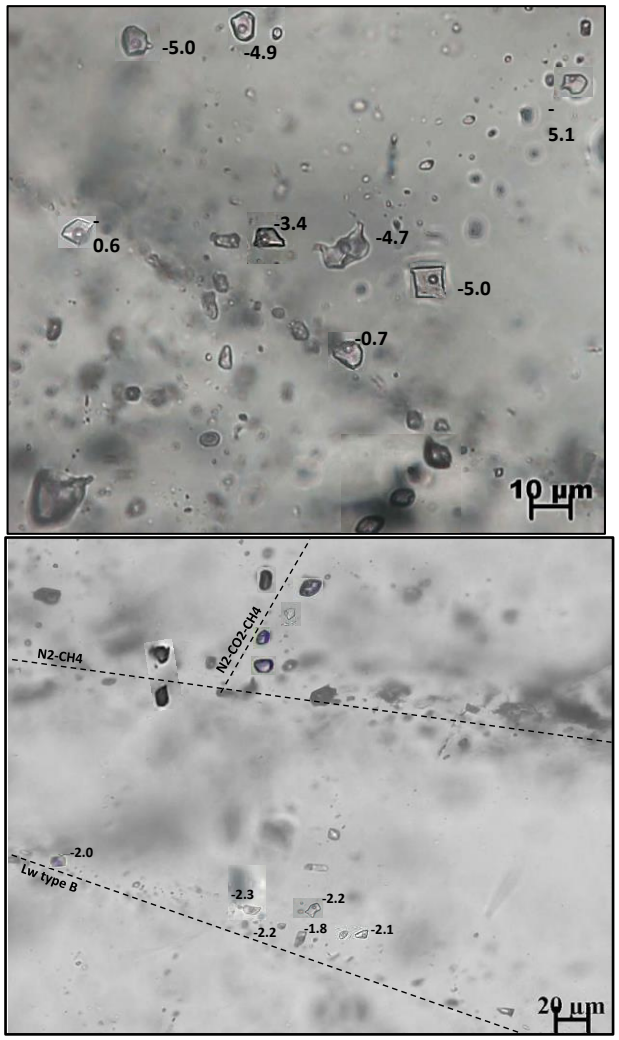

Fig. VII. 4 – High magnification photomicrographs showing the relation between the fluid inclusions in leucosome (sample FM19) and respective Ice melting temperatures of aqueous inclusions and partial homogenization temperatures of monophasic inclusions.

7.3.2. Tourmaline bearing leucogranite - VC52

Sample VC52 is a leucogranite where almost all the biotite has disappeared and, instead, dispersed crystals of tourmaline occur within a coarse grained matrix of quartz + plagioclase ± K-feldspar (Fig.VII.5). Very rare corroded garnet occurs. The K-feldspar content is relatively low (< 20 % in mode), occurs associated with tourmaline or replacing plagioclase. Biotite and garnet are considered residual in these rocks. Later retrograde alteration is marked by chloritization of biotite and muscovitization of biotite, tourmaline and feldspars.

In this sample were analyzed fluid inclusions in coarse-grained quartz crystals, and in plagioclase.

The studied quartz does not show ondulose extinction or other deformation textures. Rutile needles randomly oriented, subhedral biotite and euhedral tourmaline was observed within the quartz crystals.

Fig. VII. 5. Thick double-polished section from the tourmaline leucogranite (sample VC52).

The leucogranite contains at room-temperature mainly two inclusion types: monophasic and two-phase liquid+vapour (H_2O-NaCl) aqueous fluid inclusions (Figs. VII.6 to VII.8).

Monophasic inclusions

The monophasic inclusions were observed in poorly defined intragranular trails and clusters, exhibit regular shapes (sub-rounded to elliptical), many having a negative crystal shape. Liquid water is not visible, indicating very low water content. They range in size from 10 to 24 µm (av. 13.9 µm) (Figs. VII.6 and VII.8).

Microthermometry and Raman analyses identified N_2 and CH_4 as the main species in the volatile phase. N_2 is the dominant specie ranging from 86.1 to 91.8 mole% and CH_4 content ranges from 8.2 to 13.9 mole% (Fig. VII.15).

This type of inclusions shows temperatures of partial-homogenization ($Th_{partial}$) in the interval of -140.6 to -137.6 °C into vapor and in the range of -140.3 to 140.1°C into liquid phase (Fig. VII.10).

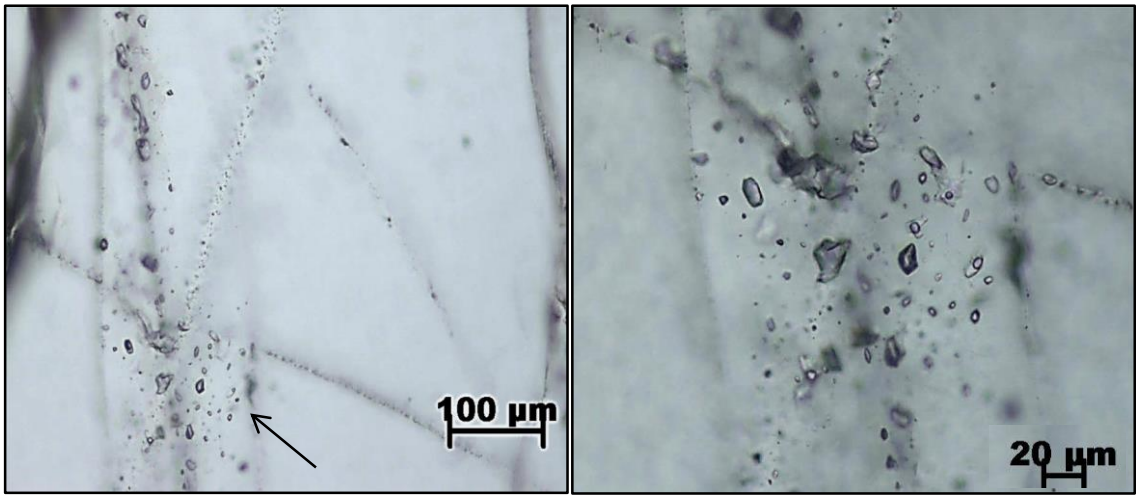

Fig. VII. 6 – Cluster of monophasic and two-phase fluid inclusions in leucogranite.

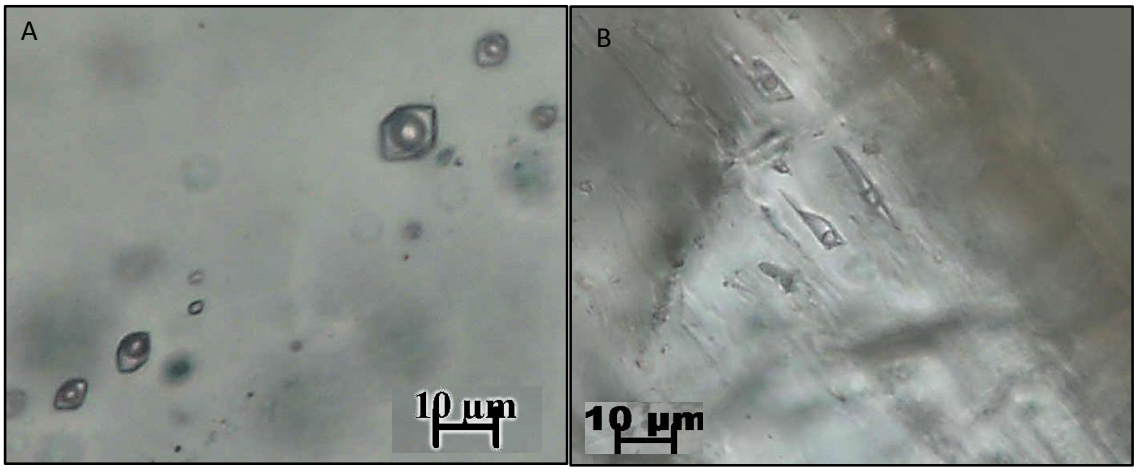

Fig. VII. 7- Photomicrographs showing aqueous two-phase fluid inclusions with A) negative crystal shape; B) Fluid inclusions in plagioclase.

Two-phase inclusions

Two-phase aqueous inclusions occur in clusters associated with the monophasic inclusions and in trails that cut the previous intragranular trails.

Two-phase inclusions show three distinct sub-types (Figs. VII. 17 and VII.11):

- Two-phase inclusions aligned in well-defined intragranular trails showing NE-SW direction (orientation relatively to the edge of the sample) and generally show 'negative' crystal shape (Fig. VII.7). Their size range from 5 to 27 µm (av. 11.6 µm) and show degree of filling varying from 0.70 to 0.90. Ice melting temperatures (Tm_{ice}) lie between -3.4 and -2.4 ºC which corresponds to salinities of 4.0 to 5.6 eq. wt.% NaCl (average of 5.0 eq. wt. % NaCl). Total homogenization occurs always in the liquid phase with Th values between 215 and 382 ºC (average of 343ºC).
- Two-phase inclusions observed in poorly defined intergranular trails and clusters, occasionally isolated. They show a degree of filling varying from 0.60 to 0.80. Ice melting temperatures (Tm_{ice}) lie between -2.6 and -1.7 ºC which corresponds to salinities of 2.9 to 4.34 eq. wt.% NaCl (average of 3.1 eq. wt. % NaCl). In this type of fluid inclusions the total homogenization was observed only in one inclusion showing 359 ºC.
- Two-phase Inclusions aligned in well-defined intragranular trails showing NW-SE direction (orientation related to the edge of the sample) and generally have irregular shape. These inclusions rang in size from 7 to 23 µm (av. 11.9 µm) and show a degree of filling (Flw) varying from 0.70 to 0.90. Ice melting temperatures (Tm_{ice}) lie between -0.9 and -0.4 ºC which corresponds to salinities of 1.7 to 0.7 eq. wt.% NaCl (average of 1.1 eq. wt. % NaCl). Total homogenization occurs always in the liquid phase and is characterized by Th between 335 and 348 ºC (average of 341ºC).

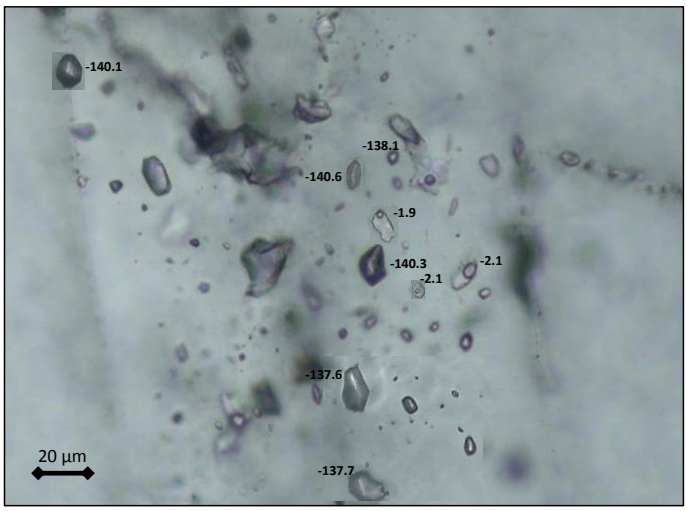

Fig. VII. 8 – Photomicrograph showing a group of monophasic and two-phase inclusions and respective partial homogenization temperature and ice-melting temperature (VC52).

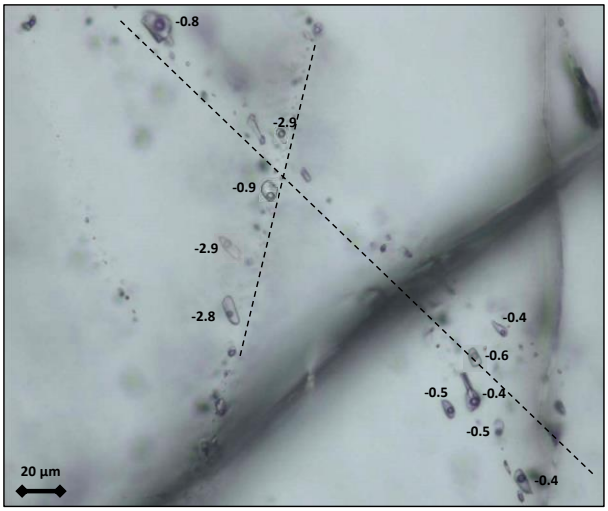

Fig. VII. 9 – Photomicrograph showing different directions of aqueous fluid inclusions trails and respective ice-melting temperatures (sample VC52).

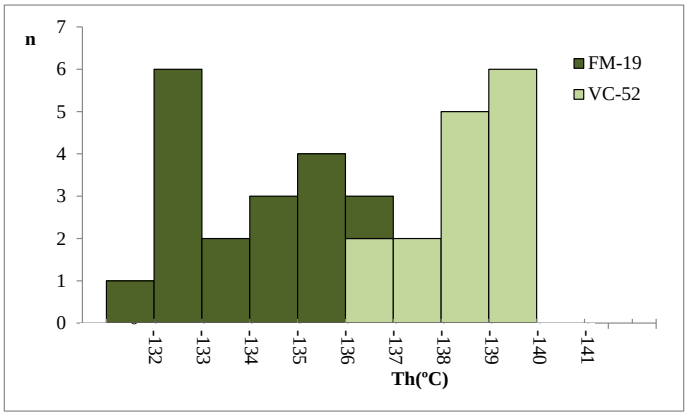

Fig. VII. 10 – Frequency histogram of partial homogenization temperatures of monophasic inclusions from leucosome and leucogranite samples (FM19 and VC52, respectively).

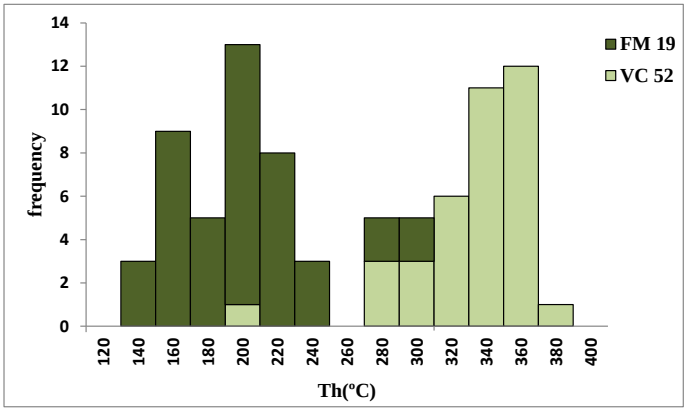

Fig. VII. 11 - Frequency histogram of two-phase inclusions total homogenization temperatures from leucosome and leucogranite samples (FM19 and VC52, respectively).

Only a few fluid inclusions have been observed in plagioclase. They occur associated with cleavages and show an elongated morphology measuring ~7.5 µm in the longest side (Fig. VII.7B). These inclusions are two-phase, showing ice melting temperatures (Tm_{ice}) between -1.2 and -0.7 ºC which corresponds to salinities of 1.2 to 2.1 eq. wt.% NaCl (average of 1.5 eq. wt. % NaCl).

7.3.3. Two-mica granite - FP21

Sample FP21 is a two-mica medium-grained granite and is composed of plagioclase + quartz + K-feldspar + biotite + apatite ± sillimanite ± garnet + muscovite (sec.) ± chlorite (sec). K-feldspar occurs as medium-grained crystals in the matrix and as sparse megacrystals of about 2 cm. K-feldspar contains inclusions of plagioclase, quartz, biotite and sillimanite. Biotite, sillimanite and rare garnet occur in aligned schlieren that are considered restitic. Biotite also occurs as dispersed flakes in the matrix (Fig. VII.12). Deformation features are rare and limited to slight ondulose extinction in quartz and incipient flame perthites in K-feldspar. This rock underwent later alteration processes revealed by the commonly observed muscovitization of biotite and feldspars and chloritization of biotite.

Fig. VII. 12 – Thick double-polished section from sample FP21

In the quartz from two-mica granite it can be mainly observed monophasic and two-phase aqueous fluid inclusions at room-temperature (Figs. VII.18 and VII.20).

Monophasic inclusions

This type of inclusions was observed in clusters and also in well-defined intragranular trails extending from border to border (Fig. VII.13). Liquid water is not visible, indicating low water content although an invisible film of water could exist. The size of the inclusions range between 5 to 38 µm (av. 18 µm).

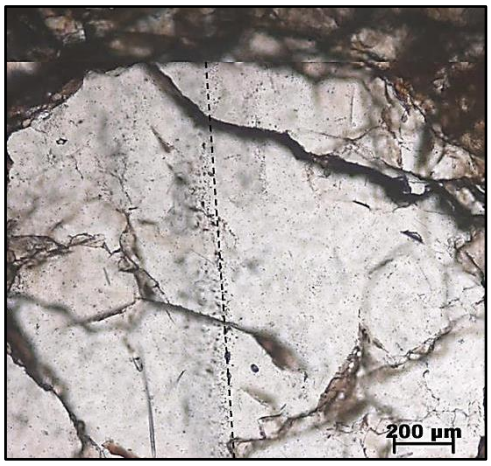

Fig. VII. 13 - Intragranular trail (grain boundary to grain boundary) in two-mica granite (FP21).

These inclusions show two distinct groups: A and B (Fig. VII.14 and VII.15):

- Group A inclusions occur in poorly defined intragranular alignments and in clusters. The melting temperature of the CO_2 phase was observed between -61.6 and -60.1ºC and the partial homogenization temperature was observed in the range of -39.0 to -32.2 (into vapor). Raman microspectroscopy analyses identify CO_2-N_2 as the main species in the volatile phase. CO_2 is dominant ranging from 61 and 66 mole% CO_2 with average of 63 mole%.
- Group B inclusions occur in well-defined intragranular alignments and appear posterior to the type A. The melting temperature of the CO_2 was observed between -61.6 and -60.5ºC and the partial homogenization temperature was observed in the range of -24.5 to -14.4 ºC (into vapor). Raman microspectroscopy analyses identify CO_2-N_2 as the main species in the volatile, being CO_2 dominant with a molar composition of 79 and 92 mole% with average of 84 mole%.

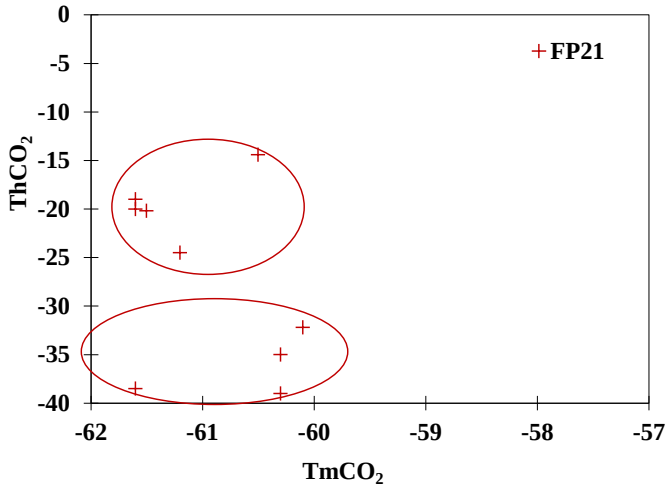

Fig. VII. 14 - Plot of homogenization temperatures *versus* melting temperatures for mixed N_2-CO_2 inclusions in two-mica granite (sample FP21).

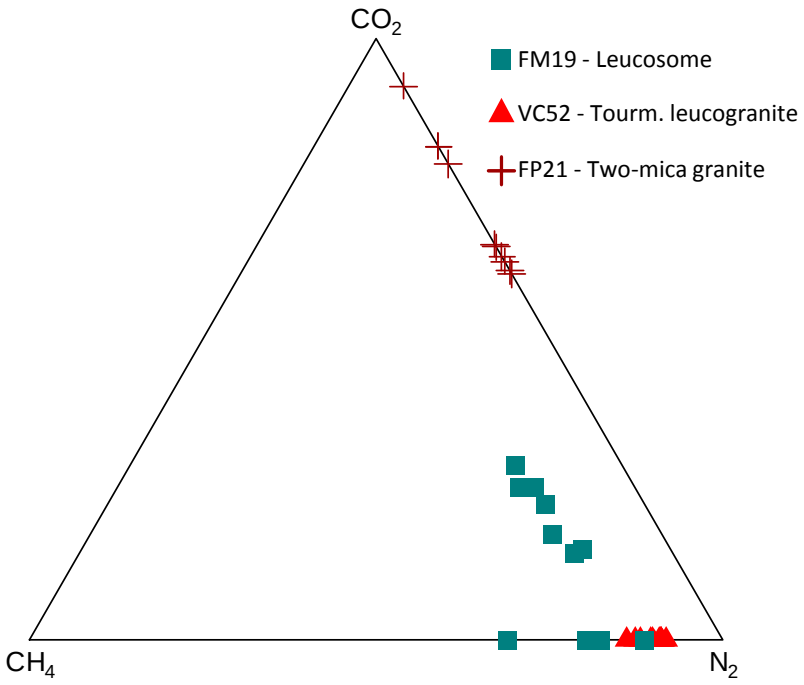

Fig. VII. 15 – Ternary plot of the volatile phase composition obtained by Raman microspectroscopy analyses of the fluids from the studied samples.

Aqueous two-phase inclusions

Two-phase inclusions show two principal types (Fig. VII.16 and VI.17).

- Inclusions occurring in intragranular trails associated or parallel to the monophasic inclusions trails. This type of inclusions show size ranging from 5 to 10 µm and a degree of filling (Flw) varying from 0.85 to 0.90. Ice melting temperatures (Tm_{ice}) lie

between -4.4 and -3.4 ºC which corresponds to salinities of 5.6 to 7.0 eq. wt.% NaCl (average 6.4 eq. wt. % NaCl);

- Inclusions occurring in well-defined alignments that seem to cut the other inclusion trails. The shape of these inclusions is irregular and the size varies between 10 to 37 µm with degree of filling between 0.85 and 0.90. Ice melting temperatures lie between -1.0 and -0.7 ºC corresponding to salinity between 1.23 and 1.74 (average 1.5 wt.% Eq. NaCl).

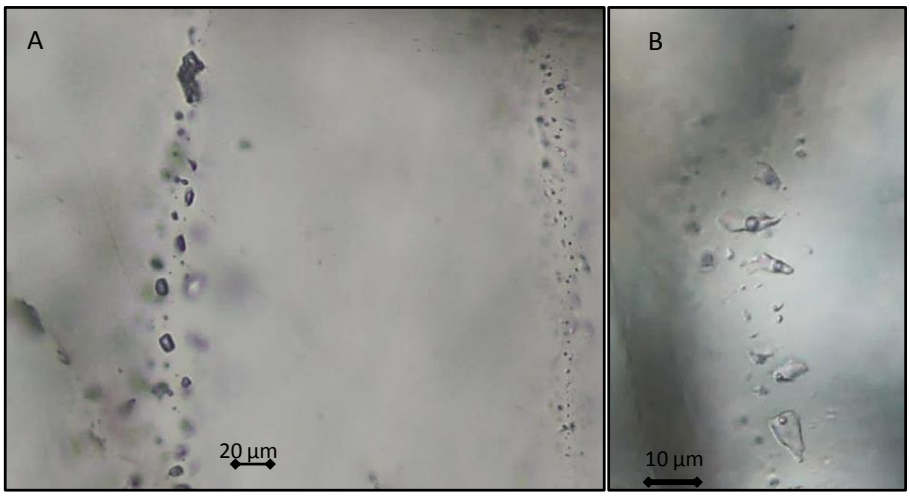

Fig. VII. 16 – Photomicrographs of sample FP25 showing: A) monophasic inclusions (group B) in trails and parallel to a trail of tiny two-phase inclusions; C) Trail of later aqueous inclusions.

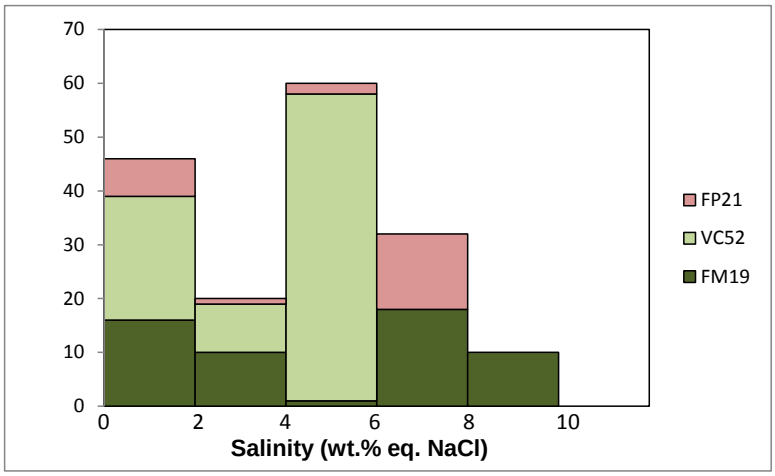

Fig. VII. 17 - Frequency histogram for fluid inclusions salinity in quartz from leucosome (FM19), leucogranite (VC52) and two-mica granite (FP21).

7.4. P-T evolution

Leucosome – FM19

Figure VII.18B represents the pressure-temperature plot of fluid inclusions isochores for sample FM19, superimposed on the aluminosilicate fields (Holdaway & Mukhopadhyay, 1993; Fig. VII.18A) and the granite minimum melt (Thompson and Tracy, 1979). The PT pseudosection calculated for a typical pelite melting in the system $Na_2O–CaO–K_2O–FeO–MgO–Al_2O_3–SiO_2–H_2O–TiO_2–Fe_2O_3$ (Brown & Korhonen, 2009; Brown, 2013) is also plotted for the paragenesis Bt + Sil + Crd + Mag/Ilm + Kfs + Qtz + Pl corresponding to the paragenesis observed in the metatexites from MMC.

The N_2-CH_4 and the N_2-CO_2-CH_4 fluid inclusions occur in clusters and in poorly-defined intragranular trails, indicating that they could have been trapped during the crystallizations of the quartz. The N_2-CH_4 inclusions isochores intersect the pressure-temperature conditions for the referred mineral paragenesis. This feature corroborates a primary origin of these fluid inclusions and permits the delimitation of the PT conditions for the crystallization of leucosomes in MMC metatexites. The values found are 400 to 500 MPa and 720 to 840 ºC. The isochores for the mixed N_2-CO_2-NH_4 fluid inclusions were not calculated. None of the aqueous fluid inclusions isochores intersect the PMC field, suggesting a re-equilibration process or secondary origin for these fluid inclusions. The higher saline fluid inclusions (eq. wt% NaCl>6) occur in clusters and associated with the monophasic inclusions. So, they are interpreted as inclusions trapped close to PMC conditions and later re-equilibrated. The inclusions that have the lowest salinities are considered secondary and could represent the later fluids affecting the MMC in subsolidus conditions.

Tourmaline leucogranite - VC52

Figure VII.19 represents the pressure-temperature plot of fluid inclusions isochores for sample VC52 superimposed on the aluminosilicate fields (Holdaway & Mukhopadhyay, 1993) and the granite minimum melt (Thompson & Tracy, 1979).

Considering the leucogranites paragenesis (absence of peritectic minerals) and whole-rock composition it is suggested that leucogranites result from a fluid-present melting in the first stages of migmatization, involving essentially quartz and plagioclase.

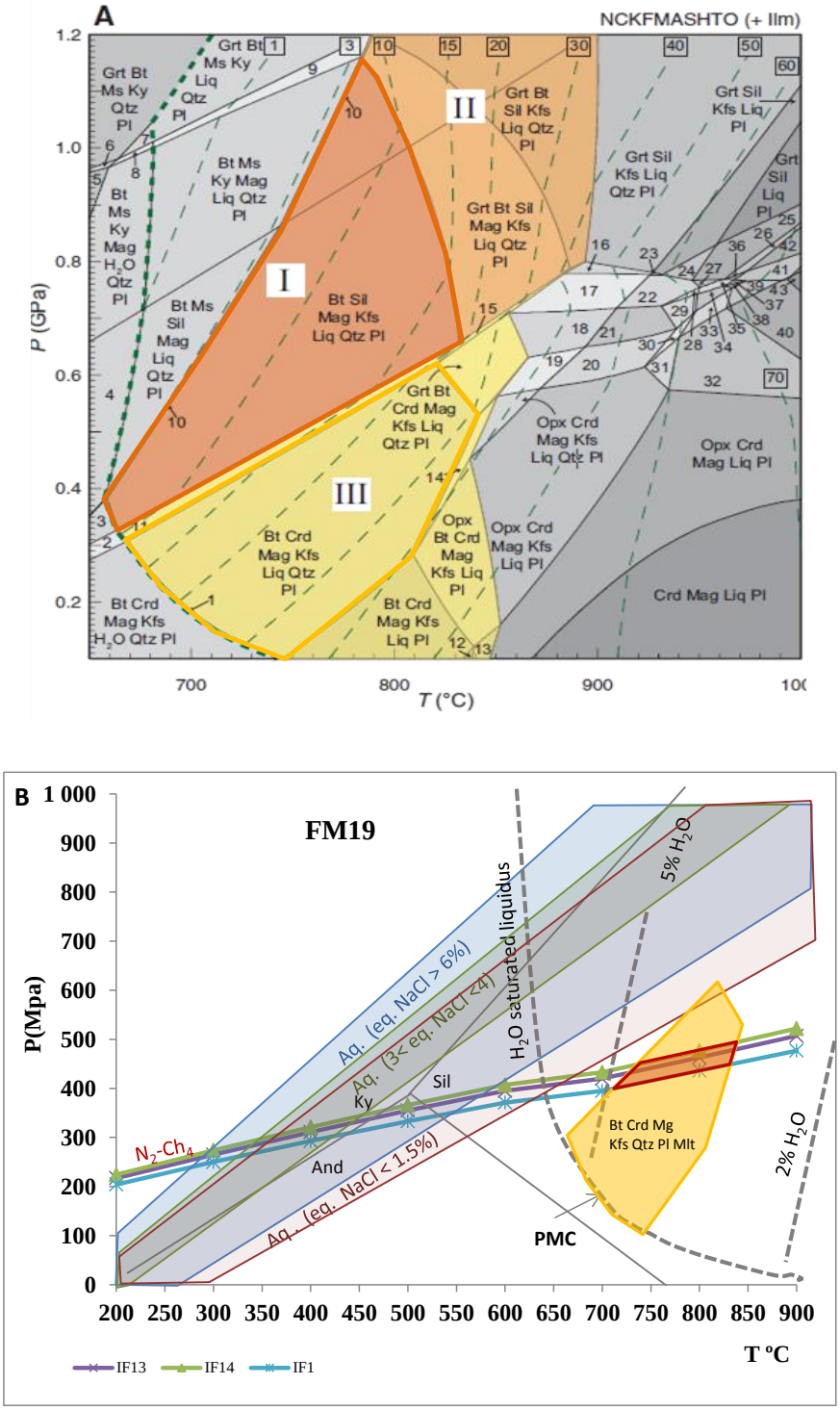

Fig. VII. 18 – A) Metamorphic PT fields for the melting of pelitic rocks accordingly to the mineral paragenesis (after Brown & Korhonen, 2009) and Brown, 2013). The fields corresponding to the metatexites mineral paragenesis (yellow shaded area) and to the two-mica granites mineral paragenesis (orang shaded area) are marked. B) Pressure-temperature plot of N_2-CH_4 fluid inclusions isochores for sample FM19 superimposed on aluminosilicate fields (Holdaway and Mukhopadhyay, 1993) and the granite minimum melt (Thompson and Tracy, 1979). Isochores of aqueous inclusions are represented by the filled stippled regions between higher and lower isochores. The migmatite mineral paragenesis is indicated by the yellow shaded area. The anatexis conditions are positioned between the intersection of the isochores and the mineral paragenesis field (red shaded area).

The T conditions of leucogranites crystallization are considered proximate to the H_2O saturated granite melting temperatures of ~ 680 ºC.

The N_2-CH_4 fluid inclusions occur in clusters and in poorly-defined intragranular trails, indicating that they could correspond to primary inclusions, i.e., inclusions trapped during the crystallizations of the quartz. These fluid inclusions isochores intersect the wet granite melting line (considered the beginning of anatexis), pointing to a primary origin, and allowing the delimitation of the P conditions (430 and 550 MPa) for the leucogranites crystallization.

None of the aqueous fluid inclusions isochores intersect the pressure-temperature field for the beginning of anatexis, suggesting its later origin and sub-solidus entrapment. The aqueous fluid inclusions showing salinity ~5 eq.wt% NaCl only occur in this sample and are absent in the leucosome and two-mica granite samples. This suggest that this fluids could be related to the influx of boron-rich fluids that lead to the development of tourmaline in this rocks (absent in the other two samples). The latest aqueous fluid inclusions are probably related to post-solidus entrapment and muscovitization and chloritization processes.

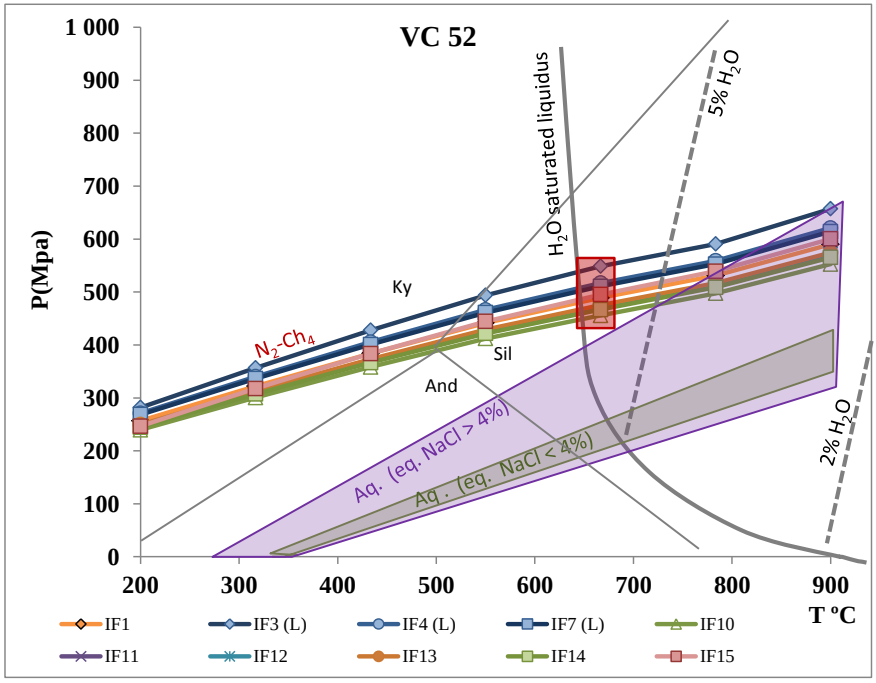

Fig. VII. 19 - Pressure-temperature plot of the N_2-CH_4 fluid inclusions isochores for sample VC52 superimposed to aluminosilicate fields (Holdaway & Mukhopadhyay, 1993) and the granite minimum melt are also represented (Thompson & Tracy, 1979). The anatexis conditions are indicated by the red shaded area. The inclusions that homogenized at liquidus are marked with (L). The aqueous fluid inclusions isochores are restricted to the filled stippled regions between higher and lower isochores.

Two-mica granite - FP21

Figure VII.20 represents the pressure-temperature plot of fluid inclusions isochores for sample FP21 superimposed on the aluminosilicate fields (Holdaway & Mukhopadhyay, 1993), the granite minimum wet melt (Thompson & Tracy, 1979) and the PT pseudosection calculated for the anatexis of pelitic rocks in the system NCKFMASHTO (Brown & Korhonen, 2009; Brown, 2013; Fig. VII.18A) for the paragenesis Bt + Sil + Mag/Ilm + Kfs + Qtz + Pl corresponding to the paragenesis observed in the two-mica granites.

The CO_2-N_2 fluid inclusions occur in poorly-defined intragranular trails, indicating that they could correspond to primary inclusions, i.e., inclusions trapped during the crystallizations of the quartz crystals.

The isochores of the N_2-CH_4 inclusions with higher and lower CO_2 proportion overlap wish other indicating that they were trapped under the same PT conditions. The fluid inclusions isochores intersect the pressure-temperature conditions of peak metamorphism, what confirms its primary origin and permits the delimitation of the PT conditions for the crystallization of two-mica granites quartz in MMC. The delimited PT conditions are 320 to 520 MPa and 680 to 780 ºC.

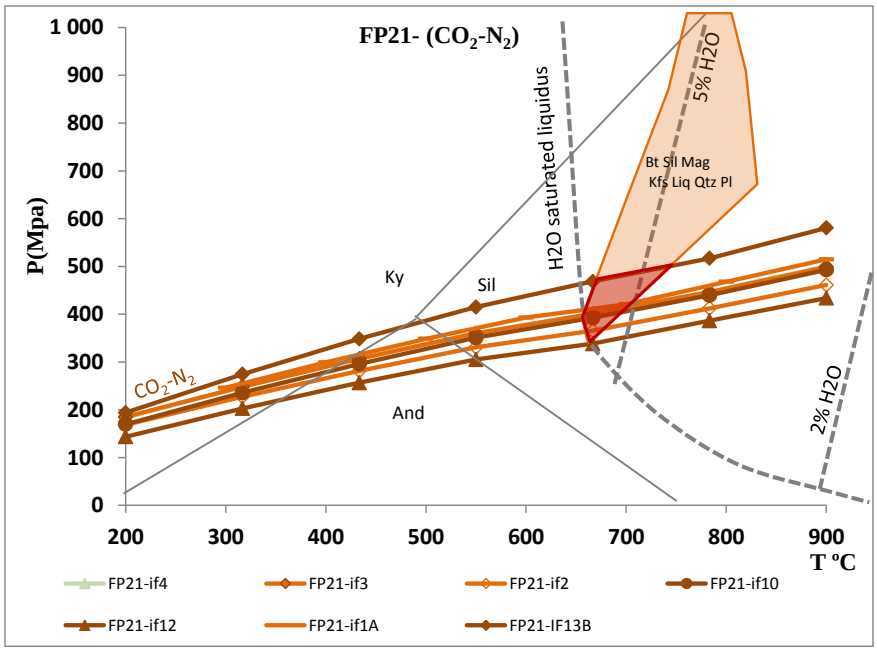

Fig. VII. 20 - Pressure-temperature plot of CO_2-N_2 fluid inclusions isochores for sample FP21 superimposed on the aluminosilicate fields (Holdaway & Mukhopadhyay, 1993) and the granite minimum melt (Thompson and Tracy, 1979). Possible metamorphic conditions are delimited by the pseudosection fields for the melting of pelitic rocks showing the mineral paragenesis of two-mica granites, proposed by Brown & Korhonen (2009) and Brown (2013). The anatexis conditions are indicated by the intersection of the isochores with the mineral paragenesis field (red shaded area).

7.5. Synthesis and discussion

Monophasic inclusions occur in all the studied samples but showing different compositions and conditions of entrapment: Leucosomes are characterized by N_2-CH_4 and N_2-CO_2-CH_4 fluids showing high N_2 content; leucogranites only show N_2-CH_4 fluids with high N_2 content as well; two-mica granites only show CO_2-N_2 fluids being CO_2 the dominant species in the volatile phase. All these fluid types occur in fluid inclusions trapped in intragranular trails or in clusters and transect the metamorphic conditions of the respective lithologies suggesting its primary character.

The generation of N_2-CH_4-rich fluids with very low water content could be the vapor phase resulted from an immiscibility process in the H_2O-CH_4-N_2 system at low pressure (Alvarenga *et al*., 1990), producing N_2-CH_4 and H_2O-bearing fluid inclusions both trapped in clusters and in parallel intragranular trails. In the studied samples there are monophasic inclusions associated with aqueous inclusions, indicating an immiscibility process during the entrapment, both, with N_2-CH_4 and CO_2-N_2 inclusions types as well.

The source for the N_2 observed in the fluid inclusions could be the micas and feldspars since these type of minerals may contain a significant amount of nitrogen in their structure in the form of NH_4^+ ions, which are released when these minerals breakdown (Andersen *et al.,* 2001). It was also observed that most N_2 in high metamorphic grade rocks is found at the stage where these minerals become unstable and such a link cannot be accidental (Cesare, 2007).

A genetic relationship between biotite melting and CO_2 content in the rock fluids is suggested by several authors in support of the model of CO_2 formation by oxidation of graphite during melting of Fe^{3+} bearing biotite. Graphite could be a stable phase at high temperatures, and probably participate in melting reactions (Giorgetti, 1996). Thus, Fe^{3+} reduction during biotite dehydration-melting could cause graphite oxidation, producing CO_2 and globally rising the fO_2 (Hollister, 1988; Georgetti *et al*., 1996 Cesare *et al*. 2005, Ferrero *et al.,* 2011). This explains the presence of CO_2-N_2 inclusions in two-mica granites and in leucosomes and its absence in leucogranites. In fact, as referred before, it is likely that a fluid-present melting pulse takes place in MMC involving essentially quartz and plagioclase and produced most of the leucogranites, through the reaction:

$$Qtz + Pl + H_2O = Melt \quad (1)$$

This reaction implies the released of melt without the break-down of biotite and occurs at lower temperatures than the biotite breakdown reactions, which favor CH_4 as the carbon-bearing gas species with respect to CO_2 (French, 1966).

The anatexis process continues by fluid-absent biotite breakdown reactions (e.g. Brown, 2008; White, 2008):

$$Bt + Pl_1 + Sil + Qtz = Crd + Pl_2 (\pm Kfs) + Melt \quad (2)$$

$$Bt + Sil + Qtz = Crd + Kfs + Melt \quad (3)$$

These reactions could be the main producers of fluids containing CO_2 if considering the model first proposed by Hollister (1988).

In migmatites (leucosomes) both processes were present. A first wet-melting producing N_2-CH_4 inclusions and, in continuum, the biotite breakdown produced the mixed N_2-CH_4-CO_2 fluid inclusions, containing high N_2 and low CO_2. This suggests that the N_2-CH_4-CO_2 inclusions resulted from a mixing process.

In two-mica granites the muscovite and biotite breakdown must be the most important reactions occurred during anatexis. Thus, it is expected that CO_2 bearing fluids were released. The absence of CH_4 in two-mica granites is indicative of higher fO_2 conditions than for leucosomes and leucogranite where CH_4 is always abundant.

The monophasic inclusions isochores of all the samples intersect the stability fields of the mineral paragenesis of metatexites, confirming its contemporaneity with the crystallization of leucosomes, leucogranites and two-mica granites, respectively. The intersection with the isochores permits a more accurate definition of the PT condition prevailing during the anatexis. For leucosomes the P values are between 400 to 500 MPa and T between 720 to 840 ºC, at H_2O percentage < 5%. For leucogranites the temperature is considered proximal to the wet granite melting (~680 ºC) and the pressures values are between 430 and 550 MPa. For two-mica granites the pressure values range from 330 - 520 MPa with temperature between 680 – 780 ºC, and H_2O percentage > 5% (Figs. VII.18, VII.19 and VII.20).

The stability field of the two-mica granites paragenesis could be more extensive, especially relatively to pressure. Field relations indicate that granites are intrusive in the metatexites what suggest ascend of granitic magma and consequently a deeper melting level and higher P values. However, the crystallization process were at the same structural level, so the PT conditions constrain by the isochores represent the quartz crystallization PT conditions, and not the melting conditions.

Bulk rock composition, AFM diagrams and pseudosection of mineral assemblages (Spear, 1995; Bucher & Grapes, 2011) were used to constrain the PT paths in the staurolite-zone (sub-chapter 4.2.5). A first metamorphic event (M1), attaining condition of P > 490 MPa and 560 < T > 600 ºC, reflects burial and heating. These conditions were followed by decompression and temperature increase leading to andalusite and cordierite development during a later metamorphic event (M2). The sillimanite-zone and migmatization are the result of the last metamorphic event.

Figure VII.21 represents possible metamorphic P–T paths followed by the studied rocks, based on the mineral paragenesis and reaction textures, the blastese / deformation relationships (Fig. IV.2.30) and the isochores intersection with the pseudosection for the mineral paragenesis.

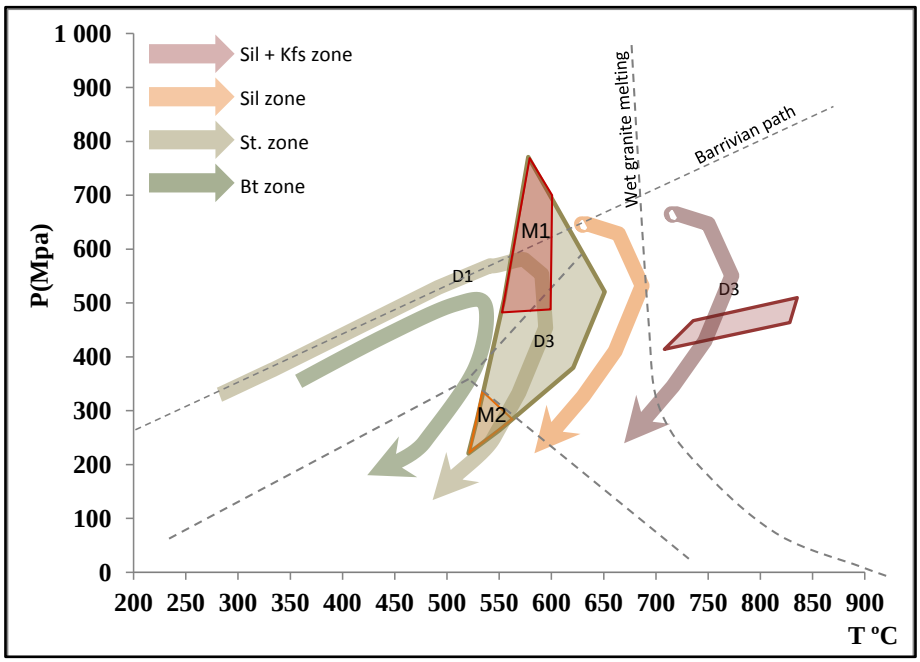

Fig. VII. 21 - Metamorphic P–T paths and relation with the major Variscan deformation phases (D1, D2 and D3) for pelitic sequences and MMC metatexites. Phase diagram for Al_2SiO_5 polymorphs (Holdaway & Mukhopadhyay, 1993), the wet granite minimum melt (Thompson and Tracy, 1979) and a Barrovian type geotherm (Bucher& Grapes, 2011)

None of the aqueous fluid inclusions isochores intersect the P-T conditions of peak metamorphism, suggesting their later origin or re-equilibration processes. Four populations of aqueous fluid inclusions (H_2O-NaCl) with different salinities occur in the studied samples (Fig. VII.17): i) the higher saline (> 6 wt.% eq. NaCl) only occur in leucosomes and two-mica granites. They are healing intragranular poorly defined trails or clusters. These aqueous inclusions often seem to be mixed with trails of primary

monophasic inclusions, indicating an immiscibility process of entrapment. However, the isochores show lower PT conditions. This probably results from late and intense reopening/rehealing process affecting a part of the earlier microstructures that lead to re-equilibration of the fluids, generally showing salt enrichment by water loss (Alvarenga *et al*., 1990). In general, the aqueous component of peak metamorphic fluids in pelitic schists and gneisses is fairly dilute, generally < 5 wt% (Crawford, 1981; Crawford and Hollister, 1986). Re-equilibration experiments (Crawford, 1979; Hall & Sterner, 1993) on saline synthetic fluid inclusions trapped in quartz showed that isothermal decompression with internal overpressures of 2 kbar provoke salinity increasing. Hall & Sterner (1993) attributed the increased salinities to preferential diffusional loss of H_2O during re-equilibration, whereas Crawford et al. (1979) suggested that retrograde hydration reactions concentrated the salts in the fluids. Thus, the higher salinities measured in the bulk of the aqueous fluid inclusions associated with the monophasic inclusions may be due to multiple processes operating during re-equilibration. The monophasic inclusions containing N_2 and CO_2 or CH_4 are less affected by re-equilibrium processes than aqueous fluid inclusions (Hall & Sterner, 1993).

Inclusion showing salinity between 4 and 6 wt.% eq. NaCl occur mainly in the tourmaline leucogranites (leucosome and two-mica granite samples show a single inclusion of this type) (Fig. VII.17). It is likely that these fluids are associated with the leucogranites tourmalinization process, which affected more intensely this type of rocks.

Lower saline inclusions showing salinity below 4 wt.% eq. NaCl occur in the three analysed lithologies, generally in well-defined alignments cutting the previous described fluid inclusions trails and clusters, therefore considered as representing the last fluid entrapment occurred in MMC and probably affected all the present lithologies and giving rise to muscovitization and chloritization processes.

CHAPTER VIII – ISOTOPE GEOLOGY

"Look deep into nature, and then you will understand everything better."

Albert Einstein

8.1. Introduction

The absolute dating of rocks and minerals is based on the laws of radioactive decay established by Rutherford & Soddy in 1902, according to which the rate of decay of an unstable atom is proportional to the number of residual atoms at any time *t*. It is known that each element tends to disintegrate at a certain velocity (λ) in a unit time (t), according to the fundamental equation of Geochronology:

$$R = R_0 + R_P / _F (e^{\lambda t} - 1) \qquad (1)$$

Where R_0 is the initial ratio and $R_P/_F$ ratio is the parent/stable ratio at time *t*. The decay constant (λ) is the probability of isotopic decaying in the time unit and is characteristic of each isotope. Solving this equation as a function of *t* yields the equation of a line whose slope depends only on time, called "isochron" (Faure & Mensing, 2005).

The choice of isotopic pairs for use in geochronology depends on its concentration in measurable levels and the compatibility between its half-life time and the period of the geological process under study (e.g. Geraldes, 2010).

There are two important assumptions or conditions on the use of radioactive isotopes in geochronological study of rocks and minerals: 1) the radiogenic isotope has its origin exclusively by decay of the radioactive isotope and 2) the system as a whole, or each of its parts, remained closed between t_0 and *t* (usually the present time) (e.g. Dickin, 2005).

In general, the measured date refers to the last time the system was open to full exchange of parent / child elements between the various analyzed subsystems, *i.e*. the last point in time when the system had an uniform and homogeneous value of R. This is usually a thermal event. Thus, an isotopic age is fundamentally a thermal dating and reflects the time since a sample became cool enough for the products of a given

radioactive decay process to be retained (effective isotopic closure) (Sardarov, 1957; Hurley *et al*., 1962; Dodson, 1973).

8.2. U-Pb system

The principle of the method U-Th-Pb is based on the decay of U and Th to isotopes of Pb. Uranium occurs in three natural isotopes, all of them radioactive: ^{238}U, ^{235}U and ^{234}U.

Thus, it is possible to obtain three ages, based on three different equations:

$^{206}Pb = {}^{206}Pbi + {}^{238}U\ (e^{\lambda t} - 1)$ showing $\lambda = 1{,}55125 \times 10^{-10}$

$^{207}Pb = {}^{207}Pbi + {}^{237}U\ (e^{\lambda t} - 1)$ showing $\lambda = 9{,}8485 \times 10^{-10}$

$^{208}Pb = {}^{208}Pbi + {}^{238}Th\ (e^{\lambda t} - 1)$ showing $\lambda = 4{,}9475 \times 10^{-11}$

These three equations are solved with reference to the stable isotope ^{204}Pb.

Although it is a decay series, if a mineral or rock behaves as a closed system, the rate of production of the stable isotope at the end of each series is equal to the decay rate of the initial radioactive isotope (Dickin, 2005; Geraldes, 2010).

The ages obtained have geological significance only when certain requirements have been met:

- The system remained closed to U, Th and Pb, as well as all intermediate isotopes of the decay series;
- Adjustments were based on values of initial Pb isotopes, which are subtracted from the isotopic values obtained analytically. The common Pb can be measured by the analysis of the whole-rock or in the case of zircons with low contents of Pb, it is an estimate from a model of terrestrial evolution of Pb (e.g. Stacey and Kramers, 1975);
- The isotopic composition of U has not undergone modification by isotopic fractionation or by ^{235}U fission.

The great advantage of the U-Pb system compared to others isotopic geochronological systems is that it is based on more than one dating and therefore allows that the ages measured could be corrected in function of the loss of the radiogenic isotope, *i.e*., it allows internal self-calibration of the method.

In an ideal situation, in which the U-Pb system remained closed, the three ages are coincident and the corresponding projection of the isotopic ratios of analyzed points

occur in a $^{206}Pb/^{238}U$ *versus* $^{207}Pb/^{235}U$ curve diagram, defined by Wetherill (1956) and Ahrens (1955), and is called concordant. However, these authors found a discrepancy in the ages obtained in the same rock or mineral, related to the loss of Pb. Indeed, the U-Pb system rarely remains closed in silicate rocks because these elements are mobile in conditions of low-grade metamorphism and weathering. In this case, the points plotted in the diagram do not coincide, although presenting a linear relationship in the *concordia* diagram. The line defined by these points is called *discordia* being the age of crystallization of minerals given by one of the two intersections of discordia with the concordia line (Wetherill 1956, Dickin, 2005; Faure & Mensing, 2005).

The obtained ages are considered to be concordant if there is. <5% of discordance, which is given by the equation (Biao *et al*., 1996):

$$\{1 - (^{206}Pb/^{238}U \text{ age})/(^{207}Pb/^{206}Pb \text{ age})\} \times 100$$

Zircon is the most common mineral use in the U-Pb dating method, due to its wide distribution in various types of rocks and high resistance to weathering, high closure temperature of the U-Pb system, its relatively high levels of uranium (which replaces Zr) and the absence of common lead in the structure. Various studies (e.g. Watson, 1996; Lee *et al*., 1997; Moller *et al*. 2002) demonstrate the preservation of age information and trace element zoning patterns in zircons with multiple magmatic and metamorphic overgrowths, despite ultra-high temperature metamorphism and partial melting.

Nevertheless, zircon can experience partial recrystallization under regional metamorphism in crustal conditions (Ashwal *et al*. 1992; Pidgeon, 1992; Hoskin & Black, 2000; Moller *et al*,. 2002). The mechanism of solid state recrystallization is believed to be related to the fact that trace element-rich oscillatory-zoned zircons are relatively unstable due to lattice strain (Koppel & Sommerauer, 1974). Hoskin & black (2000) suggest that recrystallization is initiated in points of high-lattice strain in the crystals and the recrystallization front migrates from that point throughout the crystals.

8.2.1. Morphology of zircons

Clearly, for the purpose of correct petrogenetic and tectonic interpretation it is essential to know the type of zircon under study. Electron backscatter imagery, cathodoluminescence spectroscopy and electron-microprobe trace element analysis has revealed that zircon could display complex growth and overgrowth features of both magmatic and metamorphic origin (*e.g.* Hoskin & Black, 2000; Moller *et al.* 2002). Thus, careful textural observation and chemical analysis is necessary to recognize the event that is being dated.

8.2.1.1. Magmatic zircons

Zircon is tetragonal and usually develops prismatic crystals with length-width ratios of 1:5. Typical magmatic zircons are between 20 and 250 micra in the longest side and show euhedral to subhedral shapes. The development of predominant prismatic or pyramidal structures is related to the chemical characteristics of the rock (e.g. Pupin 1980, Vavra, 1994, Corfu *et al*. 2003; Martins *et al*., 2014). One of the typical characteristics of magmatic zircons is the presence of a well-marked oscillatory zoning, generally showing bimodal succession of bands rich and poor in trace elements with virtually no intermediate composition (Fig. VIII.1). In other cases the differences are almost imperceptible, showing only a thin and light zoning. Locally, in some rocks, can be observed not zoned euhedral prisms (Paterson *et al*., 1992; Hanchar & Miller, 1993; Vavra, 1994) (Fig. VII.1). For some rocks, such as S-type granites, it is common to see multiple dissolution structures preserved within the zircon crystal, indicating zirconium sub-saturation periods followed by zirconium saturation periods in the melt (e.g., Vavra 1994, de la Rosa *et al*. 2002)

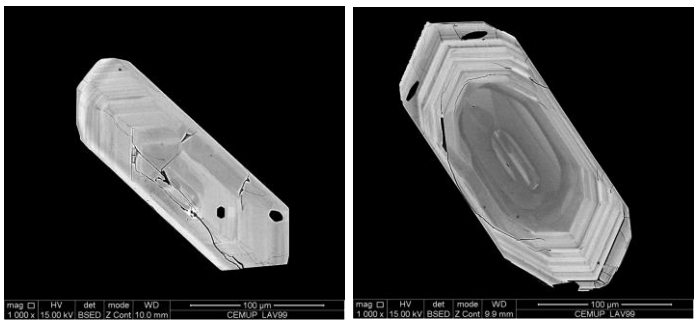

Fig. VIII. 1 – Backscattered images of magmatic zircons showing euhedral shape (prismatic) and marked oscillatory zoning (from Lavadores and Castelo do Queijo granites, NW Portugal; Abreu, (2012)).

8.2.1.2. Zircon xenocrysts

It is common the occurrence of zircon xenocrysts in many igneous rocks. When magma is supersaturated in zirconium, it does not dissolve the restitic zircons that usually become the basis of magmatic zircon regrowth. Thus, the appearance of zircon xenocrysts may vary from highly polished, without any overgrowth, to rounded grains mantled by new zircon, being usually composed of an inherited core from which develops a magmatic border. They can also occur simply as sub-rounded zircons.

The contact between the rim and the core is generally marked by an irregular discontinuity which truncates the internal zoning. In the case of a core affected by metamorphism it can show rounded or chaotic morphology and lacks zonation.

8.2.1.3. Metamorphic zircons

Metamorphic events can cause various types of changes in the shape and size of the zircon crystals. Thus, metamorphic zircons are characterized by a number of features that differ from that of igneous zircons (Hoskins & Schaltegger, 2003). The zircons from low- to high-grade metamorphic rocks are usually inherited from the protolith and may show signs of resorption or metamorphic overgrowth. The high-grade metamorphic rocks may contain zircon that grew during metamorphism, especially in rich fluid systems or in migmatites which can develop zircon in contact with a melt (Fraser *et al*, 1997; Roberts and Finger, 1997).

The external morphology of metamorphic zircons is generally characterized by rounded crystal terminations and is often reported to have ovoid morphologies (Watson & Liang, 1995). Generally they do not display oscillatory zoning but may be sector-zoned and usually shows sequential internal structures. These textures could be followed by external oscillatory zoning if new magmatic grouth occurs (Vavra *et al*. 1996, 1999; Schaltegger *et al*. 1999) (Fig.VIII.2).

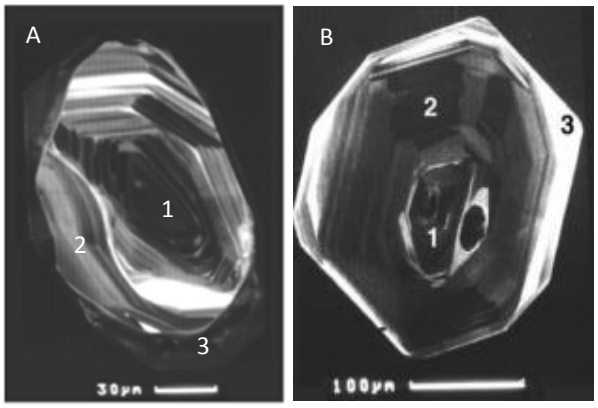

Fig. VIII. 2 _ A) Forms of recrystallization in zircon: 1 - inherited core, 2 - convoluted zone with partial recycling of U-Pb age, 3 - border with further development; B) Metamorphic zircon illustrative of sequential growth structures: 1) low-luminance core; 2) sector zoning domain; 3) outer zone with oscillatory zoning (Schaltegger *et al.* 1999).

Metamorphic zircons can be produced by internal recycling of previous igneous, detrital or metamorphic zircons. Recycling processes include solid recrystallization or dissolution-re-precipitation. These processes are negligible at low metamorphic grade, whereas in high-grade metamorphic rocks these processes create a variety of internal structures characterized by (Pidgeon, 1998; Schaltegger *et al.* 1999; Hoskin & Black, 2000; Moller *et al*., 2002):

- *Faded (blurred) oscillatory zoning* - The primary oscillatory zoning can be faded as the first indicator of disturbance of the structure;
- *Convoluted zoning* - The outer part of the metamorphic zircons may present a winding aspect and become discontinuous or truncated;
- *Transgressive recrystallization* – Local zircon recrystallization under metamorphic conditions which cuts the primary crystal textures often show lobed or sinuous aspect. Despite transgressive recrystallization, primary oscillatory zoning may be partially preserved. It is considered that zircon crystals without any internal structure result from total recrystallization that can occur under conditions of granulite facies or during anatexis.

The ages obtained from zircons in the granulite facies rocks are often interpreted as the age of peak metamorphic conditions (Pidgeon, 1992; Vavra *et al*. 1996; Pan, 1997; Hoskin & Black, 2000; Moller *et al.*, 2002; Rubatto, 2002; Tomaschek *et al*, 2003). However, processes that can produce metamorphic zircons may occur at different times and over different durations. For example, zircon formed by net-transfer reactions may record a time on the prograde P–T path prior to peak metamorphic conditions (Fraser *et al*., 1997), and zircon formed from anatectic melts may record an age later than peak conditions (Roberts & Finger, 1997).

Figures VIII.3 show cathodoluminescence images and schematic representation of the most relevant features that characterize a metamorphic zircon or/and zircon modified by metamorphic processes.

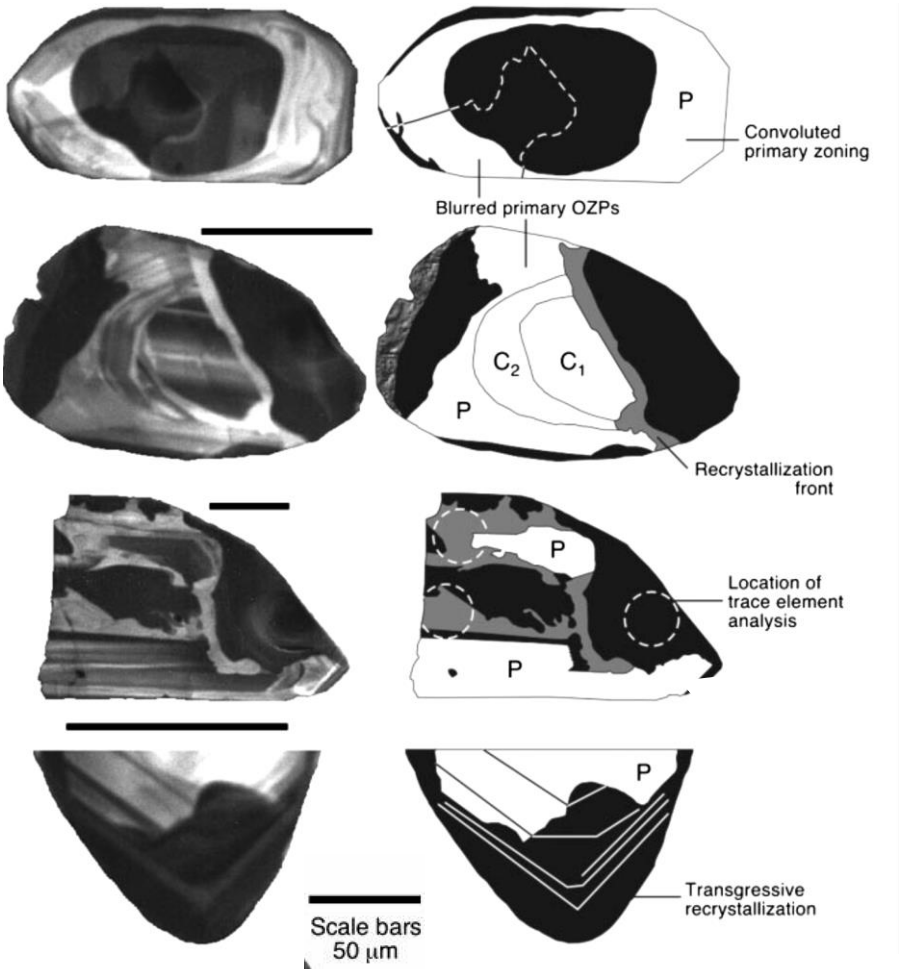

Fig. VIII. 3 – Cathodoluminescence images (left-side) and corresponding schematic diagrams (right-side) of CL-revealed internal structures for metamorphic zircons. Black: transgressive recrystallization; grey - recrystallization front; P-protolith igneous zircon, sometimes modified; C1, C2, inherited core (From Hoskin & Black, 2000).

8.2.2. Methodology

For U-Pb isotopic analyses one sample of diatexite (VC60) was selected.This sample was collected at the Metatexite Zone near Vila Chã and is part of a small body of diatexite that intruded the metatexites. It shows the typical mesoscopic aspect of the diatexites, namely mesocratic color and abundant dark schlieren consisting of biotite, sillimanite and rare garnet that are interpreted as remnants of restitic melanosomes. A

total of 64 targets were analyzed, in 36 zircon crystals. The spots for analyses were chosen in accordance with the internal structures exhibited by the zircons.

The separation and selection of zircons was carried out in the laboratories of Departmento de Geociências, Ambiente e Planeamento do Território of FCUP. Using a 50-250 µm size fraction of rock the separation of heavy minerals was made using dense liquids (bromoform + methylene iodide). The concentrates obtained were then processed in the electromagnetic separator initially using a weak intensity (0.5A) to eliminate heavy paramagnetic minerals. The non-magnetic fraction of zircon concentrate was obtained by repeating the process several times and varying the electromagnetic separator conditions. Finally the selection of zircons was done under the binocular microscope (picking), taking into account the size, shape and purity of the crystals, avoidingthe zircons with evidence of metamictization, fractured or containing inclusions.

U-Th-Pb Geochronological SHRIMP (Sensitive High Resolution Ion Microprobe) analytical procedure was performed in SHRIMP IIe/mc instrument of IBERSIMS lab (UGR). Hand-picked zircons from the studied sample, several grains of the TEMORA and one grain of the SL13 zircons standards, plus a few grain of the GAL zircon are cast on a 3.5 cm diameter epoxy mount (megamount), polished and documented using optical (reflected and transmitted light) and scanning electron microscopy (secondary electrons and cathodoluminescence). After extensive cleaning, mounts are coated with gold (80 micra thickness) and inserted into the SHRIMP for analysis. Each selected spot is rastered with the primary beam during 120 s prior to the analysis, and then analyzed during 6 scans following the isotope peak sequence $^{196}Zr_2O$, ^{204}Pb, $^{204.1}$background, ^{206}Pb, ^{207}Pb, ^{208}Pb, ^{238}U, ^{248}ThO, ^{254}UO. Every peak of every scan is measured sequentially 10 times with the following total counting times per scan: 2 s for mass 196; 5 s for masses 238, 248, and 254; 15 s for masses 204, 206, and 208; and 20 s for mass 207. The primary beam, composed of $^{16}O^{16}O2^{+}$, is set to an intensity of 4 to 5 pA, with a Kohler aperture of 120 micra, which generates 17 x 20 micra elliptical spots on the target. The secondary beam exit slit is fixed at 80 micra, achieving a resolution of about 5000 at 1% peak height. All calibration procedures are done on the standards included on the same mount. Mass calibration is done on the GAL zircon (c.a 480 Ma, very high U, Th and common lead content, Montero *et al.,* 2008). Analytical sessions start measuring the SL13 zircon (Claoué-Long *et al.,* 1995), which

is used as a concentration standard (238 ppm U). The TEMORA zircon (417 Ma, Black *et al*., 2003), used as isotope ratios standard, is then measured every 4 unknowns.

Data reduction is done with the SHRIMPTOOLS software specifically developed for IBERSIMS by F. Bea. This software is written in the programming language of the STATA commercial package which implements powerful algorithms for robust regression, outlier detection and time-series analysis. The software calculates the intensity of each measured isotope in two steps. First, it uses the STATA letter-value display algorithm to find outliers in the ten replicates measured in each peak during each scan, discarding them and averaging the rest once normalized to the SBM measurements. Then, for each isotope, it makes a robust regression of each scan average *versus* the time if was measured. The final result for each isotope is calculated as the value at the mid-time of the analysis resulting from the robust regression line.

Errors (95% confidence level) calculated as the standard error of the linear prediction at the mid-point of the analysis. $^{206}Pb/^{238}U$ is calculated from the measured $^{206}Pb+/^{238}U+$ and UO^{+}/U^{+} following the method described by Williams (1998). For high-U zircons (U > 2500 ppm) $^{206}Pb/^{238}U$ is further corrected using the algorithm of Williams & Hergt (2000). Though seldom necessary, the software also allows correction for instrumental drift with time using the sequence of replicate measurements of the TEMORA zircon. These were also used for calculating the point-to-point error for the analytical session, to which the error for the final age calculations must be expanded.

Corrected and uncorrected common Pb measurements were made and the main population age is the same within the error margin, thus uncorrected common Pb ages were considered (Fig. VIII.4).

The U-Pb isotope data are listed in the appendix E, table E.2.

Age main population	Mean	Err.
206/238	580.	± 6
207/235	582	± 5
206/238 (207-corrected)	580	± 6
206/238 (204-corrected)	579	± 6

Fig. VIII. 4 – Measured main population ages for corrected and uncorrected common lead.

8.2.3. Results

Figures VIII. 5, 6, 7 and 8 show the natural and cathodoluminescent images of each zircon crystal, the location of the analyzed points and the ages obtained, followed by a brief description of the zircon morphology and internal structure.

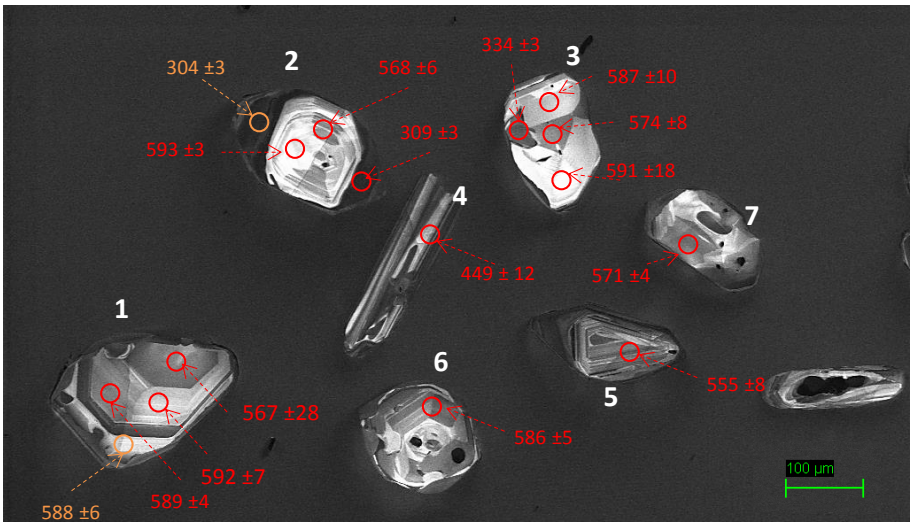

Fig. VIII. 5– Cathodoluminescence images of zircons 1 to 7 with location and obtained ages (Ma) for each analysed point. U–Pb results are indicated as ^{206}Pb / ^{238}U dates with 1σ errors. Concordant ages in red and discordant ages in orange.

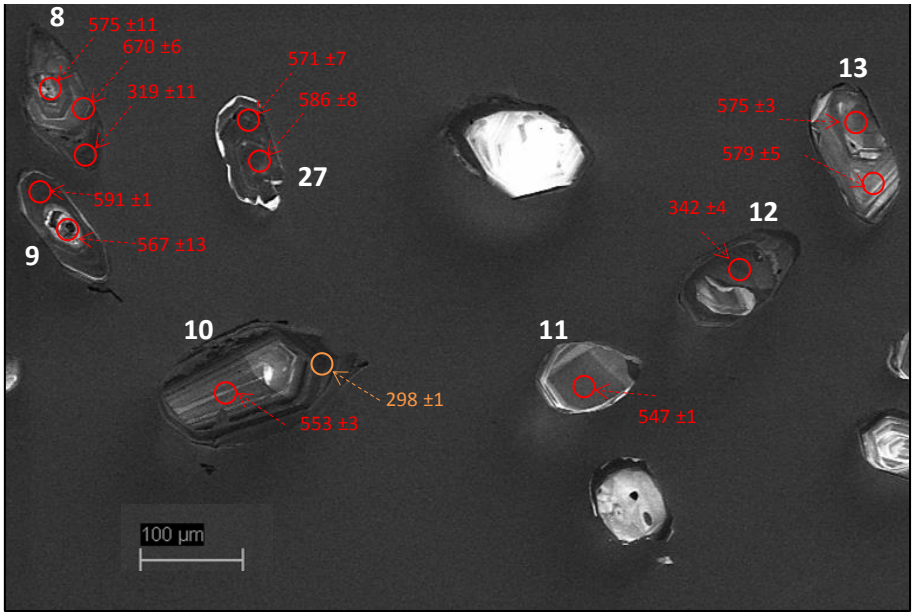

Fig. VIII. 6 - Cathodoluminescence images of zircons 8 to13 and 27 with location and measured ages (Ma) for each target point. U–Pb results are indicated as ^{206}Pb / ^{238}U dates with 1σ errors. Concordant ages in red and discordant ages in orange.

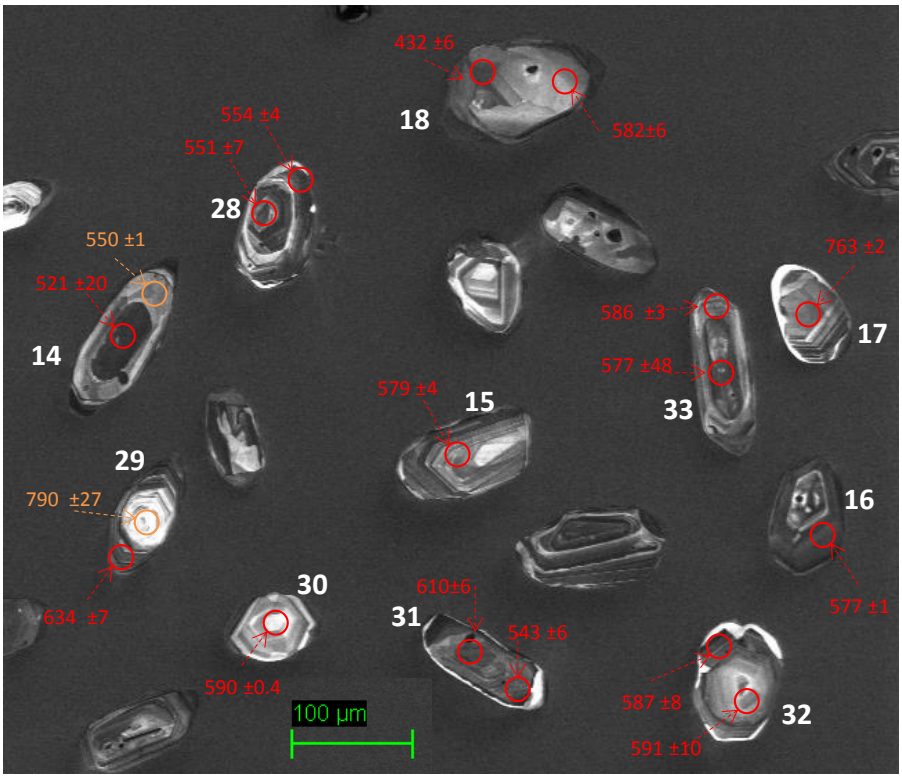

Fig. VIII. 7 - Cathodoluminescence images of zircons 14 to18 and 28 to 33 with location and measured ages (Ma) for each target point. U–Pb results are indicated as ^{206}Pb / ^{238}U dates with 1σ errors. Concordant ages in red and discordant ages in orange.

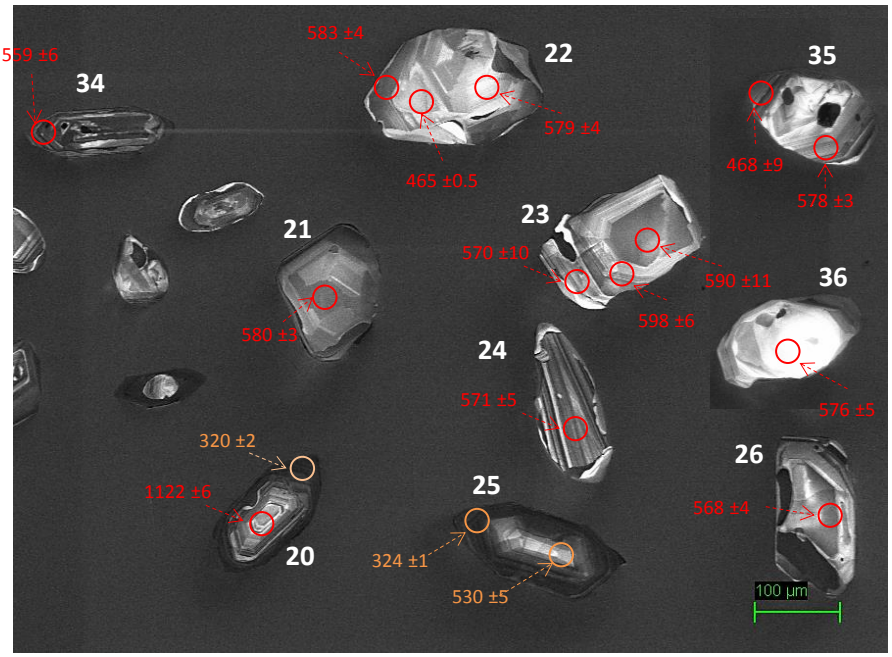

Fig. VIII. 8 - Cathodoluminescence images of zircons 20 to 26 and 34 to 36 with location and measured ages (Ma) for each target point. U–Pb results are indicated as ^{206}Pb / ^{238}U dates with 1σ errors. Concordant ages in red and discordant ages in orange.

Zircon 1 - Originally euhedral zircon mechanically fractured and damaged in one of the pyramids by etching or corrosion. It shows a nucleus that could be divided into three parts: a nebulitic core, followed by an intermediate portion showing faded fine oscillatory zoning, ending with large zoning that is disturbed by lobate transgressive overgrowth. The measured ages are the same in all the areas within the margin of error corresponding to the Ediacaran period.

Zircon 2 – Zircon with a core showing fine oscillatory zoning later changed to marked sectorial zoning. External darker zone showing pyramids development and unclear oscillatory zoning. The measured ages in different parts of the oscillatory zoning are different, varying from 568 ±6 to 593 ±3 but belonging to the Ediacaran period. The external zone shows Carboniferous (Variscan) ages.

Zircon 3 - Multifaceted zircon showing sectorial zoning and transgressive recrystallization. The measured ages in different parts of the sectorial zoning are the same under the error margin, corresponding to Ediacaran period. A Carboniferous (early Variscan) age was obtained in the transgressive recrystallization sector.

Zircon 4 - Prismatic zircon showing brown tonality and poorly defined large oscillatory zoning. It was mechanically fractured and presents partial transgressive recrystallization truncating the earlier zoning. The age measured is Ordovician.

Zircon 5 - Zircon composed of an inherited core showing large oscillatory zoning and a dark rim, especially in the pyramidal faces. The age measured in the inherited core is Ediacaran.

Zircon 6- Multifaceted zircon showing sectorial zoning transposing a diffuse oscillatory zoning. Transgressive recrystallization front and convolute zoning appear at the bottom of the crystal. Ediacaran age measured.

Zircon 7 – Zircon showing complete transgressive recrystallization and a thin overgrowth rim. Ediacaran age measured.

Zircon 8 – Zircon showing a prismatic core truncated by transgressive recrystallization. Lower region shows diffuse oscillatory zoning and a pyramidal overgrowth rim. Concordant ages measured in the core show large variation: In the center showing light color and distrurbance, the age is Ediacaran (575) and in the border showing oscillatory zoning the age is Cryogenian (670 Ma). The pyramidal overgrowth rim shows a concordant Carboniferous (Variscan age; 319 ±11 Ma).

Zircon 9 - Prismatic zircon showing diffuse oscillatory zoning and a ligther rounded nucleus. Concordant age measured in the clearer core is younger than the concordant age measured in the rim. However the core shows lighter color around inclusions indicative of later distrubance.

10 Zircon - Zircon showing diffuse oscillatory zoning and a pyramidal overgrowth rim. It shows a small recrystallization front which has developed before the rim growth since the last is not affected. Concordant measured Ediacaran age in the core and discordant Carboniferous (late-Variscan) age for the rim.

Zircon 11 - Rounded zircon showing nebulitic core and very thin oscillatory zoning edge. There is a small recrystallization front transposing the oscillatory edge. Concordant measured age is Ediacaran.

Zircon 12- Zircon with at least 3 stages of development: 1st - Small inherited magmatic core showing diffuse oscillatory zoning; 2nd - transgressive metamorphic recrystallization; 3rd – Fine rim with incipient

oscillatory zoning and development of small pyramid. Concordant age measured in the transgressive recrystallization front is Carboniferous (earlier Variscan; 342 ±11 Ma).

Zircon 13 – Ovoid zircon showing nebulitic core and diffuse oscillatory zoned edge.

Zircon 14 - Prismatic zircon showing a dark core (probably metamorphic) and an oscillatory zoned border. There is also a small rim overgrowth in the pyramids. Concordant Cambrian age measured for the dark core and discordant Ediacaran age for the rim.

Zircon 15 – Zircon mechanically fractured in one edge and showing diffuse oscillatory zoning. The oscillatory zoning is perturbed and convoluted specially in the top. Concordant age measured is Ediacaran.

Zircon 16 – Ovoid zircon showing very diffuse oscillatory zoning in the core and development of light colour recrystallization front around inclusion. There is a metamorphic low luminescent edge surrounding the core and showing concordant Ediacaran age.

Zircon 17 - Zircon which preserves a nebulitic core and oscillatory zoning. There is a development of a high luminescent edge transgressing into the interior (convoluted zoning). Concordant measured age in the core is Cryogenian (763 ±2 Ma)

Zircon 18 – "Soccer-boll" zircon with faceted faces showing concordant Ediacarian age. Darker small recrystallization front showing concordant Silurian age. There is also a very thin low luminescent rim.

Zircon 20 – Prismatic zircon showing oscillatory zoning followed by a featureless darker zone. Especially in the pyramids an overgrowth rim develops. The oscillatory zoning is perturbed by transgressive recrystallization. Mesoproterozoic concordant age measured in the core and Carboniferous (Variscan) age measured in the pyramidal overgrowth.

Zircon 21 – Irregular metamorphic zircon showing perturbed sectorial zoning and transgressive recrystallization that truncates the sectorial zoning. Concordant Ediacaran age measured in the zircon core.

Zircon 22 – Ovoid metamorphic zircon showing diffuse oscillatory zoning superimposed by sectorial zoning. Partial transgressive recrystallization truncates the sectorial zoning. Concordant ages measured in the sectorial zoning are Ediacaran and the concordant age measured in the disturbed zone is Ordovician (465 ±0.5 Ma).

Zircon 23 – Ovoid zircon showing a featureless core surrounded by oscillatory zoned border. The zircon was mechanically fractured in one edge and then acquired rounded corners. Concordant Ediacaran ages obtained in the core and in the edge of the zircon are the same within the error margin.

Zircon 24 - Prismatic zircon showing oscillatory zoning and a thin edge with high luminescence that truncates the oscillatory zoning. Concordant Ediacaran age measured in oscillatory zoning.

Zircon 25 – Prismatic zircon with brown tonality showing sector zoning in the core and a thin overgrowth darker rim with incipient oscillatory zoning that develops especially in the pyramids. Discordant Cambrian age measured in the core and discordant Carboniferous (Variscan) age measured in the overgrowth rim.

Zircon 26 – Zircon showing a featureless core truncated by a perturbed edge that shows penetrative transgressive recrystallized darker areas. Concordant Ediacaran age measured in the core.

Zircon 27 – Zircon showing irregular morphology and a pink tonality. Diffuse oscillatory zoning and a bright fine rim. Concordant ages measured are Ediacaran and the same in two zircon spots under the error margin.

Zircon 28 – Ovoid zircon showing perturbed oscillatory zoning. Concordant Ediacaran measured ages are the same in the zircon core and edge within the error margin.

Zircon 29 – Prismatic zircon with a highly luminescent core showing Cryogenian discordant age and an oscillatory zoning edge showing concordant younger age in the top of Cryogenian.

Zircon 30 – "Soccer boll" zircon showing sectorial zoning and concordant Ediacaran age.

Zircon 31 – Prismatic zircon showing a nebulitic core followed by diffuse perturbed oscillatory zoning. A thin darker recrystallization front truncating the oscillatory zoning is more pronounced in the top pyramid. A highly luminescent overgrowth rim also truncates the oscillatory zoning in the other pyramid. Although both are Ediacaran, the age measured in the nebulitic core (610 ±6 Ma) is older than the mode and the age measured in the oscillatory zone (543 ±6 Ma) is younger than the mode.

Zircon 32 – "Soccer-boll" zircon showing perturbed sectorial zoning. There is a thin highly luminescent rim whish transgresses into the area with sectorial zoning. Ediacaran ages measured in the core and in the rim of the sectorial zoning are the same within the error margin.

Zircon 34 – Prismatic zircon showing perturbed and diffused oscillatory zoning. Upper Ediacaran concordant age measured in the zircon rim.

Zircon 35 – Ovoid zircon showing a perturbed core truncated by diffuse oscillatory zoning and superposed sectorial zoning. Ediacaran age measured in the oscillatory zoning and middle Ordovician age measured in the edge.

Zircon 36 – Ovoid zircon showing high luminescent core with sector zoning. Concordant Ediacaran age was obtained in the high luminescent zone.

8.2.3.1. Summary of the results

The zircon population of diatexite sample VC60 is dominated by medium-sized grains (90–150 µm) but also includes larger grains (~200 µm). Most zircons are translucent and pinkish and a few are brown. Some grains have mineral inclusions, generally showing lighter disturbed zone around them. The zircons show a wide variety of forms ranging from subhedral grains with pyramidal terminations to strongly rounded crystals with no visible crystalline faces. The internal structure and external morphology of the zircons is characteristic of xenocrysts, showing in cathodoluminescent images the existence of three components in most of the zircons: i) an inherited core showing magmatic or metamorphic textures and ovoid external morphology, ii) a transitional

zone showing corrosion and lobate transgressive recrystallization fronts and iii) a dark rim overgrowth developing mostly in the pyramidal extremities.

8.2.3.1.1. Inherited cores

The cores show several internal structures that indicate the outcome of total or partial solid state recrystallization superimposed in magmatic textures, including diffuse nebulitic and oscillatory zoning; "soccer ball" structure resulted from sector zoning, convolute zoning, transgressive recrystallization fronts, lobate boundaries, etc.

56 cores were analyzed being 51 concordant (91%). The measured ages show the following distribution (Fig. VIII.9 and VIII.10):

- One measured age is Mesoproterozoic (1121 Ma) representing inherited zircon that preserved in the core the magmatic oscillatory zoning and shows a dark variscan rim.
- Four measured ages are Cryogenian two being around 660 Ma and two around 790 Ma (one is discordant); they were measured in the cores of zircon showing oscillatory zoning. Some of them show younger age to the borders (e.g. zircon 29 and zircon 31)
- Most of the measured ages are Ediacaran (75%) ranging from 630 to 530 Ma, showing a concentration peak around 590 Ma. The Ediacaran ages were obtained in cores showing either diffuse oscillatory zoning and/or sectorial zoning and/or in zircons without any internal structure.
- Four measured ages are Ordovician around 460 Ma and two are early Carboniferous (343 and 334 Ma). All this ages were obtained in zircons showing dark transgressive recrystallization fronts particularly in the transition between the cores and the rims.

The Th/U ratio shows large variation (between 0.02 and 0.73) and in general is higher than typical for metamorphic zircon (<0.1) and lower than typical for igneous zircons (> 0.5 ppm) (e.g. Schaltegger *et al.*, 1999; Hoskin & Black, 2000; Rubatto *et al.,* 2002; Hoskin & Schaltegger, 2003). Only 8% of the zircons cores show Th/U < 0.1 and 17% show Th/U > 0.5. The older zircons (Mesoproterozoic and Cryogenian) show Th/U ratios > 0.6 compatible with the considered to igneous zircons (Fig. VIII. 10). The

values found in the diatexite zircon cores, mostly situated between the typical for metamorphic and igneous zircons, could be the result of partial metamorphic recrystallization, indicating that the Ediacaran measured ages are mostly metamorphic whereas the older measured ages reflect the igneous not disturbed inherited cores.

There is positive correlation between Th and U suggesting a coupled exchange relationship. Exception for measurements in zircons showing intense high luminescence that show enrichment in U relatively to Th (Fig. VIII.11).

In all the zircons showing marked sectorial zoning the Th and U contents are higher in the darker parts than in the lighter parts of the zoning, what could indicate transference of elements during the metamorphic process that originate the sector zoning. Although in most of these zircons the ages measured in the different parts of the sector zoning are only slightly different (the same within the margin error), there is one zircon where the ages measured in the clear and darker zones are different (593 ±6 and 568 ±6 Ma respectively; zircon 2).

8.2.3.1.2. Rims

The rims are usually very narrow (maximum 50 µm but the majority is about 15 µm), some show incipient magmatic oscillatory zoning and growth preferentially over the pyramids sites, giving a pyramidal aspect to the zircon crystal. All possible rims were analyzed but most of them are thinner than the diameter of the SHRIMP beam. From 6 analyzed rims, two are concordant and four are discordant. The ages measured are Carboniferous, ranging from 324 to 298 Ma. The concordant ages are 319 ±11 and 309 ±3 Ma. All the rim measurements show very low Th/U ratio (< 0.02), especially due to the relatively high U content (av. 1775 ppm) and the low Th content (< 46 ppm). Some authors consider that a low Th/U ratio (<0.1 ppm) is synonymous for metamorphic zircons. (e.g. Schaltegger *et al.,* 1999; Hoskin & Black, 2000; Rubatto *et al*., 2002) while for others this division is not effective and low Th/U ratio is not always diagnostic of metamorphic processes (e.g. Moller *et al*., 2003; Kelly & Harley, 2005; Harley *et al*., 2007). In the Gyeonggi migmatitic massif, Horie *et al.* 2009 found the same characteristic for migmatitic zircons, showing an inherited core and a low Th/U rim. The authors consider that the rim is attributing to “anatectic metamorphism”.

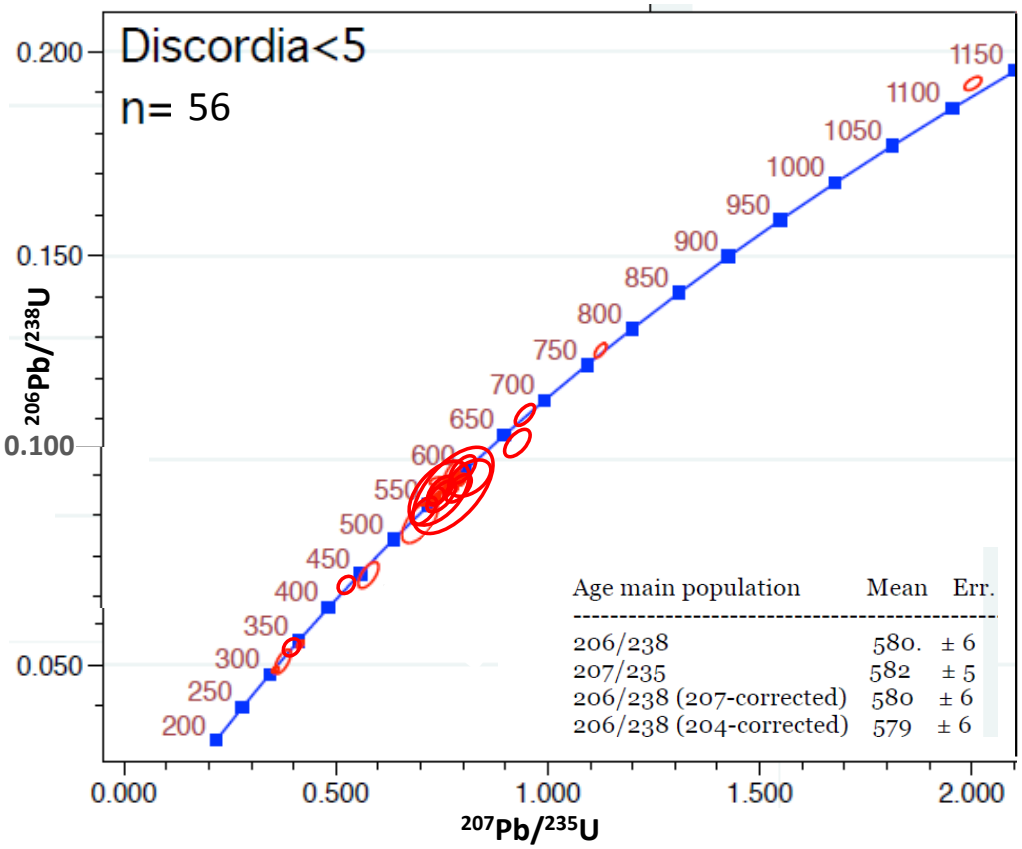

Fig. VIII. 9 – Wetherill Concordia diagram for common Pb uncorrected data of the MMC diatexite zircons considering only the concordant zircons.

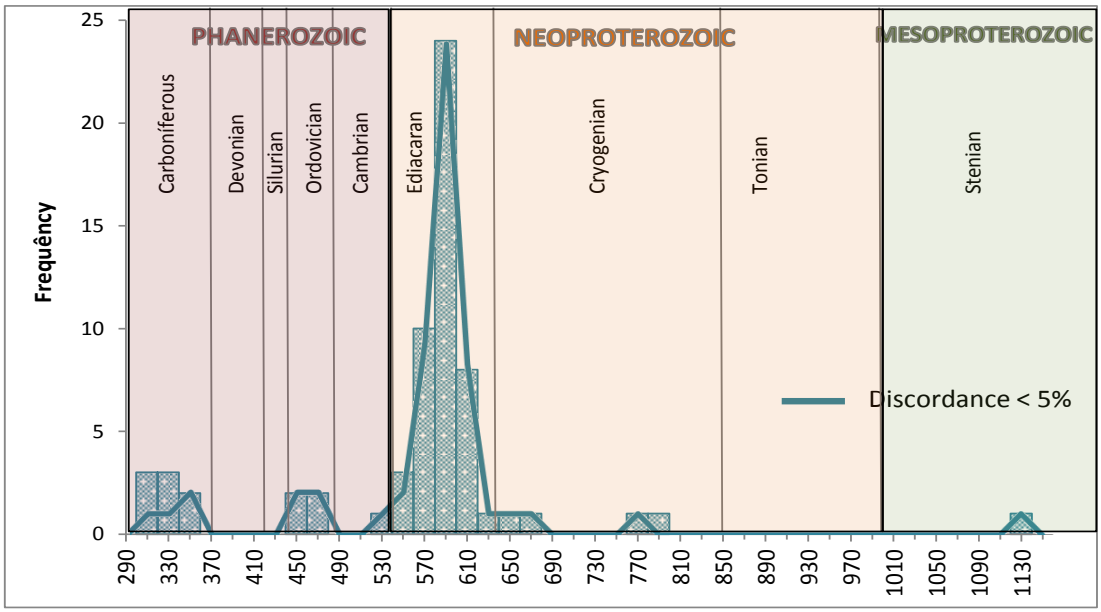

Fig. VIII. 10 - Histogram for the ^{206}Pb / ^{238}U ages measured in the diatexite sample (VC60) from MMC (64 measurements). The line represents the concordant ages (56 measurements).

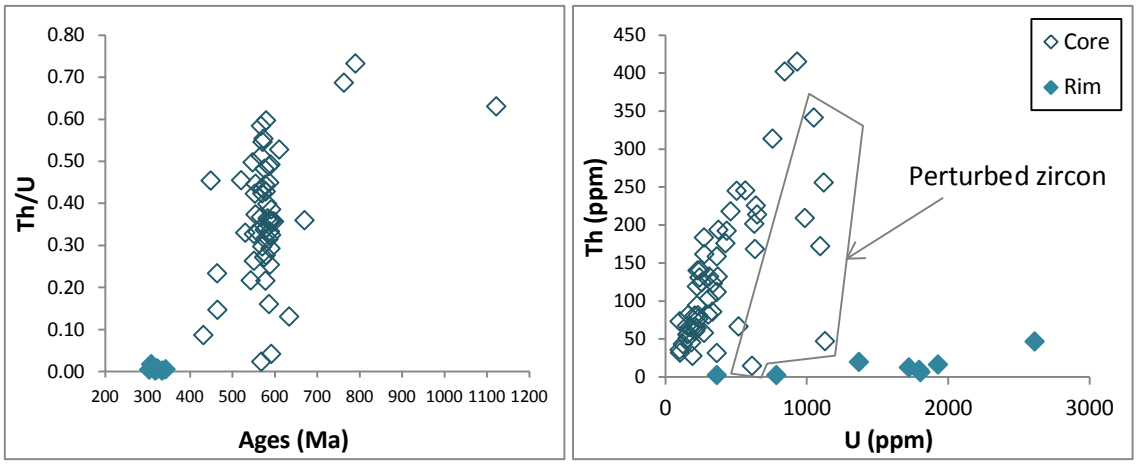

Fig. VIII. 11 – Th/U *vs.* ages and Th *vs*. U diagrams for cores and rims of MMC diatexite zircons. The "perturbed zircons" are those whish show intense high luminescence around inclusions or in the borders.

8.2.4. Interpretation and discussion of the results

Although the analyzed sample belong to a rock showing mostly magmatic petrological textures with variable amount of schlieren it is notorious the detrital provenance/aspect of the zircons cores. Moreover, these zircons were affected by partial or total recrystallization processes that are reflected in its external ovoid morphology and round crystal terminations, diffuse oscillatory zoning, sectorial zoning, convoluted borders, lobate reentrances and transgressive recrystallization fronts. Thus, the ages recorded in zircon grains from the diatexite sample could be significant in characterizing the sources of the sedimentary protolith and in estimating its depositional age (Castineiras *et al*. 2008). The rim overgrowths with Variscan ages reflect a later event.

Inherited zircons in the MMC diatexite define an age range displaying predominant Neoproterozoic populations. This group of zircons is the most abundant and fits well with materials derived from the Cadomian orogeny. In general, the probability density curve of the MMC diatexite inherited zircons shows a broad overlap with the zircon U–Pb age distribution previously reported for the Schist-Greywacke Complex ages (Gutiérrez-Alonso *et al*., 2003; Teixeira, 2008; Teixeira *et al*., 2011; Pereira, 2011, 2012; Talavera *et al*., 2012;) This similarity points to the Schist-Greywacke Complex as the most probable protolith of the MMC metatexites and granitic rocks.

Beiras-Group and Douro-Group detrital zircons belonging to low metamorphic grade metagreywackes were recently dated (Teixeira *et al*. 2011, 2013; Pereira *et al.*, 2012).

Besides Archean, Paleoproterozoic and Mesoproterozoic ages, over 75% of the Beiras-Group and Douro-Group greywackes zircon ages are late Neoproterozoic. Cryogenian ages are those most represented (c. 833–631) followed by Ediacaran and Tonian ages.

When comparing our data with data from Pereira *et al*. (2012) and Teixeira (2008) we find a number of similarities and differences. The Neoproterozoic ages are prevalent in the MMC studied sample as well in Douro-Group and Beiras-Group. However, as mentioned before, in MMC there is a noticeable greater frequency of Ediacaran ages relatively to the Cryogenian ages and the older Cryogenian ages are significantly under-represented while in the Beiras-Group and Douro-Group the Cryogenian ages dominate and there is a significant contribution of Tonian ages. The Paleoproterozoic and Archean ages are absent in MMC studied sample while in the metasedimentary sequences are well represented.

Also the absence of younger than Ediacaran ages in Beiras and Douro-Group is a noticeable feature that distinguishes the MMC studied sample from the low grade metasedimentary sequences.

Thus, unlike Beiras-Group the MMC studied sample shows mainly latter Cadomian ages. The question is to understand if the ages measured are the result of exclusively magmatic events or also have the contribution of metamorphic events within the measured age's interval. Considering: i) the continuous existence of zircons ages from 610 Ma to 520 Ma and the peak concentration around 590 Ma in zircons showing marked metamorphic internal structures, ii) the low Th/U content and iii) the correlation between Th and U (coupled exchange), it is suggested that most of the inherited zircons could result mostly from partial recrystallization processes or from total recrystallization processes that completely erased the previous zoning (featureless zircons). These recrystallization events could represent recrystallization during the main Cadomian metamorphic event whose age of 590 Ma coincide with the age concentration peak in the MMC diatexite inherited zircons. Moreover, the Mesoproterozoic and Cryogenian aged zircons and the zircons aged older than 590 Ma have probable magmatic origin, which is suggested by their higher Th/U ratios and internal structure.

The two Ordovician ages measured in the cores showing disturbed structures and abnormal U content most likely are mixed ages, probably represent sites of incomplete

homogenization during metamorphism rather than meaningful periods of growth (*e.g*. Hoskin & Black, 2000;).

The early Carboniferous ages (343 and 334 Ma) measured in the disturbed transition between cores and rims could be the result of the early Variscan metamorphic events that disturbed the borders of the Ediacaran cores, before the pyramidal overgrowths. The rims, aged 319 to 309 Ma, are interpreted as late-Variscan magmatic developments. These late variscan magmatic overgrows are probably related to the MMC migmatization and anatexis, that should have occurred during the Variscan Orogeny between 330 to 310 Ma and falls within the range of ages defined by many authors for the emplacement of syn-D3 granitic rocks in Iberian Central Zone (*e.g*. Ferreira *et al.* 1987; Dias et al.,1998; Fernandez Suarez *et al*., 2000, Almeida *et al*., 2001, 2014, Valle Aguado *et al*., 2005; Teixeira, 2008, Teixeira *et al*., 2011).

MMC diatexite zircons show Neoproterozoic inherited ages and Variscan overgrowth ages coeval with the ages found to other anatectic complexes in the Central Spain. Like MMC studied sample also the zircon ages of the Sotosalbos, Toledo and Peña Negra anatectic complexes show an important Neoproterozoic age (Castiñeiras, 2008) and a younger zircon populations dated ~330 Ma in the Sotosalbos region, 317 Ma in the Toledo complex (Castiñeiras *et al.* 2008) and 315 Ma in Peña Negra (Zeck *et al.* 2004). Montero *et al*. (2004) stated that anatexis in the Central Spain region occurred for a long period, from 352 to 297 Ma, with a maximum at 335-305 Ma, suggesting a coeval emplacement of massif-type granites.

In general the measured anatexis ages are younger than the age of the main Hercynian metamorphic events indicating that migmatization occurred late in the metamorphic cycle, after peak conditions were attained (Castiñeiras, 2008). This is in agreement with the petrologic evidence suggesting that anatexis took place late in the Hercynian cycle during the exhumation of metamorphic core complexes (Barbero 1995) and coincide with the ages stablished to the 3rd Variscan deformation phase (Noronha, 1979; Acciaioli *et al*., 2003; 2005; Valle Aguado *et al*., 2005). This late origin with respect to the thermal peak for the studied migmatite terranes in the Central Iberian Zone is also comparable with other European Hercynian terranes, where ages for intermediate P and high T granulites vary from 345 to 323 Ma (Kroner *et al*. 1998; Chen *et al*. 2003; Gordon *et al.* 2005, Be Mezeme *et al*. 2006).

The good preservation of pre-Hercynian zircons in the diatexite is remarkable even though the original metamorphic fabric of these rocks has been mostly obliterated

during the anatectic event. The preservation of inherited ages in the pelite-derived MMC diatexite also suggests that the anatexis occurred at low temperature and/or the duration of the magmatic event is short (Watson, 1996). It is possible that the zircons incorporated in the biotitic schlieren are probably the ones without any rim overgrowth and the zircons with marked rims probably are in contact with the magmatic portion of the diatexites.

8.3. Rb-Sr and Sm-Nd systems

8.3.1. Principles of Rb-Sr method

The Rb-Sr system is based on the decay of the radioactive isotope ^{87}Rb to the radiogenic isotope ^{87}Sr. The amount of ^{87}Sr in a mineral or rock containing Rb increases continuously as a function of time, allowing its use for age determinations. Furthermore, the isotope ^{87}Sr can be used as a tracer in certain geological processes. The total number of atoms of ^{87}Sr existing in any geological material at age (t) is given by the fundamental equation of Geochronology (eq. 1).

An isochron is obtained by a diagram in which the X axis represents the $^{87}Rb/^{86}Sr$ ratio and the Y axis represents the $^{87}Sr/^{86}Sr$ ratio. The slope of the line that best fits the obtained ratios corresponds to the age of crystallization or metamorphism. When the degree of scattering of the points that define the line calculated by linear regression is above a certain amount this is called an “errorchron” and should be treated with caution (Brooks *et al*., 1972). The dates and initial ratio derived from errorchron may, nevertheless, convey geologically useful information, especially in cases where additional facts or judgments support them (Faure, 2000). The MSWD parameter (Mean Square of Weighted Deviation) established by McIntyre *et al*. (1966) defines the degree of scattering of the experimental points from the best line and therefore the consistency of the isochrons. If the reason for the analytical uncertainties is only associated with scattering, the MSWD tends to be close to one. Much higher values generally indicate either or overestimated analytical errors or other source of scattering is present, often called "geologic scattering". Snelling (1976) proposed maximum values of MSWD for a line to be considered an isochron, relative to the number of analyzed points. These values are shown in table VIII.1.

Table VIII.1 - Maximum values of MSWD for an isochron (Snelling, 1976)

Nº points	3	4	5	6	7	8	9	10
$MSWD_{max}$	3,92	3,07	2,68	2,45	2,29	2,18	2,09	2,02

During magmatic differentiation or during sedimentation the behavior of the Rb and Sr ions is different. Rb is an alkali metal with a low ionic radius which allows its integration in the mineral crystal lattice replacing K. Sr is an alkaline earth metal and tends to replace Ca. The different behavior of the pair Rb-Sr and its geochemical mobility allows the easy opening of the system, which requires special attention in the interpretation of the age data (Geraldes, 2010).

With regard to the petrogenesis of igneous rock, Rb/Sr isotopic method allows distinguishing magma originated exclusively in the upper mantle or derived wholly or partly from crustal rocks. Indeed, the Earth magmatic differentiation processes lead to the formation of a continental crust more rubidium enriched than the mantle and thus in ^{87}Rb. This composition is reflected on the isotopic $^{87}Sr/^{86}Sr$ isotopic ratio, which is higher the greater the contribution of crustal material. Thus, ratios $(^{87}Sr/^{86}Sr)_i > 0.710$ indicate a source from crustal materials, meaning that strontium comes mainly from crustal rocks enriched in radiogenic ^{87}Sr. On the other hand, ratios $(^{87}Sr/^{86}Sr)_i < 0.704$ imply a mantle juvenile crustal origin without contribution of older crustal materials. For intermediate values of $(^{87}Sr/^{86}Sr)_i$ the source of the magma will be more difficult to interpret, supposing mixing models involving crustal and mantle contributions (e.g. Raymond, 1995; Faure & Mensing, 2005).

The metamorphic processes cause changes in the isotopic ratios of the pair Rb-Sr even for modest increases in temperature and therefore can be applied to the study of metamorphic events. If the system remained closed during metamorphism, the whole-rock isochron shall indicate the period of formation of the rock. However, if the system was open, both whole-rock and mineral isochronous indicate the metamorphism age (Jager *et al.*1967; Geraldes, 2010)

8.3.2. Principles of the Sm-Nd method

The Sm-Nd geochronological method is based on the radioactive decay of the ^{147}Sm radioactive isotope to the ^{143}Nd radiogenic isotope. The principles applied in this system are the same as for the Rb-Sr system, so it can be apply the isochron method

using the Fundamental Equation of Geochronology and the ^{144}Nd stable isotope as a reference:

$$^{143}Nd = (^{143}Nd)i + {}^{147}Sm\ (e^{\lambda t} - 1)$$

However, the small variations of the ratio $^{147}Sm/^{144}Nd$ make difficult or impossible the measurement of crystallization ages, especially when using only whole-rock samples. The ideal is combine analyses of whole-rock with analyses of mineral phases (Dickin, 2005).

The Sm and Nd belong to the rare-earth elements group and have similar characteristics. For this reason, these two elements have a similar behaviour in most geological processes. The immobile character of these elements during most geological processes, particularly during metamorphic episodes, hydrothermal alteration and weathering allows the system to be closed. Therefore their systematic study has been used as a geochemical indicator of the nature and composition of the protolith (DePaolo, 1988; McLennan *et al.,* 1990; Faure & Mensing, 2005;), although slight changes may occur during the sedimentary cycle (Awwiller & Mack, 1991, Zhao *et al*., 1992).

The parameters of the Sm-Nd system are distinctive of mantle *vs*. crustal origin of the rocks. Relatively low $^{143}Nd/^{144}Nd$ ratios indicate crustal sources, while high $^{143}Nd/^{144}Nd$ ratios suggest the input of mantle-derived juvenile material. Positive or near-zero εNd values near the crystallization age of an igneous suite, correspond to juvenile, mantle-derived components (DePaolo, 1988).

8.3.3. Methodology

Twenty-nine samples from MMC and the SGC were selected for Rb-Sr and Sm-Nd whole-rock isotope studies. They correspond to: four pelitic samples from Schist-Greywacke Complex (three from Fânzeres and one from Aguçadoura); three metagreywacke samples, three calc-silicate samples, two patch-metatexite samples; five banded-metatexites samples, one diatexite sample; two leucosome samples, two leucogranite samples; five two-mica granite samples and two aplite-pegmatite samples. The Rb-Sr and Sm-Nd isotope data are listed in the appendix E.

The analyses were performed at the Laboratório de Geologia Isotópica da Universidade de Aveiro, Portugal. The selected powdered samples were dissolved with HF/HNO_3 solution in Teflon Parr acid digestion bombs at 200ºC for 3 days. After evaporation of the final solution, the samples were dissolved with HCl (6N) and dried. The target elements were purified using conventional ion chromatography technique in two stages: (i) separation of Sr and REE elements in ion exchange column with AG8 50W Bio-Rad cation exchange resin; (ii) purification of Nd from other lanthanides elements in columns with Ln Resin (ElChrom Technologies) cation exchange resin. All reagents used in the preparation of the samples were sub-boiling distilled and the water produced by a Milli-Q Element (Millipore) apparatus. Sr was loaded on a single Ta filament with H_3PO_4, whereas Nd was loaded on a Ta outer side filament with HCl in a triple filament arrangement. $^{87}Sr/^{86}Sr$ and $^{143}Nd/^{144}Nd$ isotopic ratios were determined using a Multi-Collector Thermal Ionization Mass Spectrometer (TIMS) VG Sector 54. Data were acquired in dynamic mode with peak measurements at 1-2V for ^{88}Sr and 0.8-1.5V for ^{144}Nd. Sr and Nd isotopic ratios were corrected for mass fractionation relative to $^{88}Sr/^{86}Sr=0.1194$ and $^{146}Nd/^{144}Nd=0.7219$. During this study, the SRM-987 standard gave an average value of $^{87}Sr/^{86}Sr= 0.710256(16)$ (conf. lim=95%) and $^{143}Nd/^{144}Nd=0.5121057(61)$ (conf. lim=95%) to JNdi-1 standard ($^{143}Nd/^{144}Nd$ data are normalized to La Jolla standard). The concentrations of Rb, Sr, Sm and Nd in two whole-rock samples were determined by isotope dilution mass spectrometry method (IDMS), using a $^{87}Rb/^{84}Sr$ and $^{150}Nd/^{149}Sm$ double spike.

8.3.4. Results

8.3.4.1. Isochrons / Errorchrons

The isochrons/errorchrons presented in this study were calculated with ISOPLOT® software (version 3.7) developed by Ludwig (2003), with regression lines calculated by the least squares method and its adjustment assessed by the MSWD parameter. For errorchrons the model 3 of McIntyre (1966) is used where the excess scattering is absorbed by the expansion of initial proportions.

The ages obtained are significant but their precision is limited and the error margins are large due to Rb/Sr values dispersion and the small number of samples of each lithology. Being aware of these limitations, the results provide relevant information that

is discussed below. The whole-rock Rb-Sr isotope systematics provided the following ages:

- For SGC metasediments it was not possible obtain a significant isochron due to intense dispersion of the Rb/Sr values that are not collinear, giving a MSWD = 210.
- For metagreywacke resisters (Fig.VIII.12), based on 6 samples, an errorchron of 650 ± 60 Ma (MSWD = 26) was obtained. If considering only the metagreywacke resisters without the calc-silicate rocks (only three samples), an isochrone of 608 ±53 Ma (MSWD = 1.3) was obtained.
- For banded-metatexites and leucosomes (Fig.VIII.13A), based on seven samples, an errorchron of 329 ± 16 Ma (MSWD = 10.3) was obtained. Excluding the migmatitic greywacke samples (VC22 and VC16c) it is possible to obtain an isochron of 328 ±18 Ma, the same age as the errorchron (Fig. VIII.13B).
- For two-mica granites (Fig. VIII.14A), based on five samples, an errorchron of 324 ±38 Ma (MSWD = 5.8) was obtained.
- For aplite-pegmatites (Fig. VIII.14B) an age of 325 ±27 Ma, although only with two samples, was obtained.

Due to the nature of the studied rocks, a moderate to high dispersion in the Rb-Sr system is expected. These are high-grade metamorphic rocks and granitic rocks with high interaction fluid/rock and restitic component, which may produce changes in the Rb/Sr ratio that are reflected in the isotope ratio. The isotopic homogenization depends on various factors, like the nature of minerals involved, the existence of restitic phases that could both keep their isotopic signatures or reequilibrate with the melt (depending on the mineral composition, grain size and closing temperature and the extent of the thermal peak) (Dickin, 2005; Faure & Menssing, 2005)

In the case of whole-rock analyses, the question arises whether the system remained closed and what really reflect the measured ages.

The most relevant feature of the obtained results is the fact that the metagreywacke and calc-silicate resisters show an isochron of Ediacaran age, comprised in the same age range measured in the inherited cores of the diatexite by the U/Pb method. On the other hand, the MMC metatexites and granitic rocks show isochrons of Variscan age, of ~329 Ma. It is also remarkable that the errorchron ages obtained with larger number of samples coincide with the isochron ages obtained with a lesser number of samples, even though the lack of reliability of the 3-point or 2-points isochrons.

The studied rocks have different mineralogy and thus may have a different isotopic behavior during metamorphism. Metagreywacke and calc-silicate resisters, consisting mainly of quartz and Ca-plagioclase and rare biotite, thus containing minerals poor in Rb, could have remained as a closed system (for whole-rock), providing isotopic older age, coincident with the age of the protolith. In fact, it was found (Dickin, 2005 and referenced therein) that the ^{87}Sr generated by radioactive decay of unstable Rb occupies instable positions in the crystal lattice of minerals rich in Rb and tends to migrate from crystals if subjected to a heat pulse. However, if the fluids in the rock remain static, the Sr released from minerals such as feldspars and micas tend to be attached by Sr absorbing mineral as plagioclase, apatite and sphene, abundant in the metagreywacke and calc-silicate resisters. Thus, it is possible that the whole-rock system remains closed, even if the mineral system was open.

On the other hand, the migmatites are richer in K, both incorporated in the biotite and in K-feldspar, and therefore it is likely that the Rb-Sr system was been fully re-equilibrated when the migmatization occurred. Thus, it is expected that the isochron age of these rocks represent the Variscan thermal pulse that resulted in the anatectic process.

Despite some dispersion of values, the study of Rb/Sr isochrons reinforces the hypothesis of Ediacaran age for the sediments that originated the MMC lithologies and the Variscan age for migmatization and anatexis. The ages suggested for migmatization are coincident with the ages found by Acciaioli *et al*. (2005) in biotites contemporaneous of an early stage of D3 deformation phase that yielded an age of 333.5±4.4 Ma.

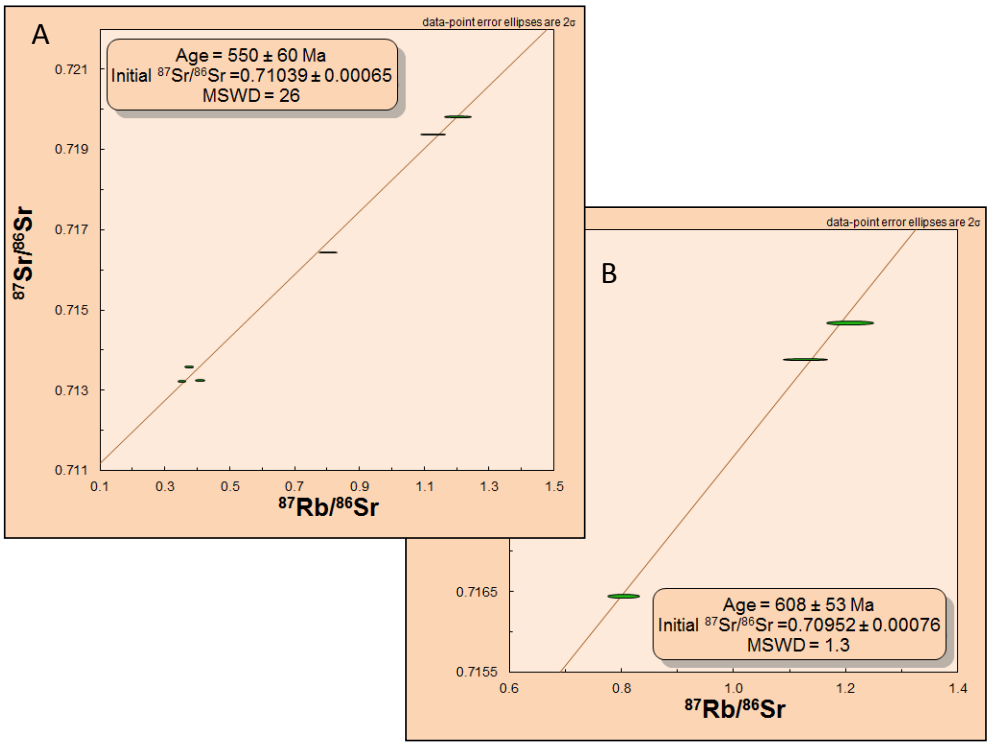

Fig. VIII. 12 - Nicolaysen diagrams for: A) Metagreywacke and calc-silicate resisters (errorchron); B) Metagreywacke resisters (isochron). Both show Ediacaran ages.

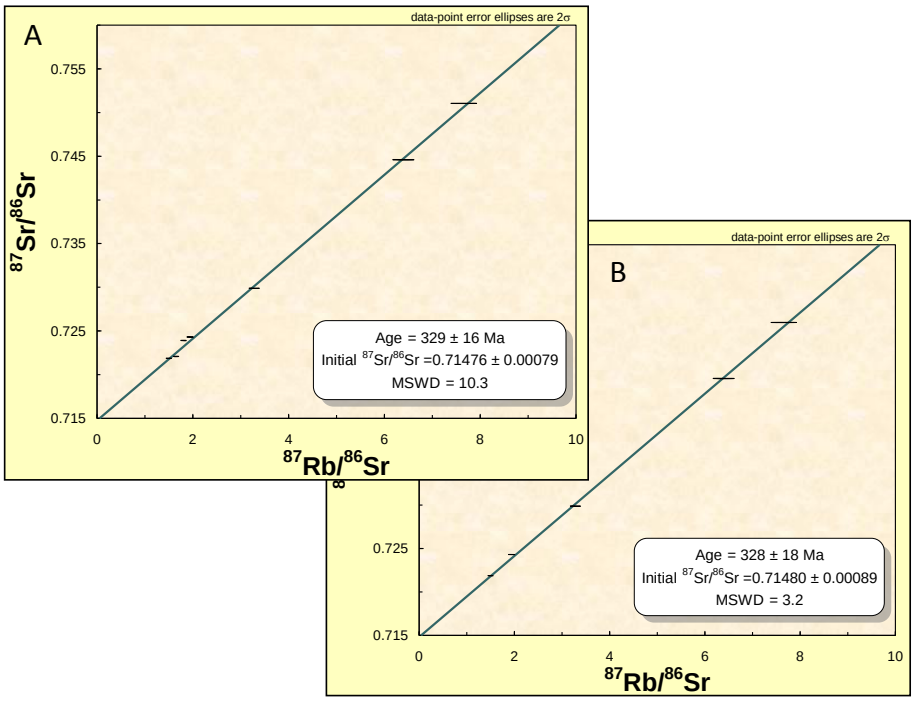

Fig. VIII. 13 – Nicolaysen diagrams for: A) Five banded-metatexites and two leucosomes samples; B) the same as in A) without two samples of migmatized metagreywackes. All the obtained ages are Variscan.

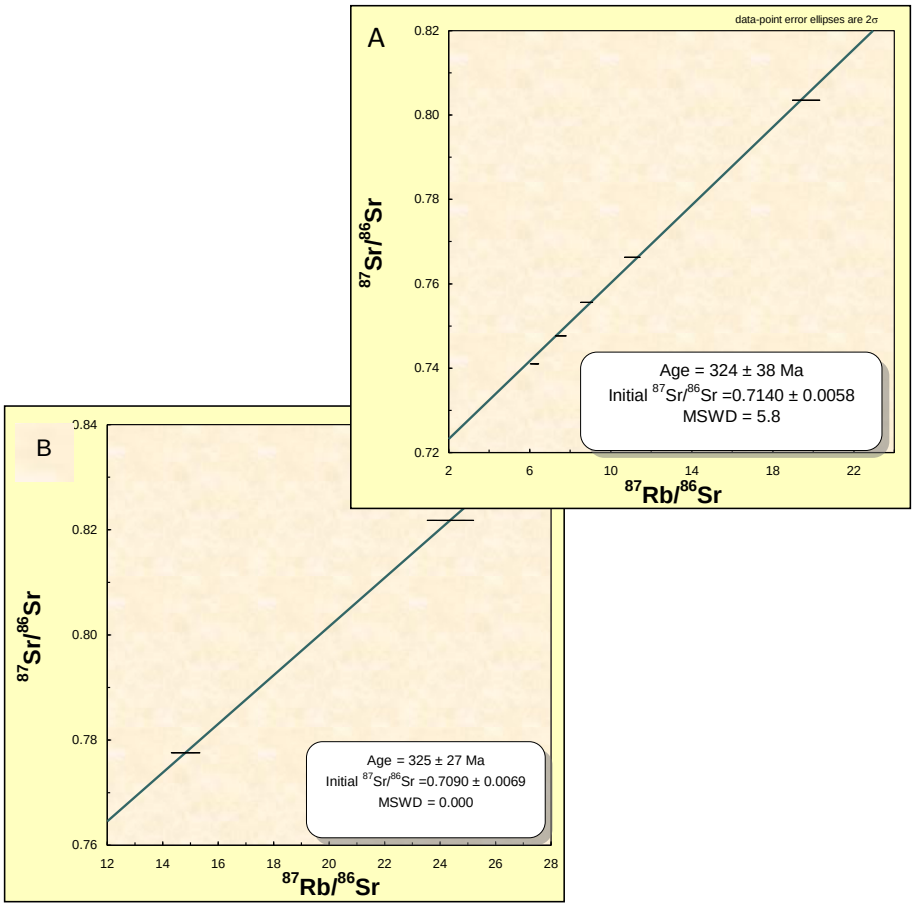

Fig. VIII. 14 - Nicolaysen diagrams for: A) Two-mica granites; B) Aplite-pegmatites.

8.3.4.2. Isotopic signature

The Sm-Nd isotopic results obtained in selected samples of SGC and MMC are presented in appendix E. For initial ratio calculations a representative Variscan age of 330 Ma is assumed since it is the age used by several authors considering the emplacement age of most syn-tectonic variscan granites (Beetsma, 1995; Teixeira, 2008), and corresponds to the isochron age obtained to the MMC metatexites.

Fig VIII.16 represents the εSr_{330} versus εNd_{330} diagram for selected MMC rocks superimposed on the fields established for other CIZ granitic and metasedimentary rocks.

Rb-Sr and Sm-Nd isotopic signatures reveal that the analysed samples have a substantial crustal component, showing εSr_{330} values ranging from +46 to +257 and εNd_{330} values ranging from -2.1 to -9.3.

The SGC metasediments show relatively wide ranges of initial $^{87}Sr/^{86}Sr_{(330)}$ (0.7139 to 0.7222) and some of them yield unrealistically low isotopic Sr ratios at the Ediacaran age (590 Ma), below BABI values. This is a geochemical feature of a significant part of the CIZ Neoproterozoic metasediments, as reported by other authors (Ugidos, *et al.*, 2003; Beetsma, 1995; Villaseca *et al*., 2014). These values clearly indicate disturbance of the Rb-Sr system during metamorphism. The Rb-Sr system may be disturbed by source-rock weathering, K-metasomatism and Rb mobility during diagenesis and metamorphism (McLennan *et al*., 1993). Thus, the $^{87}Sr/^{86}Sr$ ratio does not indicate the provenance of the rock but the conditions associated to the metamorphic processes.

The MMC lithologies (migmatites and granites) show much shorter range of initial $^{87}Sr/^{86}Sr_{330}$ (0.7113 to 0.7153) which suggests that the Rb-Sr resetting was complete, undertaking a Sr "isotopic uniformization process" (Cordani *et al.,* 2004), during the migmatization and anatectic process.

The aplite-pegmatite samples show lower values with $^{87}Sr/^{86}Sr_{330} < 0.7080$.

The range of $^{147}Sm/^{144}Nd$ values for all the analysed samples are within the limits established by Zhao *et al*. (1992) for undisturbed clastic sediments (from 0.100 to 0.130). The εNd results allows the division of the analysed lithologies into the following groups:

- Group I comprises the pelitic SGC metasediments, the patch-metatexites, the pelitic banded-metatexites and all the MMC granitic rocks, showing εNd_{330} values between -2.1 and -5.9;
- Group II comprises migmatized metagreywackes, metagreywacke resisters and calc-silicate resisters showing εNd_{330} values between -7.3 and -9.3.

The Nd isotopic composition of the MMC samples, compared with the values obtained by other authors for the granitic and metasedimentary rocks of the CIZ (Fig. VIII.15) (recalculated to the same age – 330 Ma), shows that the Group I coincide with the εNd values found in the Beiras-Group (Beetsma, 1995; Tassinari, 1995) and other Neoproterozoic metasediments (Ugidos *et al*., 1997, 2003; López-Guijarro *et al*., 2008; Villaseca *et al*., 2014). On the contrary, the isotopic signature found in the Douro-Group metasediments (Teixeira, 2008), to the lower-crust granulites (Villaseca *et al.* 1999) and to Paleozoic metasediments (Beetsma, 1995) show different Nd

isotopic ratios, generally with lower εNd than the MMC rocks and SGC metasediments (Fig. VIII.15).

The εNd_0 values for the SGC metasediments and for MMC rocks (including group I and Group II) overlap the values found by Dabard *et. al.* (1996) to Brioverian sediments from the Armorican Massif.

Relatively to the syn-tectonic two-mica granites studied by Beetsma (1995) and Teixeira (2008), the MMC granitic rocks show lower Nd isotopic dispersion and slightly higher εSr_{330} values. The MMC rocks, including two-mica granites, show εSr values between the syn-tectonic granites and the SGC metasediments. Also the comparison of the MMC granitic rocks with the values found by Almeida (2014) to the Porto granite show that the MMC lithologies have slightly higher εSr and lower εNd values for the same inferred age (313 Ma). The Porto granite samples plot in the field defined by the other CIZ two-mica granites (Beetsma, 1995).

The mixture of components with distinct elemental and isotopic composition generates a hyperbolic curve on a $^{87}Sr/^{86}Sr$ versus Sr diagram (e.g. Faure, 1986), correspondingto a straight line in $^{86}Sr/^{87}Sr$ versus 1/Sr diagrams. These diagrams are used to better understand the genetic relationship between the MMC different lithologies. The SGC samples collected at Aguçadoura, the migmatites (metatexites and diatexites), the leucogranites and the two-mica granites plot along a hyperbolic curve in the $^{87}Sr/^{86}Sr$ *versus* Sr diagram and show a collinear relation ($r^2 = 0.93$) on the $^{86}Sr/^{87}Sr$ *versus* 1/Sr diagram. The SGC samples collected at Fânzeres and the aplite-pegmatites plot outside this collinear group (Fig. VIII.16).

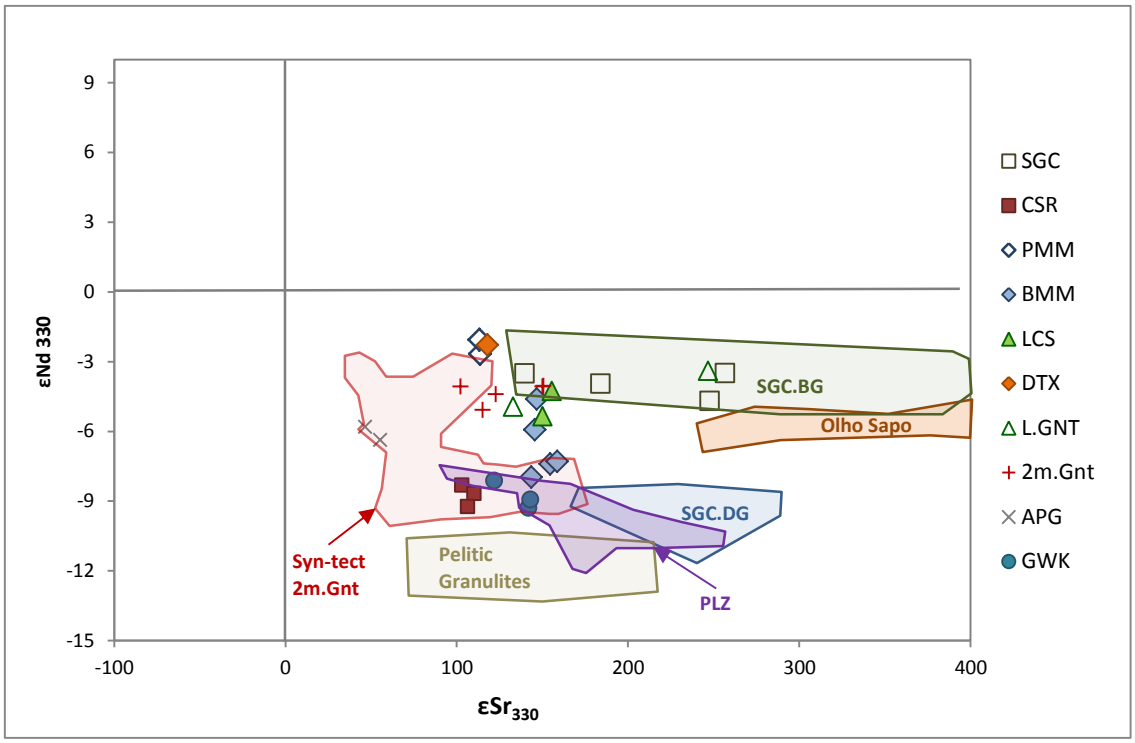

Fig. VIII. 15 – Initial Sr-Nd composition of the MMC rocks and SGC metasediments and comparison with other Central Iberian Zone granitic and metasedimentary rocks. Abbreviations: SGC.bg - field defined for Beiras-Group and other Neoproterozoic metasediments (Beetsma (1995) and Tassinary *et al*. (1995) (Beiras-Group) ; Ugidos *et al*. (1997, 2003); Villaseca *et al*. (2008, 2014) and Rodríguez-Alonso *et al*. (2004) (Neoproterozoic)); SGC.DG - Field defined for Douro-Group metasediments (Teixeira, 2008); Syn-tect 2m.Gnt – Field defined by syn-tectonic granites (Beetsma, 1995; Teixeira, 2008); Olho Sapo – Field defined for Olho de Sapo Orthogneiss (Beetsama, 1995); PLZ – field defined for Paleozoic metasediments (Beetsma, 1995); Pelitic granulites – field defined for lower crust pelitic granulites (Villaseca, 1999). Legend Key: SGC = Schist-Greywacke Complex; PMM = patch-metatexites, BMM = banded-metatexites; LCS = leucosomes; DTX = diatexites; 2m.Gnt = two-mica granites; APG – aplite-pegmatites; GWK = metagreywackes resisters;

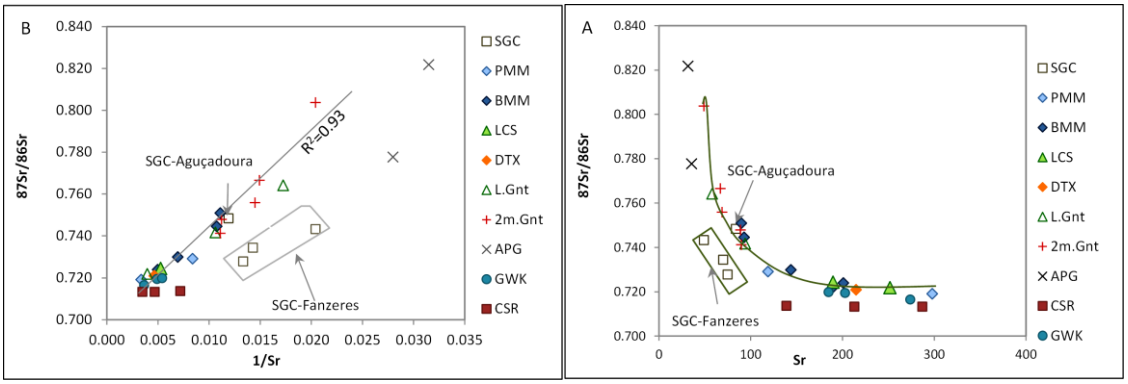

Fig. VIII. 16 – A) $^{87}Sr/^{86}Sr$ *vs* Sr diagram and B) $^{87}Sr/^{86}Sr$ vs 1/Sr diagram for MMC rocks and SGC pelitic rocks. Legend Key: SGC = Schist-Greywacke Complex pelitic samples; PMM = patch-metatexites, BMM = banded-metatexites; LCS = leucosomes; DTX = diatexites; 2m.Gnt = two-mica granites; APG – aplite-pegmatites; GWK = metagreywacke resister; CSR - calc-silicate resisters.

8.3.5. Interpretation and discussion of the results

It is generally recognized that the radiogenic parent/daughter elemental ratios are often changed on a regional scale during high-grade metamorphism. As a result, isotopic systems are strongly disturbed, and the pre-metamorphic history of high-grade terrains may be poorly constrained. In addition, the majority of anatectic granites generated during crustal melting events will be isotopically heterogeneous (Chemiak & Ryerson, 1993; Barbero *et al*. 1995; Faure & Mensing, 2005; Zeng *et al*., 2005). There are several anatectic complexes that lack isotopic homogeneity as is the case of the Manaslu anatectic Complex (Deniel et al., 1987) and the Toledo Anatectic Complex (Barbero *et al*. 1995) that exhibit large isotopic variation. Other anatectic complexes show isotopic homogeneity, as is the case of the Trois Seigneurs massif (Bickle *et al*., 1988) and St. Malo massif (Peucat, 1986).

In MMC, it was possible to observe that the initial isotopic heterogeneity shown by the two considered groups is mostly a replication of the protoliths heterogeneity: the pelite lithologies show isotopic signature different from the isotopic signature of the metagreywackes. This suggests that the Nd isotopic signatures are inherited from different levels of the sedimentary pile present in the MMC. The Nd isotope composition of terrigenous sediments is controlled by two processes: (i) mixing of detrital components derived from different source rocks in the provenance area and (ii) mechanical sorting and quartz dilution effects during erosion, transport and deposition resulting in unmixing of provenance components (McLennan, 1989). The bimodal Nd isotope variability between Group I and Group II is probably related with different type of terrigenous metasediments in these two groups – Group I comprise pelitic metasediments that resulted mainly from authigenic deposition of clays and Group II comprise metagreywackes composed mostly by allogenic material transported from elsewhere.

The relative homogeneity of the isotopic signature of the MMC granitic and metatexitic rocks is a remarkable feature despite their lithological and chemical heterogeneities and the notorious variations in the restite entrainment in the melts. The homogenization of the isotopic signature suggests that all MMC granitic rocks have a close relationship with the metatexites, probably having a cogenetic origin. Moreover, the relative isotopic

similarity among the MMC lithologies and the SGC metasediments suggests a direct genetic relationship between them and point to SGC as the protolith of the MMC lithologies. This is also suggested to other granitic anatectic complexes in Central Iberia (Beetsama, 1995; Pereira *et al*., 2008; Chicharro *et al*., 2014)

The almost coincident isotopic signature of calc-silicate and metagreywacke resisters suggests that these two apparent different rock types have the same origin and result from the same sedimentary process. This confirms the calc-silicate nodules diagenetic origin by cementation of the greywackes, as proposed before, based in petrological and chemical characteristics.

The aplite-pegmatite samples seems to be related to the syn-tectonic two-mica granites emplacement, since they plot outside the MMC groups within the field of syn-tectonic granites defined by Beetsma (1995).

CHAPTER IX – LAST REMARKS

I think and think for months and years. Ninety-nine times, the conclusion is false. The hundredth time I am right.

Albert Einstein

I have come to the conclusion, after many years of sometimes sad experience that you cannot come to any conclusion at all.

Vita Sackville-West

9.1 Synthesis general

At the beginning of this thesis it was mentioned that we would like to answer a series of questions about the lithologies outcropping in the coastal zone between Leça da Palmeira and Póvoa do Varzim, NW of Portugal. A group of intricate metasedimentary, migmatitic and granitic lithologies occurs in this area which we call “Mindelo Migmatitic Complex”.

In this chapter we will try to answer to those question based on the results and hypotheses suggested in the previous chapters.

Did partial melting produce the migmatites?

The textural and compositional evidence suggest that the dominant process for generating the MMC migmatites was partial-melting. Injection is not a major contributor since there are no traceable field relations between the leucosomes in the analyzed outcrops and the granitic intrusions (except for leucogranites). In addition, the diverse compositions exhibited by the leucosomes over short distances, as well as the diversity of granitic rocks spatially associated with the metatexites, argue against a common intrusive source,. Textural evidences of partial melting processes are widespread both in metatexites and in granitic rocks. Moreover, the abundance of peritectic cordierite and relicts of sillimanite + biotite in leucosomes support an anatectic origin through an incongruent melting reaction involving biotite and sillimanite as the reactants and cordierite plus K-feldspar as incongruent products.

What is the relationship between the migmatites and the surrounding lower grade metasediments? What was the protolith of these migmatites?

Field relationships, whole-rock chemistry and U-Pb, Rb-Sr and Sm-Nd isotopic signatures suggest that Schist-Greywacke Complex was the protolith that originated the MMC lithologies, considering that:

The SGC metasediments are spatially related to the migmatites and granitic lithologies that make up the MMC. Moreover, the lithologies present in the Metatexite Zone, i.e. pelitic rock interspersed with metagreywackes and calc-silicate rocks are similar to those that characterize the Schist-Greywacke Complex.

The chemical composition of the pelitic metatexites is almost coincident with the chemical composition of the pelitic metasediments from SGC, both in major and in trace elements, including Rare Earths.

The age of inherited zircons from a diatexite sample coincide with the age found to low grade SGC metasediments belonging to Beiras-Group and Douro-Group (Ediacaran) (Teixeira, 2011; Pereira, 2012).

The Rb-Sr and Sm-Nd isotopic signatures of the MMC lithologies coincide with the isotopic signatures of Beiras-Group samples (from this study and from other studies, see sub-chapter 7.3.4.2) and is different from the Sm-Nd signature obtained for other lithologies from ZCI, namely Paleozoic metasediments (Beetsma, 1995), Douro-Group metasediments (Teixeira, 2008) and lower-crust granulites (Villaseca *et al.* 1999). The εNd_0 values of the SGC metasediments and MMC rocks (including Group I and Group II) overlap the values found by Dabard *et. al.* (1996) to the Brioverian sediments from the Armorican Massif.

What is the metamorphic zoning and field gradient in the area?

In the studied area the metamorphic conditions show a gradual evolution from the chlorite-zone in the East, through the biotite-zone, the staurolite-zone, the sillimanite-zone and finally, near the coast, the sillimanite-K-feldspar-zone (Metatexite Zone) and anatexis.

The metamorphic sequence, the mineralogical associations and the geometric relations Si / Se suggest that the process that originated the metamorphic zones has a regional

character, reached moderate pressure and temperature conditions and is related with D1 deformation phase. During D3 an increase in temperature and decompression process occurred, conditioned by the granitization and emplacement of the two-mica syn-tectonic granites. The first metamorphic event (M1), attaining condition of P > 490 Pa and 560 < T< 600 ºC, reflects burial and heating. These conditions were followed by decompression and temperature increase leading to andalusite and cordierite development during the later metamorphic event (M2). The sillimanite-zone and migmatization are the result of the last metamorphic event.

Is there a relationship between the migmatites and the granitic rocks from MMC?

The MMC granitic rocks and the metatexites show an intimate spatial relationship. The transition from metatexites to leucogranites is gradual while the contacts between the diatexites and the two-mica granites with the metatexites are abrupt. The Sm-Nd isotopic signatures and the Rb-Sr ages of metatexites and granitic rocks are almost coincident. Moreover, the correlation between $^{86}Sr/^{87}Sr$ *and* 1/Sr suggests a co-genetic relation between the MMC rocks (except metagreywackes and aplite-pegmatites). The chemical and mineralogical dissimilarity between them result from their derivation from different crustal levels and different melting reactions rather than of a marked difference in the source lithologies involved.

What was the cause of the lithological diversity and heterogeneity in the MMC?

The lithological, petrographic, geochemical and isotopic signatures of the MMC rocks suggest that the lithological heterogeneity is related to the anatexis processes. Different melting processes, diverse melting rates and the distinct structural level in which the melting occurred led to the diversity of lithologies found in this area.

The following anatexis / crystallization events are suggested:

i) From a protolith consisting of Schist-Greywacke Complex metasediments a first fluid-presence melting, mainly of plagioclase and quartz, produced some leucosomes and mostly leucogranites. These melts were formed under stress which led to the migration of melts and subsequent crystallization in dilatant sites. After the water available has been consumed, fluid-absent biotite breakdown reactions produce peritectic cordierite and leucosomes composed of plagioclase + quartz with minor amounts of K-

feldspar. These processes occurred in relatively shallow levels at P < 3.5 KPa.

ii) At deeper levels (still below 4 Kbar) and slightly high temperature, melt rate was grater and produced diatexites that intruded metatexites.

iii) Above 4 Kbar large amounts of melt were produced by breakdown of muscovite plus biotite-bearing metasediments. The resultant melts are less dense than the host rocks, which promotes its ascent and emplacement at shallow levels, generating two-mica granites that incorporate migmatite xenoliths and intrusive dikes.

Also the influence of later fluids, probably of pneumatolytic and hydrothermal provenance, contributed to the lithological diversity in the MMC. These fluids seem to be structurally controlled and thus changed selectively the mineralogy of the MMC rocks.

What types of fluids were present during the anatectic process?

Fluid inclusions in leucosomes, tourmaline-bearing leucogranites and two-mica granites reveal the presence of monophasic inclusions in all the studied samples, although showing different composition. Leucosomes are characterized by N_2-CH_4 and N_2-CO_2-CH_4 fluids showing high N_2 content; leucogranites show N_2-CH_4 fluids with high N_2 content as well; two-mica granites only show CO_2-N_2 fluids being CO_2 the dominant species in the volatile phase. All these fluid types occur in fluid inclusions trapped in intragranular trails or in clusters and transect the metamorphic conditions of the respective lithologies, suggesting its primary character.

It seems that multiple fluid pulses affected the MMC in subsolidus conditions: a first pulse with K-bearing fluids, a second pulse with boron-bearing fluids and a third pulse containing silica-bearing aqueous fluids.

The K-bearing fluids affected all the MMC lithologies and caused structurally controlled sub-solidus K-metasomatism, revealed by: i) the filling of miarolitic cavities and micro-fractures; ii) alteration processes in the metagreywacke and calc-silicate nodules; iii) replacement of plagioclase crystals in leucosomes, leucogranites and two-mica granites; iv) wide variation in the K content, especially in leucosomes and leucogranites (unrelated to the content of silica), and the inverse correlation between the K and the Na_2O+CaO content in this lithologies.

The occurrence of leucogranites and two-mica granites showing localized replacement of biotite by tourmaline, the presence of post-kinematic tourmaline in the SGC metasediments and of tourmalinites associated with fractures, as well as the occurrence of aplite-pegmatite veins showing abundant tourmaline suggest that latte boron-rich fluids also affected the MMC and surrounding metasedimentary sequence. The isotopic signature of aplite-pegmatites coincides with the isotopic signature of syn-tectonic granites defined by Beetsma (1995) and Teixeira (2008), which can suggest a relationship between these fluids and the emplacement of the sin-D3 anatectic granites. In the tourmaline-bearing leucogranite, a group of fluid inclusions absent both in leucosomes and in two-mica granites was found, suggesting that this type of fluids could be related to the tourmalinization process.

A later extensive hydrothermal fluid flow is inferred from: i) the muscovitization of tourmaline, biotite and plagioclase all over the MMC; ii) presence of quartz-veins cutting all the lithologies; iii) large quartz-crystals bands in some calc-silicate rocks that include all the minerals of the rock; iv) retrograde alteration of staurolite, garnet, andalusite and biotite in the metasedimentary sequence.

The presence of different latter aqueous fluids inclusions in quartz from the leucosomes, leucogranites and two-mica granites could be related to this multiple fluid pulses that affected the MMC.

Is it possible to date the anatexis event?

U-Pb geochronological SHRIMP analytical techniques were performed in zircons from a diatexite sample. The zircon population shows in cathodoluminescent images the existence of three components in most of the zircons: i) an inherited core showing magmatic or metamorphic textures and ovoid external morphology, ii) a transitional zone showing corrosion and lobate transgressive recrystallization fronts and iii) a dark rim overgrowth, developing mostly in the pyramidal extremities. The ages measured in the inhered cores are Ediacaran (75%) ranging from 630 to 530 Ma, with a concentration peak around 590 Ma. The overgrowth rims show Variscan ages (Carboniferous) between 319 ±11 and 309 ±3 Ma and are suggested to reflect the age of the anatectic process.

The Rb-Sr isochrons, although showing some scattering, confirm the Ediacaran and the Carboniferous ages for the MMC lithologies. The Ediacaran age is preserved in the metagreywacke resisters and the Carboniferous/Variscan age is patent in metatexites

and two-mica granites (328 ±18 Ma to metatexites and 324 ±38 Ma to two-mica granites).

Mindelo Migmatite Complex represents an example of migmatites formed in low pressure conditions and illustrates some of the reactions involving melting in high grade pelitic rocks and subsequent mineral alterations due to infiltration of late different fluids.

The purpose behind the realization of this thesis was to better characterize the geology of the Mindelo Migmatite Complex and try understanding the processes involved in its petrogenesis. The various methodologies used led to a better understanding of the area in question and allowed to put forward some suggestions about its origin and evolution.

CHAPTER X – REFERENCES CITED

Ábalos, B., Carreras, J., Druguet, E., Escuder Viruete, J., Gómez Pugnaire, M., Lorenzo Alvarez, S., Quesada, C., Rodríguez Fernández, L., Gil Ibarguchi, J., 2002. Variscan and pre-variscan tectonics. In: Gibbons, W., Moreno, T. (Eds.), The Geology of Spain. The Geological Society of London, . 155-183.

Abdel-Rahman, A.M., 1994. Nature of biotites from alkaline, calcalkaline, and peraluminous magmas. Journal of Petrology 35, 525-541.

Abreu, J., 2012. Estudo Geoquímico de Zircão de Granitos do NW Português. Master's thesis. Faculdade de Ciências da Universidade do Porto, 176

Acciaioli, M.H., Santos J.F., Munhá, J.M., 2005. Ar – Ar dates for two different stages of the Varsican D3 recorded in metapelites of Serra da Freita (North – Central Portugal). Geophysical Research Abstracts 7,10076.

Acciaioli, M.H., Santos, J.F., Munhá, J.M., Cordani, U.G., Couto, A., Sousa P., 2003. Idades Ar – Ar em micas de metapelitos da zona de Espinho: Datação do metamorfismo relacionado com a F3 varisca. In: Neiva, A.M.R., Neves, L.J.P.F., Silva, M.M.V.G., Gomes, E.M.C. (Eds.), Resumos do IV Congresso Ibérico de Geoquímica/XIII Semana de Geoquímica, 161-163.

Acciaioli, M.H., 1997. Processos metamórficos variscos na Serra da Freita (Zona Centro Ibérica – Portugal). PhD Thesis, Universidade de Aveiro, 288 .

Adams, J.J.A., Weaver, C.E., 1958. Th–To–U ratios as indicators of sedimentary process-an example of geochemical facies. Am. Assoc. Pet. Geol. Bull. 42, 387-430.

Ague, J.J., 2003. Fluid flow in the deep crust. In: Rudnick, R.L., Holland, H.D., Turekian, K.K. (Eds.), The Crust. Treatise on Geochemistry.Elsevier, Oxford, 3, .195-228.

Ahrens, L.H., 1955. Implications of the Rhodesia age pattern. Geochim. Cosmochim. Acta 8, 1-15.

Allaz, J., Maeder, X., Vannay, J., Steck, A., 2005. Formation of aluminosilicate-bearing quartz veins in the Simano nappe (Central Alps): structural, thermobarometric and oxygen isotope constraints. Schweizerische Mineralogische und Petrographische Mitteilungen 85, 191-214.

Almeida, A., 2001. Geochemical and Geochronological Characterization of the Syntectonic Two-Mica Granite of Porto (NW Portugal). In: Lago, M., Arranz, A.,

Galé, G. (Eds.), III^{er} Congreso Ibérico de Geoquímica. VIII Congreso de Geoquímica de España, Zaragoza, . 311-315.

Almeida, A., Santos, J.F., Noronha, F. 2014. Contribuição dos sistemas isotópicos Sm-Nd e Rb-Sr para o estudo petrogenético do maciço granítico peraluminoso de duas micas da cidade do Porto (NW Portugal). Atas do IX Congresso Nacional de Geologia/2º Congresso de Geologia dos Países de Língua Portuguesa, Porto, Julho 2014.

Alvarenga, C.J.S, Cathelineau M., Dubessy J., 1990. Chronology and orientation of N_2-CH_4, CO_2-H_2O, and H_2O-rich fluid-inclusion trails in intrametamorphic quartz veins from the Cuiabfi gold district, Brazil. Mineralogical Magazine 54, 245-255.

Andersen, T., Neumann, E.R., 2001. Fluid inclusions in mantle xenoliths. Lithos 55, 301-320.

Andrade, A.S, 2005. Lições de Geologia de Portugal. Departamento de Ciências da Terra da Universidade de Coimbra.

Antunes, I.M.H.R., Neiva, A.M.R., Silva, M.M.V.G., Corfu, F., 2009. The genesis of I- and S-type granitoid rocks of the Early Ordovician Oledo pluton, Central Iberian Zone (central Portugal). Lithos 111, 168-185.

Antunes, I.M.H.R., Neiva, A.M.R., Silva, M.M.V.G., Corfu, F., 2008. Geochemistry of S-type granitic rocks from the reversely zoned Castelo Branco pluton (central Portugal). Lithos 103, 445-465.

Antunes, I.M.H.R., Neiva, A.M.R., Silva, M.M.V.G., Corfu, F., 2008. The genesis of I- and S- type granitoid rocks of the Early Ordovician Oledo pluton, Central Iberian Zone (central Portugal). Lithos 111, 168-185.

Antunes, I.M.H.R., Neiva, A.M.R., Silva, M.M.V.G., 2005. Geocronologia e petrogénese do plutão granítico de Castelo Branco, centro de Portugal. In: Actas da XIV Semana de Geoquímica/VIII Congresso de Geoquímica dos Países de Língua Portuguesa, 2, 425-427.

Areias, M., Ribeiro, M.A, Dória, A., 2011. Estudo Litogeoquímico de rochas do Complexo Xisto-Grauváquico do NW de Portugal: estudo preliminar. VIII Congresso Ibérico de Geoquímica/XVII Semana de Geoquímica, Castelo Branco, Setembro 2011, p.119. CD: Long Abstract.

Areias M., Ribeiro, M.A., Dória, A., 2012a. Petrografia dos *resisters* calcossilicatados da faixa migmatítica da costa NW de Portugal. 1º Congresso Internacional «Geociências na CPLP», Coimbra.

Areias, M., Ribeiro, M.A., Dória, A., 2012b. Chemical zoning in calc-silicate rocks: stratigraphic control versus metasomatism (Northern Portugal)", Goldschmidt Conference Abstracts. Canadá.

Areias M., Ribeiro, M.A., Dória, A., 2012c. Metasomatized calc-silicate resisters in migmatites (Variscan Orogen, NW Portugal), First European Mineralogical Conference, Frankfurt, Alemanha.

Areias, M., Ribeiro, M.A., Dória, A., 2012d. Caracterização da faixa gnaissomigmatítica da zona costeira do NW de Portugal. 1º Congresso de Geologia dos Países de Língua Portuguesa, Santos- Brasil. Outubro 2012.

Areias, M., Ribeiro, M.A., Doria, A., 2013a. Complexo Migmatitico do Mindelo (NW de Portugal). Anatexia e relações petrogenéticas. IX Congresso Ibérico de Geoquímica, Soria.

Areias M., Ribeiro, M.A., Dória, A., 2013b. Trace Element Composition in a Migmatite-Granite Complex (NW Portugal): Protolith and Melting Process Constraints. Mineralogical Magazine 77 (5), 611.

Areias M., Ribeiro, M.A., Dória, A., 2013c. Pegmatitic Rocks in a Migmatite-Granite Complex (NW Portugal). In: Simmons, W.B., Webber, K.L., Falster,. A.U., Roda-Robles, E., Hanson, S.L., Marquez-Zavalía, M.F., Galliski, M.A. (Eds.), Contributions to the 6 th international symposium on granitic pegmatites. Abstract Volume, 12-13.

Areias, M., Ribeiro, M.A., Santos, J.F., Dória, A., 2014. Sequência de processos anatéticos no Complexo Migmatítico de Mindelo (NW de Portugal). Atas do IX Congresso Nacional de Geologia/2º Congresso de Geologia dos Países de Língua Portuguesa, Porto.

Arenas R., Martínez Catalán, J.R., 2002. Low-P metamorphism following a Barrovian-type evolution. Complex tectonic controls for a common transition, as deduced in the Mondonedo thrust sheet (NW Iberian Massif). Tectonophysics 365, 143-164.

Arthaud, F., Matte, P., 1975. Les Decrochements tardi-Hercyniens du Sud-Oest de L' Europe. Geomrtry et essai de reconstitution des conditions de la deformation. Tectonophysics 25, 139-71.

Arthaud, F, Matte, P., 1977. Late Paleozoic stike-slip faulting in southern Europe and northern Africa: result of a right-lateral shear between the Appalachians and the Urals. Bull. Geol. Soc. Amer. 88, 1305-1320.

Arzi, A.A., 1978. Fusion kinetics, water diffusion and electrical conductivity in melting rock, interrelated. J. Petrology 19, 153-169.

Ashwal, L.D., Tucker, R.D., Zinner, E.K., 1999. Slow cooling of deep crustal granulites and Pb-loss in zircon. Geochimica et Cosmochimica Acta 63, 2839–2851.

Ashworth, J.R., 1979. Comparative petrography of deformed and undeformed migmatites from the Grampian Highlands of Scotland. Geological Magazine 116, 445-456.

Ashworth, J.R., 1985. Introduction. In: Ashworth, J.R. (Ed.), Migmatites. Blackie, London, 1-35.

Awwiller, D.N., Mack, L.E., 1991. Diagenetic modifications of Sm–Nd model ages in Tertiary sandstones and shales, Texas Gulf Coast. Geology 19, 311–314.

Azevedo, M., Valle Aguado, B., 2013. Origem e instalação de granitóides variscos na Zona Centro-Ibérica.. In: R. Dias, A. Araújo, P. Terrinha, J.C. Kulberg (Eds.), Geologia em Portugal. Escolar Editora, I, 377-401.

Bakker, R.J., 1999. Adaptation of the Bowers and Helgeson (1983) equation of state to the H_2O-CO_2-CH_4-N_2-NaCl system. Chemical Geology 154, 225-236.

Bakker, R.J., 2003. Package FLUIDS 1. Computer programs for analysis of fluid inclusion data and for modelling bulk fluid properties. Chemical Geology 194, 3-23.

Bandres, A., Eguiluz, L., Gil Ibarguchi, J.I., Palacios, T., 2002. Geodynamic evolution of a Cadomian arc region: the northern Ossa-Morena zone, Iberian massif. Tectonophysics 352, (1,2), 105-120.

Barbero, L., Villaseca, C., Rogers, G., Brown, P.E., 1995. Geochemical and isotopic disequilibrium in crustal melting: an insight from anatectic granitoids from Toledo, Spain. J Geophys Res. 100, 15745-15765.

Barbey, P., Cuney, M., 1982. K, Rb, Sr, Ba, U and Th geochemistry of the Lapland granulites (Fennoscandia). LILE* Fractination controlling factors. Contr. Miner. Petrology 81, 304-316.

Bard, J.P., 1978. Contribution au probleme de la signification des ceintures métamorphiques dans les orogenes antémesozoíque: elements d'aproche dans la

virgation Galaico-Armoricaine». In: Geologia de la parte Norte del Macizo Ibérico. Cuad. Sem. Est. Cero Sargadelos Edie. del Castro, La Coruña, 27, 71-92.

Barth, T.F.W., 1958. Principles of classifications and norm calculations of metamorphic rocks. Journal of Geology 67, 135-152.

Barton, M.D., Ilchik, R.P., Marikos, M.A., 1991. Metasomatism. In: Kerrick, D.M. (Ed.), Contact Metamorphism. Reviews in Mineralogy 26, Mineralogical Society of America, 321-344.

Barton, M., Sidle, W.C., 1994. Petrological and geochemical evidence for granitoid formation: The Waldoboro pluton complex, Maine. Journal of Petrology 35, 1241-1474.

Batchelor, R.A., Bowden, P., 1985. Petrogenetic interpretation of granitoid rock series using multicationic parameters. Chemical Geology 48, 43-55.

Bath A.B., Walshe, J., Cloutier, J., Verrall, M., Cleverley, J., Pownceby, M.I., Macrae, C.M., Wilson, N.C., Tunjic, J.,Nortje, G., Robinson, P., 2013. Biotite and Apatite as Tools for Tracking Pathways of Oxidized Fluids in the Archean East Repulse Gold Deposit, Australia, Economic Geology 108, 667-690.

Bau, M., 1996. Controls on the fractionation of isovalent trace elements in magmatic and aqueous systems: evidence from Y/Ho, Zr/Hf, and lanthanide tetrad effect. Contributions to Mineralogy and Petrology 123 (3), 323-333.

Be Mezeme, E., Cocherie, A., Faure, M., Legendre, O., Rossi, P.H., 2006. Electron microprobe monazite geochronology of magmatic events: examples from Variscan migmatites and granitoids, Massif Central, France. Lithos 87, 276-288.

Bea, F., González de Herrero J. G. S. & Pinto, M. S., 1987. Una compilación geoquímica (elementos mayores) para los granitóides del macizo Hesperico. In: Bea, F., Carmina, A., Gonzalo, J.C., Plaza, M.L., Rodrigues, J.M.L. (Eds.), Geologia de los granitoides y rocas asociadas del Macizo Hespérico. Libro Homenage a L.C.G. Figueirola, Madrid: Editorial Rueda, 87-193.

Bea, F., 1996. Residence of REE, Y, Th and U in granites and crustal protoliths: Implications for the chemistry of crustal melts. Journal of Petrology 37, 521-552.

Bea, F., Montero, P., 1999. Behavior of accessory phases and redistribution of Zr, REE, Y, Th, and U during metamorphism and partial melting of metapelites in the

lower crust: An example from the Kinzigite Formation of Ivrea-Verbano, NW Italy. Geochimica et Cosmochimica Acta 63, 1133-1153.

Bea, F., Montero, P., Talavera, C., Zinger, T. 2006. A revised Ordovician age for the Miranda do Douro orthogneiss, Portugal.Zircon U-Pb ion-microprobe and LA-ICPMS dating. Geologica Acta 4, 395-401.

Bea, F., Montero, P., González-Lodeiro, F., Talavera, C., 2007. Zircon inheritance reveals exceptionally fast crustal magma generation processes in Central Iberia during the Cambro-Ordovician. Journal of Petrology 48, 2327-2339.

Beetsma, J.J., 1995. The late Proterozoic/Paleozoic and Hercynian crustal evolution of the Iberian Massif, N Portugal. PhD thesis, Vrije University, Netherlands, 223.

Beitter, T., Wagner, T., Markl, G., 2008. Formation of kyanite-quartz veins of the Alpe Sponda, Central Alps Switzerland: implications for Al transport during regional metamorphism. Contributions to Mineralogy and Petrology 156, 689-707.

Bell, T.H., Johnson, S.E. 1989. Porphyroblast inclusion trails: the key to orogenesis. Journal of Metamorphic Geology 7, 279-310.

Bhatia, M.R., 1985. Rare earth element geochemistry of Australian Paleozoic greywackes and mudstones: provenance and tectonic control. Sedimentary Geology 45, 97-113.

Bhatia, M.R., Crook, K.A.W., 1986. Trace element characteristics of greywackes and tectonic setting discrimination of sedimentary basins. Contributions to Mineralogy and Petrology 92, 181-193.

Biao, S., Nutman, A.P., Liu, D., Jiashan, W., 1996. 3800 to 2500 Ma crustal evolution in the Anshan area of Liaoning Province, northeastern China. Precambrian Research 78, 79-94.

Bickle, M.J., Wickham, S.M., Chapman H., Taylor, H.P., 1988. A strontium. neodymium and oxygen isotope study of hydrothermal metamorphism and crustal anatexis in the Trois Seigneurs Massif, Pyrennes, France. Contrib. Mineral. Petrol. 100, 399-417.

Bin Fu, Touret, J.L.R., Zheng, Yong-Fei, Jahn, Bor-ming, 2003. Fluid inclusions in granulites, granulitized eclogites and garnet clinopyroxenites from the Dabie–Sulu terranes, eastern China. Lithos 70, 293-319.

Black, L.P., Kamo, S.L., Allen, C.M., Aleinikoff, J.A., Davis, D.W., Korsch, J.R., Foudolis, C., 2003. TEMORA 1: a new zircon standard for Phanerozoic U-Pb geochronology. Chemical Geology 200, 155-170.

Bodnar, R.J., 1993. Revised equation and table for determining the freezing point depression of H_2O-NaCl solutions. Geochimica et Cosmochimica Acta 57, 683-684.

Boynton W.V., 1985. Cosmochemistry of the rare earth elements: Meteorite studies. In: Henderson, P. (Ed.), Rare Earth Element Geochemistry, Developments in Geochemistry 2. Elsevier, Amsterdam, 115-1522.

Bracciali, L., Marroni, M., Pandolfi, L., Rocchi, S., 2007. Geochemistry and petrography of Western Tethy Cretaceous sedimentary covers (Corsica and Northern Apennines): from source areas to configuration of margins. In: Arribas, J., Critelli, S., Johnsson, M.J. (Eds.), Sedimentary Provenance and Petrogenesis: Perspectives from Petrography and Geochemistry. Geological Society of America Special Paper 420, 73-93.

Brooks, C., Hart, S.R., Wendt, I., 1972. Realistic use of two error regression treatments as applied to rubidium–strontium data. Rev. Geophys. Space Phys. 10, 551-77.

Brown, M. Power, G.M., Topley, C.G., D'Lemos, R.S., 1990. Cadomian magmatism in the North Armorican Massif. In: D'Lemos, R.S., Stkacnan, R.A., Topley, C.G. (Eds.), The Cadomian Orogeny. Geological Society, London, Special Publication, 51, 181-213.

Brown, M., 1994. The generation, segregation, ascent and emplacement of granite magma: the migmatite-to-crustally-derived granite connection in thickened orogens. Earth-Science Reviews 36, 83-130.

Brown, M., Solar, G.S., 1998, Granite ascent and emplacement during contractional deformation in convergent orogens. Journal of Structural Geology 20, 1365-1393.

Brown, M., 2007. Crustal melting and melt extraction, ascent and emplacement in orogens: mechanisms and consequences. Journal of the Geological Society of London 164, 709-730.

Brown, M., 2008. Granites, migmatites and residual granulites: relationships and processes. In: Sawyer, E.W. (Ed.), Mineralogical Association of Canada Short Course Quebec, 38, 97-144.

Brown, M., Korhonen, F.J., 2009. Some remarks on melting and extreme metamorphism of crustal rocks. In: Dasgupta, S. (Ed.), Physics and Chemistry of the Earth: New York, Published for the Indian National Science Academy. Springer, 67-87.

Brown, M., 2013. Granite: From genesis to Emplacement. Downloaded from gsabulletin.gsapubs.org (v. 125, no. 7/8, p. 1079–1113, doi: 10.1130/B30877.1).

Buatier, M.D., Karpoff, A., Boni M., Früh-Green, G.L., McKenzie, J.A., 1994. Mineralogic and petrographic records of sediment-fluid interaction in the sedimentary sequence at middle valley, Juan de Fuca Ridge, leg 1391. In: Mottl, M.J., Davis, E.E., Fisher, A.T., Slack, J.F. (Eds.), Proceedings of the Ocean Drilling Program, Scientific Results 139, 133-154.

Bucher, K., Grapes, R., 2011. Petrogenesis of Metamorphic Rocks. 8th ed. New York Springer, 428

Bucholz, C.E., Ague, J.J., 2010. Fluid flow and Al transport during quartz-kyanite vein formation, Unst, Shetland Islands, Scotland. Journal of Metamorphic Geology 28, 19-39.

Buick, I.S., Harley, S.L., Cartwright, I.C., 1993. Granulite facies metasomatism: zoned calc-silicate boudins from the Rauer Group, East Antarctica. Contributions to Mineralogy and Petrology 113, 557-571.

Burke, E.A.J., 2001. Raman microspectrometry of fluid inclusions. Lithos 55, 139-158.

Capdevila, R., Corretgé, L., Floor, P., 1973. Les granitoides varrisques de la Meseta Ibérique. Bull. Soc. Géol. France 15, 209-228.

Carreras, J., Druguet, E., Griera, A., 2005. Shear zone-related folds. Journal of Structural Geology 27, 1229-1251.

Carrington da Costa, M., 1950. Noticia sobre uma carta geológica do Buçaco de Nery Delgado. Comunicações dos Serviços Geológicos de Portugal, 28

Carvalho, P.C.S. Neiva, A.M.R., Silva, M.M.V.G, Corfu F., 2010. A unique sequential melting mechanism for the generation of anatectic granitic rocks from the Penafiel area, northern Portugal. Lithos 155, 110-124.

Castiñeiras, P., Villaseca, C., Barbero, L., Romera, C.M., 2008. SHRIMP U–Pb zircon dating of anatexis in high-grade migmatite complexes of Central Spain:

implications in the Hercynian evolution of Central Iberia. International Journal of Earth Sciences 97 (1), 35-50

Castro, A.L., Corretgé, G., De La Rosa E.J., Martinez, F.J., Pascual, E., Lago M., Arranz, E., Galé, C., Fernández, C., Donaire, T., López, S., 2002. Paleozoic Magmatism. In: Wes Gibbons, Teresa Moreno (Eds.), Geology of Spain, Geological Society, 117-153.

Castro, A., Corretgé, L.G., El-Biad, M., El-Hmidi, H., Fernández, C., Patiño Douce, E., 2000. Experimental constraints on hercynian anatexis in the Iberian massif, Spain. Jour. Petrol. 41(10), 1471-1488.

Castro, A., Patiño, E., Corretgé, L.G., de la Rosa, J., El-Biad, M., El-Hmidi, H., 1999. Origin of peraluminous granites and granodiorites, Iberian massif, Spain: an experimental test of granite petrogenesis. Contrib. Mineral. Petrology 135, 255-276.

Cavosie, A.J., Sharp, Z.D., Selverstone, J., 2002. Coexisting aluminium silicates in quartz veins: A quantitative approach for determining andalusite-sillimanite equilibrium in natural samples using oxygen isotopes. Am. Mineral. 87, 417-423.

Cesare, B., 1994. Synmetamorphic veining: origin of andalusite-bearing veins in the Vedretto di Ries contact aureole. Eastern Alps, Italy. Journal of Metamorphic Geology 12, 643-653.

Cesare, B., Maineri, C., Baron, T.A., Pedron, D., Acosta-Vigil, A. 2007. Immiscibility between carbonic fluids and granitic melts during crustal anatexis: a fluid and melt inclusion study in the enclaves of the Neogene Volcanic Province of SE Spain. Chemical Geology 237, 433-449.

Chappell, B.W., White A.J.R., 1974. Two contrasting granite types. Pacific Geology 8, 173-174.

Chappell, B.W., White, A.J.R. 2001. Two contrasting granite types – 25 years later. Australian Journal of Earth Sciences 48, 489-499.

Chen, F., Todt, W., Hann, H.P., 2003. Zircon and garnet geochronology of eclogites from the Moldanubian zone of the Black Forest. Journal Geology 111, 207-222.

Cherniak, D.J., Ryerson F.J., 1993. A study of strontium diffusion in apatite using Rutherford backscattering spectroscopy and ion implantation. Geochim. Cosmochimic Acta 57, 4653-4662.

Chicharro, E., Villaseca, C., Valverde-Vaquero, P., Belousova, E., López-García, J.A. 2014. Zircon U-Pb and Hf isotopic constraints on the genesis of a post-kinematic S-type Variscan tin granite: the Logrosán cupola (Central Iberian Zone). Journal of Iberian Geology 40 (3), 451-470

Claoue-Long, J.C., Compston, W., Roberts, J., Fanning, C.M., 1995. Two Carboniferous ages: a comparison of SHRIMP zircon dating with conventional zircon ages and $^{40}Ar/^{39}Ar$ analysis. In: Berggren, W.A., Kent, D.V., Aubry, M.P., Hardenbol, J. (Eds.), Geochronology Time Scales and Global Stratigraphic Correlation. SEPM (Society for Sedimentary Geology) Special Publication, 4. 3-21.

Cocks, L.R.M., Torsvik, T.H., 2006. European geography in a global context from the Vendian to the end of the Palaeozoic. In: Gee, D.G., Stephenson, R.A. (Eds.), European Lithosphere Dynamics, Geological Society of London Memoirs 32, 83-95.

Cocks, L.R.M., McKerrow, W.S., van Staal, C.R., 1997. The margins of Avalonia. Geological Magazine 134, 627-636.

Coelho J., 1993. Os “Skarns” cálcicos, pós-magmáticos, mineralizados em scheelite do Distrito Mineiro de Covas, V. N. de Cerveira, (Norte de Portugal). PhD Thesis, Universidade do Porto, 254 p.

Coke, C., Pires, C.A. C., Sá, A.A., Ribeiro, A., 2001. Volcanism as a stratigraphical reference element in the Cambrian/Ordovician transition of the Central-Iberian Zone in Trás-os-Montes region (Northern Portugal). Cadernos Lab. Xeolóxico de Laxe 26, 121-136.

Colley, S., Thomson, J., Toole, J., 1989. Uranium relocations and derivation of quasi-isochrons for a turbiditerpelagic sequence in the northeast Atlantic. Geochim. Cosmochim. Acta 53, 1223-1234.

Collins, L.G., 1997. Replacement of primary plagioclase by secondary k-feldspar and myrmekite. Myrmekite and metasomatic granite, ISSN: 1526-5757**.** Avaiable in: http://www.csun.edu/vcgeo005/Nr2Myrm.pdf.

Condie, K.C., 1991. Another look at rare earth elements in shales. Geochimica et Cosmochimica Acta 55, 2527-2531.

Condie, K.C., 1993. Chemical composition and evolution of upper continental crust: contrasting results from surface samples and shales. Chemical Geology 104, 1-37.

Conrad, W.K., Nicholls, I.A., Wall, V.J., 1988. Water saturated and undersaturated melting at 10 kbar: evidence for the origin of silicic magmas in the Taupo volcanic zone, New Zealand, and other occurrences. Journal of Petrology 29, 765-803.

Cordani, U.G., Nutman, A.P., Andrade, A.S., Santos, J.F., Azevedo, M.J., Mendes, M.H., Pinto, M.S., 2006. New U-Pb SHRIMP zircon ages for pre-variscan orthogneisses from Portugal and their bearing on the evolution of the Ossa Morena Tectonic Zone. Anais da Academia Brasileira de Ciências 78 (1), 13-149.

Corfu, F., Hanchar, J.M., Hoskin, P.W.O., Kinny, P., 2003. Atlas of Zircon Textures. In: Hanchar, J.M., Hoskin, W.O. (Eds.), Zircon: Reviews in Mineralogy and Geochemistry 53, 468-500.

Corretgé, L.G., Castro, A., El-Hmidi, H., García-Moreno, O., 2001. Characteristics and significance of the experimental products from partial melting of rocks from the "Complejo Esquisto grauváquico" at 3.5 kbar. III Congreso Ibérico de Geoquímica, VIII Congreso de Geoquímica de España, Zaragoza, 191-196.

Corretgé, L.G., Ugidos, J.M., Martínez, F.J., 1977. Les séries granitiques varisques du secteur Centre-Occidental espagnol. La chaîne varisque d´Europe moyenne occidentale. Coll. Intern. CNRS, Renne 243, 453-461.

Couto H., 1993. As mineralizações de Sb-Au da Região Dúrico-Beirã. PhD Thesis - Faculdade de Ciências da Universidade do Porto, 560 p.

Crawford, M.L., Filer, J., Wood, C., 1979. Saline fluid inclusions associated with retrograde metamorphism. Bull. Minéral. 102, 562-568.

Crawford, M.L., 1981, Phase equilibria in aqueous fluid inclusions. In: Hollister, L.S., Crawford, M.L. (Eds.), A Short Course in Fluid Inclusions: Applications to Petrology: Mineralogical Assoc. Canada, Short Course Handbook. 6, 75-100.

Crawford, M.L., Hollister, L.S., 1986. Metamorphic fluids: the evidence from fluid inclusions. In: Walther, J., Wood, B.J. (Eds.), Fluid-Rock Interactions during Metamorphism (Advances in Geochemistry, vol. 5), Springer Verlag, New York, 1-35.

Crowley, Q., Floyd, J., Winchester, J.A., Franke, W., Holland, J.G., 2000. Early Palaeozoic rift-related magmatism in Variscan Europe: Fragmentation of the Armorican Terrane Assemblage. Terra Nova 12, 171-180.

D' Lemos, R.S., Strachan, R.A., Topley, C.G. (eds), 1990. The Cadomian orogeny in the North Armorican Massif: a brief review .In: The Cadomian Orogeny, Geological Society Special Publication No. 51, 3-12.

Dabard, M.P., Loi, A., Peucat, J.J., 1996. Zircon typology combined with Sm-Nd whole-rock isotope analysis to study Brioverian sediments from the Armorican Massif. Sedimentary Geology 101, 243-260.

Dallmeyer, R.D., Martínez-Catalán, J., Arenas, R., Gil-Ibarguchi, J.I., Gutiérrez-Alonso, G., Farias, P., Bastida, F., Aller, J., 1997. Diachronous Variscan tectonothermal activity in the NW Iberian Massif: evidence from $^{40}Ar/^{39}Ar$ dating of regional fabrics. Tectonophysics 277, 307-337.

De la Rosa, J.D., Jenner, G.A., Castro A., 2002. A study of inherited zircons in granitoid rocks from the South Portuguese and Ossa-Morena Zones, Iberian Massif: support for the exotic origin of the South Portuguese Zone. Tectonophysics 352, 245-256.

Dean, W.E., Gardner, J.V., Jansa, L. F., Cepek, P., Seibold, D., 1978. Cyclic sedimentation along the continental margin of northwest Africa, Initial Report Deep Sea Drill. Project 41, 965-989

Debelmas, J., Mascle, G., 2002. As grandes Estruturas Geológicas. Fundação Calouste Gulbenkian, 389

Debon, F., Le Fort, P., 1988. A cationic classification of common plutonic rocks and their magmatic associations: principles, method, applications. Bull. Mineralogy 111, 493-510.

Debon, F., Le Fort, P., 1983. A chemical–mineralogical classification of common plutonic rocks and associations. Transactions of the Royal Society of Edinburgh, Earth Sciences 73, 135-149.

Deer, W.A., Howie, R.A., Zussman, J., 1962. Rock-Forming Minerals-Sheet Silicates. Longmans, London, 3, 270

Deer, W.A., Howie, R.A., Zussman, J., 1992. Minerais Constituintes das Rochas. Uma Introdução. Fundação Calouste Gulbenkian, 734

Deer, W.A., Howie, R.A., Zussman, J., 1997. Rock-Forming Minerals:Disilicates and Ring Silicates. Geological Society of London, 1B, 629 p.

Deer, W.A., Howie, R.A., Zussman, J., 1997. Rock-forming Minerals: Double-Chain Silicates, Volume 2B. Geological Society of London, 764

Delgado, J.F.N., 1908. Sistèm Silurique du Portugal. Étude de stratigraphie paléontologique. Memórias Comunicações Serviços Geológicos de Portugal. 247p.

Deniel. C., Vidal, P., Fernandez, A., Le Fort, P., Peucat, J.J.,1987. Isotopic study of the Manaslu granite (Himalaya. Nepal): inference on the age and source of Hirnalayan ieucogranites. Contrib. Mineral. Petrology. 96, 78-92.

De Paolo, D.J. 1988. Neodymium isotope geochemistry. Springer. 1–187.

Dias, R., Ribeiro, A., 1991. Finite strain analysis in a transpressive regime (variscan autochthon, northeast Portugal). Tectonophysics 191, 389-397.

Dias, R., Ribeiro, A., 1995. The Ibero-Armorican Arc: a collision effect against an irregular continent? Tectonophysics 246, 113-128.

Dias, G., Leterrier, J., Mendes, A., Simões, P.P., Bertrand, J.M., 1998. U-Pb zircon and monazite geochronology of post-collisional Hercynian granitoids from the Central Iberian Zone (Northern Portugal). Lithos. 45, 349-369.

Dias, G.T., 2001. Fontes de granitóides hercínios da Zona Centro-Ibérica (Norte de Portugal): evidências isotópicas (Sr, Nd). In: A.M.R. Neiva (Ed), Geoquímica e Petrogénese de Rochas Granitóides, Mem. Acad. Sci. Lisboa. 121-143.

Dickin, A.P., 2005. Radiogenic Isotope Geology. (2nd edition) Cambridge University Press, 492.

Dias, G.T. Noronha, F, Almeida, A., Simões, P., Martins, H., Ferreira, N., 2010. Geocronologia e Petrogénese do plutonismo tardi-varisco (NW de Portugal): síntese e inferências sobre os processos de acreção e reciclagem crustal da Zona Centro Ibérica. In: Cotelo Neiva, Ribeiro, Mendes, Noronha, Magalhães, Ramalho (Eds), Ciências Geológicas – Ensino e investigação e sua história. Associação Portuguesa de Geólogos Sociedade - Geológica de Portugal. 1, 143-160.

Diez Balda, M.A., 1992. El cizallamiento ductil subhorizontal de la segunda fase Hercinica al sur de Salamanca: engrosamiento y colapso extensional. Simpósios, III Congreso Geológico de España y VIII Congreso Latinoamericano de Geologia - Salamanca, 2, 365-374.

Díez Balda, M., Martínez Catalán, J., Ayarza Arribas, P., 1995. Syncollisional extensional collapse parallel to the orogenic trend in a domain of steep tectonics: the Salamanca Detachment Zone (Central Iberian Zone, Spain). Journal of Structural Geology 17, 163-182.

Dodson, M.H., 1973, Closure temperatures in cooling geochronological and petrological systems: Contributions to Mineralogy and Petrology 40, 259-274.

Dostal, J., Chatterjee, A.K., 2000. Contrasting behaviour of Nb/Ta and Zr/Hf ratios in a peraluminous granitic pluton (Nova Scotia, Canada). Chemical Geology 163 (1,4), 207-218.

Dupret, L., Dissler, E., Dore, F., Gresselin, F., Le Gall, J. 1990. Cadomian geodynamic evolution in the northeast Armorican Massif. In: D'Lemos, R.S., Stkacnan, R.A,. Topley, C.G. (Eds.), The Cadomian Orogeny. Geological Society, London, Special Publication, 51, 115-131.

Eguíluz, J.I., Gil Ibarguchi, J.I., Ábalos, B., Apraiz, A., 2000. Superposed Hercynian and Cadomian orogenic cycles in the Ossa-Morena zone and related areas of the Iberian Massif. Geological Society of America Bulletin 112 (9), 1398-1413.

El Bouseily, A.M., El Sokkary, A.A., 1975. The relation between Rb, Ba and Sr in granitic rocks. Chemical Geology 16 (3), 207-219.

Escuder Viruete, J., Arenas, R., Martinez Catalán, J.R., 1994. Tectonothermal evolution associated with Variscan crustal extension in the Tormes Gneiss Dome (NW Salamanca, Iberian Massif, Spain). Tectonophysics 238, 117-138

Eskola, P., 1915. On the relation between the chemical and mineralogical composition in metamorphic rock of the Orijarvi region. Bulletin of the Geological Society of Finland 44.

Faure G., Mensing T.M., 2005. Isotopes. Principles and applications. John Willey, New York. 897

Faure, G., 2000. Origin of Igneous Rocks: The Isotopic Evidence, Springer, 496

Fernández Suárez, J., Gutiérrez Alonso, G., Jenner, G.A., Tubrett, M.N., 2000. New ideas on the Proterozoic- Early Paleozoic evolution of NW Iberia. Insights from U–Pb detrital zircon ages. Precambrian Research 102, 185-206.

Fernández-Suarez, G., Gutiérrez Alonso, G., Jener, G., Tubrett, M.N., 2000. New ideas on the Proterozoic-Early Palaeozoic evolution of NW Iberia: Insights from U-Pb detrital zircon ages. Precambrian Research 102, 185-206.

Fernández-Suarez, J., Dunning, G.R., Jenner, G.A., Gutiérrez-Alonso, G., 2000. Variscan collisional magmatism and deformation in NW Iberia: constraints from U–Pb geo- chronology of granitoids. Journal of the Geological Society of London 157, 565-576.

Ferreira, N., Iglésias M., Noronha F., Pereira E., Ribeiro A., Ribeiro M.L., 1987. Granitóides da zona Centro- Ibérica e seu enquadramento geodinâmico. In: Bea, F., Carmina, A., Gonzalo, J.C., Plaza, M.L., Rodrigues J.M.L. (Eds.), Geologia de los granitoides y rocas asociadas del Macizo Hespérico. Libro Homenage a L. C. G. Figueirola. Editorial Rueda, Madrid, 37-53.

Ferreira, P., Ribeiro, M.A., Vasconcelos, C., 2010. Geoquímica de litologias ígneas e metamórficas da zona costeira de Vila do Conde (NW de Portugal). Estudos Preliminares. X Congresso de Geoquímica dos Países de Língua Portuguesa, XVI Semana da Geoquímica. Memórias 14, 115-124.

Ferrero, S., Bodnar, B; Cesare, A., Viti, C., 2011. Re-equilibration of primary fluid inclusions in peritectic garnet from metapelitic enclaves, El Hoyazo, Spain. Lithos 124, 117-131.

Fleet, M.E., Deer, W.D., Howie, R.A., Zussman, J., 2003. Rock-forming Minerals: Micas. Geological Society of London, 758.

Flowers, G.C., 1979. Correction of Holloway's (1977) adaption of the modified Redlich–Kwong equation of state for calculation of the fugacities of molecular species in supercritical fluids of geologic interest. Contrib. Mineral. Petrology 69, 315-319.

Floyd, P.A., Leveridge, B.E., 1987. Tectonic environment of the Devonian Gramscatho basin, south Cornwall: framework mode and geochemical evidence from turbiditic sandstones. Journal of the Geological Society London 144, 531-542.

Fonteilles, M., 1978. Les Mecanismes de la Metasomatose. Bull. Minéral. 101, 166-194.

Forster, H.J., 1998. The chemical composition of REE-Y-Th-U-rich accessory minerals in peraluminous granites of the Erzgebirge-Fichtelgebirge region, Germany. Part II: Xenotime. American Mineralogist 83, 1302-1315.

Forster, H.J., 1999. The chemical composition of uraninite in Variscan granites of the Erzgebirge, Germany. Mineralogical Magazine 63(2), 239-252.

Foster, M.D., 1960. Interpretation of the composition of trioctahedral micas. U. S. Geological Survey Professional Paper 354-B, 1-49.

Franke, W., 2000. The mid-European segment of theVariscides: Tectonostratigraphic units, terrane boundaries and plate tectonic evolution. In: W. Franke et al.(Eds.), Orogenic Processes. Quantification and Modelling, Variscan Belt. Spec. Publ. Geol. Soc. 179, 35-64.

Fraser, G, Ellis, D., Eggins, S., 1997. Zirconium abundance in granulite-facies minerals, with implications for zircon geochronology in high-grade rocks. Geology 25, 607-610.

French, B.M., 1966. Some geological implications of equilibrium between graphite and a C-H-O gas phase at high temperatures and pressures. Rev. Geophysics 4, 223-253.

Frost, B.R., Barnes, C.G., Collins, W.J., Arculus, R.J., Ellis, D.J., Frost, C.D., 2001. A geochemical classification for granitic rocks. Journal of Petrology 42, 2033-2048.

Garcìa-Casco, A., Torres-Roldan, R.L., Millan, G., Monie, P., Haissen, F., 2001. High-grade metamorphism and hydrous melting of metapelites in the Pinos terrane (W Cuba): evidence for crustal thickening and extension in the northern Carribean collisional belt. Journal of Metamorphic Geology 19, 699-715.

García-Moreno, O., Corretgé, L.G., Castro C., 2007. Processes of assimilation in the genesis of cordierite leucomonzogranites from the Iberian Massif: a short review. Canada Mineralogist 45, 71-85.

Geraldes, M.C., 2010. Introdução à Geocronologia. Sociedade Brasileira de Geologia, São Paulo, 146 p.

Giorgetti, G., Frezzotti, M.L.E., Palmeri, R, Burke, E.A.J.,1996. Role of fluids in migmatites - CO_2-H_2O fluid inclusions in leucosomes from the deep-freeze range migmatites (terra-nova bay, antarctica). Journal of Metamorphic Geology 14, 307-317.

Gluyas, J.G., 1984. Early carbonate diagenesis within Phanerozoic shales and sandstones in the NW European shelf. Clay Minerals 19, 309-321.

Gokhale, N.W., 1968. Chemical composition of biotites as a guide to ascertain the origin of granites. Bulletin of the Geological Society of Finland 40, 107-111.

Gorbatschev, R., 1970. Distribution of tetrahedral Al and Si in coexisting biotite and Ca amphibole. Contributions to Mineralogy and Petrology 28, 251-258.

Gordon, S.M., Schneider, D.A., Manecki, M., Holm, D.K., 2005. Exhumation and metamorphism of an ultrahigh-grade terrane: geochronometric investigations of the Sudetes Mountains Poland and Czech. Journal Geological Society London 162, 841-855.

Gromet, L.P., Silver, L.T., 1983. Rare earth element distribution among minerals in a granodiorite and their pctrogenetic implications. Geochimica et Cosmochimica Acta 47, 925-940.

Guedes A., 2001. Evolução das condições PVTX dos paleofluidos em contextos metamórficos do soco Hercínico. PhD Thesis, Faculdade de Ciências da Universidade do Porto, 207 p.

Guedes, A. Noronha, F., Boiron, M.A., Banks, D., 2002. Evolution of fluids associated with metasedimentary sequences from Chaves (North Portugal). Chemical Geology 190, 1-4.

Guidotti, C.V., 1984. Micas in metamorphic rocks. In: Bailey, S.W. (Ed.), Micas: Reviews in Mineralogy. Mineralogical Society of America, Wa.hington, D.C., 13, 357-467.

Gunow, A.J., Ludington, S., Muñoz, J.L., 2008. Fluorine in micas from the Henderson molybdenite deposit, Colorado. Economic Geology 108(4), 667-690.

Gutiérrez-Alonso, G., Fernández-Suárez, J., Jeffries, T.E., Johnston, S.T., Pastor-Galán, D., Murphy, J.B., Franco, M.P., Gonzalo, J.C., 2011. Diachronous post-orogenic magmatism within a developing orocline in Iberia, European Variscides. Tectonics 30, TC5008.

Hall, D.L., Sterner, S.M., 1993. Preferential water loss from synthetic fluid inclusions. Contrib. Mineral. Petrol. 114, 489-500.

Hanchar, J.M., Miller, C.F., 1993. Zircon zonation patterns as revealed by cathodoluminescence and back-scattered electron images: implications for interpretation of complex crustal histories. Chemical Geology 110, 1-13.

Harris, N.B.W., Pearce, J.A., Tindle, A.G., 1986. Geochemical characteristics of collision- zone magmatism. In: Coward, M.P, Ries, A.C (Eds.), Collision Tectonics. Geological Society of London Special Publication 19, 67-81.

Harris, N.B.W., Inger, S. 1992. Trace element modelling of pelite-derived granites. Contributions to Mineralogy and Petrology 110, 46-56.

Henry, D.J., Guidotti, C.V., 1985. Tourmaline as a petrogenetic indicator mineral: an example from the staurolite-grade metapelites of NW Maine. American Mineralogist 70, 1-15

Henry, D.J., Guidotti, C.V., 2002. Titanium in biotite from metapelitic rocks: Temperature effects, crystal-chemical controls, and petrologic applications. American Mineralogist 87, 375-382.

Herron, M.M., 1988. Geochemical classification of terrigenous sands and shales from core or log data. Journal of Sedimentary Petrology 58, 820-829.

Hibbard, M.J., 1995. Petrography to petrogenesis. New Jersey, Prentice Hall, 587 p.

Hicks, K.S., Compton, J.S., McCracken, S., Vecsei, A., 1996. Origin of diagenetic carbonate minerals recovered from the New Jersey continental slope. In: Mountain, G.S., Miller, K.G., Blum, P., Poag, C.W., Twichell, D.C. (Eds.),Proc. ODP, Sci. Results,150: College Station, TX (Ocean Drilling Program), 311-328.

Holdaway, M.J., Mukhopadhyay, B., 1993. A reevaluation of the stability relations of andalusite: Thermochemical data and phase diagram for the aluminum silicates: Am. Mineralogist 78, 298-315.

Holland, T.J.B., Powell, R., 2002. An internally consistent thermodynamic data set for phases of petrological interest. Journal of Metamorphic Geology 16, 309-343.

Hollister, L.S., 1970. Origin, mechanism, and consequences of compositional sector-zoning in staurolite. The American Mineralogist 55, 742-766.

Hollister, L.S., 1988. On the origin of CO_2,-rich fluid inclusions in migmatites. Journal of Metamorphic Geology 6, 467-474.

Holloway, M.I., Bussy, F., Vennemann, T.W, 2008. Low-pressure, water-assisted anatexis of basic dykes in a contact metamorphic aureole, Fuerteventura (Canary Islands): oxygen isotope evidence for a meteoric fluid origin. Contributions to Mineralogy and Petrology 155 (1), 111-121.

Holness, M.B., 2008. Decoding migmatite microstructures. In: Working with Migmatites. Short Course. Mineral Association of Canada, Québec 38, 57-76.

Holtz, F., Johannes, W., 1991. Genesis of peraluminous granites. I. Experimental investigation of melt composition at 3 and 5 kbar and various H_2O activities. Jour. Petrol. 32(5), 935-958.

Horie, K., Tsutsumi, Y., Kim, H., Cho, M., Hidaka, H., Terada, K., 2009. A U–Pb geochronological study of migmatitic gneiss in the Busan gneiss complex, Gyeonggi massif, Korea. Geosci. J. 13, 205-215.

Hoskin, P.W., Black, L.P., 2000. Metamorphic zircon formation by solid-state recrystallization of protolith igneous zircon. Journal of Metamorphic Geology 18, 423-439.

Hoskin, P.W.O., Schaltegger, U., 2003. The Composition of Zircon and Igneous and Metamorphic Petrogenesis. Reviews in Mineralogy and Geochemistry 53 (1), 27-62.

Hudson, N.F.C., Kearns, S.L., 2000. On the origins of layered calc-silicate rocks from the Buchan Dalradian and their bearing on the diagenetic history of the Southern Highland Group. Scottish Journal of Geology 36, 39-49.

Hunter, D.R., 1973.Granitic rocks of the Precambrian in Swaziland. Special Publication of Geological Society of South Africa 3, 131-147.

Hurley, P.M., Hughes, H., Pinson, W.H., Fairbairn, H.W., 1962. Radiogenic argon and strontium diffusion parameters in biotite at low temperatures obtained from Alpine Fault uplift in New Zealand: Geochimica et Cosmochimica Acta 26, 67-80.

Hutton, J., 1795. Theory of the Earth with Proofs and illustrations. Edinburg, U.K.

Iglésias, M., Ribeiro, A., 1981. Zones de cisaillement ductile dans l'arc ibéro-armoricain. Comunicações dos Serviços Geológicos de Portugal 67 (1), 85-87.

Jager, E., Niggli, E., Wenk, E., 1967. Rb–Sr Altersbestimmungen an Glimmern der Zentralalpen. Beitr. Geol. Karte Schweiz N.F. 134, 1-67.

Jan, M.Q., Howie, R.A., 1981. Ortho- and clinpyroxenes from the pyroxene granulites of Swat Kohistan, northern Pakistan. Mineralogical Magazine 43 (7) 15-26.

Jensen, S., Palacios, T., Marti Mus, M., 2007. A brief review of the fossil record of the Edicarian -Cambrian transition in the area of Montes de Toledo -Guadalupe,

Spain. In: Vickers Rich, P. (Ed.), The rise and fall of Ediacarian biota. Geological Society of London. Special Publication 286, 223-235.

Johannes, W., Holtz, F., 1996. Petrogenesis and Experimental Petrology of Granitic Rocks. Minerals and Rocks, Springer Berlin Heidelberg, 22, 335.

Johannes, W., 1988. What controls partial melting in migmatites?. J. Metamorphic Geology 6, 451-465

Jones, B., Manning, D.A.C., 1994. Comparison of geochemical indices used for the interpretation of paleoredox conditions in ancient mudstones. Chem. Geol. 111, 111-129.

Jung, S., 2005. Isotopic equilibrium/disequilibrium in granites, metasedimentary rocks and migmatites (Damara orogen, Namibia) - A consequence of polymetamorphism and melting. Lithos 84, 168-184.

Kelly N.M., Harley, S.L., 2005. An integrated textural and chemical approach to zircon geochronology: refining the Archaean history of the Napier Complex, east Antarctica. Contributions to Mineralogy and Petrology 149, 57-84.

Kerrick, D.M., 1990. Al_2SiO_5-bearing veins and segregations formed by crystallization within fractures and cavities. In: Kerrick, D.M., (Ed.), The Al_2SiO_5 polymorphs. Rev. Mineral. 22, 325-345.

Kleemann, G.J., Twist, D., 1989. The compositionally-zoned sheet-like granite pluton of the Bushveld Complex: evidence bearing on the nature of A-type magmatism. Journal of Petrology 30, 1383-1414.

Knight, C.L., Bodnar, R.J., 1989. Synthetic fluid inclusions: IX. Critical PVTX properties of NaCl H_2O solutions. Geochimica et Cosmochimica Acta 53, 3-8.

Koppel, V., Sommerauer, J., 1974. Trace elements and the behavior of the U-Pb system in inherited and newly formed zircons. Contributions to Mineralogy and Petrology 43, 71-82.

Korzhinskii, D.S.,1979. Theory of metasomatic zoning. Oxford University press, 162 p.

Kranz, R.L., 1983. Micro-cracks in rocks: a review. Tectonophysics 100, 449-480.

Kriz, J., Degardin, J.M., Ferreti, A., Hansch, W., Gutierrez-Marco, J.C., Paris, F., Piçarra, J.M., Robardet, M., Schonlaub, H.P., Serpagli, E., 2003. Silurian stratigraphy and paleogeography of Gondwanaa and Perunica Europe. In:

Landing, E., Johnson, M.E. (Eds.), Silurian Lands and Seas, New York State Bulletin 493, 105-178.

Kroner, A., Jaeckel, P., Reischmann, T., Kroner, U., 1998. Further evidence for an early Carboniferous (340 Ma) age of high-grade metamorphism in the Saxonian granulite complex. Geol. Runsd. 86, 751-766.

Lamb, W., Valley, J.W., Brown, P.E., 1987. Post-metamorphic CO_2,-rich fluid inclusions in granulites. Contributions to Mineralogy and Petrology 96, 485-495.

Le Fort, P., Cuney, M., Deniel, C., France-Ianord, C., Sheppard, S.M.F., Upreti, B.N., Vidal, P., 1987. Crustal generation of the Himalayan leucogranites. Tectonophysics 134, 39-57.

Le Maitre, R.W., 1989. A Classification of Igneous Rocks and Glossary of Terms. Recommendations of the IUGS Commission on the Systematics of Igneous Rocks. Oxford.

Leake, B.E., 1964. The Chemical Distinction Between Ortho- and Para-amphibolites. Journal of Petrology 5(2), 238-254.

Leake, B.E., Woolley, A.R., Arps, C.E.S., Birch, W.D., Gilbert, M.C., Grice, J.D., Hawthorne, F.C., Kato, A., Kisch, H.J., Krivovichev, V.G., Linthout, K., Laird, J., Mandarino, J.A., Maresch, W.V., Nickel, E.H., Rock, N.M.S., Schumacher, J.C., Smith, D.C., Stephenson, N.C.N., Ungaretti, L., Whittaker, E.J.W., Youzhi, G., 1997. Nomenclature of amphiboles: Report of the Subcommittee on Amphiboles of the International Mineralogical Association, Commission on New Minerals and Mineral Names. American Mineralogist 82, 1019-1037.

Lee, J.K.,W., Williams, I.S., Ellis, D.J., 1997. Pb, U and Th diffusion in natural zircon. Nature 390, 159-162.

Lopes G., Ribeiro M.A., 2008. Aspectos geológico-didácticos da Praia de Angeiras Norte In: Sant'Ovaia, H., Dória, A., Ribeiro, M.A. (Eds.), 8ª Conferencia Anual do Grupo de Geologia Estrutural e Tectónica / Sociedade Geológica de Portugal, Universidade do Porto, Faculdade de Ciências, Departamento de Geologia. Memória 13, 48-51.

Lopes, G., 2008. Trabalho de Campo no Ensino da Geologia: Diagnóstico de competências de formação inicial versus experiência docente. Master's Thesis. Faculdade Ciências da Universidade do Porto.

López-Guijarro, R., Armendáriz, M., Quesada, C., Fernández-Suárez, J., Murphy, J.B., Pin, C., Bellido, F., 2008. Ediacaran-Palaeozoic tectonic evolution of the Ossa Morena and Central Iberian zones (SW Iberia) as revealed by Sm–Nd isotope systematics. Tectonophysics 461, 202-214.

Lotze, F., 1945. Zur Gliederung der Varisziden der Iberischen Meseta. Geotekt. Forsch., 6, 78-92. (Trad. J. M. Rios, 1950. Observaciones a respecto de la división de los varíscides de la Meseta Ibérica. Publicaciones Extranjeras sobre Geologia de España, Instituto Lucas Mallada, 5, 27, 149-166.

Ludwig, K.R., 2003. Isoplot/EX version 3.0. A geochronological toolkit for Microsoft Excel. Berkeley Geochronology Center, Special Publication.

Lyell, C., 1855. Manual of Elementary Geology. (5th Ed.) John Murray, London, U.K.

Marques, F.O., Mateus, A., Tassinari, C., 2002. The Late-Variscan fault network in central-northern Portugal (NW Iberia): a re-evaluation. Tectonophysics 359, 255-270.

Martínez Catalán, J.R., Arenas, R., Díaz Garcia, F., Abati, J., 1997. Variscan accretionary complex of nortwest Iberia; Terrane correlation and sucession of tectonothermal events. Geology 25, 1103-1106.

Martínez Catalán, J., Martínez Poyatos, D., Bea, F., 2004. Zona Centro Ibérica. In: Vera Torres, J.A. (Ed.), Geologia de España, Sociedad Geológica de España, Instituto Geológico y Minero de España, 68-133.

Martínez Catalán, J.R., Rubio Pascual, F., Díez Montes, A., Díez Fernández, R., Gómez Barreiro, J., Dias da Silva, I., González Clavijo, E., Ayarza Arribas, P., Alcock, J.E., 2014. The late Variscan HT/LP metamorphic event in NW and central Iberia: Relationships with crustal thickening, extension, orocline development, and crustal evolution. In: Schulmann, K., Oggiano, G., Lardeaux, J.M., Janousek, V., Martínez Catalán, J.R., Scrivener, R. (Eds.), The Variscan Orogeny: Extent, Timescale and the Formation of the European Crust. Geological Society, London, Special Publications, London, 405, 225-247.

Martinez, F.J., Ibarguchi, I.G., 1983. El metamorfismo en el Maciço Ibérico. Libro Jubilar J. M. Rios, Inst. Geol. Y Minero España, Madrid, II, 555-569.

Martinez, F.G., Julivert, M., Sébastian, A., Arboleya, M.L., Dietsch, C., 1988. Structural and thermal evolution of high-grade areas in northwestern parts of the Iberian massif. American Journal of Science 288, 969-996.

Martins, H., 1998. Geoquímica e petrogénese dos granitóides biotíticos tarditectónico e pós-tectónicos. Implicações metalogenéticas. PhD Thesis. Universidade de Trás-os-Montes e Alto Douro, 288 p.

Martins, H.C.B., Almeida, A., Noronha, F., Leterrier, J., 2001. Novos dados geocronológicos de granitos da região do Porto: Granito do Porto e Granito de Lavadores. Livro de Actas do VI Congresso de Geoquímica dos Países de Língua Portuguesa e XII Semana de Geoquímica. Universidade do Algarve, Faro. 146-148.

Martins, H.C.B., Sant'Ovaia, H., Noronha, F.,2009. Genesis and emplacement of felsic Variscan plutons within a deep crustal lineation. The Penacova-Régua-Verín fault. An integrated geophysics and geochemical study (NW Iberian Peninsula). Lithos 111, 142-155.

Martins, H.C.B., Sant'Ovaia, H., Abreu, J., Oliveira, M., Noronha, F., 2011. Emplacement of the Lavadores granite (NW Portugal). U/Pb and AMS results. Comptes Rendus Geoscience 343 (6), 387-396.

Mateus, A., Noronha F., 2001. Late-Variscan crustal uplift of the Iberian Terrane as a response to isostatic rebound; implications for the brittle-ductile transition, fluid circulation and metallogenesis. Mem. Mus. Lab. Mineral. Geol. Univ. Porto, 7, 295-298.

Matte, P., 1991. Accretionary history and crustal evolution of the Variscan belt in Western Europe. Tectonophysics 196, 309-337.

Matte, P., 2001. The Variscan collage and orogeny (480-290 Ma) and the tectonic definition of the Armorica microplate: a review. Terra Nova 13, 122-128.

Matte, P., Ribeiro, A., 1975. Forme et orientation de l'ellipsoïde de déformation dans la virgation hercynienne de Galice. Relations avec le plissement et hypothèses sur la genèse de l'arc ibéro– armoricain. C.R. Acad. Sci., Paris 280, 2825-2828.

McIntyre, G.A., Brooks, A.C., Compston, W., Turek, A., 1966. The statistical assessment of Rb-Sr isochrons. Journal of Geophysics Res. 71, 5459-5468.

McKerrow, W.S.; Mac Niocaill, C., Dewey, J.F., 2002. The Caledonian Orogeny redefined, Journal of the Geological Society 157, 1149-1154.

McLennan, S.M., Taylor, S.R., McCulloch, M.T., Maynard, J.B., 1990. Geochemical and Nd-Sr Isotopic Composition of Deep-Sea Turbidites - Crustal Evolution and Plate Tectonic Associations. Geochimica et Cosmochimica Acta 54(7), 2015-2050.

McLennan, S.M., Taylor, S.R., 1991. Sedimentary rocks and crustal evolution: Tectonic setting and secular trends. Journal of Geology 99, 1-21.

McLennan, S.M., Hemming, S., McDanniel, D.K., Hanson, G.N., 1993. Geochemical approaches to sedimentation, provenance, and tectonics. In: Johnsson, M.J., Basu, A. (Eds.), Processes Controlling the Composition of Clastic Sediments. Geological Society of America, Special Paper 285, 21-40.

Mehnert, K.R., 1968. Migmatites and the Origin of Granitic Rocks. Elsevier, Amsterdam, 393 p.

Meinhold, G., Kostopoulos, D., Reischmann, T., 2007. Geochemical constraints on the provenance and depositional setting of sedimentary rocks from the islands of Chios, Inousses and Psara, Aegean Sea, Greece:implications for the evolution of Palaeotethys. Journal of the Geological Society, London 164, 1145-1163.

Miller, C.F., Stoddard, E.F., Bradfish, L.J., Dollase, W.A., 1981. Composition of plutonic muscovite: genetic implications. The Canadian Mineralogist 19 (1), 25-34.

Miller, C.F., Mittlefehdlt, D.W., 1982. Depletion of light rare-earth elements in felsic magmas. Geology 10, 129-133

Milord, I., Sawyer, E.W., Brown, M., 2001. Formation of diatexite migmatite and granite magma during anatexis of semipelitic metasedimentary rocks: An example from St. Malo, France. Journal of Petrology 42, 487-505.

Moller, A., O'Brien, P.J., Kennedy, A., Kroner, A., 2002. Polyphase zircon in ultrahigh-temperature granulites (Rogaland, SW Norway): constraints for Pb diffusion in zircon. Journal of Metamorphic Geology 20(8), 727-740.

Monier, G., Mergoil-Danil, J., Labernardière, H., 1984. Générations successives de muscovites et feldspaths potassiques dans les leucogranite du massif de Millevaches (Massif Central Français). Bull. Minéral. 107, 55-68.

Montero, P., Bea, F., T.F., Scarrow, J.H., Molina, J.F., Whitehouse, M., 2004. 55 million years of continuous anatexis in Central Iberia: single-zircon dating of the Pefia Negra complex. Journal Geological Society London 161, 255-263.

Montero, M.P., Bea, F., Corretge, L.G., Floor, P., Whitehouse, M.J., 2008. U-Pb ion microprobe dating and Sr-Nd isotope geology of the Galiñeiro Igneous Complex. A model for the peraluminous/peralkaline duality of the Cambro-Ordovician magmatism of Iberia. Lithos 107, 227-238.

Morand, V.J., 1994, Calc-silicate lenses in the Early Palaeozoic mud-pile of the Lachlan Fold Belt. Australian Journal of Earth Science 41, 383-386.

Morel, S.W., 1961. Amphibolite-granulite facies assemblages in southern Nyasaland. Mineralogical Magazine 32, 725-730.

Morimoto, N., Fabries, J., Ferguson, A.K., Ginzburg, I.V., Ross, M., Seifert, F.A., Zussman, J., Aoki, K., Gottardi, D., 1988. Nomenclature of pyroxenes. American Mineralogst 62, 53-62.

Mozley, P.S., 1996. The internal structure of carbonate concretions: A critical evaluation of the concentric model of concretion growth. Sedimentary Geology 103, 85-91.

Mullins, T.A., Neumann, C.R., Wilber, J., Boardman, M.R., 1980. Nodular Carbonate Sediment on Bahamian Slopes: Possible Precursors to Nodular Limestones. Journal of Sedimentary Petrology 50(1), 117-131.

Nachit, H., Ibhi, A., Abia, E.H., Ohoud, M.B., 2005. Discrimination between primary magmatic biotites, reequilibrated biotites and neoformed biotites. Comptes Rendus Geosciences 337, 1415-1420.

Nachit, H., Razafimahefa, N., Stussi, J.M., Carron, J.P., 1985. Composition chimique des biotites et typologie magmatique des granitoïdes. Comptes Rendus de L'Académie des Sciences, Paris, Sciences de la terre et des planètes 301 (II-11), 813-818.

Neiva, A.M.R., Gomes, M.E.P., 2001. Diferentes tipos de granitos e seus processos petrogenéticos: Granitos Hercínicos Portugueses. Memórias da Academia das Ciências de Lisboa XXXIX, 53-95.

Neiva, A.M.R., Williams, I.S., Ramos, J.M.F., Gomes, M.E.P., Silva, M.M.V.G., Antunes, I.M.H.R., 2009. Geochemical and isotopic constraints on the petrogenesis of Early Ordovician granodiorite and Variscan two-mica granites from the Gouveia area, central Portugal. Lithos 111, 186-202.

Nesbitt, H.W., Young, G.M., 1984. Prediction of some weathering trends of plutonic and volcanic rocks based on thermodynamics and kinetic consideration. Geochimica et Cosmochimica Acta 48, 1223-1234.

Nesbitt, H.W., Young, G.M., McLennan, S.M., Keays, R.R., 1996. Effects of chemical weathering and sorting on the petrogenesis of siliclastic sediments, with implications for provenance studies. Journal of Geology 104, 525-542.

Neubauer, F., 2003. Geology of Europe. In: De vivo, B., Grasemann, B., Stüwe, K. (Eds.), Volume Geology. Encyclopedia of Life Supporting Systems. UNESCO Publishing-Eolss Publishers, Oxford, UK (Online version: www.eolss.net).

Neuman, R.B., Max, M.D., 1989. Penobscottian-Grampian-Finnmarkian orogenies as indicators of terran linkages. In: Dallmeyer, R.D. (Ed.), Terranes in the Circum-Atlantic Paleozoic Orogens. Geol. Soc. Am Spec. Paper 230, 31-45.

Newton, R.C., 1992. Charnockitic alteration: evidence for CO_2 infiltration in granulite facies metamorphism. Journal of Metamorphic Geology 10, 383-400.

Nicolaysen, L.O., 1961. Graphic interpretation of discordant age measurements on metamorphic rocks. Ann. N.Y. Academy Science, 91, 198–206.

Noronha, F., Ramos, J. M. F., Rebelo, J. A., Ribeiro, A. & Ribeiro, M. L., 1979. Essai de córrelation des phases de déformation hercynienne dans le Nord – Ouest Péninsulaire. Boletim da Sociedade Geológica de Portuga 21, 227-237.

Noronha, F., Ramos, J.M.F., Rebelo, J., Ribeiro, A., Ribeiro, M.L.,1981. Essai de corrélation des phases de déformation hercyniennes dans le NW de la Péninsule Ibérique. Leidse Geologische Mededelingen 52 (1), 89-91.

Noronha, F., 1983. Estudo metalogénico da área tungstífera da borralha. PhD Thesis. Faculdade de Ciências da Universidade do Porto, Centro de Geologia da Universidade do Porto-INIC, 472 p.

Noronha, F., Cathelineau, M., Boiron, M.C., Banks, D.A., Dória, A., Ribeiro, M.A., Nogueira, P., Guedes, A. 2000. A three stage fluid flow model for Variscan gold metallogeneasis in northern Portugal. Journal of Geochemical Exploration 71(2), 209-224.

Oen, I.S., 1970. Granite intrusion, folding and metamorphism in central northern Portugal. Boletín Geológico y Minero LXXXI-II-III, 271-298.

Oliveira, J.T., Pereira E. (Crds), 1992. Carta Geológica de Portugal à escala 1:500 000. Serviços Geológicos de Portugal.

Olsen, S.N., Marsh, B.D., Baumgartner, L.P., 2004. Modelling mid-crustal migmatite terrains as feeder zones for granite plutons: the competing dynamics of melt transfer by bulk versus porous flow. Transactions of the Royal Society Edinburgh: Earth Sciences 95, 49-58.

Owen, J.V., Dostal, J., Church, B.N., 1994. Mineralogic reaction zones at a calc-silicate/metapelite interface: an example of trace element mobility in a metamorphic environment. Mineralogical Magazine 58, 205-214.

Pan, Y., 1997. Controls on the fractionation of isovalent trace elements in magmatic and aqueous systems: Evidence from Y/Ho, Zr/Hf, and lanthanide tetrad effect—A discussion of the article by M. Bau. Contrib. Mineral. Petrolrology 128, 405-408.

Pan, Y., 1997. Zircon- and monazite-forming metamorphic reactions at Manitouwadge, Ontario. Can Mineralogy 35,105-118.

Parga Pondal, I., Matte, P., Capdevila, R., 1964. Introduction a la geologie del “Olho de Sapo”, formation porphyroide ante-silurienne du nord ouest de l’Espagne. Not. Com. Inst. Geol. Min. España 76, 119-153.

Parga, J.R., 1969. Sistemas de Fracturas Tardihercínicas del Macizo Hespérico. Trab. Laboratório Geologico Lage 37, 3-15.

Paris, F., Robardet, M., 1990. Early Paleozoic palaeobiogeography of the Variscan regions. Tectonophysics 177, 193-213.

Paterson, B.A., Stephens, W.E., Rogers, G., Williams, I.S., Hinton, R.W., Herd, D.A., 1992. The nature of zircon inheritance in two granite plutons. Transactions of the Royal Society of Edinburgh, Earth Science 83, 459-471.

Patiño Douce, A.E., Harris, N., 1998. Experimental constraints on Himalayan anatexis. Journal of Petrology 39, 689-710.

Pattan, J.N., Parthiban, G., 2011. Geochemistry of ferromanganese nodule-sediment pairs from Central Indian Ocean Basin. Journal of Asian Earth Sciences 40(2), 569-580.

Pearce, J.A., Harris, N.W., Tindle, A.G., 1984. Trace element discrimination diagrams for the tectonic interpretation of granitic rocks. Journal of Petrology 25, 956-983.

Percival, J.A., Helmstaedt, H., 1978. Zoned epidote nodules from sedimentary rocks of the Eastport Formation, Southwest New Brunswick. Canadian Journal of Earth Sciences 15, 1200-1204.

Pereira, E., 1988. Soco Hercínico da Zona Centro-Ibérica - Evolução Geodinâmica. Geonovas 10, 13-35.

Pereira, E., Ribeiro, A., Carvalho, G., Noronha, F., Ferreira, N., Monteiro, J.H., 1992. Notícia Explicativa da Carta Geológica de Portugal na escala de 1:200 000. Serviços Geológicos de Portugal.

Pereira, E., Ribeiro, A., Meireles, C., 1993. Cisalhamentos hercínicos e controlo das mineralizações de Sn-W, Au e U na Zona Centro-Ibérica, em Portugal. Cuadernos Lab. Xeolóxico de Laxe 18, 89-119.

Pereira, M.F., Chichorro M., Solá, A.R,, Silva, J.B., Sánchez-García, T., Bellido, F. 2011.Tracing the Cadomian magmatism with detrital/inherited zircon ages by in-situ U–Pb SHRIMP geochronology (Ossa-Morena Zone, SW Iberian Massif). Lithos 123 (1), 204-217.

Pereira, M.F., Linnemann, U., Hofmannb, M., Chichorro, M.,.Solá, A.R, Medina, J., Silva, J.B. 2012. The provenance of Late Ediacaran and Early Ordovician siliciclastic rocks in the Southwest Central Iberian Zone: Constraints from detrital zircon data on northern Gondwana margin evolution during the late Neoproterozoic. Precambrian Research 195, 166-189.

Pesquera, A., Torres-Ruiz, J., Gil-Crespo, P.P., Jiang, S.Y. 2005. Petrographic, chemical, and B-isotopic insights into the origin of tourmaline-rich rocks and boron recycling in the Martinamor antiform (Central Iberian Zone, Salamanca, Spain). J. Petrol. 46, 1013-1044.

Pettijohn, F.J., Potter, P.E., Siever, R., 1972. Sands and Sandstones. Springer-Verlag, New York.

Pidgeon, R.T., 1992. Recrystallisation of oscillatory zoned zircon: some geochronological implications. Contributions to Mineralogy and Petrology 110, 463-472.

Pidgeon R.T., Nemchin A.A., Hitchen G.J., 1998. Internal structures of zircons from Archaean granites from the Darling Range batholith: implications for zircon stability and the interpretation of zircon U-Pb ages. Contributions to Mineralogy and Petrology 132, 288-299.

Pinto de Jesus, A., 1986. Bassin Mouiller du Douro (NW du Portugal). Stratigraphie et controle tectonique de la genèse et de l'évolution. Ann. Soc. Géol. Nord., Lille 106, 209-217.

Pinto, A.F.F., 1984. As rochas calcossilicatadas do Complexo Xisto Grauváquico. Mineralogia, geoquímica, evolução genética. Comunicações Serviços Geológicos de Portugal 79 (1), 55-62.

Pinto, M., Casquet, C., Ibarrola, E., Corretgé, L., Portugal Ferreira, M., 1987. Síntese geocronológica dos granitóides do Maciço Hespérico. In: Bea, F., Carmina, A., Gonzalo, J. C., Plaza, M. L., Rodrigues J.M.L. (Eds.), Geologia de los granitoides y rocas asociadas del Macizo Hespérico. Libro Homenage a L.C.G. Figueirola, Editorial Rueda, 69-86.

Pirajno, F., 1992. Hydrothermal mineral deposits. Sprinver-Verlag, Berlin, 709 p.

Pitcher, W.S., Berger, A.R., 1972. The Geology Of Donegal: A Study Of Granite Emplacement And Unroofing. Wiley Interscience, New York, 435 p.

Plank, T., Langmuir, C.H., 1998. The geochemical composition of subducting sediment and its consequences for the crust and mantle. Chemical Geology 145, 325-394.

Plank, T., 2005. Constraints from Thorium/Lanthanum on Sediment Recycling at Subduction Zones and the Evolution of the Continents. Journal of Petrology 46 (5), 921-944.

Ponte, M.J.B., Gama Pereira, L.C., 2004. Estruturação do Complexo Xisto-Grauváquico num conjunto areno-quartzítico da região de Ázere-S. Paio (Tábua, Portugal central). Cadernos do Laboratório Xeolóxico de Laxe, A Coruña 29, 53-78.

Poty, B.J, Leroy, J., Jachimowicz, L., 1976. Un nouvel appareil pour la mesure des temperatures sous le microscope: l'installation de microthermométrie Chaixmeca. Bull. Soc. Franc. Miner. Cristallogr. 21 (2/3), 182-186.

Prieto, A.C., Guedes A, Dória A, Noronha F, Jiménez J., 2012. Quantitative determination of gaseous phase compositions in fluid inclusions by Raman microspectrometry. Spectroscopy Letters, 45,156-160.

Pupin, J.P., 1980. Zircon and Granite Petrology. Contributions to Mineralogy and Petrology 73, 207-220.

Putlitz, B., Valley, J.W., Matthews, A., Katzir, Y., 2002. Oxygen isotope thermometry of quartz–Al_2SiO_5 veins in high-grade metamorphic rocks on Naxos Island (Greece). Contrib. Mineral. Petrology 143, 350-359.

Putnis, A., 2009. Mineral Replacement Reactions. Reviews in Mineralogy and Geochemistry 70, 87-124.

Putnis, A., John, T., 2010. Replacement processes in the Earth's crust. Elements 6, 159-164.

Putnis, A., Putnis, C.V., 2007. The mechanism of reequilibration of solids in the presence of a fluid phase. Journal of Solid State Chemistry 180, 1783-1786.

Putnis, C.V., Ruiz-Agudo, E., 2013. The Mineral-Water Interface: Where Minerals React with the Environment. Elements 9, 177-182.

Quesada, C., 1990. Precambrian successions in SW Iberia: Their relationship to Cadomian orogenic events. In: D'Lemos, R.S. Strachan, R.A. Topley, C.G. (Eds.), The Cadomian Orogeny, Special Publication, The Geological Society, London 51, 353-362.

Quesada, C., 1991. Geological constraints on the Paleozoic tectonic evolution of the tectonostratigraphic terrenes in the Iberian Massif. Tectonophysics 185, 225-245.

Quesada, C., 1992. Evolución tectónica del Macizo Ibérico (Una historia de crecimiento por acrecencia sucesiva de terrenos durante el Proterozoico superior y el Paleozoico). In: Gutiérrez Marco, J.C., Saavedra, J., Rábano, I. (Eds.), Paleozoico Inferior de Ibero-América. Junta de Extremadura, Mérida, Spain, 173-190.

Quesada, C., 1996. Evolucion geodinamica de la Zona de Ossa- Morena durante el ciclo Cadomiense. In: Araujo, A., Pereira, M.F.C. (Eds.), Estudos sobre a geologia da Zona de Ossa Morena (Maciço Ibérico). Univ. Evora, Evora, Portugal, 205-230.

Raju, R.D, Rao, J.S.R.K., 1972. The chemical distinction between replacement and magmatic granitic rocks. Contributions to Mineralogy and Petrology 35, 169-172.

Raymond, L.A., 1995. Petrology: The Study of Igneous, Sedimentary, Metamorphic Rocks. Wm.C. Brown, Publishers, Chicago, 742 p.

Reavy, R.J., 1989. Structural controls on metamorphism and syn-tectonic magmatism: the Portuguese Hercynian collision belt. Journal of the Geological Society 146, 649-657.

Regêncio C.A., Portugal Ferreira, M., 1981. O sinclinal paleozóico de Esposende (Porto) - Seoueros (Salamanca): o troço entre a Marofa e o Sátão (Portugal central). Cuadernos Geología ibérica 7, 633-644.

Ribeiro, A., Pereira, E., Severo, L., 1980. Análise da Deformação na Zona de Cisalhamento Porto-Tomar na transversal de Oliveira de Azeméis. Comun. Serv. Geol. Portugal 66, 161-167.

Ribeiro, A., 1983. Modelo Geodinâmico II magmatismo ácido pré--orogénico. In: Gonzalo, M., López Plaza, M., Rodríguez-Alonso, M.D. (Eds.), VIII Reunião Geol. Oeste Peninsular, Salamanca. Libro homenaje a L.C. Garcia de Figuerola, Rueda, Madrid, 37-53

Ribeiro, A., Pereira, E., Dias, R., 1990. Structure of the Northwest of the Iberian Peninsula. In: Dallmeyer, R.D., Martinez Garcia, E. (Eds.), Pre-Mesozoic Geology of Iberia, Springer-Verlag, 220-236.

Ribeiro, A., Munhá, J., Dias, R., Mateus, A., Pereira, E., Ribeiro, L., Fonseca, P., Araújo, A., Oliveira, T., Romão, J., Chaminé, H., Coke, C., Pedro, J., 2007. Geodynamic evolution of SW Europe Variscides. Tectonics 26, TC6009.

Ribeiro da Costa, I., Antunes, I.M., Farinha Ramos, J., Recio, C., Barriga, F., Mourão, C., Guimarães, F., Ferreira, N., 2013. Aspectos petrográficos do metamorfismo de contacto associado ao plutão granítico de Penamacor-Monsanto. Comunicações Geológicas 100 (1), 89-98.

Ribeiro, M.A., Sousa, M.B., Noronha, F., 1993. A Formação de Envendos e as rochas ácidas associadas. Publ. Museu e Lab. Miner. e Geológico da Fac. Ciências do Porto, Nova Série, 7, 1-20.

Ribeiro, M.A., Dória A., Sant'Ovaia H., 2008. Relações entre deformação, magmatismo e metamorfismo na região oriental do maciço do Porto. In: Sant'Ovaia, H. Dória, A., Ribeiro, M.A. (Eds.), 8ª Conferencia Anual do Grupo de Geologia Estrutural e Tectónica / Sociedade Geológica de Portugal, Resumos alargados, Universidade do Porto, Faculdade de Ciências, Departamento de Geologia. Memórias 13, 39-43.

Ribeiro, M.A, Sant'Ovaia, H., Dória, A., 2010. Zn-rich hercynite-magnetite assemblage in gneiss and metasedimentary rocks from Lavadores (Northern Portugal). Geoch. Cosmochimica Acta 74, (12, S1), A868.

Ribeiro, M.A, Sant'Ovaia, H., Dória, A.,2011. Litologias gnaisso-migmatíticas da faixa costeira Lavadores-Madalena. Possível significado das paragéneses com hercinite. In: Neves, L.J.P.F., Pereira, A.J.S.C., Gomes, C.S.R., Pereira, L.C.Ç., Tavares, A.O. (Eds.), Modelação de Sistemas Geológicos. Laboratório de Radioactividade Natural, Univ. Coimbra, 343-351.

Ribeiro, M.A., Areias, M., Dória, A., Ferreira, P., 2011. Zoned calc-silicated boudins in quartz-pelitic metatexitic rocks, NW Portugal. Mineralogical Magazine, Goldschmidt Conference Abstracts 75, 3.

Ribeiro, M.L., 1993. Western iberian granites: a contribution to their geodynamic interpretation. Caderno Lab Xeolóxico de Laxe 18, 7-25.

Ribeiro M.L., Munhá, J., Sola, A.R., Mata, J., 2010. The lower paleozoic magmatism in the southwestern Central Iberian Zone. In: Cotelo Neiva, J.M., Ribeiro, A., Mendes Victor, L., Noronha, F., Magalhães Ramalho, M. (Eds.), Ciências Geológicas - Ensino e Investigação e sua História, Lisboa, Associação Portuguesa de Geólogos, Sociedade Geológica de Portugal, 127-147.

Robardet, M., Gutiérrez-Marco J.C., 1990. Sedimentary and faunal domains in the Iberian Peninsula during Lower Paleozoic times. In: Dallmeyer, R.D, Martínez Garcia, E. (Eds.), Pre-Mesozoic Geology Iberia, 383-395.

Roberts, M.P., Finger, F., 1997. Do U-Pb zircon ages from granulites reflect peak metamorphic conditions? Geology 25, 319-322.

Rodriguez-Alonso, M.D., Peinado, M., Lopez-Plaza, M., Franco P., Carnicero, A., Gonzalo, J.C., 2004. Neoproterozoic-Cambrian Synsedimentary magmatism in the Central Iberian Zone (Spain): geology, petrology and geodynamic significance. Int. J. Earth Sci. (Geol. Rundsch.) 93, 897-920.

Roedder, E., 1979. Fluid inclusions as samples of ore fluids. In: Barnes, H.L. (Ed.), Geochemistry of Hydrothermal Ore Deposits. 2nd ed. Wiley, New York, 684-737.

Roedder, E., 1984. Fluid Inclusions. Review of Mineralogy. Mineralogical Society of America, Washington DC, 646 p.

Roedder, E., Bodnar, R.J., 1997. Fluid Inclusion Studies of Hydrothermal Ore Deposits. In: H.L. Barnes (Ed.), Geochemistry of Hydrothermal Ore Deposits, 3rd ed., Wiley & Sons, Inc, New York, 657-698.

Rogers, J.J.W., Adams, J.A.S.,1969a. Thorium. In: K.H. Wedepohl (Ed.), Handbook of Geochemistry, Springer-Verlag, Berlin, II/5, Ch. 90-E.

Rogers, J.J.W., Adams, J.A.S.,1969b. Uranium. In: K.H. Wedepohl (Ed.), Handbook of Geochemistry, Springer-Verlag, Berlin, II/5, Ch. 92-E.

Rogers. J.W., Adams A, 1978. Th: abundances in common igneous rocks. In: K.H. Wedepohl (Ed.), Handbook of Geochemistry, Springer-Verlag, Berlin, I/5, Ch. 92-E, 1-12.

Rolet, J., Gresselin, F., Jegouzo, P., Ledru, P. Wyns, R., 1994. Intracontinental Hercynian events in the Armorican Massif. In: Keppie, J.D. (Ed.), Pre-Mesozoic Geology in France and Related Areas. Springer, Berlin, 195-219.

Rollinson, H., 1993. Using Geochemical Data: evaluation, presentation, interpretation. Longman Group UK Limited.

Romão, J., 1994. Litoestratigrafia e tectónica do Grupo das Beiras (Complexo Xisto-Grauváquico) entre o rio Erges e a Serra do Moradal. Bol. Geol. Min. España 105/6, 521-530.

Romão, J., Coke C., Dias R., Ribeiro A., 2005. Transient inversion during the opening stage of the Wilson Cycle ‘‘Sardic phase’’ in the Iberian Variscides: Stratigraphic and tectonic record. Geodin. Acta 18, 15-29.

Romão, J., Metodiev, D., Dias, R., Ribeiro, A., 2013. Evolução geodinâmica dos sectores meridionais da Zona Centro-Ibérica. In: R. Dias, A. Araújo, P. Terrinha, J.C. Kullberg (Eds.), Geologia de Portugal. Escolar Editora, 1, 206-257.

Romariz, C., 1969. Graptólitos silúricos do Noroeste Peninsular. Comunicações dos Serviços Geológicos de Portugal 53, 107-155.

Rubatto, D., 2002. Zircon trace element geochemistry: partitioning with garnet and the link between U-Pb ages and metamorphism. Chemical Geology 184, 123-138.

Rubio-Ordónez, A., Valverde-Vaquero, P., Corretgé, L.G., Cuesta-Fernández, A., Callastegui, G., Fernández-González, M., Gerdes, A., 2012. An Early Ordovician tonalitic–granodioritic belt along the Schistose-Greywacke Domain of the Central Iberian Zone (Iberian Massif, Variscan Belt). Geological Magazine 149, 927-939.

Santos, J.F., Schärer, U., Gil Ibarguchi, J.I., Girardeau, J., 2002. Genesis of pyroxenite-rich peridotite at Cabo Ortegal (NW Spain): geochemical and Pb-Sr-Nd isotope data. Journal of Petrology 43, 17-43.

Sant'Ovaia, H., Bouchez, J.L., Noronha, F., Leblanc, D., Vigneresse, J.L., 2000. Composite-laccolith emplacement of the posttectonic Vila Pouca de Aguiar granite pluton (northern Portugal): A combined AMS and gravity study. Transactions of the Royal Society of Edinburgh, Earth Sciences 91 (1-2), 123-137.

Sardarov, S.S., 1957. Sokhrannost radiogennogo argona v mikroklinakh. Geokhimya 3, 193-197.

Sauniac, S.,Touret, J., 1983. Petrology and fluid inclusions of a quartz-kyanite segregation in the main thrust zone of the Himalayas. Lithos 16**,** 35-45**.**

Sawka, W.N., Chappell, B.W., 1988. Fractionation of uranium, thorium and rare earth elements in a vertically zoned granodiorite: implications for heat production distribution in the Sierra Nevada batholith, California, U.S.A. Geochimica et Cosmochimica Acta 52, 1131-1144.

Sawyer, E.W., 1996, Melt segregation and magma flow in migmatites: Implications for the generation of granite magmas: Transactions of the Royal Society Edinburgh: Earth Sciences 87, 85-94.

Sawyer, E.W., 1998. Formation and evolution of granite magma during crustal reworking: The significance of diatexites. Journal of Petrology 39, 1147-1167.

Sawyer, E.W., 2008a. Atlas of Migmatites. The Canadian Mineralogist Special Publications 387

Sawyer, E.W., 2008b. Working with migmatites: nomenclature for the constituent parts, Mineralogical Association of Canada Short Course, 38, Quebec City, Quebec, 1-28.

Sawyer, E.W., 2010. Migmatites formed by water-fluxed partial melting of a leucogranodiorite protolith: Microstructures in the residual rocks and source of the fluid. Lithos 116 (3–4), 273-286.

Scaillet, B., François, H., Pichavant, M., Schmidt M., 1996. Viscosity of Himalayan leucogranites: Implications for mechanisms of granitic magma ascent. Journal of Geophysical Research Solid Earth 101 (B12), 691-699.

Schaltegger U., Fanning C.M., Günther D., Maurin J.C., Schulmann K., Gebauer D., 1999. Growth, annealing and recrystallization of zircon and preservation of monazite in high-grade metamorphism: conventional and in-situ U-Pb isotope,

cathodoluminescence and microchemical evidence. Contribution Mineralogy and Petrology 134,186-201.

Schaltegger, U. 1997. Magma pulses in the Central Variscan Belt: episodic melt generation and emplacement during lithospheric thinning. Terra Nova 9, 242-245.

Schätz, M., Reischmann, T., Tait, J., Bachtadse, V., Bahlburg, H., Martin, U., 2002. The Early Palaeozoic break-up of northern Gondwana, new palaeomagnetic and geochronological data from the Saxothuringian Basin, Germany. International Journal of Earth Sciences 91(5), 838-849.

Schermerhorn, L., 1956. Igneous, metamorphic and ore geology of the Castro Daire - São Pedro do Sul - Sátão region (northern Portugal). Comun. Serv. Geol. Portugal 37, 617

Sederholm, J.J., 1926. On migmatites and associated Precambrian rocks of southwestern Finland. Bulletin de la Commission Géologique de Finland 77.

Shand, S.J., 1943. Eruptive Rocks. Their Genesis, Composition, Classification, and Their Relation to Ore-Deposits with a Chapter on Meteorite. New York, John Wiley & Sons.

Shaw D.M., 1968. A review of K-Rb fractionation trend by covariance analysis. Geochim. Cosmochim. Acta 32, 573-601.

Shepherd T.J., Rankin A.H., Alderton D., 1985. A Practical Guide to Fluid Inclusion Studies. Blackie & Son Ltd., Glasgowand, London, 239 p.

Simancas, J.F., Exposito, I., Azor, A., Martınez Poyatos, D., González Lodeiro F., 2001. From the Cadomian orogenis to the early Palaeozoic Variscan rifting Southwest Iberia. J. Iberian Geol. 30, 53-71.

Simmons, G., Richter, D., 1976. Micro-cracks in rock. In: Strens, R.G.J. (Ed.), The Physics and Chemistry of Minerals and Rocks. Wiley, New York, 105-137.

Smithson, S.B., Fikkan, P.R., Robert, S.H., 1971. Amphibolitization of Calc-Silicate Metasedimentary Rocks. Contribution to Mineralogy and Petrology 31, 228-237.

Snelling, N.J., 1976. Least squares fitting of straight line to analytical data geochronological applications. Institute of Geological Sciences (Report 76.18). London, 20 p.

Solá, A.R., Montero, P. Ribeiro, M.L., Neiva, A.M.R., Zinger, T.,Bea, F., 2005. Pb/Pb age of the Carrascal Massif, central Portugal. Geochimica Cosmochimica Acta, Special Supplement 69, A856.

Solá, A.R., Pereira, M.F., Williams, I.S., Ribeiro, M.L., Neiva, A.M.R., Montero, B., Bea, F., Zinger, T., 2008. New insights from U-Pb zircon dating of Early Ordovician magmatism on the northern Gondwana margin: The Urra Formation (SW Iberian Massif, Portugal). Tectonophysics, doi: 10.1016/j.tecto.2008.01.011.

Solá, A.R., Williams, I.S., Neiva, A.M.R., Ribeiro, M.L., 2009. U–Th–Pb SHRIMP ages and oxygen isotope composition of zircon from two contrasting late Variscan granitoids, Nisa Albuquerque batholith, SW Iberian Massif: Petrologic and regional implications. Lithos 111, 156-167.

Sousa, M.B., 1982. Litoestratrigrafia e estrutura do “Complexo Xisto-Grauváquico ante-Ordovícico – Grupo do Douro (Nordeste de Portugal). PhD Thesis, Universidade de Coimbra, 354 p.

Sousa, M.B., 1984. Considerações Sobre a Estratigrafia do Complexo Xisto-Grauváquico e sua relação com o Paleozóico Inferior. Cuadernos Geología Ibérica 9, 9-36.

Spear, F.S., 1995. Metamorphic Phase Equilibria and Pressure-Temperature-Time Paths. Second Printing. Mineralogical Society of America, Washington, D.C., 799 p.

Spear, F.S., Kohn, M.J., Florence, F., Menard, T., 1990. A model for garnet and plagioclase growth in pelitic schists: Implications for thermobarometry and P-T path determinations. J. Metamorphic Geology 8, 683-96.

Spicer, E.M., 2011. The low-pressure partial-melting behaviour of natural boron-bearing metapelites from the Mt Stafford area, central Australia. PhD Thesis, University of Stellenbosch, 218 p.

Stacey, J.S., Kramers, J.D., 1975. Approximation of terrestrial lead isotope evolution by a two-stage model. Earth and Planetary Science Letters 34, 207-226.

Streckeisen, A., 1974. Classification and nomenclature of plutonic rocks. Geologische Rundschau 63, 773-786.

Streckeisen, A., Le Maitre, R.W., 1979. A chemical approximation to the modal QAPF classification of the igneous rocks. Neues Jahrbuch für Mineralogie 136 (2), 169-206.

Stussi, J.M., 1989. Granitoid chemistry and associated mineralization in the French Variscan. Economic Geology 84(5), 1363-1381.

Talavera, C., Montero, P., Martínez Poyatos, D., Williams, I., 2012. Ediacaran to Lower Ordovician age for rocks ascribed to the Schist– Graywacke Complex (Iberian Massif, Spain): Evidence from detrital zircon SHRIMP U–Pb geochronology. Gondwana Research 22, 928-942.

Tassinari, C., Medina, J., Pinto, M., 1995. Rb-Sr and Sm-Nd geochronology and isotope geochemistry of Central Iberian metasedimentary rocks (Portugal). Geologie en Mijnbouw 75, 69-79.

Taylor S.R., McLennan S.M., 1985. The continental crust: its composition and evolution. Blackwell Scientific Publication, Carlton, 312 p.

Teixeira, C., 1970. Aspectos geológicos da orla litoral do Porto e de V. N. Gaia. Naturalia 10, (1), 13-29.

Teixeira, C., Cândido de Medeiros, A., 1965. Notícia explicativa da Carta Geológica à escala 1/50.000, Folha 9A-Póvoa de Varzim. Serviços Geológicos de Portugal.

Teixeira R.J.S., 2008. Mineralogia, petrologia e geoquímica dos granitos e seus encraves da região de Carrazeda de Ansiães. PhD Thesis, Universidade de Trás-os-Montes e Alto Douro-Vila Real, 430 p.

Teixeira, R.J.S., Neiva, A.M.R., Silva, P.B., Gomes, M.E.P, Andersen, T., Ramos, J.M.F., 2011. Combined U–Pb geochronology and Lu– Hf isotope systematics by LAM–ICPMS of zircons from granites and metasedimentary rocks of Carrazeda de Ansiães and Sabugal areas, Portugal, to constrain granite sources. Lithos 125, 321-334.

Teixeira, R.J.S. Coke, C., Gomes, M.E.P., Dias R., Martins, L.O., 2013. U-Pb geochronology of detrital zircons from metasedimentary rocks from Formation of Desejosa, Serra do Marão, Portugal. Mineralogical Magazine 77(5), 2318.

Teyssier, C., Whitney, D.L., 2002. Gneiss domes and orogeny. Geology 30, 1139-1142.

Thompson, A.B., Tracy, R.J., 1979. Model systems for anatexis of pelitic rocks, II. Facies series melting and reactions in the system $CaO\text{-}KAlO_2\text{-}NaAlO_2\text{-}Al_2O_3\text{-}H_2O$. Contrib. Mineral. Petrol. 70, 429-438.

Tischendorf, G., Gottesmann, B., Foster, H-J., Trumbull, R.B., 1997. On Li-bearing micas: estimating Li from electron microprobe analyses and an improved diagram for graphical representation. Mineralogical Magazine 61, 809-834.

Tischendorf, G., Foster, H-J., Gottesmann, B., 1999. The correlation between lithium and magnesium in trioctahedral micas: Improved equations for Li_2O estimation from MgO data. Mineralogical Magazine 63, 57-74.

Tomaschek F, Kennedy A, Villa I, Lagos M, Ballhaus C., 2003. Zircons from Syros, Cyclades, Greece recrystallisation and mobilization of zircon during high pressure metamorphism. Journal Petrology 44, 1977-2002.

Tombale A.R., Sinclair A.J., HcMillan W.J., 1984. Variation of k/Rb ratio in the major units of the Guichon Creek batholiths. British Columbia Geological Survey Geological Fieldwork, 419-425.

Torre de Assunção, C.F., 1962. Rochas Graníticas do Minho e Douro. Novos elementos para o seu conhecimento. Mem. Serv. Geol. Portugal, Nova Série 10, 33-65.

Touret, J., 1977. The significance of fluid inclusions in metamorphic rocks. In: Fraser, D. (Ed.), Thermodynamics in Geology, NATO ASI Series, C. 35, Reidell Pub., Dordrecht, 410 p.

Touret, J., 1981. Fluid inclusions in high grade metamorphic rocks. In: Hollister, L.S., Crawford, M.L. (Eds.), Fluid Inclusions. Mineralogical Association of Canada Short Course Handbook. Applications Petrol. 6, 182-208.

Touret, J., Olsen, S.N., 1985. Fluid Inclusions in Migmatites. In: Migmatites, 265-288.

Touret, J., 1986. Fluid inclusions in rocks from the lower continental crust. In: Dawson, J.B., Carswell, D.A., Hall, J., Wedepohl, K.H. (Eds.). The nature of the lower continental crust. Geological Society Special Publication, 24, 161-172.

Touret, J., 2001. Fluid inclusions in metamorphic rocks. Lithos 55, 1–25.

Turner, F.J., 1948. Mineralogical and Structural Evolution of Metamorphic Rocks. New York. Geological Society of America, 332 p.

Ugidos, J.M., Bea, F., 1976. Análisis comparativo de los granitos del área de Béjar-Plasencia con otros granitos “younger” peninsulares: precisiones sobre la serie mixta. Stvdia Geologica Salmanticiensis 10, 45-59.

Ugidos, J., Valladares, M.I., Recio, C., Rogers, G., Fallick, A.E., Stephens, W.E., 1997. Provenance of Upper Precambrian-Lower Cambrian shales in the Central Iberian Zone, Spain: evidence from a chemical and isotopic study. Chemical Geology 136, 55-70.

Ugidos, J.M., Valladares, M.I., Barba, P., Ellam, R.M., 2003, The Upper Neoproterozoic-Lower cambrian of the Central Iberian Zone, Spain: Chemical and isotopic (Sm-Nd) evidence that the sedimentary succesion records an inverted stratigraphy of its source. Geochimica et Cosmochimica Acta 67, 2615-2629.

Ugidos, J.M., Sánchez-Santos, J.M., Barba, P., Valladares, M.I., 2010. Upper Neoproterozoic series in the Central Iberian, Cantabrian and West Asturian Leonese Zones (Spain): Geochemical data and statistical results as evidence for a shared homogenised source area. Precambrian Research 178, 51-58.

Valladares, M.I., Barba, P., Ugidos, J.M., Colmenero, J.R., Armenteros, I., 2000. Upper Neoproterozoic-Lower Cambrian sedimentary successions in the Central Iberian Zone (Spain): sequence stratigraphy petrology and chemostratigraphy. Implications for other European zones. Int. J. Earth Sci. 89, 2-20.

Valle Aguado, B., Arenas, R., Martínez Catalán, J.R., 1993. Evolución metamórfica hercínica en la region de la Serra de Arada (Norte de Portugal). Comun. Inst. Geol. Min. Port. 79, 41- 61.

Valle Aguado, B., Martínez Catalán, J.R., Azevedo, M.R., 2000. Structure of the western termination of the Juzbado–Penalva do Castelo Shear Zone (Western Iberian Massif). Variscan–Appalachian dynamics: the building of the Upper Paleozoic basement, A Corunã, Spain, Program and Abstracts. Basement Tectonics 15, 287-291.

Valle Aguado, B., Azevedo, M.R., Schaltegger, U. Martines Catalan, J.R. Nolan, J., 2005. U–Pb zircon and monazite geochronology of Variscan magmatism related to syn-convergence extension in Central Northern Portugal. Lithos 82 (1-2), 169-184.

Valle Aguado, B., Azevedo, M., Santos, J.S., Nolan, J., 2010. O Complexo Migmatítico de Mundão (Viseu, norte de Portugal). Revista electrónica de Ciencias da Terra –

Sociedade Geológica de Portugal. VIII Congresso Nacional de Geologia. 16, 9, ISSN 1645-0388.

Van den Kerhkof, A., Hein, U.F., 2001. Fluid Inclusion Petrography. Lithos 55, 27-47.

Van den Kerkhof, A., Kronz, A., Simon, K., 2014. Deciphering fluid inclusions in high-grade rocks. Geoscience Frontiers, special issue: The role of fluids in the lower crust and upper mantle: A tribute to Jacques Touret, 5 (5), 683‑695.

Vanderhaeghe, O., 2001. Melt segregation, pervasive melt migration and magma mobility in the continental crust: the structural record from pores to orogens. Physics and Chemistry of Earth (A) 26, 213-223.

Vavra, G., 1994. Systematics of internal zircon morphology in major Variscan granitoid types. Contributions to Mineralogy and Petrology 117, 331 – 344.

Vavra, G., Gebauer, D., Schmid, R., Compston, W., 1996. Multiple zircon growth and recrystallisation during polyphase Late Carboniferous to Triassic metamorphism in granulites of the Ivrea Zone (Southern Alps): an ion microprobe (SHRIMP) study. Contrib. Mineral. Petrology 122, 337-358.

Vavra, G., Schmid, R., Gebauer, D., 1999. Internal morphology, habit and U-Th-Pb microanalysis of amphibolite-to-granulite facies zircons: geochronology of the Ivrea zone (Southern Alps). Contribution Mineralogy and Petrology 134, 380-404.

Veksler, I.V., Dorfman, A.M., Kamenetsky, M., Dulski, P., Dingwell, D.B., 2005. Partitioning of lanthanides and Y between immiscible silicate and fluoride melts, fluorite and cryolite and the origin of the tetrad effect in igneous rocks. Geochimica et Cosmochimica Acta 69 (11) 2847-2860.

Vernon, R.H., 2004. A practical guide to rock microstructure. Cambridge University Press, 594 p.

Vidal, Ph., Cocherie, A., Le Fort, P., 1982. Geochemical investigations of the origin of the Manaslu leucogranite (Himalaya, Nepal). Geochim. Cosmochim. Acta 46, 2279-2292.

Vidal, G., Palacios, T., Gámez-Vintaned, J.A., Dıéz Balda, M.A., Grant, S.W., 1994. Neoproterozoic – early Cambrian geology and paleontology of Iberia. Geol. Mag. 131, 729-765.

Villaseca, C., Barbero, L., Herreros, V., 1998. A re-examination of the typology of peraluminous granite types in intracontinental orogenic belts. Transactions of the Royal Society of Edinburgh, Earth Sciences 89, 113-119.

Villaseca, C., Downes, H., Pin, C., Barbero, L., 1999. Nature and Composition of the Lower Continental Crust in Central Spain and the Granulite-Granite Linkage: Inferences from Granulitic Xenoliths. Journal Petrolology 40, 1463-1496.

Villaseca, C., Merino, E., Oyarzun, R., Orejana, D., Pérez-Soba, C., Chicharro E., 2014. Contrasting chemical and isotopic signatures from Neoproterozoic metasedimentary rocks in the Central Iberian Zone (Spain) of pre-Variscan Europe: Implications for terrane analysis and Early Ordovician magmatic belts. Precambrian Research 245, 131-145.

Walther, J.V., Wood, B.J., 1986. Fluid-rock interactions during metamorphism. Advances in physical chemistry 5, Springer-New York, 211 p.

Watson, E.B., Vicenzi, E.P., Rapp, R.P., 1989. Inclusion/host relations involving accessory minerals in high-grade metamorphic and anatectic rocks. Contributions to Mineralogy and Petrology 101, 220-231.

Watson, E.B., Liang, Y., 1995. A simple model for sector zoning in slowly grown crystals: implications for growth rate and lattice diffusion, with emphasis on accessory minerals in crustal rocks. Am. Mineral. 80, 1179-1187.

Watson, E.B., 1996. Dissolution, growth and survival of zircons during crustal fusion: Kinetic principles, geological models and implications for isotopic inheritance. Transactions of the Royal Society of Edinburgh Earth Sciences 87, 43-56.

Watt, G.R., Burns, I.M., Graham, G.A., 1996. Chemical characteristics of migmatites: Accessory phase distribution and evidence for fast melt segregation rates. Contribution to Mineralogy and Petrology 125, 100-111.

Weinberg, R.F., Mark, G., 2008. Magma migration, folding, and disaggregation of migmatites in the Karakoram shear zone, Ladakh, NW India, Geological Society of America Bulletin, 120, 994-1009.

Wetherill, G.W., 1956. Discordant uranium-lead ages. Trans. Am. Geophysic Union 37, 320-326.

Whalen, J.B., Currie, K.L., Chappell, B.E., 1987. A-type granites: geochemical characteristics, discrimination and petrogenesis. Contributions to Mineralogy and Petrology 95, 407-419.

White, R.W., 2008. Insights into Crustal Melting and the Formation of Migmatites Gained from the Petrological Modeling of Migmatites. In: Sawyer, E.W. (Eds.), Working with migmatites. Mineralogical Association of Canada Short Course Series, 38, Quebec City, 77-96.

Whitney, D.L., Teyssier, C., Vanderhaeghe, O., 2004. Gneiss domes and crustal flow. In: Whitney, D.L., Teyssier, C., Siddoway, C.S. (Eds.), Gneiss domes in orogeny: Geological Society of America Special Paper, 380, 15-33.

Wickham, S.M., Taylor, H.P., 1987. Stable isotope constraints on the origin and depth of penetration of hydrothermal fluids associated with Hercynian regional metamorphism and crustal anatexis in the Pyrenees. Contributions to Mineralogy and Petrology 95 (3), 255-268.

Widmer, T., Thompson, A.B., 2001. Local origin of high-pressure vein material in eclogite facies rocks of the Zermatt- Saas zone, Switzerland. American Journal of Science 301, 627-656.

Wilkin, R.T., 2003. Sulfide minerals in sediments in Sedimentology Encyclopedia of Earth Science, Springer Berlin Heidelberg, 1161.

Williams, I.S., 1998. U-Th-Pb Geochronology by Ion Microprobe. In: McKibben, M.A., Shanks III, W.C., Ridley, W.I. (Eds.), Applications of microanalytical techniques to understanding mineralizing processes. Reviews in Economic Geology 7, 1-35.

Williams, I.S., Hergt, J.M., 2000. U-Pb dating of Tasmanian dolerites: a cautionary tale of SHRIMP analysis of high-U zircon. In: Woodhead, J.D., Hergt, J.M., Noble, W.P. (Eds.), Beyond 2000: New Frontiers in Isotope Geoscience, Lorne, 2000, Abstracts and Proceedings, 185-188.

Winter, J.D., 2001. An Introduction to Igneous and Metamorphic Petrology. Prentice Hall. 796 p.

Wolf, M.B., London, D., 1994. Apatite dissolution into peraluminous haplogranitic melts: an experimental study of solubilities and mechanisms. Geochimica et Cosmochimica Acta 58, 4127-4146.

Yurimoto, H., Duke, E.F., Opapike, J.J., Shearer, C.K., 1990. Are discontinuous chondrite-normalized REE patterns in pegmatic granite systems the results of monazite fractionation? Geochim. Cosmochimica Acta 54, 2141-2145.

Zeck, H.P., Wingate, M.T.D, Poo!ey, G.D., Ugidos, J.M., 2004. A sequence of Pan-African events recorded in zircons from an orthogneiss from the Belt of western Central Iberia- an ion microprobe U-Pb study. J. Petrol. 45, 1613-1629.

Zeng, L., Asimow, P.D., Saleeby, J.B., 2005. Coupling of anatectic reactions and dissolution of accessory phases and the Sr and Nd isotope systematics of anatectic melts from a metasedimentary source. Geochimica et Cosmochimica Acta 69 (14), 3671-3682.

Zeng, L., Asimow, P.D., Saleeby, J.B., 2005a. Coupling of anatectic reactions and dissolution of accessory phases and the Sr and Nd isotope systematics of ana tactic melts from a metasedimentary source. Geochimica et Cosmochimica Acta 69, 3671-3682.

Zeng, L., Saleeby, J.B., Ducea, M., 2005b. Geochemical characteristics of crustal anatexis during the formation of migmatite at the Southern Sierra Nevada, California. Contrib. Mineralogy and Petrology 150, 386–402.

Zhao, Y., Song, B., Wang, Y., Ren, L., Li, J., Chen, T., 1992. Geochronology of the late granite in the Larsemann Hills, East Antarctica. In: Yoshida, Y., Kaminuma, K., Shiraishi, K. (Eds.), Recent Progress in Antarctic Earth Science, Terra Scientific Publishing, 155-161.

Annex A – Coordinates

Table A1 – Coordinates of the points mentioned in the figures captions (WGS84).

Point n^{er}	Longitude	Latitude
434	-8.736232	41.29495
435	-8.736185	41.29487
436	-8.736149	41.29483
437	-8.735912	41.29442
438	-8.7359	41.29436
439	-8.735936	41.29434
440	-8.735781	41.29416
441	-8.735579	41.29394
442	-8.735568	41.29373
443	-8.735438	41.29354
444	-8.735188	41.29315
445	-8.730746	41.28126
446	-8.730866	41.28124
447	-8.730414	41.28073
448	-8.730522	41.28065
449	-8.729745	41.28081
450	-8.730936	41.28172
451	-8.736232	41.29494
452	-8.736197	41.29486
453	-8.7352	41.29319
454	-8.521666	41.09665
456	-8.521799	41.09627
457	-8.52096	41.09544
458	-8.514568	41.09672
459	-8.514327	41.09719
460	-8.512616	41.10302
461	-8.519425	41.08718
462	-8.735082	41.29285
463	-8.735272	41.29319
464	-8.722641	41.31732
465	-8.74188	41.31043
466	-8.741508	41.30493
467	-8.741821	41.31023
468	-8.741773	41.31019
469	-8.743328	41.30976
470	-8.741809	41.31016
472	-8.741738	41.31009
473	-8.741106	41.30986
474	-8.740868	41.30966
475	-8.740785	41.30953
476	-8.740452	41.30891
477	-8.740393	41.30882
478	-8.740692	41.30869
479	-8.740669	41.3085
480	-8.740681	41.30856
481	-8.740644	41.30876

Point n^{er}	Longitude	Latitude
482	-8.740601	41.31063
484	-8.740506	41.31061
485	-8.740589	41.31061
486	-8.740709	41.31059
487	-8.740721	41.31055
488	-8.740864	41.31053
489	-8.741832	41.31055
490	-8.741007	41.31076
492	-8.738187	41.30195
493	-8.738164	41.30175
494	-8.737937	41.30175
495	-8.737723	41.29849
496	-8.737234	41.2982
497	-8.737198	41.29824
498	-8.737068	41.298
499	-8.737128	41.29787
502	-8.737152	41.29785
503	-8.737391	41.29792
504	-8.73732	41.2977
505	-8.737428	41.29743
506	-8.737991	41.29713
507	-8.73719	41.29739
508	-8.73731	41.29728
509	-8.737202	41.29719
510	-8.736988	41.29697
511	-8.736917	41.29695
512	-8.736809	41.29691
513	-8.736858	41.29674
514	-8.736834	41.29667
515	-8.736752	41.29631
517	-8.736896	41.2962
518	-8.736944	41.296
519	-8.736932	41.29605
520	-8.736981	41.29591
521	-8.736933	41.29588
522	-8.737064	41.29595
523	-8.736707	41.29563
524	-8.736398	41.29527
525	-8.73628	41.29501
526	-8.736137	41.29484
528	-8.736221	41.29476
529	-8.736138	41.29457
530	-8.736043	41.29455
531	-8.735972	41.29433
532	-8.73602	41.2943
533	-8.735639	41.29393

Point n^{er}	Longitude	Latitude
534	-8.735604	41.29378
535	-8.735557	41.29347
536	-8.735486	41.29344
537	-8.735022	41.29286
538	-8.734999	41.29278
539	-8.731306	41.28178
540	-8.730818	41.2813
541	-8.73045	41.28075
542	-8.730344	41.28032
543	-8.729104	41.27984
544	-8.731838	41.28301
545	-8.733416	41.29122
546	-8.733691	41.29139
547	-8.733527	41.29048
548	-8.56108	40.98919
549	-8.537425	41.21444
550	-8.537689	41.21433
551	-8.48257	41.16986
552	-8.483597	41.15592
553	-8.482828	41.15067
554	-8.490975	41.10803
555	-8.517626	41.13933
556	-8.544651	41.40373
557	-8.546351	41.39674
558	-8.548898	41.39856
559	-8.548783	41.40137
560	-8.548027	41.39652
561	-8.54715	41.39878
562	-8.546951	41.39309
563	-8.556667	41.39073
564	-8.563917	41.38873
565	-8.572474	41.38617
566	-8.572243	41.38129
567	-8.578844	41.37772
568	-8.582947	41.37935
569	-8.580142	41.3767
570	-8.62361	41.36227
571	-8.623502	41.3624
572	-8.675541	41.36339
573	-8.684518	41.36629
574	-8.718378	41.36949
575	-8.754243	41.34916
576	-8.756111	41.35778
577	-8.756659	41.35828
578	-8.756801	41.35856
579	-8.754372	41.34323

Point n^{er}	Longitude	Latitude
580	-8.754705	41.34372
581	-8.752706	41.34137
582	-8.739423	41.33033
583	-8.728801	41.27526
584	-8.728729	41.27527
585	-8.729018	41.27775
586	-8.729191	41.27925
587	-8.730013	41.27964
588	-8.729119	41.27621
589	-8.70234	41.28622
590	-8.732168	41.28706
591	-8.723625	41.27672
592	-8.728973	41.277
593	-8.728669	41.27256
594	-8.728776	41.27265
595	-8.729014	41.27282
596	-8.728953	41.27322
597	-8.72861	41.27246
598	-8.728492	41.27195
599	-8.728292	41.2713
600	-8.728104	41.27066
601	-8.721416	41.27117
602	-8.720928	41.27072
603	-8.728002	41.26647
604	-8.72816	41.26582
605	-8.728461	41.26501
606	-8.728844	41.27642
607	-8.728929	41.27598
608	-8.728787	41.27565
609	-8.728978	41.27566
610	-8.728979	41.2756
611	-8.729182	41.27554
612	-8.729003	41.27554
613	-8.729388	41.27478
614	-8.728958	41.27472
615	-8.728909	41.27793
616	-8.728831	41.27947
617	-8.72895	41.27956
618	-8.728963	41.27936
619	-8.729749	41.27994
620	-8.730346	41.27981
621	-8.730059	41.27996
622	-8.725221	41.26063
623	-8.725648	41.26122
624	-8.726361	41.26187
625	-8.726491	41.26238

Point n^{er}	Longitude	Latitude
626	-8.591559	41.3102
627	-8.59474	41.31353
628	-8.597011	41.31733
629	-8.597403	41.32157
630	-8.596668	41.32446
631	-8.596578	41.32737
632	-8.617906	41.33594
633	-8.619025	41.33459
634	-8.618914	41.33313
635	-8.62945	41.32337
636	-8.631275	41.3218
637	-8.636307	41.31937
638	-8.631631	41.31384
639	-8.630568	41.31375
640	-8.626326	41.31182
641	-8.626814	41.31
642	-8.611195	41.30483
643	-8.605013	41.29202
644	-8.606317	41.29359
645	-8.610281	41.30194
646	-8.598464	41.31415
647	-8.59844	41.31421
648	-8.602034	41.30853
649	-8.602047	41.30848
650	-8.602661	41.31559
651	-8.629082	41.33784
652	-8.668449	41.33318
653	-8.72676	41.34385
654	-8.727572	41.33831
655	-8.725085	41.23595
656	-8.728602	41.24265
657	-8.726594	41.24058
658	-8.725894	41.23943
659	-8.725876	41.24955
660	-8.721478	41.22827
661	-8.720493	41.22716
662	-8.719815	41.22671
663	-8.716382	41.22321
664	-8.715686	41.22136
665	-8.714956	41.20258
666	-8.564421	41.40816
667	-8.56065	41.41028
668	-8.588195	41.39861
669	-8.623466	41.36248
670	-8.678133	41.38087
671	-8.733594	41.29169

Point n^{er}	Longitude	Latitude
672	-8.732228	41.2869
673	-8.727984	41.27083
674	-8.737793	41.30174
675	-8.700183	41.37375
676	-8.683564	41.36593
677	-8.682281	41.35434
678	-8.656921	41.37116
679	-8.687615	41.38895
680	-8.73702	41.29806
681	-8.73224	41.28693
682	-8.665236	41.40061
685	-8.737949	41.30174
686	-8.73702	41.298
687	-8.734248	41.29227
688	-8.66806	41.40977
689	-8.667944	41.40904
690	-8.668096	41.40981
691	-8.6743	41.41326
692	-8.674644	41.41385
693	-8.674524	41.41399
694	-8.67444	41.41654
695	-8.678275	41.41757
696	-8.732124	41.33278
697	-8.670985	41.30429
698	-8.668802	41.30356
699	-8.673215	41.2979
700	-8.677257	41.29684
701	-8.680866	41.29644
702	-8.687971	41.29438
703	-8.686599	41.29157
704	-8.643835	41.23797
705	-8.733535	41.29154
706	-8.732807	41.29129
707	-8.735377	41.29367
708	-8.736504	41.29556
709	-8.736774	41.29691
710	-8.737152	41.29782
711	-8.735163	41.29355
712	-8.629597	41.33749
713	-8.616875	41.33449
714	-8.587894	41.41983
715	-8.588516	41.41977
716	-8.587517	41.41689
717	-8.586948	41.41609
718	-8.586479	41.41838
719	-8.589901	41.42023

Point n^{er}	Longitude	Latitude
720	-8.596146	41.41862
721	-8.629912	41.42118
722	-8.629936	41.42119
723	-8.637846	41.4169
724	-8.664525	41.42019
725	-8.698653	41.428
726	-8.709375	41.43109
727	-8.709265	41.43165
728	-8.709324	41.43177
729	-8.713123	41.44965
730	-8.712119	41.44918
731	-8.697043	41.48859
732	-8.699263	41.48525
733	-8.701241	41.47958
734	-8.706586	41.47623
735	-8.72627	41.42931
736	-8.779153	41.39547
737	-8.674453	41.4163
738	-8.676871	41.42091
739	-8.705043	41.44158
740	-8.788288	41.41503
741	-8.787374	41.41281
742	-8.783604	41.40943
743	-8.783071	41.40777
744	-8.781604	41.40637
745	-8.781544	41.40631
746	-8.785345	41.41105
747	-8.785671	41.42114
748	-7.421852	41.21836
749	-7.421845	41.21835
750	-7.423213	41.22656
751	-7.42321	41.22656
752	-7.430873	41.21235
753	-7.430853	41.21238
754	-7.430883	41.21229
755	-8.521613	41.09649
756	-8.741757	41.31009
757	-8.74053	41.31061
758	-8.739525	41.31513
759	-8.737085	41.29784
760	-8.737088	41.29785
761	-8.736913	41.29621
762	-8.736113	41.29483
763	-8.73678	41.3019
764	-8.736787	41.30189
765	-8.545343	41.37321

Point n^{er}	Longitude	Latitude
766	-8.545823	41.37289
767	-8.545403	41.37313
768	-8.547544	41.3713
769	-8.548315	41.36705
770	-8.738199	41.3019
771	-8.737925	41.30174
772	-8.737887	41.29911
773	-8.737352	41.29852
774	-8.737139	41.29821
775	-8.736953	41.29682
776	-8.736695	41.29867
777	-8.728836	41.27269
778	-8.726862	41.2707
779	-8.526011	41.173519

Annex B – Mineral chemistry formulas

Table B. 1 - Chemical analysis (wt.%) and structural formulas of pyroxenes* from MMC calc-silicate nodules.

Sample n^{er}	GD2	GD2	GD2	VC48	VC48	VC48	VC48	VC48	VC48	VC48	VC48
Analyse n^{er}	3.00	2.00	1.00	1.00	2.00	3.00	4.00	5.00	6.00	7.00	8.00
SiO2	49.58	50.16	50.48	50.43	52.16	51.85	51.55	51.84	52.10	50.54	51.67
TiO2	0.02	0.00	0.05	0.15	0.12	0.24	0.28	0.40	0.06	0.13	0.12
Al2O3	0.53	0.22	0.29	1.00	1.51	0.74	0.71	1.01	1.41	1.03	1.67
Cr2O3	0.00	0.00	0.00	0.00	0.07	0.12	0.12	0.00	0.00	0.00	0.00
FeO	15.58	14.49	10.03	13.84	14.05	15.97	16.32	13.85	10.71	14.95	9.91
MnO	0.93	0.57	0.86	1.08	1.45	1.47	1.53	1.49	1.26	1.76	0.83
MgO	8.11	9.65	11.89	9.34	9.54	8.57	8.96	10.46	10.61	8.59	11.71
CaO	24.05	24.81	24.90	23.34	20.89	20.65	20.09	20.59	23.96	23.59	23.79
Na2O	0.03	0.02	0.08	0.11	0.10	0.28	0.24	0.23	0.09	0.07	0.17
K2O	0.00	0.00	0.00	0.00	0.11	0.11	0.18	0.14	0.00	0.00	0.00
Total	98.83	99.92	98.57	99.29	100.00	100.00	99.98	100.01	100.20	100.66	99.87
Si	1.95	1.93	1.93	1.95	2.01	2.01	2.00	1.99	1.98	1.94	1.95
Ti	0.00	0.00	0.00	0.00	0.00	0.01	0.01	0.01	0.00	0.00	0.00
Al	0.02	0.01	0.01	0.05	0.07	0.03	0.03	0.05	0.06	0.05	0.07
Cr	0.00	0.00	0.00	0.00	0.00	0.00	0.00	0.00	0.00	0.00	0.00
Fe3+	0.09	0.13	0.13	0.05	-0.08	-0.05	-0.02	-0.02	-0.01	0.07	0.03
Fe2+	0.42	0.33	0.19	0.40	0.53	0.56	0.55	0.46	0.35	0.41	0.28
Mn	0.03	0.02	0.03	0.04	0.05	0.05	0.05	0.05	0.04	0.06	0.03
Mg	0.47	0.55	0.68	0.54	0.55	0.50	0.52	0.60	0.60	0.49	0.66
Ca	1.01	1.02	1.02	0.97	0.86	0.86	0.83	0.84	0.97	0.97	0.96
Na	0.00	0.00	0.01	0.01	0.01	0.02	0.02	0.02	0.01	0.01	0.01
K	0.00	0.00	0.00	0.00	0.01	0.01	0.01	0.01	0.00	0.00	0.00
Total	4.00	4.00	4.00	4.00	4.00	4.00	4.00	4.00	4.00	4.00	4.00
Mg/(Mg+Fe^2)	0.53	0.63	0.78	0.58	0.51	0.47	0.48	0.57	0.63	0.54	0.70

Sample n^{er}	FM1	FM1	FM1	FM1	VC28e	VC28e	FM21
Analyse n^{er}	1.00	2.00	3.00	4.00	1.00	2.00	1.00
SiO2	52.80	52.12	51.67	51.69	50.16	52.03	52.55
TiO2	0.02	0.00	0.00	0.00	0.38	0.34	0.34
Al2O3	0.58	0.61	0.62	0.53	0.69	0.70	0.89
Cr2O3	0.00	0.00	0.00	0.00	0.09	0.24	0.00
FeO	10.90	11.51	11.72	11.10	19.50	16.63	12.52
MnO	1.49	1.83	1.41	1.11	1.51	1.24	1.52
MgO	10.49	10.10	10.07	10.64	5.83	6.98	11.55
CaO	24.42	24.22	23.96	24.44	21.45	21.56	20.20
Na2O	0.05	0.06	0.10	0.10	0.16	0.20	0.33
K2O	0.00	0.00	0.00	0.00	0.24	0.09	0.10
Total	100.75	100.45	99.55	99.60	100.01	100.01	100.00
Si	2.00	1.98	1.98	1.97	1.98	2.04	2.00
Ti	0.00	0.00	0.00	0.00	0.01	0.01	0.01
Al	0.03	0.03	0.03	0.02	0.03	0.03	0.04
Cr	0.00	0.00	0.00	0.00	0.00	0.01	0.00
Fe3+	-0.02	0.01	0.02	0.04	0.00	-0.11	-0.02
Fe2+	0.36	0.35	0.36	0.32	0.64	0.65	0.42
Mn	0.05	0.06	0.05	0.04	0.05	0.04	0.05
Mg	0.59	0.57	0.58	0.61	0.34	0.41	0.65
Ca	0.99	0.99	0.98	1.00	0.91	0.90	0.82
Na	0.00	0.00	0.01	0.01	0.01	0.02	0.02
K	0.00	0.00	0.00	0.00	0.01	0.00	0.00
Total	4.00	4.00	4.00	4.00	4.00	4.00	4.00
Mg/(Mg+Fe^2)	0.62	0.62	0.62	0.66	0.35	0.38	0.61

OBS: *based on 6 oxygen atoms and the formula $M_2M_1T_2O_6$.

Table B. 2 - Chemical analysis (wt.%) and structural formulas* of amphiboles from MMC calc-silicate nodules.

Sample n^{er}	FM25	VC48	VC48	VC48	VC48	VC48	GC2	GC2	GC2	FM21	VC28e	VC28e	FM1	FM1
Analyse n^{er}	1	1	2	3	4	5	1	2	3	1	1	2	1	2
SiO2	48.21	51.86	50.08	50.55	51.67	50.94	52.33	50.88	51.10	51.26	51.51	52.17	47.52	49.97
TiO2	0.43	0.38	0.61	0.59	0.43	0.71	0.07	0.44	0.44	0.29	0.52	0.27	1.23	0.40
Al2O3	9.09	2.39	5.36	6.03	5.08	5.08	1.96	4.61	5.29	3.53	2.13	2.30	8.60	6.42
Cr2O3	0.00	0.00	0.00	0.00	0.00	0.00	0.00	0.00	0.00	0.00	0.00	0.00	0.00	0.00
Fe2O3	7.26	6.64	5.77	7.19	5.89	11.02	5.96	3.97	9.97	8.52	5.02	5.45	7.19	11.51
FeO	9.73	8.95	9.84	9.29	9.83	5.33	9.14	7.64	2.18	8.94	19.12	17.34	5.43	5.11
MnO	0.36	1.17	1.16	1.13	0.95	1.06	0.63	0.53	0.73	1.03	0.87	1.14	1.14	0.80
MgO	10.98	14.11	12.69	12.78	13.18	13.74	15.05	15.75	16.68	13.34	8.03	9.31	13.61	13.43
NiO	0.00	0.00	0.00	0.00	0.00	0.00	0.00	0.00	0.00	0.00	0.00	0.00	0.00	0.00
ZnO	0.15	0.00	0.00	0.00	0.00	0.00	0.00	0.00	0.00	0.00	0.00	0.00	0.00	0.00
CaO	10.86	11.50	11.41	11.57	11.67	10.25	12.28	12.46	11.45	11.33	10.84	11.19	10.88	10.30
Na2O	0.61	0.29	0.54	0.52	0.34	0.70	0.14	0.38	0.49	0.43	0.00	0.30	0.90	0.71
K2O	0.16	0.26	0.16	0.11	0.05	0.28	0.00	0.10	0.10	0.20	0.28	0.07	0.50	0.40
BaO	0.00	0.00	0.00	0.00	0.00	0.00	0.00	0.00	0.07	0.00	0.00	0.00	0.00	0.00
SrO	0.00	0.00	0.00	0.00	0.00	0.00	0.00	0.00	0.00	0.00	0.00	0.00	0.00	0.00
PbO	0.00	0.00	0.00	0.00	0.00	0.00	0.00	0.00	0.00	0.00	0.00	0.00	0.00	0.00
F	0.00	0.00	0.00	0.00	0.00	0.00	0.03	0.07	0.17	0.00	0.00	0.00	0.00	0.00
Cl	0.03	0.00	0.00	0.00	0.00	0.00	0.00	0.00	0.00	0.00	0.00	0.00	0.00	0.00
H2O*	2.06	2.06	2.06	2.11	2.10	2.11	2.06	2.04	2.05	2.08	2.00	2.04	2.07	2.11
O=F,Cl	0.01	0.00	0.00	0.00	0.00	0.00	0.01	0.03	0.07	0.00	0.00	0.00	0.00	0.00
Total	99.9	99.6	99.7	101.9	101.2	101.2	99.6	98.8	100.7	100.9	100.3	101.6	99.1	101.2
Si	6.99	7.54	7.29	7.20	7.37	7.23	7.58	7.35	7.18	7.38	7.71	7.66	6.88	7.10
Al iv	1.01	0.41	0.71	0.80	0.63	0.77	0.33	0.65	0.82	0.60	0.29	0.34	1.12	0.90
Al vi	0.55	0.00	0.21	0.21	0.23	0.08	0.00	0.14	0.06	0.00	0.08	0.06	0.35	0.18
Ti	0.05	0.04	0.07	0.06	0.05	0.08	0.01	0.05	0.05	0.03	0.06	0.03	0.13	0.04
Cr	0.00	0.00	0.00	0.00	0.00	0.00	0.00	0.00	0.00	0.00	0.00	0.00	0.00	0.00
Fe3+	0.79	0.73	0.63	0.77	0.63	1.18	0.65	0.43	1.06	0.92	0.57	0.60	0.78	1.23
Fe2+	1.18	1.09	1.20	1.11	1.17	0.63	1.11	0.92	0.26	1.08	2.39	2.13	0.66	0.61
Mn	0.04	0.14	0.14	0.14	0.11	0.13	0.08	0.07	0.09	0.13	0.11	0.14	0.14	0.10
Mg	2.37	3.06	2.75	2.71	2.80	2.91	3.25	3.39	3.50	2.86	1.79	2.04	2.94	2.85
Ni	0.00	0.00	0.00	0.00	0.00	0.00	0.00	0.00	0.00	0.00	0.00	0.00	0.00	0.00
Zn	0.02	0.00	0.00	0.00	0.00	0.00	0.00	0.00	0.00	0.00	0.00	0.00	0.00	0.00
Ca	1.69	1.79	1.78	1.77	1.78	1.56	1.90	1.93	1.72	1.75	1.74	1.76	1.69	1.57
Na	0.17	0.08	0.15	0.14	0.09	0.19	0.04	0.11	0.13	0.12	0.00	0.09	0.25	0.20
K	0.03	0.05	0.03	0.02	0.01	0.05	0.00	0.02	0.02	0.04	0.05	0.01	0.09	0.07
Ba	0.00	0.00	0.00	0.00	0.00	0.00	0.00	0.00	0.00	0.00	0.00	0.00	0.00	0.00
Sr	0.00	0.00	0.00	0.00	0.00	0.00	0.00	0.00	0.00	0.00	0.00	0.00	0.00	0.00
Pb	0.00	0.00	0.00	0.00	0.00	0.00	0.00	0.00	0.00	0.00	0.00	0.00	0.00	0.00
F	0.00	0.00	0.00	0.00	0.00	0.00	0.01	0.03	0.08	0.00	0.00	0.00	0.00	0.00
Cl	0.01	0.00	0.00	0.00	0.00	0.00	0.00	0.00	0.00	0.00	0.00	0.00	0.00	0.00
OH*	1.99	2.00	2.00	2.00	2.00	2.00	1.99	1.97	1.92	2.00	2.00	2.00	2.00	2.00
Total	16.89	16.92	16.96	16.93	16.89	16.80	16.94	17.05	16.88	16.90	16.79	16.86	17.03	16.84

OBS: *based on 23 O and the formula $A_{0\text{-}1}B_2C_5T_8O_{22}(OH,F)_2$.

Table B. 3 - Chemical analysis (wt.%) and structural formulas* of epidote group minerals from MMC calc-silicate nodules

Sample n^{er}	FM1	FM1	FM1	FM1	GC2	GC2	GC2	VC28e	VC28e
Analyse n^{er}	1	2	3	4	1	2	3	1	2
K2O	0.02	0.00	0.00	0.00	0.00	0.00	0.00	0.26	0.07
Na2O	0.00	0.12	0.00	0.03	0.00	0.09	0.00	0.10	0.12
FeO	5.03	0.84	2.77	2.25	5.40	1.43	4.16	0.41	0.56
SiO2	40.04	41.18	39.86	40.08	38.63	38.83	41.74	41.24	40.56
P2O5	0.02	0.07	0.06	0.07	0.01	0.00	0.03	0.00	0.00
CaO	23.46	24.01	23.75	23.22	23.18	24.59	23.09	21.97	22.37
MgO	0.01	0.04	0.00	0.00	0.02	0.02	1.51	0.26	0.32
MnO	0.53	0.36	0.23	1.18	0.84	0.11	0.07	0.37	0.34
Al2O3	29.99	33.80	31.70	31.53	31.18	34.05	24.88	34.77	35.18
TiO2	0.03	0.00	0.05	0.00	0.02	0.00	0.00	0.33	0.20
SrO	0.14	0.02	0.14	0.09	0.09	0.07	0.00	0.14	0.09
Total	99.14	100.42	98.43	98.36	99.27	99.12	95.48	99.71	99.72
K	0.00	0.00	0.00	0.00	0.00	0.00	0.00	0.02	0.01
Na	0.00	0.02	0.00	0.00	0.00	0.01	0.00	0.01	0.02
Fe	0.32	0.05	0.18	0.14	0.35	0.09	0.28	0.03	0.03
Si	3.07	3.05	3.04	3.06	2.97	2.93	3.30	3.04	3.00
Ca	1.93	1.90	1.94	1.90	1.91	1.99	1.96	1.74	1.77
Mg	0.00	0.00	0.00	0.00	0.00	0.00	0.18	0.03	0.04
Mn	0.03	0.02	0.01	0.08	0.05	0.01	0.00	0.02	0.02
Al	2.71	2.95	2.85	2.84	2.83	3.03	2.32	3.02	3.07
Ti	0.00	0.00	0.00	0.00	0.00	0.00	0.00	0.02	0.01
Sr	0.01	0.00	0.01	0.00	0.00	0.00	0.00	0.01	0.00

OBS: *based on 12,5 oxygen atoms and the formula X2Y3Z3(O,OH,F)13.

Table B. 4 – Chemical analysis (wt.%) and structural formulas* of garnets from staurolite schists and MMC metatexites.

Type	St.Sch	St.Sch	St.Sch	St.Sch	St.Sch	St.Sch	St.Sch	PMM
Sample no	FM14	FM14	FM14	VC65	VC65	VC65	VC65	VC28b
Analyze no	1-b	2- c	3 -b	1	2	3	4	1
SiO2	38.06	38.08	38.38	37.43	37.26	37.87	37.65	36.87
TiO2	0.00	0.00	0.01	0.00	0.00	0.04	0.02	0.30
Al2O3	21.26	21.20	21.03	21.03	20.91	20.99	21.05	21.12
FeO	33.56	33.92	34.37	32.40	31.94	31.81	34.82	32.69
MnO	2.12	1.51	1.70	4.15	4.89	4.61	1.91	3.32
MgO	3.19	3.32	3.32	2.48	2.36	2.41	3.27	3.97
CaO	2.35	2.47	2.54	2.32	2.31	2.41	1.08	1.20
F	0.09	0.12	0.15	0.09	0.11	0.16	0.20	0.65
Cr2O3	0.00	0.00	0.03	0.09	0.11	0.08	0.08	0.08
Total	100.63	100.64	101.53	99.99	99.87	100.39	100.08	100.20
Si	3.02	3.02	3.03	3.01	3.01	3.03	3.02	2.97
Al iv	0.00	0.00	0.00	0.00	0.00	0.00	0.00	0.03
Al vi	1.99	1.99	1.96	2.00	1.99	1.98	1.99	1.97
Ti	0.00	0.00	0.00	0.00	0.00	0.00	0.00	0.02
Cr	0.00	0.00	0.00	0.01	0.01	0.01	0.01	0.01
Fe3+	0.00	0.00	0.01	0.00	0.00	0.00	0.00	0.00
Fe2+	2.25	2.27	2.27	2.20	2.17	2.15	2.36	2.20
Mn	0.14	0.10	0.11	0.28	0.33	0.31	0.13	0.23
Mg	0.38	0.39	0.39	0.30	0.28	0.29	0.39	0.48
Ni	0.00	0.00	0.00	0.00	0.00	0.00	0.00	0.00
Zn	0.00	0.00	0.00	0.00	0.00	0.00	0.00	0.00
Ca	0.20	0.21	0.22	0.20	0.20	0.21	0.09	0.10
Almandine	76	76	76	74	73	73	79	73
Andradite	0	0	0	0	0	0	0	0
Grossular	7	7	7	6	6	7	3	3
Pyrope	13	13	13	10	10	10	13	16
Spessartine	5	3	4	9	11	11	4	8

Type	PMM	PMM	PMM	PMM	PMM	PMM	PMM	BMM
Sample n^{er}	VC28a	VC28a	VC28a	VC28a	VC28a	VC28a	VC28a	FM3
Analyze n^{er}	1	2	3	4	5	6	7	1
SiO2	37.87	37.56	37.82	37.24	37.48	37.91	37.54	37.54
TiO2	0.00	0.02	0.02	0.00	0.00	0.00	0.00	0.12
Al2O3	21.88	21.85	21.80	21.86	21.65	21.61	21.69	20.78
FeO	32.40	32.41	32.70	32.95	32.81	32.40	32.63	29.65
MnO	3.63	3.65	3.67	3.71	3.65	3.66	3.49	6.49
MgO	3.25	3.35	3.15	3.12	3.11	3.15	3.36	2.93
CaO	1.19	1.19	1.19	1.18	1.19	1.18	1.20	0.96
F	0.55	0.85	0.95	1.15	0.95	0.74	0.55	0.95
Cr2O3	0.07	0.11	0.13	0.07	0.08	0.08	0.08	0.07
Total	100.85	100.98	101.42	101.29	100.93	100.74	100.54	99.49
Si	3.00	2.98	2.99	3.01	2.99	3.01	2.99	3.03
Al iv	0.00	0.02	0.01	0.00	0.01	0.00	0.01	0.00
Al vi	2.05	2.04	2.04	2.04	2.03	2.03	2.03	1.98
Ti	0.00	0.00	0.00	0.00	0.00	0.00	0.00	0.01
Cr	0.00	0.01	0.01	0.00	0.01	0.01	0.01	0.00
Fe3+	0.00	0.00	0.00	0.00	0.00	0.00	0.00	0.00
Fe2+	2.21	2.21	2.23	2.23	2.24	2.22	2.22	2.03
Mn	0.24	0.25	0.25	0.25	0.25	0.25	0.24	0.44
Mg	0.38	0.40	0.37	0.37	0.37	0.37	0.40	0.35
Ni	0.00	0.00	0.00	0.00	0.00	0.00	0.00	0.00
Zn	0.00	0.00	0.00	0.00	0.00	0.00	0.00	0.06
Ca	0.10	0.10	0.10	0.10	0.10	0.10	0.10	0.08
Almandine	75	75	76	76	76	75	75	70
Andradite	0	0	0	0	0	0	0	0
Grossular	3	3	3	3	3	3	3	3
Pyrope	13	13	13	12	13	13	13	12
Spessartine	8	8	8	8	8	8	8	15

OBS: Abbreviations: St.Sch – staurolite schist; PMM – patch metatexites; BMM – Banded metatexites. *Based on 24 oxygen atoms and the formula $A_3O_2T_3O_{12}$; OBS: b – border; c – core.

Table B. 5 - Chemical analysis (wt.%) and structural formulas* of garnets from MMC granitic rocks.

Type	DTX	DTX	DTX	DTX	DTX	DTX	TL.Gnt	TL.Gnt	TL.Gnt	TL.Gnt
Sample ner	VC59	VC59	VC59	VC59	VC59	VC59	VC62	VC62	VC62	VC62
Analyze ner	1a	1	2	3	4	5	1	2	3	4
SiO2	37.38	37.05	37.43	37.16	37.26	37.23	37.40	37.15	37.40	37.03
TiO2	0.00	0.01	0.00	0.00	0.00	0.00	0.01	0.00	0.02	0.02
Al2O3	20.46	20.86	21.06	21.02	20.94	20.93	20.96	20.97	20.95	20.88
FeO	33.37	30.78	33.40	32.81	33.06	30.18	32.74	33.10	33.07	32.60
MnO	4.03	8.36	4.40	4.93	5.28	9.00	4.94	5.35	5.56	6.25
MgO	2.76	2.05	3.05	2.94	2.69	2.10	3.07	2.81	2.72	2.31
CaO	0.57	0.68	0.64	0.64	0.64	0.65	0.64	0.36	0.35	0.31
F	1.91	0.58	0.66	0.95	0.75	0.83	0.58	0.72	0.95	0.66
Cr2O3	0.09	0.12	0.09	0.07	0.04	0.05	0.07	0.08	0.06	0.05
Total	100.63	100.50	100.72	100.50	100.66	100.97	100.39	100.54	101.07	100.11
Si	3.04	3.01	3.01	3.00	3.01	3.01	3.01	3.00	3.01	3.01
Al iv	0.00	0.00	0.00	0.00	0.00	0.00	0.00	0.00	0.00	0.00
Al vi	1.97	2.00	2.00	2.01	2.00	2.00	1.99	2.00	1.99	2.00
Ti	0.00	0.00	0.00	0.00	0.00	0.00	0.00	0.00	0.00	0.00
Cr	0.01	0.01	0.01	0.00	0.00	0.00	0.00	0.01	0.00	0.00
Fe3+	0.00	0.00	0.00	0.00	0.00	0.00	0.00	0.00	0.00	0.00
Fe2+	2.30	2.10	2.26	2.24	2.24	2.06	2.22	2.25	2.24	2.24
Mn	0.28	0.57	0.30	0.34	0.36	0.62	0.34	0.37	0.38	0.43
Mg	0.34	0.25	0.37	0.35	0.32	0.25	0.37	0.34	0.33	0.28
Ni	0.00	0.00	0.00	0.00	0.00	0.00	0.00	0.00	0.00	0.00
Zn	0.00	0.00	0.00	0.00	0.00	0.00	0.00	0.00	0.00	0.00
Ca	0.05	0.06	0.05	0.05	0.05	0.06	0.05	0.03	0.03	0.03
Almandine	78	70	76	75	75	69	74	75	75	75
Andradite	0	0	0	0	0	0	0	0	0	0
Grossular	1	2	2	2	2	2	2	1	1	1
Pyrope	11	8	12	12	11	8	12	11	11	9
Spessartine	9	19	10	11	12	21	11	12	13	14

Type	TL.Gnt	TL.Gnt	TL.Gnt	APG	APG	APG
Sample ner	VC62	VC62	VC62	VC58	VC58	VC58
Analyze ner	5	6	7	1	2	3
SiO2	37.01	36.98	37.62	35.33	35.67	35.23
TiO2	0.01	0.00	0.01	0.35	0.33	0.35
Al2O3	20.86	20.96	20.51	19.78	19.96	19.70
FeO	32.76	32.83	28.55	23.87	24.05	23.80
MnO	6.00	5.60	11.58	15.37	14.53	15.95
MgO	2.62	2.86	1.64	0.39	0.22	0.41
CaO	0.35	0.40	0.41	0.27	0.24	0.26
F	0.83	0.66	0.75	5.09	5.66	5.00
Cr2O3	0.07	0.08	0.09	0.12	0.09	0.07
Total	100.50	100.36	101.17	100.57	100.75	100.77
Si	3.00	3.00	3.04	3.01	3.03	3.01
Al iv	0.00	0.00	0.00	0.00	0.00	0.00
Al vi	2.00	2.00	1.96	2.00	2.01	1.99
Ti	0.00	0.00	0.00	0.02	0.02	0.02
Cr	0.00	0.00	0.01	0.01	0.01	0.00
Fe3+	0.00	0.00	0.00	0.00	0.00	0.00
Fe2+	2.23	2.23	1.94	1.75	1.80	1.73
Mn	0.41	0.38	0.79	1.11	1.05	1.15
Mg	0.32	0.35	0.20	0.05	0.03	0.05
Ni	0.00	0.00	0.00	0.00	0.00	0.00
Zn	0.00	0.00	0.00	0.00	0.00	0.00
Ca	0.03	0.04	0.04	0.02	0.02	0.02
Almandine	75	74	65	60	62	58
Andradite	0	0	0	0	0	0
Grossular	1	1	1	0	0	1
Pyrope	11	12	7	2	1	2
Spessartine	14	13	27	38	36	39

OBS: Abbreviations: DTX - diatexite; TL.Gnt – Tourmaline bearing leucogranite; APG – Aplite-pegmatite. *Based on 24 oxygen atoms and the formula $A_3O_2T_3O_{12}$;

Table B. 6 - Chemical analysis (wt.%) and structural formulas* of plagioclases from MMC metagreywackes.

Sample n^{er}	FM25	FM1	FM1	FM1	FM1	VC48	VC48	VC48	VC48	GC2	FM21	FM21	FM21
Analyse n^{er}	1	1	2	3	4	1	2	3	4	1	1a	1b	2b
Type	LG	CZ	CZ	CZ	OZ	CZ	CZ	CZ	OZ	OZ	CZ	GWK	GWK
SiO2	45.41	43.99	42.97	43.78	46.92	44.64	43.09	44.08	44.86	46.10	44.20	58.39	56.88
TiO2	0.00	0.00	0.00	0.04	0.00	0.01	0.28	0.00	0.09	0.00	0.12	0.00	0.02
Al2O3	35.69	35.63	35.80	35.87	33.23	35.80	36.89	37.22	36.59	35.13	36.88	25.91	27.05
FeO	0.30	0.04	0.22	0.02	0.08	0.16	0.62	0.29	0.29	0.00	0.37	0.04	0.11
MnO	0.11	0.01	0.00	0.09	0.04	0.04	0.33	0.18	0.27	0.04	0.28	0.00	0.04
MgO	0.17	0.00	0.00	0.00	0.00	0.01	0.24	0.06	0.22	0.01	0.26	0.00	0.00
CaO	16.84	19.84	19.49	19.38	16.68	19.39	17.36	17.51	16.40	18.05	16.70	7.47	9.01
Na2O	0.87	0.30	0.35	0.30	2.01	0.80	0.45	0.59	1.08	1.44	0.78	7.12	6.39
K2O	0.08	0.01	0.01	0.03	0.07	0.03	0.30	0.00	0.12	0.02	0.18	0.21	0.21
BaO	0.00	0.15	0.04	0.00	0.06	0.05	0.00	0.00	0.00	0.13	0.00	0.05	0.00
P2O5	0.36	0.01	0.00	0.00	0.04	0.00	0.44	0.08	0.09	0.00	0.22	0.03	0.00
TOTAL	99.8	100.0	99.0	99.6	99.1	100.9	100.0	100.0	100.0	101.1	100.0	99.3	99.7
Si	2.09	2.04	2.01	2.03	2.17	2.05	1.99	2.03	2.06	2.10	2.03	2.63	2.56
Al	1.93	1.95	1.98	1.96	1.81	1.94	2.01	2.02	1.98	1.89	2.00	1.37	1.44
Ti	0.00	0.00	0.00	0.00	0.00	0.00	0.01	0.00	0.00	0.00	0.00	0.00	0.00
Fe	0.01	0.00	0.01	0.00	0.00	0.01	0.02	0.01	0.01	0.00	0.01	0.00	0.00
Mn	0.00	0.00	0.00	0.00	0.00	0.00	0.01	0.01	0.01	0.00	0.01	0.00	0.00
Mg	0.01	0.00	0.00	0.00	0.00	0.00	0.02	0.00	0.02	0.00	0.02	0.00	0.00
Zn	0.00	0.00	0.00	0.00	0.00	0.00	0.00	0.00	0.00	0.00	0.00	0.00	0.00
Ca	0.83	0.98	0.98	0.96	0.83	0.95	0.86	0.86	0.81	0.88	0.82	0.36	0.43
Na	0.08	0.03	0.03	0.03	0.18	0.07	0.04	0.05	0.10	0.13	0.07	0.62	0.56
K	0.00	0.00	0.00	0.00	0.00	0.00	0.02	0.00	0.01	0.00	0.01	0.01	0.01
P	0.01	0.00	0.00	0.00	0.00	0.00	0.02	0.00	0.00	0.00	0.01	0.00	0.00
Or	1	0	0	0	0	0	2	0	1	0	1	1	1
Ab	9	3	3	3	18	7	4	6	11	13	8	63	56
An	91	97	97	97	82	93	94	94	89	87	91	36	43

Sample n^{er}	FM21	FM21	FM21	FP21c	FP21c	FP21c	FP21c	FP21c	FP21c	FP21c	FP21c	FP21c
Analyse n^{er}	3b	4b	5b	1a	2a	3a	4a	5a	6a	1b	2b	3b
Type	GWK	GWK.m	GWK.m	GWK.m	GWK.m	GWK.m	GWK.m	GWK.m	GWK.m	GWK.m	GWK.m	GWK.m
SiO2	58.07	63.43	63.09	64.87	65.48	64.85	64.91	68.97	65.12	65.04	64.80	65.47
TiO2	0.00	0.00	0.15	0.01	0.01	0.02	0.02	0.00	0.00	0.02	0.00	0.00
Al2O3	27.25	23.34	22.57	22.52	22.56	22.22	22.31	20.20	22.16	22.40	22.66	22.42
FeO	0.00	0.15	0.45	0.02	0.00	0.00	0.01	0.00	0.01	0.07	0.01	0.03
MnO	0.00	0.00	0.28	0.27	0.04	0.28	0.00	0.04	0.00	0.00	0.28	0.33
MgO	0.04	0.00	0.08	0.00	0.00	0.00	0.00	0.00	0.01	0.00	0.00	0.00
CaO	7.41	3.32	2.85	3.28	3.58	3.34	3.36	0.82	3.15	3.29	3.76	3.40
Na2O	7.12	9.30	9.86	10.10	9.86	9.88	9.78	11.57	10.05	10.02	9.77	9.91
K2O	0.11	0.27	0.42	0.17	0.08	0.23	0.22	0.02	0.13	0.11	0.13	0.17
BaO	0.00	0.05	0.03	0.01	0.00	0.00	0.00	0.03	0.00	0.00	0.00	0.00
P2O5	0.00	0.18	0.24	0.09	0.00	0.22	0.03	0.00	0.00	0.18	0.24	0.08
TOTAL	100.0	100.0	100.0	101.3	101.6	101.0	100.6	101.7	100.6	101.1	101.6	101.8
Si	2.59	2.80	2.80	2.84	2.84	2.85	2.85	2.97	2.85	2.84	2.83	2.85
Al	1.43	1.21	1.18	1.16	1.15	1.15	1.15	1.03	1.14	1.15	1.17	1.15
Ti	0.00	0.00	0.01	0.00	0.00	0.00	0.00	0.00	0.00	0.00	0.00	0.00
Fe	0.00	0.01	0.02	0.00	0.00	0.00	0.00	0.00	0.00	0.00	0.00	0.00
Mn	0.00	0.00	0.01	0.00	0.00	0.00	0.00	0.00	0.00	0.00	0.00	0.00
Mg	0.00	0.00	0.01	0.00	0.00	0.00	0.00	0.00	0.00	0.00	0.00	0.00
Zn	0.00	0.00	0.00	0.00	0.00	0.00	0.00	0.00	0.00	0.00	0.00	0.00
Ca	0.35	0.16	0.14	0.15	0.17	0.16	0.16	0.04	0.15	0.15	0.18	0.16
Na	0.62	0.80	0.85	0.86	0.83	0.84	0.83	0.97	0.85	0.85	0.83	0.84
K	0.01	0.02	0.02	0.01	0.00	0.01	0.01	0.00	0.01	0.01	0.01	0.01
P	0.00	0.01	0.01	0.00	0.00	0.00	0.00	0.00	0.00	0.00	0.00	0.00
Or	0.64	1.57	2.36	0.92	0.46	1.25	1.24	0.10	0.74	0.58	0.69	0.94
Ab	63.08	82.21	84.19	83.98	82.90	83.21	82.98	96.12	84.58	84.14	81.89	83.28
An	36.28	16.22	13.45	15.09	16.64	15.53	15.78	3.78	14.67	15.28	17.42	15.78

OBS: Abbreviations: LG – staurolite zone calc-silicate rocks; CZ – Core zone of Calc-silicate nodules; OZ – outer zone of calc-silicate nodules; GWK – metagreywacke resister; GWK.m – Metagreywacke partially migmatized; *based on 8 oxygen atoms and the formula (Ca, Na, K) Al (Al, Si) Si_2O_8.

Table B. 7 - Chemical analysis (wt.%) and structural formulas* of plagioclases from metasediments and metatexites

Sample n^{er}	FM38	VC65	VC65	VC65	VC28a	VC28	VC28	VC28	VC28	VC52
Analyse n^{er}	1	1	2	3	1	2	3	4	5	1
Type	Bt.Sch	St.Sch	St.Sch	St.Sch	PMM	PMM	PMM	PMM	PMM	PMM
SiO2	66.40	67.36	67.16	67.20	59.39	62.14	64.11	63.69	60.82	61.05
TiO2	0.08	0.00	0.00	0.00	0.00	0.03	0.00	0.00	0.33	0.21
Al2O3	19.02	21.01	21.04	20.88	24.24	24.13	23.49	23.23	24.42	23.66
FeO	0.31	0.02	0.02	0.02	0.03	0.00	0.00	0.02	0.46	0.35
MnO	0.22	0,3	0.09	0.12	0.06	0.08	0.12	0.11	0.26	0.25
MgO	0.22	0.00	0.00	0.00	0.00	0.00	0.00	0.00	0.17	0.22
CaO	0.51	1.67	1.59	1.56	5.48	5.12	4.42	4.27	4.21	3.97
Na2O	10.59	10.42	10.86	10.77	8.44	8.31	9.03	9.24	8.93	9.31
K2O	0.06	0.14	0.13	0.14	0.19	0.24	0.11	0.11	0.29	0.31
BaO	0.00	0.00	0.00	0.06	0.03	0.07	0.00	0.07	0.00	0.00
P2O5	0.20	0.22	0.14	0.16	0.12	0.14	0.25	0.30	0.12	0.67
TOTAL	98.1	100.6	100.8	100.6	98.1	100.3	101.2	100.6	100.0	100.0
Si	2.97	2.93	2.92	2.93	2.70	2.75	2.80	2.80	2.71	2.71
Al	1.00	1.08	1.08	1.07	1.30	1.26	1.21	1.20	1.28	1.24
Ti	0.00	0.00	0.00	0.00	0.00	0.00	0.00	0.00	0.01	0.01
Fe	0.01	0.00	0.00	0.00	0.00	0.00	0.00	0.00	0.02	0.01
Mn	0.01	0.00	0.00	0.00	0.00	0.00	0.00	0.00	0.01	0.01
Mg	0.01	0.00	0.00	0.00	0.00	0.00	0.00	0.00	0.01	0.01
Zn	0.02	0.00	0.00	0.00	0.00	0.00	0.00	0.00	0.00	0.00
Ca	0.02	0.08	0.07	0.07	0.27	0.24	0.21	0.20	0.20	0.19
Na	0.92	0.88	0.92	0.91	0.74	0.71	0.76	0.79	0.77	0.80
K	0.00	0.01	0.01	0.01	0.01	0.01	0.01	0.01	0.02	0.02
P	0.01	0.00	0.00	0.00	0.00	0.01	0.00	0.00	0.00	0.03
Or	0	1	1	1	1	1	1	1	2	2
Ab	97	91	92	92	73	74	78	79	78	80
An	3	8	7	7	26	25	21	20	20	19
Sample n^{er}	FM16	FM16	FM16	FM16	FM3	FM4	FM4	VC15	VC15	VC15
Analyse n^{er}	1	2	3	4	1	1	2	1	2	3
Type	BMM	BMM	BMM	BMM	BMM	BMM	BMM	BMM	BMM	BMM
SiO2	64.43	61.13	62.61	68.39	62.19	59.88	64.72	61.45	63.26	60.67
TiO2	0.00	0.00	0.03	0.03	0.08	0.20	0.25	0.13	0.00	0.00
Al2O3	21.43	23.78	23.37	19.79	23.74	25.03	21.25	23.82	23.76	23.97
FeO	0.00	0.00	0.00	0.00	0.00	0.35	0.46	0.35	0.03	0.00
MnO	0.01	0.01	0.02	0.01	0.00	0.16	0.22	0.30	0.00	0.10
MgO	0.00	0.00	0.00	0.00	0.07	0.35	0.14	0.21	0.00	0.00
CaO	2.68	5.08	4.44	0.19	4.97	4.67	1.57	3.82	4.57	4.73
Na2O	10.44	8.72	9.16	11.88	8.04	9.03	11.08	9.45	8.94	8.65
K2O	0.16	0.24	0.32	0.16	0.26	0.34	0.20	0.31	0.25	0.35
BaO	0.09	0.00	0.00	0.09	0.00	0.00	0.00	0.00	0.04	0.06
P2O5	0.25	0.16	0.20	0.18	0.00	0.00	0.09	0.17	0.13	0.06
TOTAL	99.7	99.2	100.2	100.7	99.4	100.0	100.0	100.0	101.0	98.6
Si	2.85	2.74	2.77	2.97	2.77	2.67	2.86	2.73	2.77	2.73
Al	1.12	1.25	1.22	1.01	1.24	1.32	1.11	1.25	1.23	1.27
Ti	0.00	0.00	0.00	0.00	0.00	0.01	0.01	0.00	0.00	0.00
Fe	0.00	0.00	0.00	0.00	0.00	0.01	0.02	0.01	0.00	0.00
Mn	0.00	0.00	0.00	0.00	0.00	0.01	0.01	0.01	0.00	0.00
Mg	0.00	0.00	0.00	0.00	0.00	0.02	0.01	0.01	0.00	0.00
Zn	0.01	0.00	0.00	0.00	0.00	0.00	0.00	0.00	0.00	0.00
Ca	0.13	0.24	0.21	0.01	0.24	0.22	0.07	0.18	0.21	0.23
Na	0.90	0.76	0.79	1.00	0.69	0.78	0.95	0.81	0.76	0.76
K	0.01	0.01	0.02	0.01	0.01	0.02	0.01	0.02	0.01	0.02
P	0.01	0.01	0.01	0.01	0.00	0.00	0.00	0.01	0.00	0.00
Or	1	1	2	1	2	2	1	2	1	2
Ab	87	75	77	98	73	76	92	80	77	75
An	12	24	21	1	25	22	7	18	22	23

OBS: Abbreviations: St.Sch – staurolite schist; PMM – patch metatexites; BMM – Banded metatexites; *based on 8 oxygen atoms and the formula (Ca, Na, K) Al (Al, Si) Si_2O_8.

Table B. 8 - Chemical analysis (wt.%) and structural formulas* of plagioclases from diatexites and leucogranites.

Sample n^{er}	VC60	VC60	VC60	VC60	VC60	VC60	VC60	VC60	FM6	FM6	FM6	FM6	VC59	VC3
Anal. n^{er}	1	2	3c	3b	4c	4b	5c	5b	1c	1b	2c	2b	1	1
Type	DTX	DTX	DTX	DTX	DTX	DTX	DTX	DTX	DTX	DTX	DTX	DTX	DTX	L.Gnt
SiO2	61.27	68.68	61.47	65.77	60.60	65.72	63.78	63.12	62.11	64.63	63.44	67.74	65.96	61.76
TiO2	0.07	0.02	0.00	0.26	0.22	0.23	0.00	0.00	0.22	0.13	0.21	0.12	0.00	0.21
Al2O3	24.16	19.99	24.06	20.22	24.22	20.45	23.44	23.60	22.95	21.34	22.31	19.41	19.88	21.42
FeO	0.24	0.01	0.25	0.38	0.45	0.58	0.00	0.01	0.24	0.65	0.45	0.23	0.15	0.37
MnO	0.23	0.00	0.12	0.19	0.30	0.34	0.00	0.00	0.22	0.16	0.07	0.09	0.18	0.25
MgO	0.18	0.00	0.00	0.14	0.20	0.16	0.00	0.00	0.04	0.21	0.21	0.06	0.09	0.15
CaO	3.97	0.43	3.94	0.37	4.09	0.42	4.33	4.60	4.20	1.23	3.24	0.75	0.64	2.83
Na2O	9.16	11.67	9.26	11.92	9.15	11.58	9.18	9.10	8.21	9.33	8.87	10.18	10.70	9.09
K2O	0.36	0.11	0.44	0.20	0.31	0.17	0.22	0.15	0.45	0.73	0.25	0.09	0.25	0.37
BaO	0.00	0.00	0.00	0.03	0.00	0.00	0.00	0.00	0.01	0.01	0.00	0.00	0.02	0.01
P2O5	0.36	0.27	0.18	0.55	0.46	0.35	0.56	0.36	0.00	0.00	0.00	0.00	0.33	0.30
TOTAL	100.0	100.9	99.7	100.0	100.0	100.0	100.9	100.6	99.2	99.3	99.3	99.3	98.3	97.4
Si	2.72	2.98	2.74	2.90	2.70	2.90	2.79	2.78	2.78	2.88	2.82	2.98	2.92	2.81
Al	1.26	1.02	1.26	1.05	1.27	1.06	1.21	1.22	1.21	1.12	1.17	1.01	1.04	1.15
Ti	0.00	0.00	0.00	0.01	0.01	0.01	0.00	0.00	0.01	0.00	0.01	0.00	0.00	0.01
Fe	0.01	0.00	0.01	0.01	0.02	0.02	0.00	0.00	0.01	0.02	0.02	0.01	0.01	0.01
Mn	0.01	0.00	0.00	0.01	0.01	0.01	0.00	0.00	0.01	0.01	0.00	0.00	0.01	0.01
Mg	0.01	0.00	0.00	0.01	0.01	0.01	0.00	0.00	0.00	0.01	0.01	0.00	0.01	0.01
Zn	0.00	0.00	0.00	0.00	0.00	0.00	0.00	0.00	0.02	0.03	0.01	0.02	0.00	0.02
Ca	0.19	0.02	0.19	0.02	0.20	0.02	0.20	0.22	0.20	0.06	0.15	0.04	0.03	0.14
Na	0.79	0.98	0.80	1.02	0.79	0.99	0.78	0.78	0.71	0.81	0.77	0.87	0.92	0.80
K	0.02	0.01	0.02	0.01	0.02	0.01	0.01	0.01	0.03	0.04	0.01	0.01	0.01	0.02
P	0.01	0.00	0.01	0.02	0.02	0.01	0.00	0.00	0.00	0.00	0.00	0.00	0.00	0.01
Or	2	1	2	1	2	1	1	1	3	5	2	1	1	2
Ab	79	97	79	97	79	97	78	78	76	89	82	96	95	83
An	19	2	19	2	19	2	20	22	21	6	17	4	3	14

Sample n^{er}	VC3	VC3	VC3	VC62	VC62	VC62	VC52	VC52	VC52	VC52	VC52	VC52	VC52	VC52
Anal. n^{er}	2	3c	3b	1a	2a	3a	1a	2a	3a	4a	5a	1b	2b	3
Type	L.Gnt	L.Gnt	L.Gnt	L.Gnt	L.Gnt	L.Gnt	TL.Gnt	TL.Gnt	TL.Gnt	TL.Gnt	TL.Gnt	TL.Gnt	TL.Gnt	TL.Gnt
SiO2	65.14	65.09	67.66	68.89	68.55	69.71	67.67	66.45	65.17	66.56	67.98	69.03	68.11	66.46
TiO2	0.09	0.13	0.00	0.02	0.01	0.01	0.00	0.00	0.00	0.02	0.00	0.00	0.00	0.01
Al2O3	20.10	20.54	18.76	19.52	19.67	19.48	21.48	21.81	22.42	21.50	20.95	19.67	20.59	21.94
FeO	0.16	0.17	0.15	0.00	0.01	0.00	0.00	0.03	0.00	0.00	0.01	0.01	0.02	0.01
MnO	0.11	0.00	0.12											
MgO	0.22	0.15	0.16	0.00	0.00	0.00	0.01	0.00	0.01	0.00	0.00	0.00	0.01	0.00
CaO	1.30	2.18	0.13	0.19	0.38	0.27	1.81	2.55	3.44	2.25	1.19	0.44	1.17	2.40
Na2O	9.99	9.96	11.12	11.61	11.44	11.49	10.86	10.15	9.68	10.46	11.17	11.47	11.26	10.52
K2O	0.15	0.20	0.07	0.09	0.12	0.12	0.10	0.23	0.10	0.21	0.15	0.05	0.06	0.14
BaO	0.03	0.01	0.08	0.00	0.05	0.01	0.01	0.01	0.03	0.01	0.08	0.00	0.02	0.00
P2O5	0.56	0.00	0.34	0.60	0.30	0.00	0.60	0.30	0.56	0.00	0.34	0.60	0.30	0.32
TOTAL	98.9	98.4	99.4	100.3	100.2	101.1	101.9	101.2	100.9	101.0	101.5	100.7	101.2	101.5
Si	2.90	2.91	2.99	3.00	2.99	3.01	2.91	2.89	2.85	2.90	2.94	2.99	2.95	2.88
Al	1.06	1.08	0.98	1.00	1.01	0.99	1.09	1.12	1.15	1.10	1.07	1.01	1.05	1.12
Ti	0.00	0.00	0.00	0.00	0.00	0.00	0.00	0.00	0.00	0.00	0.00	0.00	0.00	0.00
Fe	0.01	0.01	0.01	0.00	0.00	0.00	0.00	0.00	0.00	0.00	0.00	0.00	0.00	0.00
Mn	0.00	0.00	0.00	0.00	0.00	0.00	0.00	0.00	0.00	0.00	0.00	0.00	0.00	0.00
Mg	0.01	0.01	0.01	0.00	0.00	0.00	0.00	0.00	0.00	0.00	0.00	0.00	0.00	0.00
Zn	0.03	0.00	0.03	0.00	0.00	0.00	0.00	0.00	0.00	0.00	0.00	0.00	0.00	0.00
Ca	0.06	0.10	0.01	0.01	0.02	0.01	0.08	0.12	0.16	0.10	0.06	0.02	0.05	0.11
Na	0.86	0.86	0.95	0.98	0.97	0.96	0.91	0.85	0.82	0.88	0.94	0.96	0.94	0.88
K	0.01	0.01	0.00	0.01	0.01	0.01	0.01	0.01	0.01	0.01	0.01	0.00	0.00	0.01
P	0.02	0.00	0.01	0.00	0.00	0.00	0.00	0.00	0.00	0.00	0.00	0.00	0.00	0.00
Or	1	1	0	1	1	1	1	1	1	1	1	0	0	1
Ab	92	88	99	99	98	98	91	87	83	88	94	98	94	88
An	7	11	1	1	2	1	8	12	16	10	6	2	5	11

OBS: DTX - diatexite; L.Gnt – leucogranite; TL.Gnt – lourmaline bearing leucogranite; *based on 8 oxygen atoms and the formula (Ca, Na, K) Al (Al, Si) Si_2O_8

Table B. 9 - Chemical analysis (wt.%) and structural formulas* of plagioclases from two-mica granites.

Sample n^{er}	FP21b	FP21b	VC22	VC22a	VC22a	VC22a	VC22a	VC22a	VC22a	VC22a	VC39	VC39	VC39
Anal. n^{er}	1	2	1	1a	2a	3a	4a	5a	6a	7a	1	2	3
Type	2m.Gnt	2m.Gnt	2m.Gnt	2m.Gnt	2m.Gnt	2m.Gnt	2m.Gnt	2m.Gnt	2m.Gnt	2m.Gnt	2m.Gnt	2m.Gnt	2m.Gnt
SiO2	63.22	64.71	67.98	68.11	66.86	68.07	69.79	66.17	68.84	68.88	66.62	64.89	64.38
TiO2	0.00	0.20	0.00	0.00	0.00	0.00	0.00	0.02	0.00	0.00	0.00	0.28	0.00
Al2O3	21.47	19.91	20.49	19.63	21.14	19.64	19.31	21.44	19.73	19.97	20.64	20.77	19.54
FeO	0.38	0.34	0.00	0.01	0.01	0.01	0.01	0.00	0.02	0.00	0.15	0.29	0.28
MnO	0.24	0.12									0.00	0.34	0.22
MgO	0.21	0.06	0.00	0.01	0.00	0.01	0.00	0.01	0.00	0.00	0.10	0.26	0.14
CaO	2.95	1.35	1.43	0.83	2.14	0.57	0.13	2.07	0.61	0.70	1.30	1.81	1.23
Na2O	8.99	10.25	11.08	11.37	10.56	11.48	11.80	10.42	11.58	11.38	10.01	9.56	10.26
K2O	0.31	0.30	0.10	0.10	0.22	0.11	0.05	0.59	0.09	0.12	0.24	0.25	0.20
BaO	0.02	0.03	0.01	0.00	0.02	0.03	0.00	0.00	0.00	0.01	0.05	0.01	0.01
P2O5	0.43	0.07	0.36	0.18	0.46	0.55	0.35	0.00	0.60	0.30	0.00	0.00	0.60
TOTAL	98.73	98.37	101.09	100.06	100.94	99.91	101.09	100.70	100.87	101.07	99.55	99.06	97.62
Si	2.83	2.91	2.95	2.98	2.91	2.98	3.01	2.89	2.98	2.98	2.93	2.89	2.91
Al	1.13	1.06	1.05	1.01	1.08	1.01	0.98	1.10	1.01	1.02	1.07	1.09	1.04
Ti	0.00	0.01	0.00	0.00	0.00	0.00	0.00	0.00	0.00	0.00	0.00	0.01	0.00
Fe	0.01	0.01	0.00	0.00	0.00	0.00	0.00	0.00	0.00	0.00	0.01	0.01	0.01
Mn	0.01	0.00	0.00	0.00	0.00	0.00	0.00	0.00	0.00	0.00	0.00	0.01	0.01
Mg	0.01	0.00	0.00	0.00	0.00	0.00	0.00	0.00	0.00	0.00	0.01	0.02	0.01
Zn	0.02	0.04	0.00	0.00	0.00	0.00	0.00	0.00	0.00	0.00	0.02	0.02	0.03
Ca	0.14	0.07	0.07	0.04	0.10	0.03	0.01	0.10	0.03	0.03	0.06	0.09	0.06
Na	0.78	0.89	0.93	0.96	0.89	0.97	0.99	0.88	0.97	0.95	0.85	0.83	0.90
K	0.02	0.02	0.01	0.01	0.01	0.01	0.00	0.03	0.01	0.01	0.01	0.01	0.01
Or	2	2	1	1	1	1	0	3	1	1	1	2	1
Ab	83	92	93	96	89	97	99	87	97	96	92	89	93
An	15	7	7	4	10	3	1	10	3	3	7	9	6

Sample n^{er}	VC58	VC58	VC58	VC58	VC58	VC58	VC58	VC58	VC58	VC64	VC64
Anal. n^{er}	1a	1b	2b	1c	2c	3c	4c	5c	1.00	2.00	3.00
Type	APG	APG	APG	APG	APG	APG	APG	APG	APG	APG	APG
Localiz.	Aplite	Int.	Int.	Int	Bord	Bord.	Bord.	Bord.	Bord.	Bord.	Pertite
SiO2	65.63	65.20	66.66	65.38	65.45	64.71	65.17	66.58	64.69	64.84	66.35
TiO2	0.13	0.24	0.24	0.16	0.09	0.14	0.00	0.23	0.16	0.30	0.00
Al2O3	20.92	20.70	20.02	21.00	20.47	21.01	21.11	20.10	21.25	20.94	20.34
FeO	0.00	0.33	0.00	0.26	0.00	0.60	0.00	0.16	0.26	0.15	0.00
MnO	0.00	0.22	0.14	0.13	0.17	0.16	0.10	0.21	0.16	0.13	0.26
MgO	0.11	0.20	0.18	0.13	0.09	0.22	0.11	0.07	0.32	0.05	0.22
CaO	0.61	0.78	0.19	0.84	0.93	0.86	0.64	0.24	1.00	0.99	0.17
Na2O	11.46	11.21	11.91	11.28	11.77	11.37	11.74	11.84	11.16	11.46	11.75
K2O	0.21	0.29	0.27	0.27	0.19	0.30	0.19	0.19	0.37	0.29	0.17
P2O5	0.84	0.51	0.09	0.00	0.08	0.46	0.77	0.00	0.20	0.33	0.47
TOTAL	99.91	99.68	99.70	99.45	99.24	99.83	99.83	99.62	99.57	99.48	99.73
Si	2.88	2.88	2.94	2.90	2.91	2.86	2.87	2.94	2.87	2.87	2.92
Al	1.08	1.08	1.04	1.10	1.07	1.10	1.10	1.05	1.11	1.09	1.05
Ti	0.00	0.01	0.01	0.01	0.00	0.00	0.00	0.01	0.01	0.01	0.00
Fe	0.00	0.01	0.00	0.01	0.00	0.02	0.00	0.01	0.01	0.01	0.00
Mn	0.00	0.01	0.01	0.00	0.01	0.01	0.00	0.01	0.01	0.00	0.01
Mg	0.01	0.01	0.01	0.01	0.01	0.01	0.01	0.00	0.02	0.00	0.01
Zn	0.00	0.00	0.00	0.00	0.00	0.00	0.00	0.00	0.00	0.00	0.00
Ca	0.03	0.04	0.01	0.04	0.04	0.04	0.03	0.01	0.05	0.05	0.01
Na	0.98	0.96	1.02	0.97	1.01	0.98	1.00	1.01	0.96	0.98	1.00
K	0.01	0.02	0.02	0.02	0.01	0.02	0.01	0.01	0.02	0.02	0.01
Or	1	2	1	1	1	2	1	1	2	2	1
Ab	96	95	98	95	95	94	96	98	93	94	98
An	3	4	1	4	4	4	3	1	5	4	1

OBS: Abbreviations: 2m.gnt – two-mica granite; APG – aplite-pegmatite. Int: intermedian zone; bord – Comb-structure plagioclase in the border zone; *based on 8 oxygen atoms and the formula (Ca, Na, K) Al (Al, Si) Si_2O_8

Table B. 10 - Chemical analysis (wt.%) and structural formulas* of K-feldspars from Calc-silicate nodules, banded metatexites and diatexites.

Sample n^{er}	GC2	GC2	FM16	FM15	FM15	VC52a	VC60	VC60
Anal. n^{er}	1a	2a	1	2	3	4	1	2
Type	CSN	CSN	BMM	BMM	BMM	BMM	DTX	DTX
SiO2	65.74	64.28	62.54	64.65	65.85	63.75	64.09	63.90
TiO2	0.02	0.02	0.01	0.23	0.00	0.94	0.27	0.38
Al2O3	19.02	19.30	18.70	19.60	19.08	19.41	19.31	19.74
FeO	0.10	0.00	0.04	0.42	0.00	0.60	0.08	0.08
MnO	0.17	0.04	0.00	0.17	0.05	0.28	0.27	0.29
MgO	0.00	0.01	0.00	0.00	0.01	0.07	0.28	0.10
CaO	0.04	0.06	0.01	0.13	0.00	0.21	0.18	0.30
Na2O	0.41	0.43	2.01	1.42	1.54	1.44	2.43	2.15
K2O	14.75	15.01	14.26	13.07	14.03	12.94	12.69	12.50
BaO	0.68	0.40	0.28	0.44	0.45	0.00	0.33	0.26
Rb2O	0.09	0.02	0.00	0.01	0.00	0.00	0.00	0.00
Cs2O	0.02	0.02	0.02	0.03	0.00	0.00	0.00	0.00
P2O5	0.00	0.00	0.17	0.30	0.14	0.36	0.11	0.25
TOTAL	101.0	99.6	98.0	100.5	101.2	100.0	100.0	99.9
Si	3.00	2.97	2.95	2.95	2.99	2.92	2.94	2.93
Al	1.02	1.05	1.04	1.05	1.02	1.05	1.04	1.07
Ti	0.00	0.00	0.00	0.01	0.00	0.03	0.01	0.01
Fe	0.00	0.00	0.00	0.02	0.00	0.02	0.00	0.00
Mn	0.01	0.00	0.00	0.01	0.00	0.01	0.01	0.01
Mg	0.00	0.00	0.00	0.00	0.00	0.00	0.02	0.01
Zn	0.00	0.00	0.00	0.00	0.00	0.00	0.00	0.00
Ca	0.00	0.00	0.00	0.01	0.00	0.01	0.01	0.01
Na	0.04	0.04	0.18	0.13	0.14	0.13	0.22	0.19
K	0.86	0.89	0.86	0.76	0.81	0.76	0.74	0.73
Ba	0.01	0.01	0.01	0.01	0.01	0.00	0.01	0.00
Rb	0.00	0.00	0.00	0.00	0.00	0.00	0.00	0.00
Cs	0.00	0.00	0.00	0.00	0.00	0.00	0.00	0.00
Or	95.73	95.55	82.33	85.21	85.70	84.55	76.75	78.03
Ab	4.03	4.11	17.64	14.07	14.30	14.30	22.34	20.40
An	0.24	0.33	0.03	0.71	0.00	1.15	0.91	1.57

Sample n^{er}	VC60	VC60	VC60	VC60	VC60	VC60	VC60
Anal. n^{er}	3	4	5	1a	2a	3a	4a
Type	DTX	DTX	DTX	DTX	DTX	DTX	DTX
SiO2	64.02	65.50	65.71	65.46	65.28	65.88	65.33
TiO2	0.24	0.03	0.05	0.03	0.02	0.02	0.00
Al2O3	20.00	19.01	18.95	19.06	18.78	18.80	18.65
FeO	0.08	0.02	0.03	0.09	0.00	0.01	0.04
MnO	0.12	0.00	0.00	0.00	0.00	0.00	0.00
MgO	0.21	0.00	0.01	0.01	0.01	0.01	0.00
CaO	0.30	0.06	0.07	0.08	0.03	0.04	0.06
Na2O	2.30	2.03	2.02	2.21	1.37	1.43	0.95
K2O	12.32	13.81	14.00	13.13	14.93	13.94	15.20
BaO	0.29	0.30	0.31	0.39	0.22	0.15	0.20
Rb2O	0.00	0.00	0.00	0.00	0.00	0.00	0.00
Cs2O	0.00	0.00	0.00	0.00	0.00	0.00	0.00
P2O5	0.13	0.11	0.11	0.11	0.11	0.15	0.11
TOTAL	100.0	100.9	101.3	100.6	100.8	100.4	100.5
Si	2.93	2.98	2.98	2.98	2.98	3.00	2.99
Al	1.08	1.02	1.01	1.02	1.01	1.01	1.01
Ti	0.01	0.00	0.00	0.00	0.00	0.00	0.00
Fe	0.00	0.00	0.00	0.00	0.00	0.00	0.00
Mn	0.00	0.00	0.00	0.00	0.00	0.00	0.00
Mg	0.01	0.00	0.00	0.00	0.00	0.00	0.00
Zn	0.00	0.00	0.00	0.00	0.00	0.00	0.00
Ca	0.01	0.00	0.00	0.00	0.00	0.00	0.00
Na	0.20	0.18	0.18	0.19	0.12	0.13	0.08
K	0.72	0.80	0.81	0.76	0.87	0.81	0.89
Ba	0.01	0.01	0.01	0.01	0.00	0.00	0.00
Rb	0.00	0.00	0.00	0.00	0.00	0.00	0.00
Cs	0.00	0.00	0.00	0.00	0.00	0.00	0.00
Or	76.67	81.47	81.72	79.33	87.59	86.33	91.09
Ab	21.76	18.24	17.96	20.28	12.24	13.46	8.62
An	1.57	0.30	0.32	0.39	0.17	0.21	0.29

OBS: Abbreviations: CSN – calc-silicate nodule; BMM – banded metatexites; DTX – diatexite; *based on 8 oxygen atoms and the formula (Ca, Na, K) Al (Al, Si) Si_2O_8.

Table B. 11 - Chemical analysis (wt.%) and structural formulas* of K-feldspars from Leucogranites and two-mica granites..

Sample n^{er}	VC52	VC52	VC62	VC62	VC62	VC62	VC62	VC22	VC22
Anal. n^{er}	1	2	1a	2a	3a	4a	2	1	2
Type	L.Gnt	L.Gnt	TL.Gnt	TL.Gnt	TL.Gnt	TL.Gnt	TL.Gnt	2m.Gnt	2m.Gnt
SiO2	65.86	65.84	65.08	65.37	65.07	65.10	64.99	65.56	65.75
TiO2	0.00	0.00	0.00	0.00	0.00	0.02	0.02	0.00	0.00
Al2O3	18.47	18.67	18.80	18.71	18.79	18.58	18.71	18.65	18.23
FeO	0.00	0.03	0.00	0.03	0.02	0.02	0.00	0.07	0.03
MnO	0.00	0.00	0.00	0.00	0.00	0.00	0.00	0.00	0.00
MgO	0.00	0.00	0.00	0.00	0.00	0.00	0.00	0.00	0.00
CaO	0.02	0.02	0.03	0.02	0.02	0.02	0.02	0.03	0.02
Na2O	0.78	0.79	1.38	1.28	1.21	0.52	1.05	0.79	0.67
K2O	15.71	15.69	14.87	14.73	14.94	15.83	15.11	15.69	15.77
BaO	0.06	0.00	0.22	0.11	0.12	0.13	0.08	0.33	0.29
Rb2O	0.00	0.00	0.00	0.00	0.09	0.02	0.01	0.01	0.09
Cs2O	0.02	0.00	0.00	0.00	0.02	0.02	0.03	0.01	0.02
P2O5	0.14	0.17	0.36	0.11	0.25	0.11	0.11	0.13	0.13
TOTAL	100.9	101.0	100.4	100.3	100.2	100.2	100.0	101.1	100.8
Si	3.01	3.00	2.99	3.00	2.99	3.00	2.99	3.00	3.01
Al	0.99	1.00	1.02	1.01	1.02	1.01	1.01	1.00	0.98
Ti	0.00	0.00	0.00	0.00	0.00	0.00	0.00	0.00	0.00
Fe	0.00	0.00	0.00	0.00	0.00	0.00	0.00	0.00	0.00
Mn	0.00	0.00	0.00	0.00	0.00	0.00	0.00	0.00	0.00
Mg	0.00	0.00	0.00	0.00	0.00	0.00	0.00	0.00	0.00
Zn	0.00	0.00	0.00	0.00	0.00	0.00	0.00	0.00	0.00
Ca	0.00	0.00	0.00	0.00	0.00	0.00	0.00	0.00	0.00
Na	0.07	0.07	0.12	0.11	0.11	0.05	0.09	0.07	0.06
K	0.91	0.91	0.87	0.86	0.88	0.93	0.89	0.91	0.92
Ba	0.00	0.00	0.00	0.00	0.00	0.00	0.00	0.01	0.01
Rb	0.00	0.00	0.00	0.00	0.00	0.00	0.00	0.00	0.00
Cs	0.00	0.00	0.00	0.00	0.00	0.00	0.00	0.00	0.00
Or	92.93	92.81	87.56	88.22	88.93	95.12	90.39	92.78	93.87
Ab	6.97	7.09	12.31	11.66	10.96	4.78	9.50	7.09	6.05
An	0.10	0.10	0.13	0.12	0.12	0.11	0.11	0.13	0.08
Sample n^{er}	VC22	VC39	VC39	VC39	VC39	VC39	VC64	VC64	VC64
Anal. n^{er}	3	1a	2a	3a	1	2	1	2	3
Type	2m.Gnt	2m.Gnt	2m.Gnt	2m.Gnt	2m.Gnt	2m.Gnt	APG	APG	APG
SiO2	65.30	63.95	64.96	63.04	65.04	62.64	64.54	64.32	63.70
TiO2	0.00	0.27	0.00	0.21	0.21	0.18	0.00	0.11	0.25
Al2O3	18.70	18.57	18.57	18.63	18.63	18.09	19.83	19.42	19.39
FeO	0.03	0.04	0.02	0.05	0.02	0.04	0.02	0.01	0.02
MnO	0.00	0.27	0.12	0.29	0.19	0.13	0.20	0.13	0.38
MgO	0.00	0.11	0.12	0.24	0.24	0.10	0.00	0.13	0.13
CaO	0.02	0.14	0.13	0.12	0.12	0.09	0.00	0.00	0.00
Na2O	1.31	1.25	0.41	0.90	0.90	0.25	0.91	0.74	0.93
K2O	14.84	14.21	14.99	14.50	14.50	14.61	14.06	14.51	14.03
BaO	0.24	0.27	0.31	0.29	0.20	0.30	0.10	0.08	0.08
Rb2O	0.04	0.02	0.05	0.00	0.09	0.02	0.01	0.04	0.01
Cs2O	0.04	0.02	0.03	0.00	0.02	0.02	0.03	0.00	0.01
P2O5	0.11	0.17	0.14	0.13	0.00	0.32	0.00	0.50	0.38
TOTAL	100.5	99.3	99.8	98.4	100.0	96.7	99.7	100.0	99.3
Si	2.99	2.97	2.99	2.96	2.99	2.98	2.96	2.95	2.94
Al	1.01	1.02	1.01	1.03	1.01	1.01	1.07	1.05	1.06
Ti	0.00	0.01	0.00	0.01	0.01	0.01	0.00	0.00	0.01
Fe	0.00	0.00	0.00	0.00	0.00	0.00	0.00	0.00	0.00
Mn	0.00	0.01	0.00	0.01	0.01	0.01	0.01	0.01	0.01
Mg	0.00	0.01	0.01	0.02	0.02	0.01	0.00	0.01	0.01
Zn	0.00	0.00	0.00	0.00	0.00	0.00	0.00	0.00	0.00
Ca	0.00	0.01	0.01	0.01	0.01	0.00	0.00	0.00	0.00
Na	0.12	0.11	0.04	0.08	0.08	0.02	0.08	0.07	0.08
K	0.87	0.84	0.88	0.87	0.85	0.89	0.82	0.85	0.83
Ba	0.00	0.00	0.01	0.01	0.00	0.01	0.00	0.00	0.00
Rb	0.00	0.00	0.00	0.00	0.00	0.00	0.00	0.00	0.00
Cs	0.00	0.00	0.00	0.00	0.00	0.00	0.00	0.00	0.00
Or	88.05	87.57	95.34	90.80	90.80	96.98	91.04	92.81	90.85
Ab	11.83	11.71	3.96	8.57	8.57	2.52	8.96	7.19	9.15
An	0.11	0.72	0.69	0.63	0.63	0.50	0.00	0.00	0.00

OBS: Abbreviations: L.Gnt – leucogranite; TL.Gnt – Tourmaline bearing leucogranite; 2m.Gnt – two-mica granite; APG – aplite-pegmatite. *Based on 8 oxygen atoms and the formula (Ca, Na, K) Al (Al, Si) Si_2O_8.

Table B. 12 - Chemical analysis (wt.%) and structural formulas* of biotites from calc-silicate nodules and metagreywackes.

Sample n^{er}	FM1	FM1	FM21	FM21	FM21	FP21c	FP21c	FP21c	FP21c	FP21c	FP21c	FP21c
Anal. n^{er}	1	2	1	2	3	1-r	2-r	3-r	4-r	5-m	6-m	7-m
Type	CSR	CSR	GWK	GWK	GWK	GWK.m	GWK.m	GWK.m	GWK.m	GWK.m	GWK.m	GWK.m
SiO2	36.09	36.78	36.23	36.36	36.30	35.62	35.78	35.27	35.47	35.50	35.92	35.76
TiO2	3.31	3.37	3.05	3.43	3.33	3.07	3.02	2.95	3.31	2.99	3.03	3.13
Al2O3	17.31	17.62	17.54	18.84	18.00	19.28	19.62	19.57	19.18	19.49	19.65	19.45
FeO	17.66	14.59	18.24	18.89	18.90	18.84	18.47	18.81	18.69	18.75	18.57	18.65
MnO	0.30	0.25	0.27	0.26	0.17	0.23	0.27	0.26	0.17	0.23	0.20	0.25
MgO	13.33	12.54	11.11	10.96	10.07	8.93	8.64	8.89	9.08	8.78	8.65	8.63
CaO	0.16	0.01	0.01	0.00	0.05	0.00	0.00	0.01	0.00	0.00	0.00	0.00
Na2O	0.00	0.15	0.10	0.32	0.09	0.15	0.11	0.21	0.20	0.16	0.15	0.15
K2O	8.55	9.37	8.79	8.83	8.90	9.65	9.72	9.61	9.63	9.69	9.74	9.69
BaO	0.16	0.15	0.08	0.06	0.13	0.08	0.09	0.02	0.13	0.09	0.06	0.00
F	0.30	0.44	0.15	0.12	0.11	0.15	0.16	0.18	0.11	0.14	0.12	0.12
Cl	0.00	0.00	0.02	0.02	0.01	0.02	0.03	0.02	0.01	0.01	0.02	0.03
Cr2O3	0.00	0.00	0.12	0.10	0.15	0.12	0.11	0.08	0.15	0.12	0.10	0.11
Li2O*	0.07	0.07	0.10	0.10	0.11	0.14	0.15	0.14	0.13	0.14	0.15	0.15
H2O*	2.50	4.40	4.20	2.70	3.00	3.93	4.06	4.20	3.92	4.12	3.85	4.05
Subtotal	99.73	99.75	100.00	100.99	99.34	100.20	100.22	100.22	100.18	100.20	100.20	100.20
O=F,Cl	0.13	0.19	0.07	0.06	0.05	0.07	0.07	0.08	0.05	0.06	0.06	0.06
Total	99.61	99.57	99.93	100.94	99.29	100.14	100.14	100.14	100.13	100.14	100.14	100.15
Si	5.35	5.50	5.45	5.34	5.44	5.37	5.39	5.33	5.35	5.36	5.39	5.39
Al iv	2.65	2.50	2.55	2.66	2.56	2.63	2.61	2.67	2.65	2.64	2.61	2.61
Al vi	0.37	0.60	0.56	0.60	0.63	0.79	0.87	0.82	0.75	0.83	0.87	0.84
Ti	0.37	0.38	0.35	0.38	0.38	0.35	0.34	0.33	0.38	0.34	0.34	0.35
Cr	0.00	0.00	0.01	0.01	0.02	0.01	0.01	0.01	0.02	0.01	0.01	0.01
Fe	2.19	1.82	2.30	2.32	2.37	2.38	2.33	2.38	2.36	2.37	2.33	2.35
Mn	0.04	0.03	0.03	0.03	0.02	0.03	0.03	0.03	0.02	0.03	0.03	0.03
Mg	2.94	2.79	2.49	2.40	2.25	2.01	1.94	2.00	2.04	1.98	1.94	1.94
Li*	0.04	0.04	0.06	0.06	0.07	0.08	0.09	0.08	0.08	0.09	0.09	0.09
Ca	0.03	0.00	0.00	0.00	0.01	0.00	0.00	0.00	0.00	0.00	0.00	0.00
Na	0.00	0.04	0.03	0.09	0.03	0.04	0.03	0.06	0.06	0.05	0.04	0.04
K	1.62	1.79	1.69	1.65	1.70	1.86	1.87	1.85	1.85	1.87	1.86	1.86
Ba	0.01	0.01	0.00	0.00	0.01	0.00	0.01	0.00	0.01	0.01	0.00	0.00
OH*	3.86	3.79	3.93	3.94	3.95	3.93	3.92	3.91	3.95	3.93	3.94	3.94
F	0.14	0.21	0.07	0.06	0.05	0.07	0.08	0.09	0.05	0.06	0.06	0.06
Cl	0.00	0.00	0.00	0.01	0.00	0.00	0.01	0.01	0.00	0.00	0.01	0.01

OBS: Abbreviations: CSN – Calc-silicate nodules; GWK – Metagreywackes; GWK.m – Metagreywacke partially migmatized; r – biotite from the non-migmatized zone; m – biotite from the migmatized zone; *based on 24 oxygen atoms and the formula $X_2Y_{4-6}Z_8O_{20}$ $(OH,F)_4$; Li_2O = [2.1/(0.356 + MgO)] – 0.088 (Tischendorf *et al*., 1999).

Table B. 13 - Chemical analysis (wt.%) and structural formulas* of biotites from SGC metasediments.

Sample n^{er}	FM38	FM38	FM38	FM38	FM38	FM38	VC65	VC65	VC65
Anal. n^{er}	1	2	3	4	5	6	1	2	3
Type	Bt.sch	Bt.sch	Bt.sch	Bt.sch	Bt.sch	Bt.sch	St.sch	St.sch	St.sch
SiO2	35.81	36.15	36.70	36.58	36.15	36.15	35.54	35.35	35.72
TiO2	1.85	1.80	1.90	1.82	1.86	1.96	2.48	2.11	2.31
Al2O3	20.38	19.80	19.42	19.25	19.05	19.46	19.66	19.89	20.21
FeO	20.62	20.73	20.96	20.61	21.09	20.98	19.62	19.56	18.78
MnO	0.01	0.07	0.10	0.07	0.04	0.07	0.13	0.14	0.13
MgO	8.03	7.46	7.75	7.84	7.33	6.79	8.39	8.75	9.12
CaO	0.13	0.13	0.44	0.14	0.16	0.14	0.06	0.02	0.02
Na2O	0.09	0.09	0.19	0.15	0.13	0.15	0.23	0.12	0.33
K2O	5.21	5.26	5.88	6.04	5.55	5.18	8.42	8.89	8.47
BaO	0.05	0.05	0.00	0.00	0.06	0.06	0.12	0.10	0.09
F	0.07	0.04	0.75	0.07	0.04	0.04	0.06	0.06	0.06
Cr2O3	0.12	0.11	0.00	0.11	0.09	0.09	0.11	0.12	0.08
Li2O*	0.16	0.18	0.17	0.17	0.19	0.21	0.15	0.14	0.13
H2O*	7.66	8.29	6.90	7.26	8.48	8.87	5.21	4.92	4.69
Subtotal	100.20	100.20	101.26	100.11	100.21	100.17	100.18	100.17	100.16
O=F,Cl	0.03	0.02	0.34	0.03	0.02	0.02	0.03	0.03	0.02
Total	100.17	100.18	100.92	100.08	100.19	100.15	100.15	100.14	100.13
Si	5.48	5.57	5.59	5.61	5.61	5.62	5.40	5.37	5.37
Al iv	2.52	2.43	2.41	2.39	2.39	2.38	2.60	2.63	2.63
Al vi	1.16	1.17	1.07	1.09	1.10	1.18	0.92	0.93	0.96
Ti	0.21	0.21	0.22	0.21	0.22	0.23	0.28	0.24	0.26
Fe	2.64	2.67	2.67	2.64	2.74	2.73	2.49	2.49	2.36
Mn	0.00	0.01	0.01	0.01	0.01	0.01	0.02	0.02	0.02
Mg	1.83	1.71	1.76	1.79	1.70	1.57	1.90	1.98	2.04
Li*	0.10	0.11	0.10	0.10	0.12	0.13	0.09	0.09	0.08
Ca	0.02	0.02	0.07	0.02	0.03	0.02	0.01	0.00	0.00
Na	0.03	0.03	0.06	0.04	0.04	0.05	0.07	0.03	0.10
K	1.02	1.04	1.14	1.18	1.10	1.03	1.63	1.72	1.63
Ba	0.00	0.00	0.00	0.00	0.00	0.00	0.01	0.01	0.01
OH*	3.97	3.98	3.61	3.96	3.98	3.98	3.97	3.97	3.97
F	0.03	0.02	0.36	0.03	0.02	0.02	0.03	0.03	0.03
Sample n^{er}	FM14	FM14	FM14	FM14	FM14	FM14	FM11	FM11	FM11
Anal. n^{er}	1	2	3	1g	1g	1s	1	2	3
Type	St.sch	St.sch	St.sch	St.sch	St.sch	St.sch	St.sch	St.sch	St.sch
SiO2	32.72	36.44	37.21	36.18	36.36	36.47	36.52	36.21	36.45
TiO2	1.26	1.84	1.84	1.38	1.42	1.42	1.69	1.68	2.29
Al2O3	22.10	19.66	19.33	20.02	20.28	20.75	19.81	20.00	19.62
FeO	20.05	18.80	18.97	18.60	18.20	17.34	19.48	19.48	19.43
MnO	0.08	0.06	0.10	0.10	0.00	0.04	0.09	0.07	0.10
MgO	9.78	10.02	10.26	10.96	10.83	9.39	10.22	10.31	9.62
CaO	0.04	0.03	0.06	0.02	0.01	0.02	0.04	0.04	0.02
Na2O	0.20	0.32	0.34	0.46	0.44	0.32	0.35	0.32	0.39
K2O	7.31	8.72	8.58	8.24	8.42	8.35	8.01	8.01	8.18
BaO	0.68	0.10	0.11	0.06	0.16	0.11	0.06	0.11	0.11
F	0.05	0.17	0.16	0.07	0.04	0.09	0.03	0.28	0.20
Cr2O3	0.09	0.08	0.06	0.08	0.06	0.09	0.06	0.09	0.10
Li2O*	0.12	0.11	0.11	0.10	0.10	0.13	0.11	0.11	0.12
H2O*	6.20	4.10	3.99	*4.10*	*3.99*	5.20	3.66	3.49	3.59
O=F,Cl	0.02	0.07	0.07	0.11	0.10	0.08	0.01	0.12	0.08
Total	100.73	100.48	101.18	101.40	101.38	99.55	100.11	100.11	100.12
Si	5.02	5.44	5.50	5.38	5.40	5.48	5.43	5.39	5.43
Al iv	2.98	2.56	2.50	2.62	2.60	2.52	2.57	2.61	2.57
Al vi	1.02	0.89	0.86	0.89	0.95	1.16	0.90	0.89	0.87
Ti	0.15	0.21	0.20	0.15	0.16	0.16	0.19	0.19	0.26
Fe	2.57	2.35	2.34	2.31	2.26	2.18	2.42	2.42	2.42
Mn	0.01	0.01	0.01	0.01	0.00	0.00	0.01	0.01	0.01
Mg	2.24	2.23	2.26	2.43	2.40	2.10	2.26	2.29	2.14
Li*	0.07	0.07	0.07	0.06	0.06	0.08	0.07	0.07	0.07
Ca	0.01	0.01	0.01	0.00	0.00	0.00	0.01	0.01	0.00
Na	0.06	0.09	0.10	0.13	0.13	0.09	0.10	0.09	0.11
K	1.43	1.66	1.62	1.56	1.59	1.60	1.52	1.52	1.55
Ba	0.04	0.01	0.01	0.00	0.00	0.00	0.00	0.01	0.01
OH*	3.98	3.92	3.92	3.97	3.98	3.96	3.99	3.87	3.91
F	0.02	0.08	0.08	0.03	0.02	0.04	0.01	0.13	0.09

OBS: Abbreviations: Bt.Sch – biotite schist; St.sch – staurolite schist; g – biotite inside garnet; s – biotite inside staurolite; *based on 24 oxygen atoms and the formula $X_2Y_{4\text{-}6}Z_8O_{20}$ $(OH,F)_4$; Li_2O = [2.1/(0.356 + MgO)] – 0.088 de (Tischendorf *et al*. , 1999).

Table B. 14 - Chemical analysis (wt.%) and structural formulas* of biotites from patch-and banded metatexites.

Sample n^{er}	VC28	VC28	VC28	VC28	VC28	VC28	VC28	VC28	VC28	FM16
Anal. n^{er}	1	2	3	4	5	6	7	8	9	1
Type	PMM.l	PMM.l	PMM.l	PMM.m	PMM.m	PMM.m	PMM.m	PMM.m	PMM.m	BMM.m
SiO2	35.16	35.31	34.89	35.33	35.64	35.47	35.16	34.78	36.43	35.53
TiO2	3.74	3.68	3.32	2.64	3.33	3.42	3.03	3.79	3.20	3.73
Al2O3	19.92	19.86	20.30	20.06	19.97	20.04	20.29	19.74	20.33	19.72
FeO	18.57	18.56	18.72	18.41	18.58	18.53	19.15	19.00	18.22	18.95
MnO	0.25	0.29	0.23	0.18	0.31	0.23	0.18	0.23	0.30	0.20
MgO	9.07	9.14	9.04	9.61	9.55	9.60	8.41	8.00	9.20	7.66
CaO	0.01	0.02	0.03	0.03	0.03	0.02	0.02	0.00	0.02	0.00
Na2O	0.19	0.23	0.26	0.18	0.22	0.25	0.25	0.17	0.27	0.12
K2O	9.56	9.59	9.62	9.10	9.63	9.56	9.04	9.10	8.90	9.87
BaO	0.04	0.10	0.10	0.08	0.09	0.13	0.10	0.06	0.08	0.16
F	0.15	0.12	0.11	0.19	0.15	0.16	0.18	0.15	0.14	0.20
Cr2O3	0.07	0.13	0.11	0.06	0.14	0.12	0.07	0.07	0.08	0.00
Li2O*	0.13	0.13	0.14	0.12	0.12	0.12	0.15	0.16	0.13	0.17
H2O*	3.38	3.05	3.37	3.99	2.48	2.64	4.01	4.95	3.07	4.04
Subtotal	100.26	100.22	100.24	99.98	100.26	100.27	100.09	100.23	100.38	100.41
O=F,Cl	0.06	0.05	0.05	0.08	0.06	0.07	0.08	0.06	0.06	0.09
Total	100.20	100.17	100.19	99.90	100.20	100.20	100.01	100.17	100.33	100.32
Si	5.26	5.27	5.23	5.31	5.28	5.26	5.30	5.29	5.37	5.36
Al iv	2.74	2.73	2.77	2.69	2.72	2.74	2.70	2.71	2.63	2.64
Al vi	0.77	0.76	0.81	0.87	0.77	0.76	0.91	0.83	0.91	0.87
Ti	0.42	0.41	0.37	0.30	0.37	0.38	0.34	0.43	0.35	0.42
Fe	2.32	2.32	2.35	2.31	2.30	2.30	2.41	2.42	2.25	2.39
Mn	0.03	0.04	0.03	0.02	0.04	0.03	0.02	0.03	0.04	0.03
Mg	2.02	2.03	2.02	2.15	2.11	2.12	1.89	1.81	2.02	1.72
Li*	0.08	0.08	0.08	0.07	0.07	0.07	0.09	0.10	0.08	0.11
Ca	0.00	0.00	0.00	0.01	0.00	0.00	0.00	0.00	0.00	0.00
Na	0.06	0.07	0.08	0.05	0.06	0.07	0.07	0.05	0.08	0.03
K	1.82	1.82	1.84	1.75	1.82	1.81	1.74	1.77	1.67	1.90
Ba	0.00	0.01	0.01	0.00	0.01	0.01	0.01	0.00	0.00	0.01
OH*	3.93	3.94	3.94	3.91	3.93	3.93	3.91	3.93	3.93	3.90
F	0.07	0.06	0.05	0.09	0.07	0.07	0.09	0.07	0.06	0.10

Sample n^{er}	FM16	VC15	VC15	VC15	VC15	VC15	VC15
Anal. n^{er}	2	1	2	3	4	5	6
Type	BMM.l	BMM.m	BMM.m	BMM.l	BMM.l	BMM.l	BMM.l
SiO2	34.82	36.04	36.45	35.70	35.69	36.35	35.99
TiO2	3.67	4.05	4.36	4.15	4.40	2.58	3.12
Al2O3	19.17	20.23	20.19	20.07	20.01	20.79	20.51
FeO	19.22	19.14	19.40	19.67	20.38	18.64	18.83
MnO	0.13	0.28	0.25	0.12	0.31	0.20	0.19
MgO	8.02	7.82	7.89	7.69	7.92	9.17	9.05
CaO	0.00	0.00	0.00	0.00	0.20	0.00	0.00
Na2O	0.17	0.14	0.18	0.14	0.28	0.22	0.20
K2O	9.66	9.10	9.16	9.22	8.89	9.05	9.14
BaO	0.08	0.09	0.07	0.07	0.04	0.07	0.08
F	0.23	0.21	0.16	0.18	0.19	0.09	0.11
Cr2O3	0.00	0.06	0.07	0.08	0.03	0.02	0.09
Li2O*	0.16	0.17	0.17	0.17	0.17	0.13	0.14
H2O*	5.05	3.80	2.05	3.00	3.00	3.00	3.00
O=F,Cl	0.10	0.09	0.07	0.08	0.08	0.04	0.05
Total	100.30	101.04	100.35	100.22	101.43	100.30	100.40
Si	5.32	5.35	5.35	5.32	5.27	5.36	5.32
Al iv	2.68	2.65	2.65	2.68	2.73	2.64	2.68
Al vi	0.78	0.89	0.85	0.84	0.75	0.98	0.90
Ti	0.42	0.45	0.48	0.47	0.49	0.29	0.35
Fe	2.46	2.38	2.38	2.45	2.52	2.30	2.33
Mn	0.02	0.04	0.03	0.01	0.04	0.02	0.02
Mg	1.83	1.73	1.73	1.71	1.74	2.02	2.00
Li*	0.10	0.10	0.10	0.10	0.10	0.08	0.08
Ca	0.00	0.00	0.00	0.00	0.03	0.00	0.00
Na	0.05	0.04	0.05	0.04	0.08	0.06	0.06
K	1.88	1.72	1.72	1.75	1.67	1.70	1.72
Ba	0.00	0.00	0.00	0.00	0.00	0.00	0.00
OH*	3.89	3.90	3.93	3.91	3.91	3.95	3.95
F	0.11	0.10	0.07	0.09	0.09	0.04	0.05

OBS: Abbreviations: PPM.l – patch metatexite leucosome; PPM.m – patch-metatexite melanosome; BMM.l – banded metatexite leucosome; BMM.m – banded metatexite melanosome; *based on 24 oxygen atoms and the formula $X_2Y_{4-6}Z_8O_{20}(OH,F)_4$; $Li_2O = [2.1/(0.356 + MgO)] – 0.088$ (Tischendorf *et al*. , 1999).

Table B. 15 - Chemical analysis (wt.%) and structural formulas* of biotites from granitic rocks.

Sample n^{er}	VC60	VC60	VC60	VC60	VC60	VC60	VC52	VC62	VC62	VC62
Anal. n^{er}	1c	1b	2c	2b	3c	3b	1	1c	1b	2
Type	DTX	DTX	DTX	DTX	DTX	DTX	TL.Gnt	TL.Gnt	TL.Gnt	TL.Gnt
SiO2	35.29	35.59	35.14	35.56	35.27	35.17	34.01	35.82	35.02	35.40
TiO2	2.26	2.38	2.83	2.62	2.95	2.01	2.01	2.25	3.55	2.64
Al2O3	20.44	20.01	20.53	20.58	19.83	20.40	20.28	19.75	19.28	19.84
FeO	18.47	18.07	17.68	17.39	18.52	18.30	23.71	20.49	20.86	20.78
MnO	0.19	0.19	0.23	0.20	0.17	0.18	1.82	0.89	0.85	0.88
MgO	9.27	9.54	8.93	8.90	9.30	9.64	3.45	6.26	5.76	5.77
CaO	0.03	0.02	0.02	0.02	0.01	0.01	0.05	0.03	0.02	0.01
Na2O	0.13	0.12	0.11	0.19	0.23	0.20	0.18	0.06	0.07	0.06
K2O	9.52	9.59	9.64	9.58	9.50	9.57	9.19	9.47	9.41	9.49
BaO	0.06	0.00	0.08	0.00	0.11	0.08	0.02	0.09	0.00	0.09
F	0.02	0.02	0.00	0.00	0.00	0.02	0.15	0.21	0.20	0.25
Cr2O3	0.03	0.09	0.08	0.02	0.08	0.06	0.08	0.02	0.07	0.07
Li2O*	0.13	0.12	0.14	0.14	0.13	0.12	0.46	0.23	0.26	0.25
H2O*	4.29	4.39	4.72	4.92	4.02	4.36	5.09	4.70	5.00	4.84
Subtotal	100.14	100.13	100.14	100.14	100.13	100.13	100.53	100.32	100.34	100.36
O=F,Cl	0.01	0.01	0.00	0.00	0.00	0.01	0.06	0.09	0.08	0.10
Total	100.13	100.12	100.14	100.14	100.13	100.12	100.47	100.23	100.25	100.25
Si	5.31	5.35	5.30	5.36	5.31	5.30	5.32	5.48	5.39	5.43
Al iv	2.69	2.65	2.70	2.64	2.69	2.70	2.68	2.52	2.61	2.57
Al vi	0.94	0.90	0.95	1.01	0.82	0.93	1.07	1.04	0.89	1.02
Ti	0.26	0.27	0.32	0.30	0.33	0.23	0.24	0.26	0.41	0.30
Fe	2.33	2.27	2.23	2.19	2.33	2.31	3.10	2.62	2.69	2.67
Mn	0.02	0.02	0.03	0.03	0.02	0.02	0.24	0.12	0.11	0.11
Mg	2.08	2.14	2.01	2.00	2.08	2.17	0.80	1.43	1.32	1.32
Li*	0.08	0.08	0.08	0.08	0.08	0.07	0.29	0.14	0.16	0.16
Ca	0.01	0.00	0.00	0.00	0.00	0.00	0.01	0.00	0.00	0.00
Na	0.04	0.04	0.03	0.06	0.07	0.06	0.05	0.02	0.02	0.02
K	1.83	1.84	1.85	1.84	1.82	1.84	1.84	1.85	1.85	1.86
Ba	0.00	0.00	0.00	0.00	0.01	0.00	0.00	0.01	0.00	0.01
OH*	3.99	3.99	4.00	4.00	4.00	3.99	3.92	3.90	3.90	3.88
F	0.01	0.01	0.00	0.00	0.00	0.01	0.07	0.10	0.10	0.12
Sample n^{er}	FP21 z3	FP21 z6	VC22	VC22	VC22	VC22	VC22	VC22	VC39	VC39
Anal. n^{er}	1	2	1	2	3c	3b	4c	4b	5c	5b
Type	2m.Gnt	2m.Gnt	2m.Gnt	2m.Gnt	2m.Gnt	2m.Gnt	2m.Gnt	2m.Gnt	2m.Gnt	2m.Gnt
SiO2	35.52	36.09	35.68	35.79	35.75	35.52	35.94	35.44	35.26	36.23
TiO2	2.70	3.11	2.85	2.77	3.01	2.61	2.81	2.87	2.65	2.79
Al2O3	18.80	18.53	19.31	19.29	18.96	18.93	19.08	19.39	18.69	19.94
FeO	20.27	22.16	18.64	18.81	18.80	18.98	18.61	18.55	21.70	21.04
MnO	0.36	0.27	0.25	0.26	0.21	0.19	0.26	0.27	0.32	0.34
MgO	7.72	8.09	8.62	8.71	8.76	8.68	8.59	8.62	6.68	6.80
CaO	0.10	0.00	0.02	0.00	0.01	0.02	0.03	0.02	0.00	0.05
Na2O	0.00	0.24	0.15	0.18	0.14	0.13	0.16	0.16	0.09	0.27
K2O	8.62	8.74	9.69	9.71	9.66	9.75	9.72	9.66	8.46	9.24
BaO	0.02	0.02	0.00	0.00	0.11	0.02	0.00	0.08	0.08	0.07
F	0.18	0.19	0.14	0.11	0.14	0.14	0.11	0.13	0.17	0.19
Cr2O3	0.00	0.00	0.08	0.13	0.14	0.09	0.08	0.12	0.09	0.09
Li2O*	0.17	0.16	0.15	0.14	0.14	0.14	0.15	0.15	0.21	0.21
H2O*	4.93	3.30	4.61	4.27	4.36	5.00	4.59	4.76	4.10	3.00
O=F,Cl	0.09	0.08	0.06	0.05	0.06	0.06	0.05	0.06	0.07	0.08
Total	99.35	100.82	100.14	100.15	100.14	100.15	100.15	100.14	98.43	100.19
Si	5.46	5.42	5.41	5.41	5.41	5.42	5.44	5.38	5.46	5.43
Al iv	2.54	2.58	2.59	2.59	2.59	2.58	2.56	2.62	2.54	2.57
Al vi	0.87	0.69	0.86	0.84	0.80	0.82	0.85	0.85	0.88	0.96
Ti	0.31	0.35	0.32	0.31	0.34	0.30	0.32	0.33	0.31	0.31
Fe	2.61	2.78	2.36	2.38	2.38	2.42	2.36	2.36	2.81	2.64
Mn	0.05	0.03	0.03	0.03	0.03	0.02	0.03	0.03	0.04	0.04
Mg	1.77	1.81	1.95	1.96	1.98	1.97	1.94	1.95	1.54	1.52
Li*	0.11	0.10	0.09	0.09	0.09	0.09	0.09	0.09	0.13	0.12
Ca	0.02	0.00	0.00	0.00	0.00	0.00	0.00	0.00	0.00	0.01
Na	0.00	0.07	0.04	0.05	0.04	0.04	0.05	0.05	0.03	0.08
K	1.69	1.67	1.87	1.87	1.86	1.90	1.88	1.87	1.67	1.77
Ba	0.00	0.00	0.00	0.00	0.01	0.00	0.00	0.00	0.00	0.00
OH*	3.90	3.91	3.93	3.95	3.93	3.93	3.94	3.94	3.91	3.90
F	0.09	0.09	0.07	0.05	0.07	0.07	0.05	0.06	0.08	0.09

OBS: Abbreviations: DTX – diatexites; TL.Gnt – tourmaline bearing leucogranite; 2m.Gnt – two-mica granite. C – core; b – border; *Based on 24 oxygen atoms and the formula $X_2Y_{4\text{-}6}Z_8O_{20}$ $(OH,F)_4$; Li_2O = [2.1/(0.356 + MgO)] – 0.088 (Tischendorf *et al*., 1999).

Table B. 16 - Chemical analysis (wt.%) and structural formulas* of muscovites from MMC calc-silicate nodule, SGC metasediments and MMC metatexites.

Sample n^{er}	VC28e	VC28e	FP26	FM38	VC65	VC65	FM11	FM11	FM11	FM11	FM11
Anal. n^{er}	1	2	1	1	1	2	1	2	3	4	5
Type	CSN	CSN	Chl.Sch	Bt.Sch	St.Sch	St.Sch	St.Sch	St.Sch	St.Sch	St.Sch	St.Sch
SiO2	45.97	46.25	46.09	46.92	45.84	45.44	45.56	45.98	46.46	46.33	45.88
TiO2	0.17	0.33	0.29	0.42	0.85	0.93	0.12	0.42	0.65	0.47	0.20
Al2O3	37.89	36.64	36.41	36.83	36.75	36.59	37.47	37.05	36.17	36.35	36.96
FeO	0.73	0.74	1.72	0.79	1.03	0.78	0.54	0.70	0.65	0.63	0.69
MnO	0.24	0.46	0.10	0.00	0.02	0.00	0.00	0.00	0.00	0.00	0.01
MgO	0.28	0.45	0.98	0.63	0.55	0.48	0.42	0.39	0.43	0.56	0.45
CaO	0.34	0.12	0.12	0.09	0.03	0.04	0.03	0.00	0.02	0.00	0.02
Na2O	0.08	0.16	0.81	1.92	0.76	0.98	1.47	1.36	1.33	1.47	1.60
K2O	10.21	10.62	8.40	7.92	8.83	9.56	9.09	9.09	9.24	8.72	8.88
BaO	0.13	0.28	0.17	0.22	0.30	0.27	0.06	0.13	0.28	0.17	0.22
F	0.05	0.04	0.66	0.00	0.05	0.03	0.01	0.00	0.01	0.06	0.09
Li2O*	0.00	0.00	0.13	0.00	0.00	0.00	0.00	0.00	0.00	0.00	0.00
H2O*	4.54	4.52	4.24	4.59	4.94	4.83	5.15	4.81	4.68	5.14	4.94
O=F,Cl	0.02	0.02	0.28	0.00	0.02	0.01	0.00	0.00	0.00	0.03	0.04
Total	100.60	100.60	100.40	100.66	100.02	100.00	100.01	100.00	100.00	100.03	100.00
Si	6.04	6.11	6.07	6.13	6.07	6.04	6.04	6.08	6.14	6.13	6.08
Al iv	1.96	1.89	1.93	1.87	1.93	1.96	1.96	1.92	1.86	1.87	1.92
Al vi	3.91	3.81	3.73	3.79	3.80	3.76	3.89	3.85	3.78	3.80	3.85
Al VI - 2	1.91	1.81	1.73	1.79	1.80	1.76	1.89	1.85	1.78	1.80	1.85
Ti	0.02	0.03	0.03	0.04	0.08	0.09	0.01	0.04	0.07	0.05	0.02
Fe	0.08	0.08	0.19	0.09	0.11	0.09	0.06	0.08	0.07	0.07	0.08
Mn	0.03	0.05	0.01	0.00	0.00	0.00	0.00	0.00	0.00	0.00	0.00
Mg	0.05	0.09	0.19	0.12	0.11	0.10	0.08	0.08	0.08	0.11	0.09
Li*	0.00	0.00	0.07	0.00	0.00	0.00	0.00	0.00	0.00	0.00	0.00
Ca	0.05	0.02	0.02	0.01	0.00	0.01	0.00	0.00	0.00	0.00	0.00
Na	0.02	0.04	0.21	0.49	0.20	0.25	0.38	0.35	0.34	0.38	0.41
K	1.71	1.79	1.41	1.32	1.49	1.62	1.54	1.53	1.56	1.47	1.50
Sr	0.00	0.00	0.00	0.00	0.00	0.00	0.00	0.00	0.00	0.00	0.00
Ba	0.01	0.01	0.01	0.01	0.02	0.01	0.00	0.01	0.01	0.01	0.01
OH*	3.98	3.98	3.73	4.00	3.98	3.99	4.00	4.00	4.00	3.97	3.96
F	0.02	0.02	0.27	0.00	0.02	0.01	0.00	0.00	0.00	0.02	0.04

Sample n^{er}	VC52	VC28A	FM16	FM16	FM16	FM16
Anal. n^{er}	1	1	1	2	3	4
Type	MTX	MTX	MTX	MTX	MTX	MTX
SiO2	48.32	47.14	45.25	46.56	46.77	47.40
TiO2	0.82	0.42	1.51	0.02	0.02	0.08
Al2O3	36.71	38.88	35.44	36.69	33.94	34.56
FeO	1.61	1.22	0.80	0.50	1.78	1.44
MnO	0.39	0.19	0.00	0.06	0.00	0.00
MgO	1.15	0.92	0.49	0.02	0.79	0.88
CaO	0.26	0.11	0.05	0.00	0.15	0.02
Na2O	0.80	0.73	0.57	0.13	0.20	0.24
K2O	9.60	10.20	10.60	11.22	11.23	11.19
BaO	0.16	0.11	0.21	0.12	0.13	0.15
F	0.11	0.09	0.41	0.08	0.07	0.05
Li2O*	0.00	0.00	0.05	0.00	0.00	0.00
H2O*	0.00	0.00	4.29	4.48	4.43	4.50
O=F,Cl	0.05	0.04	0.17	0.03	0.03	0.02
Total	99.88	99.97	99.50	99.85	99.49	100.50
Si	6.13	5.97	6.06	6.18	6.28	6.28
Al iv	1.87	2.03	1.94	1.82	1.72	1.72
Al vi	3.62	3.78	3.65	3.91	3.65	3.68
Al VI - 2	1.62	1.78	1.65	1.91	1.65	1.68
Ti	0.08	0.04	0.15	0.00	0.00	0.01
Fe	0.17	0.13	0.09	0.06	0.20	0.16
Mn	0.04	0.02	0.00	0.01	0.00	0.00
Mg	0.22	0.17	0.10	0.00	0.16	0.17
Li*	0.00	0.00	0.03	0.00	0.00	0.00
Ca	0.04	0.01	0.01	0.00	0.02	0.00
Na	0.20	0.18	0.15	0.03	0.05	0.06
K	1.55	1.65	1.81	1.90	1.92	1.89
Sr	0.00	0.00	0.00	0.00	0.00	0.00
Ba	0.01	0.01	0.01	0.01	0.01	0.01
OH*	3.96	3.96	3.83	3.97	3.97	3.98
F	0.04	0.04	0.17	0.03	0.03	0.02

OBS: Abbreviations: CSN – calc-silicate nodule; Chl.Sch – chlorite schist; Bt.Sch – biotite-schist; St.Sch – staurolite schist; MTX – metatexites; *based on 24 oxygen atoms and the formula $X_2Y_{4-6}Z_8O_{20}$ $(OH,F)_4$; Li_2O was calculated from the equation: $Li_2O = 0.3935.F^{1.326}$ de TISCHENDORF *et al* . (1997).

Table B. 17 - Chemical analysis (wt.%) and structural formula* of muscovites from MMC granitic rocks.

Sample n^{er}	FM6	VC56	VC60	VC60	VC60	VC59	VC52	VC52	VC52	VC52	VC62	VC62
Anal. n^{er}	1	1	1	2	3	1	1	2	3	4	1	2
Type	DTX	DTX	DTX	DTX	DTX	DTX	TL.Gnt	TL.Gnt	TL.Gnt	TL.Gnt	TL.Gnt	TL.Gnt
SiO2	46.08	46.58	46.52	46.35	45.71	46.23	45.91	45.81	46.00	45.91	45.46	45.09
TiO2	1.10	1.06	0.63	0.33	0.59	0.13	1.28	0.39	0.68	0.22	0.03	0.09
Al2O3	36.18	35.52	36.51	36.69	36.25	36.86	35.05	35.29	34.59	35.12	35.89	35.20
FeO	1.22	1.25	0.87	1.25	0.86	1.16	1.68	1.56	1.72	1.58	0.97	1.36
MnO	0.00	0.00	0.00	0.24	0.01	0.10	0.07	0.10	0.12	0.09	0.08	0.06
MgO	0.95	0.92	0.53	0.79	0.49	0.74	0.54	0.48	0.60	0.46	0.38	0.72
CaO	0.00	0.00	0.03	0.06	0.02	0.08	0.04	0.06	0.02	0.03	0.01	0.03
Na2O	0.79	0.70	0.44	0.74	0.59	0.61	0.52	0.52	0.65	0.66	0.61	0.42
K2O	9.65	9.98	9.53	9.54	10.13	9.90	9.69	10.65	10.40	10.64	10.57	10.57
BaO	0.12	0.21	0.16	0.12	0.12	0.13	0.03	0.03	0.03	0.06	0.05	0.16
F	0.06	0.41	0.11	.09	0.08	0.12	0.09	0.05	0.07	0.07	0.04	0.08
Li2O*	0.00	0.05	0.00	0.00	0.00	0.00	0.00	0.00	0.00	0.00	0.00	0.00
H2O*	4.53	4.37	4.73	4.56	5.30	4.50	5.04	5.05	5.06	5.12	5.86	6.16
O=F,Cl	0.02	0.17	0.05	0.00	0.03	0.05	0.04	0.02	0.03	0.03	0.02	0.04
Total	100.7	101.1	100.1	100.6	100.2	100.9	100.0	100.0	100.0	100.0	100.0	100.0
Si	6.06	6.12	6.14	6.09	6.09	6.08	6.13	6.14	6.17	6.16	6.12	6.12
Al iv	1.94	1.88	1.86	1.91	1.91	1.92	1.87	1.86	1.83	1.84	1.88	1.88
Al vi	3.68	3.63	3.81	3.78	3.79	3.79	3.64	3.72	3.64	3.72	3.82	3.75
Al VI - 2	1.68	1.63	1.81	1.78	1.79	1.79	1.64	1.72	1.64	1.72	1.82	1.75
Ti	0.11	0.10	0.06	0.03	0.06	0.01	0.13	0.04	0.07	0.02	0.00	0.01
Cr	0.00	0.00	0.01	0.00	0.01	0.00	0.00	0.01	0.01	0.01	0.01	0.01
Fe	0.13	0.14	0.10	0.14	0.10	0.13	0.19	0.17	0.19	0.18	0.11	0.15
Mn	0.00	0.00	0.00	0.03	0.00	0.01	0.01	0.01	0.01	0.01	0.01	0.01
Mg	0.19	0.18	0.10	0.15	0.10	0.15	0.11	0.10	0.12	0.09	0.08	0.15
Li*	0.00	0.03	0.00	0.00	0.00	0.00	0.00	0.00	0.00	0.00	0.00	0.00
Ca	0.00	0.00	0.00	0.01	0.00	0.01	0.01	0.01	0.00	0.00	0.00	0.00
Na	0.20	0.18	0.11	0.19	0.15	0.16	0.13	0.13	0.17	0.17	0.16	0.11
K	1.62	1.67	1.60	1.60	1.72	1.66	1.65	1.82	1.78	1.82	1.82	1.83
Sr	0.00	0.00	0.00	0.00	0.00	0.00	0.00	0.00	0.00	0.00	0.00	0.00
Ba	0.01	0.01	0.01	0.00	0.01	0.01	0.00	0.00	0.00	0.00	0.00	0.01
OH*	3.98	3.83	3.95	4.00	3.97	3.95	3.96	3.98	3.97	3.97	3.98	3.96
F	0.02	0.17	0.05	0.00	0.03	0.05	0.04	0.02	0.03	0.03	0.02	0.04

Sample n^{er}	VC62	VC22	VC22	VC22	VC22	VC58	VC58	VC58	VC58	VC58	VC58	VC64
Anal. n^{er}	3	1c	1b	2c	2b	1	2-agl	3	4	5	6	7
Type	TL.Gnt	2m.Gnt	2m.Gnt	2m.Gnt	2m.Gnt	APG	APG	APG	APG	APG	APG	APG
SiO2	46.08	46.97	46.30	45.65	45.89	46.08	46.73	46.54	46.09	47.52	47.62	45.61
TiO2	0.32	1.07	0.95	1.31	0.92	0.48	0.12	0.09	0.00	0.12	0.13	0.41
Al2O3	35.08	34.89	34.28	34.31	34.81	35.76	35.97	37.03	36.26	36.57	37.21	37.64
FeO	1.10	0.97	1.04	1.06	1.01	1.86	0.98	1.14	1.67	0.90	1.03	2.03
MnO	0.04	0.05	0.00	0.00	0.00	0.38	0.00	0.12	0.23	0.00	0.35	0.19
MgO	0.62	0.89	0.78	0.87	0.83	0.49	0.71	0.21	0.43	0.38	0.17	0.52
CaO	0.02	0.01	0.01	0.03	0.02	0.23	0.07	0.08	0.07	0.19	0.16	0.16
Na2O	0.77	0.57	0.66	0.71	0.72	0.96	0.79	1.08	0.91	0.88	0.37	1.05
K2O	10.27	9.83	10.61	10.24	10.16	9.76	9.83	9.70	9.85	9.17	8.78	9.75
BaO	0.05	0.01	0.00	0.04	0.00	0.03	0.05	0.06	0.12	0.14	0.06	0.04
F	0.05	0.05	0.04	0.07	0.07	0.80	0.44	0.66	0.32	0.44	0.56	0.73
Li2O*	0.00	0.00	0.00	0.00	0.00	0.17	0.06	0.13	0.02	0.06	0.10	0.15
H2O*	5.54	4.61	5.23	5.68	5.49	4.16	4.33	4.26	4.37	4.38	4.34	4.25
O=F,Cl	0.02	0.02	0.02	0.03	0.03	0.34	0.19	0.28	0.13	0.19	0.24	0.31
Total	100.0	100.0	100.0	100.0	100.0	100.8	99.9	100.8	100.2	100.6	100.6	102.2
Si	6.18	6.21	6.20	6.14	6.15	6.09	6.18	6.11	6.11	6.21	6.20	5.95
Al iv	1.82	1.79	1.80	1.86	1.85	1.91	1.82	1.89	1.89	1.79	1.80	2.05
Al vi	3.73	3.65	3.62	3.59	3.65	3.66	3.79	3.83	3.78	3.85	3.91	3.73
Al VI - 2	1.73	1.65	1.62	1.59	1.65	1.66	1.79	1.83	1.78	1.85	1.91	1.73
Ti	0.03	0.11	0.10	0.13	0.09	0.05	0.01	0.01	0.00	0.01	0.01	0.04
Cr	0.00	0.01	0.01	0.01	0.01	0.00	0.00	0.00	0.00	0.00	0.00	0.00
Fe	0.12	0.11	0.12	0.12	0.11	0.21	0.11	0.13	0.19	0.10	0.11	0.22
Mn	0.00	0.01	0.00	0.00	0.00	0.04	0.00	0.01	0.03	0.00	0.04	0.02
Mg	0.12	0.18	0.16	0.17	0.17	0.10	0.14	0.04	0.09	0.07	0.03	0.10
Li*	0.00	0.00	0.00	0.00	0.00	0.09	0.03	0.07	0.01	0.03	0.05	0.08
Ca	0.00	0.00	0.00	0.00	0.00	0.03	0.01	0.01	0.01	0.03	0.02	0.02
Na	0.20	0.15	0.17	0.19	0.19	0.25	0.20	0.27	0.23	0.22	0.09	0.27
K	1.76	1.66	1.81	1.76	1.74	1.65	1.66	1.62	1.67	1.53	1.46	1.62
Sr	0.00	0.00	0.00	0.00	0.00	0.00	0.00	0.00	0.00	0.00	0.00	0.00
Ba	0.00	0.00	0.00	0.00	0.00	0.00	0.00	0.00	0.01	0.01	0.00	0.00
OH*	3.98	3.98	3.98	3.97	3.97	3.67	3.82	3.73	3.87	3.82	3.77	3.70
F	0.02	0.02	0.02	0.03	0.03	0.33	0.18	0.27	0.13	0.18	0.23	0.30

OBS: Abbreviations: DTX – diatexite; TL.Gnt – tourmaline bearing leucogranite; 2m.Gnt – two-mica granites; *Based on 24 oxygen atoms and the formula $X_2Y_{4-6}Z_8O_{20}$ $(OH,F)_4$; $Li_2O = 0.3935.F^{1.326}$ (TISCHENDORF *et al* ., 1997).

Table B. 18 - Chemical analysis (wt.%) and structural formulas* of staurolites from SGC staurolite-schists.

Sample n^{er}	FM11	FM11	FM11	FM11	FM11	FM11	FM11	FM11	FM11	FM11	FM11	FM11	FM11	FM11
Anal. n^{er}	a	b	c	d	e	1	3	3	4.	5	6	7	8	9
SiO2	27.39	27.68	27.48	28.10	27.76	27.32	27.63	27.53	27.76	27.88	27.77	28.26	27.79	28.67
TiO2	0.49	0.47	0.56	0.57	0.59	0.59	0.61	0.56	0.63	0.60	0.67	0.64	0.64	0.66
Al2O3	54.39	54.53	54.39	54.30	54.47	54.31	54.60	54.21	54.45	54.09	54.74	54.59	54.31	53.53
Cr2O3	0.10	0.07	0.07	0.08	0.09	0.05	0.08	0.13	0.09	0.12	0.13	0.14	0.17	0.12
FeO	12.90	13.01	12.90	12.87	12.48	12.97	12.65	13.16	12.52	12.86	12.50	12.37	12.79	11.82
MnO	0.33	0.28	0.27	0.26	0.26	0.25	0.25	0.26	0.25	0.23	0.29	0.22	0.22	0.22
MgO	1.66	1.68	1.66	1.96	1.65	0.78	1.61	1.70	1.81	1.81	1.54	1.54	1.90	1.63
ZnO	0.35	0.27	0.36	0.29	0.33	0.36	0.28	0.30	0.27	0.25	0.23	0.24	0.32	0.23
H2O	2.32	1.98	2.31	1.57	2.35	2.37	2.28	2.15	2.22	2.18	2.14	2.01	1.86	3.18
Total	99.9	100.0	100.0	100.0	100.0	99.0	100.0	100.0	100.0	100.0	100.0	100.0	100.0	99.7
Si	3.80	3.83	3.81	3.86	3.84	3.83	3.82	3.82	3.84	3.86	3.83	3.89	3.83	3.99
Ti	0.05	0.05	0.06	0.06	0.06	0.06	0.06	0.06	0.07	0.06	0.07	0.07	0.07	0.07
Al	8.90	8.88	8.89	8.80	8.88	8.97	8.90	8.86	8.87	8.82	8.90	8.85	8.83	8.77
Cr	0.01	0.01	0.01	0.01	0.01	0.01	0.01	0.01	0.01	0.01	0.01	0.01	0.02	0.01
Fe++	1.50	1.50	1.50	1.48	1.44	1.52	1.46	1.53	1.45	1.49	1.44	1.42	1.48	1.37
Mn	0.04	0.03	0.03	0.03	0.03	0.03	0.03	0.03	0.03	0.03	0.03	0.03	0.03	0.00
Mg	0.34	0.35	0.34	0.40	0.34	0.16	0.33	0.35	0.37	0.37	0.32	0.32	0.39	0.34
Ca	0.00	0.00	0.00	0.00	0.00	0.00	0.00	0.00	0.00	0.00	0.00	0.00	0.00	0.00
Na	0.00	0.00	0.01	0.00	0.00	0.00	0.00	0.00	0.00	0.00	0.00	0.00	0.00	0.01
K	0.00	0.00	0.00	0.00	0.00	0.00	0.00	0.00	0.00	0.00	0.00	0.00	0.00	0.00
Zn	0.04	0.03	0.04	0.03	0.03	0.04	0.03	0.03	0.03	0.03	0.02	0.02	0.03	0.00

Sample n^{er}	FM11	FM11	FM11	FM11	FM11	FM11	FM11	FM14	FM14	FM14	FM14	FM14	FM14
Anal. n^{er}	10	11	12	13	14	15	16	1	2	3	4	5	6
SiO2	27.79	27.39	26.91	27.77	27.27	27.92	27.47	27.43	27.77	28.14	28.08	27.58	28.34
TiO2	0.61	0.57	0.63	0.64	0.70	0.63	0.71	0.58	0.71	0.55	0.54	0.62	0.57
Al2O3	53.86	53.91	54.13	53.68	53.56	53.81	54.08	53.91	53.61	53.59	53.49	53.72	54.05
Cr2O3	0.08	0.10	0.07	0.10	0.14	0.10	0.10	0.11	0.17	0.07	0.06	0.10	0.07
FeO	12.47	12.71	12.78	12.93	12.88	12.09	12.41	12.78	13.12	12.67	13.25	13.10	12.25
MnO	0.26	0.24	0.27	0.28	0.26	0.24	0.25	0.35	0.21	0.19	0.20	0.18	0.19
MgO	1.60	1.82	1.80	1.82	1.84	1.73	1.61	1.56	1.92	1.93	1.95	1.91	1.81
ZnO	0.30	0.29	0.25	0.23	0.27	0.31	0.34	0.27	0.23	0.21	0.16	0.17	0.14
H2O	3.04	2.98	3.16	2.55	3.08	3.19	3.04	3.02	2.27	2.64	2.27	2.63	2.58
Total	100.0	100.0	100.0	100.0	100.0	100.0	100.0	100.0	100.0	100.0	100.0	100.0	100.0
Si	3.87	3.82	3.77	3.86	3.82	3.89	3.83	3.83	3.85	3.91	3.89	3.84	3.92
Ti	0.06	0.06	0.07	0.07	0.07	0.07	0.07	0.06	0.07	0.06	0.06	0.07	0.06
Al	8.84	8.87	8.93	8.79	8.83	8.83	8.89	8.87	8.77	8.77	8.74	8.81	8.81
Cr	0.01	0.01	0.01	0.01	0.02	0.01	0.01	0.01	0.02	0.01	0.01	0.01	0.01
Fe++	1.45	1.48	1.50	1.50	1.51	1.41	1.45	1.49	1.52	1.47	1.54	1.52	1.42
Mn	0.03	0.03	0.03	0.03	0.03	0.03	0.03	0.04	0.03	0.02	0.02	0.02	0.02
Mg	0.33	0.38	0.38	0.38	0.38	0.36	0.33	0.33	0.40	0.40	0.40	0.40	0.37
Ca	0.00	0.00	0.00	0.00	0.00	0.00	0.00	0.00	0.00	0.00	0.00	0.00	0.00
Na	0.00	0.00	0.00	0.00	0.00	0.00	0.00	0.00	0.00	0.00	0.00	0.00	0.00
K	0.00	0.00	0.00	0.00	0.00	0.00	0.00	0.00	0.00	0.00	0.00	0.00	0.00
Zn	0.03	0.03	0.03	0.02	0.03	0.03	0.03	0.03	0.02	0.02	0.02	0.02	0.01

OBS: *based on 23 Oxygen atoms and the formula $(Fe,Mg,Zn,Li)_2Al_9Si_4O_{22}(OH$

Table B. 19 - Chemical analysis (wt.%) and structural formulas* of tourmalines from SGC

Sample n^{er}	VC58	VC58	VC58	VC64	VC64	VC62b1	VC62	VC62	VC62	VC62	VC62	VC62	VC62	VC62	VC52	VC52
Anal. n^{er}	1.00	2.00	3.00	1.00	2.00	1.00	2.00	3.00	4.00	5.00	6.00	7.00	8.00	9.00	1c	2b
Type	APG	APG	APG	APG	APG	TL.Gnt	TL.Gnt	TL.Gnt	TL.Gnt	TL.Gnt	TL.Gnt	TL.Gnt	TL.Gnt	TL.Gnt	TL.Gnt	TL.Gnt
SiO2	36.09	36.63	36.08	36.09	36.16	36.54	36.40	36.06	36.22	36.15	36.38	36.33	36.44	36.40	35.71	36.36
TiO2	0.35	0.70	0.88	0.54	0.48	0.22	0.20	0.22	0.19	0.12	0.22	0.31	0.36	0.72	0.56	0.46
Al2O3	32.49	31.58	31.39	31.56	33.28	32.95	33.70	33.52	33.40	34.07	33.72	33.42	33.07	32.13	33.81	33.30
Cr2O3	n.d	n.d	n.d	n.d	n.d	0.07	0.05	0.07	0.07	0.04	0.06	0.10	0.04	0.07	0.03	0.06
FeO	12.62	11.74	13.27	12.55	11.56	9.09	9.78	10.05	9.55	10.19	9.71	9.90	9.91	9.57	9.19	9.41
MgO	1.63	2.74	1.55	2.27	2.01	3.95	2.72	3.09	3.37	2.47	3.14	2.81	3.14	4.01	3.53	3.63
CaO	0.20	0.32	0.15	0.23	0.24	0.06	0.03	0.06	0.06	0.04	0.06	0.05	0.05	0.09	0.07	0.08
MnO	0.36	0.59	0.71	0.50	0.22	0.10	0.18	0.17	0.21	0.19	0.18	0.22	0.12	0.16	0.13	0.18
ZnO	n.d.	n.d.	n.d.	n.d.	n.d.	0.08	0.11	0.05	0.12	0.09	0.11	0.08	0.07	0.01	0.05	0.06
Na2O	1.96	2.39	2.37	2.53	1.63	2.24	2.16	2.24	2.20	1.85	2.18	2.14	2.14	2.33	2.21	2.19
K2O	0.14	0.05	0.15	0.22	0.25	0.03	0.03	0.03	0.03	0.02	0.02	0.03	0.03	0.03	0.03	0.02
F	0.00	0.26	0.34	0.00	0.00	0.00	0.26	0.34	0.11	0.14	0.21	0.11	0.11	0.14	0.21	0.11
H2O	3.56	3.48	3.40	3.57	3.59	4.17	4.16	3.95	4.09	4.27	3.71	4.12	4.13	3.98	4.18	3.75
B2O3	10.33	10.44	10.32	10.35	10.41	10.50	10.50	10.50	10.50	10.50	10.50	10.50	10.50	10.50	10.50	10.50
O=F	0.00	0.11	0.14	0.00	0.00	0.00	0.00	0.00	0.00	0.00	0.00	0.00	0.00	0.00	0.00	0.00
Total	99.74	100.82	100.47	100.41	99.83	100.00	100.00	100.00	100.00	100.00	100.00	100.00	100.00	100.00	100.00	100.00
Si	6.07	6.10	6.07	6.06	6.04	6.00	5.99	5.96	5.97	5.95	6.01	5.99	6.00	6.01	5.87	6.00
Al	0.00	0.00	0.00	0.00	0.00	0.00	0.01	0.04	0.03	0.05	0.00	0.01	0.00	0.00	0.13	0.00
B	3.00	3.00	3.00	3.00	3.00	2.98	2.98	3.00	2.99	2.98	3.00	2.99	2.99	2.99	2.98	2.99
Al	6.00	6.00	6.00	6.00	6.00	6.00	6.00	6.00	6.00	6.00	6.00	6.00	6.00	6.00	6.00	6.00
Mg	0.00	0.00	0.00	0.00	0.00	0.00	0.00	0.00	0.00	0.00	0.00	0.00	0.00	0.00	0.00	0.00
Cr	0.00	0.00	0.00	0.00	0.00	0.00	0.00	0.00	0.00	0.00	0.00	0.00	0.00	0.00	0.00	0.00
Fe3+	0.00	0.00	0.00	0.00	0.00	0.00	0.00	0.00	0.00	0.00	0.00	0.00	0.00	0.00	0.00	0.00
Al	0.44	0.19	0.23	0.24	0.55	0.38	0.52	0.49	0.45	0.55	0.57	0.48	0.42	0.25	0.42	0.48
Ti	0.04	0.09	0.11	0.07	0.06	0.03	0.02	0.03	0.02	0.02	0.03	0.04	0.04	0.09	0.07	0.06
Mg	0.41	0.68	0.39	0.57	0.50	0.97	0.67	0.76	0.83	0.61	0.77	0.69	0.77	0.99	0.86	0.89
Mn	0.05	0.08	0.10	0.07	0.03	0.01	0.02	0.02	0.03	0.03	0.03	0.03	0.02	0.02	0.02	0.02
Fe2+	1.78	1.63	1.87	1.76	1.61	1.25	1.35	1.39	1.32	1.40	1.34	1.36	1.37	1.32	1.26	1.30
Zn	0.00	0.00	0.00	0.00	0.00	0.01	0.01	0.01	0.01	0.01	0.01	0.01	0.01	0.00	0.01	0.01
Li*	0.00	0.00	0.00	0.00	0.00	0.00	0.00	0.00	0.00	0.00	0.00	0.00	0.00	0.00	0.00	0.00
?Y	2.72	2.68	2.70	2.71	2.76	2.66	2.61	2.70	2.67	2.62	2.76	2.62	2.64	2.68	2.65	2.77
Ca	0.04	0.06	0.03	0.04	0.04	0.01	0.00	0.01	0.01	0.01	0.01	0.01	0.01	0.02	0.01	0.01
Ba	0.00	0.00	0.00	0.00	0.00	0.00	0.00	0.00	0.00	0.00	0.00	0.00	0.00	0.00	0.00	0.00
Na	0.64	0.77	0.77	0.82	0.53	0.71	0.69	0.72	0.70	0.59	0.70	0.68	0.68	0.75	0.70	0.70
K	0.03	0.01	0.03	0.05	0.05	0.01	0.01	0.01	0.01	0.00	0.00	0.01	0.01	0.01	0.01	0.00
Rb	0.00	0.00	0.00	0.00	0.00	0.00	0.00	0.00	0.00	0.00	0.00	0.00	0.00	0.00	0.00	0.00
Cs	0.00	0.00	0.00	0.00	0.00	0.00	0.00	0.00	0.00	0.00	0.00	0.00	0.00	0.00	0.00	0.00
r	0.29	0.16	0.17	0.09	0.38	0.27	0.30	0.26	0.28	0.40	0.29	0.30	0.30	0.23	0.28	0.28
OH	4.00	3.86	3.82	4.00	4.00	4.57	4.57	4.35	4.49	4.68	4.09	4.53	4.54	4.38	4.58	4.13
F	0.00	0.14	0.18	0.00	0.00	0.00	0.00	0.00	0.00	0.00	0.00	0.00	0.00	0.00	0.00	0.00
Cl	0.00	0.00	0.00	0.00	0.00	0.00	0.00	0.00	0.00	0.00	0.00	0.00	0.00	0.00	0.00	0.00
Mineral	Sch.I	Sch.I	Sch.I	Sch.I	Sch.I	Sch.I	Sch.I	Sch.I	Sch.I	Sch.I	Sch.I	Sch.I	Sch.I	Sch.I	Sch.I	Sch.I

OBS: Abbreviations: APG – aplitopegmatite; TL.Gnt – tourmaline bearing leucogranite.

Annex C – Geochemical data

Table C. 1 - Chemical composition of samples from Sector 1 – Metagreywackes and CSR

Sample	VC50c	FM21b	FM16b	VC47	VC48	FM16a	FM21a	GC2	VC50	VC50a	GC2a	VC50b	GC2b
Type	GWK	GWK	GWK	GWK	CSR	CSR	CSR	CSR	CSR	CSN-CZ	CSN-OZ	CSN-CZ	CSN-OZ
SiO2	75.9	74.2	73.0	73.6	59.7	57.5	67.2	63.1	67.9	63.96	66.80	71.83	59.47
Al2O3	11.6	12.2	12.0	11.8	19.2	15.2	14.4	12.9	12.3	12	10.79	12.54	15.04
Fe2O3t	3.6	3.5	4.1	3.8	4.2	4.9	4.1	6.2	4.1	4.98	5.92	3.22	6.51
MnO	0.1	0.1	0.1	0.1	0.3	0.3	0.2	0.4	0.4	0.613	0.47	0.158	0.35
MgO	1.2	1.3	1.6	1.3	1.7	1.7	1.4	1.2	1.1	1	0.42	1.24	1.88
CaO	2.0	2.9	3.0	2.0	13.1	12.9	8.9	12.7	9.4	12.88	13.76	6	11.61
Na2O	2.8	2.6	2.4	2.6	0.5	0.4	0.6	0.5	0.5	0.5	0.28	0.53	0.67
K2O	1.4	1.4	1.5	1.6	0.3	1.1	0.7	0.8	0.9	0.73	0.23	1.16	1.40
TiO2	0.5	0.5	0.6	0.5	0.6	0.6	0.7	0.6	0.5	0.492	0.52	0.561	0.71
P2O5	0.1	0.1	0.1	0.1	0.3	0.4	0.3	0.1	0.2	0.17	0.09	0.25	0.19
LOI	0.7	0.4	0.5	1.1	1.0	3.8	0.7	2.7	2.6	3.5	2.26	1.66	3.10
Total	99.7	99.2	98.7	98.6	100.7	98.8	99.0	100.9	100.0	100.8	100.80	99.14	100.90
Sc	9.0	8.0	9.0	9.0	9.0	11.0	11.0	9.5	8.0	8.00	7.00	8.00	12.00
Be	2.0	2.0	2.0	2.0	4.0	3.0	3.0	4.0	3.0	2.00	4.00	4.00	4.00
V	58.0	56.0	64.0	61.0	83.0	78.0	72.0	75.5	56.5	60	65.00	53	86.00
Ba	101.0	189.0	206.0	156.0	16.0	66.0	75.0	18.5	139.0	156	6.00	122	31.00
Sr	203.0	274.0	260.0	185.0	199.0	181.0	213.0	149.5	213.0	139	61.00	287	238.00
Y	18.0	20.0	16.0	18.0	34.0	53.0	40.0	43.0	35.0	40	49.00	30	37.00
Zr	256.0	197.0	181.0	237.0	137.0	180.0	273.0	250.5	230.5	213	263.00	248	238.00
Cr	80.0	120.0	120.0	50.0	300.0	320.0	290.0	185.0	150.0	140	120.00	160	250.00
Co	8.0	9.0	10.0	8.0	10.0	10.0	11.0	6.0	8.0	7	4.00	9	8.00
Ni	20.0	30.0	30.0	20.0	20.0	60.0	60.0	45.0	35.0	30	30.00	40	60.00
Cu	10.0	10.0	10.0	10.0	70.0	10.0	30.0	15.0	15.0	10	10.00	20	20.00
Zn	80.0	60.0	70.0	60.0	40.0	6.0	50.0	60.0	50.0	50	50.00	50	70.00
Ga	15.0	15.0	14.0	15.0	40.0	26.0	22.0	19.5	18.0	19	17.00	17	22.00
Ge	2.0	2.0	2.0	2.0	4.0	3.0	2.0	4.0	2.5	3	5.00	2	3.00
As	5.0	5.0	5.0	5.0	19.0	13.0	5.0	5.0	5.0	5	5.00	5	5.00
Rb	79.0	76.0	83.0	77.0	6.0	43.0	30.0	19.5	26.5	18	7.00	35	32.00
Mo	2.0	2.0	2.0	2.0	2.0	3.0	3.0	4.0	2.0	2	3.00	2	5.00
Ag	0.5	0.7	0.7	1.3	0.7	0.7	1.0	1.6	0.5	0.5	1.60	0.5	1.60
In	0.2	0.2	0.2	0.3	0.2	0.2	0.2	0.2	0.2	0.2	0.2	0.2	0.2
Sn	3.0	2.0	2.0	21.0	7.0	9.0	4.0	11.5	7.0	10	13.00	4	10.00
Sb	0.5	0.5	0.5	1.0	0.5	0.5	0.5	0.5	1.1	0.5	0.5	1.7	0.5
Cs	5.5	4.1	4.3	5.4	0.8	1.5	2.8	1.3	2.1	1.5	0.5	2.6	2.00
La	31.4	30.8	25.2	34.4	31.3	49.2	43.1	33.1	37.5	43.7	39.70	31.3	26.40
Ce	63.1	62.1	53.0	67.9	65.2	92.2	84.9	64.5	67.0	67.2	71.40	66.8	57.50
Pr	6.9	7.1	6.3	7.7	6.9	10.2	9.5	7.5	8.2	9.1	8.31	7.39	6.75
Nd	26.3	26.0	23.6	27.2	27.0	39.1	34.7	30.0	30.8	34.3	33.10	27.3	26.90
Sm	5.2	5.0	4.6	5.2	5.5	8.8	7.4	6.9	6.2	6.8	7.30	5.5	6.40
Eu	1.1	1.2	1.0	1.1	1.3	1.9	1.7	1.6	1.2	1.51	1.87	0.93	1.36
Gd	4.2	4.1	3.8	4.3	5.6	8.8	7.0	7.3	5.5	6.7	7.90	4.3	6.60
Tb	0.6	0.7	0.6	0.7	0.9	1.6	1.2	1.3	1.0	1.1	1.40	0.8	1.10
Dy	3.4	3.8	3.5	3.4	5.4	9.3	7.3	7.3	5.8	6.2	8.00	5.3	6.60
Ho	0.6	0.8	0.7	0.7	1.1	2.0	1.5	1.5	1.2	1.2	1.70	1.1	1.30
Er	1.7	2.2	2.0	1.9	3.1	5.6	4.3	4.3	3.3	3.5	4.80	3.1	3.80
Tm	0.3	0.4	0.3	0.3	0.5	0.9	0.7	0.6	0.5	0.57	0.67	0.45	0.60
Yb	1.8	2.2	2.1	1.9	3.3	5.7	4.4	4.1	3.4	3.7	4.20	3	4.00
Lu	0.3	0.4	0.3	0.3	0.6	0.9	0.7	0.6	0.5	0.58	0.62	0.46	0.61
Hf	5.8	5.3	5.2	6.0	3.6	5.3	7.8	6.5	5.7	5.2	6.80	6.2	6.10
Ta	0.9	0.9	0.9	3.7	0.8	1.0	1.2	0.7	0.7	0.6	0.50	0.8	0.80
Nb	10.0	12.0	10.0	16.0	20.0	15.0	17.0	10.0	11.0	11	6.00	11	14.00
W	1.0	3.0	3.0	1.0	4.0	10.0	7.0	6.5	40.5	73	5.00	8	8.00
Tl	0.5	0.5	0.6	0.6	0.1	0.3	0.2	0.1	0.3	0.3	0.1	0.3	0.10
Pb	13.0	15.0	12.0	173.0	5.0	5.0	5.0	5.0	5.0	5	5.00	5	5.00
Bi	0.4	0.4	0.4	2.9	0.5	0.4	0.4	0.4	0.4	0.4	0.4	0.4	0.4
Th	11.6	11.2	9.5	11.0	8.0	10.8	14.6	9.6	11.6	10.1	10.30	13.1	8.80
U	3.0	2.8	2.4	2.9	2.7	3.8	4.0	3.3	2.9	2.6	3.50	3.2	3.10

Table C. 2 - Chemical composition of samples from Sector 1 - Metatexites

Sample	VC37d	VC28	FM23	FM4a	VC6a	VC27b	FM18	FP46a	FP46c	FM16c	FP21c	FM22
Type	PMM	PMM	BMM	BMM	BMM	BMM	BMM	BMM	BMM	BMM	BMM	BMM
SiO2	57.4	61.0	55.4	59.2	63.8	67.7	71.9	64.3	65.9	68.4	65.1	68.4
Al2O3	18.1	19.3	21.0	17.7	16.2	14.7	13.6	14.7	14.3	15.4	15.2	15.0
Fe2O3t	7.9	8.5	8.8	8.2	7.5	5.9	3.9	6.5	5.4	4.3	6.3	4.3
MnO	0.1	0.1	0.1	0.1	0.1	0.1	0.0	0.1	0.1	0.1	0.1	0.0
MgO	3.0	2.9	3.4	3.2	2.9	2.0	1.5	2.5	2.0	1.7	2.6	1.6
CaO	2.5	0.5	0.4	1.1	0.7	0.4	1.3	1.3	2.2	1.6	1.9	1.3
Na2O	3.4	1.0	1.4	2.1	1.7	1.4	2.7	2.5	3.1	2.6	3.2	2.3
K2O	3.5	3.7	6.1	3.4	3.6	3.5	2.5	2.8	2.1	3.1	2.7	4.0
TiO2	1.1	1.1	1.1	1.0	0.9	0.8	0.6	0.9	0.9	0.5	0.8	0.6
P2O5	0.1	0.2	0.1	0.2	0.1	0.1	0.1	0.2	0.2	0.3	0.2	0.4
LOI	2.0	1.5	1.6	2.5	2.4	2.4	0.7	2.5	2.2	0.9	1.2	0.8
Total	99.1	99.4	99.3	98.6	99.9	98.8	98.8	98.4	98.3	98.7	99.4	98.7
Sc	21.0	21.0	24.0	20.0	17.0	17.0	10.0	17.0	16.0	9.0	15.0	12.0
Be	1.0	2.0	2.0	2.0	3.0	1.0	2.0	3.0	3.0	8.0	3.0	2.0
V	150.0	156.0	150.0	167.0	131.0	112.0	55.0	127.0	106.0	66.0	112.0	72.0
Ba	612.0	794.0	1006.0	380.0	584.0	571.0	289.0	365.0	394.0	445.0	498.0	600.0
Sr	298.0	119.0	90.0	144.0	126.0	93.0	180.0	143.0	165.0	190.0	243.0	201.0
Y	36.0	39.0	27.0	26.0	26.0	29.0	17.0	23.0	26.0	19.0	33.0	30.0
Zr	281.0	279.0	173.0	288.0	215.0	224.0	236.0	203.0	195.0	215.0	196.0	216.0
Cr	290.0	190.0	170.0	140.0	130.0	370.0	140.0	120.0	100.0	190.0	90.0	140.0
Co	18.0	22.0	24.0	18.0	24.0	8.0	10.0	9.0	5.0	9.0	14.0	11.0
Ni	20.0	60.0	60.0	60.0	70.0	20.0	40.0	20.0	< 20	40.0	40.0	30.0
Cu	10.0	30.0	20.0	30.0	20.0	20.0	10.0	30.0	20.0	10.0	10.0	10.0
Zn	160.0	300.0	230.0	160.0	170.0	110.0	90.0	150.0	100.0	90.0	140.0	80.0
Ga	25.0	27.0	40.0	25.0	21.0	19.0	20.0	22.0	18.0	20.0	22.0	24.0
Ge	2.0	2.0	2.0	2.0	2.0	3.0	2.0	3.0	2.0	2.0	2.0	1.0
As	5.0	5.0	5.0	5.0	5.0	6.0	5.0	5.0	< 5	5.0	20.0	5.0
Rb	153.0	148.0	237.0	164.0	169.0	205.0	107.0	177.0	118.0	110.0	225.0	127.0
Mo	2.0	2.0	2.0	2.0	2.0	2.0	2.0	2.0	< 2	2.0	2.0	2.0
Ag	2.1	0.5	0.6	1.9	1.3	0.5	0.9	0.5	< 0.5	0.8	1.3	0.7
In	0.2	0.2	0.2	0.2	0.2	0.2	0.2	0.2	< 0.2	0.2	0.2	0.2
Sn	6.0	3.0	7.0	4.0	4.0	8.0	3.0	4.0	3.0	4.0	6.0	4.0
Sb	0.6	0.5	0.5	0.5	0.5	0.5	0.5	0.5	< 0.5	0.5	0.5	0.5
Cs	7.2	7.5	11.9	10.4	11.6	85.7	6.9	10.2	7.9	7.4	14.6	5.2
La	35.0	41.4	49.3	54.4	38.0	37.7	33.3	29.6	24.1	31.6	34.0	35.1
Ce	76.6	85.5	98.9	109.0	79.3	76.4	67.2	62.5	53.7	63.8	73.3	71.6
Pr	8.5	10.1	11.6	12.5	8.8	8.5	7.7	7.6	6.2	7.5	8.2	8.4
Nd	34.6	40.9	42.7	47.9	34.2	32.2	28.5	28.8	24.3	27.8	32.8	31.6
Sm	7.0	9.0	8.2	9.5	7.0	6.6	5.6	6.1	5.2	5.9	7.0	6.8
Eu	1.8	1.2	1.3	1.4	1.5	1.3	1.2	1.4	1.5	1.3	1.4	1.4
Gd	6.5	6.9	6.5	7.6	5.9	5.1	4.4	5.1	4.6	5.1	6.5	6.1
Tb	1.1	1.2	1.0	1.1	0.9	0.8	0.7	0.8	0.8	0.8	1.1	1.1
Dy	6.5	7.2	5.4	6.0	5.3	5.0	3.8	4.5	4.6	4.6	6.5	6.3
Ho	1.3	1.5	1.1	1.1	1.1	1.1	0.7	0.8	0.9	0.8	1.3	1.2
Er	3.9	4.4	3.1	3.2	3.1	3.3	1.9	2.4	2.7	2.0	3.7	3.0
Tm	0.6	0.7	0.5	0.5	0.5	0.6	0.3	0.4	0.4	0.3	0.5	0.5
Yb	4.1	4.4	3.0	3.2	3.0	3.7	1.7	2.7	3.1	1.5	3.5	2.6
Lu	0.7	0.7	0.5	0.5	0.5	0.6	0.3	0.5	0.5	0.2	0.6	0.4
Hf	7.8	7.1	5.0	7.5	5.6	5.3	6.4	5.1	4.4	6.2	5.2	5.9
Ta	1.1	0.9	2.3	1.2	0.9	1.0	0.8	1.0	0.8	0.8	1.0	1.1
Nb	16.0	14.0	29.0	16.0	13.0	11.0	12.0	12.0	10.0	11.0	13.0	14.0
W	2.0	3.0	6.0	2.0	2.0	3.0	3.0	2.0	2.0	5.0	3.0	4.0
Tl	0.9	1.2	1.4	1.0	1.1	1.7	0.7	1.4	1.0	0.7	1.8	0.8
Pb	28.0	31.0	21.0	18.0	19.0	24.0	24.0	20.0	22.0	32.0	17.0	29.0
Bi	0.4	0.4	0.4	0.4	0.4	0.6	0.4	0.5	0.8	0.4	< 0.4	0.4
Th	13.4	13.3	16.7	16.8	11.1	11.0	12.2	8.4	7.0	10.8	9.2	12.1
U	3.7	3.8	5.3	4.8	3.0	3.5	4.2	2.8	2.6	4.4	3.5	4.3

Table C. 3 – Chemical composition of samples from Sector 1 – Diatexites (DTX) and leucogranites (L.Gnt)

Sample	FM6a	VC60	VC59	FP37	FP46b	VC8	FM19	VC43a	VC3	VC52	VC68	FP44b	VC2a	VC55
Type	DTX	DTX	DTX	DTX	DTX	LCS	LCS	TL.Gnt	TL.Gnt	TL.Gnt	L.Gnt	L.Gnt	L.Gnt	L.Gnt
SiO2	72.9	74.1	72.8	70.6	74.0	72.2	71.2	74.9	73.3	73.3	74.1	78.2	74.0	74.0
Al2O3	13.5	13.3	14.4	14.9	13.8	14.5	15.5	13.0	15.1	14.4	16.0	12.1	14.5	13.4
Fe2O3t	2.9	1.8	1.6	2.2	1.8	1.2	2.0	1.0	1.3	1.3	0.4	0.7	0.5	0.3
MnO	0.0	0.0	0.0	0.0	0.0	0.0	0.0	0.0	0.0	0.0	0.0	0.0	0.0	0.0
MgO	1.1	0.7	0.6	0.7	0.6	0.5	0.7	0.2	0.4	0.1	0.1	0.2	0.2	0.1
CaO	1.1	1.0	0.9	0.8	0.6	0.6	0.6	0.4	0.7	0.5	0.4	0.1	0.5	0.2
Na2O	2.4	2.3	1.9	2.7	2.1	2.4	2.1	3.4	3.3	4.5	5.8	2.3	3.6	2.1
K2O	4.7	4.8	4.6	4.9	3.5	6.6	6.8	4.5	4.1	3.0	1.4	3.3	5.5	7.4
TiO2	0.4	0.3	0.2	0.3	0.3	0.2	0.2	0.1	0.1	0.0	0.0	0.1	0.1	0.0
P2O5	0.3	0.3	0.3	0.1	0.1	0.4	0.1	0.3	0.1	0.2	0.1	0.1	0.3	0.2
LOI	0.8	1.3	1.1	1.4	1.6	1.1	1.1	0.6	1.0	1.1	1.3	1.6	0.8	0.7
Total	100.1	100.0	98.4	98.6	98.3	99.6	100.3	98.2	99.5	98.3	99.7	98.7	99.9	98.3
Sc	7.0	4.0	4.0	7.0	4.0	3.0	4.0	2.0	4.0	2.0	1.0	3.0	2.0	1.0
Be	2.0	9.0	3.0	2.0	2.0	5.0	2.0	5.0	12.0	13.0	11.0	2.0	2.0	10.0
V	52.0	22.0	24.0	36.0	29.0	17.0	13.0	9.0	14.0	6.0	8.0	9.0	9.0	5.0
Ba	736.0	702.0	842.0	730.0	618.0	913.0	1258.0	117.0	359.0	89.0	329.0	912.0	420.0	624.0
Sr	215.0	201.0	199.0	175.0	122.0	190.0	252.0	69.0	212.0	58.0	341.0	77.0	94.0	123.0
Y	18.0	18.0	30.0	10.0	7.0	18.0	8.0	3.0	10.0	5.0	2.0	4.0	16.0	2.0
Zr	158.0	91.0	135.0	102.0	110.0	34.0	6.0	30.0	41.0	29.0	4.0	23.0	60.0	18.0
Cr	80.0	80.0	90.0	60.0	50.0	90.0	270.0	330.0	20.0	580.0	50.0	280.0	60.0	20.0
Co	6.0	3.0	2.0	4.0	2.0	2.0	3.0	1.0	1.0	1.0	1.0	2.0	1.0	1.0
Ni	20.0	20.0	20.0	20.0	20.0	20.0	20.0	20.0	20.0	20.0	20.0	< 20	20.0	20.0
Cu	10.0	10.0	10.0	10.0	10.0	10.0	10.0	10.0	10.0	10.0	10.0	< 10	10.0	10.0
Zn	60.0	50.0	40.0	50.0	40.0	30.0	30.0	40.0	30.0	40.0	30.0	< 30	30.0	30.0
Ga	17.0	14.0	16.0	17.0	18.0	12.0	14.0	17.0	21.0	16.0	12.0	12.0	12.0	13.0
Ge	1.0	1.0	2.0	2.0	2.0	1.0	2.0	2.0	2.0	4.0	2.0	2.0	2.0	1.0
As	5.0	5.0	5.0	< 5	5.0	5.0	5.0	5.0	9.0	7.0	5.0	< 5	5.0	5.0
Rb	134.0	113.0	113.0	122.0	94.0	129.0	133.0	230.0	154.0	215.0	36.0	115.0	139.0	255.0
Mo	2.0	2.0	2.0	< 2	2.0	2.0	2.0	2.0	2.0	3.0	2.0	< 2	2.0	2.0
Ag	1.1	0.8	1.1	< 0.5	0.5	0.5	0.5	0.5	0.5	0.5	0.5	< 0.5	0.5	0.5
In	0.2	0.2	0.2	< 0.2	0.2	0.2	0.2	0.2	0.2	0.2	0.2	< 0.2	0.2	0.2
Sn	6.0	3.0	4.0	8.0	3.0	7.0	5.0	6.0	23.0	51.0	16.0	9.0	8.0	8.0
Sb	0.5	0.5	0.5	< 0.5	0.5	0.5	0.5	0.5	0.5	0.5	0.5	1.3	0.5	0.5
Cs	5.8	3.3	5.1	6.6	2.9	4.3	4.3	9.9	15.5	37.6	2.9	5.3	6.2	7.7
La	25.0	14.8	16.6	21.0	23.5	12.9	3.9	5.5	9.5	5.0	1.4	7.3	7.8	1.7
Ce	51.8	30.9	34.1	43.5	46.9	27.8	7.6	11.3	19.2	9.4	2.3	12.7	16.2	3.1
Pr	5.8	3.7	4.1	4.8	5.3	3.2	0.8	1.3	2.2	1.1	0.2	1.7	1.8	0.3
Nd	22.5	13.7	16.0	18.0	20.4	12.8	3.0	4.5	7.9	4.1	0.7	5.8	7.0	1.2
Sm	4.6	3.4	4.2	3.8	4.2	3.3	0.7	1.0	2.0	1.1	0.2	1.3	1.8	0.3
Eu	1.4	1.2	1.2	1.2	0.9	1.3	1.4	0.4	1.0	0.3	0.1	0.5	0.7	0.4
Gd	4.2	3.4	4.3	3.0	2.9	3.4	0.8	0.8	2.0	0.9	0.1	0.9	2.0	0.3
Tb	0.7	0.6	0.8	0.4	0.4	0.7	0.2	0.1	0.4	0.2	0.1	0.1	0.5	0.0
Dy	3.9	3.4	5.4	2.1	1.8	4.0	1.3	0.5	2.2	0.9	0.1	0.8	2.9	0.2
Ho	0.7	0.6	1.1	0.4	0.3	0.7	0.3	0.1	0.4	0.2	0.1	0.2	0.6	0.1
Er	1.8	1.7	3.2	1.0	0.7	1.8	1.0	0.3	1.0	0.4	0.1	0.5	1.6	0.1
Tm	0.2	0.2	0.5	0.2	0.1	0.3	0.2	0.1	0.1	0.1	0.1	0.1	0.3	0.1
Yb	1.4	1.3	3.1	1.0	0.6	1.4	1.1	0.3	0.9	0.5	0.1	0.6	1.7	0.1
Lu	0.2	0.2	0.5	0.2	0.1	0.2	0.2	0.1	0.1	0.1	0.0	0.1	0.3	0.0
Hf	4.2	2.2	3.9	2.6	2.6	1.0	0.2	1.0	1.4	0.9	0.2	0.7	1.9	0.9
Ta	0.7	0.3	0.4	0.8	0.2	0.4	0.3	1.1	1.4	4.0	0.4	0.6	0.4	0.1
Nb	9.0	4.0	3.0	6.0	4.0	3.0	4.0	2.0	8.0	6.0	2.0	3.0	2.0	1.0
W	3.0	1.0	1.0	2.0	1.0	3.0	3.0	3.0	2.0	5.0	2.0	2.0	3.0	1.0
Tl	0.8	0.7	0.7	1.0	0.8	0.7	0.8	1.4	0.8	1.8	0.3	1.1	0.9	1.6
Pb	41.0	46.0	44.0	47.0	29.0	54.0	61.0	31.0	103.0	36.0	49.0	29.0	50.0	44.0
Bi	0.4	0.4	0.4	0.6	0.4	0.4	0.4	1.8	3.2	0.9	14.2	5.4	0.4	10.1
Th	8.5	4.2	4.9	7.1	10.0	3.6	1.2	2.3	2.9	2.3	0.4	2.2	2.2	0.5
U	3.4	2.2	3.8	3.0	3.7	2.6	1.0	4.6	4.0	3.5	0.3	1.5	2.8	1.6

Table C. 4 - Chemical composition of samples from Sector 1 – Two-mica granites (2m.Gnt), fine-grained granites (F.Gnt), porphyritic granites (P.Gnt) and aplite-pegmatites (APG).

Sample	VC39	VC22	VC34a	VC45	FP21B	FP21A	FP30a	FP49	FP59	VC32	VC16	A12	A13	A21	VC64	VC58
Type	2m.Gnt	2m.Gnt	2m.Gnt	2m.Gnt	2m.Gnt	2m.Gnt	2m.Gnt	2m.Gnt	2m.Gnt	F.Gnt	F.Gnt	P.Gnt	P.Gnt	P.Gnt	APG	APG
SiO2	74.4	71.7	70.4	72.3	72.6	74.3	73.5	72.8	71.9	72.5	74.1	73.3	71.2	71.9	73.9	74.3
Al2O3	14.2	15.2	15.0	15.3	15.0	14.7	13.9	14.4	14.4	14.2	13.9	14.9	15.7	14.8	14.6	14.6
Fe2O3t	1.3	2.0	1.7	1.6	1.6	1.2	1.1	1.6	1.5	1.4	1.5	0.3	0.9	1.6	0.8	0.9
MnO	0.0	0.0	0.0	0.0	0.0	0.0	0.0	0.0	0.0	0.0	0.0	0.0	0.0	0.0	0.1	0.1
MgO	0.3	0.7	0.4	0.4	0.4	0.3	0.3	0.4	0.3	0.4	0.3	0.4	0.3	0.4	0.1	0.2
CaO	0.6	0.6	0.5	0.6	0.9	0.3	0.2	0.4	0.2	0.7	0.5	0.3	0.4	0.7	0.3	0.4
Na2O	2.9	3.0	2.5	3.4	3.2	2.7	2.2	2.7	2.3	2.7	2.9	3.1	2.8	3.5	4.5	4.3
K2O	5.5	4.6	6.0	5.1	5.5	5.2	5.1	4.9	5.2	5.6	4.8	4.9	5.2	4.7	3.4	2.5
TiO2	0.2	0.3	0.2	0.2	0.2	0.2	0.2	0.2	0.2	0.2	0.1	0.2	0.2	0.2	0.0	0.0
P2O5	0.4	0.3	0.4	0.4	0.3	0.3	0.3	0.4	0.3	0.4	0.3	0.5	0.5	0.5	0.3	0.3
LOI	1.1	1.5	1.3	1.3	1.2	1.8	2.5	1.8	2.0	1.1	1.9	**	**	**	1.0	1.0
Total	100.9	99.9	98.3	100.8	100.8	100.9	99.2	99.4	98.3	99.3	100.3	97.8	97.0	98.2	99.1	98.6
Sc	3.0	5.0	3.0	2.0	2.0	2.0	3.0	3.0	2.0	2.0	4.0	2.0	2.0	2.0	2.0	3.0
Be	3.0	6.0	5.0	7.0	2.0	7.0	7.0	1.0	4.0	2.0	5.0	8.0	8.0	7.0	34.0	9.0
V	13.0	36.0	18.0	15.0	15.0	12.0	11.0	14.0	12.0	11.0	8.0	11.0	10.0	11.0	5.0	6.0
Ba	289.0	402.0	394.0	270.0	329.0	256.0	235.0	243.0	265.0	306.0	256.0	246.0	243.0	240.0	38.0	23.0
Sr	89.0	69.0	68.0	49.0	90.0	67.0	58.0	57.0	51.0	72.0	58.0	50.0	50.0	50.5	32.0	37.0
Y	12.0	9.0	8.0	9.0	6.0	5.0	3.0	5.0	4.0	8.0	12.0	5.0	7.0	7.0	4.0	4.0
Zr	93.0	112.0	83.0	117.0	72.0	72.0	74.0	90.0	72.0	93.0	58.0	83.0	90.0	72.2	21.0	37.0
Cr	80.0	30.0	390.0	40.0	410.0	60.0	50.0	260.0	330.0	220.0	20.0	80.0	20.0	40.0	30.0	70.0
Co	2.0	2.0	2.0	2.0	2.0	1.0	1.0	1.0	2.0	2.0	1.0	2.0	1.0	2.1	1.0	1.0
Ni	20.0	20.0	20.0	20.0	20.0	20.0	20.0	20.0	20.0	20.0	20.0	20.0	20.0	20.0	20.0	20.0
Cu	10.0	10.0	10.0	10.0	10.0	10.0	10.0	10.0	10.0	10.0	10.0	10.0	10.0	10.0	10.0	10.0
Zn	50.0	60.0	60.0	60.0	50.0	30.0	40.0	50.0	40.0	60.0	60.0	30.0	60.0	30.0	50.0	40.0
Ga	22.0	22.0	21.0	24.0	20.0	21.0	21.0	21.0	21.0	19.0	18.0	24.0	24.0	20.0	21.0	19.0
Ge	2.0	2.0	2.0	2.0	1.0	2.0	2.0	2.0	2.0	1.0	3.0	**	**	**	4.0	3.0
As	5.0	5.0	5.0	5.0	5.0	5.0	13.0	5.0	12.0	5.0	5.0	**	**	**	23.0	5.0
Rb	229.0	208.0	284.0	330.0	191.0	254.0	307.0	286.0	287.0	222.0	214.0	302.0	361.0	284.7	277.0	188.0
Mo	2.0	2.0	2.0	2.0	3.0	2.0	2.0	2.0	2.0	2.0	2.0	2.0	2.0	2.0	2.0	2.0
Ag	0.5	0.7	0.5	0.5	0.5	0.5	0.5	0.5	0.5	0.5	0.5	0.5	0.5	0.5	0.5	0.5
In	0.2	0.2	0.2	0.2	0.2	0.2	0.2	0.2	0.2	0.2	0.2	2.0	2.0	2.0	0.2	0.2
Sn	7.0	12.0	12.0	14.0	9.0	25.0	20.0	16.0	14.0	5.0	21.0	8.0	10.0	15.0	27.0	26.0
Sb	0.5	0.5	0.5	0.5	0.5	1.5	4.9	5.6	3.3	0.5	0.5	3.4	4.6	xxx	0.5	0.5
Cs	5.5	11.9	38.4	32.3	5.0	22.3	18.8	25.2	19.8	4.6	15.1	22.7	20.9	24.5	24.7	19.9
La	16.0	26.4	16.6	22.3	15.3	14.9	15.5	17.3	13.9	14.7	7.6	11.7	12.4	10.9	1.8	2.7
Ce	38.1	60.6	37.9	54.6	34.7	32.5	30.6	34.8	28.9	32.9	14.6	28.2	27.6	25.4	3.5	5.4
Pr	4.7	7.5	4.8	6.8	4.2	4.2	3.9	4.1	3.8	4.0	1.9	3.2	3.1	3.2	0.4	0.7
Nd	18.8	30.3	20.0	27.4	16.8	17.3	14.3	15.1	14.0	16.3	6.8	14.4	13.8	12.6	1.4	2.1
Sm	4.8	6.3	4.3	6.1	4.3	4.5	3.3	3.2	3.9	4.6	1.9	3.8	3.7	3.1	0.5	0.6
Eu	0.6	0.7	0.5	0.5	0.6	0.7	0.4	0.5	0.5	0.7	0.4	0.5	0.5	0.4	0.1	0.1
Gd	4.2	4.1	2.8	4.1	3.4	4.0	2.1	2.5	2.6	4.1	2.1	2.9	3.0	2.8	0.5	0.5
Tb	0.6	0.5	0.4	0.5	0.5	0.6	0.2	0.3	0.4	0.6	0.4	0.3	0.4	0.4	0.1	0.1
Dy	2.6	2.3	2.1	1.9	2.0	2.3	1.0	1.3	1.4	2.0	2.3	1.3	1.6	1.8	0.7	0.8
Ho	0.4	0.4	0.3	0.3	0.3	0.3	0.1	0.2	0.2	0.2	0.4	0.2	0.2	0.2	0.1	0.2
Er	0.8	1.1	0.7	0.6	0.6	0.6	0.3	0.4	0.4	0.5	0.9	0.4	0.5	0.5	0.4	0.5
Tm	0.1	0.2	0.1	0.1	0.1	0.1	0.1	0.1	0.1	0.1	0.1	0.1	0.1	0.1	0.1	0.1
Yb	0.6	1.0	0.6	0.5	0.5	0.4	0.3	0.3	0.3	0.4	0.7	0.3	0.3	0.4	0.5	0.7
Lu	0.1	0.2	0.1	0.1	0.1	0.1	0.0	0.0	0.0	0.1	0.1	0.0	0.0	0.1	0.1	0.1
Hf	2.3	3.1	2.2	3.1	2.0	2.1	1.9	2.3	2.1	2.5	1.9	2.2	2.6	2.7	0.9	1.4
Ta	0.6	1.1	0.8	1.0	0.4	1.2	1.1	1.2	1.0	0.1	1.7	1.0	1.2	1.0	3.3	1.3
Nb	7.0	7.0	5.0	7.0	4.0	8.0	7.0	8.0	7.0	3.0	11.0	6.0	6.0	7.5	9.0	6.0
W	3.0	2.0	4.0	2.0	4.0	4.0	4.0	4.0	5.0	1.0	3.0	3.0	4.0	6.1	2.0	3.0
Tl	1.3	1.2	2.3	2.1	1.2	1.7	2.4	2.3	2.5	1.2	1.3	1.6	2.7	1.6	1.7	1.1
Pb	46.0	50.0	37.0	36.0	37.0	28.0	35.0	30.0	22.0	43.0	44.0	18.0	26.0	20.0	38.0	23.0
Bi	1.4	0.6	0.4	1.1	0.4	0.7	1.0	1.7	1.3	0.4	3.3	1.3	1.1	1.0	1.4	0.5
Th	9.9	18.6	12.6	17.6	6.4	5.9	6.8	8.6	5.9	5.7	2.6	6.1	6.1	5.3	0.7	0.8
U	6.8	6.5	4.9	7.2	4.0	8.4	8.1	7.6	7.9	6.6	6.8	8.5	8.1	9.6	4.3	4.1

Table C. 5 – Chemical composition of samples from Sector 2: Staurolite-litharenites (St. Lith); Quartzites (Quartz.); Biotite-schists (B.Sch) and Staurolite schists (St.Sch).

Sample	FM15a	FM15b	FM38b	FM38c	FM31a	FM40b	FM14	VC65	FM25
Type	St. Lith	St.Lith.	Quartz.	Bt.Scg	St. Sch	St. Sch	St. Sch	St. Sch	CSR
SiO2	84.4	83.3	91.0	65.1	58.7	56.8	64.5	59.7	74.1
Al2O3	7.0	6.7	2.6	17.0	21.4	23.8	16.8	20.2	9.8
Fe2O3t	2.6	3.2	2.5	7.0	7.2	6.5	7.2	7.5	5.0
MnO	0.0	0.0	0.0	0.0	0.0	0.0	0.1	0.1	0.1
MgO	1.1	1.0	0.7	2.2	1.9	1.8	2.4	2.3	2.1
CaO	0.4	0.4	0.0	0.1	0.1	0.0	0.4	0.6	5.1
Na2O	1.2	1.0	0.1	1.2	0.6	0.5	0.9	2.0	0.3
K2O	1.3	1.2	0.1	2.7	4.0	4.0	2.8	3.2	0.5
TiO2	0.4	0.4	0.2	0.9	0.8	0.9	0.9	0.8	0.8
P2O5	0.1	0.1	0.1	0.1	0.1	0.1	0.2	0.4	0.2
LOI	1.4	1.2	1.4	4.3	5.9	5.3	2.5	3.6	1.3
Total	99.8	98.5	98.7	100.6	100.8	99.7	98.4	100.2	99.4
Sc	6.0	6.0	3.0	18.0	21.0	22.0	16.0	18.0	10.0
Be	1.0	1.0	1.0	2.0	4.0	3.0	2.0	4.0	2.0
V	54.0	54.0	20.0	150.0	182.0	191.0	135.0	151.0	83.0
Ba	234.0	207.0	17.0	528.0	741.0	864.0	573.0	742.0	158.0
Sr	75.0	66.0	4.0	49.0	57.0	36.0	70.0	84.0	192.0
Y	11.0	16.0	4.0	26.0	24.0	28.0	26.0	36.0	26.0
Zr	159.0	180.0	54.0	211.0	163.0	178.0	205.0	215.0	259.0
Cr	90.0	80.0	100.0	100.0	160.0	140.0	160.0	150.0	310.0
Co	3.0	3.0	2.0	12.0	17.0	8.0	16.0	9.0	12.0
Ni	20.0	20.0	20.0	50.0	80.0	40.0	40.0	40.0	70.0
Cu	10.0	10.0	40.0	20.0	20.0	40.0	30.0	40.0	20.0
Zn	30.0	50.0	30.0	120.0	130.0	130.0	210.0	190.0	50.0
Ga	7.0	8.0	3.0	22.0	27.0	30.0	27.0	28.0	11.0
Ge	2.0	2.0	1.0	2.0	2.0	2.0	3.0	3.0	2.0
As	19.0	27.0	5.0	5.0	5.0	5.0	5.0	14.0	5.0
Rb	59.0	55.0	7.0	78.0	191.0	115.0	105.0	161.0	15.0
Mo	2.0	2.0	2.0	2.0	2.0	2.0	2.0	2.0	4.0
Ag	0.5	0.5	0.5	1.3	1.0	1.1	0.8	2.1	1.2
In	0.2	0.2	0.2	0.2	0.2	0.2	0.2	0.2	0.2
Sn	2.0	2.0	1.0	4.0	6.0	6.0	4.0	5.0	5.0
Sb	0.5	0.5	0.5	0.5	0.5	0.5	0.5	1.1	0.5
Cs	6.3	7.0	0.5	3.4	77.5	7.7	7.0	46.6	2.0
La	17.4	14.4	9.0	35.4	37.1	36.8	33.3	34.3	25.4
Ce	35.9	29.8	20.9	73.8	75.8	74.2	67.5	69.4	52.9
Pr	4.3	3.5	2.3	8.6	9.1	8.8	8.4	8.4	6.5
Nd	15.6	14.4	9.2	33.8	35.6	34.8	32.4	31.9	24.8
Sm	3.3	3.4	1.9	6.9	7.3	7.0	6.8	6.9	5.4
Eu	0.8	0.8	0.4	1.4	1.5	1.3	1.2	1.6	1.5
Gd	3.0	3.0	1.4	6.2	6.3	5.7	6.0	6.8	5.0
Tb	0.5	0.5	0.2	1.0	1.0	0.9	1.0	1.1	0.9
Dy	2.5	3.1	1.0	5.4	5.4	5.6	5.5	6.6	5.3
Ho	0.4	0.6	0.2	1.1	1.0	1.1	1.1	1.3	1.1
Er	1.2	1.7	0.5	3.1	3.1	3.5	3.1	3.8	3.0
Tm	0.2	0.3	0.1	0.5	0.5	0.5	0.5	0.6	0.5
Yb	1.1	1.8	0.5	3.1	3.0	3.5	3.1	3.6	3.1
Lu	0.2	0.3	0.1	0.5	0.5	0.6	0.5	0.6	0.5
Hf	3.9	3.9	1.1	5.6	4.4	4.8	5.5	5.5	7.1
Ta	0.4	0.4	0.2	0.9	0.9	0.9	0.9	0.8	0.7
Nb	6.0	5.0	2.0	12.0	12.0	12.0	13.0	10.0	10.0
W	2.0	1.0	3.0	2.0	7.0	3.0	3.0	2.0	8.0
Tl	0.2	0.5	0.1	0.4	1.0	0.5	0.6	1.1	0.8
Pb	17.0	14.0	5.0	18.0	20.0	19.0	14.0	23.0	5.0
Bi	0.4	0.4	0.4	0.4	0.4	0.4	0.4	0.4	0.5
Th	4.4	4.4	2.0	9.9	11.1	10.8	10.4	9.3	9.7
U	1.5	1.6	0.8	3.4	3.2	4.0	3.5	3.5	3.0

Annex D – Fluid inclusions data

Table D. 1 – Microthermometric data and Composition (mol%) of monophasic fluid inclusions from sample FM19. Composition obtained by Raman microspectroscopy.

FM19							
Monophasic	Microthermometry				Composition		
IF	Size(μm)	$TmCO_2$	Th(partial)	Mode	CO_2	CH_4	N_2
11	13.0	n.o.	-133.2	L	17.71	15.9	66.39
2	17.5	-78.6	-135.8	L	29.14	15.27	55.59
6	8.5	n.o	-135.4	L	25.46	16.55	57.99
7	12.3	n.o	-133.7	L	n.o	n.o	n.o
9	10.7	n.o	-134.0	n.o	n.o	n.o	n.o
10	17.7	n.o	-132.9	n.o	n.o	n.o	n.o
3	11.5	-75.1	-132.7	V	25.44	14.42	60.14
5	10.7	n.o	-132.9	V	15.09	12.64	72.27
12	13.0	n.o	-132.4	V	14.61	14.18	71.21
8	13.0	n.o	-132.9	V	22.43	14.39	63.18
15	12.0	n.o	-135.2	V	n.o	n.o	n.o
16	13.0	-64.9	-135.8	V	29	14	57
17	11.0	-65.6	-134.5	V	30	13	57
18	12.0	n.o	-136.0	V	n.o	n.o	n.o
1	17.7	n.o	-131.6	V	n.d.	11.25	88.75
13	14.6	n.o	-132.9	V	n.d.	19.69	80.31
14	13.0	n.o	-134.4	V	n.d.	17.62	82.38
4	10.0	n.o	-134.1	V	n.d.	31.17	68.83

Table D. 2 - Microthermometric data and Composition (mol%) of monophasic fluid inclusions from sample VC52. Composition obtained by Raman microspectroscopy.

VC52						
Monophasic	Microthermometry			Composition		
IF	Size(μm)	Th(partial)	Mode	CO_2	CH_4	N_2
1	13.0	-140.1	V	n.d.	11.98	88.02
2	12.5	-139.7	V	n.o.	n.o.	n.o.
3	10.0	-140.1	L	n.d.	8.24	91.76
4	14.0	-140.1	L	n.d.	12.62	87.38
5	13.0	-140.1	L	n.o.	n.o.	n.o.
6	15.8	-140.6	L	n.o.	n.o.	n.o.
7	15.0	-140.3	L	n.d.	8.86	91.14
10	24.6	-137.7	V	n.d.	9.03	90.97
11	10.0	-139.0	V	n.d.	9.20	90.80
12	10.8	-139.1	V	n.d.	8.86	91.14
13	11.0	-139.2	V	n.d.	10.13	89.87
14	11.5	-138.1	V	n.d.	13.91	86.09
15	13.0	-139.0	V	n.d.	10.43	89.57

Table D. 3 - Microthermometric data and Composition (mol%) of monophasic fluid inclusions from sample FM19. Composition obtained by Raman microspectroscopy.

VC21							
Monophasic	Microthermometry				Composition		
IF	Size(μm)	$TmCO_2$	Th(partial)	Mode	CO_2	CH_4	N_2
1	11.5	-60.3	-39.0	V	65.94	n.d.	34.06
2	15.0	-60.3	-35.0	V	63.81	n.d.	36.19
3	37.5	-60.1	-32.2	V	63.03	n.d.	36.97
4	7.7	-61.6	-38.5	V	65.46	n.d.	34.54
5	19.0	-60.7	n.o.	V	61.53	n.d.	38.47
6	10.8	-60.3	n.o.	V	60.96	n.d.	39.04
7	10.0	-60.3	n.o.	n.o.	n.o.	n.o.	n.o.
8	11.0	-61.6	-19.0	V	n.o.	n.o.	n.o.
9	9.0	-61.6	-20.0	V	n.o.	n.o.	n.o.
10	23.0	-61.2	-24.5	V	79.30	n.d.	20.70
11	15.0	-61.3	n.o.	V	82.19	n.d.	17.81
12	23.0	-60.5	-14.4	V	82.19	n.d.	17.81
13	17.0	-61.5	-20.2	V	92.19	n.d.	7.81
14	16.8	-60.2	n.o.	n.o.	n.o.	n.o.	n.o.

Table D. 4 - Microthermometric data two-phase fluid inclusions from sample VC52.

FM19 Two-phase						
FI	Size(µm)	Type	Flw	TmIce	wt%NaCl	Th(total)
1	7.0	Lw	0.90	-5.1	8.00	210
2	8.0	Lw	0.90	-5.1	8.00	223
3	10.0	Lw	0.90	-5.0	7.86	218
4	7.0	Lw	0.70	-5.1	8.00	n.o.
5	11.0	Lw	0.90	-5.2	8.14	210
6	7.7	Lw	0.90	-4.9	7.73	216
7	8.0	Lw	0.80	-5.3	8.28	n.o.
8	10.0	Lw	0.80	-4.9	7.73	211
9	11.5	Lw	0.75	-4.9	7.73	246
10	10.7	Lw	0.80	-5.6	8.68	257
11	8.5	Lw	0.80	-5.0	7.86	231
12	7.7	Lw	0.90	-5.0	7.86	209
13	5.3	Lw	0.95	-4.9	7.73	179
14	8.0	Lw	0.80	-5.0	7.86	180
15	5.3	Lw	0.95	-5.1	8.00	159
16	7.0	Lw	0.90	-4.9	7.73	167
17	7.0	Lw	0.90	-5.0	7.86	165
18	7.6	Lw	0.90	-3.4	5.56	n.o.
19	12.3	Lw	0.95	-4.7	7.45	144
20	7.7	Lw	0.95	-5.0	7.86	n.o.
22	9.0	Lw	0.95	-5.0	7.86	n.o.
23	10.0	Lw	0.85	-5.0	7.86	220
24	8.0	Lw	0.90	-4.8	7.59	n.o.
25	8.0	Lw	0.90	-5.5	8.55	n.o.
26	10.0	Lw	0.90	-4.8	7.59	n.o.
27	7.7	Lw	0.80	-5.1	8.00	216
28	6.0	Lw	0.90	-4.9	7.73	207
29	7.5	Lw	0.80	-5.0	7.86	211
30	6.0	Lw	0.90	-5.2	8.14	214
21	8.4	Lw	0.80	-0.7	1.23	208
21	8.4	Lw	0.90	-0.7	1.23	n.o.
22	11.5	Lw	0.80	-0.6	1.05	293
23	16.0	Lw	0.90	-0.4	0.71	282
24	6.0	Lw	0.80	-0.7	1.23	224
25	7.7	Lw	0.90	-0.4	0.71	233
26	11.0	Lw	0.80	-0.4	0.71	175
27	23.0	Lw	0.80	-0.7	1.23	236
28	6.0	Lw	0.90	-0.7	1.23	221
29	10.0	Lw	0.95	-0.6	1.05	176
30	9.0	Lw	0.80	-0.7	1.23	254
31	6.0	Lw	0.90	-0.6	1.05	225
32	6.9	Lw	0.80	-0.5	0.88	n.o.
33	13.0	Lw	0.90	-0.4	0.71	312
34	13.0	Lw	0.80	-0.1	0.18	199

FM19 Two-phase						
FI	Size(µm)	Type	Flw	TmIce	wt%NaCl	Th(total)
35	30.0	Lw	0.90	-0.4	0.71	168
36	9.0	Lw	0.95	-0.4	0.71	161
37	6.0	Lw	0.95	-2.1	3.55	170
38	7.7	Lw	0.95	-2.2	3.71	164
39	8.5	Lw	0.90	-2.2	3.71	192
40	11.5	Lw	0.80	-2.0	3.39	192
41	5.4	Lw	0.90	-2.2	3.71	208
42	10.0	Lw	0.80	-1.8	3.06	n.o.
43	9.0	Lw	0.90	-1.8	3.06	n.o.
44	10.0	Lw	0.80	-2.2	3.71	n.o.
45	27.0	Lw	0.90	-2.1	3.55	n.o.
46	7.7	Lw	0.95	-1.9	3.23	191

Table D. 5 - Microthermometric data two-phase fluid inclusions from sample VC52.

VC52 Two-phase						
FI	Size(μm)	Type	Flw	TmIce	wt%NaCl	Th(total)
39	11.5	Lw	0.80	-3.2	5.26	292
40	14.0	Lw	0.80	-3.2	5.26	293
41	12.5	Lw	0.80	-3.2	5.26	315
42	11.0	Lw	0.75	-3.4	5.56	leak
43	13.0	Lw	0.80	-3.5	5.71	leak
44	12.0	Lw	0.70	-3.3	5.41	365
45	12.5	Lw	0.80	-3.1	5.11	366
46	12.0	Lw	0.85	-3.4	5.56	n.o
47	10.0	Lw	0.85	-3.0	4.96	n.o
48	9.0	Lw	0.75	-3.0	4.96	decr
49	11.5	Lw	0.80	-3.3	5.41	decr
50	11.0	Lw	0.80	n.o.	n.o.	332
51	12.0	Lw	0.75	n.o.	n.o.	319
52	10.8	Lw	0.70	-3.1	5.11	350
53	27.5	Lw	0.75	-2.9	4.80	decr
54	13.0	Lw	0.70	-2.8	4.65	347
55	15.0	Lw	0.70	-3.1	5.11	371
56	10.0	Lw	0.75	-2.9	4.80	351
57	12.5	Lw	0.70	-3.3	5.41	decr
59	10.0	Lw	0.75	n.o.	n.o.	330
60	12.5	Lw	0.70	n.o.	n.o.	336
61	10.0	Lw	0.70	-3.1	5.11	354
62	10.0	Lw	0.80	-3.4	5.56	352
63	15.0	Lw	0.70	-3.4	5.56	382
64	11.5	Lw	0.70	-3.4	5.56	370
65	15.4	Lw	0.75	-3.1	5.11	354
66	15.3	Lw	0.75	n.o.	n.o.	358
67	10.8	Lw	0.70	-3.1	5.11	357
68	12.3	Lw	0.75	-3.3	5.41	370
70	10.0	Lw	0.70	-3.2	5.26	366
71	8.5	Lw	0.70	-3.1	5.11	354
73	10.0	Lw	0.70	-3.0	4.96	366
74	7.7	Lw	0.9	-2.4	4.03	215
75	8.5	Lw	0.75	-3.2	5.26	366
76	5.4	Lw	0.75	n.o.	n.o	365
77	11.5	Lw	0.70	-3.2	5.26	362
79	11.5	Lw	0.70	-3.4	5.56	366
80	6.0	Lw	0.75	-3.1	5.11	n.o.
81	6.0	Lw	0.70	-3.1	5.11	330

VC52 Two-phase						
FI	Size(μm)	Type	Flw	TmIce	wt%NaCl	Th(total)
82	7.7	Lw	0.70	-3.6	5.86	n.o.
83	8.5	Lw	0.70	-2.9	4.80	318
84	5.4	Lw	0.70	-2.8	4.65	295
86	11.5	Lw	0.70	-3.2	5.26	331
87	11.5	Lw	0.70	n.o.	n.o.	367
58	7.5	Lw	0.90	-2.4	4.03	decr
29	10.0	Lw	0.70	-2.6	4.34	n.o.
30	12.5	Lw	0.70	-2.5	4.18	n.o.
89	9.0	Lw	0.70	-2.9	4.80	n.o.
15	11.0	Lw	0.6	-1.7	2.90	n.o.
16	10.8	Lw	0.75	-1.6	2.74	n.o.
72	15.3	Lw	0.70	-1.4	2.41	359
18	11.0	Lw	0.7	-1.8	3.06	n.o.
31	14.2	Lw	0.6	-1.7	2.90	n.o.
36	8.3	Lw	0.7	-2.1	3.55	n.o.
37	10.8	Lw	0.7	-2.1	3.55	n.o.
38	13.3	Lw	0.7	-1.9	3.23	n.o.
19	9.0	Lw	0.70	-0.9	1.57	n.o.
20	22.5	Lw	0.70	-0.6	1.05	n.o.
21	20.8	Lw	0.70	-0.8	1.40	n.o.
22	14.0	Lw	0.70	-0.9	1.57	n.o.
23	9.1	Lw	0.70	-0.4	0.71	n.o.
24	7.5	Lw	0.70	-0.6	1.05	n.o.
25	18.3	Lw	0.70	-0.4	0.71	n.o.
26	9.1	Lw	0.70	-0.5	0.88	n.o.
27	8.3	Lw	0.70	-0.5	0.88	n.o.
28	12.5	Lw	0.70	-0.4	0.71	n.o.
32	5.0	Lw	0.70	-0.4	0.71	n.o.
33	6.6	Lw	0.70	-0.4	0.71	n.o.
34	7.2	Lw	0.70	-0.5	0.88	n.o.
35	16.6	Lw	0.70	-0.6	1.05	n.o.
78	7.0	Lw	0.70	-0.6	1.05	335
85	13.0	Lw	0.70	-0.7	1.23	348
92	12	Lw	0.70	-0.6	1.05	n.o.
93	11	Lw	0.70	-0.7	1.23	n.o.
94	15	Lw	0.70	-0.7	1.23	n.o.
95	12	Lw	0.70	-0.8	1.40	n.o.
96	10.0	Lw	0.70	-0.9	1.57	n.o.

Table D. 6- Microthermometric data two-phase fluid inclusions from sample FP21.

FP21 Two-phase						
FI	Size(µm)	Type	Flw	TmIce	wt%NaCl	Th(total)
1	6.6	Lw	0.90	-4.1	6.59	n.o.
2	6.0	Lw	0.95	-3.4	5.56	n.o.
3	6.6	Lw	0.85	-4.1	6.59	n.o.
4	10.0	Lw	0.90	-4.0	6.45	n.o.
5	6.6	Lw	0.90	-3.3	5.41	n.o.
6	5.0	Lw	0.85	-4.1	6.59	n.o.
7	6.0	Lw	0.90	-4.2	6.74	n.o.
8	7.0	Lw	0.90	-4.0	6.45	n.o.
9	8.0	Lw	0.90	-4.0	6.45	n.o.
10	7.7	Lw	0.85	-4.4	7.02	n.o.
11	10.0	Lw	0.90	-3.9	6.30	n.o.
12	5.4	Lw	0.90	-4.0	6.45	n.o.
13	6.6	Lw	0.85	-4.0	6.45	n.o.
14	7.0	Lw	0.90	-4.0	6.45	n.o.
15	7.0	Lw	0.90	-4.4	7.02	n.o.
16	8.0	Lw	0.90	-4.0	6.45	n.o.
17	37.5	Lw	0.85	-0.9	1.57	n.o.
18	12.5	Lw	0.90	-1.0	1.74	n.o.
19	12.5	Lw	0.90	-0.7	1.23	n.o.
20	12.5	Lw	0.85	-0.7	1.23	n.o.
21	10.0	Lw	0.80	-0.8	1.40	n.o.
23	8.0	Lw	0.90	-0.9	1.57	n.o.
24	9.0	Lw	0.95	-0.9	1.57	n.o.
25	17.0	Lw	0.90	-0.8	1.47	n.o.
26	16.0	Lw	0.95	-1.5	2.57	n.o.

Annex E – Isotopic data

Table E. 1 – Rb-Sr and Sm-Nd data for MMC rocks.

Sample	Type	Sr	Rb	$^{87}Rb/^{86}Sr$	2σ	$^{87}Sr/^{86}Sr$	2σ	Nd	Sm	$^{147}Sm/^{144}Nd$	2σ	$^{143}Nd/^{144}Nd$	2σ	εSr_0	εSr_{330}	eNd_0	eNd_{330}
FM14	SGC	70	105	4.351	0.123	0.734	2.1E-05	32.4	6.8	0.12695	4.E-03	0.51231	2.E-05	424	140	-6.4	-3.5
FM15	SGC	75	59	2.281	0.065	0.728	1.9E-05	15.6	3.3	0.12796	4.E-03	0.51229	2.E-05	330	184	-6.8	-3.9
FM38a	SGC	49	78	4.622	0.131	0.743	2.4E-05	33.8	6.9	0.12349	7.E-03	0.51224	2.E-05	550	248	-7.8	-4.7
VC65	SGC	84	161	5.567	0.157	0.748	2.4E-05	31.9	6.9	0.13084	7.E-03	0.51232	2.E-05	622	257	-6.3	-3.5
VC37	PMM	298	153	1.487	0.042	0.719	1.9E-05	34.6	7	0.12238	7.E-03	0.51237	2.E-05	207	113	-5.2	-2.1
VC28	PMM	119	148	3.606	0.102	0.729	2.5E-05	40.9	9	0.13100	7.E-03	0.51236	2.E-05	348	114	-5.4	-2.7
FM4a	BMM	144	164	3.302	0.093	0.730	1.5E-05	47.9	9.5	0.11997	3.E-03	0.51217	2.E-05	360	146	-9.2	-5.9
VC 27b	BMM	93	205	6.401	0.181	0.745	1.8E-05	32.2	6.6	0.12399	7.E-03	0.51224	2.E-05	568	147	-7.7	-4.6
FM 16	BMM	190	110	1.677	0.047	0.722	1.6E-05	27.8	5.9	0.12838	4.E-03	0.51208	1.E-05	659	155	-10.8	-7.4
FM23	BMM	90	237	7.651	0.216	0.751	2.4E-05	42.7	8.2	0.11616	3.E-03	0.51208	2.E-05	250	144	-10.8	-8.0
FM 22	BMM	201	127	1.831	0.052	0.724	1.9E-05	31.6	6.8	0.13017	4.E-03	0.51212	2.E-05	275	159	-10.1	-7.3
VC 60	DTX	215	134	1.806	0.051	0.721	2.5E-05	22.5	4.6	0.12367	7.E-03	0.51236	2.E-05	233	118	-5.4	-2.3
VC8	LCS	190	129	1.968	0.056	0.724	2.2E-05	12.8	3.3	0.15595	4.E-03	0.51233	1.E-05	281	155	-6.0	-4.3
FM19	LCS	252	133	1.529	0.043	0.722	1.7E-05	3.0	0.7	0.14114	4.E-03	0.51224	2.E-05	246	150	-7.7	-5.4
VC2a	L.Gnt	94	139	4.293	0.121	0.742	1.8E-05	7.0	1.8	0.15555	8.E-03	0.51237	1.E-05	846	133	-6.4	-5.0
VC 52	TL.Gnt	58	215	10.784	0.305	0.764	1.8E-05	4.1	1.1	0.16229	1.E-02	0.51231	2.E-05	527	247	-5.1	-3.4
FP21a	2m.Gnt	67	254	11.032	0.312	0.767	2.9E-05	17.3	4.5	0.15734	4.E-03	0.51235	1.E-05	881	151	-5.7	-4.0
FP21b	2m.Gnt	90	191	6.160	0.174	0.741	1.9E-05	16.8	4.3	0.15483	4.E-03	0.51229	1.E-05	520	115	-6.8	-5.1
VC22	2m.Gnt	69	208	8.763	0.248	0.756	2.3E-05	30.3	6.3	0.12577	4.E-03	0.51228	2.E-05	729	150	-7.1	-4.1
VC 39	2m.Gnt	89	229	7.474	0.211	0.748	2.4E-05	18.8	4.8	0.15444	8.E-03	0.51232	1.E-05	615	123	-6.2	-4.4
VC 45	2m.Gnt	49	330	19.668	0.556	0.804	1.9E-05	27.4	6.1	0.13467	7.E-03	0.51230	1.E-05	1408	102	-6.7	-4.1
FM21a	CSR	213	30	0.408	0.012	0.713	2.6E-05	34.7	7.4	0.12900	4.E-03	0.51207	1.E-05	125	103	-11.2	-8.3
VC50a	CSR	139	18	0.375	0.011	0.714	1.4E-05	34.3	6.8	0.11992	6.E-03	0.51203	2.E-05	129	110	-11.9	-8.7
VC50b	CSR	287	35	0.353	0.010	0.713	2.4E-05	27.3	5.5	0.12187	7.E-03	0.51200	1.E-05	124	106	-12.4	-9.2
FM21b	GWK	274	76	0.803	0.023	0.716	2E-05	26.0	5	0.11633	3.E-03	0.51205	2.E-05	170	122	-11.5	-8.1
VC50c	GWK	203	79	1.127	0.032	0.719	1.4E-05	26.3	5.2	0.11960	6.E-03	0.51200	2.E-05	211	142	-12.5	-9.3
VC 47	GWK	185	77	1.206	0.034	0.720	1.7E-05	27.2	5.2	0.11564	6.E-03	0.51201	2.E-05	218	143	-12.3	-8.9
VC58	APG	35.71	181.87	14.836	0.420	0.778	2.2E-05	2.1	0.6	0.17283	2.E-02	0.51226	2.E-05	1039	55	-7.4	-6.4
VC64	APG	31.76	264.39	24.355	0.689	0.822	3.9E-05	1.4	0.5	0.21604	2.E-02	0.51238	2.E-05	1665	46	-5.0	-5.8

OBS: SGC – Schist-greywacke Complex samples; PMM – patch-metatexite; BMM – banded-Metatexite; DTX – diatexites; LCS – leucosomes; L.Gnt – leucogranites; TL.Gnt – tourmaline-bearing leucogranites; 2m.Gnt – two-mica granites; CSR – calc-silicate rocks; GWK – metagreywackes; APG – aplite-pegmatites.

Table E. 2 - U-Pb isotopic data for MMC diatexite sample (VC60)

					Ratios			Ages				
id	U (ppm)	Th (ppm)	Th/U	^{206}Pb	$^{206}Pb/^{204}Pb$	$^{207}Pb/^{235}U$	±err	$^{206}Pb/^{238}U$	±err	$^{207}Pb/^{235}U$	±err	Disc. (%)
1.1	174.3	65.7	0.39	14.5	0.0689	0.798	0.015	591.8	6.5	595.5	8.4	0.6
1.2	155.3	55.7	0.37	12.4	0.0809	0.758	0.055	567.3	28.4	572.8	32.5	1.0
1.3	235.2	76.7	0.33	19.5	0.0514	0.765	0.011	588.7	4.1	576.8	6.3	-2.0
1.4	183.3	45.5	0.25	15.2	0.0660	0.903	0.015	588.4	6.4	653.2	8.0	10.0
2.1	2613.0	46.4	0.02	109.5	0.0091	0.548	0.005	304.2	2.5	443.8	3.6	31.4
2.2	784.7	2.4	0.00	33.3	0.0300	0.360	0.007	308.9	3.1	312.0	5.2	1.0
2.2	192.1	27.7	0.15	12.4	0.0804	0.582	0.007	465.1	0.5	465.8	4.2	0.2
2.3	163.0	81.6	0.51	13.0	0.0770	0.753	0.013	567.7	6.0	569.9	7.7	0.4
2.4	123.7	43.3	0.36	10.3	0.0970	0.789	0.013	592.8	2.6	590.5	7.5	-0.4
3.1	241.7	130.6	0.55	19.5	0.0514	0.742	0.012	573.6	7.6	563.5	6.9	-1.8
3.2	153.1	67.3	0.45	12.6	0.0792	0.767	0.015	587.0	9.6	578.1	8.9	-1.6
3.3	363.7	2.2	0.01	16.7	0.0597	0.402	0.007	334.1	3.4	343.0	5.3	2.6
3.4	102.2	35.8	0.36	8.5	0.1175	0.815	0.035	591.8	17.9	605.3	19.9	2.2
4.1	433.5	192.3	0.45	27.1	0.0370	0.578	0.020	448.8	12.3	463.3	12.9	3.2
5.2	363.7	158.6	0.45	28.3	0.0353	0.732	0.013	554.8	8.1	557.5	7.5	0.4
6.1	231.5	81.0	0.36	19.1	0.0524	0.769	0.013	586.4	4.7	579.1	7.7	-1.2
7.1	223.0	118.9	0.55	17.9	0.0559	0.759	0.008	571.0	3.9	573.2	4.4	0.4
8.1	1929.2	16.3	0.01	84.6	0.0118	0.374	0.016	318.5	11.4	322.4	11.7	1.2
8.2	641.1	225.4	0.36	60.8	0.0165	0.938	0.014	669.8	8.3	672.1	7.5	0.4
8.3	633.0	168.1	0.27	51.1	0.0196	0.764	0.018	574.7	10.5	576.4	10.2	0.2
9.1	1130.6	47.0	0.04	94.0	0.0106	0.774	0.004	591.4	1.4	582.1	2.1	-1.6
9.2	612.6	14.5	0.02	48.8	0.0205	0.924	0.040	567.8	12.9	664.3	21.3	14.6
10.1	1795.7	9.0	0.01	73.5	0.0136	0.512	0.006	297.8	1.1	419.6	3.8	29.0
10.2	425.5	175.8	0.42	33.0	0.0303	0.730	0.007	553.2	3.3	556.4	4.2	0.6
11.1	504.5	245.0	0.50	38.7	0.0258	0.708	0.010	547.4	0.7	543.7	6.1	-0.6
12.1	1369.0	19.5	0.01	64.7	0.0155	0.413	0.007	342.5	4.0	351.1	4.8	2.4
13.1	308.7	102.8	0.34	25.1	0.0399	0.763	0.008	578.6	5.1	575.7	4.7	-0.6
13.2	462.6	217.9	0.48	37.4	0.0268	0.766	0.005	575.3	2.7	577.3	2.9	0.4
14.1	332.0	85.5	0.26	25.6	0.0390	0.788	0.010	550.7	3.5	590.0	5.5	6.6
14.2	933.4	415.0	0.46	67.9	0.0147	0.691	0.035	520.6	20.2	533.6	21.3	2.4
15.1	302.9	82.0	0.28	24.6	0.0406	0.790	0.006	578.8	3.8	591.3	3.6	2.2
16.1	565.7	245.6	0.45	45.9	0.0218	0.759	0.005	577.2	1.0	573.2	3.1	-0.6
17.1	273.4	183.4	0.69	29.7	0.0337	1.113	0.012	762.6	6.4	759.4	5.6	-0.4
18.1	207.4	80.7	0.40	17.0	0.0589	0.771	0.014	582.3	6.0	580.3	8.2	-0.4
18.2	364.4	31.2	0.09	21.9	0.0458	0.534	0.010	431.8	5.6	434.2	6.6	0.6
20.1	1722.4	12.4	0.01	75.8	0.0132	0.422	0.004	319.6	2.3	357.2	3.0	10.6
20.2	227.7	140.3	0.63	37.5	0.0267	1.982	0.017	1122.1	6.0	1109.4	5.6	-1.2
21.1	276.9	161.4	0.60	22.5	0.0444	0.768	0.007	579.5	3.3	578.7	4.0	-0.2
22.1	224.6	94.0	0.43	18.3	0.0548	0.733	0.016	578.8	4.4	558.1	9.2	-3.8
22.3	371.4	132.2	0.37	30.4	0.0329	0.778	0.007	583.1	3.7	584.6	4.1	0.2
23.1	258.8	124.4	0.49	21.5	0.0466	0.767	0.017	590.3	10.9	577.9	9.6	-2.2
23.2	163.2	56.8	0.36	13.7	0.0728	0.791	0.009	598.3	5.1	591.9	5.0	-1.0
23.3	221.3	64.4	0.30	17.7	0.0564	0.747	0.016	570.4	10.4	566.2	9.5	-0.8
24.1	310.5	131.9	0.44	24.9	0.0402	0.760	0.008	571.2	5.2	574.0	4.7	0.4
25.1	1804.1	6.0	0.00	80.5	0.0124	0.411	0.002	323.9	1.0	349.9	1.5	7.4
25.2	159.2	51.4	0.33	11.8	0.0846	0.807	0.017	530.4	4.5	600.8	9.4	11.8
26.1	246.3	140.4	0.58	19.6	0.0510	0.763	0.015	567.6	4.3	576.0	8.7	1.4
27.1	757.8	313.5	0.42	60.7	0.0165	0.757	0.010	570.6	6.6	572.4	5.8	0.4
27.2	843.4	402.2	0.49	69.5	0.0144	0.789	0.012	586.1	7.6	590.6	6.7	0.8
28.1	337.7	123.1	0.37	26.2	0.0381	0.741	0.009	554.4	4.2	563.1	5.3	1.6
28.2	630.0	201.6	0.33	48.7	0.0205	0.726	0.012	551.1	6.9	554.0	7.0	0.6
29.1	517.9	66.3	0.13	46.3	0.0216	0.911	0.011	633.9	6.1	657.6	5.8	3.6
29.2	102.6	73.3	0.73	11.6	0.0864	1.292	0.057	789.9	27.0	842.2	25.6	6.2
30.1	211.9	60.6	0.29	17.6	0.0569	0.781	0.012	590.2	0.4	586.2	7.1	-0.6
31.1	986.7	209.0	0.22	75.1	0.0133	0.759	0.015	543.4	9.4	573.6	8.4	5.2
31.2	375.9	193.7	0.53	32.3	0.0310	0.834	0.017	610.1	6.2	616.0	9.5	1.0
32.1	1094.9	171.9	0.16	90.3	0.0111	0.777	0.012	586.6	7.8	583.6	6.9	-0.6
32.2	207.1	65.8	0.33	17.2	0.0581	0.788	0.019	591.3	10.0	590.1	10.9	-0.2
33.1	363.5	112.0	0.32	29.9	0.0334	0.779	0.006	585.6	2.8	584.7	3.2	-0.2
33.2	649.1	213.6	0.34	52.6	0.0190	0.770	0.076	576.8	48.2	579.8	44.7	0.6
34.1	1051.3	341.3	0.33	82.4	0.0121	0.756	0.010	558.9	5.9	571.4	6.0	2.2
35.1	1119.4	255.9	0.23	72.3	0.0138	0.602	0.012	463.8	8.5	478.2	7.8	3.0
35.2	273.4	57.8	0.22	22.2	0.0450	0.771	0.012	578.0	3.1	580.6	6.7	0.4
36.1	103.9	31.9	0.32	8.4	0.1189	0.781	0.009	576.3	5.3	585.8	5.0	1.6

Annex F - Figures